ESAFORM Bookseries on Material Forming

Dorel Banabic *Editor*

Multiscale Modelling in Sheet Metal Forming

Springer

ESAFORM Bookseries on Material Forming

Series editor

Elías Cueto, Zaragoza, Spain

This series publishes monographs and carefully edited books on every aspect covered by the European Scientific Association for Material Forming (ESAFORM). Like its supporting association, this collection acts as a tool for promoting applied research in University and Industry, spreading scientific information, and developing education in all aspects related to material forming in its broadest sense. Therefore, the series is aimed at establishing a platform of communication between engineers and scientists covering: (i) all forming processes, including sheet forming, bulk forming, powder forming, forming in melt or near-melt conditions, machining and cutting technologies, non-traditional processes, rapid prototyping, micro-forming, hydro-forming, thermo-forming, incremental forming, liquid composite molding, etc. (ii) all materials, including metals, ceramics, polymers, fibre reinforced materials, composites, glass, wood, materials in food processing, biomateriais, nano-materials, shape memory alloys etc., and (iii) all kinds of approaches, such as micro-macro modelling, thermo-mechanical modelling, numerical simulation, experimental analysis, inverse identification, and optimization. These volumes cover aspects related to theoretical foundations, experimental research, development of innovative numerical methods, and in general anything that could help in the development of the corps of knowledge in the field. Book proposals at a well-established research level, as well as a more basic, educationally oriented level are welcomed and can be sent to the series editor or the publisher.

More information about this series at http://www.springer.com/series/11923

Dorel Banabic
Editor

Multiscale Modelling in Sheet Metal Forming

Springer

Editor
Dorel Banabic
CERTETA Research Center
Technical University of Cluj-Napoca
Cluj-Napoca
Romania

ISSN 2198-9907 ISSN 2198-9915 (electronic)
ESAFORM Bookseries on Material Forming
ISBN 978-3-319-44068-2 ISBN 978-3-319-44070-5 (eBook)
DOI 10.1007/978-3-319-44070-5

Library of Congress Control Number: 2016948098

Printed on acid-free paper

This Springer imprint is published by Springer Nature
The registered company is Springer International Publishing AG Switzerland

The original version of the book was revised: For detailed information please see erratum. The erratum to this book is available at 10.1007/978-3-319-44070-5_8.

Preface

Virtual fabrication is a key ingredient for increasing the competitiveness of the industry, by reducing the time from concept to market and by increasing quality and reliability of the final product. Pushing more and more tasks from the usual design/test/redesign cycles to the computer-based testing of a virtual prototype reduces dramatically the research and development phase. In the metal forming industry an important part of the virtual factory relies on the numerical simulation of sheet metal forming processes by finite element (FE) programs. Among other factors, the success of an FE simulation depends essentially on the accuracy of the constitutive model describing the plastic behaviour of the sheet. Recent advances in the modelling of metals include the modelling of structural inhomogeneities, damage, porosity, twinning/untwining, non-local and second-order effects. Virtually all materials used in the metal forming industry today are anisotropic (material properties are not the same in every direction), showing both as-received (initial) anisotropy and evolving anisotropy related to plastic deformation processes. Plastic anisotropy can be most easily explained by the microstructure of the material.

The book gives a synthetic presentation of the research performed in the field of multiscale modelling in sheet metal forming during more than thirty years by the members of five international teams from Technical University of Cluj-Napoca, Romania; KU Leuven, Belgium; Clausthal University of Technology, Germany; Amirkabir University of Technology, Iran; University of Bucharest, Romania and Institute of Mathematics of the Romanian Academy, Romania.

Chapter 1 is devoted to the presentation of some recent phenomenological yield criteria. As this chapter is only a synthetic overview of the yield criteria, the reader interested in some particular formulation should also read the original papers listed in the reference section. This chapter gives a more detailed presentation of the yield criteria implemented in the commercial programs used for the finite element simulation (emphasizing the formulations proposed by the CERTETA team—BBC2005 and BBC2008 models) or the yield criteria having a major impact on the research progress.

An overview of the crystallographic texture and plastic anisotropy is presented in Chap. 2. After an introduction in the structure of polycrystalline materials and

crystallographic texture the authors present the main equipment and methods for the experimental determination of textures. The relation between texture and properties of materials is also analyzed in a subchapter. An extended subchapter presents different models used for polycrystalline materials with reference in particular to the Taylor model (Full-Constraints).

Chapter 3 is dedicated to multiscale modelling of plastic anisotropy. After an introduction in the topic the authors present the multiscale frameworks in crystal plasticity. The statistical crystal plasticity and the full-field approaches are presented in this section. The main section of this chapter is focused on the hierarchical multiscale approaches. A new hierarchical multiscale framework is presented that allows taking into account the evolution of the plastic anisotropy during sheet forming processes. This approach was followed, in which the fine-scale model provides data needed for identification of the macroscopic one. Generally, the crystal plasticity models have to be evaluated for a huge number of possible stress or strain-rate modes, sometimes exceeding one million realizations. This inspired works that aim at decreasing the computational effort related to virtual experiments. A possible way to capture the influence of microstructural changes on the anisotropic response is to use the crystal plasticity model to calculate some quantities of interest in advance and approximate these in the macroscopic simulation. The evolution of crystallographic texture, which is identified as the main source of the plastic anisotropy, is predicted by the ALAMEL crystal plasticity model. An extension to the phenomenological anisotropic plane-stress yield criterion BBC2008 is proposed, which provides adaptive updates of the local anisotropy in the integration points of the macroscopic finite element model. To this end, the BBC2008 is systematically recalibrated to data provided by the crystal plasticity virtual experiment framework (VEF). An enhanced identification algorithm is proposed. The new algorithm exploits comprehensive material characterization delivered by the VEF. The deep drawing of cylindrical cups is used as a benchmark case to validate the model.

Chapter 4 is focused on the modelling of the void growth in ductile fracture. First is presented a short introduction to Gurson-type models for predicting the fracture of ductile metals. After that an application of some anisotropic extensions of the Gurson–Tvergaard–Needleman model to the prediction of fracture in a sheet deep drawing simulation, including the identification of material parameters from tensile tests performed on sheets is presented. Having concluded that the optimal Gurson-type model for sheets must consider ellipsoidal voids and non-quadratic anisotropic yield criteria, the attention is focused on three such advanced yield criteria—Yld91, Yld2004-18p and BBC2005. A new method based on convex analysis to derive analytical expressions for the dissipation functions of these yield criteria is presented. The expressions thus obtained are not fully explicit and require some supplementary minimizations; however, it is shown that such forms are compatible with the development of Gurson-type models. In a second step Gurson's model is extended to non-quadratic yield criteria where the "cosh" term is replaced by some other function. In order to calibrate these new models, the Lee and Mear family of spheroidal axisymmetric and incompressible velocity fields are extended

to the general ellipsoidal case. The method used is based on a Piola transform of the spherical Mie decomposition to a new ellipsoidal Mie decomposition. This forms the basis of a spectral method to solve the limit-analysis problem for a spheroidal void in a confocal unit cell. Using this spectral method to find an approximate solution in the case of a hydrostatic macroscopic stress state provides the optimal velocity field describing the expansion of the cavity. The knowledge of this velocity field for a given geometry permits the calibration of the remaining parameters in Gurson-type models. At variance with previous works, the authors have not tried to fit analytical approximations to the calibrated parameters. For a given yield criterion, it has been proposed to use a new fast calibration to tabulate all parameters as functions of void geometry and porosity and to use interpolation in these tables in a finite element simulation. The new tools and techniques presented in this chapter open the way to build Gurson-type models for new anisotropic yield criteria and general ellipsoidal voids.

The advanced models for the prediction of forming limit curves are presented in Chap. 5. After presenting different types of defects in sheet metal forming operations, the discussion focuses on the Forming Limit Curves (FLC). Classical and original theoretical models for the prediction of FLCs are presented in detail. In this context, the authors emphasize their contributions to the mathematical modelling of FLCs, namely: an original implicit formulation of the Hutchinson–Neale model, a modified model based on localized and diffuse necking, an original model based on the non-zero through-thickness shear stress effect on the FLC, a model without initial inhomogeneity and a model using the Gurson–Tvergaard–Needleman (GTN) theory. A subchapter is dedicated to the comparison of the FLC's predicted by different theoretical models. The commercial programs (emphasizing the FORM-CERT program developed at the CERTETA centre) and the semi-empirical models for FLC prediction are presented in the last sections of the chapter.

Chapter 6 is devoted to anisotropic damage in elasto-plastic materials with structural defects. The material is damaged when the microstructural changes, like microcracks and microvoids, take place in the material (at the microstructural level) and no macrocracks can be observed. The failure is characterized by dominant macro cracks, which are generated as an ultimate stage during the damage (microstructural) process of the material. The author assumed that the plastic flow and the development of the microvoid and microcracks are distinct irreversible mechanisms produced during the deformation process. In contrast to the plastic behaviour, the damage affects the material elastic properties. The chapter deals with finite elasto-plastic models, which involve the defect density tensor, as a measure of the defects existing in the damaged microstructure. The author extended to finite deformation the relationships between the continuum theory of lattice defects and non-Euclidean geometry in the linear approximation, which have been presented (from geometrical aspects only) within the small strain constitutive framework. The evolution equations for the plastic distortion and the defect density tensor are compatible with the free energy imbalance on the isothermal processes, which describes the dissipative nature for the irreversible behaviour.

Chapter 7 deals with modelling the Portevin–Le Chatelier (PLC) effect. An elastic-viscoplastic model of McCormick type incorporating dynamic strain ageing and negative strain-rate sensitivity is considered. A methodology for the identification of the unstable PLC range of strain rates and mechanical parameters is considered by using a bifurcation analysis of spatial homogeneous processes. A critical condition on material parameters for the PLC effect is established. The loss of homogeneity and the strain localization phenomena are investigated numerically for both constant strain-rate and stress-rate experiments. The sensitivity of the model to the mode of testing is investigated. The influence of the testing machine is not taken into account by adding a machine equation, but by considering mixed stress- and strain-controlled boundary conditions. A discussion and comparison with existing models in the literature is also provided.

The book is of interest to both the research and industrial communities. It is useful for the students, doctoral fellows, researchers and engineers who are mainly interested in the material modelling and numerical simulation of sheet metal forming processes.

Cluj-Napoca, Romania
May 2016

Prof. Dorel Banabic

Contents

Contributors

Dorel Banabic Technical University of Cluj Napoca, Cluj Napoca, Romania

Hans Joachim Bunge (deceased) Clausthal University of Technology, Clausthal-Zellerfeld, Germany

Sanda Cleja-Ţigoiu University of Bucharest, Bucharest, Romania

Dan-Sorin Comsa Technical University of Cluj Napoca, Cluj Napoca, Romania

Philip Eyckens Department of Materials Engineering, KU Leuven, Leuven, Belgium

Cristian Făciu Simion Stoilow Institute of Mathematics of the Romanian Academy, Bucharest, Romania

Jerzy Gawad Department of Computer Science, KU Leuven, Leuven, Belgium

Mihai Gologanu Technical University of Cluj Napoca, Cluj Napoca, Romania

Abdolvahed Kami Amirkabir University of Technology, Tehran, Iran

Robert Arthur Schwarzer Herrenberg, Germany; Clausthal University of Technology, Clausthal-Zellerfeld, Germany

Albert van Bael Department of Materials Engineering, KU Leuven, Leuven, Belgium

Paul van Houtte Department of Materials Engineering, KU Leuven, Leuven, Belgium

Chapter 1
Plastic Behaviour of Sheet Metals

Dorel Banabic, Dan-Sorin Comsa and Jerzy Gawad

1.1 Anisotropy of Sheet Metals

1.1.1 Uniaxial Characteristics of Plastic Anisotropy

Due to the rolling process, sheet metals generally exhibit a significant anisotropy. In fact, the rolling process induces a particular anisotropy characterised by the symmetry of the mechanical properties with respect to three orthogonal planes. Such a mechanical behaviour is called orthotropy. The intersection lines of the symmetry planes are the orthotropy axes. In the case of rolled sheet metals, their orientation is as follows: rolling direction (RD); transverse direction (TD); normal direction (ND).

In practice, the variation of the plastic behaviour with direction is usually assessed by means of the uniaxial yield stress and the so-called anisotropy

The original version of the chapter was revised: The erratum to this chapter is available at 10.1007/978-3-319-44070-5_8

D. Banabic · D.-S. Comsa (✉)
Technical University of Cluj Napoca, 28 Memorandumului,
400114 Cluj Napoca, Romania
e-mail: dscomsa@tcm.utcluj.ro
URL: http://www.certeta.utcluj.ro

D. Banabic
e-mail: banabic@tcm.utcluj.ro

J. Gawad
Department of Computer Science, KU Leuven,
200A Celestijnenlaan, 3001 Leuven, Belgium
e-mail: jerzy.gawad@cs.kuleuven.be
URL: http://www.kuleuven.be/english

D. Banabic (ed.), *Multiscale Modelling in Sheet Metal Forming*,
ESAFORM Bookseries on Material Forming,
DOI 10.1007/978-3-319-44070-5_1

(or Lankford) coefficient (Lankford et al. 1950). These characteristic are determined by tensile tests performed on sheet specimens in the form of a strip. The anisotropy coefficient r is defined by

$$r = \varepsilon_{22}/\varepsilon_{33} \tag{1.1}$$

where $\varepsilon_{22}, \varepsilon_{33}$ are the strains in the width and thickness directions, respectively. In the case of an isotropic material, the coefficient is one because the width and thickness strains have the same value. If the coefficient is greater than one, the width strains will be dominant (the "thinning resistance' is more pronounced). On the other hand, for materials having a coefficient less than one, the thickness strains will dominate. Equation (1.1) can be written in the form

$$r = \left(\ln\frac{w}{w_0}\right) \Big/ \left(\ln\frac{t}{t_0}\right) \tag{1.2}$$

where w_0 and w are the initial and final width of the specimen, while t_0 and t are its initial and final thickness, respectively. As the thickness is very small compared to the width, the relative errors of measurement of the two strains will be quite different. Therefore Eq. (1.1) is replaced by another relationship involving quantities having the same order of magnitude: length and width of the specimen. Taking into account the condition of volume constancy

$$\varepsilon_{11} + \varepsilon_{22} + \varepsilon_{33} = 0 \tag{1.3}$$

the following form of Eq. (1.1) is obtained

$$r = -\varepsilon_{22}/(\varepsilon_{11} + \varepsilon_{22}) \tag{1.4}$$

and Eq. (1.2) becomes

$$r = -\left(\ln\frac{w}{w_0}\right) \Big/ \left(\ln\frac{l}{l_0} + \ln\frac{w}{w_0}\right) \tag{1.5}$$

where l_0 and l are the initial and final gage length of the specimen. Equation (1.5) can be rearranged as follows:

$$r = \left(\ln\frac{w}{w_0}\right) \Big/ \left(\ln\frac{l_0 w_0}{l\, w}\right) \tag{1.6}$$

This relationship is used in practice for evaluating the anisotropy coefficient.

Experiments show that r depends on the in-plane direction. If the tensile specimen is cut having its longitudinal axis inclined with the angle θ to the rolling

direction, the coefficient r_θ is obtained. The subscript specifies the angle between the axis of the specimen and the rolling direction.

An important element characterising the performances of a yield criterion is the capability to predict the variations of the uniaxial yield stress and coefficient of plastic anisotropy in the plane of the sheet metal.

In order to assess the capability of yield criteria to describe the anisotropy of metallic sheets, we shall establish relationships defining the dependence of the parameters mentioned above on the angle θ measured from the rolling direction.

Let us denote by Y_θ the uniaxial yield stress corresponding to the direction inclined at the angle θ with respect to the rolling direction. In the case of a uniaxial load, the components of the stress tensor can be expressed as follows:

$$\sigma_{11} = Y_\theta \cos^2\theta, \quad \sigma_{22} = Y_\theta \sin^2\theta, \quad \sigma_{21} = \sigma_{12} = Y_\theta \sin\theta \cos\theta \tag{1.7}$$

By replacing Eq. (1.7) in the relationship defining the equivalent stress $\bar{\sigma}$ and taking into account its first-degree homogeneity, we obtain:

$$\bar{\sigma}|_\theta = Y_\theta F_\theta \tag{1.8}$$

where F_θ is a function depending on the angle θ. Of course, F_θ is defined according to the specific formulation of the equivalent stress. If we combine Eq. (1.8) with the consistence condition,

$$\Phi(\bar{\sigma}, Y) := \bar{\sigma} - Y(h) = 0 \tag{1.9}$$

where $\Phi(\bar{\sigma}, Y)$ is the yield function associated to the yield criterion, Y—yield stress, h—scalar parameter defining the plastic strain accumulated by the material, we get:

$$Y_\theta = Y(h)/F_\theta \tag{1.10}$$

Equation (1.10) defines the uniaxial yield stress corresponding to the planar direction identified by the angle θ. If the reference yield stress is selected to be the one corresponding to the rolling direction ($Y(h) = \sigma_0$), we obtain the following relationship:

$$Y_\theta = \sigma_0/F_\theta \tag{1.11}$$

In this case, the yield stress corresponding to some planar direction will depend only on the yield stress associated to the rolling direction and the function F_θ (which is related to the yield criterion adopted in the model). The determination of the function F_θ will be presented in the next subchapters, for each type of yield criterion.

In a similar way, we can establish the relationship defining the variation of the coefficient of plastic anisotropy in the plane of the sheet metal. Let us consider the specimen inclined at the angle θ with respect to the rolling direction. According to Eq. (1.1), the instantaneous coefficient of plastic anisotropy r_θ is defined as the ratio

of the plastic strain rates associated to the width (inclined at the angle θ + 90° with respect to the rolling direction), $\dot{\varepsilon}_{\theta+90}$, and thickness, $\dot{\varepsilon}_{33}$:

$$r_\theta = \dot{\varepsilon}_{\theta+90}/\dot{\varepsilon}_{33} \tag{1.12}$$

Taking into account the incompressibility restraint (see Eq. (1.3)), as well as the expressions of the strain rate components along the principal directions,

$$\dot{\varepsilon}_\theta = \dot{\varepsilon}_{11}\cos^2\theta + \dot{\varepsilon}_{22}\sin^2\theta + \dot{\varepsilon}_{12}\sin\theta\cos\theta, \quad \dot{\varepsilon}_{33} = -(\dot{\varepsilon}_{11} + \dot{\varepsilon}_{22}) \tag{1.13}$$

we obtain the relationship defining the coefficient of plastic anisotropy associated to the direction θ:

$$r_\theta = \frac{\dot{\varepsilon}_{11}\cos^2\theta + \dot{\varepsilon}_{22}\sin^2\theta + \dot{\varepsilon}_{12}\sin\theta\cos\theta}{\dot{\varepsilon}_{11} + \dot{\varepsilon}_{22}} - 1 \tag{1.14}$$

Equation (1.14) can be rewritten in terms of the stress components if the associated flow rule is used:

$$r_\theta = \frac{\left(\sigma_{11}\frac{\partial\bar{\sigma}}{\partial\sigma_{11}} + \sigma_{22}\frac{\partial\bar{\sigma}}{\partial\sigma_{22}} + \sigma_{12}\frac{\partial\bar{\sigma}}{\partial\sigma_{12}}\right)_\theta}{\left(\sigma_{11}\frac{\partial\bar{\sigma}}{\partial\sigma_{11}} + \sigma_{22}\frac{\partial\bar{\sigma}}{\partial\sigma_{22}}\right)_\theta} - 1 \tag{1.15}$$

By coupling Eq. (1.15) with Euler's identity, we obtain:

$$r_\theta = \frac{\bar{\sigma}|_\theta}{Y_\theta\left(\frac{\partial\bar{\sigma}}{\partial\sigma_{11}} + \frac{\partial\bar{\sigma}}{\partial\sigma_{22}}\right)_\theta} - 1 \tag{1.16}$$

Finally, after replacing Eq. (1.8) in the last relationship, we get:

$$r_\theta = \frac{F_\theta}{\left(\frac{\partial\bar{\sigma}}{\partial\sigma_{11}} + \frac{\partial\bar{\sigma}}{\partial\sigma_{22}}\right)_\theta} - 1 \tag{1.17}$$

This formula defines the coefficient of plastic anisotropy as a dependence of the specimen inclination. In order to make use of it, we need the expression of the equivalent stress and the function F_θ, both of them being specific to the yield criterion adopted in the plasticity model. The planar distribution of the coefficient of plastic anisotropy will be determined in the next subchapters, for different yield criteria.

The average of the *r*-values obtained for different directions in the plane of the sheet metal represents the so-called coefficient of normal anisotropy r_n. Having determined the values of *r* at specimens cut along three directions in the plane of the sheet metal (0°, 45°, 90°, respectively), the coefficient of normal anisotropy is determined by:

$$r_n = (r_0 + 2r_{45} + r_{90})/4 \tag{1.18}$$

A measure of the variation of normal anisotropy with the angle to the rolling direction is given by the quantity:

$$\Delta r = (r_0 + r_{90} - 2r_{45})/2 \tag{1.19}$$

known as planar anisotropy. This quantity is related to the earring amplitude of the deep-drawn cups.

1.1.2 Biaxial Characteristics of Plastic Anisotropy

The experimental research has proved that the yield surfaces are not symmetric in the biaxial region (Banabic and Wagner 2002; Barlat et al. 2003). This fact is also a consequence of the plastic anisotropy. In order to give a quantitative description of such a behaviour, the so-called coefficient of biaxial anisotropy has been defined independently by Barlat et al. (2003), Pöhlandt et al. (2002). Barlat and his co-workers (Barlat et al. 2003) have proposed the use of a compression test for the experimental determination of this mechanical parameter. A set of circular specimens are subjected to a normal pressure. Due to the plastic anisotropy, the discs become elliptic during the compression. By measuring the major and minor axes of the elliptic specimen, the corresponding principal strains can be evaluated.

As in the case of the uniaxial traction, the ratio of the principal strains will define the coefficient of biaxial anisotropy:

$$r_b = \varepsilon_{22}/\varepsilon_{11} \tag{1.20}$$

If the material is isotropic, the coefficient will be one. The more pronounced is the anisotropy, the farther is the coefficient from unity. This parameter is a direct measure of the slope of the yield locus at the balanced biaxial stress state. As in the case of the uniaxial coefficient of plastic anisotropy, we shall define a general relationship defining the biaxial coefficient. The relationship will be usable for any yield criterion.

In the case of biaxial tension along the rolling and transverse directions, the planar stress components can be expressed as

$$\sigma_{11} = \sigma_{22} = Y_b, \quad \sigma_{21} = \sigma_{12} = 0 \tag{1.21}$$

where, Y_b is the theoretical biaxial yield stress. Consequently, the equivalent stress becomes:

$$\bar{\sigma}|_b = Y_b F_b \tag{1.22}$$

Here, F_b is a quantity depending on the yield criterion adopted in the plasticity model. Equation (1.22) provides the expression of the theoretical biaxial yield stress:

$$Y_b = Y(h)/F_b \tag{1.23}$$

In a very close analogy with the case of the uniaxial coefficient of plastic anisotropy (see Eqs. (1.12)–(1.17)), one may deduce the relationship defining the coefficient of biaxial plastic anisotropy:

$$r_b = \frac{F_b}{\left.\frac{\partial \bar{\sigma}}{\partial \sigma_{11}}\right|_b} - 1 \tag{1.24}$$

This relationship involves only the parameter F_b and the expression of the equivalent stress, both of them being specific to the yield criterion adopted in the plasticity model. The determination of the biaxial coefficient of anisotropy will be presented in the next subchapters, for different yield criteria.

1.2 Classical Yield Criteria for Anisotropic Sheet Metals

1.2.1 Hill (1948) Yield Criterion

In 1948 Hill (1948) proposed an anisotropic yield criterion as a generalization of the von Mises isotropic yield criterion. The material is supposed to have an anisotropy with three orthogonal symmetry planes. The yield criterion is expressed by a quadratic function of the following type:

$$\begin{aligned} 2f(\sigma_{ij}) \equiv {} & F(\sigma_{22}-\sigma_{33})^2 + G(\sigma_{33}-\sigma_{11})^2 + H(\sigma_{11}-\sigma_{22})^2 \\ & + 2L\sigma_{23}^2 + 2M\sigma_{31}^2 + 2N\sigma_{12}^2 = 1 \end{aligned} \tag{1.25}$$

Here f is the yield function; F, G, H, L, M and N are constants specific to the anisotropy state of the material, and x, y, z are the principal anisotropic axes. In the case of sheet metals, axis 1 is usually parallel to the rolling direction, 2 is parallel to the transverse direction and 3 is collinear with the normal direction. For plane stress ($\sigma_{33} = \sigma_{31} = \sigma_{23} = 0$; $\sigma_{11} \neq 0$; $\sigma_{22} \neq 0$; $\sigma_{12} \neq 0$), the yield criterion becomes

$$2f(\sigma_{ij}) \equiv (G+H)\sigma_{11}^2 - 2H\sigma_{11}\sigma_{22} + (H+F)\sigma_{22}^2 + 2N\sigma_{12}^2 = 1 \tag{1.26}$$

If we take into account Eqs. (1.26) and (1.7), the equivalent stress can be expressed as

$$\bar{\sigma} = Y_\theta \left[F \sin^4 \theta + G \cos^4 \theta + H \cos^2 2\theta + \frac{1}{2} N \sin^2 2\theta \right]^{\frac{1}{2}} \tag{1.27}$$

Consequently, F_θ will be defined by the relationship

$$F_\theta = \left[F \sin^4 \theta + G \cos^4 \theta + H \cos^2 2\theta + \frac{1}{2} N \sin^2 2\theta \right]^{\frac{1}{2}} \tag{1.28}$$

In the case of the Hill'48 yield criterion, the uniaxial yield stress corresponding to a direction inclined at the angle θ with respect to the rolling direction is

$$Y_\theta = \frac{Y(h)}{\left[F \sin^4 \theta + G \cos^4 \theta + H \cos^2 2\theta + \frac{1}{2} N \sin^2 2\theta \right]^{\frac{1}{2}}} \tag{1.29}$$

If the yield parameter *Y(h)* is set equal to the uniaxial yield stress σ_u, the uniaxial yield stress predicted by this criterion is

$$Y_0 = \frac{\sigma_u}{\sqrt{G+H}}. \tag{1.30}$$

The expression of the uniaxial coefficient of plastic anisotropy predicted by the Hill'48 yield criterion is obtained by replacing Eq. (1.28) in Eq. (1.17):

$$r_\theta = \frac{F \sin^4 \theta + G \cos^4 \theta + H \cos^2 2\theta + \frac{1}{2} N \sin^2 2\theta}{F \sin^2 \theta + G \cos^2 \theta} - 1 \tag{1.31}$$

Equations (1.30) and (1.31) are used for predicting the uniaxial yield stress and coefficient of plastic anisotropy, in the case when the parameters *F, G, H* and *N* of the Hill'48 yield criterion are related to the experimental yield stress σ_u and the experimental coefficients of plastic anisotropy r_0, r_{45} and r_{90}. The identification of the yield criterion can be also performed by using three experimental values of the yield stress and one experimental value of the coefficient of plastic anisotropy.

1.2.2 Barlat (1989) Yield Criterion

Barlat and Richmond (1987) proposed a more general form of Hosford's criterion for *isotropic* materials (Hosford 1972) by expressing it in an *x, y, z* coordinate system, not necessarily coincident with the principal directions (the so-called 'tri-component plane stress yield surface'):

$$f = |k_1 + k_2|^M + |k_1 - k_2|^M + |2k_2|^M = 2\bar{\sigma}^M \tag{1.32}$$

Here k_1 and k_2 are invariants of the stress tensor while M is an integer exponent having the same significance as the exponent used by Hosford; k_1 and k_2 are obtained from

$$k_1 = \frac{\sigma_{11} + \sigma_{22}}{2}, \quad k_2 = \sqrt{\left(\frac{\sigma_{11} - \sigma_{22}}{2}\right)^2 + \sigma_{12}^2} \tag{1.33}$$

In 1989, Barlat and Lian (1989) published a generalisation of Eqs. (1.32) and (1.33) for materials exhibiting *planar anisotropy* by introducing the following yield function:

$$f = a|k_1 + k_2|^M + a|k_1 - k_2|^M + (1-a)|2k_2|^M = \bar{\sigma}^M \tag{1.34}$$

The coefficients k_1 and k_2 are given by

$$k_1 = \frac{\sigma_{11} + h\sigma_{22}}{2}, \quad k_2 = \left[\left(\frac{\sigma_{11} - h\sigma_{22}}{2}\right)^2 + p^2\sigma_{12}^2\right]^{\frac{1}{2}} \tag{1.35}$$

while a, h and p are material parameters.

In order to establish the expression of the uniaxial yield stress, Eq. (1.7) will be replaced in Eqs. (1.34) and (1.35). We get the relationship

$$Y_\theta = \frac{Y_0}{[a(F_1 + F_2)^M + a(F_1 - F_2)^M + (1-a)(2F_2)^M]^{\frac{1}{M}}} \tag{1.36}$$

where

$$F_1 = \frac{h\sin^2\theta + \cos^2\theta}{2}, \quad F_2 = \left[\left(\frac{h\sin^2\theta - \cos^2\theta}{2}\right)^2 + p^2\sin^2\theta\cos^2\theta\right]^{\frac{1}{2}} \tag{1.37}$$

The function F_θ is obtained from Eq. (1.36):

$$F_\theta = [a(F_1 + F_2)^M + a(F_1 - F_2)^M + (1-a)(2F_2)^M]^{\frac{1}{M}} \tag{1.38}$$

The yield parameter *Y(h)* in Eq. (1.36) has been set equal to the uniaxial yield stress corresponding to the rolling direction (*Y(h)* = Y_0).

By replacing in Eq. (1.17) the F_θ expression given by Eq. (1.38) and performing some computations, we get the relationship defining the coefficient of plastic anisotropy:

$$r_\theta = \frac{a(F_1 + F_2)^M + a(F_1 - F_2)^M + (1-a)(2F_2)^M}{a(F_1 + F_2)^{M-1}(t_1 + t_2) + a(F_1 - F_2)^{M-1}(t_1 - t_2) + 2(1-a)(2F_2)^{M-1}t_2} - 1 \tag{1.39}$$

where

$$t_1 = \frac{h+1}{2},$$
$$t_2 = \frac{(h-1)(h\sin^2\theta - \cos^2\theta)}{4F_2} \tag{1.40}$$

Equations (1.36) and (1.39) allow the calculation of the uniaxial yield stress and the coefficient of plastic anisotropy corresponding to different directions in the plane of the sheet metal.

In 1991, Barlat proposed a 3D extension of his yield criterion (Barlat et al. 1991). Banabic and his coworkers (Banabic et al. 2000; Banabic et al. 2003; Banabic et al. 2005) also proposed extensions of the (Barlat and Lian 1989) yield criterion (with seven and eight coefficients), aiming to remove some of its intrinsic limitations.

1.3 BBC (2005) Yield Criterion

1.3.1 Equation of the Yield Surface

The sheet metal is assumed to behave as a plastically orthotropic membrane under plane stress conditions. By making this assumption, we can use the following description of the yield surface:

$$\Phi\left(\sigma_{\alpha\beta}, Y\right) := \overline{\sigma}\left(\sigma_{\alpha\beta}\right) - Y = 0 \tag{1.41}$$

where $\overline{\sigma}\left(\sigma_{\alpha\beta}\right) > 0$ is the BBC (2005) equivalent stress (see next section), $Y > 0$ is a yield parameter, and $\sigma_{\alpha\beta} = \sigma_{\beta\alpha}(\alpha, \beta = 1, 2)$ are planar components of the stress tensor expressed in an orthonormal basis superimposed to the axes of plastic orthotropy: 1—rolling direction (RD), 2—transverse direction (TD), 3—normal direction (ND). The other components are subjected to the restriction

$$\sigma_{3i} = \sigma_{i3} = 0, \ (i = 1, 2, 3) \tag{1.42}$$

arising from the plane stress hypothesis. Whenever not clearly specified, we shall use the following convention: Greek indices take the values 1 and 2, while the Latin ones take the values 1, 2 and 3.

The BBC (2005) yield criterion does not enforce some special constraints on the choice of the yield parameter (Y). In fact, any quantity representing a yield stress

can act as Y. For example, Y may be the uniaxial yield stress Y_θ associated to a direction defined by the angle θ measured from RD, an average of several uniaxial yield stresses, or the biaxial yield stress Y_b associated to RD and TD.

1.3.2 Flow Rule Associated to the Yield Surface

The flow rule associated to the yield surface described by Eq. (1.41) is

$$\dot{\varepsilon}^p_{\alpha\beta} = \dot{\lambda}\frac{\partial \Phi}{\partial \sigma_{\alpha\beta}}, \quad \alpha, \beta = 1, 2 \tag{1.43}$$

where $\dot{\varepsilon}^p_{\alpha\beta} = \dot{\varepsilon}^p_{\alpha\beta}$ $(\alpha, \beta = 1, 2)$ are planar components of the plastic strain-rate tensor (expressed in the same basis as the corresponding components of the stress tensor), and $\dot{\lambda} \geq 0$ is a scalar multiplier (its significance is not essential for our discussion). The out of plane components of the plastic strain-rate tensor are subjected to the restrictions

$$\dot{\varepsilon}^p_{3\alpha} = \dot{\varepsilon}^p_{\alpha 3} = 0, \quad \alpha = 1, 2 \tag{1.44}$$

$$\dot{\varepsilon}^p_{33} = -\dot{\varepsilon}^p_{11} - \dot{\varepsilon}^p_{22} \tag{1.45}$$

arising from the plane stress hypothesis and the isochoric character of the plastic deformation.

When using Eq. (1.43) we need the partial derivatives of the function Φ with respect to the planar components of the stress tensor. Equation (1.41) allows us to calculate them as partial derivatives of the equivalent stress:

$$\frac{\partial \Phi}{\partial \sigma_{\alpha\beta}} = \frac{\partial \overline{\sigma}}{\partial \sigma_{\alpha\beta}}, \quad \alpha, \beta = 1, 2 \tag{1.46}$$

1.3.3 BBC (2005) Equivalent Stress

The equivalent stress used in Eq. (1.41) is defined by the following formula:

$$\bar{\sigma} = \left[a(\Lambda + \Gamma)^{2k} + a(\Lambda - \Gamma)^{2k} + b(\Lambda + \Psi)^{2k} + b(\Lambda - \Psi)^{2k}\right]^{\frac{1}{2k}} \tag{1.47}$$

where $k \in \mathbf{N}^*$ and $a, b > 0$ are material parameters, while Γ, Λ and Ψ are functions depending on the planar components of the stress tensor:

$$\begin{aligned} \Gamma &= L\sigma_{11} + M\sigma_{22} \\ \Lambda &= \sqrt{(N\sigma_{11} - P\sigma_{22})^2 + \sigma_{12}\sigma_{21}} \\ \Psi &= \sqrt{(Q\sigma_{11} - R\sigma_{22})^2 + \sigma_{12}\sigma_{21}} \end{aligned} \tag{1.48}$$

The coefficients L, M, N, P, Q, and R involved in Eqs. (1.48) are also material parameters.

Despite the fact that Eqs. (1.47) and (1.48) do not enforce any constraint on the sign of the coefficients L, M, N, P, Q, and R, the numerical tests performed by the authors have shown that positive values of these parameters lead to better predictions of the BBC (2005) yield criterion.

The conditions $\mathrm{k} \in \mathbf{N}^{\geq 1}$ and $a, b > 0$ ensure the convexity of the yield surface defined by Eqs. (1.41), (1.47) and (1.48). The parameters L, M, N, P, Q, and R are not subjected to any constraint from this point of view.

Nine material parameters are involved in the expression of the BBC (2005) equivalent stress: k, a, b, L, M, N, P, Q, and R (see Eqs. (1.47) and (1.48)). The integer exponent k has a special status, due to the fact that its value is fixed from the very beginning in accordance with the crystallographic structure of the material: $k = 3$ for BCC materials, $k = 4$ for FCC materials.

The identification procedure calculates the other parameters (a, b, L, M, N, P, Q, and R) by forcing the constitutive equations associated to the BBC (2005) yield criterion to reproduce the following experimental data:

- The uniaxial yield stresses associated to the directions defined by 0°, 45° and 90° angles measured from RD (denoted as Y_0, Y_{45} and Y_{90})
- The coefficients of uniaxial plastic anisotropy associated to the directions defined by 0°, 45° and 90° angles measured from RD (denoted as r_0, r_{45} and r_{90})
- The biaxial yield stress associated to RD and TD (denoted as Y_b)
- The coefficient of biaxial plastic anisotropy associated to RD and TD (denoted as r_b).

There are 8 constraints acting on 8 material parameters. The identification procedure has enough data to generate a set of equations having a, b, L, M, N, P, Q, and R as unknowns. The structure of this set of equations, as well as the solution strategy will be presented in the next section.

When using the flow rule given by Eq. (1.43), we need the partial derivatives of the function Φ with respect to the planar components of the stress tensor. Equations (1.46), (1.47) and (1.48) lead to the following formula:

$$\frac{\partial \Phi}{\partial \sigma_{\alpha\beta}} = \frac{\partial \bar{\sigma}}{\partial \Gamma}\frac{\partial \Gamma}{\partial \sigma_{\alpha\beta}} + \frac{\partial \bar{\sigma}}{\partial \Lambda}\frac{\partial \Lambda}{\partial \sigma_{\alpha\beta}} + \frac{\partial \bar{\sigma}}{\partial \Psi}\frac{\partial \Psi}{\partial \sigma_{\alpha\beta}}, \quad \alpha, \beta = 1, 2 \tag{1.49}$$

where

$$\begin{aligned}
\frac{\partial \bar{\sigma}}{\partial \Gamma} &= \frac{a}{\bar{\sigma}^{2k-1}}\left[(\Lambda+\Gamma)^{2k-1} - (\Lambda-\Gamma)^{2k-1}\right] \\
\frac{\partial \bar{\sigma}}{\partial \Lambda} &= \frac{1}{\bar{\sigma}^{2k-1}}\left\{a\left[(\Lambda+\Gamma)^{2k-1} + (\Lambda-\Gamma)^{2k-1}\right] + b\left[(\Lambda+\Psi)^{2k-1} + (\Lambda-\Psi)^{2k-1}\right]\right\} \\
\frac{\partial \bar{\sigma}}{\partial \Psi} &= \frac{b}{\bar{\sigma}^{2k-1}}\left[(\Lambda+\Psi)^{2k-1} - (\Lambda-\Psi)^{2k-1}\right]
\end{aligned} \tag{1.50}$$

and

$$\begin{aligned}
\frac{\partial \bar{\sigma}}{\partial \Gamma} &= \frac{a}{\bar{\sigma}^{2k-1}}\left[(\Lambda+\Gamma)^{2k-1} - (\Lambda-\Gamma)^{2k-1}\right] \\
\frac{\partial \bar{\sigma}}{\partial \Lambda} &= \frac{1}{\bar{\sigma}^{2k-1}}\left\{a\left[(\Lambda+\Gamma)^{2k-1} + (\Lambda-\Gamma)^{2k-1}\right] + b\left[(\Lambda+\Psi)^{2k-1} + (\Lambda-\Psi)^{2k-1}\right]\right\} \\
\frac{\partial \bar{\sigma}}{\partial \Psi} &= \frac{b}{\bar{\sigma}^{2k-1}}\left[(\Lambda+\Psi)^{2k-1} - (\Lambda-\Psi)^{2k-1}\right]
\end{aligned} \tag{1.51}$$

Equations (1.47)–(1.51) allow expressing the flow rule given by Eq. (1.43) as a dependency of the stress components $\sigma_{\alpha\beta}$ $(\alpha, \beta = 1, 2)$.

1.3.4 Identification Procedure

As mentioned in the previous section, the parameters a, b, L, M, N, P, Q, and R are obtained by constraining the constitutive equations associated to the BBC 2005 yield criterion to reproduce the following experimental data: Y_0, Y_{45}, Y_{90}, r_0, r_{45}, r_{90}, Y_b, and r_b. In fact, the identification procedure will solve the following set of 8 equations considering a, b, L, M, N, P, Q, and R as unknowns:

$$\tilde{Y}_0 = Y_0, \tilde{Y}_{45} = Y_{45}, \tilde{Y}_{90} = Y_{90}, \tilde{r}_0 = r_0, \tilde{r}_{45} = r_{45}, \tilde{r}_{90} = r_{90}, \tilde{Y}_b = Y_b, \tilde{r}_b = r_b \tag{1.52}$$

where: $\tilde{Y}_0$, $\tilde{Y}_{45}$ and $\tilde{Y}_{90}$ are the theoretical yield stresses corresponding to pure tension along the directions defined by 0°, 45° and 90° angles measured from RD; $\tilde{r}_0$, $\tilde{r}_{45}$ and $\tilde{r}_{90}$ are the theoretical coefficients of uniaxial anisotropy associated to the directions mentioned above; $\tilde{Y}_b$ is the theoretical yield stress in biaxial tension along RD and TD; $\tilde{r}_b$ is the theoretical coefficient of biaxial anisotropy associated to RD and TD. It is obvious that the identification procedure needs formulas for evaluating $\tilde{Y}_0$, $\tilde{Y}_{45}$, $\tilde{Y}_{90}$, $\tilde{r}_0$, $\tilde{r}_{45}$, $\tilde{r}_{90}$, $\tilde{Y}_b$, and $\tilde{r}_b$. These formulas will be presented below.

1.3.5 Theoretical Yield Stress in Pure Tension

Let $\tilde{Y}_\theta$ be the theoretical yield stress corresponding to pure tension along a direction defined by the angle θ measured from RD. The planar components of the stress tensor are

$$\sigma_{11} = \tilde{Y}_\theta \cos^2\theta, \quad \sigma_{22} = \tilde{Y}_\theta \sin^2\theta, \quad \sigma_{12} = \sigma_{21} = \tilde{Y}_\theta \sin\theta \cos\theta \tag{1.53}$$

The quantities Γ, Λ and Ψ defined by Eqs. (1.48) become

$$\Gamma = \tilde{Y}_\theta \Gamma_\theta, \quad \Lambda = \tilde{Y}_\theta \Lambda_\theta, \quad \Psi = \tilde{Y}_\theta \Psi_\theta \tag{1.54}$$

where

$$\begin{aligned} \Gamma_\theta &= L\cos^2\theta + M\sin^2\theta \\ \Lambda_\theta &= \sqrt{\left(N\cos^2\theta - P\sin^2\theta\right)^2 + \sin^2\theta\cos^2\theta} \\ \Psi_\theta &= \sqrt{\left(Q\cos^2\theta - R\sin^2\theta\right)^2 + \sin^2\theta\cos^2\theta} \end{aligned} \tag{1.55}$$

Equations (1.47) and (1.54) lead to the following expression of the equivalent stress when pure tension is applied along the θ direction:

$$\bar{\sigma}|_\theta = \tilde{Y}_\theta F(\theta) \tag{1.56}$$

where

$$F(\theta) = \left[a(\Lambda_\theta + \Gamma_\theta)^{2k} + a(\Lambda_\theta - \Gamma_\theta)^{2k} + b(\Lambda_\theta + \Psi_\theta)^{2k} + b(\Lambda_\theta - \Psi_\theta)^{2k}\right]^{\frac{1}{2k}} \tag{1.57}$$

$\bar{\sigma}|_\theta$ given by Eq. (1.56) should be replaced in Eq. (1.41). We thus obtain the desired formula of the theoretical yield stress $\tilde{Y}_\theta$:

$$\tilde{Y}_\theta = Y/F(\theta) \tag{1.58}$$

$\tilde{Y}_0$, $\tilde{Y}_{45}$ and $\tilde{Y}_{90}$ can be calculated from Eqs. (1.58) and (1.57) using $\theta = 0°$, $45°$ and $90°$, respectively.

1.3.6 Theoretical Coefficient of Uniaxial Plastic Anisotropy

The theoretical coefficient of uniaxial plastic anisotropy associated to a direction inclined at the angle θ measured from RD is defined as follows:

$$\tilde{r}_\theta = \dot{\varepsilon}^p_{\theta+90^\circ} / \dot{\varepsilon}^p_{DN} \tag{1.59}$$

where: $\dot{\varepsilon}^p_{\theta+90^\circ}$ is the plastic strain-rate component associated to the direction defined by the angle $\theta + 90^\circ$, and $\dot{\varepsilon}^p_{DN}$ is the component of the same tensor associated to ND. After using the condition of plastic incompressibility

$$\dot{\varepsilon}^p_\theta + \dot{\varepsilon}^p_{\theta+90^\circ} + \dot{\varepsilon}^p_{DN} = 0 \tag{1.60}$$

Equation (1.59) becomes

$$\tilde{r}_\theta = -\frac{\dot{\varepsilon}^p_\theta}{\dot{\varepsilon}^p_{DN}} - 1 \tag{1.61}$$

The symbol $\dot{\varepsilon}^p_\theta$ denotes the plastic strain-rate component associated to the θ direction. $\dot{\varepsilon}^p_\theta$ and $\dot{\varepsilon}^p_{DN}$ may be rewritten using the components of the plastic strain-rate tensor expressed in the orthotropy basis:

$$\begin{aligned} \dot{\varepsilon}^p_\theta &= \dot{\varepsilon}^p_{11}\cos^2\theta + \dot{\varepsilon}^p_{22}\sin^2\theta + \left(\dot{\varepsilon}^p_{12} + \dot{\varepsilon}^p_{21}\right)\sin\theta\cos\theta \\ \dot{\varepsilon}^p_{DN} &= \dot{\varepsilon}^p_{33} = -\dot{\varepsilon}^p_{11} - \dot{\varepsilon}^p_{22} \end{aligned} \tag{1.62}$$

We can replace now $\dot{\varepsilon}^p_\theta$ and $\dot{\varepsilon}^p_{DN}$ given by Eqs. (1.62) into Eq. (1.61):

$$\tilde{r}_\theta = \frac{\dot{\varepsilon}^p_{11}\cos^2\theta + \dot{\varepsilon}^p_{22}\sin^2\theta + \left(\dot{\varepsilon}^p_{12} + \dot{\varepsilon}^p_{21}\right)\sin\theta\cos\theta}{\dot{\varepsilon}^p_{11} + \dot{\varepsilon}^p_{22}} - 1 \tag{1.63}$$

The right-hand side of Eq. (1.63) should be expressed in terms of the planar stress components. This transformation is achieved using the flow rule (see Eqs. (1.43) and (1.46), as well as Eq. (1.53)):

$$\tilde{r}_\theta = \frac{1}{\tilde{Y}_\theta}\frac{\left(\sigma_{\alpha\beta}\frac{\partial\bar{\sigma}}{\partial\sigma_{\alpha\beta}}\right)\Big|_\theta}{\left(\frac{\partial\bar{\sigma}}{\partial\sigma_{11}} + \frac{\partial\bar{\sigma}}{\partial\sigma_{22}}\right)\Big|_\theta} - 1 \tag{1.64}$$

The notation $(\cdot)|_\theta$ means that the expression enclosed by parentheses should be calculated for pure tension along the θ direction. The summation rule for tensor components has been used in Eq. (1.64). The equivalent stress defined by Eqs. (1.47) and (1.48) is a first-degree homogeneous function of the stress components $\sigma_{\alpha\beta}$ $(\alpha, \beta = 1, 2)$. Thus we can use Euler's theorem:

$$\bar{\sigma} = \sigma_{\alpha\beta}\frac{\partial\bar{\sigma}}{\partial\sigma_{\alpha\beta}} \tag{1.65}$$

Equations (1.64), (1.65) and (1.56) lead to the following formula for $\tilde{r}_\theta$:

$$\tilde{r}_\theta = \frac{F(\theta)}{\left(\frac{\partial\bar{\sigma}}{\partial\sigma_{11}} + \frac{\partial\bar{\sigma}}{\partial\sigma_{22}}\right)\Big|_\theta} - 1 \tag{1.66}$$

We shall express now $\left(\frac{\partial\bar{\sigma}}{\partial\sigma_{11}} + \frac{\partial\bar{\sigma}}{\partial\sigma_{22}}\right)\Big|_\theta$ as a dependency of the θ angle. We start by rewriting Eq. (1.49) both for $\alpha = \beta = 1$ and $\alpha = \beta = 2$, assuming a uniaxial stress state along the θ direction. We have two relationships that can be added, thus obtaining

$$\begin{aligned}\left(\frac{\partial\bar{\sigma}}{\partial\sigma_{11}} + \frac{\partial\bar{\sigma}}{\partial\sigma_{22}}\right)\Big|_\theta &= \frac{\partial\bar{\sigma}}{\partial\Gamma}\Big|_\theta \left(\frac{\partial\Gamma}{\partial\sigma_{11}} + \frac{\partial\Gamma}{\partial\sigma_{22}}\right)\Big|_\theta \\ &+ \frac{\partial\bar{\sigma}}{\partial\Lambda}\Big|_\theta \left(\frac{\partial\Lambda}{\partial\sigma_{11}} + \frac{\partial\Lambda}{\partial\sigma_{22}}\right)\Big|_\theta + \frac{\partial\bar{\sigma}}{\partial\Psi}\Big|_\theta \left(\frac{\partial\Psi}{\partial\sigma_{11}} + \frac{\partial\Psi}{\partial\sigma_{22}}\right)\Big|_\theta\end{aligned} \tag{1.67}$$

Equations (1.50), (1.54) and (1.56) allow us to express the derivatives $\frac{\partial\bar{\sigma}}{\partial\Gamma}\Big|_\theta$, $\frac{\partial\bar{\sigma}}{\partial\Lambda}\Big|_\theta$ and $\frac{\partial\bar{\sigma}}{\partial\Psi}\Big|_\theta$ as functions of the θ angle:

$$\begin{aligned}\frac{\partial\bar{\sigma}}{\partial\Gamma}\Big|_\theta &= \frac{a}{[F(\theta)]^{2k-1}}\left[(\Lambda_\theta + \Gamma_\theta)^{2k-1} - (\Lambda_\theta - \Gamma_\theta)^{2k-1}\right] \\ \frac{\partial\bar{\sigma}}{\partial\Lambda}\Big|_\theta &= \frac{1}{[F(\theta)]^{2k-1}}\left\{a\left[(\Lambda_\theta + \Gamma_\theta)^{2k-1} + (\Lambda_\theta - \Gamma_\theta)^{2k-1}\right] + b\left[(\Lambda_\theta + \Psi_\theta)^{2k-1} + (\Lambda_\theta - \Psi_\theta)^{2k-1}\right]\right\} \\ \frac{\partial\bar{\sigma}}{\partial\Psi}\Big|_\theta &= \frac{b}{[F(\theta)]^{2k-1}}\left[(\Lambda_\theta + \Psi_\theta)^{2k-1} - (\Lambda_\theta - \Psi_\theta)^{2k-1}\right]\end{aligned} \tag{1.68}$$

where Γ_θ, Λ_θ and Ψ_θ are defined by Eqs. (1.55). The other derivatives appearing on the right-hand side of Eq. (1.67) can be also expressed as functions of the θ angle (see Eqs. 1.51), (1.53) and (1.54)):

$$\begin{aligned}\left(\frac{\partial\Gamma}{\partial\sigma_{11}} + \frac{\partial\Gamma}{\partial\sigma_{22}}\right)\Big|_\theta &= L + M, \\ \left(\frac{\partial\Lambda}{\partial\sigma_{11}} + \frac{\partial\Lambda}{\partial\sigma_{22}}\right)\Big|_\theta &= \frac{(N-P)\left(N\cos^2\theta - P\sin^2\theta\right)}{\Lambda_\theta}, \\ \left(\frac{\partial\Psi}{\partial\sigma_{11}} + \frac{\partial\Psi}{\partial\sigma_{22}}\right)\Big|_\theta &= \frac{(Q-R)\left(Q\cos^2\theta - R\sin^2\theta\right)}{\Psi_\theta}\end{aligned} \tag{1.69}$$

After replacing the quantities given by Eqs. (1.68) and (1.69) into Eq. (1.67) and making some rearrangements, we get the following relationship for

$$\begin{aligned}&\left(\frac{\partial\bar{\sigma}}{\partial\sigma_{11}} + \frac{\partial\bar{\sigma}}{\partial\sigma_{22}}\right)\Big|_\theta : \\ &\left(\frac{\partial\bar{\sigma}}{\partial\sigma_{11}} + \frac{\partial\bar{\sigma}}{\partial\sigma_{22}}\right)\Big|_\theta = \frac{G(\theta)}{[F(\theta)]^{2k-1}}\end{aligned} \tag{1.70}$$

where

$$
\begin{aligned}
G(\theta) = a&\left[\frac{(N-P)\left(N\cos^2\theta - P\sin^2\theta\right)}{\Lambda_\theta} + L + M\right](\Lambda_\theta + \Gamma_\theta)^{2k-1} \\
&+ a\left[\frac{(N-P)\left(N\cos^2\theta - P\sin^2\theta\right)}{\Lambda_\theta} - L - M\right](\Lambda_\theta - \Gamma_\theta)^{2k-1} \\
&+ b\left[\frac{(N-P)\left(N\cos^2\theta - P\sin^2\theta\right)}{\Lambda_\theta} + \frac{(Q-R)\left(Q\cos^2\theta - R\sin^2\theta\right)}{\Psi_\theta}\right](\Lambda_\theta + \Psi_\theta)^{2k-1} \\
&+ b\left[\frac{(N-P)\left(N\cos^2\theta - P\sin^2\theta\right)}{\Lambda_\theta} - \frac{(Q-R)\left(Q\cos^2\theta - R\sin^2\theta\right)}{\Psi_\theta}\right](\Lambda_\theta - \Psi_\theta)^{2k-1}
\end{aligned}
\tag{1.71}
$$

We can now combine Eqs. (1.66) and (1.70) to obtain a formula for evaluating the coefficient of uniaxial plastic anisotropy:

$$
\tilde{r}_\theta = \frac{[F(\theta)]^{2k}}{G(\theta)} - 1 \tag{1.72}
$$

$\tilde{r}_0$, $\tilde{r}_{45}$ and $\tilde{r}_{90}$ can be calculated from Eqs. (1.72), (1.71) and (1.57) using $\theta = 0°$, 45° and 90°, respectively.

1.3.7 Theoretical Yield Stress in Biaxial Tension Along RD and TD

Let $\tilde{Y}_b$ be the theoretical yield stress corresponding to biaxial tension along RD and TD. The planar components of the stress tensor are

$$
\sigma_{11} = \tilde{Y}_b, \quad \sigma_{22} = \tilde{Y}_b, \quad \sigma_{12} = \sigma_{21} = 0 \tag{1.73}
$$

The quantities Γ, Ψ and Λ defined by Eqs. (1.48) become

$$
\Gamma = \tilde{Y}_b \Gamma_b, \quad \Lambda = \tilde{Y}_b \Lambda_b, \quad \Psi = \tilde{Y}_b \Psi_b \tag{1.74}
$$

where

$$
\begin{aligned}
\Gamma_b &= L + M, \\
\Lambda_b &= \sqrt{(N-P)^2} = |N-P|, \\
\Psi_b &= \sqrt{(Q-R)^2} = |Q-R|
\end{aligned}
\tag{1.75}
$$

Equations (1.47) and (1.74) lead to the following expression of the equivalent stress when biaxial tension is applied along RD and TD:

$$\bar{\sigma}|_b = \tilde{Y}_b F_b \tag{1.76}$$

where

$$F_b = \left[a(\Lambda_b + \Gamma_b)^{2k} + a(\Lambda_b - \Gamma_b)^{2k} + b(\Lambda_b + \Psi_b)^{2k} + b(\Lambda_b - \Psi_b)^{2k}\right]^{\frac{1}{2k}} \tag{1.77}$$

$\bar{\sigma}|_b$ given by Eq. (1.76) should be replaced in Eq. (1.40). We thus obtain the desired formula of the theoretical yield stress $\tilde{Y}_b$:

$$\tilde{Y}_b = Y/F_b \tag{1.78}$$

$\tilde{Y}_b$ can be calculated from Eqs. (1.78) and (1.77).

1.3.8 Theoretical Coefficient of Biaxial Plastic Anisotropy

The theoretical coefficient of biaxial plastic anisotropy associated to RD and TD is defined as follows:

$$\tilde{r}_b = \dot{\varepsilon}^p_{TD}/\dot{\varepsilon}^p_{RD} \tag{1.79}$$

where $\dot{\varepsilon}^p_{RD}$ and $\dot{\varepsilon}^p_{TD}$ are the components of the plastic strain-rate tensor corresponding to RD and TD, respectively. The choice of the orthonormal basis allows us to write the equalities

$$\dot{\varepsilon}^p_{RD} = \dot{\varepsilon}^p_{11}, \quad \dot{\varepsilon}^p_{TD} = \dot{\varepsilon}^p_{22} \tag{1.80}$$

We can replace now $\dot{\varepsilon}^p_{RD}$ and $\dot{\varepsilon}^p_{TD}$ given by Eq. (1.80) into Eq. (1.79):

$$\tilde{r}_b = \frac{\dot{\varepsilon}^p_{22}}{\dot{\varepsilon}^p_{11}} = \frac{\dot{\varepsilon}^p_{11} + \dot{\varepsilon}^p_{22}}{\dot{\varepsilon}^p_{11}} - 1 \tag{1.81}$$

The right-hand side of Eq. (1.81) should be expressed in terms of the planar stress components. This transformation is achieved using the flow rule (see Eqs. (1.43) and (1.46)), as well as Eq. (1.73)):

$$\tilde{r}_b = \frac{1}{\tilde{Y}_b} \frac{\left(\sigma_{\alpha\beta} \frac{\partial \bar{\sigma}}{\partial \sigma_{\alpha\beta}}\right)\Big|_b}{\left(\frac{\partial \bar{\sigma}}{\partial \sigma_{11}}\right)\Big|_b} - 1 \tag{1.82}$$

The notation $(\cdot)|_b$ means that the expression enclosed by parentheses should be calculated for biaxial tension along RD and TD. Equations (1.82), (1.65) and (1.76) lead to the following formula for $\tilde{r}_b$:

$$\tilde{r}_b = \frac{F_b}{\left(\frac{\partial \bar{\sigma}}{\partial \sigma_{11}}\right)\Big|_b} - 1 \tag{1.83}$$

We shall find now the expression of the denominator $\left(\frac{\partial \bar{\sigma}}{\partial \sigma_{11}}\right)\Big|_b$. We start by rewriting Eq. (1.49) for $\alpha = \beta = 1$, assuming a biaxial stress state along RD and TD:

$$\left(\frac{\partial \bar{\sigma}}{\partial \sigma_{11}}\right)\Big|_b = \frac{\partial \bar{\sigma}}{\partial \Gamma}\Big|_b \frac{\partial \Gamma}{\partial \sigma_{11}}\Big|_b + \frac{\partial \bar{\sigma}}{\partial \Lambda}\Big|_b \frac{\partial \Lambda}{\partial \sigma_{11}}\Big|_b + \frac{\partial \bar{\sigma}}{\partial \Psi}\Big|_b \frac{\partial \Psi}{\partial \sigma_{11}}\Big|_b \tag{1.84}$$

Equations (1.50), (1.74) and (1.76) allow us to express the derivatives $\frac{\partial \bar{\sigma}}{\partial \Gamma}\Big|_b$, $\frac{\partial \bar{\sigma}}{\partial \Lambda}\Big|_b$ and $\frac{\partial \bar{\sigma}}{\partial \Psi}\Big|_b$:

$$\begin{aligned}
\frac{\partial \bar{\sigma}}{\partial \Gamma}\Big|_b &= \frac{a}{F_b^{2k-1}}\left[(\Lambda_b + \Gamma_b)^{2k-1} - (\Lambda_b - \Gamma_b)^{2k-1}\right] \\
\frac{\partial \bar{\sigma}}{\partial \Lambda}\Big|_b &= \frac{1}{F_b^{2k-1}}\left\{a\left[(\Lambda_b + \Gamma_b)^{2k-1} + (\Lambda_b - \Gamma_b)^{2k-1}\right] + b\left[(\Lambda_b + \Psi_b)^{2k-1} + (\Lambda_b - \Psi_b)^{2k-1}\right]\right\} \\
\frac{\partial \bar{\sigma}}{\partial \Psi}\Big|_b &= \frac{b}{F_b^{2k-1}}\left[(\Lambda_b + \Psi_b)^{2k-1} - (\Lambda_b - \Psi_b)^{2k-1}\right]
\end{aligned} \tag{1.85}$$

where Γ_b, Λ_b and Ψ_b are defined by Eqs. (1.75). The other derivatives appearing on the right-hand side of Eq. (1.84) can be also expressed from Eqs. (1.51), (1.73) and (1.74):

$$\frac{\partial \Gamma}{\partial \sigma_{11}}\Big|_b = L, \quad \frac{\partial \Lambda}{\partial \sigma_{11}}\Big|_b = \frac{N(N-P)}{\Lambda_b}, \quad \frac{\partial \Psi}{\partial \sigma_{11}}\Big|_b = \frac{Q(Q-R)}{\Psi_b} \tag{1.86}$$

After replacing the quantities given by Eqs. (1.85) and (1.86) into Eq. (1.84), we get the following relationship for $\left(\frac{\partial \bar{\sigma}}{\partial \sigma_{11}}\right)\Big|_b$ (see also Eqs. (1.75)):

$$\left(\frac{\partial \bar{\sigma}}{\partial \sigma_{11}}\right)\Big|_b = \frac{G_b}{F_b^{2k-1}} \tag{1.87}$$

where

$$G_b = a\left[\frac{N(N-\mathrm{P})}{\Lambda_b} + L\right](\Lambda_b + \Gamma_b)^{2k-1} + a\left[\frac{N(N-P)}{\Lambda_b} - L\right](\Lambda_b - \Gamma_b)^{2k-1} + b\left[\frac{N(N-P)}{\Lambda_b} + \frac{Q(Q-R)}{\Psi_b}\right](\Lambda_b + \Psi_b)^{2k-1} + b\left[\frac{N(N-P)}{\Lambda_b} - \frac{Q(Q-R)}{\Psi_b}\right](\Lambda_b - \Psi_b)^{2k-1} \tag{1.88}$$

We can combine Eqs. (1.83) and (1.87) to obtain a formula for evaluating the coefficient of biaxial plastic anisotropy:

$$\tilde{r}_b = \frac{F_b^{2k}}{G_b} - 1 \tag{1.89}$$

1.3.9 Identification Constraints

Now we have all the quantities needed to construct the identification conditions (see Eqs. (1.52)). Equations (1.58) and (1.78) allow us to rewrite the constraints referring to the yield stresses in a more convenient form:

$$[F(0^\circ)]^{2k} = y_0^{2k}, \quad [F(45^\circ)]^{2k} = y_{45}^{2k}, \quad [F(90^\circ)]^{2k} = y_{90}^{2k}, \quad F_b^{2k} = y_b^{2k} \tag{1.90}$$

where

$$y_0 = Y/Y_0, \quad y_{45} = Y/Y_{45}, \quad y_{90} = Y/Y_{90}, \quad y_b = Y/Y_b \tag{1.91}$$

are normalized values of the experimental yield stresses. In a similar way, Eqs. (1.70), (1.89) and (1.90) lead to the following expressions of the constraints associated to the coefficients of plastic anisotropy:

$$\begin{aligned} G(0^\circ) &= \tfrac{1}{r_0+1} y_0^{2k}, & G(45^\circ) &= \tfrac{1}{r_{45}+1} y_{45}^{2k}, \\ G(90^\circ) &= \tfrac{1}{r_{90}+1} y_{90}^{2k}, & G_b &= \tfrac{1}{r_b+1} y_b^{2k}. \end{aligned} \tag{1.92}$$

Finally, we use Eqs. (1.57), (1.55), (1.77), (1.75), (1.71), and (1.88) to put into evidence the unknown material parameters a, b, L, M, N, P, Q, and R on the left-hand sides of Eqs. (1.90) and (1.92):

$$
\begin{aligned}
&a(N+L)^{2k}+a(N-L)^{2k}+b(N+Q)^{2k}b(N-Q)^{2k}=y_0^{2k}\\
&a\left[\sqrt{(N-P)^2+1}+L+M\right]^{2k}+a\left[\sqrt{(N-P)^2+1}-L-M\right]\\
&\quad+b\left[\sqrt{(N-P)^2+1}+\sqrt{(Q-R)^2+1}\right]^{2k}\\
&\quad+b\left[\sqrt{(N-P)^2+1}-\sqrt{(Q-R)^2+1}\right]^{2k}=(2y_{45})^{2k}\\
&a(P+M)^{2k}+a(P-M)^{2k}+b(P+R)^{2k}+b(P-R)^{2k}=y_{90}^{2k}\\
&a(N-P+L+M)^{2k}+a(N-P-L-M)^{2k}\\
&\quad+b(N-P+Q-R)^{2k}+b(N-P-Q+R)^{2k}=y_b^{2k}\\
&a(P-M)(N+L)^{2k-1}+a(P+M)(N-L)^{2k-1}\\
&\quad+b(P+R)(N+Q)^{2k-1}+b(P-R)(N-Q)^{2k-1}=\frac{r_0}{r_0+1}y_0^{2k}\\
&a\sqrt{(Q-R)^2+1}\left\{\left[\sqrt{(N-P)^2+1}+L+M\right]^{2k-1}+\left[\sqrt{(N-P)^2+1}-L-M\right]^{2k-1}\right\}\\
&\quad+b\left\{\left[\sqrt{(N-P)^2+1}+\sqrt{(Q-R)^2+1}\right]^{2k}\right.\\
&\quad\left.-\left[\sqrt{(N-P)^2+1}-\sqrt{(Q-R)^2+1}\right]^{2k}\right\}\\
&\quad=\sqrt{(N-P)^2+1}\sqrt{(Q-R)^2+1}\frac{r_{45}+1/2}{r_{45}+1}(2y_{45})^{2k}\\
&a(N-L)(P+M)^{2k-1}+a(N+L)(P-M)^{2k-1}\\
&\quad+b(N+Q)(P+R)^{2k-1}+b(N-Q)(P-R)^{2k-1}=\frac{r_{90}}{r_{90}+1}y_{90}^{2k}\\
&a(N+L)(N-P+L+M)^{2k-1}+a(N-L)(N-P-L-M)^{2k-1}\\
&\quad+b(N+Q)(N-P+Q-R)^{2k-1}\\
&\quad+b(N-Q)(N-P-Q+R)^{2k-1}=\frac{1}{r_b+1}y_b^{2k}
\end{aligned}
\tag{1.93}
$$

Equations (1.93) form together a set of eight non-linear equations. The identification procedure uses Newton's method to obtain its numerical solution.

From now on we shall manipulate Eqs. (1.93) in a generic form:

$$f_i(a,\,b,\,L,\,M,\,N,\,P,\,Q,\,R)\,=\,0,\quad i\,=\,1,\,2,\ldots,\,8 \tag{1.94}$$

where

$$
\begin{aligned}
f_1 &= a(N+L)^{2k} + a(N-L)^{2k} + b(N+Q)^{2k} + b(N-Q)^{2k} - y_0^{2k} \\
f_2 &= a\left[\sqrt{(N-P)^2+1} + L + M\right]^{2k} + a\left[\sqrt{(N-P)^2+1} - L - M\right]^{2k} \\
&\quad + b\left[\sqrt{(N-P)^2+1} + \sqrt{(Q-R)^2+1}\right]^{2k} \\
&\quad + b\left[\sqrt{(N-P)^2+1} - \sqrt{(Q-R)^2+1}\right]^{2k} - (2\,y_{45})^{2k} \\
f_3 &= a(P+M)^{2k} + a(P-M)^{2k} + b(P+R)^{2k} + b(P-R)^{2k} - y_{90}^{2k} \\
f_4 &= a(N-P+L+M)^{2k} + a(N-P-L-M)^{2k} \\
&\quad + b(N-P+Q-R)^{2k} + b(N-P-Q+R)^{2k} - y_b^{2k} \\
f_5 &= a(P-M)(N+L)^{2k-1} + a(P+M)(N-L)^{2k-1} \\
&\quad + b(P+R)(N+Q)^{2k-1} + b(P-R)(N-Q)^{2k-1} - \frac{r_0}{r_0+1} y_0^{2k} \\
f_6 &= a\sqrt{(Q-R)^2+1}\left\{\left[\sqrt{(N-P)^2+1} + L + M\right]^{2k-1}\right. \\
&\quad \left. + \left[\sqrt{(N-P)^2+1} - L - M\right]^{2k-1}\right\} \\
&\quad + b\left\{\left[\sqrt{(N-P)^2+1} + \sqrt{(Q-R)^2+1}\right]^{2k}\right. \\
&\quad \left. - \left[\sqrt{(N-P)^2+1} - \sqrt{(Q-R)^2+1}\right]^{2k}\right\} \\
&\quad - \sqrt{(N-P)^2+1}\sqrt{(Q-R)^2+1}\,\frac{r_{45}+1/2}{r_{45}+1}(2\,y_{45})^{2k} \\
f_7 &= a(N-L)(P+M)^{2k-1} + a(N+L)(P-M)^{2k-1} \\
&\quad + b(N+Q)(P+R)^{2k-1} + b(N-Q)(P-R)^{2k-1} - \frac{r_{90}}{r_{90}+1} y_{90}^{2k} \\
f_8 &= a(N+L)(N-P+L+M)^{2k-1} + a(N-L)(N-P-L-M)^{2k-1} \\
&\quad + b(N+Q)(N-P+Q-R)^{2k-1} \\
&\quad + b(N-Q)(N-P-Q+R)^{2k-1} - \frac{1}{r_b+1} y_b^{2k}
\end{aligned}
\tag{1.95}
$$

As mentioned previously, the parameters involved in the expression of the equivalent stress are subjected to constraints: $a > 0$, $b > 0$, $L > 0$, $M > 0$, $N > 0$, $P > 0$, $Q > 0$, and $R > 0$. Aiming to ensure a natural treatment of these restrictions, the identification procedure replaces the parameters a, b, L, M, N, P, Q, and R with the following substitutes:

$$\begin{aligned} &a = (a')^2, \quad b = (b')^2, \quad L = (L')^2, \quad M = (M')^2, \\ &N = (N')^2, \quad P = (P')^2, \quad Q = (Q')^2, \quad R = (R')^2, \\ &a', b', L', M', N', P', Q', R' \in \mathbb{R} \end{aligned} \tag{1.96}$$

In this way, $f_1, f_2, \ldots, f_8$ will become functions of the variables a', b', L', M', N', P', Q', and R'. As a consequence, Eqs. (1.94) should be rewritten in the form

$$\begin{aligned} &f_i\left[a(a'), b(b'), L(L'), M(M'), N(N'), P(P'), Q(Q'), R(R')\right] = 0, \\ &i = 1, 2, \ldots, 8 \end{aligned} \tag{1.97}$$

The identification procedure solves Eqs. (1.97) considering a', b', L', M', N', P', Q', and R' as unknowns. After finding the numerical solution, the values of the actual parameters a, b, L, M, N, P, Q, and R can be obtained from Eqs. (1.96). Let a'_k, b'_k, L'_k, M'_k, N'_k, P'_k, Q'_k, and R'_k be the approximations of the numerical solution corresponding to the k-th Newton iteration. Equations (1.97) are linearised in the vicinity of this approximation using a Taylor expansion:

$$\begin{aligned} &\left.\frac{\partial f_i}{\partial a}\right|_k \left.\frac{\partial a}{\partial a'}\right|_k (\Delta a'_k) + \left.\frac{\partial f_i}{\partial b}\right|_k \left.\frac{\partial b}{\partial b'}\right|_k (\Delta b'_k) \\ &+ \left.\frac{\partial f_i}{\partial L}\right|_k \left.\frac{\partial L}{\partial L'}\right|_k (\Delta L'_k) + \left.\frac{\partial f_i}{\partial M}\right|_k \left.\frac{\partial M}{\partial M'}\right|_k (\Delta M'_k) \\ &+ \left.\frac{\partial f_i}{\partial N}\right|_k \left.\frac{\partial N}{\partial N'}\right|_k (\Delta N'_k) + \left.\frac{\partial f_i}{\partial P}\right|_k \left.\frac{\partial P}{\partial P'}\right|_k (\Delta P'_k) \\ &+ \left.\frac{\partial f_i}{\partial Q}\right|_k \left.\frac{\partial Q}{\partial Q'}\right|_k (\Delta Q'_k) + \left.\frac{\partial f_i}{\partial R}\right|_k \left.\frac{\partial R}{\partial R'}\right|_k (\Delta R'_k) = -f_i|_k, \; i = 1, 2, \ldots, 8 \end{aligned} \tag{1.98}$$

The symbol $\cdot|_k$ means that the associated expression should be evaluated considering $a' = a'_k$, $b' = b'_k$, $L' = L'_k$, $M' = M'_k$, $N' = N'_k$, $P' = P'_k$, $Q' = Q'_k$ and $R' = R'_k$. The unknowns of the linearised set are the corrections $\Delta a'_k$, $\Delta b'_k$, $\Delta L'_k$, $\Delta M'_k$, $\Delta N'_k$, $\Delta P'_k$, $\Delta Q'_k$, and $\Delta R'_k$. After adding them to a'_k, b'_k, L'_k, M'_k, N'_k, P'_k, Q'_k, and R'_k, respectively, we obtain a new approximation of the numerical solution that should be used in the next iteration:

$$\begin{aligned}
a'_{k+1} &= a'_k + \Delta a'_k \\
b'_{k+1} &= b'_k + \Delta b'_k \\
L'_{k+1} &= L'_k + \Delta L'_k \\
M'_{k+1} &= M'_k + \Delta M'_k \\
N'_{k+1} &= N'_k + \Delta N'_k \\
P'_{k+1} &= P'_k + \Delta P'_k \\
Q'_{k+1} &= Q'_k + \Delta Q'_k \\
R'_{k+1} &= R'_k + \Delta R'_k
\end{aligned} \tag{1.99}$$

Two convergence criteria are used to stop the iterations:

$$\begin{aligned}
&\sqrt{\frac{\left(\Delta a'_k\right)^2 + \left(\Delta b'_k\right)^2 + \left(\Delta L'_k\right)^2 + \left(\Delta M'_k\right)^2 + \left(\Delta N'_k\right)^2 + \left(\Delta P'_k\right)^2 + \left(\Delta Q'_k\right)^2 + \left(\Delta R'_k\right)^2}{\left(a'_{k+1}\right)^2 + \left(b'_{k+1}\right)^2 + \left(L'_{k+1}\right)^2 + \left(M'_{k+1}\right)^2 + \left(N'_{k+1}\right)^2 + \left(P'_{k+1}\right)^2 + \left(Q'_{k+1}\right)^2 + \left(R'_{k+1}\right)^2}} < 10^{-7} \\
&\sqrt{\sum_{i=1}^{8} \left(f_i|_k\right)^2} < 10^{-5}
\end{aligned} \tag{1.100}$$

The convergence of the Newton iterations is strongly influenced by the so-called 'initial guess'. Due to the difficulties encountered when trying to define such an initial guess suitable for all situations that may occur in practice, the authors have been forced to adopt a special identification strategy.

1.3.10 Particular Formulations of the BBC (2005) Yield Criterion

We can reduce BBC (2005) to Hill (1948) yield criterion if we choose the material parameters as follows:

$$\begin{aligned}
Y &= Y_0 \\
k &= 1 \\
a &= \frac{\sqrt{\frac{1+r_0}{r_0}\frac{1+r_{90}}{r_{90}}} - 1}{\sqrt{\frac{1+r_0}{r_0}\frac{1+r_{90}}{r_{90}}} + 1} \frac{1}{1+r_0}\left(1 + \frac{r_0}{r_{90}}\right)\left(r_{45} + \frac{1}{2}\right) \\
b &= \frac{a}{\sqrt{\frac{1+r_0}{r_0}\frac{1+r_{90}}{r_{90}}} - 1} \\
L &= N = Q = \frac{1}{2\sqrt{a+b}} \\
M &= P = R = \frac{1}{2}\sqrt{\frac{\frac{r_0}{1+r_0}\frac{1+r_{90}}{r_{90}}}{a+b}}
\end{aligned} \tag{1.101}$$

In this case, the identification procedure needs only r_0, r_{45} and r_{90} as input data.

The yield criterion proposed by Barlat and Lian (1989) can be also obtained by enforcing the following constraints on the material parameters:

$$Y = Y_0, \quad k = 3\,or\,4, \quad L = N = Q, \quad M = P = R \tag{1.102}$$

As above, the identification procedure needs only r_0, r_{45} and r_{90} as input data.

Another situation of practical interest is the so-called normal anisotropy ($r_0 = r_{45} = r_{90} = r$, $Y_0 = Y_{45} = Y_{90} = Y$). In this case, BBC (2005) also reduces to the Hill (1948) or Barlat and Lian (1989) yield criteria (depending on the value of the exponent k):

$$\begin{array}{ll} k = 1\,(\text{Hill}\,1948), & k = 3\,or\,4\,(\text{Barlat}\,1989), \\ a = \frac{1}{1+r}, b = \frac{r}{1+r}, & L = N = Q = M = P = R = \frac{1}{2} \end{array} \tag{1.103}$$

1.4 BBC (2008) Yield Criterion

In order to enhance the flexibility of the BBC 2005 yield criterion, a new version of this model has been developed (Comsa and Banabic 2008). The model is expressed as a finite series that can be expanded to retain more or less terms, depending on the volume of experimental data. Different identification strategies (using 8, 16, 24, etc. input values) could be used in order to determine the coefficients of the yield function.

1.4.1 BBC 2008 Equivalent Stress

The equivalent stress used in Eq. (1.41) is defined as follows:

$$\begin{aligned} \frac{\bar{\sigma}^{2k}}{w-1} &= \sum_{i=1}^{s}\left\{w^{i-1}\left\{\left[L^{(i)}+M^{(i)}\right]^{2k}+\left[L^{(i)}-M^{(i)}\right]^{2k}\right\}\right. \\ &\left.+\,w^{s-i}\left\{\left[M^{(i)}+N^{(i)}\right]^{2k}+\left[M^{(i)}-N^{(i)}\right]^{2k}\right\}\right\} \\ k, s \in \mathbf{N}^*, w &= (3/2)^{1/s} > 1 \\ L^{(i)} &= \ell_1^{(i)}\sigma_{11} + \ell_2^{(i)}\sigma_{22} \\ M^{(i)} &= \sqrt{\left[m_1^{(i)}\sigma_{11} - m_2^{(i)}\sigma_{22}\right]^2 + \left[m_3^{(i)}(\sigma_{12}+\sigma_{21})\right]^2} \\ N^{(i)} &= \sqrt{\left[n_1^{(i)}\sigma_{11} - n_2^{(i)}\sigma_{22}\right]^2 + \left[n_3^{(i)}(\sigma_{12}+\sigma_{21})\right]^2} \\ \ell_1^{(i)}, \ell_2^{(i)}, m_1^{(i)}, m_2^{(i)}, m_3^{(i)}, n_1^{(i)}, n_2^{(i)}, n_3^{(i)} &\in \mathbf{R}. \end{aligned} \tag{1.104}$$

The quantities denoted $k, \ell_1^{(i)}, \ell_2^{(i)}, m_1^{(i)}, m_2^{(i)}, m_3^{(i)}, n_1^{(i)}, n_2^{(i)}, n_3^{(i)}$ $(i = 1, \ldots, s)$ are material parameters. One may prove that $k \in \mathbf{N}^*$ is a sufficient condition for the convexity of the yield surface defined by Eqs. (1.41) and (1.104). From this point of view, there is no constraint acting on the admissible values of the other material parameters.

It is easily noticeable that Eqs. (1.104) reduce to the isotropic formulation proposed by Barlat and Richmond (1987) if

$$\ell_1^{(i)} = \ell_2^{(i)} = m_1^{(i)} = m_2^{(i)} = m_3^{(i)} = n_1^{(i)} = n_2^{(i)} = n_3^{(i)} = 1/2, \quad i = 1, \ldots, s \tag{1.105}$$

Under these circumstances, the exponent k may be chosen as in Barlat and Richmond's model, i.e. according to the crystallographic structure of the sheet metal: $k = 3$ for BCC materials $(2k = 6)$, and $k = 4$ for FCC materials $(2k = 8)$.

The other parameters involved in Eqs. (1.104) result from an identification procedure (see the next section). Their number (n_p) is defined by the summation limit s :

$$n_p = 8s \tag{1.106}$$

Let n_e be the number of experimental values describing the plastic anisotropy. The summation limit should be chosen according to the following constraint:

$$n_p = 8s \leq n_e \tag{1.107}$$

i.e.

$$s \leq n_e/8, \quad s \in \mathbf{N}^* \tag{1.108}$$

Apparently, Eqs. (1.104) are usable only when $n_e \geq 8$. In fact, they also work with less experimental values. When such a situation occurs, the summation limit should be $s = 1$, and the $n_e < 8$ identification constraints arisen from experiments should be accompanied by at least $8 - n_e$ artificial conditions involving the material parameters. For example, if $n_e = 6$, we may enforce the equalities $m_1^{(1)} = n_1^{(1)}$ and $m_2^{(1)} = n_2^{(1)}$.

1.4.2 Basic Identification Procedure

Due to the expandable structure of the yield criterion, many identification strategies can be devised. We shall restrict our discussion to a procedure that uses only normalized yield stresses and r-coefficients obtained from uniaxial and biaxial tensile tests.

Let Y_θ be the yield stress predicted by the yield criterion in the case of a uniaxial traction along the direction defined by the angle θ measured from RD. The planar components of the stress tensor are in this case

$$\sigma_{11}|_\theta = Y_\theta \cos^2\theta, \quad \sigma_{22}|_\theta = Y_\theta \sin^2\theta, \quad \sigma_{12}|_\theta = \sigma_{21}|_\theta = Y_\theta \sin\theta\cos\theta \tag{1.109}$$

After replacing them in Eqs. (1.104), we get the associated equivalent stress

$$\bar{\sigma}|_\theta = Y_\theta F_\theta \tag{1.110}$$

where F_θ is defined by the relationships

$$\begin{aligned}
\frac{F_\theta^{2k}}{w-1} &= \sum_{i=1}^{s}\left\{ w^{i-1}\left\{ \left[L_\theta^{(i)} + M_\theta^{(i)}\right]^{2k} + \left[L_\theta^{(i)} - M_\theta^{(i)}\right]^{2k} \right\} \right. \\
&\quad \left. + w^{s-i}\left\{ \left[M_\theta^{(i)} + N_\theta^{(i)}\right]^{2k} + \left[M_\theta^{(i)} - N_\theta^{(i)}\right]^{2k} \right\} \right\} \\
L_\theta^{(i)} &= \ell_1^{(i)}\cos^2\theta + \ell_2^{(i)}\sin^2\theta \\
M_\theta^{(i)} &= \sqrt{\left[m_1^{(i)}\cos^2\theta - m_2^{(i)}\sin^2\theta\right]^2 + \left[m_3^{(i)}\sin 2\theta\right]^2} \\
N_\theta^{(i)} &= \sqrt{\left[n_1^{(i)}\cos^2\theta - n_2^{(i)}\sin^2\theta\right]^2 + \left[n_3^{(i)}\sin 2\theta\right]^2}
\end{aligned} \tag{1.111}$$

Equations (1.41) and (1.110) lead to the following expression of the normalized uniaxial yield stress:

$$y_\theta = Y_\theta / Y = 1/F_\theta \tag{1.112}$$

The r-coefficient corresponding to the uniaxial traction along a direction inclined at the angle θ measured from RD is defined by the formula

$$r_\theta = \dot{\varepsilon}_{\theta+90^\circ}^{(p)} \Big/ \dot{\varepsilon}_{ND}^{(p)} \tag{1.113}$$

where $\dot{\varepsilon}_{\theta+90^\circ}^{(p)}$ is the plastic strain-rate component associated to the $\theta + 90^\circ$ planar direction, and $\dot{\varepsilon}_{ND}^{(p)}$ is the through-thickness component of the same tensor. After some simple mathematical manipulations, Eq. (1.113) becomes

$$r_\theta = \frac{F_\theta}{G_\theta} - 1 \tag{1.114}$$

where G_θ is defined by the relationships

$$\begin{aligned}
\frac{F_\theta^{2k-1}G_\theta}{w-1} &= \sum_{i=1}^{s}\left\{w^{i-1}\left[\hat{L}_\theta^{(i)}+\hat{M}_\theta^{(i)}\right]\left[L_\theta^{(i)}+M_\theta^{(i)}\right]^{2k-1}\right. \\
&+ w^{i-1}\left[\hat{L}_\theta^{(i)}-\hat{M}_\theta^{(i)}\right]\left[L_\theta^{(i)}-M_\theta^{(i)}\right]^{2k-1} + w^{s-i}\left[\hat{M}_\theta^{(i)}+\hat{N}_\theta^{(i)}\right]\left[M_\theta^{(i)}+N_\theta^{(i)}\right]^{2k-1} \\
&+ \left. w^{s-i}\left[\hat{M}_\theta^{(i)}-\hat{N}_\theta^{(i)}\right]\left[M_\theta^{(i)}-N_\theta^{(i)}\right]^{2k-1}\right\} \\
\hat{L}_\theta^{(i)} &= \ell_1^{(i)}+\ell_2^{(i)} \\
\hat{M}_\theta^{(i)} &= \left[m_1^{(i)}-m_2^{(i)}\right]\left[m_1^{(i)}\cos^2\theta - m_2^{(i)}\sin^2\theta\right]\Big/M_\theta^{(i)} \\
\hat{N}_\theta^{(i)} &= \left[n_1^{(i)}-n_2^{(i)}\right]\left[n_1^{(i)}\cos^2\theta - n_2^{(i)}\sin^2\theta\right]\Big/N_\theta^{(i)}
\end{aligned} \tag{1.115}$$

together with Eqs. (1.111).

Let us denote by Y_b the yield stress predicted in the case of a biaxial traction along RD and TD. The corresponding planar components of the stress tensor are

$$\sigma_{11}|_b = Y_b, \quad \sigma_{22}|_b = Y_b, \quad \sigma_{12}|_b = \sigma_{21}|_b = 0 \tag{1.116}$$

After replacing them in Eqs. (1.104), we get the associated equivalent stress

$$\bar{\sigma}|_b = Y_b F_b \tag{1.117}$$

where F_b is defined by the relationships

$$\begin{aligned}
\frac{F_b^{2k}}{w-1} &= \sum_{i=1}^{s}\left\{w^{i-1}\left\{\left[L_b^{(i)}+M_b^{(i)}\right]^{2k}+\left[L_b^{(i)}-M_b^{(i)}\right]^{2k}\right\}\right. \\
&+ \left. w^{s-i}\left\{\left[M_b^{(i)}+N_b^{(i)}\right]^{2k}+\left[M_b^{(i)}-N_b^{(i)}\right]^{2k}\right\}\right\} \\
L_b^{(i)} &= \ell_1^{(i)}+\ell_2^{(i)},\ M_b^{(i)} = m_1^{(i)}-m_2^{(i)},\ N_b^{(i)} = n_1^{(i)}-n_2^{(i)}
\end{aligned} \tag{1.118}$$

Equations (1.41) and (1.117) lead to the following expression of the normalized biaxial yield stress:

$$y_b = Y_b/Y = 1/F_b \tag{1.119}$$

The r-coefficient corresponding to the biaxial traction along RD and TD is defined by the formula

$$r_b = \dot{\varepsilon}_{TD}^{(p)}\Big/\dot{\varepsilon}_{RD}^{(p)} \tag{1.120}$$

where $\dot{\varepsilon}_{RD}^{(p)}$ and $\dot{\varepsilon}_{TD}^{(p)}$ are the plastic strain-rate components associated to the rolling and transverse directions, respectively. After some simple mathematical manipulations, Eq. (1.120) becomes

$$r_b = \frac{F_b}{G_b} - 1 \tag{1.121}$$

where G_b is defined by the relationships

$$\begin{aligned}
&\frac{F_b^{2k-1} G_b}{w-1} = \sum_{i=1}^{s} \left\{ w^{i-1} \left[\hat{L}_b^{(i)} + \hat{M}_b^{(i)} \right] \left[L_b^{(i)} + M_b^{(i)} \right]^{2k-1} \right. \\
&+ w^{i-1} \left[\hat{L}_b^{(i)} - \hat{M}_b^{(i)} \right] \left[L_b^{(i)} - M_b^{(i)} \right]^{2k-1} + w^{s-i} \left[\hat{M}_b^{(i)} + \hat{N}_b^{(i)} \right] \left[M_b^{(i)} + N_b^{(i)} \right]^{2k-1} \\
&\left. + w^{s-i} \left[\hat{M}_b^{(i)} - \hat{N}_b^{(i)} \right] \left[M_b^{(i)} - N_b^{(i)} \right]^{2k-1} \right\} \\
&\hat{L}_b^{(i)} = \ell_1^{(i)}, \quad \hat{M}_b^{(i)} = m_1^{(i)}, \quad \hat{N}_b^{(i)} = n_1^{(i)}
\end{aligned} \tag{1.122}$$

together with Eqs. (1.118).

An identification procedure that strictly enforces a large number of experimental constraints on the yield criterion would be inefficient in practical applications. The failure probability of such a strategy increases when the external restrictions become stronger. Taking into account this aspect, the authors have developed an identification procedure based on the minimization of the following error-function:

$$\begin{aligned}
&E\left[\ell_1^{(i)}, \ell_2^{(i)}, m_1^{(i)}, m_2^{(i)}, m_3^{(i)}, n_1^{(i)}, n_2^{(i)}, n_3^{(i)} \middle| i = 1, \ldots, s \right] \\
&= \sum_{\theta_j} \left[\frac{y_{\theta_j}^{(\exp)}}{y_{\theta_j}} - 1 \right]^2 + \sum_{\theta_j} \left[r_{\theta_j}^{(\exp)} - r_{\theta_j} \right]^2 + \left[\frac{y_b^{(\exp)}}{y_b} - 1 \right]^2 + \left[r_b^{(\exp)} - r_b \right]^2
\end{aligned} \tag{1.123}$$

where θ_j represents an individual element from a finite set of angles defining the orientation of the specimens used in the uniaxial tensile tests. One may notice that Eq. (1.123) describes a square-distance between the experimental and predicted values of the anisotropy characteristics.

Two versions of the BBC 2008 yield criterion have been evaluated from the point of view of their performances (see (Comsa and Banabic 2008)). They include 8 and 16 material coefficients, respectively, and correspond to the smallest values of the summation limit ($s = 1$ and $s = 2$). The identification of the BBC 2008

(16 parameters) model has been performed using the following mechanical parameters: $y_{0^\circ}^{(\exp)}$, $y_{15^\circ}^{(\exp)}$, $y_{30^\circ}^{(\exp)}$, $y_{45^\circ}^{(\exp)}$, $y_{60^\circ}^{(\exp)}$, $y_{75^\circ}^{(\exp)}$, $y_{90^\circ}^{(\exp)}$, $y_b^{(\exp)}$, $r_{0^\circ}^{(\exp)}$, $r_{15^\circ}^{(\exp)}$, $r_{30^\circ}^{(\exp)}$, $r_{45^\circ}^{(\exp)}$, $r_{60^\circ}^{(\exp)}$, $r_{75^\circ}^{(\exp)}$, $r_{90^\circ}^{(\exp)}$ and $r_b^{(\exp)}$. In the case of BBC 2008 (8 parameters), the input data has been restricted to the values $y_{0^\circ}^{(\exp)}$, $y_{45^\circ}^{(\exp)}$, $y_{90^\circ}^{(\exp)}$, $y_b^{(\exp)}$, $r_{0^\circ}^{(\exp)}$, $r_{45^\circ}^{(\exp)}$, $r_{90^\circ}^{(\exp)}$ and $r_b^{(\exp)}$.

The predictions of the BBC (2008) model with 16 parameters are superior to those given by the 8-parameter version. The improvement is noticeable especially in the case of the r-coefficients. This capability of the 16-parameter version is relevant for the accurate prediction of the thickness when simulating sheet metal forming processes. For the materials exhibiting a distribution of the anisotropy characteristics that would lead to the occurrence of 8 ears in a cylindrical deep-drawing process (Yoo 2006) the planar distribution of the *r*-coefficient predicted by the BBC (2008) yield criterion with 8 parameters is very inaccurate (see (Comsa and Banabic 2008)). This model would not be able to predict the occurrence of more than 4 ears at the top edge of a cup deep-drawn from a circular blank. In contrast, the variation of the r-coefficient described by BBC 2008 with 16 parameters closely follows the reference data. In conclusion, this model would predict the occurrence of 8 ears as reported by Yoon et al. (2006). As compared with other formulations described in the literature, the new model does not use linear transformations of the stress tensor. Due to this fact, its computational efficiency should be superior in the simulation of sheet metal forming processes.

1.4.3 Enhanced Identification Procedure

It is forthright to realize that the identification procedure outlined in Sect. 1.4.2 uses data points that can be obtained by means of relatively uncomplicated mechanical tests. These tests are typically standardized, which is of a clear advantage to reliability and reproducibility of the results, but they do not explore all relevant deformation modes. Owing to a recent progress in mechanical testing, several more advanced techniques become technically feasible. These include biaxial stress setups, such as the ISO-standardized cruciform shape test (Kuwabara et al. 2002; Kuwabara 2007; ISO 2013) or the multiaxial tube expansion test (Kuwabara and Sugawara 2013) that allow one to study the anisotropic behaviour of sheet metals under more complex loading conditions. The Digital Image Correlation (DIC) technique can provide accurate readings of strain fields in a broad spectrum of experiments. Yet another alternative is to use crystal plasticity models, further elaborated in Chap. 3, which can provide almost unlimited number of data points that the calibration procedure could exploit. In many cases there is more experimental data available than would be needed to calibrate a flexible and generously parameterised yield locus model. This abundance of data can only be utilized if some extensions to the calibration method are introduced.

The identification procedure outlined in Sect. 1.4.2 can be then further extended and generalized with the aim to consider a broader group of data points. The

generalization may also take into account various nature of inputs that can be provided in calibration of the yield criteria (Gawad et al. 2015). Let $\mathbf{p}$ denote an N-dimensional vector that parameterizes the yield criterion. The vector $\mathbf{p}$ can be in principle found from the minimization of the vector-valued error function $\mathbf{E}: \mathbb{R}^N \rightarrow \mathbb{R}^M$:

$$\begin{aligned} \mathbf{E}(\mathbf{p}) &= \{\Delta\mathbf{Y}_1(\mathbf{p}), \ldots, \Delta\mathbf{Y}_i(\mathbf{p}), \ldots, \Delta\mathbf{Y}_M(\mathbf{p})\}^T \\ &= \{v_1 - f_1(\mathbf{p}), \ldots, v_i - f_i(\mathbf{p}), \ldots, v_M - f_M(\mathbf{p})\}^T \end{aligned} \tag{1.124}$$

To calculate the residuals $v_i - f_i(\mathbf{p})$, the error-function considers M data points $v_1, \ldots, v_M$, which are typically obtained from a series of different experiments. Regardless of the means how the data points have been acquired, they all serve as the reference data for the calibration of the yield locus. The quantities $v_i, i = 1, \ldots, M$, are in general non-commensurable, thus a proper scaling may be necessary to make them dimensionless. To emphasize the physical meaning of the components in $\mathbf{E}$, one may conveniently group the residuals into K sub-vectors:

$$\mathbf{E}(\mathbf{p}) = \{\Delta\mathbf{Y}_1(\mathbf{p}), \ldots, \Delta\mathbf{Y}_i(\mathbf{p}), \ldots, \Delta\mathbf{Y}_K(\mathbf{p})\}^T \tag{1.125}$$

where the contributions $\Delta\mathbf{Y}_i$ are differences between the quantities derived from the yield locus and the corresponding calibration data of a given type i. The contributions $\Delta\mathbf{Y}_i$ can be further parameterized, e.g. by adding parameters that control the data acquisition (e.g. parameters of the experiments).

The minimization problem can be conveniently solved by means of general non-linear least squares solvers, such as the Levenberg-Marquardt or the Trust Region algorithms. From the mathematical point of view, the uniqueness of the solution requires that $N \leq M$, but this is not a sufficient condition. Furthermore, as in many optimization problems, many local minima may be encountered. These issues can be alleviated if the identification problem is posed as an over-determined minimization, i.e. $N < M$, or in other words, an over-determined least squares problem. The solution is then constrained by more equations, and by the consequence the solution has to simultaneously fulfil more requirements.

Another difficulty is related to the choice of the calibration data, which in principle should be done in such a way that most of relevant deformation modes are sampled. On one hand, the data points should sufficiently reflect the size of the yield locus. On the other hand, they should provide a link between the direction of the yield stress and resulting plastic strain, therefore also the shape of the yield locus could be determined.

Another difficulty is related to the choice of the calibration data, which in principle should be done in such a way that most of relevant deformation modes are sampled. On one hand, the data points should sufficiently reflect the size of the yield locus. On the other hand, they should provide a link between the direction of the yield stress and resulting plastic strain, therefore also the shape of the yield locus could be determined.

Let us consider the BBC (2008) plane stress yield criterion as an example of a yield locus model. Suppose the criterion contains 16 parameters assembled in the vector $\mathbf{p}$, therefore it can be calibrated by supplying at least 16 data points. Following the formalism introduced in (1.125), let us define the error-function

$$\mathbf{E}(\mathbf{p}) = \begin{Bmatrix} w_y \Delta \mathbf{y}(\mathbf{p}) \\ w_r \Delta \mathbf{r}(\mathbf{p}) \\ w_{yb} \Delta \mathbf{y}_b(\mathbf{p}) \\ w_{rb} \Delta \mathbf{r}_b(\mathbf{p}) \\ w_S \Delta \mathbf{S}(\mathbf{p}) \\ w_\beta \Delta \boldsymbol{\beta}(\mathbf{p}) \end{Bmatrix} \tag{1.126}$$

that takes into account the residual error with respect to the uniaxial yield stresses $\Delta \mathbf{y}$, Lankford coefficient (uniaxial r-values) $\Delta \mathbf{r}$, balanced biaxial tensile yield stress $\Delta \mathbf{y}_b$, and the corresponding r_b- value, respectively, as well as yield stresses for arbitrary plane stress ratios $\Delta \mathbf{S}$ and the corresponding normals to the yield locus $\Delta \boldsymbol{\beta}$. The weighing factors w_y, w_r, w_{yb}, w_{rb}, w_S, and w_β allow one to control the relative importance of the individual components.

The components of vectors $\Delta \mathbf{y}(\mathbf{p})$ and $\Delta \mathbf{r}(\mathbf{p})$ include the residuals pertaining to the series of n uniaxial tensile tests performed at the angles α_i with respect to RD:

$$\Delta \mathbf{y}(\mathbf{p}) = \left\{ 1 - \frac{y(\mathbf{p}, \alpha_1)}{y^{(\exp)}(\alpha_1)}, \ldots, 1 - \frac{y(\mathbf{p}, \alpha_n)}{y^{(\exp)}(\alpha_n)} \right\}^T \tag{1.127}$$

$$\Delta \mathbf{r}(\mathbf{p}) = \left\{ 1 - \frac{r(\mathbf{p}, \alpha_1)}{r^{(\exp)}(\alpha_1)}, \ldots, 1 - \frac{r(\mathbf{p}, \alpha_n)}{r^{(\exp)}(\alpha_n)} \right\}^T \tag{1.128}$$

where $y^{(\exp)}(\alpha)$ and $y(\mathbf{p}, \alpha)$ denote the yield stress in the direction α and its counterpart derived from the yield criterion (1.104), respectively, while $r^{(\exp)}(\alpha)$ and $r(\mathbf{p}, \alpha)$ are the r-values obtained in analogous way. The residual errors regarding the balanced biaxial point are calculated likewise:

$$\Delta \mathbf{y}_b(\mathbf{p}) = \left\{ 1 - \frac{y_b(\mathbf{p})}{y_b^{(\exp)}} \right\}^T \tag{1.129}$$

$$\Delta \mathbf{r}_b(\mathbf{p}) = \left\{ 1 - \frac{r_b(\mathbf{p})}{r_b^{(\exp)}} \right\}^T \tag{1.130}$$

Equation (1.126) introduces the terms $\Delta \mathbf{S}(\mathbf{p})$ and $\Delta \boldsymbol{\beta}(\mathbf{p})$ that provide additional constraints on the solution in the regions of the yield locus that can be specified by a ratio between σ_{11} and σ_{22} and the value of the shear stress $\tau = \sigma_{12}$:

$$\Delta \mathbf{S}(\mathbf{p}) = \left\{ 1 - \frac{S(\mathbf{p}, \theta_1, \tau_1)}{S^{(\exp)}(\theta_1, \tau_1)}, \ldots, 1 - \frac{S(\mathbf{p}, \theta_m, \tau_n)}{S^{(\exp)}(\theta_m, \tau_n)} \right\}^T \tag{1.131}$$

$$\Delta \boldsymbol{\beta}(\mathbf{p}) = \left\{ \cos\left(\beta^{(\exp)}(\theta_1, \tau_1) - \beta_1(\mathbf{p}, \theta_1, \tau_1)\right), \ldots, \cos\left(\beta^{(\exp)}(\theta_m, \tau_n) - \beta_m(\mathbf{p}, \theta_m, \tau_n)\right) \right\}^T \tag{1.132}$$

As a matter of convenience, the angle θ is used to express the relation between the σ_{11} and σ_{22} components: $\tan\theta = \sigma_{22}/\sigma_{11}$. The magnitude of the yield stress in the direction given by the angle θ is denoted as $S(\mathbf{p}, \theta, \tau)$. The normal to the yield contour and the σ_{11} direction form the angle $\beta(\theta)$. Figure 1.1 presents the relations between these quantities in a normalized yield section. From the normality rule, $\beta(\theta)$ corresponds to the direction of the plastic strain rate. In principle, both quantities can be measured experimentally, e.g. (Kuwabara et al. 2002; Kuwabara 2007). Therefore, the amount of information acquired from the data points can be maximized by capturing the size of the yield locus and its curvature at the same time. Furthermore, two special cases can be considered: $\beta(\theta) = 0°$ and $\beta(\theta) = 90°$, which correspond to the plane strain conditions, provided that $\tau = 0$.

It can be expected that some local minima of the function (1.123) would not be necessarily the extreme values of $\|\mathbf{E}(\mathbf{p})\|$, since the latter uses also other terms to quantify the quality of the solution. Figure 1.2 exemplifies such a case. The figure compares two solutions of the BBC (2008) p 16 identification problem. The method that makes use of Eq. (1.123) is referred to as the *basic identification*, while the *enhanced identification* exploits the function (1.126). The calibration data (marked with symbols) comprises all the data points needed by both methods. Although the yield locus section shown in Fig. 1.2d includes the calibration points that correspond to the uniaxial and balanced biaxial tension, the contributions from these

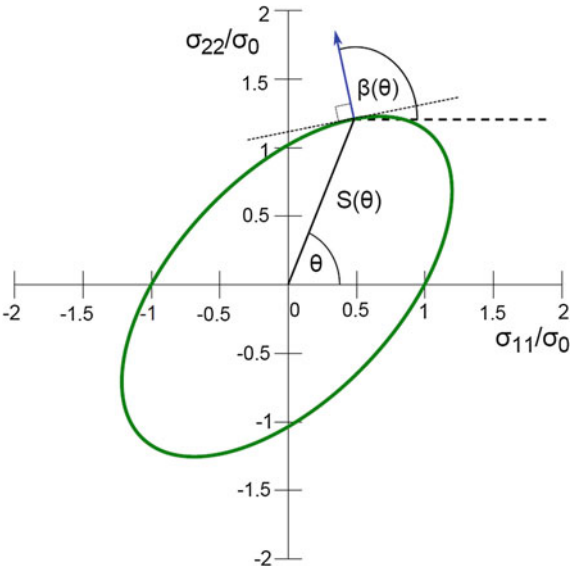

Fig. 1.1 Schematic illustration of $S(\theta)$ and $\beta(\theta)$ in a normalized yield locus section. The direction of σ_{11} coincides with RD, while σ_{22} is parallel to TD. $S(\theta)$ denotes the distance from the origin to the yield locus, while $\beta(\theta)$ is the angle between the normal to the yield locus and σ_{11} direction

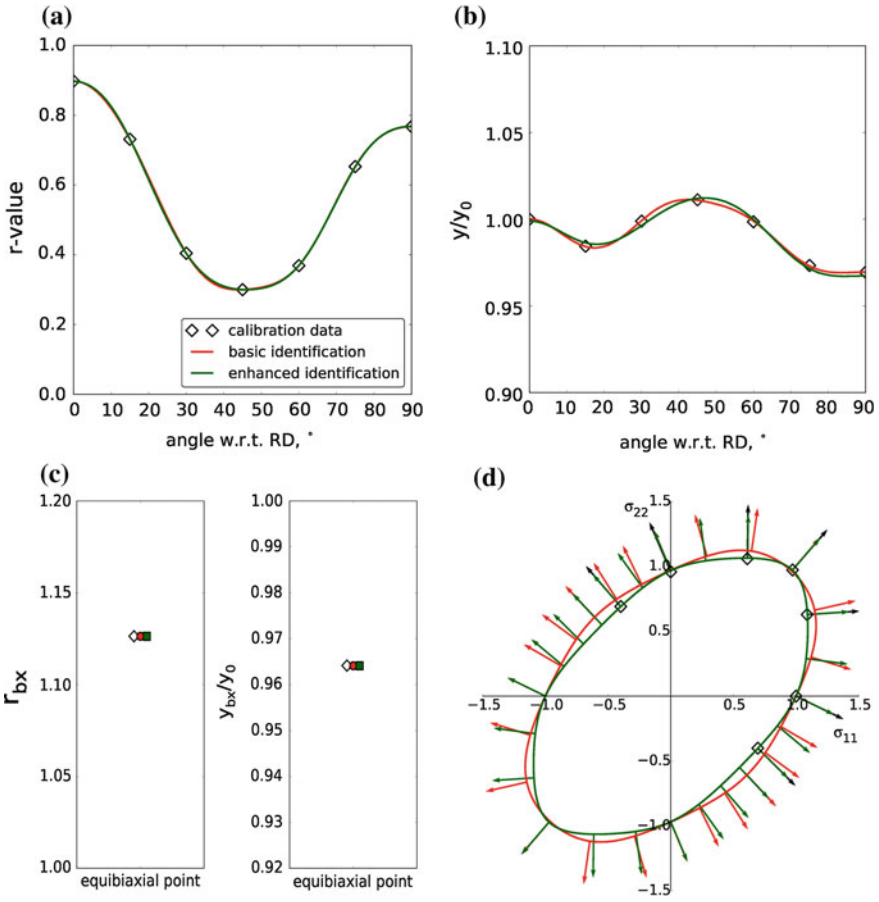

Fig. 1.2 Comparison of BBC (2008) p 16 calibrated by means of the basic identification procedure (1.123) and the enhanced procedure, which utilizes (1.127)–(1.132). **a** *r*-value, **b** the scaled uniaxial yield stress, **c** balanced biaxial *r*-value and scaled balanced biaxial yield stress, **d** contour of the yield locus in the σ_{11}—σ_{22} section. The calibration data points are marked with *black* symbols. The *arrows* denote the normal directions to the yield locus sections. The *arrows* related to the calibration points are drawn longer merely for a clearer visual appearance

points were not used in (1.131) and (1.132), since they are already tackled by the terms (1.127)–(1.130). For the sake of simplicity, only the yield locus section with no shear component is considered, thus $\tau = 0$ in (1.131)–(1.132).

To localize the minima of the respective error functions, the Levenberg-Marquardt algorithm was followed. For each function the identification procedure started from an identical initial guess and it was carried out until good numerical convergence was reached. As seen in Figs. 1.2a, b, both runs result in a very accurate prediction of the *r*-values and uniaxial yield stresses over a broad range of directions. In this respect, it is hard to discriminate between the calibration data and the BBC (2008) p 16 approximation, even though the minimization of the

function (1.123) appears to perform slightly better in terms of the normalized uniaxial yield stresses. The balanced biaxial tension is ideally reproduced in both cases, as can be seen in Fig. 1.2c.

However, from the normalized yield locus sections shown in Fig. 1.2d it emerges that the enhanced identification method provides much higher fidelity of the yield locus approximation. The figure reveals considerable discrepancies if the basic identification algorithm is used. The divergence is particularly striking in the regions that are distant from the uniaxial or balanced biaxial stress states, which are the only points in that section that the basic method considers.

The enhanced identification method can benefit from both the size of the yield surface and its curvature. It is worth mentioning that these two contributions (from the components (1.131) and (1.132), respectively) are in many cases complementary. For instance, in Fig. 1.2d the points at $\theta = 135^{\circ}$ on the green and red curves are clearly different in terms of the distance $S(\theta)$, yet there is hardly any difference with respect to the angle $\beta(\theta)$. If the point at $\theta = 15^{\circ}$ is considered, the deviation with regard to the contour curvature noticeably prevails.

1.5 3D Extensions of the BBC (2005, 2008) Yield Criteria

The methodology proposed by van Riel and van den Boogaard (2007) allows extending the BBC (2005, 2008 yield criteria to 3D formulations. These formulations can be expressed generically as follows:

$$\bar{\sigma}(\sigma_{11} - \sigma_{33}, \sigma_{22} - \sigma_{33}, \sigma_{12}, \sigma_{21}, \sigma_{23}, \sigma_{32}, \sigma_{31}, \sigma_{13}) = Y. \tag{1.133}$$

In the above relationship, the symbols $\sigma_{ij} = \sigma_{ji}, i,j \in \{1,2,3\}$, denote Cartesian components of the Cauchy stress tensors expressed in a basis superimposed to the plastic orthotropy axes (by convention, the indices of the stress components are associated to the rolling direction (1), transverse direction (2), and normal direction (3)), $\bar{\sigma} \geq 0$ is the equivalent stress (first-degree homogeneous function of the Cauchy stresses $\sigma_{ij} = \sigma_{ji}, i,j \in \{1,2,3\}$), and $Y > 0$ is the yield parameter.

The 3D extension of the BBC (2005) equivalent stress involved in Eq. (1.133) reads (see Eqs. (1.47) and (1.48) for comparison)

$$\begin{aligned}\bar{\sigma}^2 = &\left[a(\Lambda+\Gamma)^{2k} + a(\Lambda-\Gamma)^{2k} + b(\Lambda+\Psi)^{2k} + b(\Lambda-\Psi)^{2k}\right]^{\frac{1}{k}} \\ &+ 3(\sigma_{23}\sigma_{32} + \sigma_{31}\sigma_{13}),\end{aligned} \tag{1.134}$$

where $k \in \mathbf{N}^*$ and $a, b > 0$ are material parameters, while Γ, Λ and Ψ are functions depending on $\sigma_{11} - \sigma_{33}$, $\sigma_{22} - \sigma_{33}$, and $\sigma_{12} = \sigma_{21}$:

$$\begin{aligned}
\Gamma &= L(\sigma_{11}-\sigma_{33})+M(\sigma_{22}-\sigma_{33})\\
\Lambda &= \sqrt{\left[N(\sigma_{11}-\sigma_{33})-P(\sigma_{22}-\sigma_{33})\right]^2+\sigma_{12}\sigma_{21}}\\
\Psi &= \sqrt{\left[Q(\sigma_{11}-\sigma_{33})-R(\sigma_{22}-\sigma_{33})\right]^2+\sigma_{12}\sigma_{21}}
\end{aligned} \tag{1.135}$$

The coefficients L, M, N, P, Q, and R involved in Eqs. (1.135) are also material parameters. In the case of the BBC (2008) equivalent stress, the 3D extension is (see Eqs. (1.104) for comparison)

$$\begin{aligned}
\bar{\sigma}^2 &= \left\{(w-1)\sum_{i=1}^{s}\left\{w^{i-1}\left\{\left[L^{(i)}+M^{(i)}\right]^{2k}+\left[L^{(i)}-M^{(i)}\right]^{2k}\right\}\right.\right.\\
&\quad \left.\left.+\ w^{s-i}\left\{\left[M^{(i)}+N^{(i)}\right]^{2k}+\left[M^{(i)}-N^{(i)}\right]^{2k}\right\}\right\}\right\}^{\frac{1}{k}}\\
&\quad +\ 3(\sigma_{23}\sigma_{32}+\sigma_{31}\sigma_{13})\\
k,s\in\mathbf{N}^*, w &= (3/2)^{1/s}>1\\
L^{(i)} &= \ell_1^{(i)}(\sigma_{11}-\sigma_{33})+\ell_2^{(i)}(\sigma_{22}-\sigma_{33})\\
M^{(i)} &= \sqrt{\left[m_1^{(i)}(\sigma_{11}-\sigma_{33})-m_2^{(i)}(\sigma_{22}-\sigma_{33})\right]^2+\left[m_3^{(i)}(\sigma_{12}+\sigma_{21})\right]^2}\\
N^{(i)} &= \sqrt{\left[n_1^{(i)}(\sigma_{11}-\sigma_{33})-n_2^{(i)}(\sigma_{22}-\sigma_{33})\right]^2+\left[n_3^{(i)}(\sigma_{12}+\sigma_{21})\right]^2}\\
&\ell_1^{(i)},\ell_2^{(i)},m_1^{(i)},m_2^{(i)},m_3^{(i)},n_1^{(i)},n_2^{(i)},n_3^{(i)}\in\mathbf{R}.
\end{aligned} \tag{1.136}$$

Because Eqs. (1.133)–(1.136) reduce to the 2D formulations of the BBC (2005, 2008) yield criteria by enforcing $\sigma_{i3}=\sigma_{3i}=0, i\in\{1,2,3\}$, the 3D versions of both plasticity models can be efficiently adapted to finite elements accommodating either 2D or 3D stress states. One may also notice that the 2D identification procedures of the BBC (2005, 2008) yield criteria are still usable for calibrating their 3D versions.

1.6 Advanced Anisotropic Yield Criteria

During the last years, the competition in the automotive and aeronautical industry has become more intense. This fact has lead to the development of new steel alloys (Bake Hardenable, Dual Phase, Complex Phase, Transformation Induced Plasticity-TRIP, Martensitic Steels, Hot-stamping boron-alloyed steels), aluminium alloys having better performances and increased interest on the use of magnesium and superplastic alloys. Since 2000, the modelling of the anisotropic behaviour of

these materials has encouraged the research activities focused on the development of yield criteria. Several new models have been proposed during the last years. These models allow a very good description of the anisotropic behaviour both of steel alloys (BCC crystallographic structure), aluminium alloys (FCC structure) and magnesium alloys (HCP structure). The new yield criteria incorporate a large number of coefficients (usually, at least 8 coefficients). Due to this fact, they are able to give an accurate description of the yield surface and follow closely the planar variations of the uniaxial yield stress and the coefficient of plastic anisotropy. Even more, some of the recently developed models can also capture the non-symmetric response in tension/compression specific to the HCP alloys. Due to the significant impact of these advanced yield criteria, they are described in a separate subchapter entitled 'Advanced Anisotropic Yield Criteria'.

1.6.1 Barlat Yield Criteria

In order to remove the disadvantages of the Barlat 1994 and Barlat 1996 yield criteria, but aiming to preserve their flexibility, Barlat proposed in 2000 (Barlat et al. 2000, 2003) a new model particularized for plane stress (2D). Barlat considers a linear transformation defined as follows:

$$X = \mathrm{C} \cdot \boldsymbol{s} \tag{1.137}$$

where $\boldsymbol{s}$ is the deviatoric stress tensor and $\mathbf{X}$ is the linearly transformed stress tensor. This gives 9 independent anisotropy coefficients for the general case and 7 for plane stress. However, when applied to plane stress conditions, only one coefficient is available to account for σ_{45} and r_{45}. As pointed out in Barlat et al. (2003) additional coefficients in the context of linear transformations can be obtained by using two transformations associated to different isotropic yield functions, respectively. As a consequence, Barlat et al. (2003) proposed a yield function expressed by the relationship

$$\Phi = \Phi' + \Phi'' = 2\sigma^a, \tag{1.138}$$

where

$$\Phi' = |S_1 - S_2|^a \tag{1.139}$$

and

$$\Phi'' = |2\mathrm{S}_2 + \mathrm{S}_1|^{\mathrm{a}} + |2\mathrm{S}_2 + \mathrm{S}_2|^{\mathrm{a}} \tag{1.140}$$

S_1, and S_2 are principal deviatoric stresses and 'a' is an exponent depending on the crystallographic structure of the material. Applying a linear transformation to each

of the isotropic functions defined by Eqs. (1.139) and (1.140) one obtains the yield function

$$\Phi = \Phi'(X') + \Phi''(X'') = 2\bar{\sigma}^a \tag{1.141}$$

where $\bar{\sigma}$ is the effective stress, a is a material coefficient and

$$\Phi' = \left|X'_1 + X'_2\right|^a \tag{1.142}$$

$$\Phi'' = \left|2X''_2 + X''_1\right|^a + \left|2X''_1 + X''_2\right|^a \tag{1.143}$$

and

$$\begin{aligned} \mathbf{X}' &= \mathbf{C}'.\mathbf{s} = \mathbf{C}'.\mathbf{T}.\boldsymbol{\sigma} = \mathbf{L}'.\boldsymbol{\sigma} \\ \mathbf{X}'' &= \mathbf{C}''.\mathbf{s} = \mathbf{C}''.\mathbf{T}.\boldsymbol{\sigma} = \mathbf{L}''.\boldsymbol{\sigma} \end{aligned} \tag{1.144}$$

$\mathbf{T}$ is a matrix that transforms the Cauchy stress tensor $\boldsymbol{\sigma}$ into its deviator $\mathbf{s}$:

$$\mathbf{T} = \begin{bmatrix} 2/3 & -1/3 & 0 \\ -1/3 & 2/3 & 0 \\ 0 & 0 & 1 \end{bmatrix} \tag{1.145}$$

$\boldsymbol{C}'$ and $\boldsymbol{C}''$ being the linear transformations. In the reference frame associated with the material symmetry,

$$\begin{bmatrix} X'_{11} \\ X'_{22} \\ X'_{12} \end{bmatrix} = \begin{bmatrix} C'_{11} & C'_{12} & 0 \\ C'_{21} & C'_{22} & 0 \\ 0 & 0 & C'_{66} \end{bmatrix} \begin{bmatrix} s_{11} \\ s_{22} \\ s_{12} \end{bmatrix} \tag{1.146}$$

and

$$\begin{bmatrix} X''_{11} \\ X''_{22} \\ X''_{12} \end{bmatrix} = \begin{bmatrix} C''_{11} & C''_{12} & 0 \\ C''_{21} & C''_{22} & 0 \\ 0 & 0 & C''_{66} \end{bmatrix} \begin{bmatrix} s_{11} \\ s_{22} \\ s_{12} \end{bmatrix} \tag{1.147}$$

Because Φ' depends on $X'_1 - X'_2$, only three coefficients remain independent in $\boldsymbol{C}'$ (see more details in (Barlat et al. 2003)). There are five independent coefficients in $\boldsymbol{C}''$. In both transformations, there are 8 independent anisotropy coefficients.

The principal values X_1 and X_2 of there X' and X'' are as follows:

$$X_1 = \frac{1}{2}\left(X_{11} + X_{22} + \sqrt{(X_{11} - X_{22})^2 + 4X_{12}^2}\right), \tag{1.148}$$

$$X_2 = \frac{1}{2}\left(X_{11} + X_{22} - \sqrt{(X_{11} - X_{22})^2 + 4X_{12}^2}\right). \tag{1.149}$$

The coefficients of $\mathbf{L}'$ and $\mathbf{L}''$ are

$$\begin{bmatrix} L'_{11} \\ L'_{12} \\ L'_{21} \\ L'_{22} \\ L'_{66} \end{bmatrix} = \begin{bmatrix} 2/3 & 0 & 0 \\ -1/3 & 0 & 0 \\ 0 & -1/3 & 0 \\ 0 & 2/3 & 0 \\ 0 & 0 & 1 \end{bmatrix} \begin{bmatrix} \alpha_1 \\ \alpha_2 \\ \alpha_7 \end{bmatrix} \tag{1.150}$$

$$\begin{bmatrix} L''_{11} \\ L''_{12} \\ L''_{21} \\ L''_{22} \\ L''_{66} \end{bmatrix} = \frac{1}{9}\begin{bmatrix} -2 & 2 & 8 & -2 & 0 \\ 1 & -4 & -4 & 4 & 0 \\ 4 & -4 & -4 & 1 & 0 \\ -2 & 8 & 2 & -2 & 0 \\ 0 & 0 & 0 & 0 & 1 \end{bmatrix} \begin{bmatrix} \alpha_3 \\ \alpha_4 \\ \alpha_5 \\ \alpha_6 \\ \alpha_8 \end{bmatrix} \tag{1.151}$$

Due to the fact that 8 coefficients are incorporated in the linear transformations, 8 material characteristics are needed for identification. The uniaxial tension test along the rolling, diagonal and transversal directions, together with the biaxial tension test can provide only 7 characteristics (3 uniaxial yield stresses, 3 coefficients of uniaxial anisotropy and the biaxial yield stress). Barlat adopted the coefficient of biaxial anisotropy r_b as the eighth characteristic in the identification procedure.

By using the same methodology as the one described above, Barlat et al. (2005) proposed a 3D yield criterion called Barlat 2004–18p:

$$\begin{aligned} \Phi = &\left|s'_1 - s''_1\right|^a + \left|s'_1 - s''_2\right|^a + \left|s'_1 - s''_3\right|^a + \left|s'_2 - s''_1\right|^a + \left|s'_2 - s''_2\right|^a + \\ &+ \left|s'_2 - s''_3\right|^a + \left|s'_3 - s''_1\right|^a + \left|s'_3 - s''_2\right|^a + \left|s'_3 - s''_3\right|^a = 4\bar{\sigma}^a, \end{aligned} \tag{1.152}$$

where, $\bar{\sigma}$ represents the uniaxial yield stress (any other yield stress may be use as reference yield stress) and a is an exponent determined based on the crystallographic structure of the material. The associated linear transformation on the stress deviator is defined as follows:

$$\mathbf{C} = \begin{bmatrix} 0 & -c_{12} & -c_{13} & 0 & 0 & 0 \\ -c_{21} & 0 & -c_{23} & 0 & 0 & 0 \\ -c_{31} & -c_{32} & 0 & 0 & 0 & 0 \\ 0 & 0 & 0 & c_{44} & 0 & 0 \\ 0 & 0 & 0 & 0 & c_{55} & 0 \\ 0 & 0 & 0 & 0 & 0 & c_{66} \end{bmatrix} \tag{1.153}$$

and $\boldsymbol{C}'$ and $\boldsymbol{C}''$ are obtained by adding prime and double prime symbols. Each transformation provides 9 coefficients and totally both transformations give 18 coefficients. In order to determine all this coefficients an the minimization of the error function method is used (see (Banabic et al. 2000)). If only one linear transformation is assumed the Barlat 2004–18p formulation reduces to Banabic et al. (2005) yield criterion.

The uniaxial yield stresses and anisotropy coefficients in seven directions in the plane of the sheet (0, 15, 30, 45, 60, 75 and 90° to the rolling direction), the biaxial yield stress, the biaxial anisotropy coefficient and four additional data characterizing out-of-plane properties (two tensile and two simple shear yield stresses) are used in the identification of all the coefficients. For the determination of the out-of-plane parameters, crystal plasticity models are also needed (see (Barlat et al. 2005)).

If one adopts a yield function defined by the relationship

$$\begin{aligned}\Phi = &\left|s_1' - s_2''\right|^a + \left|s_2' - s_3''\right|^a + \left|s_3' - s_1''\right|^a - \left\{\left|s_1'\right|^a + \left|s_2'\right|^a + \left|s_3'\right|^a\right\} \\ &+ \left|s_1''\right|^a + \left|s_2''\right|^a + \left|s_3''\right|^a = 4\bar{\sigma}^a,\end{aligned} \tag{1.154}$$

the number of coefficients included in the linear transformations will reduce to 13:

$$\mathrm{C}' = \begin{bmatrix} 0 & -1 & -c_{13}' & 0 & 0 & 0 \\ -c_{21}' & 0 & -c_{23}' & 0 & 0 & 0 \\ -1 & -1 & 0 & 0 & 0 & 0 \\ 0 & 0 & 0 & c_{44}' & 0 & 0 \\ 0 & 0 & 0 & 0 & c_{55}' & 0 \\ 0 & 0 & 0 & 0 & 0 & c_{66}' \end{bmatrix} 0 \tag{1.155}$$

$$\mathrm{C}'' = \begin{bmatrix} 0 & -c_{12}'' & -c_{13}'' & 0 & 0 & 0 \\ -c_{21}'' & 0 & -c_{23}'' & 0 & 0 & 0 \\ -1 & -1 & 0 & 0 & 0 & 0 \\ 0 & 0 & 0 & c_{44}'' & 0 & 0 \\ 0 & 0 & 0 & 0 & c_{55}'' & 0 \\ 0 & 0 & 0 & 0 & 0 & c_{66}'' \end{bmatrix} 0 \tag{1.156}$$

For the plane stress case the number of coefficients reduces from 13 to 9.

The yield function has been tested for different aluminium alloys exhibiting a pronounced anisotropy. The model has proved its capability to provide an accurate prediction of the planar variations of the uniaxial yield stress and coefficient of plastic anisotropy.

The implementation of the Barlat 2004–18p model in finite-element codes (Yoon et al. 2006) has proved its capability to predict the occurrence of six and eight ears in the process of cup drawing. This is the most important advantage of the yield criterion. Of course, it is possible to develop models incorporating more and more linear transformations and thus having a larger number of coefficients. The practical difficulty related to the use of such yield criteria consists in the

experimental determination of the mechanical parameters needed for the evaluation of the coefficients. The disadvantages of the models presented above are:

- Due to the complexity of the formulation, they are not user-friendly.
- They need crystal plasticity models for the evaluation of some parameters.

1.6.2 Cazacu-Barlat Yield Criteria

To introduce orthotropy in the expression of an isotropic criterion, (Cazacu and Barlat 2001) proposed an alternative method based on the theory of representation of tensor functions. They developed a method for generalizing the invariants of the stress deviator J_2 and J_3. Based on this method, an anisotropic yield criterion is obtained by substituting the expression of the stress deviator invariants in the isotropic criterion by their respective anisotropic forms.

The generalized forms of the invariants, J_3^o and J_2^o, respectively, are:

$$\begin{aligned} J_3^o = & \frac{1}{27}(b_1+b_2)\sigma_{11}^3 + \frac{1}{27}(b_3+b_4)\sigma_{22}^3 + \frac{1}{27}[2(b_1+b_4)-b_2-b_3]\sigma_{33}^3 \\ & - \frac{1}{9}(b_1\sigma_{22}+b_2\sigma_{33})\sigma_{11}^2 - \frac{1}{9}(b_3\sigma_{33}+b_4\sigma_{11})\sigma_{22}^2 \\ & - \frac{1}{9}[(b_1-b_2+b_4)\sigma_{11}+(b_1-b_3+b_4)\sigma_{22}]\sigma_{33}^2 \\ & + \frac{2}{9}(b_1+b_4)\sigma_{11}\sigma_{22}\sigma_{33} - \frac{\sigma_{xz}^2}{3}[2b_9\sigma_{22}-b_8\sigma_{33}-(2b_9-b_8)\sigma_{11}] \\ & - \frac{\sigma_{12}^2}{3}[2b_{10}\sigma_{33}-b_5\sigma_{22}-(2b_{10}-b_5)\sigma_{11}] - \frac{\sigma_{23}^2}{3}[(b_6+b_7)\sigma_{11}-b_6\sigma_{22}-b_7\sigma_{33}] \\ & + 2b_{11}\sigma_{12}\sigma_{13}\sigma_{23}. \end{aligned} \tag{1.157}$$

where the coefficients b_k (k = 1, …, 11) describe the anisotropy and reduce to unity for isotropic conditions.

$$J_2^o = \frac{a_1}{6}(\sigma_{11}-\sigma_{22})^2 + \frac{a_2}{6}(\sigma_{22}-\sigma_{33})^2 + \frac{a_3}{6}(\sigma_{11}-\sigma_{33})^2 + a_4\sigma_{12}^2 + a_5\sigma_{13}^2 + a_6\sigma_{23}^2 \tag{1.158}$$

where the coefficients a_k (k = 1, …, 6) describe the anisotropy and reduce to unity in the isotropic case. Note that J_2^0 is Hill's (1948) quadratic yield function.

In Cazacu and Barlat (2001), this approach was used to extend Drucker's isotropic yield criterion (Drucker 1949) to an orthotropic formulation. For this case the expression of the proposed orthotropic criterion is:

$$f^O = \left(J_2^o\right)^3 - c\left(J_3^o\right)^2 = k^2. \tag{1.159}$$

where c is a constant,

$$k^2 = 18\left(\frac{Y}{3}\right)^6 \tag{1.160}$$

and Y is the uniaxial yield stress.

For the in-plane case, the yield function may be written in the form

$$f_2^O \equiv \left[\frac{1}{6}(a_1+a_3)\,\sigma_{11}^2 - \frac{a_1}{3}\,\sigma_{11}\sigma_{22} + \frac{1}{6}(a_1+a_2)\sigma_{22}^2 + a_4\,\sigma_{12}^2\right]^3 - c\left\{\begin{array}{l}\frac{1}{27}(b_1+b_2)\sigma_{11}^3 + \frac{1}{27}(b_3+b_4)\sigma_{22}^3 - \frac{1}{9}(b_1\sigma_{11}+b_4\sigma_{22})\sigma_{11}\sigma_{22}\\ -\frac{1}{3}\sigma_{12}^2[(b_5-2\,b_{10})\sigma_{11} - b_5\sigma_{22}]\end{array}\right\}^2 = k^2. \tag{1.161}$$

where a_1–a_4 and b_1–b_5 and b_{10} are coefficients describing the anisotropy, c is a constant and k is expressed by Eq. (1.160). As one may see, the yield function incorporates 10 anisotropy coefficients and an extra constant c. The 10 anisotropy coefficients and the value of c can be determined from the measured uniaxial yield stresses σ_θ and strain ratios r_θ in 5 different orientations and σ_b, the value of the equibiaxial tensile stress. In the 3D case, the model incorporates 18 coefficients.

The yield stress in uniaxial tension along an axis at orientation θ to the rolling direction is predicted by:

$$\sigma_\theta = k^{\frac{1}{3}}\left\{\begin{array}{l}\left[\frac{1}{6}(a_1+a_3)\cos^4\theta + (a_4 - a_1/3)\cos^2\theta\,\sin^2\theta + \frac{1}{6}(a_1+a_2)\sin^4\theta\right]^3\\ -c\left[\begin{array}{l}\frac{1}{27}(b_1+b_2)\cos^6\theta + \frac{1}{27}(b_3+b_4)\sin^6\theta\\ -\frac{1}{9}\left[\begin{array}{l}(b_1+3b_5-6b_{10})\cos^2\theta\\ +(b_4-3b_5)\sin^2\theta\end{array}\right]\sin^2\theta\,\cos^2\theta\end{array}\right]^2\end{array}\right\}^{-1/6} \tag{1.162}$$

and the biaxial yield stress by:

$$\sigma_b = k^{\frac{1}{3}}\left[\left(\frac{a_2+a_3}{6}\right)^3 - c\left(\frac{-2\,b_1+b_2+b_3-2b_4}{27}\right)^2\right]^{-\frac{1}{6}} \tag{1.163}$$

Yielding under pure shear parallel to the orthotropic axes occurs when σ_{xy} is equal to

$$\tau = k^{\frac{1}{3}}(a_4)^{-\frac{1}{2}} \tag{1.164}$$

In order to predict the distribution of the anisotropy coefficient r_θ, the function f_2^0 defined by Eq. (1.161) should be replaced in the relationship

$$r_\theta = -\frac{\sin^2\theta\,\frac{\partial f^o}{\partial \sigma_x} - \sin 2\theta\,\frac{\partial f^o}{\partial \sigma_{xy}} + \cos^2\theta\,\frac{\partial f^o}{\partial \sigma_y}}{\frac{\partial f^o}{\partial \sigma_x} + \frac{\partial f^o}{\partial \sigma_y}} \tag{1.165}$$

Cazacu and Barlat (2003) also applied the representation theorems for transverse isotropy and cubic symmetries. The general expressions of the invariants of the stress deviators in these cases are detailed in (Cazacu and Barlat 2001). The method is applied for the extension of Drucker's isotropic yield criterion to transverse isotropy and cubic symmetries.

Aiming to develop models of the asymmetrical tension/compression behaviour specific to the alloys having a Hexagonal Closed Packed-HCP structure, Cazacu and Barlat have successfully used the representation theory of tensor functions. They have proposed an isotropic yield function in the form (Cazacu and Barlat 2004):

$$f = (\mathrm{J}_2)^{3/2} - cJ_3 = \tau_Y^3 \tag{1.166}$$

where τ_Y is the yield stress in pure shear and c is a constant. This constant can be expressed in the terms of the uniaxial yield stresses in tension σ_T and compression σ_C, respectively, as follow:

$$c = \frac{3\sqrt{3}(\sigma_T^3 - \sigma_C^3)}{2(\sigma_T^2 + \sigma_C^2)}. \tag{1.167}$$

Anisotropy was introduced in the formulation using the method presented above.

For plane stress conditions, the yield locus is:

$$\left[\frac{1}{3}\left(\sigma_1^2 - \sigma_1\sigma_2 + \sigma_2^2\right)\right]^{3/2} - \frac{c}{27}[2\sigma_1^3 + \sigma_2^3 - 3(\sigma_1 + \sigma_2)\sigma_1\sigma_2] = \tau_Y^3, \tag{1.168}$$

where σ_1 and σ_2 are principal stresses.

The expressions of the anisotropic yield function and the uniaxial yield stresses in tension and compression along an axis having the angular orientation θ to the rolling direction are presented in (Cazacu and Barlat 2004). The predictions of the biaxial yield stresses corresponding to the tension and compression, as well as the planar distribution of the anisotropy coefficient are also presented in the referenced paper.

Experimental researches (Liu et al. 1997) have shown that for some HCP alloys (e.g., titanium based alloys) the yield surface is better described by fourth order

functions. As a consequence, in order to describe such a behaviour, (Cazacu et al. 2006) proposed an isotropic yield function for which the degree of homogeneity a is not fixed:

$$\Phi = ||S_1| - kS_1|^a + ||S_2| - kS_2|^a + ||S_3| - kS_3|^a, \tag{1.169}$$

where S_1, S_2, S_3 are principal values of the stress deviator, a is a positive integer and k is the strength differential parameter.

In order to extend the isotropic criterion defined by Eq. (1.169) to an anisotropic formulation, the principal values of the deviatoric stress (S_1, S_2, S_3) are replaced by the principal values of the transformed tensor (Σ_1, Σ_2, Σ_3), obtained after applying a linear transformation. In this way, the new anisotropic yield criterion (CPB05) can be written as

$$\Phi = ||\Sigma_1| - k\Sigma_1|^a + ||\Sigma_2| - k\Sigma_2|^a + ||\Sigma_3| - k\Sigma_3|^a. \tag{1.170}$$

The paper (Cazacu et al. 2006) gives a detailed presentation of the relationships used to predict the uniaxial yield stresses and the coefficients of plastic anisotropy both for tension and compression states. Additional linear transformations can be incorporated into the CPB05 criterion for an improved representation of the anisotropy. The most important advantage of this yield criterion consists in its capability to provide an accurate description of the tension/compression behaviour specific to the magnesium and titanium alloys.

1.6.3 Vegter Yield Criterion

Using points of the yield locus determined directly by experiments, (Vegter et al. 1995; Vegter and van den Boogaard 2006) obtained the yield locus in the first quadrant by applying a Bezier interpolation. Vegter's criterion requires the determination of three parameters for each reference point (two principal stresses σ_1 and σ_2 and the strain vector $\rho = d\varepsilon_2/d\varepsilon_1$). In order to describe the planar anisotropy Vegter's criterion needs as many as 17 parameters. The analytical expression of the criterion is

$$\begin{pmatrix}\sigma_1\\ \sigma_2\end{pmatrix} = (1-\lambda)^2\begin{pmatrix}\sigma_1\\ \sigma_2\end{pmatrix}_i^r + 2\lambda(1-\lambda)\begin{pmatrix}\sigma_1\\ \sigma_2\end{pmatrix}_i^h + \lambda^2\begin{pmatrix}\sigma_1\\ \sigma_2\end{pmatrix}_{i+1}^r \tag{1.171}$$

for σ_e and angle φ where

$$\begin{pmatrix}\sigma_1\\ \sigma_2\end{pmatrix}_{i+1}^r = \sum_{j=0}^{m\,\cos}\begin{pmatrix}a_1^j\\ a_2^j\end{pmatrix}_i^r \cos(2j\varphi) \tag{1.172}$$

is a trigonometric expansion associated to the reference point,

$$R(\varphi) = \sum_{j=0}^{m\ cos} b^j \cos(2j\varphi) \tag{1.173}$$

is a cosine interpolation of the function $R(\varphi)$, φ is the angle between the principal directions and the orthotropic axes, λ is a parameter of the Bézier function, r is a superscript denoting the reference point, h is a superscript denoting the breaking point, $\begin{pmatrix} a_1^j \\ a_2^j \end{pmatrix}_i^r$ are parameters of the trigonometric interpolation to be determined at the reference points, and b^j are parameters of the trigonometric interpolation of the R-function.

The most important advantage of the criterion is the flexibility ensured by the large number of parameters. The disadvantages are related to the unfriendly form of the yield function making it improper for analytical computation, the large number of experiments required (uniaxial tension, biaxial tension, plane strain and pure shearing), and the need of mathematical abilities of the user. The Vegter's model has been implemented in the PAMSTAMP FE commercial program.

1.7 Recommendations on the Choice of the Yield Criteria

The most important factors that must be taken into account when choosing the yield criterion are as follows:

- Accuracy of the prediction both of the yield locus and the uniaxial yield stress and uniaxial coefficient of plastic anisotropy
- Computational efficiency and ease of implementation in numerical simulation codes
- Flexibility of the yield criterion
- Degree of generality
- Number of mechanical parameters needed by the identification procedure
- Robustness of the identification procedure
- Experimental difficulties caused by the determination of the mechanical parameters involved in the identification procedure
- User-friendliness of the yield criterion
- Acceptance of the yield criterion in the scientific/industrial community.

Usually, the best quality of the predictions will be ensured by the yield criteria having an identification procedure based both on uniaxial and biaxial tension experimental data. As concerns the experimental data obtained by uniaxial tension tests, the identification should use at least the yield stresses and the coefficients of plastic anisotropy corresponding to three planar directions (0^0, 45^0 and 90^0).

The yield criteria that use a larger number of mechanical parameters in the identification (13 or even more—Barlat 2004, BBC 2008 etc.) are able to provide

highly accurate descriptions of the anisotropic behaviour. It is especially notable their capability to capture the occurrence of six or eight ears in the case of deep-drawing of cylindrical cups.

1.8 Perspectives

As it can be seen from the previous sections of this chapter, advanced yield criteria allow an accurate prediction of the anisotropic behaviour of materials. On the one hand, it is possible to simultaneously describe the distribution of both the uniaxial yield stress and the anisotropy coefficient in the surface of the metallic sheet. On the other hand, it is also possible to model both "first and second order anisotropic behaviour anomalies".

The future research in this field will be oriented towards developing new models which include special properties (superplastic materials, shape memory materials, etc.). By including the evolution of the coefficients in the yield functions it will be possible to predict the yield loci for nonlinear loading. Stochastic modelling will be used for a more robust prediction of the yield loci (taking into account the variability of the mechanical parameters). Coupling the phenomenological models with the ones based on crystal plasticity will allow better simulation of the parameters evolution in technological processes (these include temperature, strain rate, strain path, structural evolution).

Therefore, the virtual process chain will be described more accurately, allowing it to be used in real fabrication processes.

References

Banabic D, Balan T, Comsa DS (2000) A new yield criterion for orthotropic sheet metals under plane–stress conditions. In: 7th Conference on TPR2000 Cluj Napoca, pp 217–224

Banabic D, Wagner S (2002) Anisotropic behaviour of aluminium alloy sheets. Aluminium 78:926–930

Banabic D, Kuwabara T, Balan T, Comsa DS, Julean D (2003) Non-Quadratic yield criterion for orthotropic sheet metals under plane-stress conditions. Int J Mech Sciences 45:797–811

Banabic D, Aretz H, Comsa DS, Paraianu L (2005) An improved analytical description of orthotropy in metallic sheets. Int J Plasticity 21:493–512

Barlat F, Richmond O (1987) Prediction of tricomponent plane stress yield surfaces and associated flow and failure behaviour of strongly textured FCC polycrystalline sheets. Mat Sci Eng 91:15–29

Barlat F, Lian J (1989) Plastic behaviour and stretchability of sheet metals (Part I): A yield function for orthotropic sheet under plane stress conditions. Int J Plasticity 5:51–56

Barlat F, Lege DJ, Brem JC (1991) A six-component yield function for anisotropic materials. Int J Plasticity 7:693–712

Barlat F et al (2000) Constitutive modeling for aluminium sheet forming simulations. In: Khan AS, Zhang H, Yuan Y (eds.) Proceedings of the of 8th international symposium in plasticity and its current applications. Whistley, Canada, Neat Press, Fulton, MD, pp 591–593

Barlat F et al (2003) Plane stress yield function for aluminium alloy sheets-Part 1: theory. Int J Plasticity 19:297–319

Barlat F et al (2005) Linear transformation-based anisotropic yield functions. Int J Plasticity 21:1009–1039

Cazacu O, Barlat F (2001) Generalization of Drucker's yield criterion in orthotropy. Math Mech Solids 6:613–630

Cazacu O, Barlat F (2003) Application of representation theory to describe yielding of anisotropic aluminium alloys. Int J Eng Sci 41:1367–1385

Cazacu O, Barlat F (2004) A criterion for description of anisotropy and yield differential effects in pressure insensitive metals. Int J Plasticity 20:2027–2045

Cazacu O, Plunkett B, Barlat F (2006) Orthotropic yield criterion for hexagonal close packed metals. Int J Plasticity 22:1171–1194

Comsa DS, Banabic D (2008) Plane-stress yield criterion for highly-anisotropic sheet metals. In: Hora P (ed) Proceedings of the 7th international conference workshop on numerical simulation of 3D sheet metal forming processes, NUMISHEET 2008, Interlaken, pp 43–48

Drucker DC (1949) Relations of experiments to mathematical theories of plasticity. J Appl Mech 16:349–357

Gawad J, Banabic D, Van Bael A, Comsa DS, Gologanu M, Eyckens P, Van Houtte P, Roose D (2015) An evolving plane stress yield criterion based on crystal plasticity virtual experiments. Int J Plasticity 75:141–169

Hill R (1948) A theory of the yielding and plastic flow of anisotropic metals. Proc Roy Soc London A 193:281–297

Hosford WF (1972) A generalised isotropic yield criterion. J Appl Mech 39:607–609

ISO/FDIS 16842 (2013) Metallic materials—sheet and strip—biaxial tensile testing method using cruciform specimen

Kuwabara T, Van Bael A, Iizuka E (2002) Measurement and analysis of yield locus and work hardening characteristics of steel sheets with different r-values. Acta Mater 50:3717–3729

Kuwabara T (2007) Advances in experiments on metal sheets and tubes in support of constitutive modeling and forming simulations. Int J Plasticity 23:385–419

Kuwabara T, Sugawara F (2013) Multiaxial tube expansion test method for measurement of sheet metal deformation behavior under biaxial tension for a large strain range. Int J Plasticity 45:103–118

Lankford WI, Snyder SC, Bauscher JA (1950) New criteria for predicting the press performance of deep-drawing sheets. Trans ASM 42:1196–1232

Liu C, Huang Y, Stout MG (1997) On the asymmetric yield surface of plastically orthotropic materials: A phenomenological study. Acta Mater 45:2397–2406

Pöhlandt K, Banabic D, Lange K (2002) Equi-biaxial anisotropy coefficient used to describe the plastic behavior of sheet metal. In: Proceedings of the ESAFORM conference, Krakow, pp 723–727

van Riel M, van den Boogaard AH (2007) Consistent plane stress-3D conversion of hardening models and yield criteria. In: Computational plasticity IX—Fundamentals and applications, COMPLAS 2007, Barcelona, Spain, pp 624–627

Vegter H, Drent P, Huetink J (1995) A planar isotropic yield criterion based on material testing at multi-axial stress state. In: Shen SF, Dawson PR (eds) Simulation of materials processing-Theory, methods and applications. Balkema, pp 345–350

Vegter D, van den Boogaard AH (2006) A plane stress yield function for anisotropic sheet material by interpolation of biaxial stress states. Int J Plasticity 22:557–580

Yoon JW et al (2006) Prediction of six or eight ears in a drawn cup based on a new anisotropic yield function. Int J Plasticity 22:174–193

Chapter 2
Crystallographic Texture and Plastic Anisotropy

Hans Joachim Bunge and Robert Arthur Schwarzer

2.1 The Structure of Polycrystalline Materials

Anisotropy includes elastic and plastic anisotropy. The macroscopic anisotropy is closely related to the anisotropic behavior of the single crystal and to the structure of the poylcrystalline material. The anisotropy of the elastoplastic behavior of the single crystal results from the crystallographic nature of plastic glide, interactions between the glide systems (reflecting the dislocation—dislocation—precipitation interactions) and eventually anisotropy of elastic constants. The mechanical anisotropy associated with the granular aspect of the material is caused by the crystallographic texture, morphology (size, shape and mutual arrangement of grains, grain boundaries) and internal stresses caused by intragranular incompatibilities of plastic strain. In cold rolled sheets, elastic deformation is much smaller than plastic deformation.

The structure of crystalline materials can be characterized by four structure levels:

1. The *Crystal Structure* specifies the kind and position of atoms in the unit cell of the ideal crystal lattice.
2. The *Phase Structure* specifies the sizes, shapes and mutual arrangement of single-phase volumes (volumes with constant crystal structure) in polyphase materials.
3. The *Grain Structure* specifies the sizes, shapes, crystal lattice orientations, and mutual arrangement of monocrystal volumes (within the single-phase volumes).

Hans Joachim Bunge—deceased.

R.A. Schwarzer (✉)
Kappstr. 65, 71083 Herrenberg, Germany
e-mail: post@robert-schwarzer.de
URL: http://www.crystaltexture.com

H.J. Bunge · R.A. Schwarzer
Clausthal University of Technology, Leibnizstr. 4, 38678 Clausthal-Zellerfeld, Germany

D. Banabic (ed.), *Multiscale Modelling in Sheet Metal Forming*,
ESAFORM Bookseries on Material Forming,
DOI 10.1007/978-3-319-44070-5_2

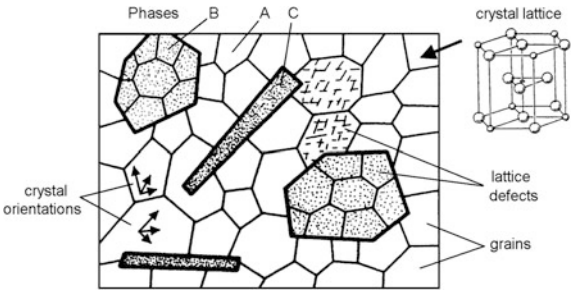

Fig. 2.1 The structure of a polycrystalline material can be characterized by four structure levels: crystal structure, phase structure, grain structure, substructure

4. The *Substructure* specifies the kind, amount, arrangement, crystallographic orientation of all lattice defects, i.e. all deviations from the ideal crystal lattice such as point defects, dislocations, stacking faults, grain and phase boundaries, the surface, elastic strain, magnetization, electric polarization.

This is illustrated schematically in Fig. 2.1. Any crystalline material is thus completely characterized by the *Microstructure Function* G(**x**) which specifies the phase, orientation and defects in all small (monocrystalline) volume elements V_x at the loci **x** in the material (Bunge and Schwarzer 2001):

$$G(\mathbf{x}) = \left\{ \begin{array}{ll} i(\mathbf{x}) & \text{Phase Locus Function} \\ g(\mathbf{x}) & \text{Orientation Locus Function} \\ D(\mathbf{x}) & \text{Substructure Function} \end{array} \right\} \quad \text{Microstructure Function} \quad (2.1)$$

2.2 Definition of Crystallographic Texture

The term *Crystallographic Texture* or *Preferred Orientations,* in its widest sense, may be identified with the Orientation Locus Function g(**x**). In a narrower (conventional) sense, however, it is understood as the set of volume fractions of all crystallites in the sample having any given crystal orientation g. Its mathematical formulation is the *Orientation Density Function* or *Orientation Distribution Function* ODF (Bunge 1982):

$$\frac{dV_g/V}{dg} = f(g); \quad g = \{\varphi_1, \Phi, \varphi_2\} \quad \text{Global Texture.} \quad (2.2)$$

The same definition can also be applied to smaller (but still polycrystalline) *subsamples* of the size $V_{\mathbf{X}}$ at the locus **X** in the sample. The ODF in the subsample $V_{\mathbf{X}}$ is called the *Local Texture*, and all local textures together form a *Texture Field*. In order to make clear that the definition Eq. (2.2) applies to the *whole sample* it may then be called the *global texture*.

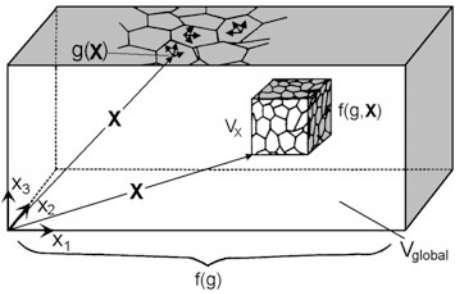

Fig. 2.2 Illustration of the three texture functions: the global texture f(g); the local textures f(g, **X**) forming together a texture field; the orientation locus function g(**x**)

$$\frac{dV_g/V_{\mathbf{X}}}{dg} = f(g, \mathbf{X}); \quad \mathbf{X} = \{X_1, X_2, X_3\} \quad \text{Texture Field} \tag{2.3}$$

Finally, by considering still smaller (monocrystalline) subvolumes $V_{\mathbf{X}}$ at the locus **X**, we obtain the complete *Orientation Locus Function* g(**x**) (contained in Eq. (2.1)) (Bunge and Schwarzer 2001)

$$g = g(\mathbf{x}); \quad \begin{matrix} g = \{\varphi_1, \Phi, \varphi_2\} \\ \mathbf{x} = \{x_1, x_2, x_3\}. \end{matrix} \quad \text{Orientation Locus Function} \tag{2.4}$$

The Orientation Locus Function g(**x**) corresponds to a Cosserat continuum (Cosserat and Cosserat 1909) (if we do not take the atomistic structure of matter into account). The three definitions, Eqs. (2.2)–(2.4), are illustrated in Fig. 2.2. The ODF, Eq. (2.2), is three-dimensional, whereas texture fields and the Orientation Locus Function require six dimensions for their complete representation. Hence, if we want to "visualize" them, some further data reduction is required (to no more than three dimensions). In mathematical models of materials properties, e.g. the plastic properties as considered in this volume, both six-dimensional quantities, however, can be taken fully into account.

2.2.1 Crystal Orientation

The basic quantity in the Eqs. (2.2)–(2.4) is crystal orientation g. It is defined by choosing a crystallographic coordinate system K_B consisting of three crystal directions, e.g. [100][010][001] in cubic materials or $[1\,\bar{1}\,0\,0]\,[11\,\bar{2}\,0]\,[0\,0\,0\,1]$ in hexagonal materials. A second coordinate system, K_A, is (somehow) fixed in the sample. In sheet metals, for instance, one may choose the rolling, transverse and normal direction. In principle, the choice of both coordinate systems is deliberate.

It is, however, convenient to choose them in relation to symmetry, i.e. *sample symmetry* in the case of K_A and *crystal symmetry* in the case of K_B. An often considered sample symmetry is orthorhombic symmetry (which is in this case often

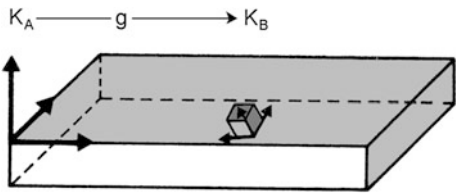

Fig. 2.3 The orientation g of a single-crystalline volume element is described by the rotation which transfers the sample coordinate system K_A into the crystal coordinate system K_B

called *orthotropic* symmetry). Crystal orientation g is the rotation which transfers K_A into K_B. This may be written in the form

$$K_B = g \cdot K_A \qquad \text{Crystal Orientation} \tag{2.5}$$

and is illustrated in Fig. 2.3. Cubic-cubic coordinate systems are assumed. So a non-cubic crystal and/or a non-cubic sample coordinate system have to be defined first in orthonormal frames (Schumann 1979). Crystal orientation can be specified in many different "parameterizations", e.g. by a transformation matrix $[g_{ij}]$, the Euler angles $\{\varphi_1, \Phi, \varphi_2\}$, a rotation axis **r** and angle ω, the Rodrigues vector, quaternions, or others:

$$g = [g_{ij}] = \{\varphi_1, \Phi, \varphi_2\} = \{\mathbf{r}, \omega\} \qquad \text{Orientation Parameters.} \tag{2.6}$$

In this chapter we shall mainly use the Euler angles $\{\varphi_1, \Phi, \varphi_2\}$ as was already done in Eqs. (2.2) and (2.4).

2.3 Experimental Determination of Textures

Texture measurement in the classical sense, Eq. (2.2), can be carried out with a *Texture Goniometer*, Fig. 2.4, using X-ray or Neutron Diffraction. The "output" of such an instrument are *Direction Distribution Functions*, $P_{(hkl)}(\alpha, \beta)$, of the normal directions **h** to low-index reflecting crystal lattice planes (hkl) which are commonly called *Pole Figures* (Wassermann and Grewen 1962):

$$\frac{dV/V}{d\Omega} = P_{(hkl)}(\alpha, \beta) = \frac{1}{2\pi} \int\limits_{h \| \{\alpha\beta\}} f(g)\, dg; \quad d\Omega = \sin\alpha\, d\alpha\, d\beta \quad \text{Pole Figure} \tag{2.7}$$

where (α, β) specifies a direction referred to the sample coordinate system K_A. These functions are two-dimensional projections of the three-dimensional function f(g) as is expressed on the right hand side of Eq. (2.7). The function f(g) can be calculated from several pole figures by a mathematical procedure, solving the

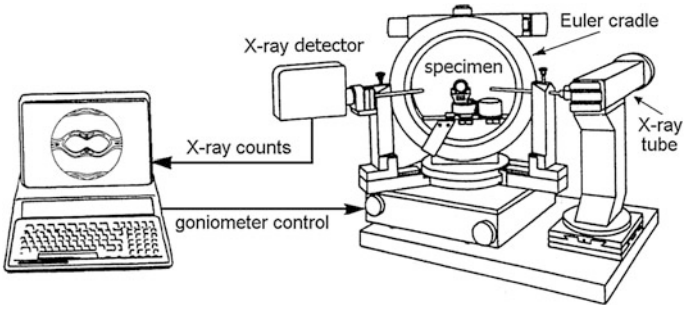

Fig. 2.4 An automated X-ray texture goniometer (schematic) consisting of a two-circle diffractometer supplemented by a Eulerian Cradle as the sample orientation device

integral equation (Eq. (2.7)), called *Pole Figure Inversion* as shown schematically in Fig. 2.5. "Experimental" pole figures measured in reflection mode of X-ray diffraction are incomplete with a non-acquired circular range at large angles of specimen tilt. Since the ODF represents the full orientation distribution of the sampled volume, complete "theoretical" pole figures, however, can be recalculated from the ODF. For more details see e.g. Bunge (1982); Spiess et al. (2016).

In order to measure local textures and texture fields, a collimated fine primary beam (X-rays or synchrotron radiation), e.g. of 0.05 mm in diameter, is used and the specimen is scanned in steps of similar size. This can be done with an *X-ray Scanning Apparatus* which is essentially an "upgraded" conventional texture goniometer with a computer-controlled x–y specimen stage (see e.g. (Fischer and Schwarzer 1998; Schwarzer 2005)). Pole intensity distribution maps (Fig. 2.6a), texture fields, f(g, **X**), and pole figures of small selected specimen areas are acquired. In addition residual lattice strain is determined simultaneously with the same high spatial resolution by evaluating the profile and shift of the X-ray diffraction peaks (Fig. 2.6b). If "white" primary X-rays and an energy dispersive X-ray detector are employed, the chemical composition can furthermore be obtained by X-ray micro-fluorescence analysis (XFA), and thus—in combination with checking for characteristic diffraction peaks—the Phase Locus Function i(**x**) is so acquired (Schwarzer 2005).

The complete Microstructure Function G(**x**) (at least in a two-dimensional section $\mathbf{x} = \{x_1, x_2, 0\}$), Eq. (2.1), can be measured by backscatter electron diffraction in the *Scanning Electron Microscope* as is shown schematically in Fig. 2.7 (see e.g. (Schwarzer 1997; Schwartz et al. 2009)). The results of such measurements, known as EBSD (*Electron Backscatter Diffraction*) or COM (*Crystal Orientation Microscopy*), may be *visualized* by color-coding of g(**x**) in microstructural images as is shown, as an example, in Fig. 2.8. For the use in mathematical models e.g. of plastic anisotropy, the individual grain orientations of the Orientation Locus Function g(**x**) are available in the complete six-dimensional form, Eq. (2.4) (or at least five-dimensional if measurement is restricted to one sample plane). Phases can be discriminated simultaneously to determine the Phase

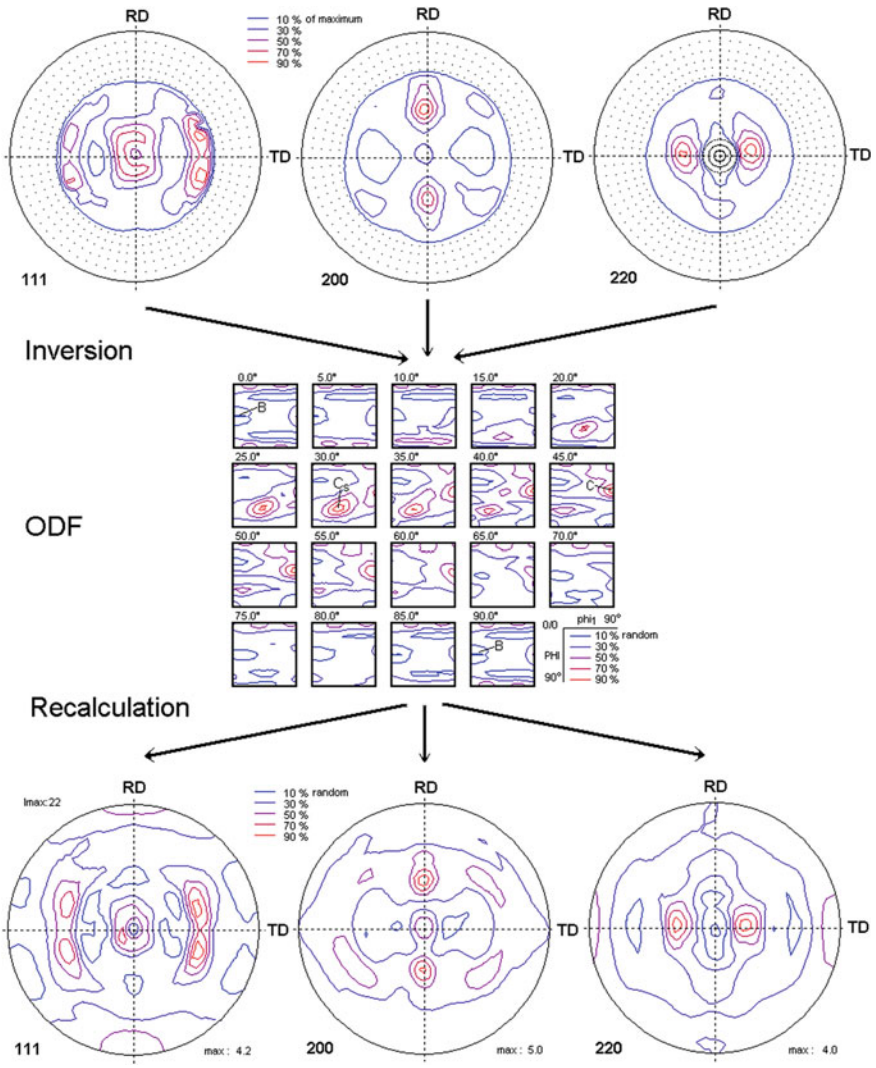

Fig. 2.5 Calculation of the Orientation Distribution Function (ODF) (*center*) from several incomplete experimental pole distribution functions (*top*). The procedure is called "Pole Figure Inversion". From the ODF complete pole figures can be recalculated (*bottom*)

Locus Function i(**x**) by checking, in a trial with all assumed crystal structures, for best indexing the diffraction patterns if the lattice constants differ sufficiently, as well as by supplementing electron beam microanalysis (Energy Dispersive X-Ray Spectroscopy, EDS, or Auger Electron Spectroscopy, AES). The pattern quality (PQ), i.e. the sharpness of the backscatter Kikuchi patterns, is a (semi-)quantitative measure of the perfection of the diffracting crystallite volume thus providing an estimate of the Substructure Function D(**x**).

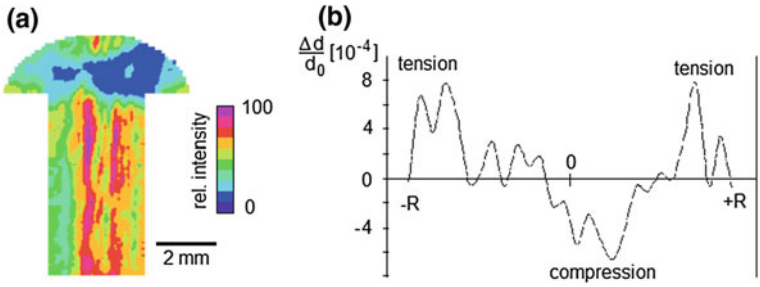

Fig. 2.6 Cross section of an aluminum rivet. **a** Spatial distribution map of the 220 pole intensity. The 220 planes were placed parallel to the reference direction $\alpha = 35°$ and $\beta = 83°$, $2\vartheta = 40.2°$; **b** The lattice strain across the rivet bolt was calculated from the width of the 220 peaks

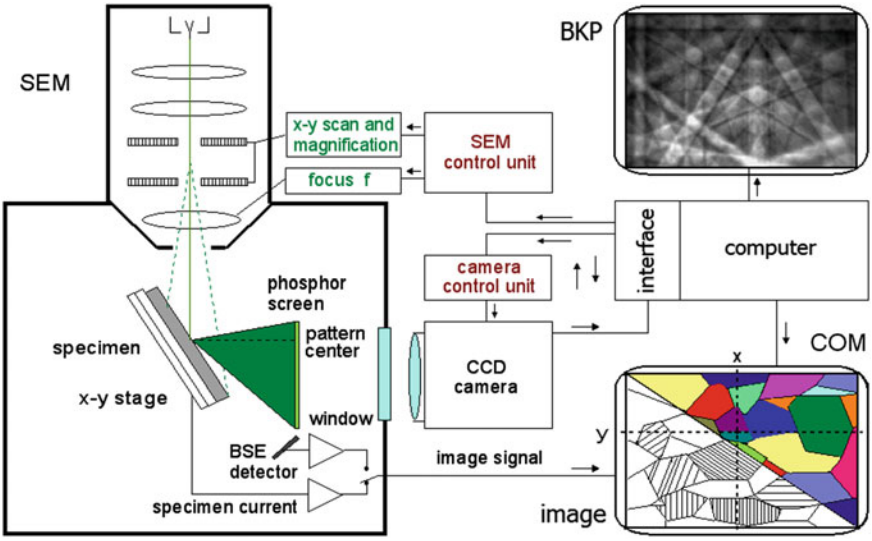

Fig. 2.7 Backscatter electron diffraction in a scanning electron microscope (schematic). The points (x, y) on the specimen are scanned automatically. A wide-angle Kikuchi diffraction pattern (see insert on *top right*) is acquired in every point with a sensitive CCD camera, evaluated automatically for crystal orientation, and represented by a pixel with orientation specific color on the monitor screen to form a crystal orientation map (COM) (Schwarzer 1997)

The properties of a polycrystalline aggregate depend markedly on the arrangement and distribution of its constituent elements of all four structure levels as stated in Sect. 2.1. Hence, the general concept of orientation stereology, rather than merely texture or conventional stereology alone (i.e. Quantitative Materialography), must be taken as a basis for comprehensive models which describe and simulate anisotropic properties of the real polycrystalline material. Orientation stereology is based on the Microstructure Function G(**x**), Eq. (2.1). Both fields of materials science, texture and

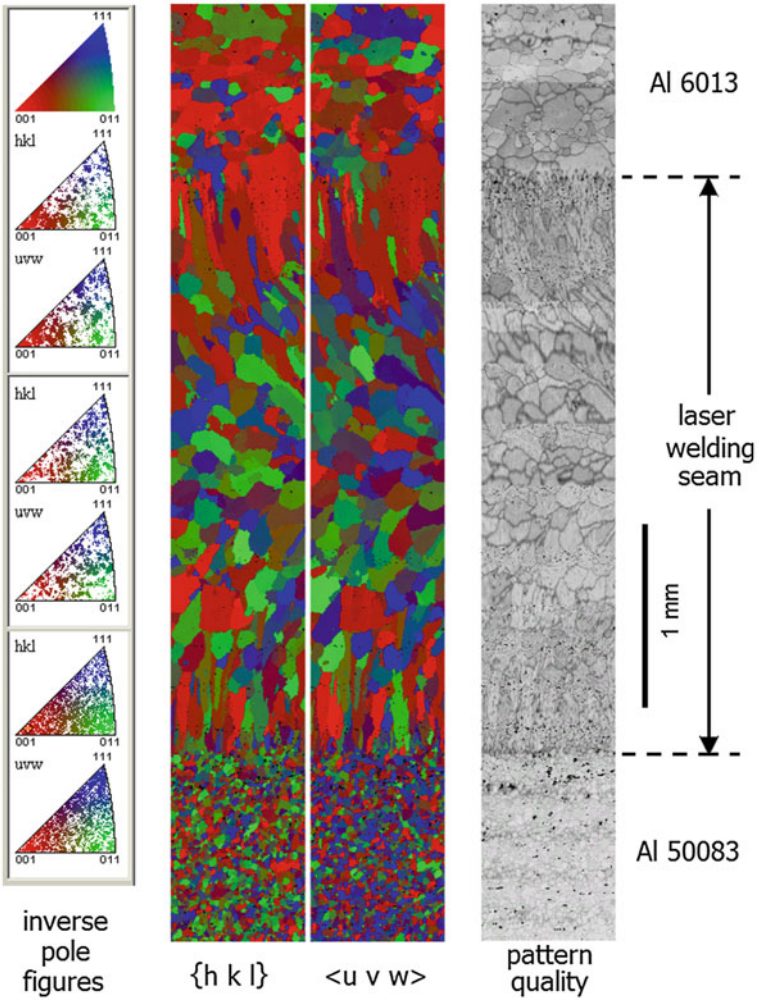

Fig. 2.8 Representation of individual crystal data g(**x**) by *color coding*. A laser welding seam connects an *Al6013* with an *Al5083* metal sheet. The crystal directions, {*hkl*} in welding direction and <*uvw*> in the reference direction (perpendicular to the welding direction and in the sheet plane), have been coded by the color triangle (*top left*) to form crystal orientation maps. The inverse pole figures of *Al6013* (*upper left*), of the welding seam (*center left*), respectively of *Al5083* (*bottom left*) have been constructed from the individual grain orientations. The grain structure is clearly reproduced in the pattern quality map (PQ) (Brokmeier et al. 2007)

stereology, and their conventional functions characterizing the microstructure are contained, but many other functions can be derived from G(**x**) which are hard or in no way accessible to direct measurement (Bunge and Schwarzer 2001).

2.4 Texture and Properties of Materials

Crystallographic texture, or even more generally the Microstructure Function G(**x**), influences the physical properties of materials as is shown schematically in the right half of Fig. 2.9. On the other hand, texture is formed (or modified) by physical processes as is shown schematically on the left side of Fig. 2.9. With respect to the topic of this book we consider here particularly *Plastic Anisotropy* as a property and *Plastic Deformation* as a process. In technological forming processes both are directly related to each other as is also illustrated in this figure. The relationships are to be expressed in terms of mathematical models. It is evident that the relationship Process → Structure → Properties, illustrated in Fig. 2.9, holds for virtually all crystalline materials, be they metals, ceramics, (partly) crystalline polymers, or even geologic or natural biologic materials.

Crystallographic texture influences the properties of a material via *Crystal Anisotropy* as is illustrated schematically in Fig. 2.10:

- If the orientation distribution of the crystallites is not random, then the material may be macroscopically anisotropic. The effect can be understood (at least in a good first approximation) in terms of the classical texture function f(g). This is the main topic of this chapter.
- At the grain boundaries the (local) properties are discontinuous. This may have a strong influence on the material's properties, too, even if the material is macroscopically isotropic.
- And finally the near-boundary zones of the crystallites may have deviating physical properties (e.g. higher diffusion or lower strength).

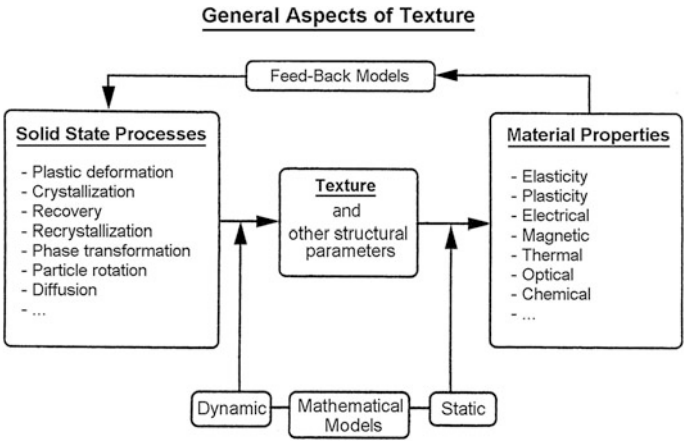

Fig. 2.9 The two aspects of texture analysis: the "Process → Texture" relationship (*left side*); the "Texture → Property" relationship (*right side*)

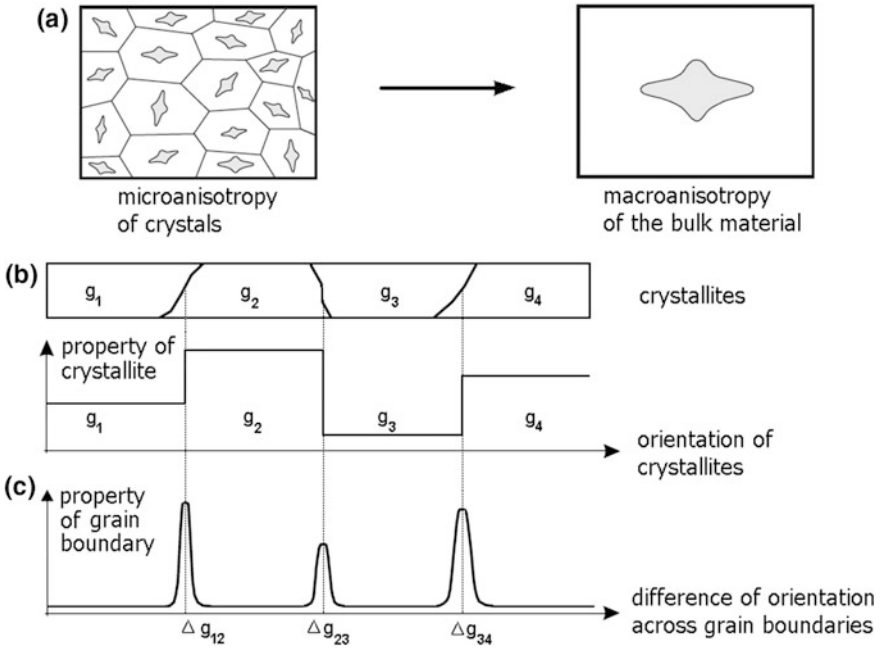

Fig. 2.10 Effect of crystal anisotropy on material properties (schematic): **a** macro-anisotropy, **b** micro-discontinuity, **c** grain boundary properties

These latter two effects require the full Orientation Locus Function g(**x**) for their understanding rather than only the classical concept of texture f(g).

In this book plastic formability of materials is considered for sheet materials. In this case it is convenient to subdivide plastic anisotropy into planar and normal anisotropy, as is shown schematically in Fig. 2.11. The *normal anisotropy* influences the maximum drawability of sheet material and should thus be as high as possible, as is shown in Fig. 2.12. For the correlation of r with deep-drawability see also Chap. 5.

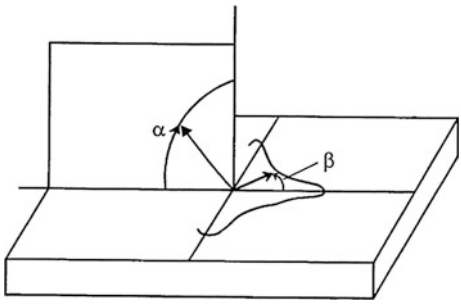

Fig. 2.11 The anisotropy of sheet material is subdivided into normal and planar anisotropy

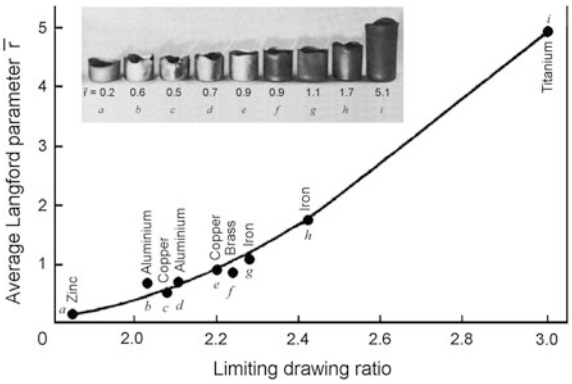

Fig. 2.12 Normal anisotropy expressed by the average r-value enhances the deep drawability of sheet metals. The same material, e.g. aluminum, copper, iron, may have different textures and hence different r̄-values (after (Wilson 1966))

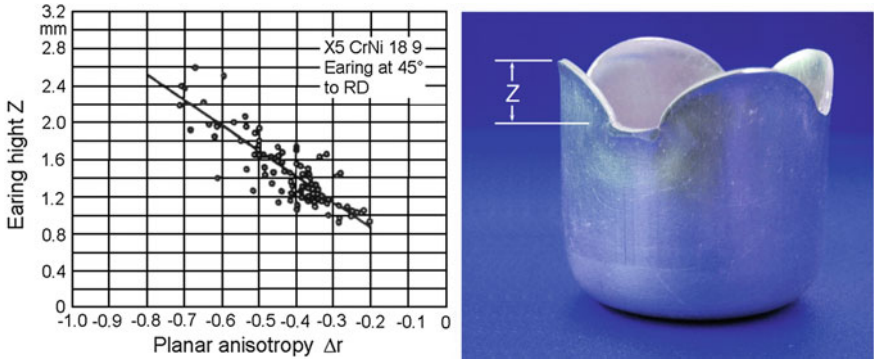

Fig. 2.13 Planar anisotropy expressed by Δr leads to earing after deep drawing

Planar anisotropy leads to earing as is shown in Fig. 2.13. Hence, it should be as low as possible, ideally it should be zero. Both quantities are directly related to crystallographic texture. In fact, earing shown in Fig. 2.13 and the means how to avoid it, has become the very mark of crystallographic texture (see e.g. (Wassermann and Grewen 1962)).

2.5 Plasticity of Polycrystalline Materials

Plasticity of crystalline materials must be considered on many different length-scales as is illustrated in Fig. 2.14. The following scales may be distinguished:

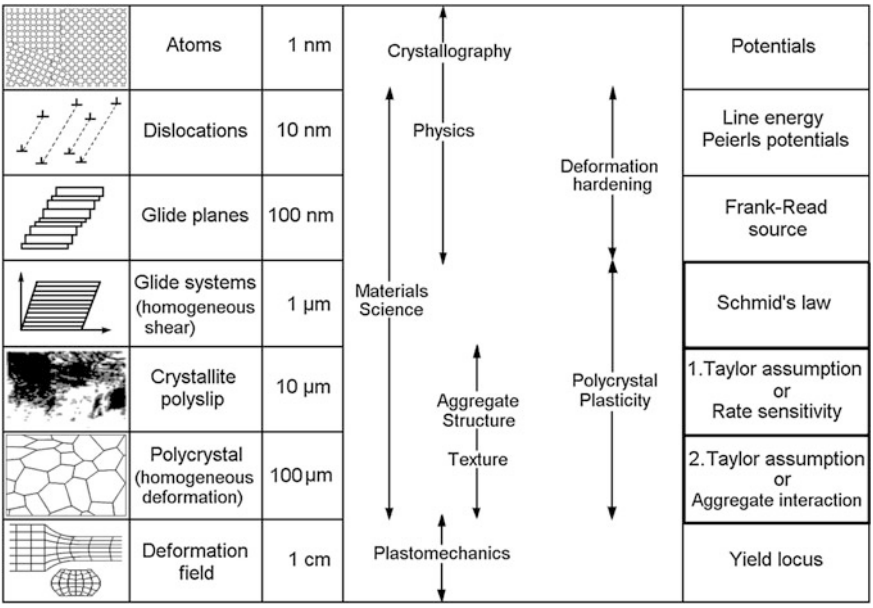

Fig. 2.14 Plasticity of polycrystalline materials is to be considered on many different length scales ranging from atomistic to macroscopic-technological dimensions

Microscopic	→	Hardening relevant
Mesoscopic	→	Texture relevant
Macroscopic	→	Process relevant.

In this chapter we consider mainly the mesoscopic—texture relevant—scale. As is illustrated in Fig. 2.15, two volume elements of different length scales are distinguished:

- A small *monocrystalline* volume element (a) at the locus **x**, with the crystal orientation g, Eq. (2.4), which undergoes *homogeneous* deformation $\varepsilon(\mathbf{x})$ (as the average of individual dislocation movements considered on the microscopic scale).
- A bigger, *polycrystalline* volume element (d) at the locus **X** with the texture f(g), Eq. (2.3), which undergoes the *quasi-homogeneous* deformation $\bar{\varepsilon}(X)$ (as the average of the local deformations $\varepsilon(\mathbf{x})$ of all monocrystalline volume elements (a) which it contains).

Any mathematical model of polycrystal plasticity must contain *model assumptions* about the monocrystalline as well as the polycrystalline volume element. Plastic deformation of the *monocrystalline* volume element has been considered in terms of the following models:

- The *Sachs model* assumes glide in only *one glide system* which is subjected to the highest shear stress according to its maximum Schmid factor (Sachs 1928).

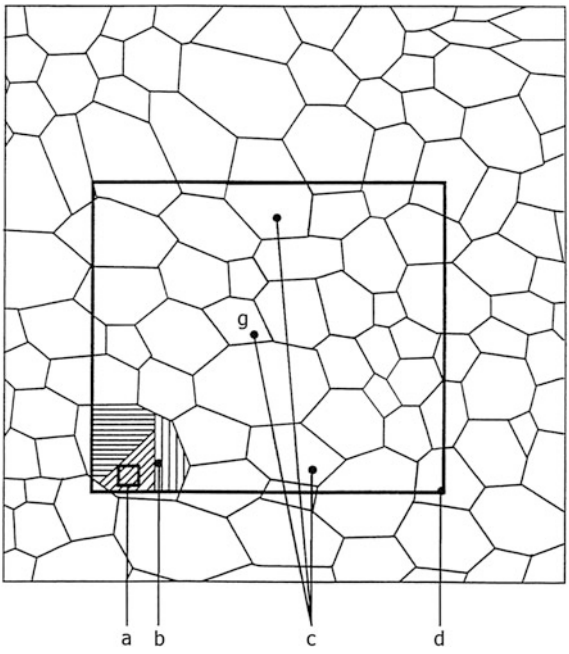

Fig. 2.15 Different volume elements considered in a polycrystalline material: *a* small volume element which is single crystalline with homogeneous deformation, V_x, *b* single crystalline with inhomogeneous deformation, *c* volume fraction with same orientation g, *d* bigger polycrystalline volume V_x with texture f(g)

- The *viscoplastic (strain rate sensitive) model* assumes glide in *all glide systems*. The glide rates γ^n in these systems depend on the shear stresses τ^n falling into the systems (according to their Schmid factors).

$$\gamma^n = \gamma_0 \cdot \left[\frac{\tau^n}{\tau_0^n}\right]^{\frac{1}{m}} \tag{2.8}$$

The exponent m is a measure of strain rate sensitivity (Canova et al. 1984; Tóth et al. 1997).

- The *Taylor-Bishop-Hill model* assumes glide in *all glide systems*. The glide rates γ^n guarantee minimum deformation work (see Eq. (2.13)) (Bishop and Hill 1951; Taylor 1938).

Also the *polycrystalline* volume element has been considered with different model assumptions:

- The *Taylor-Bishop-Hill model (full constraints)* assumes constant deformation throughout the whole material

$$\varepsilon(x) = \bar{\varepsilon}(X). \tag{2.9}$$

This assumption allows the polycrystalline volume element to be treated solely on the basis of the classical texture f(g), Eq. (2.3).

- The *relaxed constraints (Taylor) model* allows deviations from Eq. (2.9). Particularly one or two shear strain components in $\varepsilon(\mathbf{x})$ are "relaxed", i.e. they are allowed to assume non-fixed values which are deduced, later on, from the model (Honneff and Mecking 1978).
- The *self-consistent model* considers one grain with the orientation g (at a time) individually which is embedded in a homogeneous matrix the properties of which are texture averages over all orientations g according to the texture f(g) (Kröner 1961; Molinari et al. 1987; Tomé and Canova 1998).
- Finally, model calculations have also been carried out *without any model hypotheses about the polycrystal*, i.e. they are based on the Orientation Locus Function g(**x**), Eq. (2.4), the changes of which follow as a result of the model (Dawson et al. 1994; Dawson and Beaudoin 1998).

All of the polycrystal assumptions may be combined with any of the monocrystal assumptions, hence leading to a great variety of different model variants.

Plastic deformation is necessarily combined with *elastic deformation*. Hence, strictly speaking plasticity cannot be considered without taking elasticity into account. The maximum elastic strains are, however, much smaller than the maximum plastic strains. This applies particularly to metal forming processes in which the elastic strains can be neglected as compared with the plastic ones. It does not apply to the range of yield stresses, i.e. to the very onset of plasticity.

In this case some of the crystallites may have already been deformed plastically, whereas others are still in the elastic range. Hence, all models of plastic anisotropy and plastic deformation have been considered in two approximations, i.e. with and without elasticity (see e.g. (Iwakuma 1984; Masson and Zaoui 1999)).

Reviews over the various models are given, for instance, in (Van Houtte 1984, 1996; Kocks et al. 1998; Leffers et al. 1988; Leffers 1988; Lowe et al. 1991; Raabe 1998; Zaoui 1986). In the following we shall consider the full-constraints Taylor model in some more detail.

2.5.1 The Taylor Model (Full-Constraints)

Plastic deformation in a small volume element, $V_{\mathbf{x}}$, may be described by the displacement vector d**u** of a point **x** after a small deformation step dη

$$du_i = d\eta \cdot \varepsilon_{ij} \cdot x_j \tag{2.10}$$

as is illustrated schematically in Fig. 2.16.

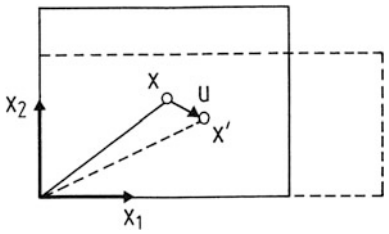

Fig. 2.16 A small deformation step dη in a small volume element characterized by the displacement vector **u**

Monocrystalline Volume Element

If the volume element is *monocrystalline* the deformation tensor ε_{ij} is composed of glide deformations in the glide systems n with the glide rates γ^n. Glide in one glide system is assumed to be a homogeneous shear described by the shear tensor (averaged over individual dislocation glide)

$$G_{ij}^{n}(g) = \mathbf{d}_i^n \cdot \mathbf{n}_j^n \tag{2.11}$$

with **d** being the vector of the glide direction and **n** the normal to the glide plane, respectively (referred to the chosen *sample* coordinate system K_A).

In a given crystal structure, glide plane and glide direction are usually known with respect to the *crystal* coordinate system K_B, e.g. in the form $\{hkl\}\langle uvw\rangle$ as glide plane and glide direction. In fcc metals, for instance, the glide systems $\{111\}\langle 110\rangle$ are assumed active. The orientations of the glide systems must be transformed by the rotation g, using the transformation matrix $[g_{ij}]$, Eq. (2.6), into the sample coordinate system K_A which was assumed in Eq. (2.11).

Plastic deformation may also proceed by twinning which we do not consider here for the sake of simplicity. Diffusion processes such as grain boundary glide are not taken into account here either.

Glide, by itself, does not change the orientation of the crystal lattice. However, the external forces may induce a torque on the deformed volume element which leads to a rigid rotation R as is illustrated schematically in Fig. 2.17. Hence, the

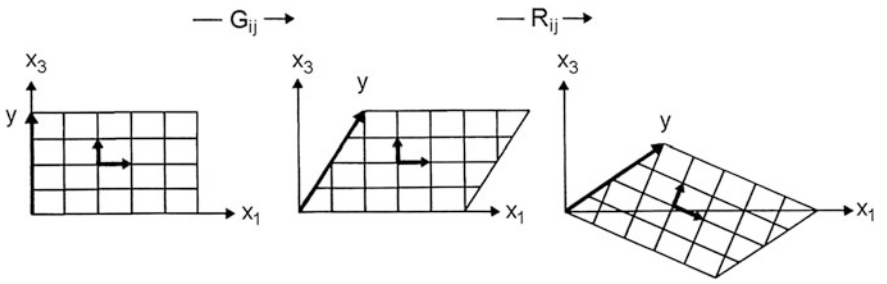

Fig. 2.17 Plastic deformation of a single-crystalline volume element by glide and rigid rotation. The intermediate state (only glide without rotation) is only imaginary

deformation tensor ε_{ij} in Eq. (2.10) must be composed of glide in all glide systems and a rigid rotation R:

$$\varepsilon_{ij} = \sum_{n=1}^{N} \gamma^n \cdot G_{ij}^n(g) + R_{ij}. \tag{2.12}$$

In most cases, the number N of available glide systems is greater than the number of independent components in ε. Hence, Eq. (2.12) leaves a high degree of freedom to the choice of the γ^n. Any physically realistic choice must, however, guarantee minimum deformation work which requires

$$\sum_{n=1}^{N} |\gamma^n| a^n = \min \rightarrow M; \quad a^n = \tau_0^n/\tau_0 \tag{2.13}$$

where τ_0^n are the critical resolved shear stresses in the glide systems, and τ_0 is some average value of them. In Eqs. (2.12) and (2.13), ε_{ij} and g are the *input variables*, the rotation R_{ij} and the Taylor factor M are the *output quantities* of the model, the glide system tensors G_{ij}^n described by **d** and **n**, Eq. (2.11), depend on the crystal structure of the considered material, and the critical resolved shear stresses τ_0^n depend on the state of deformation hardening reached after a finite degree η of deformation, i.e. they depend on D(**x**), Eq. (2.1).

The matrices ε_{ij}, G_{ij}, R_{ij} in Eq. (2.12) may be split into their respective symmetric and antisymmetric parts. Hence, Eq. (2.12) can be written in the form

$$\varepsilon_{ij}^{sym} = \sum_{n=1}^{N} \gamma^n \cdot G_{ij}^n(g)^{sym} \tag{2.12a}$$

$$\varepsilon_{ij}^{ant} = \sum_{n=1}^{N} \gamma^n \cdot G_{ij}^n(g)^{ant} + R_{ij}. \tag{2.12b}$$

Since R_{ij} is antisymmetric it is not contained in Eq. (2.12a). Hence, this equation can be solved together with Eq. (2.13) for the γ^n. In the most general case this system of equations has several linearly independent solutions γ_m^n (notwithstanding the minimum condition in Eq. (2.13) which enforces a *unique* solution for M). Substituting the γ_m^n in Eq. (2.12b) gives the rotations R_{ij}^m which are thus also not unique. Hence, the Taylor model has two (external) output quantities

$$M(\varepsilon_{ij}, g) \qquad \text{Taylor Factor} \tag{2.14}$$

$$R_{ij}(\varepsilon_{ij}, g) = \sum_{m} \alpha^m \cdot R_{ij}^m(\varepsilon_{ij}, g) \quad \text{Axis Rotation Rate.} \tag{2.15}$$

(Then the "internal" quantities γ_m^n are no more required.) The Taylor factor M expresses the deformation work dW needed during the deformation step dη, Eq. (2.10). It is

$$dW = d\eta \cdot \tau_0 \cdot M. \tag{2.16}$$

Hence, its dependence on ε_{ij}, Eq. (2.14) describes the plastic anisotropy of the monocrystalline volume element. M has been called the *plastic potential*. It is the basis for the calculation of the plastic properties of the material (for small deformations).

The rigid rotation rate R changes the crystallographic orientation g of the volume element by Δg

$$\Delta g = d\eta \cdot R \qquad \text{Lattice Spin.} \tag{2.17}$$

Corresponding to the Cosserat continuum (Lippmann 1969, 1995) this may be called the "lattice spin" of the monocrystalline volume element. The Cosserat theory of elasticity, also known as micropolar elasticity, incorporates the translation due to force stress assumed in classical elasticity as well as a local orientation of volume elements due to a couple stress (torque). Lattice spin is the basis for the change of texture in the course of plastic deformation. Considered as a function of the starting orientation g it describes the *Orientation Flow Field* (in the orientation space) (Bunge and Klein 1993, 1991).

The Taylor model does not fix the factors α^m in Eq. (2.15) which may assume any values under the conditions

$$\sum_m \alpha^m = 1; \quad 0 \le \alpha^m \le 1. \tag{2.18}$$

The actual values of the α^m depend on the environment of the considered volume element, i.e. on g(**x**) in this environment. They may also be influenced by the local defect substructure D(**x**), Eq. (2.1). These quantities are, however, not taken into consideration in the classical Taylor model. Rather, as was mentioned in the context of Eq. (2.9), this model stays within the scope of the classical texture function f(g). Hence, within the Taylor model, some reasonable assumptions for some average values of the α^m are usually introduced (see e.g. (Chin 1969)). It is worth mentioning that the non-uniqueness of the rotation Δg, for volume elements with the same starting orientation g, leads to deformation textures which are flatter than the ones described later on in Eq. (2.24). For details see e.g. (Bunge and Klein 1993).

In Fig. 2.18 the Taylor factor is shown as a function of crystal orientation g, calculated for plane-strain deformation q = 0 (see Eq. (2.26)) for fcc metals with the glide systems $\{111\}\langle 110\rangle$ (Bunge 1970). In Fig. 2.19 one section, $\varphi_1 = 90°$, of the orientation flow field is shown for the same parameters as for the Taylor factor in Fig. 2.18 (Bunge 1970).

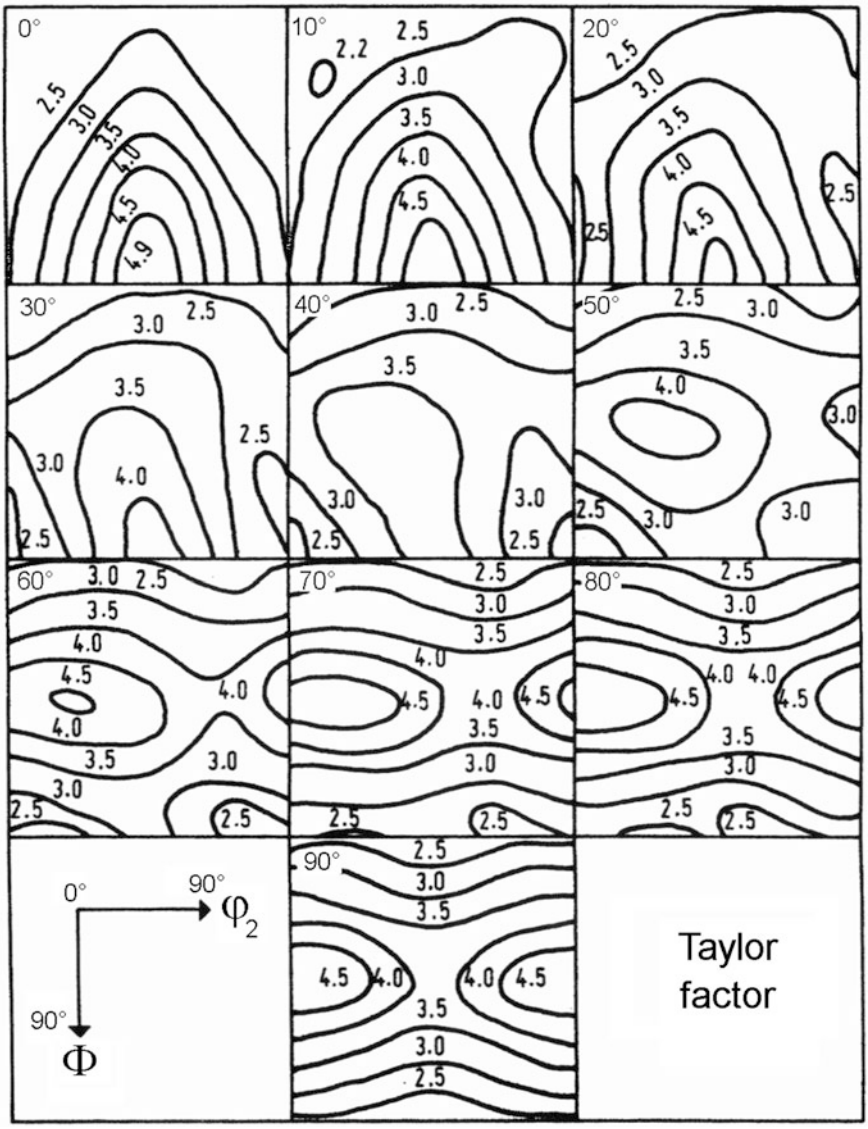

Fig. 2.18 The single-crystal Taylor factor M(g) as a g function of crystal orientation expressed by Euler angles φ_1, Φ, φ_2

Polycrystalline Volume Element

The monocrystal quantities M and R, Eqs. (2.14) and (2.15), are to be averaged in the *polycrystalline volume element* $V_{\mathbf{x}}$ with the texture f(g) as weight function:

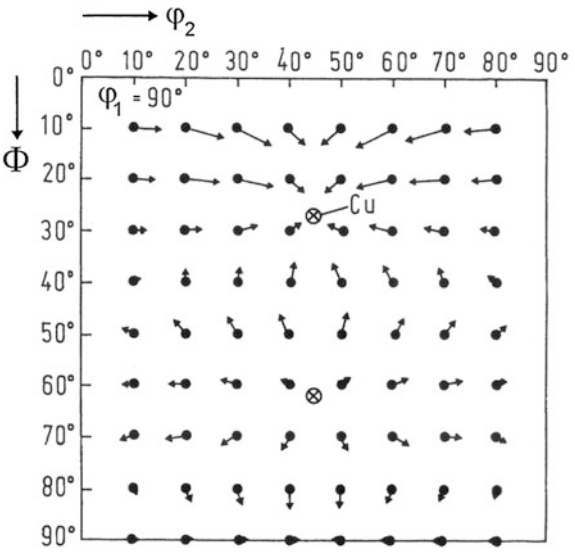

Fig. 2.19 Lattice rotation R (g) as a function of the initial orientation g (only one section, $\varphi_1 = 90°$, of the Euler space is shown). Crystal orientations rotate toward the main orientation (Cu) of the copper rolling texture

$$\overline{M}(\varepsilon_{ij}) = \int_g M(\varepsilon_{ij}, g) \cdot f(g)\, dg \tag{2.19}$$

$$\overline{R}_{ij}(\varepsilon_{ij}) = \int_g R_{ij}(\varepsilon_{ij}, g) \cdot f(g)\, dg. \tag{2.20}$$

The polycrystal Taylor factor $\overline{M}$ expresses the deformation work needed during the deformation step $d\eta$ in the polycrystalline volume element $V_{\mathbf{x}}$

$$d\overline{W} = d\eta \cdot \tau_0 \cdot \overline{M}. \tag{2.21}$$

Hence, its dependence on ε_{ij}, Eq. (2.19) describes the plastic anisotropy of this volume element. It is the *plastic potential* for this volume element.

The averaged rotation rate $\overline{R}$ describes a "common" rotation component of all monocrystalline volume elements contained in the polycrystalline one, Fig. 2.20. If the crystallites would do only this rotation, the texture f(g) would only be rotated *as a whole* to the new one

$$f'(g) = f(\overline{\Delta g} \cdot g); \quad \overline{\Delta g} = d\eta \cdot \overline{R} \quad \text{Texture Spin}. \tag{2.22}$$

With reference to the Cosserat continuum (Lippmann 1969, 1995) this may be called the *Texture Spin*. It is, however, evident from Fig. 2.20 that this texture spin represents only a small part of the total texture change. This is corroborated by Fig. 2.21. In this figure the deviation of the texture from its original orthotropic

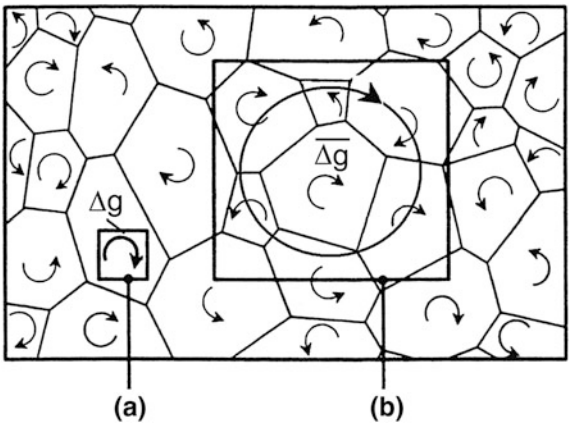

Fig. 2.20 Individual lattice rotation Δg (lattice spin) *a* and the average rotation $\overline{\Delta g}$ (texture spin) *b*

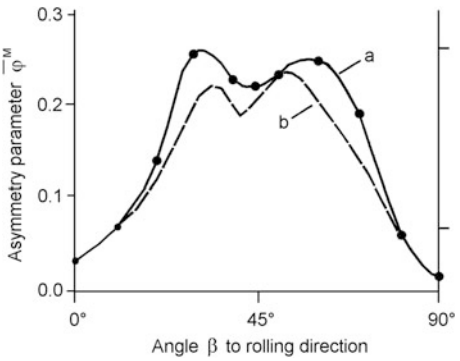

Fig. 2.21 Deviation of the texture symmetry from the original orthotropic symmetry (as a measure of texture change) for samples cut out of an aluminum sheet and elongated by 20 % under the angle β to the rolling direction: *a* total asymmetry; *b* remaining asymmetry after carrying out the "texture spin" rotation according to Eqs. (2.20) and (2.22)

symmetry (expressed by an asymmetry parameter) is plotted for samples cut out of an aluminum sheet under different angles β to the rolling direction (i.e. to the original orthotropic axes) and elongated by 20 % (Bunge and Nielsen 1997). The upper curve a is the total change, the lower curve b is obtained after carrying out the texture spin, Eq. (2.22), i.e. the average rotation shown in Fig. 2.20b. The still remaining deviation from orthotropic symmetry, curve b, is due to the *individual rotations* shown in Fig. 2.20a. They are much stronger than the "common" rotation component, the texture spin which is shown in Fig. 2.22, as a function of the angle β. It assumes a maximum value of only 5° in this case. Hence, the Cosserat continuum is not an appropriate model to treat plastic deformation to large plastic strains *in terms of polycrystalline volume elements*. In the isotropic Cosserat solid there are six elastic constants, in contrast to the classical elastic solid in which there are two. A polycrystalline volume element requires many more internal parameters, e.g. the texture coefficients $C_{\lambda}^{\mu\nu}$, Eq. (2.41).

In order to obtain the *complete texture change* the rotations R(g) must be considered individually for all orientations g together with the orientation densities f(g)

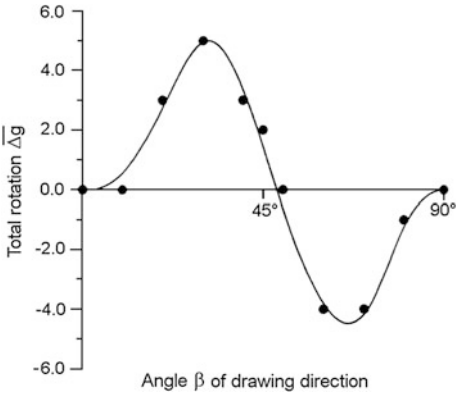

Fig. 2.22 The texture spin Δg according to Eqs. (2.20) and (2.22) and Fig. 2.20 for samples cut out of an aluminum sheet and elongated 20 % under the angle β to the rolling direction

in these orientations. Hence, the texture change during a *small deformation step* dη is described by the *continuity equation* in the orientation space g (Clement and Coulomb 1979):

$$\frac{\partial f(g,\eta)}{\partial \eta} = -\mathrm{div}\{f(g,\eta)\cdot R(g)_\varepsilon\} = \phi(g,\eta)_\varepsilon \quad \text{Continuity Equation.} \tag{2.23}$$

Equation (2.23) expresses the fact that no orientations "get lost" in the orientation space. They rather move continuously into and out of any volume element in this space in which the density f(g) is defined. In this respect the texture is analogous to a compressible fluid in the orientation space with local density f(g). After larger deformation the end-texture $f^{end}(g)$ is reached. It is obtained by integration over all small steps dη. Thereby it must be admitted that the deformation tensor ε_{ij} (i.e. the deformation geometry) may vary with the deformation degree η. Hence, the *deformation path* ε(η) must be taken into account, and it is obtained after *large deformations* by

$$f^{end}(g) = f^{start}(g) + \int_{\eta^{start}}^{\eta^{end}} \phi(g,\eta,\eta(\varepsilon))\, d\eta \qquad \text{Large Deformations.} \tag{2.24}$$

As a special case, the deformation path ε(η) may also be constant, as for instance during uniaxial elongation in the homogeneous range.

2.5.2 Special Plasticity Parameters

Having Eqs. (2.12a) and (2.12b) in mind, it is meaningful to split the deformation tensor, Eq. (2.10), into its symmetric and antisymmetric part

$$\varepsilon_{ij} = \varepsilon_{ij}^{sym} + \varepsilon_{ij}^{ant}. \tag{2.25}$$

The first one is a shape change of the volume element, the second one is a rigid rotation (which is to be distinguished from the lattice rotation R_{ij} in Eq. (2.12)). The symmetric part can be referred to its *principle axes* which are related to the chosen sample coordinate system K_A by the rotation g_ε

$$\varepsilon_{kl}^{sym} = \begin{bmatrix} 1 & 0 & 0 \\ 0 & -q & 0 \\ 0 & 0 & -(1-q) \end{bmatrix}_{g_\varepsilon} \qquad \text{Principle Strain Axes.} \tag{2.26}$$

By the choice of $d\eta$ the component ε_{11} in Eq. (2.26) can always be normalized to one. As is seen in Eqs. (2.12a) and (2.13), the monocrystal Taylor factor M depends only on the symmetric part of the imposed strain ε^{sym}. With Eq. (2.19) the same holds for the polycrystal Taylor factor $\overline{M}$. Hence, we can write

$$\overline{M}(\varepsilon) = \overline{M}(\varepsilon^{sym}) = \overline{M}(q, g_\varepsilon). \tag{2.27}$$

If we know the principle strain axes a priori then we can choose them as the sample coordinate system K_A. In this case the polycrystal Taylor factor depends only on one parameter, namely q (assuming of course that the texture is given and does not change during the small deformation step).

According to Eq. (2.21) the Taylor factor $\overline{M}$ describes the deformation work needed during the deformation step $d\eta$. If the parameters q and g_ε in Eq. (2.27) are not fixed by the deformation device, then they will assume such values which minimize Eq. (2.27):

$$\overline{M}(q, g_\varepsilon) \rightarrow \min. \tag{2.28}$$

The minimum values depend on the texture and hence, they are material property parameters, describing plastic anisotropy.

We consider particularly the following two simple experimental conditions:

Uniaxial Stress, r-Value

In a uniaxial tensile test a uniaxial *stress* is applied. This enforces a strong *strain* component along the stress direction. Nevertheless, the principle strain axes may deviate from the principle stress axes, Fig. 2.23. In many cases (of not too strong texture) these deviations may, however, be neglected. Then g_ε in Eq. (2.28) is fixed and $\overline{M}$ has to be minimized with respect to q only:

$$\frac{d\overline{M}(q)}{dq} = 0 \quad \rightarrow \quad q_{min}. \tag{2.29}$$

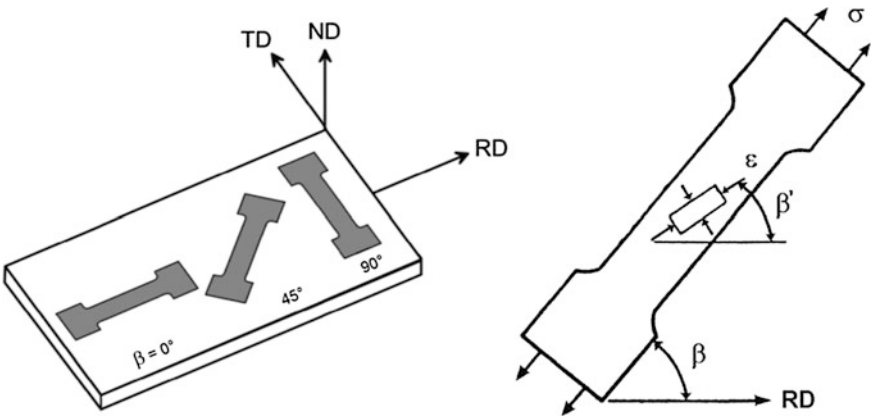

Fig. 2.23 In a uniaxial tensile test under the angle β towards sheet-rolling direction the principle strain axes ε may deviate from the principle stress axes σ

The minimum value of q is related to the *Lankford parameter* r by

$$r = \frac{q_{min}}{1 - q_{min}}. \tag{2.30}$$

This is illustrated in Fig. 2.24 for two samples cut in rolling direction and under 45° from a rolled iron sheet. The curves were calculated from the measured texture by Eq. (2.19) as a function of q. The experimental q-value agrees quite well with the calculated minimum value according to Eq. (2.29) (Bunge and Roberts 1969; Bunge 1970).

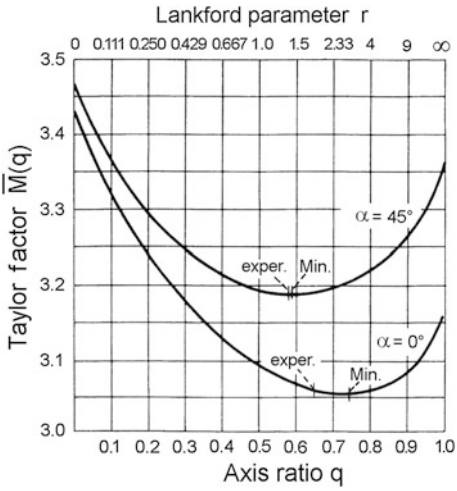

Fig. 2.24 The polycrystal Taylor factor $\overline{M}(q)$ as a function of q (for a given texture) compared with the experimentally determined q-value, respectively r-value according to Eq. (2.30)

Biaxial Stress, Yield Locus
A biaxial stress may be applied to the material. It can be represented in the *principle stress axes* which have the orientation g_σ with respect to the sample coordinate system K_A:

$$\sigma_{ij} = \begin{bmatrix} \sigma_1 & 0 & 0 \\ 0 & \sigma_2 & 0 \\ 0 & 0 & 0 \end{bmatrix}_{g_\sigma} \qquad \text{Principle Stress Axes.} \tag{2.31}$$

In the most general case the *principle strain axes* g_ε in Eq. (2.26) need not be parallel to the principle stress axes of Eq. (2.31) as was illustrated in Fig. 2.23. If, however, the material has orthorhombic (orthotropic) symmetry, as in the case of sheet metals, and if we choose the principle stress axes parallel to the orthotropic axes of the material, i.e. to the symmetry axes of the texture, then they are also the principle strain axes g_ε of Eq. (2.26). The deformation work (Eq. (2.21)) can then be expressed by the stress and strain tensor

$$\begin{aligned} d\overline{W} &= d\eta \cdot \varepsilon_{ij} \cdot \sigma_{ij} \\ &= d\eta \cdot [\sigma_1 - q \cdot \sigma_2] = \tau_0 \cdot d\eta \cdot \overline{M}(q). \end{aligned} \tag{2.32}$$

For any given value of q, Eq. (2.32) represents a straight line in the principle stress-space σ_1, σ_2 which is a tangent to the yield locus. The yield locus is then obtained as the inner envelope of the bunch of these straight lines. By differentiating Eq. (2.32) with respect to q one obtains, together with Eq. (2.32), (Bunge et al. 1980; Park et al. 1993)

$$\begin{aligned} \sigma_1 &= \left[\overline{M}(q) - q \cdot \frac{d\overline{M}(q)}{dq}\right] \cdot \tau_0 \\ \sigma_2 &= -\frac{d\overline{M}(q)}{dq} \cdot \tau_0 \end{aligned} \tag{2.33}$$

This is illustrated in Fig. 2.25. The *shape* of the yield locus follows from $\overline{M}(q)$ and hence from the texture, its *size* is given by the hardness parameter τ_0.

2.5.3 *Plasticity of Cubic Metals*

Crystal structure enters plastic behavior, e.g. in the Taylor model, via the glide systems, i.e. via the G_{ij}^n in Eq. (2.12) expressed by $\mathbf{d}_i^n$ and $\mathbf{n}_j^n$ in Eq. (2.11). The glide systems are (in a good first approximation)

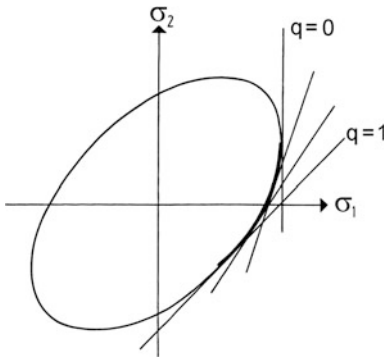

Fig. 2.25 The yield locus is obtained as the inner envelope of a bundle of straight lines as a function of q (cf. Eq. (2.32))

$$\begin{array}{llll} \text{for} & \text{fcc} & \text{metals}: & \{111\}\langle 110\rangle \\ \text{for} & \text{bcc} & \text{metals}: & \{110\}\langle 111\rangle \end{array} \tag{2.34}$$

i.e. glide plane normal and glide direction are exchanged in the two crystal structures. Then it follows immediately from Eq. (2.11)

$$\begin{aligned} G^{n}_{ij}(g)^{sym}_{bcc} &= G^{n}_{ij}(g)^{sym}_{fcc} \\ G^{n}_{ij}(g)^{ant}_{bcc} &= -G^{n}_{ij}(g)^{ant}_{fcc} \end{aligned} \tag{2.35}$$

and for the two principle quantities of plasticity, M and R:

$$\begin{aligned} M(g)_{bcc} &= M(g)_{fcc} \\ R_{ij}(g)_{bcc} &= -R_{ij}(g)_{fcc}. \end{aligned} \tag{2.36}$$

Hence, with the same texture, fcc and bcc metals have the same (polycrystal) Taylor factor

$$\overline{M}_{bcc} = \overline{M}_{fcc} \qquad \text{Same Texture f}(g) \tag{2.37}$$

and therefore the same plastic anisotropy expressed, for instance, by the r-value, Eq. (2.30), or by the yield locus, Eq. (2.33).

As an example Fig. 2.26 shows the yield loci of three different fcc and bcc materials calculated from their respective textures. All three yield loci are in between those according to the von Mises and Tresca hypotheses. The differences are due to the different rolling textures. Because of Eq. (2.37), fcc and bcc materials *with the same given texture* need not be distinguished in plasticity model calculations *for small deformations*. Because of Eq. (2.36b), however, the orientation changes of fcc and bcc crystals by plastic deformation go into opposite directions. Hence, with the *same starting texture different end-textures* will result after the

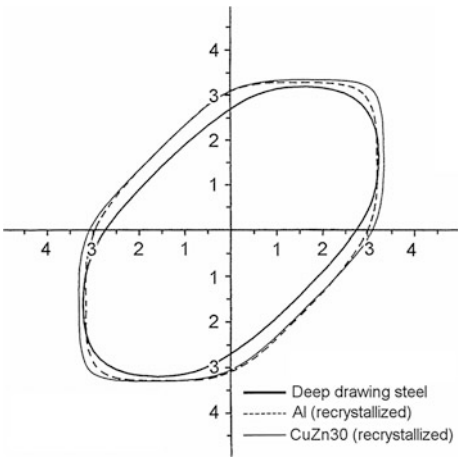

Fig. 2.26 Yield loci of various materials calculated from their textures

same (large) plastic deformation according to Eq. (2.24). Therefore, plastic behavior of these two kinds of materials is different *after large deformation*.

Finally Fig. 2.27 illustrates the influence of different glide systems on the yield locus with the same texture (in this case random crystal orientation distribution is assumed). Glide systems $\{111\}\langle 112\rangle$ have been considered (at least in addition to $\{111\}\langle 110\rangle$) for fcc metals with low stacking fault energy such as brass and silver. Pencil glide $\{hkl\}\langle 111\rangle$ is assumed to be the best-fitting deformation mode for bcc metals. Taking different glide systems into account then Eq. (2.36) is no more strictly valid, but it is still a good first approximation.

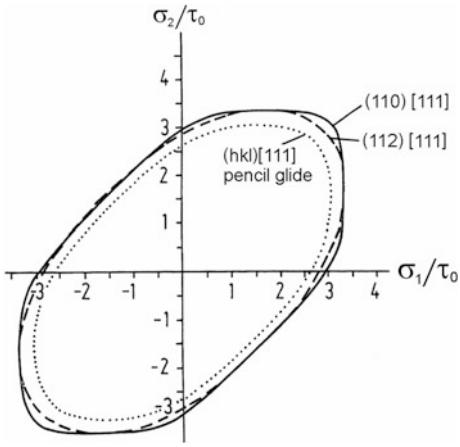

Fig. 2.27 Yield loci calculated for three different glide systems

2.5.4 Deformation Hardening

Any change of the flow stresses σ in the course of deformation is generally called *deformation hardening*. The stresses are obtained by minimizing the deformation work, Eq. (2.21), from which particularly Eq. (2.33) was obtained in that special case.

Hence, total hardening can be split into the following three contributions due to changes of the three parameters τ_0, a^n and f(g) entering this expression

$$\left(\frac{\partial\sigma}{\partial\eta}\right)_{a^n,f(g)} = \frac{\partial\sigma}{\partial\tau_0}\cdot\frac{d\tau_0}{d\eta} \qquad \text{Isotropic Strain Hardening} \tag{2.38}$$

$$\left(\frac{\partial\sigma}{\partial\eta}\right)_{\tau_0,f(g)} = \frac{\partial\sigma}{\partial a^n}\cdot\frac{da^n}{d\eta} \qquad \begin{array}{l}\text{Anisotropic Strain Hardening}\\ \text{“Latent Hardening”}\end{array} \tag{2.39}$$

$$\left(\frac{\partial\sigma}{\partial\eta}\right)_{\tau_0,a^n} = \frac{\partial\sigma}{\partial\, f(g)}\cdot\frac{df(g)}{d\eta} \qquad \text{Texture Hardening.} \tag{2.40}$$

It is worth mentioning that all three parts may assume also negative values (softening). This is particularly known as the *Bauschinger Effect* and as *deformation softening* (negative strain hardening) as well as *texture softening*. The prevailing case is, however, positive hardening.

Anisotropic strain hardening (latent hardening) is often assumed to be small compared with isotropic strain hardening. In this case strain hardening is a multiplicand factor τ_0, Eqs. (2.21) and (2.33). This factor does not enter Eqs. (2.29) and (2.30). Hence, the r-value is a plasticity parameter which is independent of the actual hardening state of the material (which may be different when different samples are being compared). Texture hardening (or softening) can be deduced from the texture change according to Eq. (2.23) for small deformation steps (where it is generally small compared to strain hardening), and from Eq. (2.24) for large strains in which case it must not be neglected.

2.5.5 Plasticity of Macroscopic Bodies

On the *mesoscopic* scale we have considered a polycrystalline volume element $V_{\mathbf{X}}$ (type d in Fig. 2.15) which is characterized by its texture f(g) and its hardness described by τ_0^n. Both quantities may vary as a consequence of deformation.

On the *macroscopic* scale (process-relevant scale) many such polycrystalline volume elements at the loci $\mathbf{X}$ must be considered. They undergo the local deformation $\bar{\varepsilon}(\mathbf{X})$(deformation field) which may even vary in the course of deformation as a function of η (deformation path). Hence, each volume element may develop its own texture (texture field f(g, $\mathbf{X}$)) as well as its own hardness $\tau_0^n(\mathbf{X})$, both as a

function of the actual deformation degree η. The deformation field $\bar{\varepsilon}(\mathbf{X})$ is not uniquely fixed by the external conditions. Rather, stresses and/or strains are given only on the surface of the body. The stress and strain *fields* $\bar{\varepsilon}(\mathbf{X})$ and $\sigma(\mathbf{X})$ develop according to minimum *total* deformation energy which involves the actual materials *property fields* $f(g, \mathbf{X}, \eta)$ and $\tau_0^n(\mathbf{X}, \eta)$. Hence, any plasticity model of macroscopic bodies must consider local textures and local hardness simultaneously (see e.g. (Hoferlin et al. 1999)).

2.6 Parameterization of the Texture Function

The texture function f(g), defined in Eq. (2.2), is the basic quantity for the calculation of the plastic properties of a polycrystalline material from the known properties of monocrystals expressed in Eq. (2.19). The function f(g) is a function of three variables. It requires several thousand function values for its numerical representation and treatment (depending on the required angular resolution and hence accuracy). This number can be drastically reduced by choosing an appropriate *parameterization* of this function. For this purpose we express f(g) by a series expansion in terms of generalized spherical harmonics $T_\lambda^{\mu\nu}(g)$ (Bunge 1982):

$$f(g) = \sum_{\lambda=0}^{L} \sum_{\mu=1}^{M(\lambda)} \sum_{\nu=1}^{N(\lambda)} C_\lambda^{\mu\nu} \cdot T_\lambda^{\mu\nu}(g). \tag{2.41}$$

The "resolving power" of this representation is given by the series truncation value L. The function f(g) is then represented by its coefficients $C_\lambda^{\mu\nu}$, the number of which depends on L. The coefficients are obtained from experimental measurements of pole figures by a mathematical procedure called *Pole Figure Inversion* for which routine computer programs have been developed (Dahms and Bunge 1989; Dahlem-Klein et al. 1993; Schäfer 1998). The positivity of ODF and pole figures, as statistical density functions, is taken into account during the iterative calculation so that "ghost" errors are eliminated. The result of this procedure was illustrated in Fig. 2.5.

In order to calculate the basic integral Eq. (2.19), the function M(g) is represented in the same way (Bunge 1970) as well:

$$M(g) = \sum_{\lambda=0}^{L_0} \sum_{\mu=1}^{M(\lambda)} \sum_{\nu=1}^{N(\lambda)} m_\lambda^{\mu\nu} \cdot T_\lambda^{\mu\nu}(g). \tag{2.42}$$

Thereby the truncation value L_0 may be chosen different from L in Eq. (2.41). The coefficients $m_\lambda^{\mu\nu}$ can be obtained from M(g) by a known mathematical procedure, see e.g. (Bunge 1982). The integral Eq. (2.19) then takes on the form

$$\overline{M} = \sum_{\lambda=0}^{L_{min}} \sum_{\mu=1}^{M(\lambda)} \sum_{\nu=1}^{N(\lambda)} \frac{C_\lambda^{\mu\nu} \cdot m_\lambda^{\mu\nu}}{2\lambda+1}; \quad L_{min} = \min[L, L_0]. \tag{2.43}$$

It turns out that usually the series Eq. (2.42) converges much faster than that of Eq. (2.41), i.e. $L_0 < L$. In fact, rather low values of L_{min} are often satisfactory. Hence, Eq. (2.43) provides a very "economic" mathematical treatment of the "Texture → Property" relationship illustrated on the right side of Fig. 2.9 (here applied to plastic properties).

In cubic materials the lowest-order non-random approximation is $L_{min} = 4$. With this approximation the r-value in sheet metals, according to Eqs. (2.29) and (2.30), in the sheet plane, Fig. 2.11, can be written in the form

$$r(\beta) = 1 + r_1 C_4^{11} + r_2 C_4^{12} \sin 2\beta + r_3 C_4^{13} \sin 4\beta. \tag{2.44}$$

It contains only three texture coefficients $C_4^{1\nu}$. Since a similar fourth-order expression describes the elastic properties in sheet materials, too, this may be used as the basis for an (indirect) determination of plastic properties from the more convenient measurement of elastic properties, as was done, for the first time, by Stickels and Mould (Stickels and Mould 1970) and was found satisfactory in many applications.

It must be mentioned, however, that the "Process → Texture" relationship does not allow a satisfactory low-order approximation. This relationship, expressed in Eqs. (2.23) and (2.24), requires the full series expansion Eq. (2.41) with the value L guaranteeing good convergence of the series (which is the higher the sharper the texture is). As a rule $L \sim 30$ may be satisfactory in many cases, corresponding to some hundred coefficients $C_\lambda^{\mu\nu}$. This is much more than the four coefficients of the approximation, but Eq. (2.44) is still one order of magnitude lower than the representation of the texture function f(g) by several thousand function values. Hence, the parameterization of this function by Eq. (2.41) is "most economic" also for the "Process → Texture" relationship. For details see e.g. (Klein and Bunge 1991).

2.7 Other Modes of Plasticity

In the preceding sections we have considered plastic deformation on the basis of dislocation glide (which was averaged to homogeneous shear in the glide systems). In the most general case, however, many other physical processes may also contribute to plastic deformation of materials:

- *Mechanical twinning* leads to homogeneous shear in the twin lamellae, similar to Eq. (2.11). Crystal orientation in these lamellae is, however, changed discontinuously with respect to the starting crystal orientation. Furthermore, the shear stresses τ_0^n, by which twinning is "triggered", are quite different in

twinning and "anti-twinning" direction. Twinning is the main reason for non-centrosymmetric yield loci in the *hexagonal materials*. This is not treated in the present chapter.

- *Grain boundary sliding* leads to highly localized shear strains in the grain boundaries, based on diffusion processes. In this case texture formation contains a strong contribution of rigid rotation of grains with respect to each other. It is assumed that this effect plays an important role in *superplastic deformation* which is also not considered in this chapter.
- *Hot deformation* is characterized by recrystallization processes occurring simultaneously with dislocation glide and hardening. Hence, the texture, and as a result of that plastic anisotropy, are changing in a different way compared to that considered in this chapter. It may be mentioned that the deformation of *low-melting-point materials*, such as lead, may be "hot-deformation" in this sense even at room temperature.
- *Martensitic phase transformation* may be induced by plastic deformation (deformation martensite). This process bears strong analogy to mechanical twinning mentioned above. This process plays a role, for instance, in some steels. It is also the basic process for *shape memory materials*, the deformation of which is also not considered in this chapter.
- *Green-forming* of (moist) ceramic masses is based on sliding and rotation of rigid particles and follows completely different mechanisms as those considered here.
- Finally, the present considerations deal only with crystalline materials as shown in Fig. 2.1 and described in the Microstructure Function, Eq. (2.1). This does not include materials with *amorphous structures* (either completely or partly amorphous) such as polymers or glasses. Plasticity of these materials is thus also not included in this chapter.

Mathematical models for the Process → Texture, Texture → Property relationships (Fig. 2.9) and hence, the plasticity of materials, based on the mentioned mechanisms, are much more complicated than the case treated here, i.e. plasticity based only on dislocation glide. Nevertheless, plasticity based on dislocation glide only is still the most prominent case applicable to the formability of many technologically important materials.

References

Bishop JFW, Hill R (1951) A theoretical derivation of the plastic properties of a polycrystalline face-centered metal. Phil Mag Ser 7:1298–1307

Brokmeier HG, Lenser S, Schwarzer R, Ventzke V, Riekehr S, Kocak M, Homeyer J (2007) Crystallographic texture of dissimilar laser welded Al5083-Al6013 sheets. Mat Sci Forum 539–543:3894–3899

Bunge HJ (1970) Some applications of the Taylor theory of polycrystal plasticity. Kristall Tech 5:145–175

Bunge HJ (1982) Texture analysis in materials science—mathematical methods. Butterworths, London. http://www.ebsd.info/pdf/Bunge_TextureAnalysis.pdf
Bunge HJ, Klein H (1993) Model calculations of texture changes by non-unique orientation flow fields. In: Lee WB (ed) Advances in engineering plasticity and its applications. Elsevier, Amsterdam, pp 109–117
Bunge HJ, Nielsen I (1997) Experimental determination of plastic spin in polycrystalline material. Int J Plast 13:435–446
Bunge HJ, Roberts WT (1969) Orientation distribution, elastic and plastic anisotropy in stabilized steel sheet. J Appl Cryst 2:116–128
Bunge HJ, Schwarzer RA (2001) Orientation stereology—a new branch in texture research. Adv Eng Mat 3:25–39
Bunge HJ, Schulze M, Grzesik D (1980) Calculation of the yield locus of polycrystalline materials according to the Taylor theory. Peine+Salzgitter Berichte, Sonderheft
Canova GR, Kocks UF, Jonas JJ (1984) Theory of torsion texture development. Acta Met 32:211–266
Chin GY (1969) Tension and compression textures. In: Grewen J, Wassermann G (eds) Textures in research and practice. Springer, Berlin, pp 51–80
Clement A, Coulomb P (1979) Eulerian simulation of deformation textures. Scr Met 13:899–901
Cosserat E, Cosserat F (1909) Theory of deformable bodies (in French). A. Hermann et Fils, Paris
Dahlem-Klein E, Klein H, Park NJ (1993) Program system ODF analysis. Cuvillier Verlag, Göttingen
Dahms M, Bunge HJ (1989) The iterative series-expansion method for quantitative texture analysis: I. General outline. J Appl Cryst 22:439–447
Dawson PR, Beaudoin AJ (1998) Finite element simulation of metal forming. In: Kocks UF, Tomé CN, Wenk HR (eds) Texture and anisotropy. Cambridge University Press, pp 532–558
Dawson PR, Beaudoin AJ, Mathur KK (1994) Finite element modelling of polycrystalline solids. Mat Sci Forum 157–162:1703–1712
Fischer AH, Schwarzer RA (1998) Mapping of local residual strain with an X-ray scanning apparatus. Mat Sci Forum 273–275:673–677
Hoferlin E, van Bael A, van Houtte P (1999) Influence of texture evolution on finite element simulation of forming processes. In: Szpunar J (ed) Proceedings of 12th international conference on textures of materials (ICOTOM-12). NRC Research Press, Ottawa, pp 249–254
Honneff H, Mecking H (1978) A method for the determination of the active slip systems and orientation changes during single crystal deformation. In: Gottstein G, Lücke K (eds) Proceedings of 5th international conference on texture of materials (ICOTOM-5), vol 1. Springer, Berlin, pp 265–275
Iwakuma T, Nemat-Nasser S (1984) Finite element elastic-plastic deformation of polycrystalline metals. Proc Roy Soc London A 394:87–119
Klein H, Bunge HJ (1991) Modelling deformation texture formation by orientation flow-field. Steel Res 62:548–559
Kocks UF, Tomé CN, Wenk HR (1998) Texture and anisotropy. Cambridge University Press
Kröner E (1961) On the plastic deformation of the polycrystal (in German). Acta Met 9:155–161
Leffers T (1988) Deformation textures: simulation principles. Panelist's contribution. In: Kallend JS, Gottstein G (eds) Proceedings of 8th international conference on textures of materials (ICOTOM-8). The Metallurgical Society of AIME, Warrendale, pp 273– 284
Leffers T, Asaro RJ, Driver JH, Kocks UF, Mecking H, Tomé C, Van Houtte P (1988) Deformation textures: simulation principles. Panel report, pp. 265–272
Lippmann H (1969) A Cosserat theory of plastic flow (in German). Acta Met 8:255–284
Lippmann H (1995) Cosserat plasticity and plastic spin. Appl Mech Rev 48:753–762
Lowe TC, Rollett AD, Follansbee PS, Daehn GS (1991) Modelling the deformation of crystalline solids: physical theory, applications, and experimental comparison. The Metallurgical Society of AIME, Warrendale
Masson R, Zaoui A (1999) Self-consistent estimates for the rate-dependent elastoplastic behaviour of polycrystalline materials. J Mech Phys Solids 47:1543

Molinari A, Canova GR, Ahzi S (1987) A self-consistent approach of the large deformation polycrystal viscoplasticity. Acta Met 35:2983–2994

Park NJ, Klein H, Dahlem-Klein E (1993) Program system physical properties of textured materials. Cuvillier Verlag, Göttingen

Raabe D (1998) Computational materials science. Wiley-VCH, Weinheim

Sachs G (1928) On the derivation of a yield condition (in German). Z Ver Dtsch Ing (Z VDI) 72:734–736

Schäfer B (1998) ODF computer program for high-resolution texture analysis of low-symmetry materials. Mat Sci Forum 273–275:113–118

Schumann H (1979) Crystal geometry—introduction to the theory of lattice transformations of metallic materials (in German). VEB Deutscher Verlag für Grundstoffindustrie, Leipzig

Schwartz AJ, Kumar M, Adams BL, Field DP (eds) (2009) Electron backscatter diffraction in materials science. Springer Science+Business Media, New York

Schwarzer RA (1997) Automated crystal lattice orientation mapping using a computer controlled SEM. Micron 28:249–265

Schwarzer RA (2005) Texture mapping by scanning X-ray diffraction and related methods. In: Singh AK (ed) Advanced X-ray techniques in research and industry. IOS Press, Amsterdam, pp 50–65

Spiess L, Teichert G, Schwarzer R, Behnken H, Genzel C (2016) Modern X-Ray diffraction (in German), 3rd edn. Springer Fachmedien GmbH, Wiesbaden

Stickels CA, Mould RR (1970) The use of Young's modulus for predicting the plastic strain ratio of low carbon steels. Met Trans 1:1303–1312

Taylor GI (1938) Plastic strain in metals. J Inst Metals 62:307–324

Tomé CN, Canova GR (1998) Self-consistent modelling of heterogeneous plasticity. In: Kocks UF, Tomé CN, Wenk R (eds) Texture and anisotropy. Cambridge University Press

Tóth LS, Molinari A, Raabe D (1997) Modelling of rolling texture development in a ferritic chromium steel. Met Trans A 28:2343–2351

Van Houtte P (1984) Some recent developments in the theories for deformation texture prediction. In: Brakman CM, Jongenburger P, Mittemeijer EJ (eds) Proceedings of 7th international conference on textures of materials (ICOTOM-7). Netherlands Society for Materials Science, Zwijndrecht, pp 7–13

Van Houtte P (1996) Microscopic strain heterogeneity and deformation texture prediction. In: Liang Z, Zuo L, Chu Y (eds) Proceedings of 11th international conference on textures of materials (ICOTOM-11). International Academic Publishers, Beijing, pp 236–247

Wassermann G, Grewen J (1962) Textures of metallic materials (in German). Springer, Berlin

Wilson DV (1966) Plastic anisotropy in sheet metals. J Inst Metals 94:84–93

Zaoui A (1986) Quasi-physical modelling of plastic behaviour of polycrystals. In: Gittus J, Zarka J (eds) Modelling small deformations of polycrystals. Elsevier, Amsterdam, pp 187–225

Chapter 3
Multiscale Modelling of Mechanical Anisotropy

Jerzy Gawad, Albert van Bael and Paul van Houtte

3.1 Introduction

Let us first recall one of the most fundamental observations in the material science and engineering: the overall chemical composition of a material does not fully determine the properties of the material. The internal structure of the material, which can be observed on the microscopic scale, influences its macroscopic properties as well. The term 'microstructure' is commonly used when referring to that structure, yet the meaning of the term remains somewhat ambiguous. In the first place, the definitions of the microstructure vary from one research field to another. The differences in what is understood by the term reach down to the list of features that are considered as belonging to the microstructure. Even the length scale associated with the microstructure is not unambiguously defined, although the name itself suggests that order of micrometers would be the proper scale.

The original version of the chapter was revised: The erratum to this chapter is available at 10.1007/978-3-319-44070-5_8

J. Gawad (✉)
Department of Computer Science, KU Leuven,
200A Celestijnenlaan, 3001 Leuven, Belgium
e-mail: jerzy.gawad@cs.kuleuven.be
URL: http://www.kuleuven.be/english

A. van Bael · P. van Houtte
Department of Materials Engineering, KU Leuven,
44 Kasteelpark Arenberg, 3001 Leuven, Belgium
e-mail: albert.vanbael@mtm.kuleuven.be
URL: http://www.kuleuven.be/english

P. van Houtte
e-mail: paul.vanhoutte@mtm.kuleuven.be

D. Banabic (ed.), *Multiscale Modelling in Sheet Metal Forming*,
ESAFORM Bookseries on Material Forming,
DOI 10.1007/978-3-319-44070-5_3

This chapter does not attempt to define the microstructure as such. We will rather follow the notion of microstructure-property relationships. From this point of view, the microstructure includes all features of the material needed to explain a certain property of interest. By the same token, the microstructure contains all information needed to *derive* or *compute* that property. This notion of deriving properties by means of microstructure simulations is nowadays well accepted, see for example the textbook by Ghosh and Dimiduk (2011).

The mechanical behaviour of polycrystalline metals and alloys is controlled by several factors generally attributed to the microstructure of the material. To enumerate just a few most recognized in the literature:

- phase composition,
- crystal structure of the phases, which also determines the deformation mechanisms of each phase,
- grain size and shape,
- preferential orientation of the crystals, usually referred to as crystallographic texture,
- substructure, which is typically a self-organized dislocations pattern,
- interfaces of the phases and grain boundaries,
- presence of non-metalic or intermetalic phases,
- presence of voids and other imperfections at the grain boundaries,
- presence of micro-cracks and other intra-grain discontinuities.

This short enumeration can already give us an impression what order of complexity one has to deal with to derive the properties from the microstructure. Most of these factors cannot be considered in isolation, which makes the matters yet more convoluted. Another source of difficulty intrinsically lies in hierarchical nature of polycrystalline materials: larger structures have a substructure (Fig. 3.1). A length scale suitable to tackle phenomena occurring in the structure is rarely convenient to concurrently analyse the substructure. Even if we limit our interest to plasticity, it remains a highly coupled phenomenon which involves at least large part of the factors listed above. Certain factors have a direct consequence on the plastic

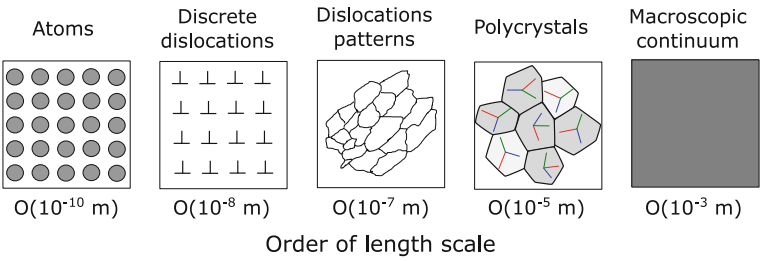

Fig. 3.1 Hierarchy of length scales in metallic materials: from macroscopic, via multiple differently oriented crystals, via patterns of dislocations (substructure), via dislocation cores, to atomistic level. Different modelling and simulation methods are used at each length scale

deformability of the material. For instance, the crystal lattice largely determines the available deformation mechanisms. Some types of crystals may primarily deform by crystallographic slip, other tend to accommodate the deformation also by activating twinning mechanisms. It is also possible that a crystal subjected to an external mechanical loading may also undergo a phase transformation. Yet the crystal structure alone does not give us a complete picture. The activation of the crystallographic deformation mechanisms largely depends on the direction of loading, which means the crystals are mechanically anisotropic. As we can see, there is a link between microstructure and micro-scale properties. If an aggregate comprising a finite number of individual crystals is deformed, its mechanical anisotropy depends on the orientation of the constituents. Therefore, the crystallographic texture, which is a microstructural feature, influences the mechanical anisotropy of polycrystalline. This brings us to the clue that a link between the microstructure and effective properties observed in a lager scale can be also derived. In other words, a microstructure can be exploited to characterize a homogeneous continuous medium (Miehe et al. 1999). Note that the effective properties are usually associated with a constitutive description of the material in continuum mechanics, and as such are very much applicable in numerous engineering problems, including simulation of metal forming.

It is extremely complex to directly include some of microstructural features in continuum mechanics constitutive modelling. For instance, reorientation of individual crystals due to deformation is hard to describe in that manner. Thus, another theoretical framework is needed to derive homogenized properties from the microstructure. It is useful to introduce two different phenomenological scales:

- *micro-scale* that is characterized by a statistically representative volume of material that comprises microstructural constituents. An assembly of microstructural features enumerated above can be conveniently modelled in this scale.
- *macro-scale* that considers the material as a continuous medium.

The two scales can be more generally named as *fine-scale* and *coarse-scale*, respectively, but the terms micro-scale and macro-scale put more emphasis on the relation with the microstructure. For this reason we will only occasionally use the generic names in this chapter. A two-level hierarchy, nevertheless, constitutes one of fundamental building blocks of a more general multi-scale approach.

It is important to note that state variables used in the micro- and macro-scale are typically different, but some of the variables have counterparts in both scales, as presented in Fig. 3.2. This framework is commonly known as Representative Volume Element (RVE), sometimes also referred to as Representative Elementary Volume. The RVE concept is one of the foundations of homogenization theories.

In essence, the RVE is considered as a sub-volume of the whole bulk of material. The RVE allows one to estimate statistically representative coarse-scale responses

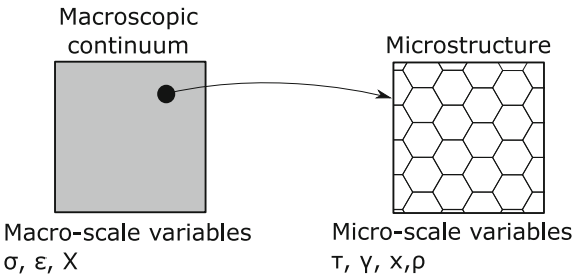

Fig. 3.2 Continuum with micro-structure modelled as RVE. A typical point in the macro-scale is characterized by a representative assembly of microstructural elements. The relations between variables in the coupled scales may vary. For instance, state variables σ, ϵ in the macroscale are defines as volume averages of τ, γ in the micro-scale, respectively, the variable X is a direct counterpart of micro-scale variable x, whereas the variable ρ is relevant only in the micro-scale

or properties of a heterogeneous volume where fine-scale evolution laws hold. A prerequisite needed for this coupling is that a sufficient scale separation must be satisfied (Ostoja-Starzewski 2005, 2006). In other words, an RVE has to be large enough compared to the characteristic length scale of its constituents and processes altering the constituents. Since the RVE is supposed to generate a description that represents the whole material, it must include a sufficient sampling of the variety of microstructural features that exist in the material. This implies that the minimal size of an RVE must be set in such a way that any smaller sub-volume would be insufficient to statistically represent the variation of its constituents. An RVE needs also to satisfy the requirement that further increase of its size does not significantly change the resulting homogenized response or properties (McDowell 2010). As a corollary, a properly constructed RVE shall approximately provide the same response and properties as any other proper RVE.

A natural question arises what is the proper size of the RVE if random polycrystals are modelled. A closely related question is how many grains are necessary to homogenize the response of polycrystalline aggregates. It is essential to realize that the necessary size of an RVE depends on the type of responses and effective properties accounted for. These may present considerably different sensitivity to the microstructural composition of the RVE. The factors that play a role in this context typically include spatial distribution of microstructural constituents inside the RVE, grain size distribution, as well as phase contrast with respect to certain properties. Furthermore, the required RVE size is also influenced. For instance, the elastic properties (the elastic moduli) or responses (such as stiffness) in non-evolving stationary microstructures are less sensitive to local configurations of the constituents than plastic properties in evolving microstructures (McDowell 2010). Therefore, for the same microstructure, the RVE size differs depending on what effective properties are considered (Kanit et al. 2003).

3.2 Multiscale Frameworks in Crystal Plasticity

As we have discussed in the previous section, the plastic anisotropy, as well as many other properties of polycrystalline metals, is controlled by the microstructure. Several microstructural factors are involved, yet crystallographic texture is often the most prevailing feature in this respect. Given its importance, the literature contains a broad variety of reported attempts to take the texture into account in numerical simulations of metal forming processes. Broadly speaking, the microstructure can be explicitly dealt with if a physics-based model is employed to resolve deformation mechanisms in individual crystals. This can be done along with homogenizing the response over a polycrystal. Several crystal plasticity (CP) frameworks exist that allow one not only to derive macroscopic mechanical response of polycrystalline materials, but that also provide insights on how the microscopic state evolves with an increasing deformation. The crystal plasticity frameworks are typically used in one of the following contexts:

- We can use a crystal plasticity framework at the micro-scale, where the microstructure of a small volume of material is represented in a much detailed manner. If the microstructure is explicitly modelled and discretized (either in 2D or 3D), the resolution of the discretization is sufficiently fine to study intra- and inter-granular effects. The RVE method is typically used in this case to obtain effective properties or responses of the microstructure.
- We can also directly use a crystal plasticity framework inside a macroscopic simulation. Although various microstructural features (such as texture evolution, plastic slip, phase transformation etc.) can be tracked, the spatial resolution is usually coarser than in the previous case and typically enables tackling whole grains. Properties of the material or the constitutive relations needed by the macroscopic simulation are directly extracted from the crystal plasticity framework. The direct coupling may follow the RVE approach, but direct embedding is also possible.
- We can combine the two ways and indirectly employ a crystal plasticity framework inside a macroscopic simulation. The microstructure evolution is dealt with by a crystal plasticity RVE, while some other means are used to get the properties or responses needed in the calculations of the macroscopic model. For instance, an approximation function can be fitted to the responses of interest calculated by the RVE. The approximation can be either calculated before the macroscopic simulation starts (i.e. as a part of pre-processing), or during the simulation. The latter case can also include adjusting the approximation to the evolved microstructural state as the macroscopic simulation advances.

The two first approaches are somewhat complementary, but their focus is different. Whereas the former usually attempts to elucidate *why and how* certain fine-scale interactions develop and *how* they impact the coarse-scale, the latter usually tries to answer only the second question. Conversely, the third approach is based on a different paradigm: given a sufficiently predictive CP framework, a computationally efficient coupling has to be established to answer both questions at once.

Several crystal plasticity frameworks have been proposed over the last decades to answer these challenges. In this chapter we shall restrict the discussion to those that explicitly deal with microstructure to recover the properties of interest. We will put particular emphasis on several existing strategies to incorporate the texture data into macroscopic Finite Element simulations.

At this point we only remind the reader that another approach to handle plastic anisotropy exists: phenomenological models that neglect the microstructural evolution and restrict their scope to the macroscopic mechanical response of the material. Chapter 1 provides an extensive overview of models belonging to this category.

3.2.1 Statistical Crystal Plasticity

The RVE concept can be used even if the microstructure is not fully resolved in 3D, but in a statistical manner as a set of crystals. This approach is often called statistical or mean-field crystal plasticity.

3.2.1.1 Sachs-Type Models

The iso-stress model (also called "static model"), which is commonly attributed to Sachs (1928),[1] assumes that the stress mode is the same in all crystals of a polycrystalline aggregate. It is then possible to apply the Generalized Schmid law (see Chap. 2 and Gottstein (2004) for comprehensive explanation of the Schmid law) to each of the crystals. It would then be found, at gradually increasing stress level, that at first there would be no plastic deformation anywhere, until a stress level is reached for which plastic deformation would start in the grain or grains with the most favorable lattice orientation. Since all the grains experience the same state of stress, the plastic deformation that results from it can vary from one grain to another, thus the compatibility conditions in the aggregate are violated. The iso-stress assumption is nowadays considered as an oversimplification, so this group of models is rarely used.

[1] In fact, the work by Sachs (1928) does not assume a uniform stress field in the polycrystal, but it considers a uniaxial tensile test on a polycrystalline material, where the Schmid law (for a uniaxial tensile test!) is applied to find the first activated slip system in all grains, treated as stand-alone single crystals in which one slip system is activated. Sachs proposed a model that assumes the average of all local flow stresses to be the macroscopic flow stress (also tensile, of course).

3.2.1.2 Taylor-Type Models

The Full Constraints (FC) Taylor-Bishop-Hill homogenization scheme, which was originally proposed by Taylor (1938) and later taken up again by Bishop and Hill (1951a), who proposed a different but equivalent solution method, assumes identical plastic deformation throughout all the grains in the considered volume of the material. The constitutive equations are thus formulated for a single grain that is considered in isolation. Although the compatibility conditions are automatically satisfied since the entire aggregate experiences the same state of deformation, yet the stress equilibrium condition is neglected. These authors proposed two different solution methods, which are both based on the Generalized Schmid Law as the constitutive model for a metallic crystal. An approximate but mathematically convenient alternative is the visco-plastic method by Asaro and Needleman (1985).

It is well recognized that the Full Constraints approach overestimates both texture intensity and the homogenized stresses. To answer these limitations, several improvements have been proposed, among which the Relaxed Constraint Taylor (RCT) (Raphanel and Van Houtte 1985; Van Houtte 1982, 1987, 1988). The relaxed constraints models drop Taylor's strict requirement of strain homogeneity and allow certain violations in compatibility conditions. In other words, relaxations are imposed on certain components of the velocity gradient tensor. Although the RCT scheme led to moderate improvements in predictability, the concept itself turned out to be quite influential.

3.2.1.3 Grain Interaction Models

The relaxations are the core part of so-called 'cluster' models (also known as 'grain interaction models'), which define more elaborated homogenization schemes. The homogenization deals with small clusters of grains in place of single crystals. It is assumed that the average plastic velocity gradient of the cluster is equal to the macroscopic velocity gradient. Therefore, the 'cluster' models abandon the assumption that each grain is treated separately and introduce interactions between crystals in the aggregate.

The Advanced LAMEL (ALAMEL) model was proposed by Van Houtte et al. (2005) as a generalization of the LAMEL (Liu et al. 2002; Van Houtte et al. 1999). The ALAMEL model considers interactions in clusters of two grains, separated by an interface, which represents a grain boundary. The interface can be arbitrarily oriented according to a certain distribution function. In the ALAMEL scheme local strains deviate from the macroscopic strain according to admissible relaxation modes, and the extent of the relaxation is calculated by minimizing the collective plastic work inside the cluster. Several improvements to the ALAMEL model scheme have been recently proposed, for example by Arul Kumar et al. (2011), Mahesh (2010), Mánik and Holmedal (2013), Zhang et al. (2014). The multisite approach (Delannay 2002; Delannay et al. 2002, 2009; Van Houtte et al. 2002), which extends the ALAMEL, postulates that each grain interacts exclusively with

one or several of the surrounding grains. Furthermore, it adds elastic part to the governing equations.

A similar model was proposed by Evers et al. (2002), who used the RTC homogenization to calculate deformation of bi-crystal volume elements, each having the crystallographic lattice orientations of two adjacent crystals.

The Grain InterAction (GIA) model, which also puts forward the concept of grain clusters, was proposed by Crumbach et al. (2001) and further elaborated by Engler et al. (2005). The GIA model takes into account short-range interactions between next-neighbour grains in an aggregate consisting of eight hexahedral grains. The structure of GIA was further developed as the Relaxed Grain Cluster (RGC) model by Eisenlohr et al. (2009a, b), Tjahjanto et al. (2010, 2015). It was recently extended to deal with multi-phase materials (Tjahjanto et al. 2015).

3.2.1.4 Self-consistent Schemes

The Visco-Plastic Self-Consistent (VPSC) (Lebensohn and Tomé 1993; Lebensohn et al. 2007; Molinari et al. 1987, 1997) model was originally inspired by Eshelby's (1957) analytical solution of elasticity problem for an ellipsoidal inclusion embedded in an effective medium. In the VPSC the effective medium comprises all the grains in the representative volume and it is considered homogeneous. The individual crystals are treated as plastically deformable ellipsoidal inclusions constrained by the medium, so short-range interactions are basically neglected. However, the model resolves long-range interactions the in the polycrystalline, which originate in the contributions from all the crystals and are carried by the medium. The VPSC model imposes both strain compatibility and stress continuity between grains and their surrounding, as opposed to the Taylor-type models that postulate homogeneous strain in the sample (possibly with relaxations). The VPSC model has gained numerous applications, most remarkably to successfully simulate the deformation of hcp materials, e.g. Beausir et al. (2008), Ebeling et al. (2009), Plunkett et al. (2006), Steglich et al. (2012), Tomé (2001), Walde and Riedel (2007a), Wang et al. (2010) and extensions, see e.g. Knezevic et al. (2013a).

3.2.2 Full-Field Approaches

Here, "full-field" denotes a category of models that make use of a discrete grid to compute certain fields variables (e.g. stress or strain) in the microstructure. The models that belong to this category resolve both long-range and short range interactions. In particular, if a sub-grain resolution of the grid is used, heterogeneities of these fields inside individual crystals can also be considered. Therefore, the full-field approaches apply crystal plasticity theories to predict the actual micromechanical fields that develop inside the grains of a polycrystal.

Consequently, various localized phenomena, such as orientation gradients inside individual grains, can be calculated as well.

The models belonging to this group are usually much more computationally demanding than the statistical models presented in the previous section, although the increase in computing performance over the last decade has allowed conducting statistically meaningful simulations.

As a general remark, the ability to include intra-granular state variables, in particular strain and stress fields, is supposed to enhance the accuracy of microstructure evolution predictions. However, as it was shown in recent studies (see e.g. Héripré et al. 2007; Pokharel et al. 2014; St-Pierre et al. 2008), comparison with intra-granular strain measurements often shows only qualitative agreement suffering clear local discrepancies between modelling and experimental results (Pinna et al. 2015). This can be attributed to various factors, including simplifications in reproducing the initial microstructure, since simulations of more controllable oligocrystals typically deliver better agreement with experiments (Delaire et al. 2000; Klusemann et al. 2012, 2013; Lim et al. 2011, 2014; Raabe et al. 2001; Turner et al. 2013; Zhang et al. 2015a). It has also been shown that the full field models do not necessarily provide considerably better predictions than the statistical ones, neither with respect to texture evolution (see e.g. Li et al. 2004) nor macroscopic anisotropy (see e.g. Zhang et al. 2015b).

3.2.2.1 Crystal Plasticity Finite Element Method

A large body of work exists on incorporating crystal plasticity frameworks as constitutive relation in the Finite Element method. An excellent review of these attempts has been published by Roters et al. (2010a, b). The reader is referred to these works for a comprehensive overview of the constitutive laws, kinematics, homogenization and multiscale methods in the CP-FEM modeling.

Generally, CP-FEM resolves the equilibrium of the forces and the compatibility of the displacements based on a weak form of the principle of virtual work. This is in essence what the Finite Element method does. What differentiates the CP-FEM is the incorporation of a certain crystal plasticity constitutive law to provide the constitutive behavior of the material. This law typically include calculating the slip and twinning activity and the resulting material flow. Constitutive models extending the works of Asaro (1983a, b), Asaro and Rice (1977), Peirce et al. (1982, 1983) are very commonly used and include visco-plastic, elasto-viscoplastic and elastic-plastic constitutive behaviour. Plastic deformation of the material and evolution of texture results from activation of deformation mechanisms, such as slip and twinning. The CP-FEM models are formulated as either rate-dependent or rate-insensitive with respect to the material response. The hardening at the level of crystallographic slip and twinning is taken into account as well. A power law is often chosen to relate the applied resolved shear stress on the slip or twinning system to the shear rate in the slip or twinning direction. Large inelastic deformation can be reached in CP-FEM. However, we have to keep in mind that

accuracy of the FE method may be undermined if large distortions of elements are experienced. This issue can be addressed by advanced mesh refinement methods, see e.g. Quey et al. (2011), Resk et al. (2009).

In CP-FEM the FE mesh represents an aggregate of grains, each having a specific set of attributes, such as shape, orientation, phase, etc. The method offers several advantages over statistical approaches. Most remarkably:

- If several finite elements constitute a grain, the gradients of stress and strain inside individual crystal can be taken into account. This holds even if low order elements (e.g. linear) are used to discretize the domain.
- Gradients of other fields inside the grains can be captured as well. For instance, crystal orientation gradient may be accounted for, which is crucial in modelling intra-granular localization processes.
- Complicated geometry of individual crystals can be explicitly dealt with in the model.
- Since the grains are spatially bound by each other, explicit grain boundaries are introduced in the model. This also allows to take into consideration grain boundary properties.
- Boundary conditions can be imposed on the RVE in a flexible manner.

Despite of all these advantages, the CP-FEM is rarely considered as a feasible approach in modelling component-scale sheet forming processes. Since the number of elements in the RVE grows with the number of grains considered, simulation of the deformation becomes extremely computationally expensive for the solution of complex problems at the macroscopic level. For example, let us consider a realistic size of a cubic three dimensional RVE being 500 nodes at each edge, which transforms into $N = 500^3$ elements. For the sake of simplicity, suppose that the number of DOF required in an FEM calculation is roughly of the same order as the total number of elements. To solve the displacement field at each given deformation increment, one has to invert a matrix of the size of order N^2. This gives us sufficient estimate of the huge computational cost of the CP-FEM.

3.2.2.2 Crystal Plasticity FFT

Recently, considerable attention has been attracted by the Crystal Plasticity Fast Fourier Transform (CP-FFT) method (Eisenlohr et al. 2013; Lebensohn 2001; Lebensohn et al. 2004, 2011, 2012; Liu et al. 2010; Prakash and Lebensohn 2009; Roters et al. 2012; Shanthraj et al. 2015), which promises substantial improvement over the CP-FEM in terms of calculation time, while keeping high spatial resolution in order to capture the details of complex microstructures. As opposed to the CP-FEM, the CP-FFT is meshless, so it uses voxels to discretize 3D domain.

The CP-FFT-based formulation consists in finding a strain-rate field, associated with a kinematically admissible velocity field, that minimizes the average of local work-rate, under the compatibility and equilibrium constraints (Lebensohn et al.

2008). The method is based on the fact that the local mechanical response of a heterogeneous medium can be calculated as a convolution integral between Green functions associated with appropriate fields of a linear reference homogeneous medium and the actual heterogeneity field. This approach is suitable for finding the solution of a unit cell problem with periodic boundary conditions. If a periodic medium is considered, one can use the Fourier transform to reduce convolution integrals in real space to simple products in Fourier space. Thus, the Fast Fourier Transform algorithm can be utilized to transform the heterogeneity field into Fourier space. Afterwards, the mechanical fields can be calculated by applying the transformation back to real space.

The CP-FFT has several advantages over the CP-FEM. It basically eliminates the major computational bottlenecks of the CP-FEM, namely the need for inverting large matrices. In addition, no advanced meshing is needed to discretize the domain since the method is meshless and requires just a simple regular grid of voxels. This also eliminates several related issues, such as degeneration of finite elements on excessive localized deformation. On the disadvantage side, the grid in Fourier space is assumed to be regular, which is less flexible in discretizing complex geometries than a free FE mesh. To date, the CP-FFT solvers can only make use of uniform grid, which might be too coarse to properly approximate stress and strain fields near grain boundaries. To keep the grid regular, simplifications to the kinematic equations have to be made (Liu et al. 2010; Prakash and Lebensohn 2009). Moreover, the fundamental requirement of periodic boundary conditions renders the CP-FFT somewhat less flexible than the CP-FEM. The CP-FEM also permits local mesh refinements to capture localization of strain and abrupt discontinuities of material properties.

3.3 Multi-scale Modelling of Plastic Anisotropy

All crystal plasticity frameworks presented in the previous section are inherently multi-scale: they are designed to predict coarse-scale effects of fine-scale interactions in the microstructure upon imposed coarse-scale boundary conditions. Nonetheless, the macroscopic boundary conditions that are inflicted on a simulated microstructure are relatively simple, either with respect to the geometry (e.g. displacements imposed on a face of a unit cube), or with regard to fundamental assumptions on geometry (e.g. periodicity of the system, thus a unit cube with periodic boundary conditions is assumed), or other basic assumptions in the model (e.g. identical strain everywhere in the material). Even if completely arbitrary boundary conditions can be prescribed, it is not always obvious how to choose the ones that would be most relevant in a given sheet forming process. Typical idealizations, such as plane strain deformation, pure shear, uniaxial tension/compression etc. are often just very rough approximations of the actual conditions, which are nearly always affected by the geometry of the process (including for instance shape of the sheet and the dies) as well as contact conditions and other sources of non-linearities.

For this reason it is usually not straightforward to use any of these models in simulations of sheet forming processes. The CP model can be still used as a component of a macroscopic analysis if it is provided with realistic boundary conditions. To this end, a proper coupling or embedding scheme must be established. In particular, the Finite Element Method, which is nowadays an indispensable engineering tool, has been successfully used as a macroscopic host framework for various CP models. In this section we shall present an overview of the most prominent coupling techniques.

3.3.1 Direct Micro-Macro Coupling

If a micro-scale full field model is available as an RVE, one may use it as a constitutive model in a macroscopic FE simulation. In fact, direct coupling typically discards the notion of deriving properties from RVE, since the micro-model replaces the entire constitutive law, and not just the parameters in a constitutive equation. Thus, it is the homogenized RVE *response* that becomes then an integral part of the macroscopic model.

3.3.1.1 Embedded Full-Field Models

Provided that an FEM RVE is coupled with a macroscopic FE model, this computational framework is called multi-level FEM (ML-FEM) (Smit et al. 1998) or FE^2 (Feyel 1999, 2000; Feyel and Chaboche 2003). Within this general framework one conducts an embedded micro-scale RVE FE computation in order to extract from the RVE the quantities required at integration points of the macroscale finite element mesh.

In the simplest variant, the coupling is rather straightforward. The multi-level FE computes the displacement fields on both macroscopic and microscopic level (Smit et al. 1998). The micro-scale FE RVE provides the homogenized stiffness matrix, which is returned to the corresponding integration point in the macroscopic mesh as the local macroscopic tangential stiffness matrix.

Such embedding scheme has a clear advantage: no analytical constitutive equation needs to be specified at the macroscopic scale, since the constitutive behaviour comes directly from the microscale. For certain types of materials, such as multi-phase steels, constitutive equations that account for the presence of multiple phases are very difficult to specify. The use of ML-FEM bypasses this problem because all the complexity of a multi-phase material is handled by the micro-scale FE simulation.

Admittedly, the FE^2 is excessively costly if used to simulate macroscopic systems discretized with dense FE meshes. For this reason, practical applications of the method are pretty much limited, although extensive fundamental research has been conducted on this topic, see e.g. Coenen et al. (2012a, b), Feyel (1999, 2003), Feyel and Chaboche (2000), Geers et al. (2010), Kouznetsova et al. (2004a, b),

Kouznetsova and Geers (2008), Larsson and Runesson (2011), Miehe (1996), Miehe et al. (1999), Reis and Andrade Pires (2013), Temizer and Wriggers (2008, 2011), Werwer and Cornec (2000).

3.3.1.2 Embedded Mean-Field Models

The macroscopic continuum-mechanics model model can use mean-field homogenization theories, in which the effective behavior of a polycrystal is used to derive its response, but the microstructure is represented in a statistical way. To this end, an aggregate of grains underlies every material point in the macro-scale model. Local macroscopic deformation is imposed on the aggregate, which causes changes in the orientation of the aggregate components. At the same time the averaged response of the aggregate defines the macroscopic behavior of the corresponding material point, thus deformation induced changes in plastic anisotropy is incorporated in the macroscopic finite element model. It has to be noted that we speak here of *direct embedding*, in which the crystal plasticity model is called during each increment of the macroscopic model and provides constitutive response.

Several embedded polycrystalline plasticity models were devised to describe the metal anisotropy in this way. The Taylor-type model (Asaro and Needleman 1985) was incorporated in works of Mathur and Dawson (1989, 1990) to simulate the evolution of crystallographic texture in Finite Element analysis of steady state forming simulations. The fully-implicit scheme based on the same Taylor-type model was later proposed in Kalidindi et al. (1992). Despite the relative simplicity of the Taylor assumption, this approach has proved to be quite predictive, as shown in by Jung et al. (2013), Kalidindi and Schoenfeld (2000), Schoenfeld (1998), to mention just a few examples. Yet from purely computational perspective, the models turned out to be costly, in particular if 3D macro-scale systems were simulated, which prompted research on accelerating the coupling. Massive parallel computing (e.g. Beaudoin et al. 1993; Mellbin et al. 2014) on one hand, and exploiting certain assumptions of the Taylor formulation[2] (see e.g. Zecevic et al. 2015a, b) on the other hand have served that purpose.

The mesoscopic viscoplastic self-consistent schemes have been successfully embedded into explicit time integration Finite Element codes. In particular, this coupling was tested on strongly anisotropic aggregates, such as hcp alloys in which plasticity at single-crystal level can be accommodated not only by slip but also by mechanical twinning (Tomé 2001; Walde and Riedel 2007a, b). This group of materials is particularly interesting, since such alloys typically develop pronounced crystallographic texture and rapidly evolve in terms of plastic anisotropy. The challenges to be addressed include rapid textural changes originating from twinning, and associated strong directional hardening/softening, as well as the highly anisotropic slip-twin interaction (Segurado et al. 2012). It is then argued that the

[2]See also Sect. 3.3.2.

fine-scale model has to be frequently queried for the homogenized response in order to accurately follow the microstructural changes.

Recently, several strategies of fully embedding the VPSC mean-field model also in the macroscopic implicit Finite Element analysis model have been proposed (Galán et al. 2014; Knezevic et al. 2013b, c; Segurado et al. 2012). Each integration point of the FE model is considered as a polycrystal that provides the stress and tangent stiffness matrix. The grain orientations approximate the initial texture, which may subsequently evolve with deformation. The strategies attempt to accelerate the calculations by extracting and reusing quantities that are computed as part of the nonlinear self-consistent homogenization scheme. For instance, the FE Jacobian matrix is expressed as a function of the viscoplastic tangent moduli, the elastic stiffness of the aggregate, and the FE time increment (Segurado et al. 2012).

Advanced coupling strategies have been developed to preserve fine-scale variables upon mesh adaptation in the FE macroscopic model, e.g. Prakash et al. (2015).

3.3.1.3 Embedded Reduced Texture Models

Yet the number of the crystals associated to an individual integration point of a macroscopic FE mesh remains a hindering factor in terms of computational performance. To address this issue, an interesting concept to reduce the number of orientations per integration point was proposed by Raabe et al. (2004), Raabe and Roters (2004), Roters (2005), Zhao et al. (2004), where the authors suggested to de-associate the concepts of crystal and orientation and initially only consider some selected texture components. A similar idea was later elaborated in work (Knezevic and Landry 2015). The components are defined as compact functions, each characterized by its orientation (such as the ideal orientations: Goss, Brass or Cube component, etc.), a scatter around the orientation and the volume fraction of the component. The key concept is to exploit the fact that a huge number of crystals can be described by a single representative texture component. Since usually only a small number of texture components is present in a macrotexture, it is sufficient to map a relatively small number of ideal orientations to the macroscopic FE integration points. This is done in such a way that the superposition of all mapped components reproduce the initial texture of the material. However, during the simulation each of the mapped texture components undergoes its individual reorientation under local deformation conditions. Although the method allows reproducing the initial texture, it may not necessarily offer reliable predictions of the final texture at individual integration points. To understand why, let us suppose that just a single texture component is initially sufficient at a given integration point. If the component is unstable under a given deformation mode and, as a consequence, it breaks down into more than one component, the method will track just one of these evolved components and neglect all the others. On this basis, it is also doubtful whether local anisotropy can be accurately extracted from texture data that may become increasingly incomplete during the deformation.

As an alternative, the representative discrete orientations that are needed to reproduce the crystallographic texture can be spatially distributed over several neighboring integration points (Béringhier et al. 2007; Delannay et al. 2005; Logé and Chastel 2006). The way of distributing crystallographic orientations among the finite elements may be either proportional to the volume of the finite elements, or independent of it. In any case, the goal is obtain a good approximation of the ODF by merging contributions (discrete orientations) from several integration points. This way the ODF becomes a local material property of a group of several integration points, as opposed to fully embedded models that attempt to get the ODF locally approximated at every integration point.

3.3.2 Hierarchical Coupling

3.3.2.1 Database and Sampling Techniques

A possible way to capture the influence of microstructural changes on the anisotropic response is to use a crystal plasticity model to calculate some homogenized quantities of interest in advance and later approximate these in a macroscopic simulation. This can be done by sampling followed by calculating a response surface, for instance by means of multivariate Kriging, as reported by Barton et al. (2008), Knap et al. (2008), Rouet-Leduc et al. (2014), or generalized in situ tabulation technique (Arsenlis et al. 2006). Alternatively, a sequence of explicit algebraic yield criteria can be pre-calculated for a finite set of strain levels and linearly interpolated during the macroscopic simulation (Knezevic et al. 2013b; Nixon et al. 2010a, b; Plunkett et al. 2006). In this case the database contains the parameters of the yield locus model expressed as a function of strain and possibly some other variables.

Since the exploited CP model is considered as a black box, the method can be virtually used with any CP model. However, the sampling is very expensive if it has to cover the evolution of the microstructural state variables in a multi-dimensional space. In practice, it is difficult to ascertain that the entire relevant part of that space is sufficiently probed. Nevertheless, it appears problematic that the local material state evolution may lead outside the validity range of the interpolation.

3.3.2.2 Spectral Crystal Plasticity (SCP)

The Spectral Crystal Plasticity (SCP) can be seen as a special case of database-type coupling. Whereas it also relies on sampling responses of a crystal plasticity framework, the way how the results are stored and queried greatly differentiates the SCP from the approach presented in the previous section. The database techniques store the homogenized responses of the RVE, while the SCP stores the intermediate results of a Taylor-type model.

Observe that if a Taylor-type model is used, each crystal is treated separately, and any per-grain solution of the crystal plasticity model depends solely on the orientation of the crystal and the strain rate imposed on it. The solution may include stress, lattice spin, shearing rates, Taylor factor etc. It is then possible to first evaluate a Taylor-type model for a large number of orientations and strain rates and subsequently store the results in an easily retrievable manner. As long as no other factors are taken into account, such as hardening of slip systems or grain interactions, these calculations can be done once and for all.

To achieve this, Fourier (spectral) representation of orientation distribution function (Bunge and Esling 1984) can be conveniently used for storing the results of a Taylor-type model, see Kalidindi and Duvvuru (2005), Kalidindi et al. (2006), Li et al. (2003), Van Houtte (2001). The one-time, but time consuming task is to find coefficients in Fourier series of the spectral representation for the functions that represent the per-grain solutions of the Taylor-type CP model. These solutions must be computed for each crystal orientation in Euler space subjected to all possible strain rates. This way, a database of spectral coefficients is generated. The advantage of the approach is that the result of the CP model can be later retrieved just by querying the database without doing any actual CP calculations.

The spectral method was first demonstrated using generalized spherical harmonics (GSH) (Kalidindi et al. 2006; Knezevic and Kalidindi 2007; Shaffer et al. 2010; Van Houtte 2001), and later employing Discrete Fourier Transforms (DFT) (Al-Harbi et al. 2010; Alharbi and Kalidindi 2015; Kalidindi et al. 2009; Knezevic et al. 2008, 2009). The DFT promises much higher computational performance since it exploits Fast Fourier Transform (FFTs) algorithm for fast retrieval of pre-computed crystal plasticity solutions. The solutions are stored on a uniform grid in the orientation space and subsequently a local spectral interpolation using Fast Fourier Transform is applied to recover the solutions for any orientation and deformation mode of interest (Knezevic et al. 2008).

A DFT-based SCP framework has been embedded into Finite Element model (Alharbi and Kalidindi 2015; Zecevic et al. 2015a, b). This is basically equivalent to embedding a Taylor-type model at each integration point of the FE model, however the constitutive response of the material can be evaluated much faster compared to a direct embedding scheme such as the CP-FEM.

The computational advantage of the SCP comes with certain drawbacks, though. Independent sampling of individual grains is implicitly required, thus the accuracy of the SCP is bound by the limitations of the Taylor assumptions. It is now well known that Taylor-type models do not offer best texture and anisotropy prediction. Furthermore, the SCP approach is hardly capable of going beyond quite simple Taylor-type models. For instance, adding internal variable hardening models would render the SCP impractical, since constructing the database of spectral coefficients would require exploring a high dimensional space.

3.3.3 Yield Criteria Based on Crystal Plasticity

As we have seen in the previous section, the direct coupling of microstructure evolution in a component-scale FE simulations is conceptually straightforward, but computationally complex. Therefore, more robust and efficient alternatives have been sought. It is quite easy to notice that the FE solver requires stress integration in the macroscopic domain, whereas the fine-scale crystal plasticity framework, if directly embedded, calculates much more than that.

This observation results in a concept to partly dissociate the evolution of properties and the evolution of the microstructure. To this end, the evolution of crystallographic texture and possibly other microstructural features are calculated by means of an appropriate crystal plasticity framework, but the macroscopic constitutive relation used in the FE only approximates the homogenized response of the fine-scale model. The microstructural evolution is directly implemented in this approach, since the orientations of the representative crystals and other microstructural state variables are updated according to the macroscopic plastic deformation. However, the mechanical description of the homogenized material response utilizes a different mathematical model, which can be efficiently plugged into the FE stress integration algorithm.

3.3.3.1 Yield Criteria Defined by Interpolation

If a given deformation process is considered, the material is locally subjected to a certain stress state that slowly varies with increasing stain. Therefore, only a limited zone of the yield locus is probed by the stress integration algorithm. This was exploited by the works (Dawson et al. 2005; Duchêne et al. 2002; Habraken and Duchêne 2004), which proposed that the crystal plasticity yield locus is only sampled in a confined subspace of deviatoric stresses. Once the yield locus is locally known in a point-by-point manner, an interpolation method allows calculating a continuous function that approximates the yield locus. It needs to be emphasised that the interpolated yield locus is valid only within the range of the discrete set of known data points. When the available local description of the yield locus does not cover the region of interest anymore, one has to find another local description enclosing the new active part of the yield locus. The approach does neither explicitly enforce nor require any analytical yield locus model, since a generic interpolation scheme is sufficient. This has a drawback, though: the normals of locally interpolated yield loci may not be smooth, and thus stress integration that relies on the normality rule may experience convergence problems. Even though the interpolated function is continuously differentiable (e.g. C^2), there is still no guarantee that the interpolated yield locus is convex, with similar consequences as mentioned before.

3.3.3.2 Yield Criteria Defined by Approximation

Recall from Chap. 1 that the phenomenological descriptions of plastic anisotropy have proved their enormous usefulness in modelling plastic anisotropy. Numerous successful efforts have been made in the last decades to improve the macroscopic anisotropy models, for example Aretz and Barlat (2012, 2013), Banabic et al. (2000, 2003, 2005, 2010), Barlat et al. (1991, 1997a, b, 2003b, 2005, 2007), Cazacu and Barlat (2004), Cazacu et al. (2006), Comsa and Banabic (2008), Hill (1948) Hosford (1979), Plunkett et al. (2006, 2008), Soare and Barlat (2010), Soare et al. (2008), Van Houtte and Van Bael (2004), Van Houtte et al. (2009), Vegter and van den Boogaard (2006), Vegter et al. (2003), Yoon et al. (2004, 2006, 2010, 2014), Yoshida et al. (2013). The improvements were attained not only in terms of predictive capabilities, but also with respect to computational performance. Due to these advantages, the phenomenological yield loci are nowadays most commonly adopted in commercial Finite Element (FE) packages dedicated for simulations of metal forming operations. If a yield locus model is used in a combination with flow theories, such as the normality flow theory, the phenomenological yield loci provide an efficient technique for capturing the effects of material anisotropy during the simulation of deformation processes. These advantages make the existing yield loci models perfect candidates for becoming components of a *hierarchical approach* that approximates the finer-scale model by a coarser-scale model.

The phenomenological yield criteria consider the polycrystalline material as homogeneous at the macroscopic level, and the yield surface depends merely on the macroscopic stress, strain rate, certain strain measures as well as their rates. The microstructural features of the material, such as crystallographic texture, can be indirectly taken into account by means of extensive parametrization of these models. The phenomenological yield loci are generally limited to the initial anisotropy of the material, since it is hardly possible to accurately predict the evolution of the yield surface without taking into account how the microstructure develops during the deformation. Usually it is assumed that the changes to the initial yield locus due to deformation are negligible. The assumption is approximately valid if the plastic strains are not excessively large, which admittedly holds in some sheet metal forming processes.

One can also find several examples that combine the strength of the two approaches: crystal plasticity frameworks and phenomenological yield loci mentioned above. The hierarchical multi-scale approach was followed, in which the fine-scale model provides data needed for identification of the macroscopic one that is based on a different mathematical framework. The yield criteria are given as parametrized closed-form functions. A least squares method can be then used to determine the parameters by fitting them to data points generated by virtual CP experiments. For instance, parameters of orthotropic Hill yield criterion can be easily derived by means of a Taylor-type model as shown in Kalidindi et al. (2004). Other phenomenological yield criteria have been also calibrated by means of the crystal plasticity frameworks, most remarkably FC Taylor, VPSC, ALAMEL and CP-FEM, see e.g. An et al. (2011), Barlat et al. (2005), Gawad et al. (2010, 2013),

Grytten et al. (2008), He et al. (2014), Inal et al. (2010), Kalidindi et al. (2004), Kim et al. (2007, 2008), Kraska et al. (2009), Plunkett et al. (2006), Saai et al. (2013), Savoie and MacEwen (1996), Van Bael et al. (2010), Van Houtte et al. (2009, 2011), Yoon et al. (2014), Zhang et al. (2014, 2015b).

Generally, to provide data for calibration, the crystal plasticity models have to be evaluated for a huge number of possible stress or strain rate modes, sometimes exceeding one million realizations. Given the fact that the number of parameters in the yield criteria is typically small, an overdetermined least squares approach was employed in some previous works, for instance in Grytten et al. (2008), Rabahallah et al. (2009) that focused on identifying the Yld2004 3D yield criterion (Barlat et al. 2005). However, indiscriminate selection of data points was typically used, which resulted in large data sets, varying in size from few thousands (Grytten et al. 2008; Zhang et al. 2015b) to tens of thousands of data points (Rabahallah et al. 2009).

This inspired works that aim at decreasing the computational effort related to evaluating necessary data points by running crystal plasticity virtual experiments. In order to maximize the amount of information acquired from every data point, not only the size of the yield locus, but also its curvature and derivatives can be simultaneously used (Gawad et al. 2010, 2013).

It has to be emphasized that the majority of the aforementioned efforts focuses on calibrating the initial yield locus, leaving the evolution of the plastic anisotropy unaddressed. The evolution of the yield locus can still be captured, though. If the strain path can be pre-determined, a sequence of explicit yield criteria can be pre-computed along that path for a finite set of strain levels and subsequently interpolated during the macroscopic FE simulation, as it was done in Knezevic et al. (2013b), Nixon et al. (2010a, b), Plunkett et al. (2006). Similarly as in the case of database and sampling techniques (see Sect. 3.3.2), the local deformation conditions in the FE mesh may fall outside the assumed deformation path, thus the evolution of the yield locus of may also lead outside the validity range of the interpolation.

Another viable method to tackle anisotropy evolution in the macroscopic FE problem is to use an adaptive hierarchical multi-scale approach. As opposed to the hierarchical methods outlined above, the adaptive scheme is capable of deriving macroscopic yield locus that reflects changes to the material along the actual deformation path. This can be expediently done by systematic updating of the material state, such as texture, by applying local macroscopic deformation rates and subsequent recalibration of the phenomenological plasticity model. Each Gauss integration point of a macroscopic FE mesh can be linked with an evolving yield locus function, as it was successfully demonstrated by Gawad et al. (2010, 2013), Van Bael et al. (2010), Van Houtte et al. (2011) using the Facet plastic potential (Van Houtte et al. 2009), and recently by He et al. (2014) that used the CPB06ex2 yield criterion (Cazacu et al. 2006). The evolution of the plastic anisotropy is therefore taken into account, as well as the evolution of the material state. In the next section we are going to closely examine a practical implementation of this concept.

3.3.3.3 Evolving BBC2008 Yield Criterion

In this section we demonstrate how the adaptive hierarchical multi-scale approach can be utilized to model evolution of plastic anisotropy in a finite element simulation. For sake of simplicity, the texture is assumed to be the microstructural factor that primarily explains plastic anisotropy. A crystal plasticity framework will be then employed to predict changes in the crystallographic texture and to provide data needed for accommodating a macroscopic yield criterion in an adaptive manner. The yield criterion can be then incorporated into Finite Element model as a user-defined material model.

More specifically, we shall use an explicit time integration FEM, since this type of FE solvers is prevalently used in simulating sheet metal forming operations. For the same reason, elastic-plastic constitutive model will be assumed. The BBC2008 yield criterion will be calibrated by virtual experiments conducted by means of the ALAMEL crystal plasticity model.

We shall begin with a notion that material properties may evolve independently within small volumes of material, typically in individual finite elements. To achieve that, each integration point in the macroscopic mesh is associated with a collection of state variables:

macroscopic state variables (denoted as **Z**) that comprise a parametric yield locus function (along with a current set of parameters). Additionally, control variables are included that decide when and how the yield locus function should be reconstructed.
microscopic state variables (denoted as **z**) consist of variables that are relevant to the crystal plasticity framework. The state variables must be sufficient to construct an RVE. In our case, the variables in **z** are limited to the Orientation Distribution Function given in a discrete form, i.e. as a list of crystal orientations associated with their relative volume fractions. Although in the currently presented case the texture is the only micro-scale state variable, other microstructural features can be added, so the material would be described in a much more extensive way if the CP model permits so. For instance, **z** can be enriched by including phase composition, grain size and shape, ODF and/or MODF of individual phases, resistance of available deformation mechanisms (slip and twinning systems), substructure (dislocation densities or patterns), and many others.

Of course, the macroscopic state variables must include the stress state at the integration point and a local measure of plastic strain, both needed by the stress integration algorithm. The details of incorporating the yield criterion as such into the elastic-plastic explicit time integration FE are skipped here, since they are not essential in the presented method. The reader may refer to Chap. 1 for examples how this can be achieved in the context of implicit or explicit time integration FE codes. We have to mention however that the presented multi-scale model makes the assumption that a macroscopic hardening model is available in the FE code.

If an explicit time integration FE solver is used, the total deformation is subdivided into many small time increments, satisfying the stability conditions of the time integration scheme. It is quite obvious that recalculations of the parameters of the yield criterion at each integration point in every time increment would be highly inefficient. Given small strains associated to the time increments, one may postpone updating the state variables $\mathbf{z}$ and the subsequent recalculation of $\mathbf{Z}$ until a certain criterion is met at the considered integration point.

A possible criterion, as proposed in Gawad et al. (2013), is based on tracking the plastic strain accumulated since the previous update of the anisotropy model. The accumulated plastic strain is calculated by integrating instantaneous plastic strain rate $\mathbf{D}$ over time increments as

$$\mathbf{P} = \int_{t_{i-1}}^{t_i} \mathbf{D}(t)\,\mathrm{d}t \tag{3.1}$$

where t_i is the current time since the start of the simulation, and t_{i-1} is the time of the previous update. This quantity is used as the control variable in making decision if $\mathbf{Z}$ needs to be updated. The criterion is fulfilled if

$$\|\mathbf{P}\| \geq P_{cr} \tag{3.2}$$

where P_{cr} is a control parameter interpreted as a critical value to trigger the update. Again, we emphasize that the tracking is carried out independently at each integration point. Similarly, the decision about the update is made independently from one integration point to another.

Once the criterion is satisfied, both the microstructural state variables and the anisotropy model at the integration point are updated. To do so, three steps are taken:

1. evolution of $\mathbf{z}$ along the recent deformation path $\mathbf{P}$ is calculated by the crystal plasticity model,
2. necessary crystal plasticity virtual experiments are conducted to characterize the material in its updated state, and finally
3. a new vector of yield locus parameters coefficients in $\mathbf{Z}$ is computed to fit the results of the virtual experiments.

In the next paragraphs we will reiterate over these steps, however they will be presented in a slightly different order.

Macroscopic yield locus Chap. 1 provides several examples of yield loci, which vary with respect to their capability to describe plastic anisotropy of the material. The formulae presented there are typically used to describe the initial yield locus or the yield locus that corresponds to a small level of plastic strain. Let us use as an example the BBC2008 plane stress yield criterion, which was originally proposed by Comsa and Banabic (2008). The formulae of the BBC2008 yield criterion can be found in Chap. 1. To exploit the plane stress yield locus, we make a constitutive assumption

that the macroscopic material is a plastically orthotropic membrane under plane-stress conditions. Given the plane-stress constraint, the only non-zero components of the Cauchy stress tensor $\boldsymbol{\sigma}$ are σ_{11}, σ_{22} and $\sigma_{12} = \sigma_{21}$. Notwithstanding, the plane stress assumption and its consequences are not mandatory and the coupling scheme can be easily generalized to full 3D tensors, as shown in Gawad et al. (2013).

Recall from Chap. 1 that in order to distinguish whether the material is deformed elastically or plastically, a scalar-valued yield function is usually defined:

$$F(\boldsymbol{\sigma}) = \bar{\sigma}(\boldsymbol{\sigma}) - Y \leq 0 \tag{3.3}$$

where $\bar{\boldsymbol{\sigma}} \geq 0$ is the equivalent yield stress and $Y > 0$ is an arbitrary reference yield stress. The function F describes the yield locus or, more specifically, the shape and size of the yield surface. The yield surface holds the property that $F(\boldsymbol{\sigma}) = 0$ when the deformation occurs elasto-plastically, whereas purely elastic stress state satisfies the strict inequality $F(\boldsymbol{\sigma}) < 0$.

The formalism used in (3.3) does not explicitly account for the influence of the material state on plastic anisotropy, not to mention the impact of the microstructural state variables. Let $\mathbf{z}$ denote the instantaneous material state variables that in our case specifically include texture of the material. We assume that the state variables evolve as

$$\mathbf{z} = \mathbf{z}(\varepsilon_{pl}) \tag{3.4}$$

Apart from the dependency on plastic strain ε_{pl}, the state variables may also be expressed as depending on a combination of time, temperature, plastic work and possibly other variables. The evolution equation of $\mathbf{z}$ is rarely given in a closed form. In fact, in most cases the evolution of the microscopic state variables is only known from a simulation.

An extension to the yield criterion can be introduced by adding parameters that depend on $\mathbf{z}$:

$$F(\boldsymbol{\sigma}, \mathbf{z}) = \bar{\sigma}(\boldsymbol{\sigma}, \mathbf{z}) - Y \leq 0 \tag{3.5}$$

Therefore, the extended form (3.5) also discards the assumption that the plastic anisotropy does not change during the plastic deformation. Let us now re-write the formulae of the BBC2008 yield criterion using the formalism provided by Eq. (3.5).

The BBC2008 yield criterion defines the equivalent stress as:

$$\bar{\sigma}(\boldsymbol{\sigma}, \mathbf{z}) = \left[(w-1) \sum_{i=1}^{s} \{ w^{i-1} P(\boldsymbol{\sigma}, \mathbf{z}) + w^{s-1} Q(\boldsymbol{\sigma}, \mathbf{z}) \} \right]^{\frac{1}{2k}} \tag{3.6}$$

$$P(\boldsymbol{\sigma}, \mathbf{z}) = \left[L^{(i)}(\boldsymbol{\sigma}, \mathbf{z}) + M^{(i)}(\boldsymbol{\sigma}, \mathbf{z}) \right]^{2k} + \left[L^{(i)}(\boldsymbol{\sigma}, \mathbf{z}) - M^{(i)}(\boldsymbol{\sigma}, \mathbf{z}) \right]^{2k} \tag{3.7}$$

$$Q(\boldsymbol{\sigma},\mathbf{z}) = \left[M^{(i)}(\boldsymbol{\sigma},\mathbf{z}) + N^{(i)}(\boldsymbol{\sigma},\mathbf{z})\right]^{2k} + \left[M^{(i)}(\boldsymbol{\sigma},\mathbf{z}) - N^{(i)}(\boldsymbol{\sigma},\mathbf{z})\right]^{2k} \tag{3.8}$$

The coefficient w is defined as $w = (3/2)^{1/s} > 1$, where $s \in \mathbb{N}$. The choice of the exponent k must satisfy the condition that $s \in \mathbb{N}$ to ensure convexity of the yield surface (Comsa and Banabic 2008). Furthermore, Comsa and Banabic (2008) recommended to use $k = 4$ and $k = 3$ for fcc and bcc materials, respectively. The scalar functions L, M and N are given by:

$$L^{(i)}(\boldsymbol{\sigma},\mathbf{z}) = L^{(i)}(\sigma_{11},\sigma_{22},\mathbf{z}) = l_1^{(i)}(\mathbf{z})\sigma_{11} + l_2^{(i)}(\mathbf{z})\sigma_{22} \tag{3.9}$$

$$\begin{aligned} M^{(i)}(\boldsymbol{\sigma},\mathbf{z}) &= M^{(i)}(\sigma_{11},\sigma_{22},\sigma_{12},\mathbf{z}) \\ &= \sqrt{\left[m_1^{(i)}(\mathbf{z})\sigma_{11} - m_2^{(i)}(\mathbf{z})\sigma_{22}\right]^2 + \left[m_3^{(i)}(\mathbf{z})(\sigma_{12}+\sigma_{21})\right]^2} \end{aligned} \tag{3.10}$$

$$\begin{aligned} N^{(i)}(\boldsymbol{\sigma},\mathbf{z}) &= N^{(i)}(\sigma_{11},\sigma_{22},\sigma_{12},\mathbf{z}) \\ &= \sqrt{\left[n_1^{(i)}(\mathbf{z})\sigma_{11} - n_2^{(i)}(\mathbf{z})\sigma_{22}\right]^2 + \left[n_3^{(i)}(\mathbf{z})(\sigma_{12}+\sigma_{21})\right]^2} \end{aligned} \tag{3.11}$$

Equations (3.9)–(3.11) contain several parameters that depend on the material state $\mathbf{z}$. These parameters can be conveniently gathered into the vector:

$$\mathbf{p} = \{l_1^{(i)}(\mathbf{z}), l_2^{(i)}(\mathbf{z}), m_1^{(i)}(\mathbf{z}), m_2^{(i)}(\mathbf{z}), m_3^{(i)}(\mathbf{z}), n_1^{(i)}(\mathbf{z}), n_2^{(i)}(\mathbf{z}), n_3^{(i)}(\mathbf{z})\ (i = 1,\ldots,s)\} \tag{3.12}$$

Depending on the parameter s, the BBC2008 yield criterion may include 8 components in $\mathbf{p}$ for $s = 1$, 16 components if $s = 2$, 24 components for $s = 3$ and so forth. To simplify the notation, BBC2008pN stands for the BBC2008 yield criterion comprising N parameters. To determine N parameters, at least the same number of data points has to be provided by means of crystal plasticity virtual experiments. We emphasize this experimental nature (even though the experiments are virtual) by marking the data points with the superscript '(exp)'.

In Chap. 1 we presented an extensive calibration procedure that allows one to use arbitrary points of the plane stress yield locus. To recapitulate the most important points, the identification problem is posed as minimisation of square norm of the vector-valued error function:

$$\mathbf{E}(\mathbf{p}) = \begin{Bmatrix} w_y\mathbf{y}(\mathbf{p}) \\ w_r\mathbf{r}(\mathbf{p}) \\ w_{yb}\mathbf{y}_b(\mathbf{p}) \\ w_{rb}\mathbf{r}_b(\mathbf{p}) \\ w_S\mathbf{S}(\mathbf{p}) \\ w_\beta\boldsymbol{\beta}(\mathbf{p}) \end{Bmatrix} \tag{3.13}$$

where

$$\mathbf{y}(\mathbf{p}) = \left\{1 - \frac{y(\mathbf{p}, \alpha_1)}{y^{(\exp)}(\alpha_1)}, \ldots, 1 - \frac{y(\mathbf{p}, \alpha_n)}{y^{(\exp)}(\alpha_n)}\right\}^T \tag{3.14}$$

$$\mathbf{r}(\mathbf{p}) = \left\{1 - \frac{r(\mathbf{p}, \alpha_1)}{r^{(\exp)}(\alpha_1)}, \ldots, 1 - \frac{r(\mathbf{p}, \alpha_n)}{r^{(\exp)}(\alpha_n)}\right\}^T \tag{3.15}$$

$$\mathbf{y}_b(\mathbf{p}) = \left\{1 - \frac{y_b(\mathbf{p})}{y_b^{(\exp)}}\right\}^T \tag{3.16}$$

$$\mathbf{r}_b(\mathbf{p}) = \left\{1 - \frac{r_b(\mathbf{p})}{r_b^{(\exp)}}\right\}^T \tag{3.17}$$

$$\mathbf{S}(\mathbf{p}) = \left\{1 - \frac{S(\mathbf{p}, \theta_1)}{S^{(\exp)}(\theta_1)}, \ldots, 1 - \frac{S(\mathbf{p}, \theta_m)}{S^{(\exp)}(\theta_m)}\right\}^T \tag{3.18}$$

$$\boldsymbol{\beta}(\mathbf{p}) = \left\{\cos\left(\beta^{(\exp)}(\theta_1) - \beta_1(\mathbf{p}, \theta_1)\right), \ldots, \cos\left(\beta^{(\exp)}(\theta_m) - \beta_m(\mathbf{p}, \theta_m)\right)\right\}^T \tag{3.19}$$

The components of vectors $\mathbf{y}(\mathbf{p})$ and $\mathbf{r}(\mathbf{p})$ include residuals pertaining to the series of n uniaxial tensile tests along angles α_i w.r.t. RD. Uniaxial yield stress $y^{(\exp)}(\alpha)$ and $y(\mathbf{p}, \alpha)$ are calculated in the direction α by the CP virtual experiments and derived from the yield criterion (3.6), respectively, while $r^{(\exp)}(\alpha)$ and $r(\mathbf{p}, \alpha)$ are the r-values obtained in analogous way. The contribution of the equibiaxial point to the error function is included via terms (3.16) and (3.17). Other points that lie on the σ_{11} and σ_{22} section are indicated by the angle θ, which defines the ratio between σ_{11} and σ_{22}: $\tan\theta = \frac{\sigma_{22}}{\sigma_{11}}$. The contribution (3.18) provides the magnitude of the yield stress $S(\mathbf{p}, \theta)$ in the direction given by the angle θ. The normal to the yield contour and the σ_{11} direction form the angle $\beta(\theta)$. The weighting factors w_y, w_r, w_{yb}, w_{rb}, w_S and w_β allow one to control the relative importance of the individual components of the error function. This minimization problem can be conveniently solved by means of general non-linear least squares solvers, such as the Levenberg-Marquardt or the Trust Region algorithms (Conn et al. 2000).

Crystal Plasticity Virtual Experiments The data needed by (3.18) and (3.19) can be calculated by the crystal plasticity framework, which accounts for the evolution of fine-scale material state $\mathbf{z}$.

At this moment we assume that the CP framework can be seen as a black box that provides:

- homogenized stress $\sigma(\mathbf{D}, \mathbf{z})$,
- evolution of $\mathbf{z}$.

As a matter of fact, many crystal plasticity models are *strain rate driven*, similarly as the black box mentioned above. The homogenized stresses calculated by the black box can be seen as evaluations of function f: $\sigma_H(\dot{\varepsilon}, \mathbf{z}) = f(\dot{\varepsilon}, \mathbf{z})$, even though f is not given in a closed form. However, in many deformation processes it is the stress state that is either known or assumed by certain idealization. In such case the crystal plasticity model would need to predict what macroscopic deformation might be reached under a superimposed macroscopic stress $\boldsymbol{\sigma}$. This also poses certain inconveniences in (3.13). On one hand, the components of the residual vector (3.13) are expressed as stress-state dependent. On the other hand, the opaque nature of a black box does not permit any direct inversion of the function it provides. For these reasons, a numerical inversion of f must be employed. An iterative procedure can be then employed to to analyze deformation paths defined by macroscopic stress modes, even though a strain-rate driven crystal plasticity model is used. Note that the homogenization scheme in the CP model does not require imposing stress boundary condition on every individual grain, and therefore it is not necessarily satisfied on the grain level.

An iterative procedure can be then employed to analyze deformation paths defined by macroscopic stress modes, even though a strain-rate driven crystal plasticity model is used. Again, it has to be remarked that the homogenization scheme does not require imposing stress boundary condition on every individual grain, and therefore it is not necessarily satisfied on the grain level. On the grain level Eqs. (3.39)–(3.50) still hold and the microscopic boundary conditions are defined in terms of the velocity gradient. The crystal plasticity model is then considered as a black-box implementing a purely plastic rate-insensitive material. It must allow evaluating the homogenized macroscopic deviatoric stress $\mathbf{S}_H$ as a response to the macroscopic plastic strain rate $\mathbf{D}$, while keeping the state variables unmodified. An update of the state variables can be independently requested from the black-box.

Since the underlying crystal plasticity model neglects the elastic components of stress and strain rate, the homogenized stress is inherently deviatoric and the corresponding macroscopic strain rate has to satisfy the volumetric incompressibility condition. Therefore, any of these tensor quantities contains only five independent components, which can be utilized by converting the second-order tensor quantities of deviatoric nature into five-dimensional vectors. In this context the primary reason for preferring the five-dimensional vector representation is that the conversion allows one to reduce the dimensionality of the search space, since the constraint $\operatorname{tr} \mathbf{x} = 0$ is automatically satisfied by the five-dimensional vector representation.

One can conveniently reduce the dimensionality of the search space by exploiting the fact that symmetric second-order tensors of deviatoric nature contain only five independent components. This property is commonly found in tensors used in mechanics; for instance, deviatoric stresses and plastic strain rates belong to this category. The reduction of dimensionality can be done by converting

appropriate tensors into five-dimensional vectors, e.g. by following the transformation proposed in Van Houtte and Van Bael (2004). Other variants of the transformation exist in the literature, see e.g. Grytten et al. (2008), Lequeu et al. (1987), Van Houtte (1988). Throughout the remaining part of the paper the convention will be used that $\hat{\mathbf{x}}$ denotes vector representation of rank-two tensor $\mathbf{x}$.

Let $\mathbf{x}$ be a symmetric, second-order tensor that has the property that $\mathbf{x}_{11} + \mathbf{x}_{22} + \mathbf{x}_{33} = 0$. It can be then completely described by only five independent components. According to Van Houtte and Van Bael (2004), the components of the corresponding 5D vector $\hat{\mathbf{x}}$ can be calculated as:

$$\hat{\mathbf{x}}_1 = \frac{1}{\sqrt{2}}(\mathbf{x}_{11} - \mathbf{x}_{22}) \tag{3.20}$$

$$\hat{\mathbf{x}}_2 = -\sqrt{\frac{3}{2}}\mathbf{x}_{33} \tag{3.21}$$

$$\hat{\mathbf{x}}_3 = \sqrt{2}\mathbf{x}_{23} \tag{3.22}$$

$$\hat{\mathbf{x}}_4 = \sqrt{2}\mathbf{x}_{31} \tag{3.23}$$

$$\hat{\mathbf{x}}_5 = \sqrt{2}\mathbf{x}_{12} \tag{3.24}$$

It is trivial to convert back the 5D vector into the second-order tensor:

$$\mathbf{x}_{11} = \frac{1}{\sqrt{2}}\hat{\mathbf{x}}_1 + \frac{1}{\sqrt{6}}\hat{\mathbf{x}}_2 \tag{3.25}$$

$$\mathbf{x}_{22} = -\frac{1}{\sqrt{2}}\hat{\mathbf{x}}_1 + \frac{1}{\sqrt{6}}\hat{\mathbf{x}}_2 \tag{3.26}$$

$$\mathbf{x}_{33} = -\sqrt{\frac{2}{3}}\hat{\mathbf{x}}_2 \tag{3.27}$$

$$\mathbf{x}_{23} = \mathbf{x}_{32} = \frac{1}{\sqrt{2}}\hat{\mathbf{x}}_3 \tag{3.28}$$

$$\mathbf{x}_{31} = \mathbf{x}_{13} = \frac{1}{\sqrt{2}}\hat{\mathbf{x}}_4 \tag{3.29}$$

$$\mathbf{x}_{12} = \mathbf{x}_{21} = \frac{1}{\sqrt{2}}\hat{\mathbf{x}}_5 \tag{3.30}$$

It can be easily shown that the scalar product is preserved, i.e. $\mathbf{x} : \mathbf{x} = \hat{\mathbf{x}} \cdot \hat{\mathbf{y}}$. As a corollary, the length of the vector $\hat{\mathbf{x}}$ is equal to the magnitude of the corresponding tensor $\mathbf{x}$.

The 5D representation of plastic strain rate and deviatoric stress is used in the inversion of the function $\sigma(\dot{\varepsilon}, \mathbf{z}) = f(\dot{\varepsilon}, \mathbf{z})$.

Algorithm 1 is able to deliver m data points corresponding to biaxial stress state with arbitrary stress ratios.

The fundamental part of the algorithm is to find the macroscopic plastic strain rate mode $\hat{\mathbf{A}}^*$ that corresponds to the imposed deviatoric stress mode $\hat{\mathbf{U}}^*$, where

$$\hat{\mathbf{U}} = \frac{\hat{\mathbf{S}}}{\|\hat{\mathbf{S}}\|} \tag{3.31}$$

and $\hat{\mathbf{S}}$ is a five-dimensional vector representing the deviatoric part of the stress tensor $\boldsymbol{\sigma}$ that defines the requested deformation path:

$$\mathbf{S} = \boldsymbol{\sigma} - \frac{\operatorname{tr}\boldsymbol{\sigma}}{3}\mathbf{I} \tag{3.32}$$

where $\mathbf{I}$ is the identity tensor. This is achieved by solving an unconstrained optimization problem, in which the square norm of the vector-valued residual function

$$\mathbf{f}(\hat{\mathbf{A}}, \hat{\mathbf{U}}^*) = \hat{\mathbf{U}}^* - \frac{\hat{\mathbf{S}}_H(\hat{\mathbf{A}})}{\|\hat{\mathbf{S}}_H(\hat{\mathbf{A}})\|} \tag{3.33}$$

is minimized. In the subsequent derivations a simplified notation will be used: $\mathbf{f}(\hat{\mathbf{A}}, \hat{\mathbf{U}}^*) = \mathbf{f}(\hat{\mathbf{A}})$, since the imposed stress mode is considered a constant. The evaluation of the residual function involves a call to the underlying crystal plasticity to calculate the homogenized stress $\mathbf{s}_H$. The search starts from an initial guess $\hat{\mathbf{A}}_0$, typically chosen as $\hat{\mathbf{A}}_0 = \hat{\mathbf{U}}^*$, which corresponds to the property of an isotropic von Mises plastic material. From a current point $\hat{\mathbf{A}}_{\text{old}}$, the algorithm iteratively uses the trust-region minimization approach (Conn et al. 2000)

$$\min_{\hat{\mathbf{A}} \in \mathbb{R}^5} \|\mathbf{f}(\hat{\mathbf{A}}_{\text{old}}) + \mathbf{J}(\hat{\mathbf{A}}_{\text{old}})\left(\hat{\mathbf{A}}_{\text{new}} - \hat{\mathbf{A}}_{\text{new}}\right)\| \quad \text{subject to} \quad \|\hat{\mathbf{A}}_{\text{new}} - \hat{\mathbf{A}}_{\text{old}}\| \leq \delta \tag{3.34}$$

to find a new guess $\hat{\mathbf{A}}_{\text{new}} = \hat{\mathbf{A}}_{\text{old}} + \Delta\hat{\mathbf{A}}$ that satisfies

$$\min_{\hat{\mathbf{A}} \in \mathbb{R}^5} \|\mathbf{J}^T(\hat{\mathbf{A}})\mathbf{J}(\hat{\mathbf{A}})\Delta\hat{\mathbf{A}} + \mathbf{J}(\hat{\mathbf{A}})\mathbf{f}(\hat{\mathbf{A}})\| \tag{3.35}$$

where $\Delta\hat{\mathbf{A}}$ is the trial step, δ is the size of the trial step and $\mathbf{J}$ is the Jacobian matrix of the function $\mathbf{f}$. The search is terminated when any of the following criteria is fulfilled:

- $\|\mathbf{f}(\hat{\mathbf{A}}_{\text{new}})\|$ is smaller than a pre-defined threshold f_{tol}, or
- $\|\Delta\hat{\mathbf{A}}\|$ is smaller than a pre-defined minimal step size, or
- the number of iterations exceeds its maximal value.

As can be seen from Eqs. (3.34) and (3.35), the Jacobian matrix has to be calculated very often. Since it is not available in a closed form, one has to compute it numerically by a finite difference scheme, which is associated with a considerable cost. However, if the initial guess $\hat{\mathbf{A}}_0$ is sufficiently close to the solution, one may attempt to locate the minimum under the auxiliary assumption that $\mathbf{J}(\hat{\mathbf{A}}) = \mathbf{J}(\hat{\mathbf{A}}_0) = const$. From this assumption it follows that the linearized problem is solved, so (3.34) and (3.35) become:

$$\min_{\hat{\mathbf{A}}\in\mathbb{R}^5} \|\mathbf{f}(\hat{\mathbf{A}}_{\text{old}}) + \mathbf{J}(\hat{\mathbf{A}}_0)\left(\hat{\mathbf{A}}_{\text{new}} - \hat{\mathbf{A}}_{\text{new}}\right)\| \quad \text{subject to} \quad \|\hat{\mathbf{A}}_{\text{new}} - \hat{\mathbf{A}}_{\text{old}}\| \leq \delta \tag{3.36}$$

$$\min_{\hat{\mathbf{A}}\in\mathbb{R}^5} \|\mathbf{J}^T(\hat{\mathbf{A}}_0)\mathbf{J}(\hat{\mathbf{A}}_0)\Delta\hat{\mathbf{A}} + \mathbf{J}(\hat{\mathbf{A}}_0)\mathbf{f}(\hat{\mathbf{A}})\| \tag{3.37}$$

where the matrix product $\mathbf{J}^T(\hat{\mathbf{A}}_0)\mathbf{J}(\hat{\mathbf{A}}_0)$ can be conveniently pre-calculated. If the trust region algorithm fails to converge to an acceptable solution, one may drop the assumption on constant Jacobian and restart the minimization from the initial guess.

Incidentally, in many cases there is a sufficiently accurate initial guess available. For instance, it may be obtained from a previous run of the method that had explored a similar stress mode, which holds as long as an identical material state was used by the underlying crystal plasticity model. Such condition is frequently fulfilled if one systematically calculates a point-by-point yield locus section (for instance, the section defined by $\sigma_{11} - \sigma_{22}$ plane). Yet another example is that the initial guess may be provided by an analytical yield locus model calibrated for a very similar material state.

The generic procedure outlined above can be straightforwardly utilized for determining data points that are commonly used in calibration of analytical yield loci. The authors have implemented it in a set of algorithms, collectively known as the Virtual Experimentation Framework (VEF) that allows conducting crystal plasticity virtual experiments either in stress or strain rate driven mode. For instance, uniaxial tension, uniaxial compression and biaxial stress state can be studied by means of the VEF. Suppose that the material state variables, such as texture, are expressed in a reference frame defined by the $\mathbf{e}_1, \mathbf{e}_2, \mathbf{e}_3$ directions. In many practical applications these directions coincide with the rolling direction (RD), transverse direction (TD) and normal direction (ND). Algorithm 2 allows calculating instantaneous r-values and corresponding yield stresses for a sequence of angles defining rotation around $\mathbf{e}_3$ from the $\mathbf{e}_1$ axis.

A similar algorithm (see Algorithm 3) can be used for calculating evolution of the material state under the stress mode $\hat{\mathbf{U}}^*$. The algorithm provides a convenient way to determine whether the microscopic state (e.g. crystallographic texture) is stable under the imposed stress mode and to estimate how the associated strain rate

evolves. In principle, the algorithm splits the deformation path into smaller increments of plastic strain which results from the stress mode $\mathbf{U}^*$, given the microstructural state of the material. The size of increments is specified by the input parameter $\Delta\varepsilon$. At the end of each increment the state of the microstructure is updated to reflect the changes caused by the deformation. Eventually the procedure returns a sequence of triplets $(\varepsilon, \mathbf{A}, \mathbf{S}_H(\mathbf{A}))$. Non-essential operations, such as reporting the history of microstructural state variables, are omitted for clarity.

Suppose one wants to determine the contour of the yield locus. Algorithm 1 presents how the normalized σ_{11}, σ_{22} yield locus section can be calculated. The algorithm can be also used for collecting data needed for calculating the Cartesian tangent to the yield locus contour:

$$\frac{d\sigma_{22}}{d\sigma_{11}} = \frac{\frac{dS(\theta)}{d\theta}\sin\theta + S(\theta)\cos\theta}{\frac{dS(\theta)}{d\theta}\cos\theta - S(\theta)\sin\theta} \tag{3.38}$$

where $S(\theta)$ is the distance from the origin of the coordinate system to the yield locus contour in that section. The polar derivative $\frac{dS(\theta)}{d\theta}$ can be numerically estimated from a single run of Algorithm 1.

Crystal plasticity ALAMEL In the previous paragraph we considered the crystal plasticity model as a generic black box. Let us now consider a specific CP framework, namely the rate-independent ALAMEL model proposed by Van Houtte et al. (2005). As mentioned in Sect. 3.2.1, the ALAMEL belongs to the family of statistical grain interaction models. The reader is referred to the paper (Van Houtte et al. 2005), which provides a comprehensive discussion of the statistical crystal plasticity theories relevant to this work, including foundations of Taylor's theory.

This section briefly summarizes basic concepts of the ALAMEL model. Since the remaining part of the work concentrates mostly on mechanical aspects, such as yielding, the discussion of texture evolution is much limited for brevity. Let us now just mention that the ALAMEL crystal plasticity model deals with an aggregate of grains (a polycrystal). Each grain is characterized by its orientation assigned from the Orientation Distribution Function (ODF) $f(g)$ where $g \in \mathcal{R}^3$ represents the crystal orientation. The whole aggregate of grains thus corresponds to a discrete form of the ODF $f_d(g)$. The slips on individual slip systems cause rotations of the grains, and as a result evolution of texture, which is the primary component of micro-scale state $\mathbf{z}$. More details on how the lattice rotations are related to the crystallographic slip can be found in Chap. 2.

A macroscopic deformation may be imposed onto an aggregate of crystals by specifying the velocity gradient $\mathbf{L}$. This velocity gradient tensor can be additively decomposed into a symmetric part $\mathbf{D}$, which is the plastic strain rate, and anti-symmetric part $\mathbf{W}$:

Algorithm 1: VEF algorithm for calculating scaled σ_{11}, σ_{22} yield locus section

Input: angular range: θ_0, $\theta_{\max}$, angular resolution: $\Delta\theta$, scaling stress: S_s, shear stress: σ_{12}, logical flag: $reusePrevious$

Result: sequence of pairs $(\theta, S(\theta)/S_s)$: $\mathbf{o}$

$\mathbf{o} \leftarrow \emptyset$

for $\theta = \theta_0$ *to* $\theta_{\max}$ *every* $\Delta\theta$ **do**

$\boldsymbol{\sigma} \leftarrow \begin{bmatrix} \cos\theta & \sigma_{12} & 0 \\ \sigma_{12} & \sin\theta & 0 \\ 0 & 0 & 0 \end{bmatrix}$

$\mathbf{S} \leftarrow \boldsymbol{\sigma} - \frac{1}{3}\mathrm{tr}\,\boldsymbol{\sigma}\,\mathbf{I}$

$\mathbf{U}^* \leftarrow \dfrac{\mathbf{S}}{\|\mathbf{S}\|}$

if $\theta \neq \theta_0$ *and reusePrevious* **then** $\hat{\mathbf{A}}_0 \leftarrow \hat{\mathbf{A}}^*$

$\hat{\mathbf{A}}^* \leftarrow \underset{\hat{\mathbf{A}} \in \mathbb{R}^5}{\mathrm{argmin}} \|\mathbf{F}(\hat{\mathbf{A}}, \hat{\mathbf{U}}^*)\|$ given $\hat{\mathbf{A}}_0$ `// see (3.33)-(3.37)`

$S \leftarrow \|\mathbf{S}_H(\mathbf{A}^*)\|$

$\mathbf{o} \leftarrow \mathbf{o} + (\theta, \dfrac{S}{S_s})$ `// extend the sequence o`

end

$$\mathbf{L} = \mathbf{D} + \mathbf{W} \tag{3.39}$$

Let us first consider a single-phase polycrystalline aggregate, consisting of a number of grains. In the Taylor-type models, it is supposed that each grain has homogeneous properties, such as crystal orientation, as well as homogeneous stress and strain distributions over the volume. If a single grain is considered, a local constitutive law has to establish relations between the local stress, strain and rigid body rotation inside the volume of the grain. A crystal plasticity theory, for instance the Generalized Schmid Law, allows one to account for internal processes, such as slip on various slip systems and the rotation of the crystal lattice, which occur as a response to the external stimuli.

Suppose the local velocity gradient $\mathbf{l}$ is imposed on a single grain. Additive decomposition of the velocity gradient tensor leads to

$$\mathbf{l} = \mathbf{d} + \mathbf{w} \tag{3.40}$$

where the symmetric part $\mathbf{d}$ is referred to as the local strain rate, and the anti-symmetric part $\mathbf{w}$ is called the local spin. Provided that elasticity is neglected, the strain rate needs to be accommodated through plastic deformation, which is carried by dislocation slip on a number of slip systems and/or by twinning on twinning systems. The further discussion is confined to the plastic slip as the only mechanism of plastic deformation.

Algorithm 2: VEF algorithm for calculating r-values and normalized yield stresses for a sequence of uniaxial loadings defined by directions $\boldsymbol{\alpha}$

Input: sequence of angles: $\boldsymbol{\alpha} = [\alpha_1, \ldots, \alpha_n]$, stress state: m (either 1 for tension or -1 for compression), accuracy threshold: f_{tol}, logical flag: *reusePrevious*

Result: sequence of triplets $(\alpha, r_\alpha, y_\alpha)$: $\mathbf{o}$

$\boldsymbol{\sigma}_0 \leftarrow m \begin{bmatrix} 1 & 0 & 0 \\ 0 & 0 & 0 \\ 0 & 0 & 0 \end{bmatrix}$

$\mathbf{o} \leftarrow \emptyset$

hasConverged $\leftarrow$ False

foreach α *in* $\boldsymbol{\alpha}$ **do**

  $\mathbf{R} \leftarrow \begin{bmatrix} \cos\alpha & -\sin\alpha & 0 \\ \sin\alpha & \cos\alpha & 0 \\ 0 & 0 & 1 \end{bmatrix}$ `// Rotation matrix`

  $\boldsymbol{\sigma}_r \leftarrow \mathbf{R}^T \boldsymbol{\sigma}_0 \mathbf{R}$

  $\mathbf{S}_r \leftarrow \boldsymbol{\sigma}_r - \frac{1}{3} \operatorname{tr} \boldsymbol{\sigma}_r \, \mathbf{I}$

  $\mathbf{U}_r^* \leftarrow \dfrac{\mathbf{S}_r}{\|\mathbf{S}_r\|}$

  if *reusePrevious AND hasConverged* **then**

    $\mathbf{A}_0 \leftarrow \mathbf{R}^T \mathbf{A} \mathbf{R}$

  else

    $\hat{\mathbf{A}}_0 \leftarrow \hat{\mathbf{U}}_0$

  end

  hasConverged $\leftarrow$ False

  $\hat{\mathbf{A}}_r^* \leftarrow \underset{\hat{\mathbf{A}} \in \mathbb{R}^5}{\operatorname{argmin}} \|\mathbf{F}(\hat{\mathbf{A}}_r, \hat{\mathbf{U}}_r^*)\|$ given $\hat{\mathbf{A}}_0$ `// see` (3.33)-(3.37)

  if $\|\mathbf{F}(\hat{\mathbf{A}}_r^*, \hat{\mathbf{U}}_r^*)\| < f_{\text{tol}}$ **then**

    hasConverged $\leftarrow$ True

    $\mathbf{A} \leftarrow \mathbf{R} \mathbf{A}_r^* \mathbf{R}^T$

    $r_\alpha \leftarrow \frac{\mathbf{A}_{22}}{\mathbf{A}_{33}}$

    $y_\alpha \leftarrow \sqrt{3/2} \|\mathbf{S}_H(\mathbf{A})\|$

    $\mathbf{o} \leftarrow \mathbf{o} + (\alpha, r_\alpha, y_\alpha)$ `// extend the sequence o`

  end

end

return o

Algorithm 3: VEF algorithm for calculating material state evolution under the imposed deviatoric stress mode $\mathbf{U}^*$

Input: stress mode: $\mathbf{U}^*$, maximal von Mises strain: $\varepsilon_{\max}$, increment of von Mises strain: $\Delta\varepsilon$, accuracy threshold: f_{tol}
Result: sequence of triplets $(\varepsilon, \mathbf{A}, \mathbf{S}_H(\mathbf{A}))$: $\mathbf{o}$

$\boldsymbol{\varepsilon}_{\text{total}} \leftarrow 0$
$\hat{\mathbf{A}}_0 \leftarrow \hat{\mathbf{U}}^*$
$\mathbf{o} \leftarrow \emptyset$
while $\sqrt{2/3}\|\boldsymbol{\varepsilon}_{\text{total}}\| < \varepsilon_{\max}$ **do**
  $\hat{\mathbf{A}}^* \leftarrow \underset{\hat{\mathbf{A}}\in\mathbb{R}^5}{\text{argmin}}\|\mathbf{F}(\hat{\mathbf{A}}, \hat{\mathbf{U}}^*)\|$ given $\hat{\mathbf{A}}_0$ `// see (3.33)-(3.37)`
  if $\|\mathbf{F}(\hat{\mathbf{A}}^*, \hat{\mathbf{U}}^*)\| < f_{\text{tol}}$ **then**
    $\Delta\boldsymbol{\varepsilon} \leftarrow \Delta\varepsilon\mathbf{A}^*$
    $\mathbf{o} \leftarrow \mathbf{o} + (\varepsilon, \mathbf{A}^*, \mathbf{S}_H(\mathbf{A}^*))$ `// extend the sequence o`
    Update CP state variables by applying $\Delta\boldsymbol{\varepsilon}$
    $\boldsymbol{\varepsilon}_{\text{total}} \leftarrow \boldsymbol{\varepsilon}_{\text{total}} + \Delta\boldsymbol{\varepsilon}$
  else
    return o
  end
end

The slip systems are defined by the family of symmetrically equivalent slip planes and associated family of slip directions. For instance, in fcc materials there are 12 slip systems given by $\{011\}\langle 100\rangle$. The definition of a slip system (s) includes the unit vector $\mathbf{m}^{(s)}$, which is normal to a slip plane that allows shear deformation realized by a dislocation glide. The kinematical equation that relates $\mathbf{d}$ with the slip rates $\dot{\gamma}^{(s)}$ of all active slip systems reads

$$\mathbf{d} = \sum_{s=1}^{N} \mathbf{M}^{(s)}\dot{\gamma}^{(s)} \tag{3.41}$$

where the Schmid tensor $\mathbf{M}^{(s)}$ relates the normal to the slip plane with the normalized shear direction $\mathbf{b}^{(s)}$ in which the slip occurs:

$$\mathbf{M}^{(s)} = \frac{1}{2}\left(\mathbf{b}^{(s)} \otimes \mathbf{m}^{(s)} + \mathbf{m}^{(s)} \otimes \mathbf{b}^{(s)}\right) \tag{3.42}$$

The slip systems that satisfy $\dot{\gamma}^{(s)} \neq 0$ are referred to as the active slip systems. The unknown slip rates can be determined under the energetic assumption, which postulates that minimal plastic work is dissipated per unit time:

$$\dot{W} = \sum_{s=1}^{N} \tau_c^{(s)} |\dot{\gamma}^{(s)}| \rightarrow \min \tag{3.43}$$

where τ_c^s is the critical resolved shear stress (CRSS) of the slip system (s). Although the CRSS can in principle be expressed as a function of the accumulated shear in the slip system, in the present considerations the hardening of the slip systems is neglected. Furthermore, all the slip systems are supposed to have identical CRSS. The generality of the presented approach is not undermined by these assumptions, since they can be easily lifted. Moreover, one may argue that for certain classes of materials, such as fcc, the texture evolution and induced plastic anisotropy remain practically insensitive to the microscopic hardening model. This of course does not generally hold for all types of materials. On the other hand, even a very simple microscopic hardening law may become beneficial in handling complex hardening phenomena (e.g. differential hardening effect), as it was recently demonstrated by Eyckens et al. (2015).

Unfortunately, many combinations of slip systems may possibly satisfy (3.41) and (3.43) simultaneously, which is called Taylor ambiguity. To determine which slip systems are actually activated, an additional criterion is generally needed. The interested reader is referred to a recent review by Mánik and Holmedal (2014) for a comprehensive study of various means to solve the Taylor ambiguity. One of possible solutions to the issue is to consider a cluster of grains that impose constraints on each other (Van Houtte et al. 2005).

Once the slip rates are known, the deviatoric stress tensor $\mathbf{s}$ can be calculated, either directly by using the Bishop-Hill theory (Bishop and Hill 1951b), or by using the minimization method (3.43) and considering it as the work-conjugate to the imposed strain rate:

$$\dot{W} = \mathbf{s} : \mathbf{d} \tag{3.44}$$

It also follows that texture evolution can be then predicted as well. The lattice spin $\mathbf{w}^L$, which causes reorientation of the crystal lattice and in turn texture evolution, can be found from the slip rates in each grain:

$$\mathbf{w} = \mathbf{w}^L + \sum_{s=1}^{N} \mathbf{M}_A^{(s)} \dot{\gamma}^s \tag{3.45}$$

given the anti-symmetric part of the velocity gradient tensor (3.40). $\mathbf{M}_A^{(s)}$ is the anti-symmetric complement to the Schmid tensor:

$$\mathbf{M}_A^{(s)} = \mathbf{b}^{(s)} \otimes \mathbf{m}^{(s)} - \mathbf{M}^{(s)} = \frac{1}{2} \left(\mathbf{b}^{(s)} \otimes \mathbf{m}^{(s)} - \mathbf{m}^{(s)} \otimes \mathbf{b}^{(s)} \right) \tag{3.46}$$

As we can see, this way the evolution of the microscopic state variables $\mathbf{z}$ is accounted for.

The ALAMEL homogenization scheme postulates that clusters of two grains have to be treated jointly. The two grains are assumed to be neighbours, i.e. they are separated by a grain boundary. The boundary is characterized by its orientation, which at the same time defines a local orthogonal reference frame. By convention, the 3rd axis of the grain boundary reference frame is parallel to the grain boundary normal. The scheme allows relaxations of the macroscopic velocity gradient with respect to simple shear along the boundary between the grains:

$$\mathbf{l}^{(grain_1)} = \mathbf{L} + \sum_{j=1}^{2} \mathbf{K}_{RLX}^{(j)} \dot{\gamma}_{RLX}^{(j)} \tag{3.47}$$

$$\mathbf{l}^{(grain_2)} = \mathbf{L} - \sum_{j=1}^{2} \mathbf{K}_{RLX}^{(j)} \dot{\gamma}_{RLX}^{(j)} \tag{3.48}$$

As can be seen, the relaxations in both grains are equal with respect to the magnitude, but oriented in opposite directions. The relaxation slip rates $\dot{\gamma}_{RLX}^{(j)}$ conceptually operate on pseudo slip systems which are shared by the two grains, whereas the slip rates and local spin rates of the clustered grains are different. The relaxation matrices in the grain boundary reference frame are defined as:

$$\mathbf{K}_{RLX}^{(1)} = \begin{bmatrix} 0 & 0 & 1 \\ 0 & 0 & 0 \\ 0 & 0 & 0 \end{bmatrix} \quad \mathbf{K}_{RLX}^{(2)} = \begin{bmatrix} 0 & 0 & 0 \\ 0 & 0 & 1 \\ 0 & 0 & 0 \end{bmatrix} \tag{3.49}$$

Assuming that the two grains have to simultaneously satisfy the energetic assumption, Eq. (3.43) has to be reformulated as:

$$\dot{W} = \sum_{i=1}^{2} \sum_{s=1}^{N} \left\{ \tau_c^{(i,s)} |\dot{\gamma}^{(i,s)}| \right\} + \sum_{j}^{2} \tau_r^{(j)} \dot{\gamma}_{RLX}^{(j)} \rightarrow \min \tag{3.50}$$

where the index i refers to the grains in the pair. Van Houtte et al. (2005) suggest to neglect the pseudo-slip term, although some artificial resistance of the pseudo-slip systems can, in principle, be introduced by letting $\tau_r^{(j)} \neq 0$.

The homogenized stress in the polycrystal is considered as the volume average of contributions from all the grains in the polycrystalline. Let V_i denote the volume of the ith grain. Provided that the stress tensor in the individual crystals is expressed in the sample reference frame, the homogenized deviatoric part of Cauchy stress is calculated as follows:

$$\boldsymbol{S}_H = \left(\sum_{i=1}^{n} V_i \right)^{-1} \sum_{i=1}^{n} V_i \boldsymbol{s}_i \tag{3.51}$$

It is worth mentioning in this context that the virtual experiments used in calibrating macroscopic yield loci are often stress driven (or at least some idealized stress state is more opportune as the boundary condition), whereas the ALAMEL model requires macroscopic velocity gradient or strain rate as input. In the previous paragraphs we presented a method how to numerically convert a strain rate driven model so the stress is imposed as the input. It is clear from (3.43) to (3.44) that the stress state of individual grains in the polycrystalline may deviate from the imposed stress, yet the homogenized stress over the aggregate can still satisfy

$$\|\mathbf{S}_H - \mathbf{S}\| < \delta \tag{3.52}$$

where δ is a sufficiently small number. A stronger requirement (i.e. $\|\mathbf{S}_H - \mathbf{S}\| = 0$) might be difficult to satisfy given the fact that only a finite number of crystals is used in the discretized texture.

It can be argued that (3.52) introduces long range interactions in the model, since certain conditions have to be met over the whole polycrystal. Yet it needs to be emphasized that no iso-stress assumption is made concerning the aggregate.

Hierarchical multi-scale model of cup drawing test The presented modelling framework allows one to simulate the deformation of large parts, comparable in size to body car components. In this example we use it to simulate one of the most convenient mechanical tests assessing anisotropy of the sheet metal: the cup drawing process that forms cylindrical cups from circular blanks. We shall also investigate how the results of the adaptive multi-scale model compare to more conventional simulation of the same process and to experimental data.

Briefly, let us consider the following test cases:

HMS-BBC2008: adaptive hierarchical multi-scale model is used. The plastic anisotropy is modelled by adaptively recalculated BBC2008p16 yield criterion. The crystal plasticity model predicts texture evolution and calculates data needed for recalibration of the BBC2008p16, as it was described in the previous sections.

CP-BBC2008: hierarchical multi-scale model is used, but the plastic anisotropy is kept constant throughout the simulation. This means the crystal plasticity model uses just the initial texture data at the pre-processing stage, and thus it provides only the initial yield surface data for identifying the BBC2008p16.

Mech-BBC2008: The BBC2008p16 is conventionally calibrated by mechanical testing data.

In the case study presented below we use Al alloy AA6016 metallic sheet (1 mm nominal thickness). This material is a precipitation hardening alloy, containing aluminum, magnesium and silicon as major components. The sheet has been delivered in the T4 status (solution heat treated and naturally aged). One of the major applications of this material is in the automotive industry. Admittedly, the AA6016-T4 has a rather mild anisotropy, which furthermore does not change much

during mechanical tests. Modern sheet metal materials are designed (on very purpose!) to retain their anisotropic properties approximately constant during processing. Keeping that in mind, we decided to choose a material that is realistic and actually used in industrial practice. If we selected a material that is more suitable for illustrative purposes, such as commercial purity aluminum, it would be less relevant from the application point of view.

The most conventional way of calibrating the BBC2008 yield criterion is to conduct a series of mechanical experiments. The characterization methods needed for calibrating the BBC2008 to mechanical data include uniaxial tensile tests and biaxial tension.[3] In order to determine the uniaxial mechanical parameters, tensile tests were performed on specimens cut at 0°, 15°, 30°, 45°, 60°, 75°, 90° from the rolling direction. The experiments were carried out using a Zwick-Roell 150kN universal tensile testing machine equipped with an extensometer with 20 mm gauge-length. The tensile tests have also provided the values of the conventional yield stress $y = R_{p0.2}$ and the Lankford coefficients (r-values), see Fig. 3.4a, b. The measured r-values reflect the plastic anisotropy at the beginning of yield. The mechanical response of the sheet in biaxial tension stress state was studied by means of two experimental setups: hydraulic bulging and thickness compression tests. The hydraulic bulging experiments allowed determining the balanced biaxial yield stress according to the methodology described by Lazarescu et al. (2011), while the thickness compression tests were performed to determine the biaxial coefficient of plastic anisotropy (Barlat et al. 2003a). The balanced biaxial yield stress was found $y_{bx} = 160.1\,\text{MPa}$, while the measurement of the biaxial coefficient of plastic anisotropy resulted in $r_{bx} = 1.037$ (cf. Fig. 3.4c).

While the conventional calibration of the BBC2208 requires fairly extensive experimental work, the virtual calibration is much more straightforward. The multi-scale model presented in the previous section requires texture data as the main microstructural input. A single experiment is needed and it consumes approximately 1 of the material. As presented in Gawad et al. (2015), X-ray diffraction technique provided the through-thickness texture and the mid-plane texture at the depth of 50 % of the sheet. The $\phi_2 = 45°$ sections of the measured ODF along with schematically depicted measurement positions are shown in Fig. 3.3.

The figure also shows the texture index (TI), which gives an overall view of texture sharpness, defined as integral over entire orientation space:

$$\text{TI} = \int f^2(g)dg \tag{3.53}$$

where $f(g)$ is the ODF. As can be seen, the sheet features a much sharper texture at the mid-plane than over the complete thickness. This indicates a presence of a complex texture gradient across the thickness, yet we shall not elaborate on this

[3]The results of mechanical experiments and texture measurements used in this section are taken from Gawad et al. (2015).

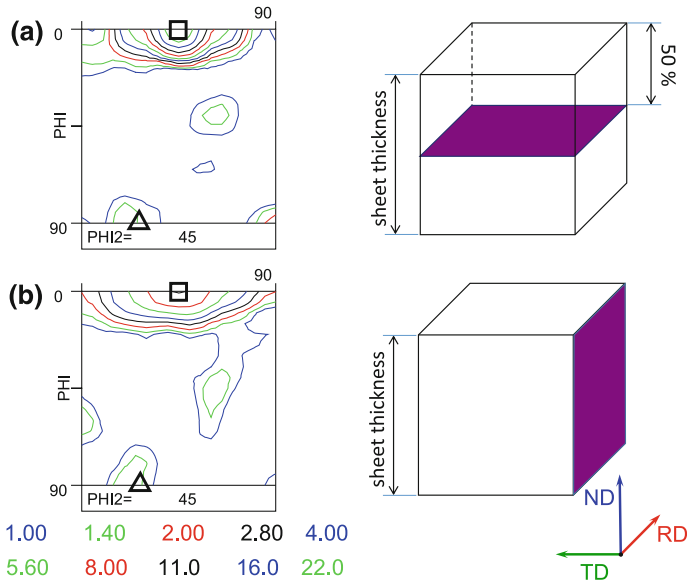

Fig. 3.3 $\phi_2 = 45°$ ODF sections (with ϕ_1 and Φ on horizontal and vertical axis, respectively) of the experimental textures: **a** mid-plane texture (50 % depth), TI = 4.96, and **b** through-thickness texture, TI = 2.45. Annotations indicate the *Cube component* (*square*) and the P component (*triangle*). The ODFs are expressed in identical reference frame: $x_1 = \text{RD}$, $x_2 = \text{TD}$ and $x_3 = \text{ND}$. Schematic sketch of the experimental texture measurement scheme is presented on the right. The *violet plane* depicts the surface exposed to the X-ray beam (Color figure online)

aspect here. Generally, the texture of this material is mostly attributed to the Cube component, i.e. the orientation given by $(\phi_1, \Phi, \phi_2) = (45°, 0°, 45°)$ in the presented ODF sections. Moreover, the spread around Cube forms a fibre towards $(45° + x, 0°, 45°)$ and $(45° - x, 0°, 45°)$. At the mid-plane however, the Cube fibre is only partial, i.e. $x < 45°$. The P texture component $(29.5°, 90°, 45°)$, which is generally attributed to the recrystallization solutionizing annealing (Engler and Hirsch 2002), can also be identified. The analyzed textures contain also some minor Goss component $\{011\}\langle 100\rangle$, which is seen in this section as a small intensity maximum at $(\phi_1, \Phi, \phi_2) = (90°, 90°, 45°)$.

The measured textures were further processed to obtain input data for the virtual experiments. Discrete ODFs, needed by the ALAMEL model, were probed from the continuous ODFs using the STAT algorithm described in Tóth and Van Houtte (1992) and implemented in the MTM-FHM software (Van Houtte 1995). Each of the initial data sets consisted of $N = 5000$ crystallographic orientations, expressed as Euler angles in Bunge (1982) convention: ϕ_1, Φ and ϕ_2. The number of orientations is sufficient to guarantee that the RVE represents the local macro-texture of the material.

In the next step, the crystal plasticity stress-driven virtual experiments were conducted to calculate the data points needed for identification of the BBC2008

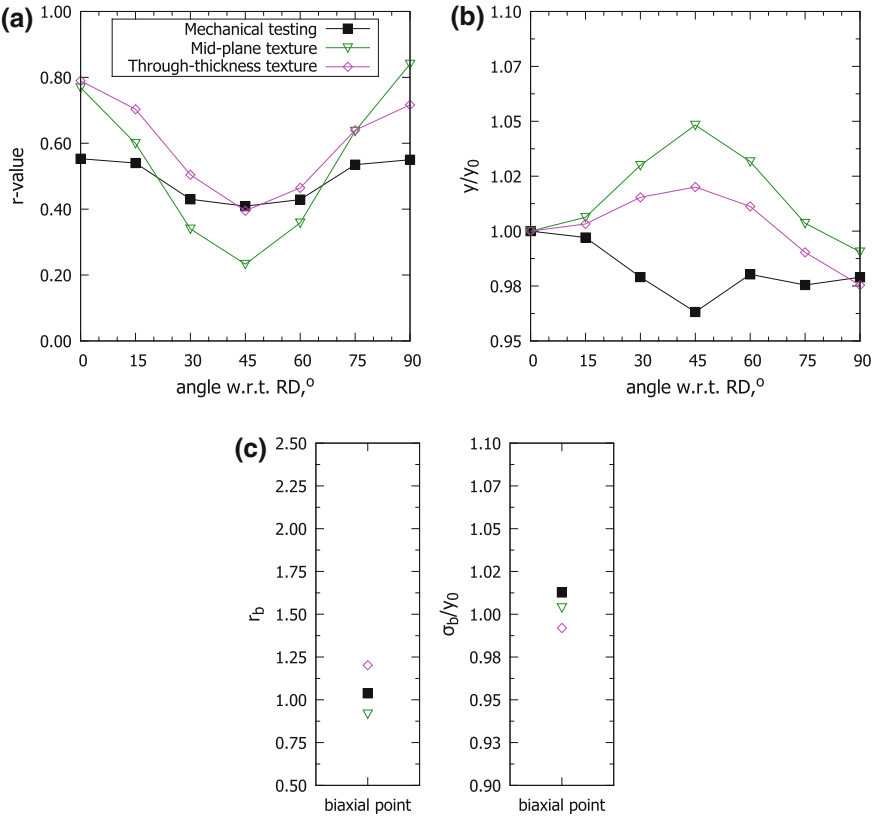

Fig. 3.4 Initial characterization of plastic anisotropy obtained by means of the mechanical testing and virtual experiments: **a** Lankford coefficient (*r*-value), **b** uniaxial yield stress, and **c** biaxial yield stress and *r*-values. All yield stresses are scaled by the uniaxial yield stress along 0° to RD. The legend in **a** applies also to the other plots. The initial experimental textures (cf. Fig. 3.3) were used in the virtual experiments

yield criterion. Figure 3.4 presents the calculated *r*-values and the yield stresses. The directions of uniaxial loading were chosen as $\alpha = 0°, 15°, \ldots, 90°$ (cf. (3.14) and (3.15)). Since the extended identification algorithm was used (see (3.13) and more extensive description in Chap. 1), the following directions θ were used in (3.18) and (3.19) to define biaxial stress ratios: 7°, 30°, 45°, 60°, 83°, 120°, 330°. The point evaluated at $\theta = 45°$ was also used in Eqs. (3.16) and (3.17) for calculating the r_b and y_b. Identical selection of data points was used in the simulations exploiting the CP-BBC2008 and HMS-BBC2008 model. All the weighting factors in (3.13) were set to unity, except for $w_\beta = 4$.

It can be seen from Fig. 3.4 that the uniaxial *r*-values resulting from the mechanical testing are generally consistent with the data provided by the virtual experiments. However, this is not the case if other quantities are considered. In

terms of the scaled uniaxial yield stresses, the virtual and the mechanical tests predict opposite trends: the maximum around 45° is consistently obtained in all virtual experiments, whereas the mechanical testing resulted in a minimum in this direction. As can be seen in Fig. 3.3, the variability of the experimental normalized uniaxial yield stress is bound in the range of (≈0.97, 1.0), therefore only a minor fluctuation of ≈3 % is present. Therefore, it is perfectly possible that the experimental result does not fully reflect the actual material behavior, since every measurand includes certain measurement uncertainty. At this point it remains debatable whether the crystal plasticity or the mechanical experiment provides better estimate of the actual material behavior in the considered case. Another prominent difference between the mechanical and the virtual testing is found at the equibiaxial yield point. Apart from the discrepancy in magnitude, the crystal plasticity predicts pretty much variation in the equibiaxial r-value, either below unity if the sharper mid-plane texture is used, or above unity for the milder through-thickness texture.

All the multi-scale simulations presented in the subsequent paragraphs use the macroscopic Swift hardening law

$$\bar{\sigma}(\varepsilon_{vM}) = K(\varepsilon_{vM} + \varepsilon_0)^n \tag{3.54}$$

where the coefficients $K = 479.7$ MPa, $n = 0.239$ and $\varepsilon_0 = 0.00096$ were determined from the average of the mechanical uniaxial tensile tests.

Concerning the cup drawing experiments, a set of cups was formed on an adapted Erichsen device. The following dimensions characterize the geometry of the tools: punch diameter: 50 mm, punch lip radius: 6 mm, die diameter: 52.82 mm and die lip radius: 3 mm, while the diameter of the blank is 90 mm. After the deep drawing, cup profiles were measured and averaged over symmetrically equivalent positions.

An Abaqus Explicit FE model was set up to reproduce the experimental cup drawing setup. Due to the symmetry of the process, it is possible to simulate one-quarter of the blank. To accelerate the computations, a mass scaling procedure was used, although quasi-static conditions were ensured. The blank was discretized using 3247 reduced integration wedge continuum shell elements (in Abaqus nomenclature: SC6R). Although only one layer of elements was used, the elements were set to include 3 integration points across the thickness. Frictional contact between the blank and the tools (punch, die and blankholder) was controlled using Coulomb law with the coefficient of friction $\mu = 0.2$, which approximately corresponds to conditions in a moderately lubricated steel-aluminum contact pair.

The HMS-BBC2008 simulations were executed on ten 12-core Westmare nodes. On average it took 5 h for an HMS-BBC2008 simulation to complete, while each of the corresponding Mech-BBC2008 and CP-BBC2008 simulations required 1 h on a single node.

The results of the simulations and experiments are summarized in Fig. 3.5. Although none of the simulations perfectly reproduces the experimental profile, it is clear that the texture-based simulations deliver superior predictions of the earing behavior. While the CP-BBC2008 and HMS-BBC2008 simulations both result in

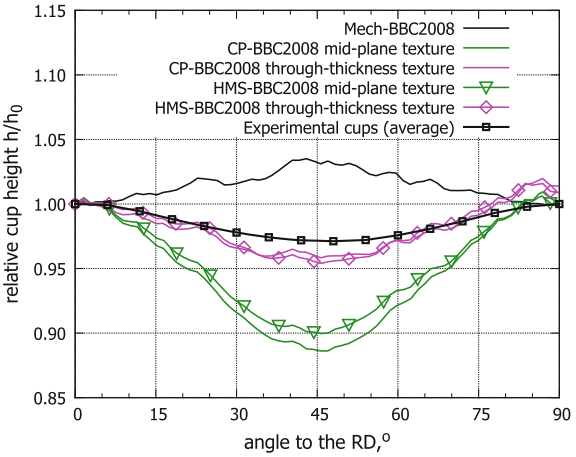

Fig. 3.5 Comparison of experimental and predicted relative cup profiles, scaled by cup height at 0° w.r.t. RD

correctly positioned ears, the modeling that relies on mechanical testing (Mech-BBC2008) wrongly predicts the ears at 45° w.r.t. RD.

Another aspect of the cup geometry prediction is related to the intensity of texture used as the starting point. As it could be anticipated from Fig. 3.4, the sharper mid-plane texture resulted in excessively pronounced ears. With respect to the impact of anisotropy evolution on the macroscopic geometry, both CP-BBC2008 and HMS-BBC2008 provide very similar cup profile prediction. Although the results of HMS-BBC2008 are slightly closer to the experimental cup, the improvement over CP-BBC2008 is only clearly visible if the sharper mid-plane texture is used as the starting point. Furthermore, the correction due to anisotropy evolution is very minor when the relative cup profile almost agrees with the experimental cups.

This raises at least two questions: why the Mech-BBC2008 produces a considerably different cup profile, and why the anisotropy evolution accounted for in HMS-BBC2008 simulations results only in limited improvement over CP-BBC2008.

The first question can be partly answered if we recall the most significant distinction between the mechanical testing and the texture-based virtual experiments found in Fig. 3.4. The mechanical testing resulted in a minimum of uniaxial yield stresses in the direction around 45° w.r.t. RD, as opposed to the virtual tests that predict it elsewhere. This minimum may appear to be a factor associated with the position of the valleys, for the reason that they correspond to higher resistance to tension in both RD and TD.

The stress state in the flange, nevertheless, is dominantly imposed by the geometry of the process. Furthermore, it considerably differs from uniaxial tension. Depending on the radial position in the flange, it may vary from nearly pure compression along the circumferential direction (at the outer rim) to a superposition of tension along the radial direction and predominant compression along the circumference. Suppose the total strain tensor is expressed in a cylindrical coordinate

system given by the axes $(\mathbf{e}_r, \mathbf{e}_\psi, \mathbf{e}_z)$. The origin of the coordinate system is fixed and coincides with the centre of the blank, while the axes correspond to the radial direction of the blank, angular position along the circumference and the sheet normal, respectively. The ratio between the radial and tangential stress in a single material point also changes while the process advances. It may be ≈–0.1 at the beginning of the process, whereas it may reach ≈–0.8 when the material point approaches the bending zone near the die lip. The plastic flow, which is a consequence of the stress state, can be then described by the ratio

$$e = \frac{\varepsilon_{rr}}{\varepsilon_{\psi\psi}} \tag{3.55}$$

between the radial and tangential strains (ε_{rr} and $\varepsilon_{\psi\psi}$, respectively). Since the strain components are in a direct relation with the yield locus through the strain rates calculated from the normality rule, the e-ratio depends on the yield locus shape as well. The strain evolution of the e-ratio was tracked in three finite elements, initially located at identical radius $r = 40$ mm along the RD, TD and 45° w.r.t. RD. Since the instantaneous stress state is used, different points on the yield locus are probed. The strain range was chosen to ensure that the considered material points remain sufficiently far from the die lip, and at the same time $\sigma_{zz} \approx 0$.

Figure 3.6 shows the e-ratio calculated for a subset of the considered cup drawing simulations. For the sake of clarity, the figure includes just the results of the Mech-BBC2008, and two CP-BBC2008 and HMS-BBC2008 that are both started from the through-thickness texture. The most pronounced difference between the two crystal plasticity based simulations and the one based on the mechanical testing data is visible at the RD and TD locations. This particularly holds at the onset of the plastic deformation, when the stress state in the given coordinate system remains nearly identical in all the cases. Thus, the divergence in the material flow is most likely attributed to the shape of the explored yield locus regions. It appears that the relatively limited deviation from the uniaxial tension state results in probing the yield surface in regions of remarkably different curvature.

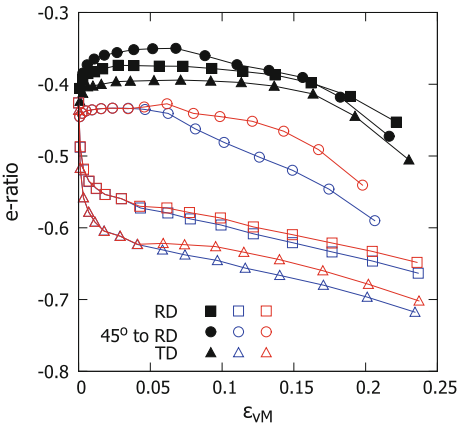

Fig. 3.6 Evolution of e-ratio as a function of equivalent von Mises plastic strain in the cup drawing simulations at the selected points in the flange: RD, 45° to RD and TD: Mech-BBC2008 (*closed black symbols*), CP-BBC2008 (*open blue symbols*) and HMS-BBC2008 (*open red symbols*), respectively (Color figure online)

If the yield locus model is calibrated primarily to the uniaxial tension data, as it is the case if the mechanical testing data are used, the regions of the yield locus that are actually reached in the cup drawing simulation are relatively distant from the measurement points. The yield loci derived from the virtual experiments, by contrast, are constructed by exploiting data points of various stress ratios. One may hence expect these yield loci to be more reliable, since the stress states more relevant to the cup drawing process are sampled.

Figure 3.6a also offers a hint why and the anisotropy evolution has only a minor effect on the cup profile. It is clearly visible that the strain history of the e-ratio coincides in the CP-BBC2008 and HMS-BBC2008 simulations only until the very first update of the yield locus model. Nonetheless, the subsequent change in the flow direction appears minor.

To explain this, let us examine how the fine-scale material state evolves and to what extent it impacts the anisotropy. Figure 3.7 presents an example of simulated cups with a superimposed field showing the count of anisotropy updates. As can be expected from Eq. (3.1), the field variable is tightly correlated with the magnitude of the plastic strain. Thus, the regions of the highest plastic strain have been updated multiple times and possibly the texture has been altered to a large extent. This is indeed the case, as seen in Fig. 3.8 showing the texture index derived from the micro-scale state and superimposed on the deformed finite element mesh. In both HMS-BBC2008 simulations we can observe a complex texture pattern that develops in the formed cup. It is remarkable that the overall texture sharpness rapidly decreases if the stronger mid-plane texture is used as the starting point, whereas the milder through-thickness texture in certain zones of the cup slightly intensifies.

It is difficult to examine evolution histories in all individual integration points. Let us then explore more in detail how the micro-scale material state and anisotropy evolve in a selected integration point located approximately 3 away from the cup rim at the RD. Figure 3.9 presents the final deformation textures that the HMS-BBC2008 model predicted in that location. In principle, texture evolution may destroy the original orthorhombic symmetry (as it was used in Fig. 3.3), thus no symmetries are imposed in the figure. The ODFs are plotted in the coordinate system coinciding with the material co-rotational reference frame. A visual inspection reveals a substantial change from the initial ODFs shown in Fig. 3.3. Even though the Cube component remains the most intense texture feature, a new texture component is regularly found. The Cu (Copper) component of varying intensity emerges in both analyzed textures, most remarkably in the evolved mid-plane texture, where it appears almost equally pronounced as the Cube component. Interestingly, the Goss component remains at similar intensity level as it used to be in the initial textures. At this point we may conclude the texture has undergone a considerable evolution during the deformation.

One might expect that not only the texture but also the anisotropic properties shall be far from the initial ones. The local anisotropy indeed evolves, as shown in yield loci shown in Fig. 3.10. The initial yield locus and the one that evolved at the considered location are substantially different, yet the largest changes are seen in the

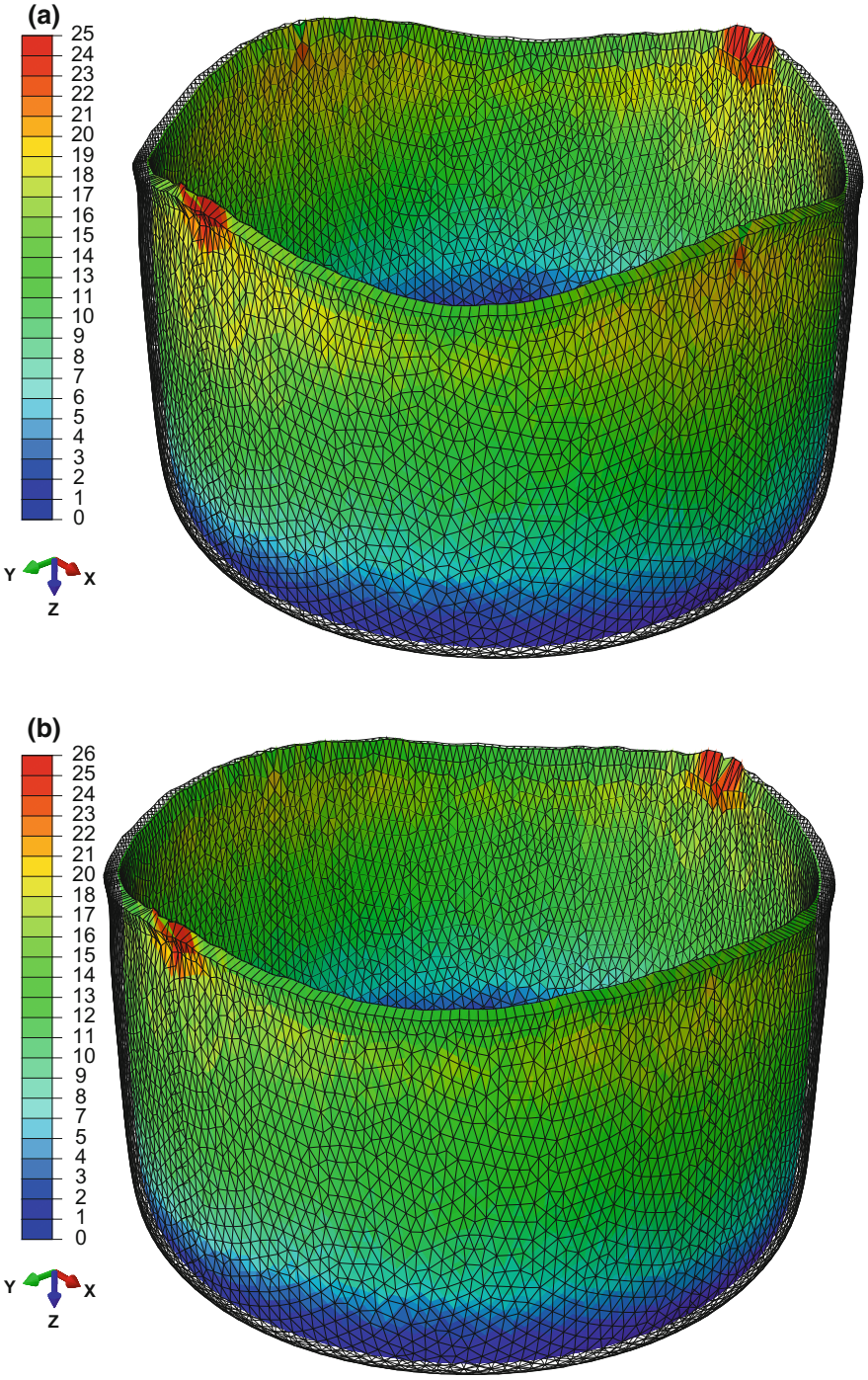

Fig. 3.7 Number of updates of texture and anisotropy in the HMS-BBC2008 simulations, presented as a field projected on the final cups (symmetries on the XZ and YZ planes are superimposed). **a** Mid-plane texture, and **b** through-thickness texture are used as the initial textures

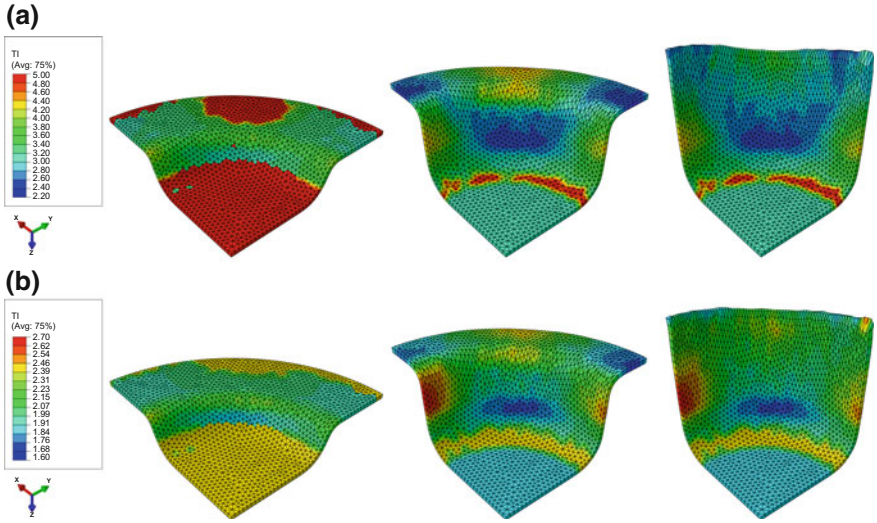

Fig. 3.8 Texture index at successive deformation stages superimposed on the deformed FE mesh in simulations started from **a** mid-plane texture (initial TI = 4.96), and **b** through-thickness texture (initial TI = 2.45), respectively

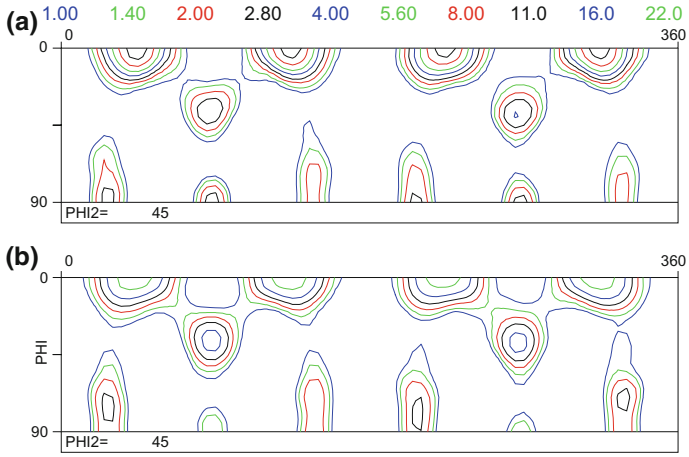

Fig. 3.9 $\phi_2 = 45°$ ODF sections (with ϕ_1 and Φ on the horizontal and the vertical axis, respectively) of the final texture textures that evolved from: **a** mid-plane texture (TI = 3.05), and **b** through-thickness texture (TI = 2.26) in the analysed position. Both sections are presented in the identical corotational reference frame, which initially was given by x_1 = RD, x_2 = TD and x_3 is the normal to the sheet

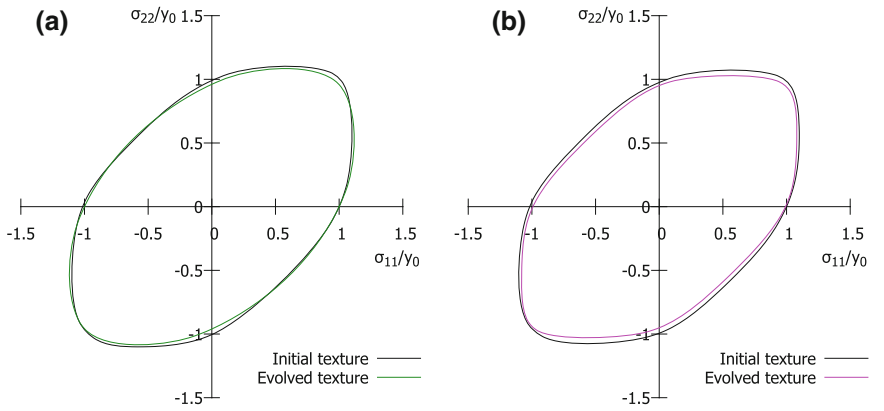

Fig. 3.10 Comparison of the initial and final yield loci obtained in the HMS-BBC2008 simulations that used **a** mid-plane texture, and **b** through-thickness texture, respectively

yield locus regions that are not active in the cup drawing process. This basically suggests a texture-induced cross-effect, which partly explains limited impact of texture evolution on the macroscopic geometry of the cup. Figure 3.11 summarises the uniaxial characteristics of plastic anisotropy that were obtained for the final deformation textures in the same geometrical location. With regard to the effects of texture evolution on the plastic behavior under uniaxial loading, the *r*-values are moderately affected. Much more complex evolution is observed when the uniaxial yield stresses are considered. Those not only tend to decrease, but the monotonicity is influenced as well: the maximum at direction 45° in the initial material clearly diminishes for the mid-plane texture.

Let us finally check a key aspect in the adaptive hierarchical modelling, namely the ability of the macroscopic yield locus to provide a good approximation of virtual experiments. From Fig. 3.11, which also shows how the BBC2008p16 predicts uniaxial material response, it is clear that the BBC2008 reproduces the virtual experiments remarkably well and is generally capable of following the changes in anisotropy that occur during the deformation.

3.3.4 Other Concepts in Multi-scale Modelling of Plastic Anisotropy

It is hardly possible to give a complete and comprehensive overview of all the concepts that have been investigated in the field of multi-scale modelling of plastic anisotropy. In this short section we want to mention a few interesting approaches that explore areas beyond the scope presented in the previous sections.

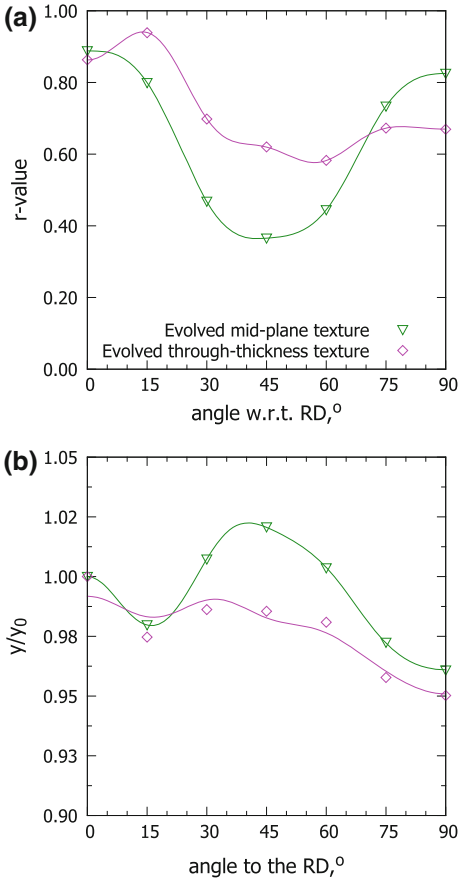

Fig. 3.11 **a** *r*-values, and **b** scaled uniaxial yield stresses calculated from evolved textures in the simulated fully formed cups: ALAMEL-based virtual experiments (*symbols*), BBC2008 local yield locus calibrated to the virtual experiments (*lines*). The legend in **a** applies to both plots

One of such concepts is to develop a macroscopic constitutive model that would allow deriving the current plastic anisotropy directly from instantaneous crystallographic texture or from constituents of crystal plasticity frameworks, see e.g. Arminjon and Bacroix (1991), Kowalczyk and Gambin (2004), Tsotsova and Böhlke (2009). Several attempts to derive macroscopic yield loci directly from texture data (i.e. without using any CP framework) have been reported in the literature. For instance, one can try to associate various texture components with their contributions to the global mechanical behaviour. This way an analytical yield locus can be constructed, as it has been tested in Darrieulat and Montheillet (2003), Darrieulat and Piot (1996). The authors investigated how parameters of quadratic Hill yield criterion can be analytically derived for the most common rolling textures. In the further step, a rule of mixture was followed to construct the Hill criterion that combines contributions from individual texture components. However, this method silently ignores the contribution from minor texture components, which may be more than subtle if interactions between the contributing terms play a role.

As the CP appears to set more reliable and robust means to recover mechanical data from the microstructure, computational performance of virtual experiments becomes crucial. This point is recognized for instance in the Reduced Texture Methodology (RTM) proposed in Rousselier and Leclercq (2006), Rousselier et al. (2009). The RTM aims neither at a complete representation of the real material texture, nor at an accurate modeling of its evolution, but it focuses on accelerating the virtual experiments. This can be achieved by simplifying the crystal plasticity model (e.g. Rousselier and Leclercq 2006). At the expense of dropping certain physical grounds, some computational gains can be reached. For example, a concept of individual crystals with smooth yield surfaces was investigated in Arminjon and Bacroix (1991), Gambin and Barlat (1997), Gambin (1992), Zamiri et al. (2007), Zamiri and Pourboghrat (2010), among others. In this formulation one yield function is used at the crystal level to calculate the crystal spin and the shear rates at the same time. Since these yield surfaces have rounded corners, as opposed to crystal yield surfaces calculated by resolving slip systems, the problem of non-uniqueness in the choice of active slip systems vanishes.

Since simplifications in the fundamental parts of the crystal plasticity may possibly impair predictive capabilities of the model, another way of accelerating virtual experiments (or to put it broader: enhancing computational performance of RVEs) is to reduce the number of crystal orientations per integration point of the macroscopic FE mesh. This is built on an observation that in many cases crystallographic textures can be approximated by a rather small number of texture components. Several attempts have been proposed to limit the number of orientations that have to be processed by the crystal plasticity while retaining a good prediction of both texture and anisotropy evolution, see e.g. Béringhier et al. (2007), Böhlke et al. (2005), Delannay et al. (2005), Knezevic and Landry (2015), Logé and Chastel (2006), Raabe et al. (2004), Raabe and Roters (2004), Roters (2005), Zhao et al. (2004).

Acknowledgments The authors would like to extend sincere gratitude to the co-authors of their previous papers on hierarchical multi-scale modelling. In particular, the authors gratefully acknowledge fruitful and formulating discussions with Profs. D. Roose and D. Banabic, and Dr. P. Eyckens. We also gratefully acknowledge financial support from the Knowledge Platform M2Form, funded by the Industrial Research Fund of KU Leuven.

References

Al-Harbi HF, Knezevic M, Kalidindi SR (2010) Spectral approaches for the fast computation of yield surfaces and first-order plastic property closures for polycrystalline materials with cubic-triclinic textures. Comput Mater Contin 15(2):153–172

Alharbi HF, Kalidindi SR (2015) Crystal plasticity finite element simulations using a database of discrete Fourier transforms. Int J Plast 66:71–84

An Y, Vegter H, Carless L, Lambriks M (2011) A novel yield locus description by combining the Taylor and the relaxed Taylor theory for sheet steels. Int J Plast 27(11):758–1780

Aretz H, Barlat F (2012) Unconditionally convex yield functions for sheet metal forming based on linear stress deviator transformation. Key Eng Mater 504–506:667–672. ISBN:978-3-03785-366-5

Aretz H, Barlat F (2013) New convex yield functions for orthotropic metal plasticity. Int J Non-linear Mech 51:97–111

Arminjon M, Bacroix B (1991) On plastic potentials for anisotropic metals and their derivation from the texture function. Acta Mech 88(3–4):219–243

Arsenlis A, Barton NR, Becker R, Rudd RE (2006) Generalized in situ adaptive tabulation for constitutive model evaluation in plasticity. Comput Methods Appl Mech Eng 196(1–3):1–13

Arul Kumar M, Mahesh S, Parameswaran V (2011) A 'stack' model of rate-independent polycrystals. Int J Plast 27(6):962–981

Asaro RJ (1983a) Crystal plasticity. J Appl Mech 50(4b):921

Asaro RJ (1983b) Advances in applied mechanics, vol 23. Elsevier. ISBN:9780120020232

Asaro RJ, Needleman A (1985) Overview no. 42 texture development and strain hardening in rate dependent polycrystals. Acta Metall 33:923–963

Asaro RJ, Rice JR (1977) Strain localization in ductile single crystals. J Mech Phys Solids 25(5):309–338

Banabic D, Comsa DS, Balan T (2000) A new yield criterion for orthotropic sheet metals under plane stress conditions. In The 7th Conference TPR2000, Cluj Napoca, pp 217–224

Banabic D, Kuwabara T, Balan T, Comsa DS, Julean D (2003) Non-quadratic yield criterion for orthotropic sheet metals under plane-stress conditions. Int J Mech Sci 45(5):797–811

Banabic D, Aretz H, Comsa DS, Paraianu L (2005) An improved analytical description of orthotropy in metallic sheets. Int J Plast 21(3):493–512

Banabic D, Barlat F, Cazacu O, Kuwabara T (2010) Advances in anisotropy and formability. Int J Mater Forming 3(3):165–189

Barlat F, Becker RC, Hayashida Y, Maeda Y, Yanagawa M, Chung K, Brem JC, Lege DJ, Matsui K, Murtha SJ, Hattori S (1997a) Yielding description for solution strengthened aluminum alloys. Int J Plast 13(4):385–401

Barlat F, Maeda Y, Chung K, Yanagawa M, Brem JC, Hayashida Y, Lege DJ, Matsui K, Murtha SJ, Hattori S, Becker RC, Makosey S (1997b) Yield function development for aluminum alloy sheets. J Mech Phys Solids 45(11–12):1727–1763

Barlat F, Brem JC, Yoon JW, Chung K, Dick RE, Lege DJ, Pourboghrat F, Choi S-H, Chu E (2003a) Plane stress yield function for aluminum alloy sheets—part I: theory. Int J Plast 19(9):1297–1319

Barlat F, Ferreira Duarte JM, Gracio JJ, Lopes AB, Rauch EF (2003b) Plastic flow for non-monotonic loading conditions of an aluminum alloy sheet sample. Int J Plast 19(8):1215–1244

Barlat F, Aretz H, Yoon JW, Karabin ME, Brem JC, Dick RE (2005) Linear transformation-based anisotropic yield functions. Int J Plast 21(5):1009–1039

Barlat F, Yoon JW, Cazacu O (2007) On linear transformations of stress tensors for the description of plastic anisotropy. Int J Plast 23:876–896

Barlat F, Lege DJ, Brem JC (1991) A six-component yield function for anisotropic materials. Int J Plast 7(7):693–712

Barton NR, Knap J, Arsenlis A, Becker R, Hornung RD, Jefferson DR (2008) Embedded polycrystal plasticity and adaptive sampling. Int J Plast 24(2):242–266

Beaudoin AJ, Mathur KK, Dawson PR, Johnson GC (1993) Three-dimensional deformation process simulation with explicit use of polycrystal plasticity models. Int J Plast 9(7):833–860

Beausir B, Suwas S, Tóth LS, Neale KW, Fundenberger J-J (2008) Analysis of texture evolution in magnesium during equal channel angular extrusion. Acta Mater 56(2):200–214

Béringhier M, Delannay L, Chastel Y, Logé R (2007) Using Lagrangian particles to efficiently describe microstructure evolution in metal forming—application to texture-induced mechanical anisotropy. Model Simul Mater Sci Eng 15(3):191–204

Bishop JFW, Hill R (1951a) A theory of the plastic distortion of a polycrystalline aggregate under combined stresses. Philos Mag 42:414–427

Bishop JFW, Hill R (1951b) A theoretical derivation of the plastic properties of a face-centred metal. Philos Mag 42:1298–1307
Böhlke T, Risy G, Bertram A (2005) A texture component model for anisotropic polycrystal plasticity. Comp Mat Sci 32(3–4):284–293
Bunge HJ (1982) Texture analysis in materials science. Butterworth, London
Bunge HJ, Esling C (1984) Texture development by plastic deformation. Mat Metall 18(3):191–195
Cazacu O, Barlat F (2004) A criterion for description of anisotropy and yield differential effects in pressure-insensitive metals. Int J Plast 20(11):2027–2045
Cazacu O, Plunkett B, Barlat F (2006) Orthotropic yield criterion for hexagonal closed packed metals. Int J Plast 22(7):1171–1194
Coenen EWC, Kouznetsova VG, Bosco E, Geers MGD (2012a) A multi-scale approach to bridge microscale damage and macroscale failure: a nested computational homogenization-localization framework. Int J Fract 178(1–2):157–178
Coenen EWC, Kouznetsova VG, Geers MGD (2012b) Multi-scale continuous–discontinuous framework for computational–homogenization–localization. J Mech Phys Solids 60(8):1486–1507
Comsa D, Banabic D (2008) Plane-stress yield criterion for highly-anisotropic sheet metals. In: Numisheet 2008. Interlaken pages, pp 43–48
Conn AR, Gould NIM, ToInt PL (2000) Trust-region methods. SIAM Society for Industrial and Applied Mathematics
Crumbach M, Pomana G, Wagner P, Gottstein G (2001) Taylor type deformation texture model considering grain interaction and material properties. part I—fundamentals. In: Gottstein G, Molodov DA (eds) Proceedings of the 1st joint international conference on recrystallisation and grain growth. Springer, Berlin, pp 1053–1060
Darrieulat M, Montheillet F (2003) A texture based continuum approach for predicting the plastic behaviour of rolled sheet. Int J Plast 19(4):517–546
Darrieulat M, Piot D (1996) A method of generating analytical yield surfaces of crystalline materials. Int J Plast 12(5):575–610
Dawson PR, Boyce DE, Hale R, Durkot JP (2005) An isoparametric piecewise representation of the anisotropic strength of polycrystalline solids. Int J Plast 21(2):251–283
Delaire F, Raphanel JL, Rey C (2000) Plastic heterogeneities of a copper multicrystal deformed in uniaxial tension: experimental study and finite element simulations. Acta Mater 48(5):1075–1087
Delannay L (2002) Prediction of intergranular strains in cubic metals using a multisite elastic-plastic model. Acta Mater 50(20):5127–5138
Delannay L, Kalidindi SR, Van Houtte P (2002) Quantitative prediction of textures in aluminium cold rolled to moderate strains. Mat Sci Eng: A 336(1–2):233–244
Delannay L, Béringhier M, Chastel Y, Logé RE (2005) Simulation of cup-drawing based on crystal plasticity applied to reduced grain samplings. Mat Sci Forum 495–497:1639–1644
Delannay L, Melchior MA, Signorelli JW, Remacle J-F, Kuwabara T (2009) Influence of grain shape on the planar anisotropy of rolled steel sheets—evaluation of three models. Comput Mater Sci 45(3):739–743
Duchêne L, Godinas A, Cescotto S, Habraken AM (2002) Texture evolution during deep-drawing processes. J Mat Proc Tech 125–126:110–118
Ebeling T, Hartig Ch, Laser T, Bormann R (2009) Material law parameter determination of magnesium alloys. Mater Sci Eng A 527(1–2):272–280
Eisenlohr P, Tjahjanto DD, Hochrainer T, Roters F, Raabe D (2009a) Texture prediction from a novel grain cluster-based homogenization scheme. Int J Mater Form 2(S1):523–526
Eisenlohr P, Tjahjanto DD, Hochrainer T, Roters F, Raabe D (2009b) Comparison of texture evolution in fcc metals predicted by various grain cluster homogenization schemes. Int J Mater Res 100(4):500–509
Eisenlohr P, Diehl M, Lebensohn RA, Roters F (2013) A spectral method solution to crystal elasto-viscoplasticity at finite strains. Int J Plast 46:37–53

Engler O, Crumbach M, Li S (2005) Alloy-dependent rolling texture simulation of aluminium alloys with a grain-interaction model. Acta Mater 53(8):2241–2257

Engler O, Hirsch J (2002) Texture control by thermomechanical processing of AA6xxx Al–Mg–Si sheet alloys for automotive applications—a review. Mat Sci Eng A 336(1–2):249–262

Eshelby JD (1957) The determination of the elastic field of an ellipsoidal inclusion, and related problems. Proc R Soc A Math Phys Eng Sci 241(1226):376–396

Evers LP, Parks DM, Brekelmans WAM, Geers MGD (2002) Crystal plasticity model with enhanced hardening by geometrically necessary dislocation accumulation. J Mech Phys Solids 50(11):2403–2424

Eyckens P, Mulder H, Gawad J, Vegter H, Roose D, van den Boogaard TH, Van Bael A, Van Houtte P (2015) The prediction of differential hardening behaviour of steels by multi-scale crystal plasticity modelling. Int J Plast accepted (available on-line)

Feyel F (1999) Multiscale FE2 elastoviscoplastic analysis of composite structures. Comput Mater Sci 16(1–4):344–354

Feyel F (2003) A multilevel finite element method (FE2) to describe the response of highly non-linear structures using generalized continua. Comput Methods Appl Mech Eng 192(28–30):3233–3244

Feyel F, Chaboche J-L (2000) FE2 multiscale approach for modelling the elastoviscoplastic behaviour of long fibre SiC/Ti composite materials. Comput Methods Appl Mech Eng 183(3–4):309–330

Galán J, Verleysen P, Lebensohn RA (2014) An improved algorithm for the polycrystal viscoplastic self-consistent model and its integration with implicit finite element schemes. Model Simul Mater Sci Eng 22(5):055023

Gambin W (1992) Refined analysis of elastic-plastic crystals. Int J Solids Struct 29(16):2013–2021

Gambin W, Barlat F (1997) Modeling of deformation texture development based on rate independent crystal plasticity. Int J Plast 13(1–2):75–85

Gawad J, Van Bael A, Eyckens P, Van Houtte P, Samaey G, Roose D (2010) Effect of texture evolution in cup drawing predictions by multiscale model. Steel Res Int 81(Supplement Metal Forming):1430–1433

Gawad J, Van Bael A, Eyckens P, Samaey G, Van Houtte P, Roose D (2013) Hierarchical multi-scale modeling of texture induced plastic anisotropy in sheet forming. Comp Mater Sci 66:65–83

Gawad J, Banabic D, Van Bael A, Comsa DS, Gologanu M, Eyckens P, Van Houtte P, Roose D (2015) An evolving plane stress yield criterion based on crystal plasticity virtual experiments. Int J Plast 75:141–169

Geers MGD, Kouznetsova VG, Brekelmans WAM (2010) Multi-scale computational homogenization: trends and challenges. J Comput Appl Math 234(7):2175–2182

Ghosh S, Dimiduk D (eds) (2011) Computational methods for microstructure-property relationships. Springer, US

Gottstein G (2004) Physical foundations of materials science. Springer, Berlin

Grytten F, Holmedal B, Hopperstad OS, Børvik T (2008) Evaluation of identification methods for YLD2004-18p. Int J Plast 24(12):2248–2277

Habraken AM, Duchêne L (2004) Anisotropic elasto-plastic finite element analysis using a stress-strain interpolation method based on a polycrystalline model. Int J Plast 20(8–9):1525–1560

He WJ, Zhang SH, Prakash A, Helm D (2014) A hierarchical multi-scale model for hexagonal materials taking into account texture evolution during forming simulation. Comp Mater Sci 82:464–475

Héripré E, Dexet M, Crépin J, Gélébart L, Roos A, Bornert M, Caldemaison D (2007) Coupling between experimental measurements and polycrystal finite element calculations for micromechanical study of metallic materials. Int J Plast 23(9):1512–1539

Hill R (1948) A theory of the yielding and plastic flow of anisotropic metals. Proc Roy Form London A193:281–297

Hosford WF (1979) On yield loci of anisotropic cubic metals. In: Proceedings of the 7th North American metalworking conference (NMRC), SME, Dearborn, pp 191–197
Inal K, Mishra RK, Cazacu O (2010) Forming simulation of aluminum sheets using an anisotropic yield function coupled with crystal plasticity theory. Int J Solids Struct 47(17):2223–2233
Jung K-H, Kim D-K, Im Y-T, Lee Y-S (2013) Prediction of the effects of hardening and texture heterogeneities by finite element analysis based on the Taylor model. Int J Plast 42:120–140
Kalidindi SR, Schoenfeld SE (2000) On the prediction of yield surfaces by the crystal plasticity models for fcc polycrystals. Mater Sci Eng A 293(1–2):120–129
Kalidindi SR, Duvvuru HK (2005) Spectral methods for capturing crystallographic texture evolution during large plastic strains in metals. Acta Mater 53(13):3613–3623
Kalidindi SR, Bronkhorst CA, Anand L (1992) Crystallographic texture evolution in bulk deformation processing of FCC metals. J Mech Phys Solids 40(3):537–569
Kalidindi SR, Duvvuru HK, Knezevic M (2006) Spectral calibration of crystal plasticity models. Acta Mater 54(7):1795–1804
Kalidindi SR, Houskamp JR, Lyons M, Adams BL (2004) Microstructure sensitive design of an orthotropic plate subjected to tensile load. Int J Plast 20(8–9):1561–1575
Kalidindi SR, Knezevic M, Niezgoda S, Shaffer J (2009) Representation of the orientation distribution function and computation of first-order elastic properties closures using discrete Fourier transforms. Acta Mater 57(13):3916–3923
Kanit T, Forest S, Galliet I, Mounoury V, Jeulin D (2003) Determination of the size of the representative volume element for random composites: statistical and numerical approach. Int J Solids Struct 40(13–14):3647–3679
Kim D, Barlat F, Bouvier S, Rabahallah M, Balan T, Chung K (2007) Non-quadratic anisotropic potentials based on linear transformation of plastic strain rate. Int J Plast 23(8):1380–1399
Kim JH, Lee M-G, Barlat F, Wagoner RH, Chung K (2008) An elasto-plastic constitutive model with plastic strain rate potentials for anisotropic cubic metals. Int J Plast 24(12):2298–2334
Klusemann B, Svendsen B, Vehoff H (2012) Investigation of the deformation behavior of Fe–3 % Si sheet metal with large grains via crystal plasticity and finite-element modeling. Comput Mater Sci 52(1):25–32
Klusemann B, Svendsen B, Vehoff H (2013) Modeling and simulation of deformation behavior, orientation gradient development and heterogeneous hardening in thin sheets with coarse texture. Int J Plast 50:109–126
Knap J, Barton NR, Hornung RD, Arsenlis A, Becker R, Jefferson DR (2008) Adaptive sampling in hierarchical simulation. Int J Numer Methods Eng 76(4):572–600
Knezevic M, Kalidindi SR (2007) Fast computation of first-order elastic-plastic closures for polycrystalline cubic-orthorhombic microstructures. Comput Mater Sci 39(3):643–648
Knezevic M, Landry NW (2015) Procedures for reducing large datasets of crystal orientations using generalized spherical harmonics. Mech Mater 88:73–86
Knezevic M, Kalidindi SR, Fullwood D (2008) Computationally efficient database and spectral interpolation for fully plastic Taylor-type crystal plasticity calculations of face-centered cubic polycrystals. Int J Plast 24(7):1264–1276
Knezevic M, Al-Harbi HF, Kalidindi SR (2009) Crystal plasticity simulations using discrete Fourier transforms. Acta Mater 57(6):1777–1784
Knezevic M, Beyerlein IJ, Brown DW, Sisneros TA, Tomé CN (2013a) A polycrystal plasticity model for predicting mechanical response and texture evolution during strain-path changes: application to beryllium. Int J Plast 49:185–198
Knezevic M, Lebensohn RA, Cazacu O, Revil-Baudard B, Proust G, Vogel SC, Nixon ME (2013b) Modeling bending of α-titanium with embedded polycrystal plasticity in implicit finite elements. Mater Sci Eng A 564:116–126
Knezevic M, McCabe RJ, Lebensohn RA, Tomé CN, Liu C, Lovato ML, Mihaila B (2013c) Integration of self-consistent polycrystal plasticity with dislocation density based hardening laws within an implicit finite element framework: application to low-symmetry metals. J Mech Phys Solids 61(10):2034–2046

Kouznetsova VG, Geers MGD, Brekelmans WAM (2004a) Size of a representative volume element in a second-order computational homogenization framework. Int J Multiscale Comput Eng 2(4):575–598

Kouznetsova VG, Geers MGD, Brekelmans WAM (2004b) Multi-scale second-order computational homogenization of multi-phase materials: a nested finite element solution strategy. Comput Methods Appl Mech Eng 193(48–51):5525–5550

Kouznetsova VG, Geers MGD (2008) A multi-scale model of martensitic transformation plasticity. Mech Mater 40(8):641–657

Kowalczyk K, Gambin W (2004) Model of plastic anisotropy evolution with texture-dependent yield surface. Int J Plast 20(1):19–54

Kraska M, Doig M, Tikhorimov D, Raabe D, Roters F (2009) Virtual material testing for stamping simulations based on polycrystal plasticity. Comp Mat Sci 46:383–392

Larsson F, Runesson K (2011) On two-scale adaptive FE analysis of micro-heterogeneous media with seamless scale-bridging. Comput Methods Appl Mech Eng 200(37–40):2662–2674

Lazarescu L, Comsa DS, Banabic D (2011) Analytical and experimental evaluation of the stress-strain curves of sheet metals by hydraulic bulge test. Key Eng Mater 473:352–359

Lebensohn RA (2001) N-site modeling of a 3D viscoplastic polycrystal using fast Fourier transform. Acta Mater 49(14):2723–2737

Lebensohn RA, Tomé CN (1993) A self-consistent anisotropic approach for the simulation of plastic deformation and texture development of polycrystals: application to zirconium alloys. Acta Metall Mater 41:2611–2624

Lebensohn RA, Liu Y, Ponte Castañeda P (2004) On the accuracy of the self-consistent approximation for polycrystals: comparison with full-field numerical simulations. Acta Mater 52(18):5347–5361

Lebensohn RA, Tomé CN, Ponte Castañeda P (2007) Self-consistent modelling of the mechanical behaviour of viscoplastic polycrystals incorporating intragranular field fluctuations. Philos Mag 87(28):4287–4322

Lebensohn RA, Brenner R, Castelnau O, Rollett AD (2008) Orientation image-based micromechanical modelling of subgrain texture evolution in polycrystalline copper. Acta Mater 56 (15):3914–3926

Lebensohn RA, Rollett AD, Suquet P (2011) Fast Fourier transform-based modeling for the determination of micromechanical fields in polycrystals. JOM 63(3):13–18

Lebensohn RA, Kanjarla AK, Eisenlohr P (2012) An elasto-viscoplastic formulation based on fast Fourier transforms for the prediction of micromechanical fields in polycrystalline materials. Int J Plast 32–33:59–69

Lequeu Ph, Gilormini P, Montheillet F, Bacroix B, Jonas JJ (1987) Yield surfaces for textured polycrystals-I. Crystallographic approach. Acta Metall 35(2):439–451

Li DS, Garmestani H, Schoenfeld S (2003) Evolution of crystal orientation distribution coefficients during plastic deformation. Mat Mater 49(9):867–872

Li S, Van Houtte P, Kalidindi SR (2004) A quantitative evaluation of the deformation texture predictions for aluminium alloys from crystal plasticity finite element method. Model Simul Mater Sci Eng 12(5):845–870

Lim H, Lee M-G, Kim JH, Adams BL, Wagoner RH (2011) Simulation of polycrystal deformation with grain and grain boundary effects. Int J Plast 27(9):1328–1354

Lim H, Carroll JD, Battaile CC, Buchheit TE, Boyce BL, Weinberger CR (2014) Grain-scale experimental validation of crystal plasticity finite element simulations of tantalum oligocrystals. Int J Plast 60:1–18

Liu YS, Delannay L, Van Houtte P (2002) Application of the Lamel model for simulating cold rolling texture in molybdenum sheet. Acta Mater 50(7):1849–1856

Liu B, Raabe D, Roters F, Eisenlohr P, Lebensohn RA (2010) Comparison of finite element and fast Fourier transform crystal plasticity solvers for texture prediction. Model Simul Mater Sci Eng 18(8):085005

Logé RE, Chastel YB (2006) Coupling the thermal and mechanical fields to metallurgical evolutions within a finite element description of a forming process. Comput Methods Appl Mech Eng 195(48–49):6843–6857
Mahesh S (2010) A binary-tree based model for rate-independent polycrystals. Int J Plast 26 (1):42–64
Mánik T, Holmedal B (2013) Additional relaxations in the Alamel texture model. Mat Sci Eng A 580:349–354
Mánik T, Holmedal B (2014) Review of the Taylor ambiguity and the relationship between rate-independent and rate-dependent full-constraints Taylor models grain interaction model. Int J Plast 55:152–181
Mathur KK, Dawson PR (1989) On modeling the development of crystallographic texture in bulk forming processes. Int J Plast 5(1):67–94
Mathur KK, Dawson PR (1990) texture development during wire drawing. J Eng Mater Technol 112(3):292
McDowell DL (2010) A perspective on trends in multiscale plasticity. Int J Plast 26(9):1280–1309
Mellbin Y, Hallberg H, Ristinmaa M (2014) Accelerating crystal plasticity simulations using GPU multiprocessors. Int J Numer Methods Eng 100(2):111–135
Miehe C (1996) Numerical computation of algorithmic (consistent) tangent moduli in large-strain computational inelasticity. Comput Methods Appl Mech Eng 134(3–4):223–240
Miehe C, Schröder J, Schotte J (1999) Computational homogenization analysis in finite plasticity Simulation of texture development in polycrystalline materials. Comput Methods Appl Mech Eng 171(3–4):387–418
Molinari A, Canova GR, Ahzi S (1987) A self consistent approach of the large deformation polycrystal viscoplasticity. Acta Metall 35(12):2983–2994
Molinari A, Ahzi S, Kouddane R (1997) On the self-consistent modeling of elastic-plastic behavior of polycrystals. Mech Mater 26(1):43–62
Nixon ME, Cazacu O, Lebensohn RA (2010a) Anisotropic response of high-purity α-titanium: Experimental characterization and constitutive modeling. Int J Plast 26(4):516–532
Nixon ME, Lebensohn RA, Cazacu O, Liu C (2010b) Experimental and finite-element analysis of the anisotropic response of high-purity α-titanium in bending. Acta Mater 58(17):5759–5767
Ostoja-Starzewski M (2005) Scale effects in plasticity of random media: status and challenges. Int J Plast 21(6):1119–1160
Ostoja-Starzewski M (2006) Material spatial randomness: from statistical to representative volume element. Probab Eng Mech 21(2):112–132
Peirce D, Asaro RJ, Needleman A (1982) An analysis of nonuniform and localized deformation in ductile single crystals. Acta Metall 30(6):1087–1119
Peirce D, Asaro RJ, Needleman A (1983) Material rate dependence and localized deformation in crystalline solids. Acta Metall 31(12):1951–1976
Pinna C, Lan Y, Kiu MF, Efthimiadis P, Lopez-Pedrosa M, Farrugia D (2015) Assessment of crystal plasticity finite element simulations of the hot deformation of metals from local strain and orientation measurements. Int J Plast 73:24–38
Plunkett B, Lebensohn RA, Cazacu O, Barlat F (2006) Anisotropic yield function of hexagonal materials taking into account texture development and anisotropic hardening. Acta Mater 54 (16):4159–4169
Plunkett B, Cazacu O, Barlat F (2008) Orthotropic yield criteria for description of the anisotropy in tension and compression of sheet metals. Int J Plast 24(5):847–866
Pokharel R, Lind J, Kanjarla AK, Lebensohn RA, Li SF, Kenesei P, Suter RM, Rollett AD (2014) Polycrystal plasticity: comparison between grain—scale observations of deformation and simulations. Annu Rev Condens Matter Phys 5(1):317–346
Prakash A, Lebensohn RA (2009) Simulation of micromechanical behavior of polycrystals: finite elements versus fast Fourier transforms. Model Simul Mater Sci Eng 17(6):064010
Prakash A, Nöhring WG, Lebensohn RA, Höppel HW, Bitzek E (2015) A multiscale simulation framework of the accumulative roll bonding process accounting for texture evolution. Mater Sci Eng A 631:104–119

Quey R, Dawson PR, Barbe F (2011) Large-scale 3D random polycrystals for the finite element method: generation, meshing and remeshing. Comput Methods Appl Mech Eng 200(17–20):1729–1745

Raabe D, Roters F (2004) Using texture components in crystal plasticity finite element simulations. Int J Plast 20(3):339–361

Raabe D, Zhao Z, Roters F (2004) Study on the orientational stability of cube-oriented FCC crystals under plane strain by use of a texture component crystal plasticity finite element method. Mat Mater 50(7):1085–1090

Raabe D, Sachtleber M, Zhao Z, Roters F, Zaefferer S (2001) Micromechanical and macromechanical effects in grain scale polycrystal plasticity experimentation and simulation. Acta Mater 49(17):3433–3441

Rabahallah M, Balan T, Bouvier S, Bacroix B, Barlat F, Chung K, Teodosiu C (2009) Parameter identification of advanced plastic strain rate potentials and impact on plastic anisotropy prediction. Int J Plast 25(3):491–512

Raphanel JL, Van Houtte P (1985) Simulation of the rolling textures of b.c.c. metals by means of the relaxed Taylor theory. Acta Metall 33(8):1481–1488

Reis FJP, Andrade Pires FM (2013) An adaptive sub-incremental strategy for the solution of homogenization-based multi-scale problems. Comput Methods Appl Mech Eng 257:164–182

Resk H, Delannay L, Bernacki M, Coupez T, Logé R (2009) Adaptive mesh refinement and automatic remeshing in crystal plasticity finite element simulations. Model Simul Mater Sci Eng 17(7):075012

Roters F (2005) Application of crystal plasticity FEM from single crystal to bulk polycrystal. Comput Mater Sci 32(3–4):509–517

Roters F, Eisenlohr P, Hantcherli L, Tjahjanto DD, Bieler TR, Raabe D (2010a) Overview of constitutive laws, kinematics, homogenization and multiscale methods in crystal plasticity finite-element modeling: theory, experiments, applications. Acta Mater 58(4):1152–1211

Roters F, Eisenlohr P, Bieler TR, Raabe D (2010b) Crystal plasticity finite element methods. Wiley-VCH Verlag GmbH & Co, KGaA

Roters F, Eisenlohr P, Kords C, Tjahjanto DD, Diehl M, Raabe D (2012) DAMASK: the Düsseldorf Advanced MAterial Simulation Kit for studying crystal plasticity using an FE based or a spectral numerical solver. Procedia IUTAM 3:3–10

Rouet-Leduc B, Barros K, Cieren E, Elango V, Junghans C, Lookman T, Mohd-Yusof J, Pavel RS, Rivera AY, Roehm D, McPherson AL, Germann TC (2014) Spatial adaptive sampling in multiscale simulation. Comput Phys Commun 185(7):1857–1864

Rousselier G, Leclercq S (2006) A simplified "polycrystalline" model for viscoplastic and damage finite element analyses. Int J Plast 22(4):685–712

Rousselier G, Barlat F, Yoon JW (2009) A novel approach for anisotropic hardening modeling. Part I: Theory and its application to finite element analysis of deep drawing. Int J Plast 25 (12):2383–2409

Saai A, Dumoulin S, Hopperstad OS, Lademo OG (2013) Simulation of yield surfaces for aluminium sheets with rolling and recrystallization textures. Comp Mater Sci 67:424–433

Sachs G (1928) Zur ableitung einer filebedingung. Zeitschrift des Vereines Deutscher Ingenieure 72:734–736

Savoie J, MacEwen SR (1996) A sixth order inverse potential function for incorporation of crystallographic texture into predictions of properties of aluminium sheet. Texture MicroStruct 26(C):495–512

Schoenfeld SE (1998) Dynamic behaviour of polycrystalline tantalum. Int J Plast 14(9):871–890

Segurado J, Lebensohn RA, LLorca J, Tomé CN (2012) Multiscale modeling of plasticity based on embedding the viscoplastic self-consistent formulation in implicit finite elements. Int J Plast 28 (1):124–140

Shaffer JB, Knezevic M, Kalidindi SR (2010) Building texture evolution networks for deformation processing of polycrystalline fcc metals using spectral approaches: applications to process design for targeted performance. Int J Plast 26(8):1183–1194

Shanthraj P, Eisenlohr P, Diehl M, Roters F (2015) Numerically robust spectral methods for crystal plasticity simulations of heterogeneous materials. Int J Plast 66:31–45

Smit RJM, Brekelmans WAM, Meijer HEH (1998) Prediction of the mechanical behavior of nonlinear heterogeneous systems by multi-level finite element modeling. Comput Methods Appl Mech Eng 155(1–2):181–192

Soare S, Barlat F (2010) Convex polynomial yield functions. J Mech Phys Solids 58(11):1804–1818

Soare S, Whan Yoon J, Cazacu O (2008) On the use of homogeneous polynomials to develop anisotropic yield functions with applications to sheet forming. Int J Plast 24(6):915–944

St-Pierre L, Héripré E, Dexet M, Crépin J, Bertolino G, Bilger N (2008) 3D simulations of microstructure and comparison with experimental microstructure coming from O.I.M analysis. Int J Plast 24(9):1516–1532

Steglich D, Jeong Y, Andar MO, Kuwabara T (2012) Biaxial deformation behaviour of AZ31 magnesium alloy: crystal-plasticity-based prediction and experimental validation. Int J Solids Struct 49(25):3551–3561

Taylor GI (1938) Plastic strain in metals. J Inst Metals 62:307–324

Temizer I, Wriggers P (2008) On the computation of the macroscopic tangent for multiscale volumetric homogenization problems. Comput Methods Appl Mech Eng 198(3–4):495–510

Temizer I, Wriggers P (2011) An adaptive multiscale resolution strategy for the finite deformation analysis of microheterogeneous structures. Comput Methods Appl Mech Eng 200(37–40):2639–2661

Tjahjanto DD, Eisenlohr P, Roters F (2010) A novel grain cluster-based homogenization scheme. Modell Simul Mater Sci Eng 18(1):015006

Tjahjanto DD, Eisenlohr P, Roters F (2015) Multiscale deep drawing analysis of dual-phase steels using grain cluster-based RGC scheme. Model Simul Mater Sci Eng 23(4):045005

Tomé CN (2001) Mechanical response of zirconium—I. Derivation of a polycrystal constitutive law and finite element analysis. Acta Mater 49(15):3085–3096

Tóth L-S, Van Houtte P (1992) Discretization techniques for orientation distribution functions. Texture MicroStruct 19:229–244

Tsotsova R, Böhlke T (2009) Representation of effective flow potentials for polycrystals based on texture data. Int J Mater Form 2(S1):451–454

Turner TJ, Shade PA, Schuren JC, Groeber MA (2013) The influence of microstructure on surface strain distributions in a nickel micro-tension specimen. Model Simul Mater Sci Eng 21 (1):015002

Van Bael A, Eyckens P, Gawad J, Samaey G, Roose D, Van Houtte P (2010) Evolution of crystallographic texture and mechanical anisotropy during cup drawing. Steel Res Int 81 (Supplement Metal Forming):1392–1395

Van Houtte P (1982) On the equivalence of the relaxed Taylor theory and the Bishop-Hill theory for partially constrained plastic deformation of crystals. Mater Sci Eng 55(1):69–77

Van Houtte P (1987) Calculation of the yield locus of textured polycrystals using the Taylor and the relaxed Taylor theory. Textures MicroStruct 7(C):29–72

Van Houtte P (1988) A comprehensive mathematical formulation of an extended Taylor–Bishop–Hill model featuring relaxed constraints, the Renouard–Wintenberger theory and a strain rate sensitivity model. Textures MicroStruct 8(C):313–350

Van Houtte P (1995) The MTM-FHM software system Version 2

Van Houtte P (2001) Fast calculation of average Taylor factors and Mandel spins for all possible strain modes. Int J Plast 17(6):807–818

Van Houtte P, Van Bael A (2004) Convex plastic potentials of fourth and sixth rank for anisotropic materials. Int J Plast 20(8–9):1505–1524

Van Houtte P, Delannay L, Samajdar I (1999) Quantitative prediction of cold rolling textures in low-carbon steel by means of the Lamel model. Texture MicroStruct 31(3):109–149

Van Houtte P, Delannay L, Kalidindi SR (2002) Comparison of two grain interaction models for polycrystal plasticity and deformation texture prediction. Int J Plast 18(3):359–377

Van Houtte P, Li S, Seefeldt M, Delannay L (2005) Deformation texture prediction: from the Taylor model to the advanced Lamel model. Int J Plast 21(3):589–624
Van Houtte P, Kumar Yerra S, Van Bael A (2009) The Facet method: a hierarchical multilevel modelling scheme for anisotropic convex plastic potentials. Int J Plast 25(2):332–360
Van Houtte P, Gawad J, Eyckens P, Van Bael A, Samaey G, Roose D (2011) A full-field strategy to take texture induced anisotropy into account during FE simulations of metal forming processes. JOM 63:37–43
Vegter H, van den Boogaard TH (2006) A plane stress yield function for anisotropic sheet material by interpolation of biaxial stress states. Int J Plast 22(3):557–580
Vegter H, ten Horn CHLJ, An Y, Atzema EH, Pijlman HH, van den Boogaard TH, Huétink H (2003) Characterisation and modelling of the plastic material behaviour and its application in sheet metal forming simulation. In: Oñate E, Owen DRJ (eds) Proceedings of COMPLAS VII, CIMNE, Barcelona pages (on CD-ROM)
Walde T, Riedel H (2007a) Simulation of earing during deep drawing of magnesium alloy AZ31. Acta Mater 55(3):867–874
Walde T, Riedel H (2007b) Modeling texture evolution during hot rolling of magnesium alloy AZ31. Mater Sci Eng A 443(1–2):277–284
Wang H, Wu Y, Wu PD, Neale KW (2010) Numerical analysis of large strain simple shear and fixed-end torsion of HCP polycrystals. Comput Mater Contin 19(3):255–284
Werwer M, Cornec A (2000) Numerical simulation of plastic deformation and fracture in polysynthetically twinned (PST) crystals of TiAl. Comput Mater Sci 19(1–4):97–107
Yoon JW, Barlat F, Dick RE, Karabin ME (2006) Prediction of six or eight ears in a drawn cup based on a new anisotropic yield function. Int J Plast 22(1):174–193
Yoon J-H, Cazacu O, Yoon JW, Dick RE (2010) Earing predictions for strongly textured aluminum sheets. Int J Mech Sci 52(12):1563–1578
Yoon J-W, Lou Y, Yoon J-H, Glazoff MV (2014) Asymmetric yield function based on the stress invariants for pressure sensitive metals. Int J Plast 56:184–202
Yoon J-W, Barlat F, Dick RE, Chung K, Kang TJ (2004) Plane stress yield function for aluminum alloy sheets–part II: FE formulation and its implementation. Int J Plast 20(3):495–522
Yoshida F, Hamasaki H, Uemori T (2013) A user-friendly 3D yield function to describe anisotropy of steel sheets. Int J Plast 45:119–139
Zamiri A, Pourboghrat F, Barlat F (2007) An effective computational algorithm for rate-independent crystal plasticity based on a single crystal yield surface with an application to tube hydroforming. Int J Plast 23(7):1126–1147
Zamiri AR, Pourboghrat F (2010) A novel yield function for single crystals based on combined constraints optimization. Int J Plast 26(5):731–746
Zecevic M, McCabe RJ, Knezevic M (2015a) Spectral database solutions to elasto-viscoplasticity within finite elements: Application to a cobalt-based FCC superalloy. Int J Plast 70:151–165
Zecevic M, McCabe RJ, Knezevic M (2015b) A new implementation of the spectral crystal plasticity framework in implicit finite elements. Mech Mater 84:114–126
Zhang K, Holmedal B, Hopperstad OS, Dumoulin S (2014) Modelling the plastic anisotropy of aluminum alloy 3103 sheets by polycrystal plasticity. Model Simul Mater Sci Eng 22 (7):075015
Zhang C, Li H, Eisenlohr P, Liu W, Boehlert CJ, Crimp MA, Bieler TR (2015a) Effect of realistic 3D microstructure in crystal plasticity finite element analysis of polycrystalline Ti-5Al-2.5Sn. Int J Plast 69:21–35
Zhang K, Holmedal B, Hopperstad OS, Dumoulin S, Gawad J, Van Bael A, Van Houtte P (2015b) Multi-level modelling of mechanical anisotropy of commercial pure aluminium plate: crystal plasticity models, advanced yield functions and parameter identification. Int J Plast 66:3–30
Zhao Z, Mao W, Roters F, Raabe D (2004) A texture optimization study for minimum earing in aluminium by use of a texture component crystal plasticity finite element method. Acta Mater 52(4):1003–1012

Chapter 4
Modelling the Voids Growth in Ductile Fracture

Mihai Gologanu, Dan-Sorin Comsa, Abdolvahed Kami and Dorel Banabic

4.1 Models for Ductile Fracture

Ductile fracture in metals and metallic alloys is due to the evolution of microscopic voids during plastic deformation. Voids nucleate around foreign inclusions or at grain boundaries and grow in regions with large triaxial stresses. Larger voids promote the formation of bands of localized deformation where new small voids are nucleated, thus forming a macroscopic crack. The microscopic dimples present on ductile fracture faces are a direct proof for such a mechanism.

Following the pioneering work of McClintock (1968), Rice and Tracey (1969), who studied the growth of voids in a rigid-plastic infinite medium, Gurson (1977) proposed a new model for porous ductile materials that predicted both the growth of such voids and their effect on the yield criterion. Later, Tvergaard (1981, 1982),

M. Gologanu (✉) · D.-S. Comsa · D. Banabic
Technical University of Cluj Napoca, 28 Memorandumului,
400114 Cluj Napoca, Romania
e-mail: gologanu@protonmail.com
URL: http://www.certeta.utcluj.ro

D.-S. Comsa
e-mail: dscomsa@tcm.utcluj.ro

D. Banabic
e-mail: banabic@tcm.utcluj.ro

A. Kami
Amirkabir University of Technology,
424 Hafez Avenue, Tehran, Iran
e-mail: vahed.kami@gmail.com

D. Banabic (ed.), *Multiscale Modelling in Sheet Metal Forming*,
ESAFORM Bookseries on Material Forming,
DOI 10.1007/978-3-319-44070-5_4

Tvergaard and Needleman (1984) included models for void nucleation and coalescence; the so-called Gurson-Tvergaard-Needleman (GTN) model has found wide adoption in the engineering community in the last 30 years and is included in all major finite element codes.

Gurson used limit analysis to study a spherical void in a concentric unit cell made of a rigid-plastic material with von Mises isotropic plasticity. He obtained the following yield criterion and void volume fraction evolution law:

$$\left(\frac{\sigma_{eq}}{\sigma_0}\right)^2 + 2f\cosh\left(\frac{3}{2}\frac{\sigma_m}{\sigma_0}\right) - 1 - f^2 = 0, \quad \dot{f} = 3(1-f)d_m \tag{4.1}$$

Here σ_{eq}, σ_m are the von Mises equivalent stress and the mean or hydrostatic stress, σ_0 is the yield stress of the matrix, f the porosity (ratio of void volume to the overall volume) and d_m the mean deformation rate. This is essentially a homogenization result—the highly heterogeneous material with its many microscopic voids is replaced with a homogeneous one, without any voids, but with a new, macroscopic plasticity criterion. The macroscopic effect of the voids is hidden in the porosity, which plays the role of a scalar damage parameter—the yield criterion shrinks progressively to zero when the porosity increases. Note also that, in contrast to the microscopic plasticity criterion which does not depend on the mean stress, the new macroscopic one is pressure sensitive. Also, the "cosh" term gives an exponential dependence of the growth rate of the porosity as a function of the stress triaxiality, defined as $T = \sigma_m/\sigma_{eq}$.

The modifications made by Tvergaard and Needleman were mostly semi-empirical and were meant to provide a better fit between model predictions and elasto-plastic finite element studies of some unit cells containing also a single void:

$$\left(\frac{\sigma_{eq}}{\sigma_0}\right)^2 + 2q_1 f^*\cosh\left(\frac{3q_2}{2}\frac{\sigma_m}{\sigma_0}\right) - 1 - q_3 f^* = 0 \tag{4.2}$$

where q_1, q_2, q_3 are empirical parameters and $f^*(f)$ is a pseudo porosity describing the coalescence of voids via a critical porosity value marking the start of the coalescence and an accelerated growth of the porosity during coalescence.

We like to believe that the main reason for the success of the Gurson model lies with the rigorous, micromechanically based approach used for its development. Alternatively, Gurson's approach can be realized in a purely numerical manner by studying, via finite elements, the evolution of some cylindrical or cubical unit cell containing one or several voids. This approach was pioneered by Koplik and Needleman (1988) who studied the coalescence of a single void in a cylindrical unit cell under constant triaxiality loading, with the effect of neighbouring voids taken indirectly into account by imposing that all boundaries remain straight during deformation. Numerous such studies have appeared in the literature, many for validating or checking various ductile fracture models, others for describing new

mechanical effects (see as a typical and recent example Tekoğlu 2014). We argue that the ease of setting up such a finite element model of a periodic unit cell and the great flexibility in choosing material properties, (including plastic anisotropy, strain hardening, viscoplasticity, single crystal plasticity, etc.), void size and shape, loading conditions, second population of voids, combined with the physical insight one gains into various fracture mechanisms, has indirectly contributed to the great success of the GTN model, perceived as being potentially able to provide the same advantages.

However, the pace of development of new Gurson type models to include the above mentioned properties and mechanisms has been rather slow. For more detailed information, we suggest the reviews by Tvergaard (1990), Benzerga and Leblond (2010), Besson (2010).

4.1.1 Void Shape Effects

Gurson's model assumes that voids have initially a spherical shape and preserve this shape during deformation. However, real voids are far from being spherical and deformation can further change their shape. Lee and Mear (1992) used a spectral approach to study the growth of spheroidal (oblate and prolate) voids in an infinite matrix with a rigid-plastic isotropic behaviour. Gologanu et al. (1993, 1994) considered the same spheroidal voids but in a finite unit cell (a spheroidal unit cell confocal with the cavity) and were able to extend Gurson's rigorous analysis to this configuration; this has been known as the Gologanu-Leblond-Devaux (GLD) model. Independently, Garajeu (2000) has proposed a similar model for the case of prolate spheroidal voids; he also considered the case of a matrix with a power-law rigid-viscoplastic constitutive behaviour.

Comparing the GLD model with the results of unit cell simulations showed some limitations regarding the prediction of void shape effects on void growth. In Gologanu (1997) we introduced a calibration method that replaces some of the analytical parameters in the original model by new expressions fitted on numerical results obtained with the Lee and Mear (1992) spectral method, modified for a finite unit cell; this will be discussed in a later section.

Recently, Madou and Leblond (2012a, b) obtained a highly significant result. They were able to extend Gurson's model to the case of a general ellipsoidal void in an isotropic rigid-plastic matrix. In the absence of a suitable spectral method for such a geometry to calibrate the model, they used finite element simulations with a clever hack to treat limit analysis problems using an elasto-plastic solver.

In a different vein, recall that Gurson's model is essentially an approximate homogenization procedure for a porous plastic material. Starting with the pioneering work of Talbot and Willis (1985), who proposed a new procedure to obtain rigorous macroscopic bounds for nonlinear composites, Ponte Castaneda and coworkers have greatly extended these nonlinear homogenization methods (see Danas 2009 for a review of recent results). The main idea is to transform the nonlinear problem, via

some suitable variational principle, to a linear homogenization one and take advantage of the well-known Hashin-Shtrikman or Willis bounds. Similar results have been obtained by Michel and Suquet (1992) using Hölder-type inequalities. These methods have provided constitutive models for porous materials with power-law viscoplastic or rigid-plastic behaviour, containing general ellipsoidal voids with arbitrary distribution and submitted to general loading conditions. One limitation of these models has been the rather stiff behaviour at large triaxialities. However, because at low triaxialities they have proven very accurate, there has been a tendency to use these models to calibrate the quadratic term in Gurson type models. We also note that recently, Agoras and Ponte Castaneda (2014) have introduced an iterated variational approach which predicts high triaxiality behaviour in line with Gurson type models.

4.1.2 Anisotropic Plasticity

We have seen in previous chapters that sheet metals exhibit a significant anisotropy due to processing. In view of the intended application of Gurson type models to sheet metals, it is important to take plastic anisotropy into account. Benzerga and Besson (2001) extended Gurson's limit analysis and model for spherical voids from a matrix obeying isotropic von Mises plasticity to one obeying Hill's orthotropic criterion (Hill 1948). Later, Monchiet et al. (2006, 2008), Keralavarma and Benzerga (2008, 2010) extended the anisotropic Gurson model to spheroidal voids. Recently, Morin et al. (2015) developed a Gurson type model for general ellipsoidal voids in an anisotropic Hill matrix.

Stewart and Cazacu (2011) extended Gurson's model for anisotropic porous aggregates displaying tension–compression asymmetry (e.g. metals with hexagonal crystal structure) and containing spherical voids. The matrix material behaviour was defined by the anisotropic Cazacu et al. (2006) yield criterion.

4.2 Anisotropic GTN Model for Sheet Metal Forming

Do voids play any role in the behaviour of metal sheets? In contrast to bulk components where ductile failure is clearly due to the evolution of voids, metal sheets fail mainly by necking—the formation of thin bands where the thickness of the sheet drastically decreases up to fracture. Note that softening is the culprit in both failure mechanisms. However, voids can influence the normal to the yield criterion well before necking, and we have seen that the prediction of forming limits is highly influenced by small variations in the direction of plastic flow. Also, voids provide the final fracture mechanism in the necking region, especially for biaxial strain conditions. We expect that accurate predictions of sheet fracture will be useful for example in crash simulations by the automotive industry. There is also experimental evidence

that forming limits of superplastic aluminium alloys are related to failure by void growth and coalescence, see Tagata et al. (2004).

In order to explore the role of voids in sheet metal forming, we present in this section the implementation of a simple anisotropic GTN model in ABAQUS and the results of the numerical simulation of a deep drawing process.

4.2.1 GTN Models for Sheet Metal Forming

One of the limitations of the GTN damage model is the assumption of isotropic behaviour for the metal matrix. In fact, because of the cold rolling production procedure, sheet metals usually exhibit a non-negligible anisotropic behaviour.

Assuming that voids are spherical and remain so during deformation, the main problem is to include in the GTN the anisotropy of the matrix material. Most studies have focused on Hill48 quadratic anisotropy. We already mentioned in Sect. 4.1.2 the work of Benzerga and Besson (2001) for spherical voids in a Hill48 matrix. Liao et al. (1997) derived an approximate potential close to the original Gurson formulation for anisotropic sheets containing through thickness holes. Wang et al. (2004) modified the Liao et al. model by using the average anisotropy parameter in the constitutive equations. Chen and Dong (2009) extended the GTN model to characterize the matrix material through Hill quadratic and Barlat-Lian 3-component (Barlat and Lian 1989) expressions of the equivalent stress.

4.2.2 Anisotropic GTN Model with Hill 48 Yield Criterion

Abaqus/Explicit allows the implementation of solid material models by means of the VUMAT routine. Because Abaqus/Explicit uses corotational components of the Cauchy stress and logarithmic strain as input/output when communicating with VUMAT, plain time derivatives of such tensor quantities can be involved in the formulation of the rate-type constitutive relationships, without any concern about their objectivity. The model presented below assumes that the Abaqus/Explicit corotational frame also reflects the plastic orthotropy of the sheet metal, being initially coincident with the frame defined by the rolling direction—RD (axis 1), transverse direction—TD (axis 2) and normal direction—ND (axis 3).

Let ε_{ij} denote the components of the corotational logarithmic strain tensor separable into elastic and plastic terms:

$$\varepsilon_{ij} = \varepsilon_{ij}^{(e)} + \varepsilon_{ij}^{(p)} \tag{4.3}$$

Let σ_{ij} denote the components of the corotational Cauchy stress tensor with mean stress $\sigma_m = \sigma_{ii}/3$. The Hill48 quadratic anisotropic yield surface is given by:

$$\varphi(\sigma) = \sigma_{eq} - \sigma_0 \equiv \left(\frac{3}{2}\sigma_{ij}P_{ijkl}\sigma_{kl}\right)^{1/2} - \sigma_0 \tag{4.4}$$

with σ_{eq} the Hill equivalent stress and where the orthotropic tensor P satisfies both major and minor symmetries and plastic incompressibility. In the frame of the sheet, σ_{eq} has only six non-zero components and it is given by:

$$\begin{aligned}\sigma_{eq} = \Big[&H(\sigma_{11} - \sigma_{22})^2 + G(\sigma_{11} - \sigma_{33})^2 + \\ &F(\sigma_{22} - \sigma_{33})^2 + 2N\sigma_{12}^2 + 2M\sigma_{13}^2 + 2L\sigma_{23}^2\Big]^{1/2}\end{aligned} \tag{4.5}$$

The yield stress σ_0 is defined as a strictly positive function of the equivalent plastic strain $\bar{\varepsilon}^p$ by means of a hardening law $\sigma_0(\bar{\varepsilon}^{(p)})$. The elasticity of the sheet metal is described by the isotropic Hooke's law with Young modulus E and Poisson ratio ν.

The plastic part of the constitutive model is based on the GTN yield surface:

$$\Phi = \left(\frac{\sigma_{eq}}{\sigma_0}\right)^2 + q_1 f^* \left[2\cosh\left(\frac{3q_2}{2}\frac{\sigma_m}{\sigma_0}\right) - q_1 f^*\right] - 1, \tag{4.6}$$

where f^* is a porosity parameter related to the void volume fraction f by:

$$f^* = \begin{cases} f, & f \le f_c, \\ f_c + \frac{f_f^* - f_c}{f_f - f_c}(f - f_c), & f_c < f < f_f, \\ f_f^*, & f \ge f_f, \end{cases} \tag{4.7}$$

Here, $f_f^* = 1/q_1$ and q_1, q_2, f_c, f_f are material parameters.

The flow rule associated to the yield criterion Φ can be expressed in the form:

$$\dot{\varepsilon}_{ij}^{(p)} = \dot{\lambda}\frac{\partial \Phi}{\partial \sigma_{ij}}, \quad \text{with} \begin{cases} \dot{\lambda} = 0, & \text{if } \Phi < 0, \\ \dot{\lambda} \ge 0, & \text{if } \Phi = 0, \end{cases} \tag{4.8}$$

or, if Eqs. (4.4) and (4.6) are taken into account:

$$\dot{\varepsilon}_{ij}^{(p)} = \frac{1}{\bar{\sigma}}\dot{\varepsilon}^{(p,dev)}P_{ijk\ell}\sigma_{k\ell} + \frac{1}{3}\dot{\varepsilon}^{(p,vol)}\delta_{ij}, \tag{4.9}$$

where:

$$\dot{\varepsilon}^{(p,dev)} = \dot{\lambda}\frac{\partial \Phi}{\partial \sigma_{eq}}, \quad \dot{\varepsilon}^{(p,vol)} = -\dot{\lambda}\frac{\partial \Phi}{\partial \sigma_m}, \tag{4.10}$$

and

$$\frac{\partial \Phi}{\partial \sigma_{eq}} = \frac{2\sigma_{eq}}{\sigma_0^2}, \qquad \frac{\partial \Phi}{\partial \sigma_m} = 3q_1 q_2 \frac{f^*}{\sigma_0} \sinh\left(q_2 \frac{3\sigma_m}{2\sigma_0}\right). \tag{4.11}$$

Equation (4.10) allows deducing the following consistency condition that accompanies the constraint $\Phi = 0$ in the elastoplastic states of the sheet metal:

$$\dot{\varepsilon}^{(p,dev)} \frac{\partial \Phi}{\partial \sigma_m} + \dot{\varepsilon}^{(p,vol)} \frac{\partial \Phi}{\partial \sigma_{eq}} = 0. \tag{4.12}$$

The evolution of the parameter $\bar{\varepsilon}^{(p)}$ is given by the equivalent plastic work rule:

$$\sigma_{ij} \dot{\varepsilon}_{ij}^{(p)} = (1-f)\sigma_0 \dot{\bar{\varepsilon}}^{(p)}. \tag{4.13}$$

The evolution of the porosity combines the growth of existing voids due to the incompressibility of the matrix and the continuous nucleation of new voids:

$$\dot{f} = \dot{f}^{(g)} + \dot{f}^{(n)}, \quad \dot{f}^{(g)} = (1-f)\dot{\varepsilon}^{(p,vol)} \tag{4.14}$$

and where the nucleation term depends on the equivalent plastic strain and its time derivative:

$$\dot{f}^{(n)} = A\left(\bar{\varepsilon}^{(p)}\right)\dot{\bar{\varepsilon}}^{(p)}. \tag{4.15}$$

and the function A is given by the following Gaussian:

$$A = \begin{cases} \frac{f_N}{s_N\sqrt{2\pi}} \exp\left\{-\frac{1}{2}\left[\frac{\bar{\varepsilon}^{(p)} - \bar{\varepsilon}_N}{s_N}\right]^2\right\}, & \sigma_m > 0, \\ 0, & \sigma_m \leq 0, \end{cases} \tag{4.16}$$

This models a void nucleation that is strain controlled, is activated only for positive hydrostatic stresses and mainly around a strain $\bar{\varepsilon}_N$ with a standard deviation s_N. Also, the total amount of nucleated voids is fixed by the porosity f_N. Note that once nucleated, voids will continue to grow due to the growth term in (4.14).

We have implemented the above model as a VUMAT subroutine in ABAQUS/Explicit with two state variables, the equivalent plastic strain and the porosity. One advantage of this approach, compared to an implementation as a UMAT subroutine in ABAQUS/Standard, is that there is no need to provide the Jacobian of the strain-stress relationship at the current step. Also, time steps are very small in an explicit time integration scheme; this has encouraged the use of approximate local solvers of the elasto-plastic equations like the cutting plane algorithm of Simo and Hughes (1998). However, for the GTN model (4.6), the porosity has a softening behaviour, with the yield surface shrinking for increasing porosity. This can jeopardize the use of the cutting plane algorithm, especially

during the final stages of the numerical simulation, when the porosity is large and the carrying capability of the metallic sheet suffers a sudden drop. We have therefore preferred to use a nonlinear (Newton) solver to find the correct plastic strain increment and state variables at the end of the time step.

4.2.3 Determination of GTN Parameters from Uniaxial Tests

A typical uniaxial tensile test of sheet metals is the simple tension of a strip. This test is routinely performed to extract the mechanical properties of the sheet, such as yield stress and anisotropy parameters. It is possible to take advantage of the experimental force versus displacement curves to calibrate the GTN model parameters (see Fratini et al.1996; Abbasi et al. 2011; Abbassi et al. 2013; Kami et al. 2014a, b). Despite the different tools used by these authors, the procedure for parameter identification is the same: fitting the force versus displacement curve obtained from numerical simulations to the experimental one.

Among the material constants included in the constitutive relationships presented in previous sections, q_1, q_2, q_3,f_0, f_c, f_f, f_N, S_N, and $\bar{\varepsilon}_N$ need a special attention, because the predictive performances of the GTN model are strongly dependent on their values. In general, an identification procedure that tries to determine all these parameters would be very inefficient because of the large amount of experimental data needed for calibration and the non-uniqueness of the solution.

Most of the researchers use the values proposed by Needleman and Tvergaard for q_1, q_2 and q_3 parameters, namely, $q_1 = 1.5$, $q_2 = 1$ and $q_3 = q_1^2 = 2.25$. Furthermore, from the six remaining parameters i.e. f_0, f_c, f_f, f_N, S_N and $\bar{\varepsilon}_N$, usually four or five of them are selected for calibration and the values of the other ones are selected arbitrarily or based on the recommendations available in the literature.

For the AA6016-T4 sheet metal with the nominal thickness of 1 mm, Kami et al. (2014a, b) assumed typical values for $\bar{\varepsilon}_N, s_N$ and calibrated the other four parameters f_0, f_c, f_f and f_N from results of uniaxial tests. They used an identification procedure based on a face centred central composite RSM design of experiments, implemented in the software package Design-Expert®. A total of 27 uniaxial tensile tests with different parameter combinations have been performed.

The hardening of the AA6016-T4 alloy has been taken as:

$$\sigma_0 = K(\varepsilon_0 + \bar{\varepsilon}^p)^n \tag{4.17}$$

and the material parameters have been fitted to first part of the tensile curves where the effect of voids is negligible. Also the anisotropy coefficients r_θ have been determined from tensile tests on strips cut at various angles θ to the rolling direction. Table 4.1 provides all material parameters for this sheet alloy.

Figure 4.1 shows a comparison between the force versus elongation curve predicted by the GTN model and the experimental curve obtained by averaging the

Table 4.1 Material parameters for AA6016-T4

f_0	2.42×10^{-4}	s_N	0.1	n	0.2704
f_c	0.047674	E	70 GPa	r_0	0.5529
f_f	0.2	v	0.33	r_{45}	0.4091
f_N	0.041546	K	525.8 MPa	r_{90}	0.5497
$\bar{\varepsilon}_N$	0.3	ε_0	0.011252		

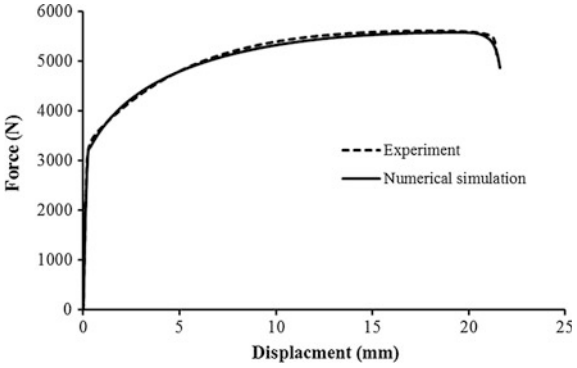

Fig. 4.1 Force versus elongation curves corresponding to uniaxial tensile tests performed along the rolling direction

results of all uniaxial tensile tests performed along the rolling direction. One may easily notice that the numerical results are in very good agreement with the experimental data, showing that material parameters obtained by identification are representative for the AA6016-T4 sheet metal with the nominal thickness of 1 mm and can be used for the simulation of more complex forming processes.

Figure 4.2 presents the distribution of the porosity (denoted as SDV2 in the legend) at several stages of a tensile test simulated with ABAQUS/Explicit. Starting from a uniform distribution, we observe an accelerated growth of the porosity at later stages and a concentration in some narrow regions in the final stage where coalescence of voids and necking or strain localization promote one another.

4.2.4 Simulation of a Deep Drawing Process

Deep drawing is a very common processes in the automotive industry. As the sheet metals are deformed by applying large strains, they are prone to fracture during the process. In recent years there has been increased interest to improve the prediction of sheet fracture during deep drawing. The common approach is to use forming limit curves; however, their experimental buildup is costly and time consuming.

We apply the anisotropic GTN damage model developed in the previous sections to model a deep drawing process. The tooling setup used in the deep-drawing experiments is shown in Fig. 4.3 (see Nicodim et al. 2013). The tests have been performed on circular blanks with 85 mm diameter lubricated on both faces with a mixture of oil and graphite. In all cases, the punch speed has been set to a constant value of 33 mm/min. Deep drawing tools have been installed on the Erichsen

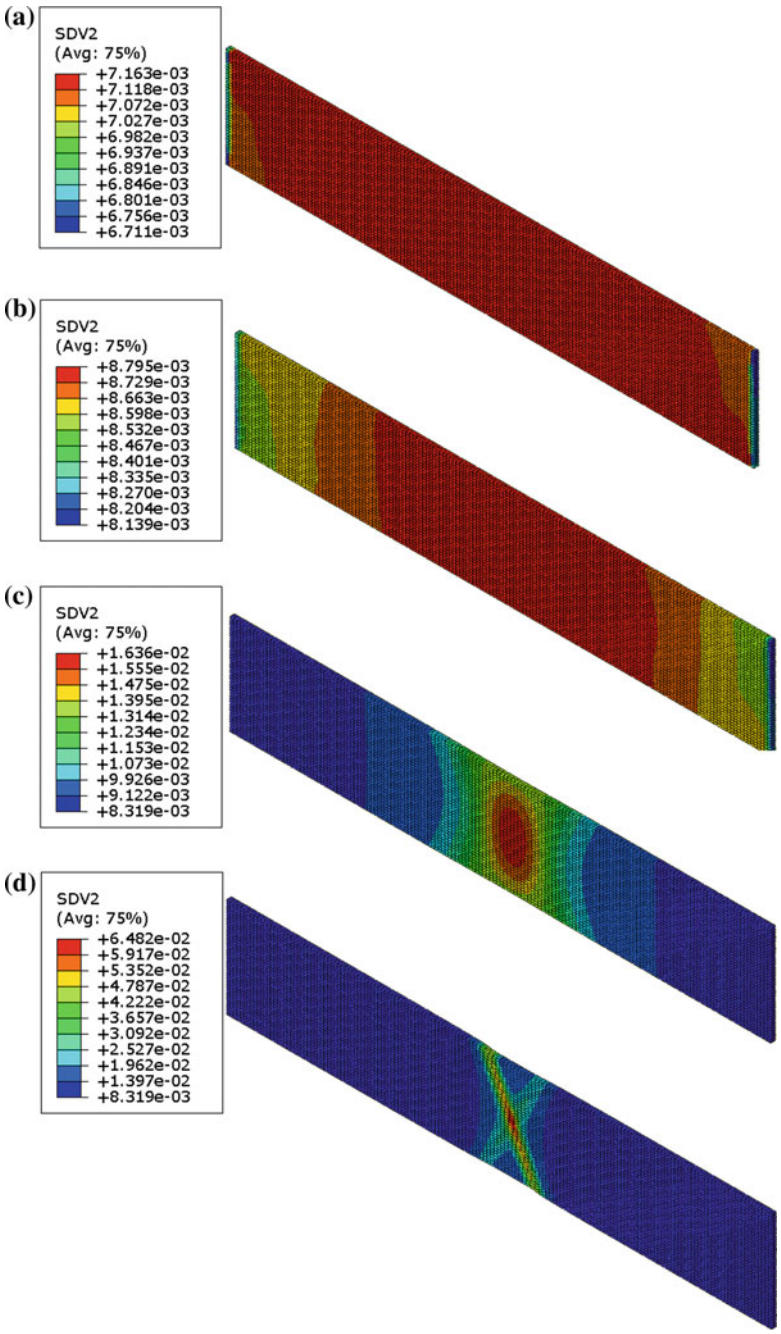

Fig. 4.2 Evolution of the void volume fraction during the uniaxial tensile test. **a** 17.99 mm, **b** 19.48 mm, **c** 20.47 mm, **d** 21.22 mm elongation

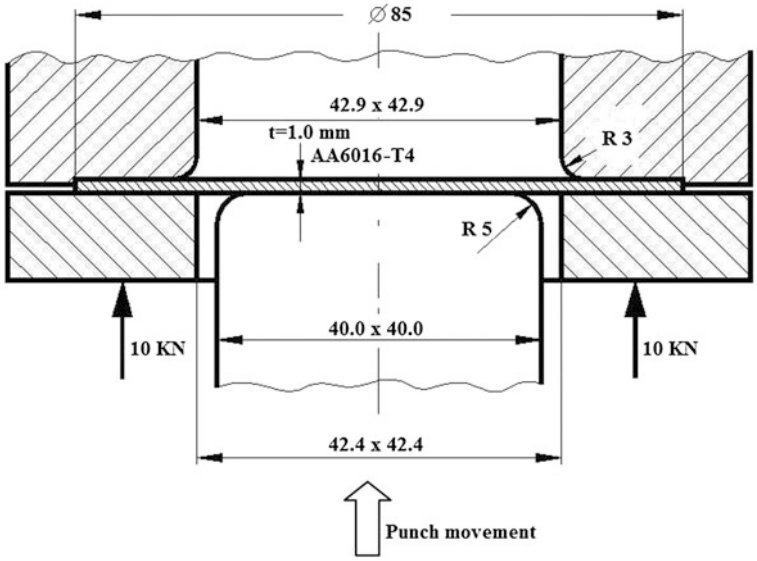

Fig. 4.3 Tooling setup used in the deep-drawing experiments

universal testing machine which ensures a hydraulic control of the blank holding force and punch displacement. Blank holding forces greater than 10 kN have caused the fracture of the deep-drawn parts. The experimental results obtained in the case of the maximum holding force (10 kN) will be used for comparison with the predictions of the GTN model.

In the finite element model, the essential surfaces of the tools (punch, die and blank holder) have been meshed using rigid shell elements (R3D4), while solid deformable elements (8-node hexahedra C3D8R with the average edge size of 0.5 mm) have been adopted for meshing the circular blank. Due to the geometric and mechanical symmetry of the deep-drawing process, only one quarter of the tool surfaces and blank volume have been included in the finite-element model. Three layers of solid elements have been generated in the thickness direction of the blank. A concentrated force of 2.5 kN has been applied to the reference point of the blank holder (one quarter of actual blank holding force—10 kN). The die has been kept fixed in its position, the punch and the blank holder being allowed to perform vertical translations. The frictional contact between blank and tools has been modelled using a penalty formulation. Taking into account the lubrication conditions of the laboratory experiments, the friction coefficient has been set to a value of 0.05 on all the contact surfaces.

Figure 4.4 illustrates the fracture of the AA6016-T4 metallic sheet during the deep-drawing tests performed with a blank holding force set to 10 kN (Kami et al. 2014). Comparing the predictions of the anisotropic GTN model with the experimental data, one may notice that fracture path has almost the same shape and position in both images.

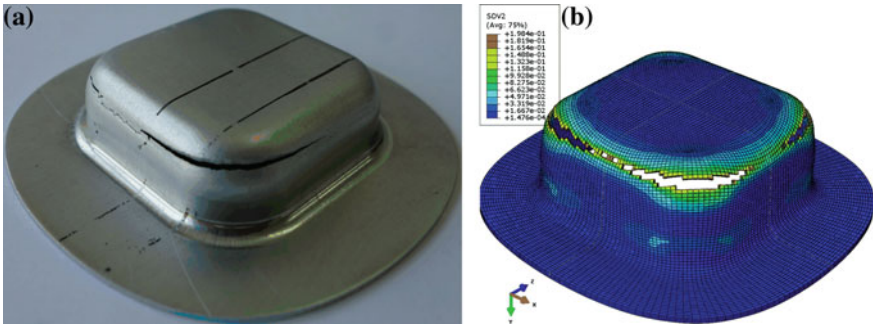

Fig. 4.4 Fractured specimens, **a** experiment, **b** numerical simulation

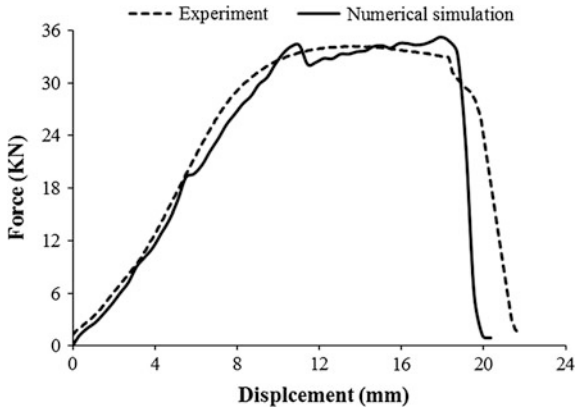

Fig. 4.5 Comparison of forming forces for blank holder of 10 kN

Figure 4.5 shows the evolution of the punch force during the deep-drawing process. Experimental data and numerical predictions are superimposed on the same diagram. One may notice that the maximum level of the punch force predicted by ABAQUS/Explicit (32.27 kN) is almost equal to the experimentally determined value (34.24 kN). The diagram also allows the evaluation of the drawing depth at which the fracture occurs. This depth corresponds to the sudden drop of the punch force towards zero: 17.9 mm—predicted by ABAQUS/Explicit, in very good agreement with the depth of 18.7 mm measured on the experimental curve.

4.3 Development of a Gurson Type Model for Some Advanced Yield Criteria for Sheet Metals

We know from the previous section that modelling of voids is of interest for sheet metals. We assumed there that voids are spherical and remain so during deformation. However, experimental evidence shows that voids in metallic sheets in the

as received condition are neither spherical nor spheroidal, but much better approximated by a general ellipsoid, relative flat in the thickness direction and elongated in the rolling direction. Further processing happens at rather low triaxiality, due to the through-thickness stress component being close to zero (one exception are hydrostatic forming processes where a large pressure is applied to the sheet to improve formability). We expect that deformation at low triaxiality will further enhance the departure of void shapes from spherical or spheroidal ones.

We have also used in the previous section the simplest Hill48 model for anisotropic plasticity. However, we have seen that accurate prediction of sheet behaviour in later processing stages like deep forming, requires the use of advanced, complex plasticity criteria. Typically, yield surfaces show a combination of regions that are almost flat, with small curvature, joined by others with large curvature. A successful yield criterion should include accurate yield stresses (affecting the prediction of drawing forces), an accurate strain hardening model (affecting the prediction of spring-back) and an accurate prediction of the normal to the yield surface (affecting, via the plastic flow, the prediction of necking and forming limits).

Concluding this preliminary analysis, it appears that the optimal Gurson type model for metal sheets should apply to ellipsoidal voids and use an advanced anisotropic yield criterion for the matrix. The closest model in the literature is that of Morin et al. (2015), which considers ellipsoidal voids in a Hill matrix. However, it is clear that quadratic yield criteria, like that of Hill, however pronounced the anisotropy, will have difficulties in accurately capturing the flat regions of yield surfaces typical for metal sheets. We present in this section the steps needed for the development of a Gurson type model for some advanced plasticity criteria and provide a detailed discussion of the entire methodology.

4.3.1 Limit Analysis and Homogenization

Limit analysis is a method to estimate the load-carrying capacity of a structure. The only information it uses is the yield region defined as a convex region in stress space (containing the zero stress). Consider some external loading applied to the structure and multiply it by a scalar load parameter. The main problem of limit analysis is to find the maximum value of the load parameter for which there is a stress field that respects equilibrium (statically admissible) and lies inside the yield convex at each point of the structure (plastically admissible). Beyond this critical load value, the structure collapses. Limit analysis admits a dual, kinematical formulation which permits the estimation of the critical load from above by using trial velocity fields. These fields should be kinematically admissible (they should be zero on the complement of the boundary part where the loading is applied) and they represent competing collapse mechanisms. Normalizing these velocity fields such that the power of external forces is unity, the collapse mechanism corresponding to the critical load parameter is precisely the one which minimizes the total plastic dissipation inside the structure. We note that this dual formulation may admit

several solutions (non-unicity of the collapse mechanism) and solutions with discontinuities (rigid blocks sliding one along the other). We recommend Suquet (1988) for a rigorous treatment of limit analysis with several applications including homogenization problems.

How is the dissipation defined for a given velocity field? Let k denote the yield convex in stress space, usually defined by $\kappa = \{\boldsymbol{\sigma} | \varphi(\boldsymbol{\sigma}) \leq 0\}$ with $\varphi(\boldsymbol{\sigma})$ the yield criterion or yield surface and let its indicator function define a potential in stress space. Then the dissipation is the dual potential in strain rate space, defined as the Legendre dual or conjugate of the indicator function:

$$\mathrm{ind}_\kappa(\boldsymbol{\sigma}) = \begin{cases} 0 & \boldsymbol{\sigma} \in \kappa \\ +\infty & \boldsymbol{\sigma} \notin \kappa \end{cases}, \quad w(\mathbf{d}) = \mathrm{ind}^*_\kappa(\mathbf{d}) = \sup_{\boldsymbol{\sigma} \in \kappa} \boldsymbol{\sigma} : \mathbf{d} \tag{4.18}$$

Here $\boldsymbol{\sigma}, \mathbf{d}$ represent stress and strain rate tensors. The most important property of the dissipation function w is that is a convex function, homogeneous of degree 1.

For a given strain tensor $\mathbf{d}$, the stress tensor $\boldsymbol{\sigma}$ that attains the sup in $(4.18)_2$ will be located on the boundary of the yield convex and $\mathbf{d}$ will be the outgoing normal at the convex at this point (or more generally will be in the normal cone if this point is a vertex). This is equivalent to the associated flow rule for plasticity. More precisely, if $\boldsymbol{\sigma}$ is a point on the yield surface with $\varphi(\boldsymbol{\sigma}) = 0$, then we have:

$$\mathbf{d} = \dot{\lambda} \frac{\partial \varphi}{\partial \boldsymbol{\sigma}}, \quad \dot{\lambda} \geq 0, \qquad \boldsymbol{\sigma} = \frac{\partial w}{\partial \mathbf{d}} \tag{4.19}$$

Note that the last equation is actually a parametric description of the yield surface.

For a yield criterion which is pressure independent, it is easy to show that the dissipation function is given by:

$$w(\mathbf{d}) = \mathrm{ind}^*_\kappa(\mathbf{d}) = \begin{cases} \sup_{\sigma \in \kappa} \boldsymbol{\sigma} : \mathbf{d} & \mathrm{tr}\, \mathbf{d} = 0 \\ +\infty & \mathrm{tr}\, \mathbf{d} \neq 0 \end{cases} \tag{4.20}$$

Let us now consider a unit cell or representative volume element Ω, containing a single or several voids noted with V and having a matrix characterized by some microscopic yield convex k and its associated dual potential or dissipation function w. There are three types of boundary conditions that provide meaningful results for the macroscopic yield region K and its associated dissipation function W, namely homogeneous strain rate, homogeneous stress and periodic boundary conditions. Let us first choose homogeneous strain rate boundary conditions:

$$\mathbf{v} = \mathbf{D}\mathbf{x}|_{\partial \Omega}, \tag{4.21}$$

where $\mathbf{D}$ represents the macroscopic strain rate tensor and $\mathbf{x}$ is the position vector. For any microscopic stress field $\boldsymbol{\sigma}$ which is statically and plastically admissible, and

for each velocity field $\mathbf{v}$ respecting the boundary conditions (4.21), we write the principle of virtual work:

$$\int_{\partial\Omega} \sigma_{ij} n_j v_i = \int_{\Omega\backslash V} \boldsymbol{\sigma} : \mathbf{d}(\mathbf{v}) \leq \int_{\Omega\backslash V} w(\mathbf{d}(\mathbf{v})) \tag{4.22}$$

where we have used the equilibrium condition $\operatorname{div}\boldsymbol{\sigma} = 0$, the fact the void boundaries are stress-free, and, for the last inequality, the definition $(4.18)_2$ of the plastic dissipation. The notation $\Omega\backslash V$ means the unit cell minus the voids and represent the matrix. Now, if we plug the boundary conditions (4.21) in the first term of (4.22), we obtain:

$$\int_{\partial\Omega} \sigma_{ij} n_j v_i = \int_{\partial\Omega} \sigma_{ij} n_j D_{ik} x_k = D_{ik} \int_{\partial\Omega} \sigma_{ij} n_j x_k = |\Omega| \boldsymbol{\Sigma} : \mathbf{D} \tag{4.23}$$

where $|\Omega|$ is volume of the unit cell, and the last equation is actually the definition of the macroscopic stresses:

$$\boldsymbol{\Sigma} = \frac{1}{|\Omega|} \int_{\partial\Omega} \boldsymbol{\sigma} : (\mathbf{n} \otimes \mathbf{x}) \tag{4.24}$$

As a side note, we can use Gauss' theorem to show that the definitions of the macroscopic quantities $\mathbf{D}$ via the boundary conditions (4.21) and $\boldsymbol{\Sigma}$ via the surface average (4.24) are both equivalent to volume averages of the microscopic quantities:

$$\mathbf{D} = \frac{1}{|\Omega|} \int_{\Omega} \mathbf{d}(\mathbf{v}) = \langle \mathbf{d} \rangle_{\Omega}, \quad \boldsymbol{\Sigma} = \frac{1}{|\Omega|} \int_{\Omega} \boldsymbol{\sigma} = \langle \boldsymbol{\sigma} \rangle_{\Omega}, \tag{4.25}$$

Combining now (4.22) and (4.23), we obtain the following result, valid for all stress fields that are statically and plastically admissible and all velocity fields that are kinematically admissible:

$$\boldsymbol{\Sigma} : \mathbf{D} \leq \frac{1}{|\Omega|} \int_{\Omega\backslash V} w(\mathbf{d}(\mathbf{v})) \tag{4.26}$$

This result permits the definition of the macroscopic dissipation function as:

$$W(\mathbf{D}) = \inf_{v = Dx|_{\partial\Omega}} \frac{1}{|\Omega|} \int_{\Omega\backslash V} w(\mathbf{d}(\mathbf{v})) \tag{4.27}$$

This is a convex function, homogeneous of degree 1 and therefore has a Legendre dual that is the indicator of a convex region in macroscopic stress space—the sought after macroscopic yield convex K. Similar to the microscopic case (4.19), if we define now the yield surface Φ by $K = \{\boldsymbol{\Sigma} | \Phi(\boldsymbol{\Sigma}) \leq 0\}$ we obtain the associated flow rule and the parametric description of the yield surface:

$$\mathbf{D} = \dot{\lambda} \frac{\partial \Phi}{\partial \boldsymbol{\Sigma}}, \quad \boldsymbol{\Sigma} = \frac{\partial W}{\partial \mathbf{D}} \tag{4.28}$$

The same approach applies to homogeneous stress boundary conditions; the only differences are the definitions for macroscopic strain rates and stresses:

$$\sigma_{ij} n_j = \Sigma_{ij} n_j|_{\partial\Omega}, \quad D_{ij} = \frac{1}{|\Omega|} \int\limits_{\partial\Omega} \frac{1}{2} (v_i n_j + v_j n_i) \tag{4.29}$$

Again, these are equivalent to the average type definitions given by (4.25). The definition of macroscopic dissipation function becomes now:

$$W^s(\mathbf{D}) = \inf_{\mathbf{D} = \frac{1}{|\Omega|} \int\limits_{\partial\Omega} \mathbf{v} \otimes_s \mathbf{n}} \frac{1}{|\Omega|} \int\limits_{\Omega \setminus V} w(\mathbf{d}(\mathbf{v})) \tag{4.30}$$

with associated yield convex K^s. It also results from (4.27) and (4.30) that $K^s \subseteq K$. We do not treat here in detail the case of periodic boundary conditions, but we note first that they give a macroscopic yield convex intermediate between the ones above and second that they are precisely those obtained from a rigorous homogenization procedure (see Suquet 1988).

4.3.2 An Introduction to Gurson Type Models

Consider a porous von Mises material with spherical, spheroidal or ellipsoidal voids. In order to apply the homogenization procedure of the previous section, we first need to choose some representative volume element or unit cell containing a single void. The selection of a unit cell concentric or confocal with the void is a rather crude approximation and is motivated only by the simplifications it brings to the mathematical treatment of the problem. Next we need to decide on boundary conditions. Because such rounded unit cells do not stack to fill up space, periodic boundary conditions are not applicable. Among homogeneous stress or homogeneous strain rate boundary conditions, the latter are preferred simply because they impose more conditions on the velocity field and the two-field approach used in Gurson type models has more chances to be accurate.

The dissipation of the von Mises isotropic yield criterion is readily available:

$$\begin{aligned}\varphi(\boldsymbol{\sigma}) &= \sigma_{eq} - \sigma_0 = \sqrt{\frac{3}{2}\boldsymbol{\sigma}' : \boldsymbol{\sigma}'} - \sigma_0,\\ w(\mathbf{d}) &= \begin{cases} \sigma_0\sqrt{\frac{2}{3}\mathbf{d} : \mathbf{d}} & \mathrm{tr}\,\mathbf{d} = 0\\ +\infty & \mathrm{tr}\,\mathbf{d} \neq 0 \end{cases}\end{aligned} \tag{4.31}$$

Here $\boldsymbol{\sigma}'$ is the stress deviator and σ_0 is the uniaxial yield stress. Note that $\mathrm{tr}\mathbf{d}(\mathbf{v}) = 0$ is equivalent to $\mathrm{div}\mathbf{v} = 0$ or the incompressibility of admissible velocity fields. The next step is to find and estimate the macroscopic dissipation defined by:

$$W(\mathbf{D}) = \inf_{\mathbf{v}} \left\{ \frac{1}{|\Omega|} \int_{\Omega\setminus V} w(\mathbf{d}(\mathbf{v})) \middle| \mathbf{v} = \mathbf{D}\mathbf{x}|_{\partial\Omega}, \mathrm{div}\mathbf{v} = 0 \right\} \tag{4.32}$$

Note that contrary to the microscopic velocity field which is incompressible, the macroscopic mean strain rate defined by $3D_m = \mathrm{tr}\mathbf{D}$ is not required to be zero. This will give a macroscopic yield convex that is pressure sensitive, contrary to the microscopic von Mises criterion; this effect is entirely due to the presence of the void. The velocity field $\mathbf{v}$ is written as a sum:

$$\mathbf{v} = A\mathbf{v}^A + B\mathbf{v}^B + \cdots \tag{4.33}$$

where $\mathbf{v}^A, \mathbf{v}^B, \ldots$ are fixed velocity fields and $A, B, \ldots$ are unknown parameters to be determined by minimizing the macroscopic dissipation (4.32). Actually, the number of fields and unknown parameters is taken to be precisely the number of parameters describing the macroscopic strain rate $\mathbf{D}$, so that the parameters $A, B, \ldots$ are fully determined solely from the boundary conditions in (4.32) and the infimum in (4.32) is never calculated in Gurson's approach.

The next step is to choose the fixed velocity fields in Eq. (4.33). By convention, the first one $\mathbf{v}^A$ describes the expansion of the cavity and is related to the macroscopic mean strain rate D_m; all other fields have a constant strain rate over the entire volume and correspond to the deviatoric part of the macroscopic strain rate. For example, in the spherical case and for axisymmetric loading with respect to the 3rd axis (the original Gurson model), the velocity fields are given by:

$$\begin{aligned} \mathbf{v}^A &= \tfrac{b^3}{r^2}\mathbf{e}_r & \mathbf{v}^B &= -\tfrac{x}{2}\mathbf{e}_x - \tfrac{y}{2}\mathbf{e}_y + z\mathbf{e}_z\\ A = D_m &= \tfrac{1}{3}(2D_{xx} + D_{zz}) & B = D' &= \tfrac{2}{3}(D_{zz} - D_{xx}) \end{aligned} \tag{4.34}$$

where r, θ, ϕ are spherical polar coordinates, x, y, z are Cartesian coordinates and a, b are the radii of the void and unit cell, respectively. For the spheroidal and ellipsoidal case, the approach is similar, the main difficulty being in finding a "good" incompressible velocity field $\mathbf{v}^A$ describing the expansion of the cavity and respecting conditions of homogeneous strain rate on the boundary of the unit cell. The choice so far, valid for spherical, spheroidal and ellipsoidal voids, has been the

unique velocity field that respects conditions of homogeneous strain rate on *all* surfaces confocal with the cavity, see Leblond and Gologanu (2008).

In the spherical case, we can now easily calculate the strain rates for these velocity fields:

$$\begin{aligned} \mathbf{d}^A &= \frac{b^3}{r^3}(-2\mathbf{e}_r \otimes \mathbf{e}_r + \mathbf{e}_\theta \otimes \mathbf{e}_\theta + \mathbf{e}_\phi \otimes \mathbf{e}_\phi) \\ \mathbf{d}^B &= \frac{1}{2}(-\mathbf{e}_x \otimes \mathbf{e}_x - \mathbf{e}_y \otimes \mathbf{e}_y + 2\mathbf{e}_z \otimes \mathbf{e}_z) \end{aligned} \tag{4.35}$$

and the plastic dissipation for the full velocity field (4.33).

$$w = \sigma_0 \sqrt{4A^2 \frac{b^6}{r^6} + 2AB\frac{b^3}{r^3}(1 - 3\cos^2\theta) + B^2} \tag{4.36}$$

We now plug this into the definition (4.32) of the macroscopic plastic dissipation:

$$W = \frac{3\sigma_0}{4\pi b^3} \int_a^b \int_0^\pi \int_0^{2\pi} \left(4A^2 \frac{b^6}{r^6} + 2AB\frac{b^3}{r^3}(1 - 3\cos^2\theta) + B^2\right)^{\frac{1}{2}} r^2 \sin\theta dr d\theta d\phi \tag{4.37}$$

We note that for the spheroidal and ellipsoidal case we obtain similar expressions[1] but with more complicated coefficients for the quadratic form in A, B. Next, we need an approximate way to get rid of the integral over the angular coordinates; usually this is based on the Cauchy-Schwartz inequality over the surface of the unity sphere:

$$\frac{1}{4\pi} \int_{\theta=0}^{\pi} \int_{\phi=0}^{2\pi} w \sin\theta d\theta d\phi \leq \left(\frac{1}{4\pi} \int_{\theta=0}^{\pi} \int_{\phi=0}^{2\pi} w^2 \sin\theta d\theta d\phi\right)^{1/2} \tag{4.38}$$

followed by an explicit calculation of the right hand side. This reduces the triple integral (4.37) to a single one in the radial or pseudo-radial coordinate. Now, one needs to find a change of coordinates $x = x(r)$ and to further reduce this single integral to the following expression:

$$W = \sigma_0 \int_{x_1}^{x_2} \sqrt{\bar{A}^2 x^2 + \bar{B}^2} \frac{dx}{x^2} \tag{4.39}$$

[1]We anticipate here the use of Tabanov's natural coordinates r, θ, ϕ for the spheroidal and ellipsoidal coordinates, with a pseudo-radial and two angular coordinates; see Sect. 4.3.

where $\bar{A} = F(x)A + G(x)B, \bar{B} = H(x)B$ are linear forms in A, B, and via (4.34) linear forms in D_m, D'. In the spheroidal or ellipsoidal case and for more general loading conditions that are not axisymmetric, the approach is similar but the relationship between $\bar{A}, \bar{B}$ and the components of $\mathbf{D}$ is more complex, being a sum of linear forms in $\mathbf{D}$ and terms of the form $(\mathbf{D} : \mathbf{C} : \mathbf{D})^{1/2}$ with C some constant fourth-order tensor.

We arrive now at the main step in the derivation of Gurson-type models. It consists in replacing the relative complicated functions $F(x), G(x), H(x)$ with some constant values $\bar{F}, \bar{G}, \bar{H}$. The only justification for such a crude approximation is a posteriori—it is the only way we know to arrive at a compact form for the macroscopic yield criterion. To make this approximation more palatable, we put forward the minimal requirement that these functions have finite limits when $x \to 0$ and $x \to +\infty$. This actually provides a guide to the selection of the most appropriate change of coordinates $x = x(r)$.

From now on, the derivation is straightforward and is essentially the original one discovered by Gurson (1977). In Madou and Leblond (2012a), it has been formalized in a so called Gurson's lemma, asserting that for a dissipation function of the form (4.39), its derivatives are related by:

$$\left(\frac{1}{\sigma_0}\frac{\partial W}{\partial \bar{B}}\right)^2 + \frac{2}{x_1 x_2}\cosh\left(\frac{1}{\sigma_0}\frac{\partial W}{\partial \bar{A}}\right) - \frac{1}{x_1^2} - \frac{1}{x_2^2} = 0 \tag{4.40}$$

For completeness, we have included the derivation of this lemma:

$$\begin{aligned}
\frac{1}{\sigma_0}\frac{\partial W}{\partial \bar{A}} &= \int_{x_1}^{x_2} \frac{\bar{A}dx}{\sqrt{\bar{A}^2x^2 + \bar{B}^2}} = \sinh^{-1}\lambda x_2 - \sinh^{-1}\lambda x_1 \\
\frac{1}{\sigma_0}\frac{\partial W}{\partial \bar{B}} &= \int_{x_1}^{x_2} \frac{\bar{B}dx}{x^2\sqrt{\bar{A}^2x^2 + \bar{B}^2}} = -\frac{\sqrt{\lambda^2 x_2^2 + 1}}{x_2} + \frac{\sqrt{\lambda^2 x_1^2 + 1}}{x_1}
\end{aligned} \tag{4.41}$$

where we have noted $\lambda = \bar{A}/\bar{B}$. These are the parametric equations of a surface and the parameter λ can be eliminated to give (4.40).

Due the relationship between $\bar{A}, \bar{B}$ and the macroscopic strain rate tensor D and taking into account Eq. $(4.28)_2$ that relates the macroscopic stresses located on the yield surface to the derivatives of W with respect to D, Eq. (4.40) becomes the sought after expression for the macroscopic yield surface.

In the spherical case and for axisymmetric loading we obtain:

$$\begin{gathered}
x = \frac{b^3}{r^3},\ x_1 = 1,\ x_2 = \frac{1}{f},\ f = \frac{a^3}{b^3}, \\
\bar{A} = 2D_m,\ \bar{B} = D',\ \frac{\partial W}{\partial D_m} = 3\Sigma_m,\ \frac{\partial W}{\partial D'} = \Sigma_{zz} - \Sigma_{xx}
\end{gathered} \tag{4.42}$$

showing that the functions $F(x), G(x), H(x)$ are true constants in this case and giving the classical Gurson criterion:

$$\frac{(\Sigma_{zz} - \Sigma_{xx})^2}{\sigma_0^2} + 2f \cosh\left(\frac{3}{2}\frac{\Sigma_m}{\sigma_0}\right) - 1 - f^2 = 0 \tag{4.43}$$

In the prolate or oblate spheroidal and ellipsoidal cases, the same approach gives the following result:

$$\frac{Q(\boldsymbol{\Sigma})}{\sigma_0^2} + 2(g+1)(g+f)\cosh\left(\frac{k\Sigma_h}{\sigma_0}\right) - (g+1)^2 - (g+f)^2 = 0 \tag{4.44}$$

where g is a parameter similar to the porosity—it depends only on the geometry of the void and unit cell and, contrary to the porosity f, has a non-zero limit when the void is flatten out to an elliptic crack. Also, k is a parameter, Σ_h is a linear form and $Q(\Sigma)$ is a quadratic form in the components of the macroscopic stress:

$$\begin{gathered}\Sigma_h = \alpha_x\Sigma_{xx} + \alpha_y\Sigma_{yy} + \alpha_z\Sigma_{zz} \quad \alpha_x + \alpha_y + \alpha_z = 1 \\ Q(\Sigma) = \boldsymbol{\Sigma} : \mathbf{Q} : \boldsymbol{\Sigma}\end{gathered} \tag{4.45}$$

Here $\mathbf{Q}$ is a constant symmetric tensor that depends on α_i and two supplementary parameters C, η and reduces to the von Mises equivalent stress when $C = 1, \eta = 0$. We note that all the parameters k, α_i, C, η appearing in the Gurson criterion (4.44) depend explicitly on the geometry of the void and unit cell and on the constants $\bar{F}, \bar{G}, \bar{H}$. One still needs some expression for these last parameters and this may be obtained from a detailed study and approximation of the functions $F(x), G(x), H(x)$. However, in Gologanu et al. (1997) it was observed that the model thus obtained showed rather poor predictions when compared to results of numerical simulations. The cause has been tracked down (see Gologanu et al. 1997) to the specific choice of the velocity field describing the expansion of the cavity. A better accuracy can be obtained by directly calibrating the parameters k, α_i, C, η as functions of void and unit cell geometries using selected numerical results. An alternative for the quadratic term $Q(\Sigma)$ consists in replacing it with another quadratic form deduced from nonlinear homogenization results, valid for the same void geometry and same matrix. In this case, only the parameters k, α_i need to be calibrated.

The local evolution of the void's shape can be easily deduced from the expression of the velocity given by (4.33) and depending linearly on the macroscopic strain rate tensor $\mathbf{D}$. Unfortunately, this approach implies that the void will not preserve an ellipsoidal shape. A better solution is to define a homogeneous rate of deformation $\mathbf{D}^{void}$ on the surface of the void by using the homogenization type expression (4.29):

$$D_{ij}^{void} = \frac{1}{|V|} \int_{\partial V} \frac{1}{2}\left(v_i n_j + v_j n_i\right) \tag{4.46}$$

Like for the yield criterion, the two-field approach gives rather poor accuracy and better results are obtained by calibrating some of the parameters in the resulting expression via numerical simulations.

Consider now the development of Gurson type models for a porous material with a matrix obeying Hill's anisotropic plasticity. The approach is similar to that presented above. The plastic dissipation is easily determined, the same velocity fields are used and one arrives at the same expression (4.39) for the macroscopic dissipation function that is amenable to a Gurson type model of the form (4.44). The only differences are that the quadratic form (4.45) will reduce not to the von Mises equivalent stress when $C = 1, \eta = 0$ but to Hill's equivalent stress. The parameters $k, \alpha_i, C, \eta_1, \eta_2$ need to be recalibrated, but some of them depend not only on the void and unit cell geometry but also on all mechanical parameters present in Hill's yield criterion, which highly complicates the guessing of analytical expressions and fitting via numerical simulations. Morin et al. (2015) partially reduced this complexity by linearizing some of the model parameters with respect to mechanical parameters in Hill's yield criterion.

4.3.3 *Dissipation Functions for Some Non-quadratic Anisotropic Yield Criteria*

Our goal is to develop Gurson type models for some advanced anisotropic yield criteria. Note that we intend to apply such models to study the evolution of microscopic voids in the bulk material of the sheet and therefore we need a full 3D plasticity model for the matrix. Many modern yield criteria for sheets are given only for plane stress conditions and must be first extended to 3D. The experimental determination of the through-thickness plastic properties is difficult or impossible; one solution is to use texture based models to predict these properties from experimental texture determination.

As we have seen in the previous sections, the first step in the development of a Gurson-type model is the calculation of the dissipation function associated to the yield criterion. This is extremely difficult if not impossible and drastically restricts the class of non-quadratic anisotropic yield criteria amenable to some analytical treatment.

We will consider three non-quadratic and orthotropic yield criteria, specifically developed to better represent the strong anisotropy of aluminium sheets. The first two are based on linear transformations, Yld91 proposed by Barlat et al. (1991) and Yld2004-18p proposed by Barlat et al. (2005). The third one is the BBC2005 criterion proposed by Banabic et al. (2000, 2005).

4.3.3.1 Yield Criteria Yld91 and Yld2004-18p

The Yld91 and Yld2004-18p criteria are based on some linear transformations of the deviator of the stress tensor:

$$\mathbf{s}' = \mathbf{C}'\mathbf{s} = \mathbf{C}'\mathbf{K}\sigma = \mathbf{L}'\boldsymbol{\sigma}, \quad \mathbf{s}'' = \mathbf{C}''\mathbf{s} = \mathbf{C}''\mathbf{K}\boldsymbol{\sigma} = \mathbf{L}''\boldsymbol{\sigma}, \tag{4.47}$$

where $\boldsymbol{\sigma}, \mathbf{s}$ are the stress tensor and its deviator, $\mathbf{C}', \mathbf{C}''$ are fourth order tensors defining the anisotropy and $\mathbf{K}$ is the projection on the deviatoric space. In the reference frame related to the rolling, transverse and through-thickness directions of the sheet, these tensors are defined in Voigt notation by:

$$\mathbf{C}' = \begin{pmatrix} 0 & -c'_{12} & -c'_{13} & 0 & 0 & 0 \\ -c'_{21} & 0 & -c'_{23} & 0 & 0 & 0 \\ -c'_{31} & -c'_{32} & 0 & 0 & 0 & 0 \\ 0 & 0 & 0 & c'_{44} & 0 & 0 \\ 0 & 0 & 0 & 0 & c'_{55} & 0 \\ 0 & 0 & 0 & 0 & 0 & c'_{66} \end{pmatrix} \tag{4.48}$$

and a similar expression for $\mathbf{C}''$ depending on other nine constants c''_{ij}, while $\mathbf{K}$ is a singular matrix defined in any orthogonal reference frame by:

$$\mathbf{K} = \frac{1}{3}\begin{pmatrix} 2 & -1 & -1 & 0 & 0 & 0 \\ -1 & 2 & -1 & 0 & 0 & 0 \\ -1 & -1 & 2 & 0 & 0 & 0 \\ 0 & 0 & 0 & 3 & 0 & 0 \\ 0 & 0 & 0 & 0 & 3 & 0 \\ 0 & 0 & 0 & 0 & 0 & 3 \end{pmatrix} \tag{4.49}$$

Recall that in the Voigt notation the stress tensor is defined by the six-component vector $\boldsymbol{\sigma} = (\sigma_{11}, \sigma_{22}, \sigma_{33}, \sigma_{12}, \sigma_{13}, \sigma_{23})$, while the strain tensor is defined by $\mathbf{d} = (d_{11}, d_{22}, d_{33}, 2d_{12}, 2d_{13}, 2d_{23})$.

We note that the transformed stress tensors $\mathbf{s}', \mathbf{s}''$ are not deviatoric but, because they are defined via the deviatoric stress $\mathbf{s}$, they do not depend on some arbitrary pressure added to the stress tensor $\boldsymbol{\sigma}$ and therefore they are pressure independent. Note also that the tensors $\mathbf{C}', \mathbf{C}''$ are not symmetric (as fourth order tensors they have only the minor symmetries but not the major ones), which increases the number of free parameters from six to nine for each tensor.

We consider a slight generalization of the yield criterion Yld91 given by:

$$\varphi(\boldsymbol{\sigma}) = |s'_1 - s'_2|^m + |s'_2 - s'_3|^m + |s'_3 - s'_1|^m - 2\sigma_0^m = 0 \tag{4.50}$$

where s'_1, s'_2, s'_3 are the eigenvalues of the tensor $\mathbf{s}'$ defined by the linear transformation (4.48), σ_0 is a scaling factor for stresses and the exponent m is 6 for BCC metals and 8 for FCC metals. The original yield criterion considered only the case

of a symmetric $\boldsymbol{C}'$ and used a different presentation based on the product $\mathbf{L}' = \mathbf{C}'\mathbf{K}$. Note that choosing $m = 2$ and a symmetric $\mathbf{C}'$ gives a quadratic yield criterion identical to Hill48 yield criterion. When all nonzero coefficients c'_{ij} are equal to 1, the yield criterion reduces to von Mises isotropic criterion.

The yield criterion Yld2004-18p is defined by:

$$\begin{aligned}\varphi(\boldsymbol{\sigma}) = {} & |s'_1 - s''_1|^m + |s'_1 - s''_2|^m + |s'_1 - s''_3|^m + \\ & + |s'_2 - s''_1|^m + |s'_2 - s''_2|^m + |s'_2 - s''_3|^m + \\ & + |s'_3 - s''_1|^m + |s'_3 - s''_2|^m + |s'_3 - s''_3|^m - 4\sigma_0^m = 0\end{aligned} \tag{4.51}$$

where s'_1, s'_2, s'_3, and s''_1, s''_2, s''_3 are the eigenvalues of the transformed tensors $\mathbf{s}', \mathbf{s}''$ defined in (4.48), while σ_0 and m have the same interpretation as for the Yld91 yield criterion.

Omitting for brevity the prime or double prime, note that the decomposition $\mathbf{L} = \mathbf{CK}$ in (4.47) is not unique, as one can add some arbitrary value to each row of the 3×3 matrix in the upper left corner of $\mathbf{C}$. A more suitable decomposition for our purposes is $\mathbf{L} = \tilde{\mathbf{C}}K$ where $\tilde{\mathbf{C}}$ is defined in Voigt notation by:

$$\tilde{\mathbf{C}} = \begin{pmatrix} 1 - \tilde{c}_{12} - \tilde{c}_{13} & \tilde{c}_{12} & \tilde{c}_{13} & 0 & 0 & 0 \\ \tilde{c}_{21} & 1 - \tilde{c}_{21} - \tilde{c}_{23} & \tilde{c}_{23} & 0 & 0 & 0 \\ \tilde{c}_{31} & \tilde{c}_{32} & 1 - \tilde{c}_{31} - \tilde{c}_{32} & 0 & 0 & 0 \\ 0 & 0 & 0 & c_{44} & 0 & 0 \\ 0 & 0 & 0 & 0 & c_{55} & 0 \\ 0 & 0 & 0 & 0 & 0 & c_{66} \end{pmatrix} \tag{4.52}$$

with

$$\begin{aligned} 3\tilde{c}_{12} &= 1 + c_{13} - 2c_{12}, \quad 3\tilde{c}_{13} = 1 + c_{12} - 2c_{13}, \\ 3\tilde{c}_{21} &= 1 + c_{23} - 2c_{21}, \quad 3\tilde{c}_{23} = 1 + c_{21} - 2c_{23}, \\ 3\tilde{c}_{31} &= 1 + c_{32} - 2c_{31}, \quad 3\tilde{c}_{32} = 1 + c_{31} - 2c_{32}. \end{aligned} \tag{4.53}$$

The defining property of such a decomposition is that the linear transformation $\tilde{\mathbf{C}}$ is the direct sum of two linear transformations, the first being the identity on pressure like tensors, while the second transforms the space of deviatoric tensors into itself:

$$\tilde{\mathbf{C}}(\mathbf{s} + p\mathbf{I}) = \tilde{\mathbf{C}}s + p\mathbf{I} = \tilde{\mathbf{s}} + p\mathbf{I}, \quad \mathbf{K}\tilde{\mathbf{s}} = \tilde{\mathbf{s}} \tag{4.54}$$

where $\mathbf{I}$ is the 3×3 identity matrix.

In the next subsections we will calculate the dissipation functions for the Yld91, Yld2004-18p and BBC2005 yield criteria.

4.3.3.2 Dissipation Function for the Yld91 Criterion

Recall that the dissipation function is defined as the Legendre conjugate of the indicator function of the yield convex, see Eq. (4.18). Our method is based entirely on results of convex analysis.

From now on we use a different definition of a convex region. Instead of defining it by $k = \{\boldsymbol{\sigma} | \varphi(\boldsymbol{\sigma}) \leq 0\}$ for some arbitrary φ we use $k = \{\boldsymbol{\sigma} | \varphi(\boldsymbol{\sigma}) \leq \sigma_0\}$, where σ_0 is a scaling factor and φ is a homogeneous function of degree 1.

For a convex surface defined by the following function of n variables:

$$\varphi(x_1, \ldots, x_n) = (|x_1|^p + \cdots + |x_n|^p)^{\frac{1}{p}} = \sigma_0 \tag{4.55}$$

the dissipation function is given by:

$$w(y_1, \ldots, y_n) = \sigma_0 (|y_1|^q + \cdots + |y_n|^q)^{\frac{1}{q}}, \quad \frac{1}{p} + \frac{1}{q} = 1 \tag{4.56}$$

where y_i are the dual variables of x_i.

The proof of this result is elementary and based on the relationships (4.18) and (4.19) which in our case give:

$$\begin{aligned} y_i &= \dot{\lambda} \frac{\partial \varphi}{\partial x_i} = \dot{\lambda}\, \mathrm{sgn}(x_i) |x_i|^{p-1} \sigma_0^{1-p}, \\ w &= y_1 x_1 + \cdots + y_n x_n = \dot{\lambda} \left(x_1 \frac{\partial \varphi}{\partial x_1} + \cdots + x_n \frac{\partial \varphi}{\partial x_n} \right) = \dot{\lambda} \varphi = \dot{\lambda} \sigma_0 \end{aligned} \tag{4.57}$$

Solving the first equation for x_i and plugging the result in (4.55) gives an equation for $\dot{\lambda}$ whose solution gives directly the dissipation function w. In the second line of (4.57) we have used the homogeneity of degree 1 of $\varphi(x)$.

We now consider general convex functions on symmetric matrices defined by some convex and symmetric function of their eigenvalues. This is entirely similar to the case of Hermitian matrices treated by Lewis (1996). We consider only the case of symmetric 3×3 matrices. Let $f(x, y, z)$ be some *symmetric* convex function of three variables and, for a 3×3 symmetric matrix $\boldsymbol{\sigma}$, let $\lambda(\boldsymbol{\sigma}) = (\sigma_1, \sigma_2, \sigma_3)$ denote its eigenvalues. Define a function of symmetric matrices by $F(\boldsymbol{\sigma}) = f(\lambda(\boldsymbol{\sigma})) = f(\sigma_1, \sigma_2, \sigma_3)$. Then F is convex and its Legendre dual is given by:

$$F^*(\mathbf{d}) = f^*(\lambda(\mathbf{d})) = f^*(d_1, d_2, d_3). \tag{4.58}$$

where f^* is the Legendre dual of f This result reduces the calculation of the Legendre dual of a function of 6 variables (the independent components of a 3×3 symmetric matrix) to that of a function of only 3 variables. However, its deep

relevance is that one no longer needs explicit solutions for the eigenvalues via a 3rd degree equation to prove convexity and calculate Legendre duals.[2] The proof of this result can be found in Lewis (1996) and is essentially based on a result of von Neumann, stating that for two symmetric (or Hermitian) matrices $\boldsymbol{\sigma}, \boldsymbol{d}$ of order n we have the following inequality:

$$\boldsymbol{\sigma} : \mathbf{d} \leq \langle \lambda(\boldsymbol{\sigma}), \lambda(\mathbf{d}) \rangle = \sigma_1 d_1 + \cdots + \sigma_n d_n \tag{4.59}$$

with equality iff the two matrices are simultaneously diagonalizable (there is an orthogonal matrix $\mathbf{Q}$ such that $\mathbf{Q}^T\boldsymbol{\sigma}\mathbf{Q}$ and $\mathbf{Q}^T\mathbf{d}\mathbf{Q}$ are both diagonal).

We need another result from convex analysis related to the linear transformation of a convex function, see Rockafellar (1997). Let $g : \mathbb{R}^m \to \mathbb{R}$ be a convex function of a variable y and $L : \mathbb{R}^n \to \mathbb{R}^m$ some linear transformation, eventually singular. Then the function $f : \mathbb{R}^n \to \mathbb{R}$ defined by $f(x) = g(Lx)$ is convex and its Legendre dual is given by:

$$f^*(x^*) = \inf_{y^*} \left\{ g^*(y^*) \middle| L^T y^* = x^* \right\} \tag{4.60}$$

where $L^T : \mathbb{R}^m \to \mathbb{R}^n$ is the transpose of L and we use the convention that the infimum over an empty set is equal to $+\infty$.

For example, if $m = n$ and the linear transformation L is not singular and therefore admits an inverse, then the infimum in (4.60) is taken over the set with the single element $y^* = L^{-T}x^*$ and we obtain $f^*(x^*) = g^*(L^{-T}x^*)$.

A second example concerns a direct sum where $m = 2n$ and $y = (y', y'')$, while the linear transformation is defined by $y = L(x) = (L'(x), L''(x))$ with $L', L'' : \mathbb{R}^n \to \mathbb{R}^n$ two linear transformations. Then a simple application of (4.60) results in

$$f^*(x^*) = \inf_{y'^*, y''^*} \left\{ g^*(y'^*, y''^*) \middle| L'^T y'^* + L''^T y''^* = x^* \right\} \tag{4.61}$$

Let us now consider the case of the yield criterion Yld91. Consider the convex surface in $\mathbb{R}^3$ defined by the symmetric function:

$$g(u_1, u_2, u_3) = (|u_1|^m + |u_2|^m + |u_3|^m)^{\frac{1}{m}} = \sigma_1, \quad \sigma_1 = 2^{\frac{1}{m}}\sigma_0 \tag{4.62}$$

Then, by (4.55) and (4.56) we know that its dissipation function, or the Legendre dual of its indicator function is given by:

$$w_g(u_1^*, u_2^*, u_3^*) = \sigma_1(|u_1^*|^q + |u_2^*|^q + |u_3^*|^q)^{\frac{1}{q}}, \quad q = \frac{m}{m-1} \tag{4.63}$$

[2]There is also a similar result in Lewis (1996) for the gradient of F.

Consider now the linear transformation $\bar{L}$ defined by:

$$\bar{L} = \begin{pmatrix} 1 & -1 & 0 \\ 0 & 1 & -1 \\ -1 & 0 & 1 \end{pmatrix} \tag{4.64}$$

and the surface $f(x) = g(\bar{L}x)$ having the following expression:

$$f(x_1, x_2, x_3) = \left(|x_1 - x_2|^m + |x_2 - x_3|^m + |x_3 - x_1)|^m\right)^{\frac{1}{m}} = \sigma_1 \tag{4.65}$$

Then, by (4.60) we know that f is convex and its dissipation function is:

$$w_f(x^*) = \inf_{u^*} \left\{ w_g(u^*) \middle| \bar{L}^T u^* = x^* \right\} \tag{4.66}$$

The transformation $\bar{L}$ is singular (has rank 2) but it can be decomposed as a product $\bar{L} = \bar{C}\bar{K}$ of some invertible matrix and a projection operator on the $x_1 + x_2 + x_3 = 0$ plane. Note that this decomposition is not unique, as $\bar{C}$ depends on 3 arbitrary parameters. However, imposing that the sum of coefficients of each row is equal to one, we obtain a direct sum of two linear operators, the first being the identity on the normal to the plane above, while the second transforms the plane in itself. Thus, we obtain:

$$\bar{C} = \frac{1}{3}\begin{pmatrix} 4 & -2 & 1 \\ 1 & 4 & -2 \\ -2 & 1 & 4 \end{pmatrix}, \quad \bar{K} = \frac{1}{3}\begin{pmatrix} 2 & -1 & -1 \\ -1 & 2 & -1 \\ -1 & -1 & 2 \end{pmatrix} \tag{4.67}$$

Let us now analyze the equation $\bar{L}^T u^* = \bar{K}^T \bar{C}^T u^* = K \bar{C}^T u^* = x^*$ defining the infimum in (4.66). First, if x^* does not lie in the image of the projection operator $\bar{K}$, then these equation has no solution. Second, if x^* lies in this image then there is a one parameter family of solutions defined by $u^* = \bar{C}^{-T}(x^* + a^*)$ for an arbitrary $a^* = \frac{1}{3}(a, a, a)$ with $\bar{K}a^* = 0$. A simple calculation then gives the following dissipation function:

$$w_f(x^*) = \begin{cases} \inf\limits_a \bar{w}_f(x^*, a) & x_1^* + x_2^* + x_3^* = 0 \\ +\infty & x_1^* + x_2^* + x_3^* \neq 0 \end{cases} \tag{4.68}$$

where $\bar{w}_f$ is defined by:

$$\bar{w}_f = \frac{\sigma_1}{3}\left(\left|x_1^* - x_2^* + a\right|^q + \left|x_2^* - x_3^* + a\right|^q + \left|x_3^* - x_1^* + a\right|^q\right)^{\frac{1}{q}} \tag{4.69}$$

In the quadratic case with $m = q = 2$, one can easily show that the infimum over a in (4.68) is attained at $a = 0$. In the non-quadratic case this is no longer true; however, we will see that the formulation (4.68) is compatible with the development of an approximate Gurson-type model.

Note that if we apply the function f defined by (4.65) to the eigenvalues of the symmetric matrix $\mathbf{s}' = \mathbf{L}'\boldsymbol{\sigma} = \tilde{\mathbf{C}}'\mathbf{K}\boldsymbol{\sigma}$ we obtain precisely the Yld91 yield criterion. Using the general result (4.58) for calculating Legendre duals for functions of symmetric matrices and Eq. (4.60) giving the effect of a linear transformation, we obtain the following expression for the dissipation function:

$$w(\mathbf{d}) = \begin{cases} \inf\limits_{a,\mathbf{d}'} \bar{w}_f(\lambda(\mathbf{d}'), a) & \mathbf{L}'^T\mathbf{d}' = \boldsymbol{d},\ \mathrm{tr}\,\mathbf{d}' = 0 \\ +\infty & \mathrm{tr}\,\mathbf{d}' \neq 0 \end{cases} \tag{4.70}$$

where $\lambda(\mathbf{d}) = (d_1, d_2, d_3)$ is the list of eigenvalues of the symmetric matrix $\mathbf{d}$ and $\mathrm{tr}\mathbf{d} = d_1 + d_2 + d_3$ represents its trace. Let us now analyze the equation $\mathbf{L}'^T\mathbf{d}' = \mathbf{K}\tilde{\mathbf{C}}'^T\mathbf{d}' = \mathbf{d}$ defining the infimum in Eqs. (4.70). First, if $\mathbf{d}$ is not deviatoric, then there is no solution and the dissipation function is $+\infty$. Second, if $\mathbf{d}$ is deviatoric, then we have $\mathbf{d}' = \tilde{\mathbf{C}}'^{-T}(\mathbf{d} + p\mathbf{I})$ for some arbitrary p. Now, the linear transformation $\tilde{\mathbf{C}}'$ is a direct sum as shown in Eq. (4.54) and it is easy to show that the same holds true for $\tilde{\mathbf{C}}'^{-T}$:

$$\mathbf{d}' = \tilde{\mathbf{C}}'^{-T}(\mathbf{d} + p\mathbf{I}) = \tilde{\mathbf{C}}'^{-T}\mathbf{d} + p\mathbf{I} = \tilde{\mathbf{d}} + p\mathbf{I}, \quad \mathbf{K}\tilde{\mathbf{d}} = \tilde{\mathbf{d}} \tag{4.71}$$

where $\tilde{\mathbf{d}}$ is a deviatoric tensor. But from (4.70) we know that $\mathrm{tr}\,\mathbf{d}' = 3p$ should be zero for the dissipation to be finite, implying $p = 0$ and therefore there is a single solution defined by $\mathbf{d}' = \tilde{\mathbf{C}}'^{-T}\mathbf{d}$ with both $\mathbf{d}$,$\mathbf{d}'$ deviatoric tensors.

Summarizing, we obtain the following expression for the dissipation function of the Yld91 anisotropic yield criterion:

$$w_1(\mathbf{d}) = \inf_a \frac{\sigma_1}{3}\left(\left|d_1' - d_2' + a\right|^q + \left|d_2' - d_3' + a\right|^q + \left|d_3' - d_1' + a\right|^q\right)^{\frac{1}{q}} \tag{4.72}$$

where $\sigma_1 = 2^{1/m}\sigma_0$, $q = m/(m-1)$ and d_1', d_2', d_3' are the eigenvalues of the linearly transformed strain rate $\mathbf{d}' = \tilde{\mathbf{C}}'^{-T}\mathbf{d}$ of the deviatoric strain rate $\mathbf{d}$. If the strain rate $\mathbf{d}$ is not deviatoric, then the dissipation function is $+\infty$. The fourth-order tensor tensor $\tilde{\mathbf{C}}'^{-T}$ is the inverse of the transpose of the matrix $\tilde{\mathbf{C}}'$ defined in (4.52) and (4.53) as a function of the original matrix $\mathbf{C}'$ given in (4.48).

4.3.3.3 Dissipation Function for the Yld2004-18p Criterion

Considering now the Yld2004-18p yield criterion, the approach to calculate the dissipation function is similar to the Yld91 case and we give only the main steps. The starting point is the following convex surface of nine variables:

$$g(u_1,\ldots,u_9)=(|u_1|^m+\cdots+|u_9|^m)^{1/m}=\sigma_1,\quad \sigma_1=4^{1/m}\sigma_0 \tag{4.73}$$

Its dissipation function is:

$$w_g(u_1^*,\ldots,u_9^*)=\sigma_1(|u_1^*|^q+\cdots+|u_9^*|^q)^{1/q},\quad q=\frac{m}{m-1} \tag{4.74}$$

Consider now the linear transformation $\bar{L}:\mathbb{R}^6\to\mathbb{R}^9$ defined by:

$$\bar{L}^T=\begin{pmatrix} 1 & 1 & 1 & 0 & 0 & 0 & 0 & 0 & 0\\ 0 & 0 & 0 & 1 & 1 & 1 & 0 & 0 & 0\\ 0 & 0 & 0 & 0 & 0 & 0 & 1 & 1 & 1\\ -1 & 0 & 0 & -1 & 0 & 0 & -1 & 0 & 0\\ 0 & -1 & 0 & 0 & -1 & 0 & 0 & -1 & 0\\ 0 & 0 & -1 & 0 & 0 & -1 & 0 & 0 & -1 \end{pmatrix} \tag{4.75}$$

Then the function of six variables $f(x)=g(\bar{L}x)$ defines a convex surface:

$$\begin{aligned} f(x)=\{&|x_1-x_4|^m+|x_1-x_5|^m+|x_1-x_6|^m+\\ &+|x_2-x_4|^m+|x_2-x_5|^m+|x_2-x_6|^m+\\ &+|x_3-x_4|^m+|x_3-x_5|^m+|x_3-x_6|^m\}^{\frac{1}{m}}=\sigma_1 \end{aligned} \tag{4.76}$$

and its dual is given by:

$$w_f(x^*)=\inf_{u^*}\left\{\sigma_1(|u_1^*|^q+\cdots+|u_9^*|^q)^{1/q}\middle|\bar{L}^Tu^*=x^*\right\} \tag{4.77}$$

The rank of the matrix $\bar{L}^T$ is 5 and its image is the 4 dimensional subspace defined by the intersection of two hyperplanes: $x_1^*+x_2^*+x_3^*=x_4^*+x_5^*+x_6^*=0$. If x^* is not in this image, then the equation defining the infimum in (4.77) has no solution and the dissipation is $+\infty$. If x^* lies in the image of $\bar{L}^T$ then the general solution for u^* will depend on 4 arbitrary parameters a,b,c,d. Using now (4.58) and (4.61), we obtain the following expression for the dissipation function of the Yld2004-18p yield criterion:

$$\begin{aligned} w(\mathbf{d})=\inf_{\substack{a,b,c,d\\ \mathbf{K}(\tilde{\mathbf{C}}'^T\mathbf{d}'+\tilde{\mathbf{C}}''^T\mathbf{d}'')=\mathbf{d}}}&\frac{\sigma_1}{3}\{|d_1'-d_1''+a|^q+|d_1'-d_2''+b|^q+\\ &+|d_1'-d_3''-a-b|^q+|d_2''-d_1''+c|^q+|d_2'-d_2''+d|^q+\\ &+|d_2'-d_3''-c-d|^q+|d_3'-d_1''-a-c|^q+\\ &+|d_3'-d_2''-b-d|^q+|d_3'-d_3''+a+b+c+d|^q\}^{1/q} \end{aligned} \tag{4.78}$$

where $\mathbf{d}$ is a *deviatoric* strain rate tensor, $\sigma_1=4^{1/m}\sigma_0$, $q=m/(m-1)$ and d_1',d_2',d_3' and d_1'',d_2'',d_3'' are the eigenvalues of two symmetric and *deviatoric* tensors

$\mathbf{d}', \mathbf{d}''$ such that $\mathbf{K}(\tilde{\mathbf{C}}'^T\mathbf{d}' + \tilde{\mathbf{C}}''^T\mathbf{d}'') = \mathbf{d}$. The fourth-order tensors $\tilde{\mathbf{C}}', \tilde{\mathbf{C}}''$ are defined in (4.52) and (4.53) as functions of the original matrix $\mathbf{C}', \mathbf{C}''$ given in (4.48). If the strain rate $\mathbf{d}$ is not deviatoric, then the dissipation function is $+\infty$.

4.3.3.4 BBC2005 Criterion and Dissipation Function

The BBC2005 yield criterion was originally developed as a plane stress criterion and therefore needs first to be extended to a 3D criterion in order to fully describe the matrix around a microscopic void in a Gurson-type model. We will consider the following modification of the BBC2005-3D criterion proposed in Chap. 1:

$$\begin{aligned}\varphi(\boldsymbol{\sigma}) = [a(\Lambda+\Gamma)^m + a(\Lambda-\Gamma)^m + b(\Lambda+\Psi)^m a + \\ b(\Lambda-\Psi)^m + c\sigma_{13}^m + c\sigma_{23}^m]^{1/m} = \sigma_0\end{aligned} \tag{4.79}$$

where a, b are material parameters, $c = 3^{m/2}$, while Γ, Λ and Ψ are given by:

$$\begin{aligned}\Gamma &= L(\sigma_{11}-\sigma_{33}) + M(\sigma_{22}-\sigma_{33}) \\ \Lambda &= \sqrt{[N(\sigma_{11}-\sigma_{33}) - P(\sigma_{22}-\sigma_{33})]^2 + \sigma_{12}\sigma_{21}} \\ \Psi &= \sqrt{[Q(\sigma_{11}-\sigma_{33}) - R(\sigma_{22}-\sigma_{33})]^2 + \sigma_{12}\sigma_{21}}\end{aligned} \tag{4.80}$$

and where stresses are given in the reference frame aligned with sheet. Note that the proposed modification affects only the out-of-plane shear stresses.

We start with the following convex surface of six variables:

$$g(u_1, \ldots, u_6) = (|u_1|^m + \cdots + |u_6|^m)^{1/m} = \sigma_0 \tag{4.81}$$

with dissipation function:

$$w_g(u_1^*, \ldots, u_6^*) = \sigma_0(|u_1^*|^q + \cdots + |u_6^*|^q)^{1/q} \tag{4.82}$$

where $q = m/(m-1)$.

Consider now the linear transformation $\bar{\mathbf{L}} : \mathbb{R}^5 \to \mathbb{R}^6$ defined by:

$$\bar{\mathbf{L}} = \begin{pmatrix} a^{1/m} & a^{1/m} & 0 & 0 & 0 \\ -a^{1/m} & a^{1/m} & 0 & 0 & 0 \\ 0 & b^{1/m} & b^{1/m} & 0 & 0 \\ 0 & b^{1/m} & -b^{1/m} & 0 & 0 \\ 0 & 0 & 0 & c^{1/m} & 0 \\ 0 & 0 & 0 & 0 & c^{1/m} \end{pmatrix} \tag{4.83}$$

Then the function of five variables $f(\mathbf{x}) = g(\bar{\mathbf{L}}\mathbf{x})$ defines a convex surface:

$$f(\mathbf{x}) = (a|x_2+x_1|^m + a|x_2-x_1|^m + b|x_2+x_3|^m + \\ + b|x_2-x_3|^m + cx_4^m + cx_5^m)^{1/m} = \sigma_0 \tag{4.84}$$

with dissipation function:

$$w_f(\mathbf{x}^*) = \sigma_0 \inf_{u^*}\left\{(|u_1^*|^q + \cdots + |u_6^*|^q)^{1/q} \middle| \mathbf{L}^{\mathbf{T}}\mathbf{u}^* = \mathbf{x}^*\right\} \tag{4.85}$$

Working out the constraint in the previous equation gives:

$$w_f(\mathbf{x}^*) = \inf_{d^*}\frac{\sigma_0}{2}\left(\frac{|d^*+x_1^*|^q}{a^{q-1}} + \frac{|d^*-x_1^*|^q}{a^{q-1}} \right. \\ \left. + \frac{|d^*+x_2^*+x_3^*|^q}{b^{q-1}} + \frac{|d^*+x_2^*-x_3^*|^q}{b^{q-1}} + \frac{x_4^{*q}}{c^{q-1}} + \frac{x_5^{*q}}{c^{q-1}}\right)^{1/q} \tag{4.86}$$

Let us now define a non-linear transformation $\bar{\mathbf{S}} : \mathbb{R}^7 \to \mathbb{R}^5$ by:

$$x_1 = y_1, x_2 = \sqrt{y_2^2+y_6^2}, x_3 = \sqrt{y_3^2+y_7^2}, x_4 = y_4, x_5 = y_5 \tag{4.87}$$

Then a simple calculation shows that the function $h(\mathbf{y}) = f(\bar{\mathbf{S}}(\mathbf{y}))$ defines a convex surface:

$$h(\mathbf{y}) = \left(a\left|\sqrt{y_2^2+y_6^2}+y_1\right|^m + a\left|\sqrt{y_2^2+y_6^2}-y_1\right|^m + cy_4^m + cy_5^m + \right. \\ \left. + b\left|\sqrt{y_2^2+y_6^2}+\sqrt{y_3^2+y_7^2}\right|^m + b\left|\sqrt{y_2^2+y_6^2}+\sqrt{y_3^2+y_7^2}\right|^m\right)^{1/m} = \sigma_0 \tag{4.88}$$

with dissipation function:

$$w_h(\mathbf{y}^*) = w_f\left(y_1^*, \sqrt{y_2^*+y_6^*}, \sqrt{y_3^*+y_7^*}, y_4^*, y_5^*\right) \tag{4.89}$$

The last step is to relate the stress tensor (as a vector in Voigt notation and with components taken in the frame of the sheet) to $\mathbf{y}$ by a linear transformation $\bar{\mathbf{T}} : \mathbb{R}^6 \to \mathbb{R}^7$ written as a direct sum:

$$(y_1, y_2, y_3) = \begin{pmatrix} L & M & -L-M \\ N & -P & -N+P \\ Q & -R & -Q+R \end{pmatrix}\begin{pmatrix}\sigma_{11}\\ \sigma_{22}\\ \sigma_{33}\end{pmatrix} \quad \begin{matrix} y_4 = \sigma_{13} \\ y_5 = \sigma_{23} \\ y_6 = y_7 = \sigma_{12}\end{matrix} \tag{4.90}$$

Then the convex surface defined by $\varphi(\boldsymbol{\sigma}) = h(\overline{\mathbf{T}}\boldsymbol{\sigma})$ is precisely the BBC2005 yield criterion (4.79), (4.80) and its dissipation function is:

$$w(\mathbf{d}) = \inf_{y^*} \left\{ w_h(\mathbf{y}^*) | \bar{\mathbf{T}}\mathbf{y}^* = \mathbf{d} \right\} \tag{4.91}$$

We note that care has to be taken when calculating the dual variables for the shear stresses; for example the term σ_{12} is actually a condensed form for $\frac{\sigma_{12}}{2} + \frac{\sigma_{21}}{2}$. There are two difficulties in solving the constraint $\bar{\mathbf{T}}\mathbf{y}^* = \mathbf{d}$ appearing in (4.91), but both have been treated already. The first difficulty is related to the double employ of σ_{12} in $(4.90)_4$. This has the simple solution $y_6^* + y_7^* = d_{12}$ with one free parameter. The second difficulty is that the 3×3 matrix $\mathbf{T}$ in $(4.90)_1$ is not invertible. Let $\mathbf{K}$ be the projection operator defined in $(4.67)_2$, and the invertible matrix $\bar{C}$ given by:

$$\tilde{\mathbf{C}} = \frac{1}{3} \begin{pmatrix} 1+3L & 1+3M & 1-3M-3L \\ 1+3N & 1-3P & 1+3P-3N \\ 1+3Q & 1-3R & 1+3R-3Q \end{pmatrix} \tag{4.92}$$

Then we have $\mathbf{T} = \mathbf{CK}$ and the equation $\mathbf{T}\mathbf{y}^* = (d_{11}, d_{22}, d_{33})$ has a solution if and only if $d_{11} + d_{22} + d_{33} = 0$. If this condition is satisfied, then the most general solution is given by:

$$(y_1^*, y_2^*, y_3^*) = \tilde{\mathbf{C}}^{-T}(d_{11}, d_{22}, d_{33}) + (e, e, e). \tag{4.93}$$

for some arbitrary value e. It is possible to calculate the inverse of the transpose of $\tilde{\mathbf{C}}$; however, for our purpose it is sufficient to give its product with the projection operator $\mathbf{K}$:

$$\tilde{\mathbf{C}}^{-T}\mathbf{K} = \begin{pmatrix} L' & M' & -L'-M' \\ N' & P' & -N'-P' \\ Q' & R' & -Q'-R' \end{pmatrix} \tag{4.94}$$

where:

$$\begin{aligned} L' &= \tfrac{2(P-R)+N-Q}{3D}, \quad M' = \tfrac{R-P+2(Q-N)}{3D} \\ N' &= \tfrac{2(R-M)+Q-L}{3D}, \quad P' = \tfrac{M-R+2(L-Q)}{3D} \\ Q' &= \tfrac{2(M-P)+L-N}{3D}, \quad R' = \tfrac{P-M+2(N-L)}{3D} \\ D &= LR + PQ + MQ - LP - MN - NR \end{aligned} \tag{4.95}$$

Combining these results with Eq. (4.91), we obtain the following form of the BBC2005 dissipation function:

$$w(\mathbf{d}) = \inf_{d,e,f} \frac{\sigma_0}{2} \left(\frac{|d+\Gamma'|^q}{a^{q-1}} + \frac{|d-\Gamma'|^q}{a^{q-1}} + \frac{|d+\Lambda'+\Psi'|^q}{b^{q-1}} + \frac{|d+\Lambda'-\Psi'|^q}{b^{q-1}} + \frac{2^q d_{23}^q}{c^{q-1}} + \frac{2^q d_{13}^q}{c^{q-1}} \right)^{1/q} \tag{4.96}$$

where

$$\begin{aligned} \Gamma' &= L'(d_{11}-d_{33}) + M'(d_{22}-d_{33}) + e \\ \Lambda' &= \sqrt{[N'(d_{11}-d_{33}) + P'(d_{22}-d_{33}) + e]^2 + 4(d_{12}-f)^2} \\ \Psi' &= \sqrt{[Q'(d_{11}-d_{33}) + R'(d_{22}-d_{33}) + e]^2 + 4f^2} \end{aligned} \tag{4.97}$$

This expression is valid only if $\mathbf{d}$ is a deviatoric strain rate tensor; otherwise the dissipation function is $+\infty$.

Note that the dissipation functions for the Yld91, Yld2004-18p and BBC2005 yield criteria are not fully explicit. However, we will see in the next section that these expressions can be used to obtain approximate Gurson-type models.

From a numerical point of view, a simpler approach to calculate the dissipation function for an arbitrary yield convex $k = \{\boldsymbol{\sigma} | \varphi(\boldsymbol{\sigma}) \leq 0\}$ is as follows. For a given strain rate tensor $\mathbf{d}$ one needs to find the point $\boldsymbol{\sigma}$ on the yield surface with normal parallel to $\mathbf{d}$; then $w(\mathbf{d}) = \boldsymbol{\sigma} : \mathbf{d}$.

4.3.4 Gurson-Type Models for Some Anisotropic Yield Criteria Based on Linear Transformations

Our approach to develop Gurson-type models for Yld91 and Yld2004-18p yield criteria is based on Gologanu et al. (1997), Keralavarma and Benzerga (2010), Madou and Leblond (2012a). Consider a spherical, spheroidal or ellipsoidal void V in a confocal unit cell Ω with homogeneous strain rate boundary conditions. Let $f = |V|/|\Omega|$ denote the porosity. We have seen in Sect. 4.2.2 that we need to estimate the macroscopic dissipation function, defined by Eq. (4.32), conveniently reproduced here:

$$W(\mathbf{D}) = \inf_{\mathbf{v}} \left\{ \frac{1}{|\Omega|} \int_{\Omega \setminus V} w(\mathbf{d}(\mathbf{v})) \middle| \mathbf{v} = \mathbf{D}\mathbf{x}|_{\partial\Omega}, \mathrm{div}\mathbf{v} = 0 \right\}$$

The macroscopic yield convex then has an indicator function which is the Legendre dual of the macroscopic dissipation function; equivalently the macroscopic yield surface or criterion is defined parametrically by:

$$\boldsymbol{\Sigma} = \frac{\partial W}{\partial \mathbf{D}} \tag{4.98}$$

The microscopic dissipation function w is given by (4.72) for the Yld91 yield criterion and by (4.78) for the Yld2004-18p yield criterion.

Consider a velocity field of the form:

$$\begin{gathered} \mathbf{v} = A\mathbf{v}^A + B\mathbf{v}^B + C\mathbf{v}^C + D_{xy}\mathbf{v}^D + D_{yz}\mathbf{v}^E + D_{xz}\mathbf{v}^F \\ \mathbf{v}^B = -\tfrac{x}{2}\mathbf{e}_x - \tfrac{y}{2}\mathbf{e}_y + z\mathbf{e}_z, \quad \mathbf{v}^C = -x\mathbf{e}_x + y\mathbf{e}_y \\ \mathbf{v}^D = x\mathbf{e}_y + y\mathbf{e}_x, \quad \mathbf{v}^E = y\mathbf{e}_z + z\mathbf{e}_y, \quad \mathbf{v}^F = x\mathbf{e}_z + z\mathbf{e}_x \end{gathered} \tag{4.99}$$

where $\mathbf{v}^A$ is an incompressible velocity field that respects homogeneous strain rate boundary conditions and describes the expansion of the cavity, while all other velocity fields are also incompressible and have homogeneous strain rate. Although there are six independent velocity fields in Eqs. (4.99), all parameters are determined uniquely by the boundary conditions. This is similar to the original Gurson approach and therefore we still call (4.99) a "two-field" approach.

There are two steps in our development of a Gurson-type criteria. The first one is generic and applies to an arbitrary microscopic yield criterion. It defines the "best" expansion velocity field and shows how this field determines several critical features of the macroscopic model. This definition will also permit us later to determine $\mathbf{v}^A$ numerically during the calibration phase of the model.

Writing explicitly the boundary conditions gives:

$$\begin{aligned} D_{xx} &= \alpha_x A - \frac{B}{2} - C \\ D_{yy} &= \alpha_y A - \frac{B}{2} + C \\ D_{zz} &= \alpha_z A + B \end{aligned} \tag{4.100}$$

with $\alpha_x, \alpha_y, \alpha_z$ parameters that depend only on the velocity field $\mathbf{v}^A$. Note that:

$$D_{xx} + D_{yy} + D_{zz} = 3D_m = A(\alpha_1 + \alpha_2 + \alpha_3) \tag{4.101}$$

where D_m is the mean macroscopic strain rate. Now, the only reasonable requirement for an expansion velocity field is that it should change the *volume* of the void. Due to the incompressibility of the matrix this is equivalent to $D_m \neq 0$. Assuming that the velocity field $\mathbf{v}^A$ is normalized such that $A = 3D_m$, we obtain:

$$\alpha_x + \alpha_y + \alpha_z = 1 \tag{4.102}$$

Taking into account Eq. (4.98), we obtain the derivatives of W:

$$\begin{gathered}\frac{\partial W}{\partial A}=\alpha_x\Sigma_{xx}+\alpha_y\Sigma_{yy}+\alpha_z\Sigma_{zz}\equiv\Sigma_h\\ \frac{\partial W}{\partial B}=-\frac{\Sigma_{xx}}{2}-\frac{\Sigma_{yy}}{2}+\Sigma_{zz},\quad \frac{\partial W}{\partial C}=\Sigma_{yy}-\Sigma_{xx}\\ \frac{\partial W}{\partial D_{xy}}=\Sigma_{xy},\quad \frac{\partial W}{\partial D_{yz}}=\Sigma_{yz},\quad \frac{\partial W}{\partial D_{xz}}=\Sigma_{xz}\end{gathered}\tag{4.103}$$

Recall now that for any macroscopic stress located on the yield surface we have:

$$\boldsymbol{\Sigma}:\mathbf{D}\le W(\mathbf{D})\tag{4.104}$$

with equality if and only if $\mathbf{D}$ is proportional to the normal to the yield surface at $\boldsymbol{\Sigma}$. For a pure hydrostatic stress defined by a pressure p we obtain:

$$p\mathbf{I}:\mathbf{D}=3pD_m=\inf_{\mathbf{v}^A=\mathbf{D}\mathbf{x}|_{\partial\Omega}}\frac{1}{|\Omega|}\int\limits_{\Omega\setminus\mathrm{V}}w(\mathbf{d}(\mathbf{v}^A))\tag{4.105}$$

Taking into account the homogeneity of degree 1 of the microscopic dissipation and the normalization of the velocity field given by (4.102), we obtain:

$$p=\inf_{\substack{\mathrm{div}\mathbf{v}^A=0,\quad \mathbf{v}^A=\mathbf{D}\mathbf{x}|_{\partial\Omega}\\ D_{xx}+D_{yy}+D_{zz}=1,\ D_{xy}=D_{xz}=D_{yz}=0}}\frac{1}{|\Omega|}\int\limits_{\Omega\setminus\mathrm{V}}w(\mathbf{d}(\mathbf{v}^A))\tag{4.106}$$

This shows that the expansion velocity field $\mathbf{v}^A$ is precisely the one that is associated to a pure hydrostatic stress and that the normal at the macroscopic yield criterion is proportional to the tensor having $(\alpha_1,\alpha_2,\alpha_3)$ on its diagonal.

Note that we have here tacitly assumed that the homogeneous boundary conditions for $\mathbf{v}^A$ do not have off-diagonal components. While this simplification seems reasonable in the case of ellipsoidal voids aligned with the orthotropy directions of the matrix, in the general case we may expect that the normal to the macroscopic yield surface at the hydrostatic point has some non-zero off-diagonal components. In this case, the condition $D_{xy}=D_{xz}=D_{yz}=0$ in the definition (4.106) of the expansion velocity field should be dropped.

Let us now consider some exact points located on the approximate macroscopic yield criterion calculated via the "two-field" approach. The microscopic strain rate is given by:

$$\mathbf{d}=A\mathbf{d}^A+\begin{pmatrix}-\frac{B}{2}-C & D_{xy} & D_{xz}\\ D_{xy} & -\frac{B}{2}+C & D_{yz}\\ D_{xz} & D_{yz} & B\end{pmatrix}=A\mathbf{d}^A+\tilde{\mathbf{d}}\tag{4.107}$$

where $\tilde{\mathbf{d}}$ is a deviatoric tensor that collects all constant strain rate tensors. Let $\tilde{\boldsymbol{\sigma}}=\partial w/\partial\tilde{\mathbf{d}}$ be the stress tensor located on the microscopic yield criterion with normal $\tilde{\mathbf{d}}$. Then, the derivatives of W with respect to A and $\tilde{\mathbf{d}}$ at $A=0$ are:

$$\begin{aligned}\left.\frac{\partial W}{\partial A}\right|_{A=0} &= \frac{1}{|\Omega|}\int\limits_{\Omega\setminus \mathrm{V}} \left.\frac{\partial w}{\partial \mathbf{d}}\right|_{A=0} : \mathbf{d}^A = \tilde{\sigma} : \left(\frac{1}{|\Omega|}\int\limits_{\Omega\setminus \mathrm{V}} \mathbf{d}^A\right) \\ \left.\frac{\partial W}{\partial \tilde{\mathbf{d}}}\right|_{A=0} &= \frac{1}{|\Omega|}\int\limits_{\Omega\setminus \mathrm{V}} \left.\frac{\partial w}{\partial \mathbf{d}}\right|_{A=0} = \frac{\tilde{\boldsymbol{\sigma}}}{|\Omega|}\int\limits_{\Omega\setminus \mathrm{V}} 1 = (1-f)\tilde{\boldsymbol{\sigma}}\end{aligned} \tag{4.108}$$

The mean value of $\mathbf{d}^A$ over the matrix can be calculated using Gauss' theorem:

$$\frac{1}{|\Omega|}\int\limits_{\Omega\setminus V} \mathbf{d}^A = \frac{1}{|\Omega|}\left(\int\limits_{\partial\Omega} \mathbf{v}^A \otimes_s \mathbf{n} - \int\limits_{\partial \mathrm{V}} \mathbf{v}^A \otimes_s \mathbf{n}\right) = \mathbf{D}^A - \mathbf{D}^{A,V} \tag{4.109}$$

Due to the homogeneous strain rate boundary conditions imposed on the boundary of the unit cell, the first tensor on the right hand is simply $\mathbf{D}^A = \mathrm{diag}(\alpha_x, \alpha_y, \alpha_z)$ while the tensor $\mathbf{D}^{A,V} = \mathrm{diag}(\alpha_x^V, \alpha_y^V, \alpha_z^V)$ is related to the mean deformation rate of the void.

Particularizing now (4.108) for $\tilde{\mathbf{d}} = \mathbf{d}^B = \mathrm{diag}(-1/2, -1/2, 1)$, let $\tilde{\boldsymbol{\sigma}}_B$ be the deviatoric stress tensor located on the microscopic yield criterion with normal $\mathbf{d}^B$. Then the following point is located on the macroscopic yield criterion and has also normal $\mathbf{d}^B$:

$$\begin{cases} \Sigma_h = \tilde{\boldsymbol{\sigma}}_B : (\mathbf{D}^A - \mathbf{D}^{A,V}) \\ \mathrm{dev}\boldsymbol{\Sigma} = (1-f)\tilde{\boldsymbol{\sigma}}_B \end{cases} \tag{4.110}$$

Similarly, taking $\tilde{\mathbf{d}} = \mathbf{d}^C = \mathrm{diag}(-1, 1, 0)$ gives a point with normal $\mathbf{d}^C$:

$$\begin{cases} \Sigma_h = \tilde{\boldsymbol{\sigma}}_C : (\mathbf{D}^A - \mathbf{D}^{A,V}) \\ \mathrm{dev}\boldsymbol{\Sigma} = (1-f)\tilde{\boldsymbol{\sigma}}_C \end{cases} \tag{4.111}$$

Finally, the evolution of the void shape and size can be calculated from the mean rate of deformation $\mathbf{D}^{void}$ due to the total velocity field and defined by Eq. (4.46). It is easy to show that by neglecting the off-diagonal components of $\tilde{\boldsymbol{d}}$ we obtain:

$$\mathbf{D}^{void} = \frac{A}{f}\mathbf{D}^{A,V} + B\mathbf{d}^B + C\mathbf{d}^C \tag{4.112}$$

where A, B, C are related to the diagonal components of the macroscopic strain rate $\mathbf{D}$ via Eqs. (4.100).

Summarizing the results obtained so far for an arbitrary microscopic yield criterion, the key element is the cavity expansion velocity field which determines:

- The hydrostatic point on the macroscopic yield criterion and its normal.
- Two points on the approximate macroscopic yield criterion having specified (deviatoric) normals.
- The evolution law for the shape of the void.

The second step in developing Gurson-type yield criteria is to find suitable approximations to reduce the macroscopic dissipation function to the form (4.39) which permits the application of the Gurson lemma (4.40).

Consider first the Yld91 yield criterion where the dissipation function is given by:

$$\begin{aligned} W &= \frac{1}{\Omega}\int\limits_{\Omega/V} \inf_{a} \bar{w}(A\mathbf{d}^A + \tilde{\mathbf{d}}, a) \\ \bar{w}(\mathbf{d}, a) &= \frac{\sigma_1}{3}\left(\left|d'_1 - d'_2 + a\right|^q + \left|d'_2 - d'_3 + a\right|^q + \left|d'_3 - d'_1 + a\right|^q\right)^{\frac{1}{q}} \end{aligned} \tag{4.113}$$

where $\sigma_1 = 2^{1/m}\sigma_0$ is a scaling factor for stresses and d'_1, d'_2, d'_3 are the eigenvalues of the linearly transformed tensor $\mathbf{d}' = \tilde{\mathbf{C}}^{'-T}(A\mathbf{d}^A + \tilde{\mathbf{d}})$. Note that the parameter a over which the infimum is taken in (4.113) should be calculated independently at each point of the matrix and therefore is a variable scalar field. The first approximation is to take the infimum only over *constant* fields $\bar{a}$, so that we can switch the integral and the infimum:

$$W \approx \frac{1}{\Omega}\inf_{\bar{a}} \int\limits_{\Omega/V} \bar{w}(A\mathbf{d}^A + \tilde{\mathbf{d}}, \bar{a}) \tag{4.114}$$

The next step is to reduce the triple integral to a single one over the pseudo-radial variable r and to find a change of variables $x = x(r)$ such that $||\mathbf{d}^A|| = F(x)x$ for some suitable norm for strain rate tensors and where $F(x(r))$ has finite limits when $r \to 0$ and $r \to +\infty$. Other approximations are then needed to arrive at the form (4.39) for the macroscopic dissipation function. Unfortunately, none of these approximations can be justified in our case. For example, there is no simple relationship between the eigenvalues for a sum of two matrices and the eigenvalues of the matrices themselves. Only the change of variable $x = x(r)$ is feasible as it depends only on the geometry of the void and unit cell and the properties of the cavity expansion velocity field $\mathbf{v}^A$. We can therefore use results from (Gologanu et al. 1997) for the spheroidal case and from (Madou and Leblond 2012a) for the ellipsoidal case. Therefore, without further ado, we propose the following approximation:

$$W = \inf_{\bar{a}} \int\limits_{x_1}^{x_2} \left\{\left[(AF + BG_1 + CG_2)\sigma_1 x\right]^q + \left[\bar{w}(\mathbf{H}\tilde{\mathbf{d}}, \bar{a})\right]^q\right\}^{\frac{1}{q}} \frac{dx}{x^2} \tag{4.115}$$

Here F, G_1, G_2 are constants and H is a constant linear transformation from the space of deviatoric tensors into itself, equal to the identity on the off-diagonal components of $\tilde{\mathrm{d}}$ and transforming the on-diagonal components by:

$$(B, C) \rightarrow (H_{11}B + H_{12}C, H_{21}B + H_{22}C) \tag{4.116}$$

The limits of integration are defined by:

$$x_1 = \frac{1}{g+1}, \quad x_2 = \frac{1}{g+f} \tag{4.117}$$

where f is the porosity and g depends only on the geometry of the void and cell.

The justification for all these terms comes from the quadratic isotropic case, where F^2x^2 is an approximation of $\mathbf{d}^A : \mathbf{d}^A$ while the other constants provide an approximation of the two cross-terms $\mathbf{d}^A : \mathbf{d}^B$ and $\mathbf{d}^A : \mathbf{d}^C$.

The linear transformation $\mathbf{H}$ can be written as a product $\mathbf{H} = \tilde{\mathbf{H}}K$ of some invertible matrix and the projection on the deviatoric space. We will need in the sequel the inverse of the transpose of the matrix $\tilde{\mathbf{H}}$ given by:

$$\tilde{\mathbf{H}}^{-T} = \begin{pmatrix} h_{11} & h_{12} & h_{13} & 0 & 0 & 0 \\ h_{21} & h_{22} & h_{23} & 0 & 0 & 0 \\ h_{31} & h_{32} & h_{33} & 0 & 0 & 0 \\ 0 & 0 & 0 & 1 & 0 & 0 \\ 0 & 0 & 0 & 0 & 1 & 0 \\ 0 & 0 & 0 & 0 & 0 & 1 \end{pmatrix} \tag{4.118}$$

where

$$\begin{gathered} h_{22} = \frac{-4C_{21} + 6C_{22} - 3C_{12} + 2C_{11} + 4}{12} \\ h_{23} = \frac{1 - C_{11} + 2C_{21}}{3}, \; h_{32} = \frac{2 - 2C_{11} + 3C_{12}}{6}, \; h_{33} = \frac{1 + 2C_{11}}{3} \\ C_{11} = \frac{H_{11}}{\Delta}, C_{22} = \frac{H_{22}}{\Delta}, C_{12} = -\frac{H_{12}}{\Delta}, C_{21} = -\frac{H_{21}}{\Delta}, \\ \Delta = H_{11}H_{22} - H_{12}H_{21} \end{gathered} \tag{4.119}$$

and all other parameters $h_{11}, h_{12}, h_{13}, h_{21}, h_{23}$ are uniquely determined from the condition that the sum over each row and column of the 3×3 upper left corner of $\tilde{\boldsymbol{H}}^{-T}$ is equal to one.

We can now transfer back the infimum over $\bar{a}$ inside the integral and obtain:

$$W = \int_{x_1}^{x_2} \left\{ [(AF + BG_1 + CG_2)\sigma_1 x]^q + [w(\tilde{\mathbf{H}}\tilde{\mathbf{d}})]^q \right\}^{\frac{1}{q}} \frac{dx}{x^2} \tag{4.120}$$

Finally, using the notations:

$$\bar{A} = (AF + BG_1 + CG_2)\sigma_1, \quad \bar{B} = w(\tilde{\mathbf{H}}\tilde{\mathbf{d}}) \tag{4.121}$$

we obtain the following expression for the macroscopic dissipation:

$$W(\bar{A},\bar{B}) = \int_{x_1}^{x_2} (\bar{A}^q x^q + \bar{B}^q)^{\frac{1}{q}} \frac{dx}{x^2} \tag{4.122}$$

For the quadratic case $m = q = 2$ this is precisely the form required by Gurson's lemma (4.40). In the non-quadratic case, the integral is resoluble by elementary means only when m is a natural number. Introducing a new parameter μ and a change of variables defined by:

$$\mu = \frac{|\bar{B}|}{\bar{A}}, \quad y = \operatorname{sgn}\mu \frac{(x^q + |\mu|^q)^{(q-1)/q}}{x^{q-1}} \tag{4.123}$$

we obtain for the derivatives of W:

$$\frac{\partial W}{\partial \bar{A}} = \frac{\operatorname{sgn}\mu}{1-q} \int_{y_1}^{y_2} \frac{y^{m-2}dy}{y^m - 1}, \quad \frac{\partial W}{\partial \bar{B}} = \frac{\operatorname{sgn}\bar{B}}{|\mu|(1-q)} \int_{y_1}^{y_2} y^{m-2}dy \tag{4.124}$$

While the second integral is elementary for all values of m, the first one $S_m(y)$ is elementary[3] only when m is a natural number. For selected values we obtain:

$$\begin{gathered} S_2(y) = \tfrac{1}{2}\ln\tfrac{y+1}{y-1}, \quad S_4(y) = \tfrac{3}{4}\ln\tfrac{y+1}{y-1} - \tfrac{3}{2}\tan^{-1} y \\ S_6(y) = \tfrac{5}{12}\ln\tfrac{(y+1)^2(y^2+y+1)}{(y-1)^2(y^2-y+1)} + \tfrac{5}{2\sqrt{3}}\tan^{-1}\tfrac{\sqrt{3}y}{y^2-1} \\ S_8(y) = \tfrac{7}{8\sqrt{2}}\ln\tfrac{y^2+\sqrt{2}y+1}{y^2-\sqrt{2}y+1} + \tfrac{7\sqrt{2}}{8}\tan^{-1}\tfrac{\sqrt{2}y}{y^2-1} \\ + \tfrac{7}{8}\ln\tfrac{y+1}{y-1} - \tfrac{7}{4}\tan^{-1} y \end{gathered} \tag{4.125}$$

Similar to the proof of Gurson's lemma, the macroscopic yield criterion in parametric form can be obtained via the following receipt: relate the derivatives of W with respect to $A, B, C, D_{xy}, D_{xz}, D_{yz}$, to the macroscopic stresses via (4.103) and to the derivatives of W with respect to $\bar{A}, \bar{B}$ via (4.121). However, in our case we need to generalize a key technical point from the quadratic case to that of an arbitrary yield surface $\varphi(\boldsymbol{\sigma}) = \sigma_1$ defined by a homogeneous function of degree 1 and with dissipation function $w(\mathbf{d})$. The simplest case still showing this difficulty is one where the yield surface is isotropic, the macroscopic strain rate and stress tensors are diagonal and the cross terms are neglected in (4.121):

$$W = W(\bar{A},\bar{B}), \quad \bar{A} = FA, \bar{B} = w(\tilde{\mathbf{d}}), \quad \tilde{\mathbf{d}} = B\mathbf{d}^B + C\mathbf{d}^C \tag{4.126}$$

where the diagonal tensors $\mathbf{d}^B, \mathbf{d}^C$ are defined in (4.103). Then we have:

[3]For arbitrary values of the exponent, this integral is expressible as a hypergeometric function.

$$\begin{array}{c} \frac{\partial W}{\partial B} = \frac{\partial W}{\partial B}\left(\tilde{\boldsymbol{\sigma}} : \mathbf{d}^B\right), \quad \frac{\partial W}{\partial C} = \frac{\partial W}{\partial B}\left(\tilde{\boldsymbol{\sigma}} : \mathbf{d}^C\right), \quad \tilde{\boldsymbol{\sigma}} \equiv \frac{\partial w}{\partial \mathbf{d}} \\ \mathrm{dev}\boldsymbol{\Sigma} \equiv \frac{\partial W}{\partial B}\mathbf{Q}_1 + \frac{\partial W}{\partial C}\mathbf{Q}_2 = \frac{\partial W}{\partial B}\tilde{\boldsymbol{\sigma}}, \quad \varphi(\mathrm{dev}\boldsymbol{\Sigma}) = \left|\frac{\partial W}{\partial B}\right|\sigma_1 \end{array} \tag{4.127}$$

where the stress $\tilde{\boldsymbol{\sigma}}$ in the first line lies on the on yield surface, and where, in the second line, we have used the linear homogeneity of φ. Here the tensors $\mathbf{Q}_1, \mathbf{Q}_2$ are the duals $\mathbf{d}^B, \mathbf{d}^C$ and are given by:

$$\begin{array}{c} \mathbf{Q}_1 = -\frac{1}{3}\left(\mathbf{e}_x \otimes \mathbf{e}_x + \mathbf{e}_y \otimes \mathbf{e}_y\right) - \frac{2}{3}\mathbf{e}_z \otimes \mathbf{e}_z, \\ \mathbf{Q}_2 = -\frac{1}{2}\mathbf{e}_x \otimes \mathbf{e}_x + \frac{1}{2}\mathbf{e}_y \otimes \mathbf{e}_y. \end{array} \tag{4.128}$$

The same method applied to the general case gives the sought after macroscopic criterion in parametric form:

$$\begin{cases} k\Sigma_h \equiv k(\alpha_1\Sigma_{11} + \alpha_2\Sigma_{22} + \alpha_3\Sigma_{33}) = \sigma_1 \,\mathrm{sgn}\,\mu[S_m(y_2) - S_m(y_1)] \\ \left(|s'_1 - s'_2|^m + |s'_2 - s'_3|^m + |s'_3 - s'_1|^m\right)^{\frac{1}{m}} = \frac{\sigma_1}{|\mu|}\left(y_1^{m-1} - y_2^{m-1}\right) \end{cases} \tag{4.129}$$

where $\sigma_1 = 2^{1/m}\sigma_0, k = \frac{1}{F}, \eta_1 = \frac{G_1}{F}, \eta_2 = \frac{G_2}{F}$ and s'_1, s'_2, s'_3 are the eigenvalues of the following linearly transformed tensor of the macroscopic stresses:

$$\boldsymbol{\Sigma}' = \tilde{\mathbf{H}}^{-T}\tilde{\mathbf{C}}'(\mathrm{dev}\boldsymbol{\Sigma} - \eta_1\Sigma_h\mathbf{Q}_1 - \eta_2\Sigma_h\mathbf{Q}_2) \tag{4.130}$$

We recall that the linear transformation $\tilde{\mathbf{C}}'$ is given by Eq. (4.52) as a function of the original linear transformation $\mathbf{C}'$ appearing in the Yld91 yield criterion. Finally, $S_m(y)$ is defined in (4.125) for several values of m and:

$$y_i = \frac{\left(x_i^q + |\mu|^q\right)^{(q-1)/q}}{x_i^{q-1}}, x_1 = \frac{1}{1+g}, x_2 = \frac{1}{g+f} \tag{4.131}$$

In the quadratic case, we can eliminate the parameter μ from (4.129) and obtain:

$$\frac{\varphi^2(\lambda(\boldsymbol{\Sigma}'))}{\sigma_1^2} + 2(g+1)(g+f)\cosh\frac{k\Sigma_h}{\sigma_1} - (g+1)^2 - (g+f)^2 = 0 \tag{4.132}$$

In the general case this is no longer possible and we are forced to use the parametric form. We still need to prescribe the parameters of the model: the factor k multiplying the pressure-dependent stress Σ_h, the two factors η_1, η_2 in front of the cross terms in (4.130), the coefficients $\alpha_1, \alpha_2, \alpha_3 = 1 - \alpha_1 - \alpha_2$ defining Σ_h via (4.103), the parameter g and the coefficients $C_{11}, C_{22}, C_{12}, C_{21}$ defining the linear tensor $\tilde{\mathbf{H}}^{-T}$ via (4.119). As discussed above, the choice of the expansion velocity field $\mathbf{v}^A$ determines three points located on the yield criterion (the hydrostatic stress and those defined by (4.110) and (4.111)). These 3 points together with their normal to the yield criterion give nine conditions to be satisfied by the nine parameters

above. We will discuss in the next section how to find, via a spectral method, the expansion velocity field in the case of an arbitrary microscopic yield criterion and for a general ellipsoidal void. We call this a numerical calibration of the Gurson model.

Note that the effect of the voids on the macroscopic yield criterion (4.129) is twofold. First, the original anisotropy given by the linear transformation $\mathbf{C}'$ is amended to $\tilde{\mathbf{H}}^{-T}\tilde{\mathbf{C}}'$; this can be interpreted as a supplementary anisotropy due to the void geometry. Second, there is a pressure-dependent term Σ_h affecting in multiple ways the yield criterion. The exponent m affects the Gurson-type criterion via the function $S_m(y)$. A subtler effect is visible in Fig. 4.6 where we compare, for several values of m, Gurson-type isotropic yield criteria of the form (4.129), with $\eta_1 = \eta_2 = C_{12} = C_{21} = g = 0$, $C_{11} = C_{22} = 1$, $k = \frac{3}{2}, \alpha_i = \frac{1}{3}$ and a porosity $f = 0.01$. Note that for larger values of the exponent the yield surface shows flatter regions joined by a high curvature region.

The case of the Yld2004-18p is similar and does not present any new difficulty. The multiple infimum appearing in the expression (4.78) of the dissipation function is again pushed out of the integral by assuming all fields constant. Later, the infimum is pushed back inside the integral so that this takes precisely the form (4.120) but expressed via the Yld2004-18p dissipation function. The final result is again the parametric form:

$$\begin{cases} k\Sigma_h \equiv k(\alpha_1\Sigma_{11} + \alpha_2\Sigma_{22} + \alpha_3\Sigma_{33}) = \sigma_1 \operatorname{sgn}\mu[S_m(y_2) - S_m(y_1)] \\ \varphi(\lambda(\boldsymbol{\Sigma}'), \lambda(\boldsymbol{\Sigma}'')) = \frac{\sigma_1}{|\mu|}\left(y_1^{m-1} - y_2^{m-1}\right) \end{cases} \tag{4.133}$$

where $\sigma_1 = 4^{1/m}\sigma_0$, φ is the homogeneous function of degree 1 implicitly defined by the Yld2004-18p criterion (4.51) and $\lambda(\boldsymbol{\Sigma}'), \lambda(\boldsymbol{\Sigma}'')$ are the eigenvalues of two linearly transformed tensors of the macroscopic stresses:

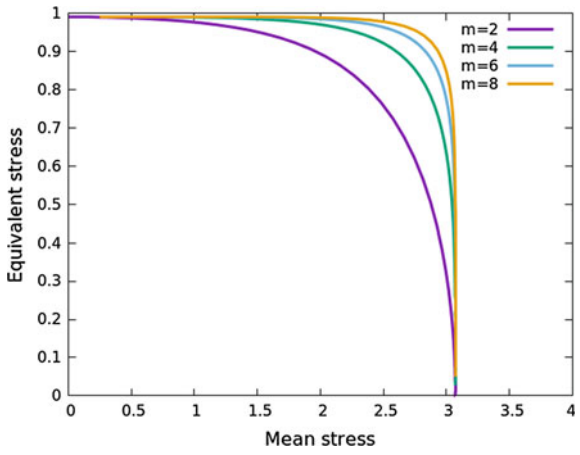

Fig. 4.6 Quadratic $m = 2$ versus non-quadratic $m > 2$ Gurson-type yield surfaces for an isotropic material with spherical voids and porosity 0.01

$$\begin{aligned}\boldsymbol{\Sigma}' &= \tilde{\mathbf{H}}^{-T}\tilde{\mathbf{C}}'(\mathrm{dev}\boldsymbol{\Sigma} - \eta_1\Sigma_h\mathbf{Q}_1 - \eta_2\Sigma_h\mathbf{Q}_2)\\ \Sigma'' &= \tilde{\mathbf{H}}^{-T}\tilde{\mathbf{C}}''(\mathrm{dev}\boldsymbol{\Sigma} - \eta_1\Sigma_h\mathbf{Q}_1 - \eta_2\Sigma_h\mathbf{Q}_2)\end{aligned} \tag{4.134}$$

Here, all other parameters have similar definitions as for the Yld91 criterion.

Consider now the BBC2005 yield criterion defined by Eqs. (4.79) and (4.80) with dissipation function given by Eqs. (4.96) and (4.97). The development of the Gurson-type model is again similar to the Yld91 case and will not be further detailed here. The final Gurson model is given in parametric form by:

$$\begin{cases} k\Sigma_h \equiv k(\alpha_1\Sigma_{11} + \alpha_2\Sigma_{22} + \alpha_3\Sigma_{33}) = \sigma_0\,\mathrm{sgn}\,\mu[S_m(y_2) - S_m(y_1)] \\ \Big[a\big(\tilde{\Lambda}+\tilde{\Gamma}\big)^m + a\big(\tilde{\Lambda}-\tilde{\Gamma}\big)^m + b\big(\tilde{\Lambda}+\tilde{\Psi}\big)^m + \\ \qquad + b\big(\tilde{\Lambda}-\tilde{\Psi}\big)^m + c\sigma_{13}^m + c\sigma_{23}^m\Big]^{1/m} = \frac{\sigma_0}{|\mu|}\big(y_1^{m-1} - y_2^{m-1}\big) \end{cases} \tag{4.135}$$

where $S_m(y)$ is defined by (4.125) and y_1, y_2 by (4.131). Here, the new variables $\tilde{\Gamma}, \tilde{\Lambda}, \tilde{\Psi}$ depend on the components of a deviatoric stress tensor $\tilde{\boldsymbol{\Sigma}}$ defined in terms of the macroscopic stress tensor by:

$$\tilde{\boldsymbol{\Sigma}} = \mathrm{dev}\boldsymbol{\Sigma} - \eta_1\Sigma_h\mathbf{Q}_1 - \eta_2\Sigma_h\mathbf{Q}_2 \tag{4.136}$$

with $\mathbf{Q}_1, \mathbf{Q}_2$ defined by Eqs. (4.128). The expressions for $\tilde{\Gamma}, \tilde{\Lambda}, \tilde{\Psi}$ are:

$$\begin{aligned}\tilde{\Gamma} &= \tilde{L}\big(\tilde{\Sigma}_{11} - \tilde{\Sigma}_{33}\big) + \tilde{M}\big(\tilde{\Sigma}_{22} - \tilde{\Sigma}_{33}\big)\\ \tilde{\Lambda} &= \sqrt{\big[\tilde{N}\big(\tilde{\Sigma}_{11} - \tilde{\Sigma}_{33}\big) - \tilde{P}\big(\tilde{\Sigma}_{22} - \tilde{\Sigma}_{33}\big)\big]^2 + \tilde{\Sigma}_{12}\tilde{\Sigma}_{21}}\\ \tilde{\Psi} &= \sqrt{\big[\tilde{Q}\big(\tilde{\Sigma}_{11} - \tilde{\Sigma}_{33}\big) - \tilde{R}\big(\tilde{\Sigma}_{22} - \tilde{\Sigma}_{33}\big)\big]^2 + \tilde{\Sigma}_{12}\tilde{\Sigma}_{21}}\end{aligned} \tag{4.137}$$

The new parameters $\tilde{L}, \tilde{M}, \tilde{N}, \tilde{P}, \tilde{R}, \tilde{Q}, \tilde{R}$ are related to the original parameters of the BBC2005 criterion by the following relationship:

$$\begin{pmatrix} \tilde{L} & \tilde{M} & -\tilde{L}-\tilde{M} \\ \tilde{N} & -\tilde{P} & -\tilde{N}+\tilde{P} \\ \tilde{Q} & -\tilde{R} & -\tilde{Q}+\tilde{R} \end{pmatrix} = \begin{pmatrix} h_{11} & h_{12} & h_{13} \\ h_{21} & h_{22} & h_{23} \\ h_{31} & h_{32} & h_{33} \end{pmatrix} \begin{pmatrix} L & M & -L-M \\ N & -P & -N+P \\ Q & -R & -Q+R \end{pmatrix} \tag{4.138}$$

where the coefficients h_{ij} are given by Eqs. (4.119). Note that actually the matrix (h_{ij}) is the upper left corner of $\tilde{\mathbf{H}}^{-T}$ and that it depends on only four parameters $C_{11}, C_{22}, C_{12}, C_{21}$. We still need to specify these four parameters and also the other parameters of the Gurson type criterion: $k, \alpha_1, \alpha_2, \alpha_3, \eta_1, \eta_2, g$. All these parameters will be determined during the calibration of the Gurson model using a spectral numerical method.

As a preliminary conclusion, we have found analytical Gurson type approximations (in parametric form) for porous materials, containing spherical, spheroidal and ellipsoidal voids and with the matrix having a rigid-plastic behaviour defined by the advanced, non-quadratic, anisotropic yield criteria Yld91, Yld2004-18p and BBC2005. These models still need to be calibrated, which means finding numerically via a spectral method a "good" velocity field describing the expansion of the void and using it to calculate some of the parameters of the Gurson models.

Note that although the dissipation functions for all three yield criteria were so complicated that we were not able to fully justify some of the approximations made to arrive at a Gurson-type criterion, their analytical expressions played a paramount role in defining the function S_m or the pressure-dependent term in the Gurson models (4.129), (4.133) and (4.135).

4.4 Mie Decomposition of Incompressible Vector Fields in Ellipsoidal Coordinates

We have seen that one essential ingredient in developing and calibrating Gurson type models was the Lee and Mear (1992) family of axisymmetric incompressible fields for prolate and oblate spheroidal voids. The recent Gurson type models for general ellipsoidal voids (both von Mises isotropic plasticity and Hill anisotropic plasticity) were based on the discovery in (Leblond and Gologanu 2008) of a velocity field describing the expansion of such voids and respecting conditions of homogeneous strain rate on every ellipsoid confocal with the cavity. However, this field (when added to some uniform strain rate incompressible field as in the original two-field approach used by Gurson), does not provide alone a very accurate description of the cavity expansion under various loading conditions and material properties. We have seen that an essential step is the *calibration* of a new Gurson type model by some semi-empirical method. Practically, key parameters in the Gurson model are fitted on numerical results obtained for the same elementary representative volume. Spectral methods are fast and accurate; unfortunately they require velocity fields respecting both the incompressibility condition and the boundary conditions. In absence of these, recent work by Madou and Leblond (2012b) has used the finite element method to calibrate their Gurson-type model, albeit with a clever hack to simulate limit analysis problems with isotropic or Hill plasticity via elasto-plastic solvers. For the moment we do not know how to extend these finite element methods to other models of anisotropic plasticity.

In the next section we present a complete solution for the missing tools needed to calibrate new Gurson type models. First we obtain a complete family of incompressible velocity fields for general ellipsoidal voids that extends that of Lee and Mear (1992) which was limited to spheroidal voids and axisymmetric conditions. Second we extend the spectral numerical method to an arbitrary anisotropic plasticity model.

4.4.1 Natural Ellipsoidal Coordinates

Ellipsoidal coordinates were discovered by Lamé when searching for closed-form solutions for geodesics on the surface of an ellipsoid.

Consider a reference ellipsoid with semi-axes (a, b, c), ordered such that:

$$a > b > c. \tag{4.139}$$

For the moment we require strict inequalities, but in the sequel these will be relaxed. We choose Cartesian coordinates (x, y, z) aligned with the ellipsoid's axis; the ellipsoid's surface is then defined by the equation:

$$\frac{x^2}{a^2} + \frac{y^2}{b^2} + \frac{z^2}{c^2} = 1. \tag{4.140}$$

For any value of t, the surface defined by:

$$\frac{x^2}{t+a^2} + \frac{y^2}{t+b^2} + \frac{z^2}{t+c^2} = 1, \tag{4.141}$$

represents a quadric *conformal* with the initial ellipsoid. After rearrangement, we obtain a cubic equation for t:

$$\begin{aligned} S(t) = (t+a^2)(t+b^2)(t+c^2) - x^2(t+b^2)(t+c^2) \\ - y^2(t+a^2)(t+c^2) - z^2(t+a^2)(t+b^2) = 0 \end{aligned} \tag{4.142}$$

Inspection of the sign of $S(t)$ at $t = -a^2, -b^2, -c^2$ and ∞ shows that the cubic always has three real and distinct roots (λ, μ, ν) located in between these values:

$$\lambda \geq -c^2 \geq \mu \geq -b^2 \geq \nu \geq -a^2 \tag{4.143}$$

Writing $S(t) = (t-\lambda)(t-\mu)(t-\nu)$, inserting in turn $t = -a^2, -b^2, -c^2$ and solving for x^2, y^2, z^2 we obtain:

$$\begin{cases} x^2 = \frac{(a^2+\lambda)(a^2+\mu)(a^2+\nu)}{(a^2-c^2)(a^2-b^2)} \\ y^2 = \frac{(b^2+\lambda)(b^2+\mu)(b^2+\nu)}{(b^2-c^2)(b^2-a^2)} \\ z^2 = \frac{(c^2+\lambda)(c^2+\mu)(c^2+\nu)}{(c^2-b^2)(c^2-a^2)} \end{cases} \tag{4.144}$$

These relations connect Cartesian coordinates to curvilinear ones (λ, μ, ν). Through any point in space there passes three mutually orthogonal surfaces: one ellipsoid ($\lambda = \text{cst.}$), one hyperboloid with one sheet ($\mu = \text{cst.}$) and one hyperboloid with two sheets ($\nu = \text{cst.}$).

There are two problems with these classical ellipsoidal coordinates. First, the relationship (4.144) is not one-to-one as there are in general 8 different points in space having the same (λ, μ, ν). To solve this, Hermite introduced *uniformising* variables by expressing the algebraic relationships (4.144) in terms of Jacobian elliptic functions of three new variables. Modern mathematical treatments like Arscott (1964) tend to use them extensively.

Second, Eqs. (4.144) become degenerate in the limit of axisymmetric ellipsoids —oblate spheroids $(a = b)$, prolate ones $(b = c)$ and spheres. Imagine now a void that starts with a prolate/oblate/spherical shape or evolves arbitrary close to such one. This will correspond to various $0/0$ limits or other degeneracies and any analytical or numerical method will need to devise special methods to treat them.

We now follow Tabanov (1998), Burnett and Holford (1998) and introduce "natural" variables (r, θ, ϕ) defined by:

$$\begin{aligned} \lambda &= r^2 - c^2 \\ \mu &= -b^2 \cos^2\theta - c^2 \sin^2\theta \\ \nu &= -b^2 \cos^2\phi - a^2 \sin^2\phi \end{aligned} \tag{4.145}$$

in terms of which the relationships (4.144) become:

$$\begin{cases} x = (r^2 + h_1^2 + h_2^2)^{1/2}(1 - k'^2 cos^2\theta)^{1/2} \cos\phi \\ y = (r^2 + h_2^2)^{1/2} \sin\theta \, \sin\phi \\ z = r \, \cos\theta(1 - k^2 \cos^2\phi)^{1/2} \end{cases} \tag{4.146}$$

where:

$$h_1^2 = a^2 - b^2 \quad h_2^2 = b^2 - c^2 \quad k = \left(\frac{h_1^2}{h_1^2 + h_2^2}\right)^{1/2} \quad k' = (1 - k^2)^{1/2} \tag{4.147}$$

We note the striking similarity of the new coordinates to spherical (polar) ones, with r playing the role of the radial variable and θ, ϕ those of angular ones. Surfaces of constant r are ellipsoids, those of constant θ are hyperboloids with one sheet and those of constant ϕ are hyperboloids with two sheets, all being confocal with the reference ellipsoid. Taking $r = 0$, we obtain the double face parametrization of the focal ellipse in the $z = 0$ plane with demi-axes h_2, $(h_1^2 + h_2^2)^{1/2}$.

In order to have a one-to-one correspondence between points in space x, y, z and coordinates r, θ, ϕ, we have two choices for the ranges of the new variables, either:

$$0 \leq r < +\infty, \quad 0 \leq \theta \leq \pi, \quad 0 \leq \phi \leq 2\pi, \tag{4.148}$$

or:

$$0 \leq r < +\infty, \quad 0 \leq \theta \leq 2\pi, \quad 0 \leq \phi \leq \pi. \tag{4.149}$$

We can now lift the restriction of strict inequalities in (4.139) for the reference ellipsoid. The oblate spheroidal case corresponds to the direct substitution $h_1 = 0$ with $k = 0,\ k' = 1$. Then the relationships (4.146) reduce to:

$$\begin{cases} x = (r^2 + h_2^2)^{1/2} \sin\theta \cos\phi \\ y = (r^2 + h_2^2)^{1/2} \sin\theta \sin\phi \\ z = r \cos\theta \end{cases} \tag{4.150}$$

These are equivalent to the classical oblate spheroidal coordinates if we replace the radial coordinate with a new one given by $r = h_2 \sinh\lambda$ and use (4.148).

The prolate spheroidal case corresponds to $h_2 = 0$ with $k = 1,\ k' = 0$. The relationships (4.146) reduce to:

$$\begin{cases} x = (r^2 + h_1^2)^{1/2} \cos\phi \\ y = r \sin\theta \sin\phi \\ z = r \cos\theta \sin\phi \end{cases} \tag{4.151}$$

Again, these are equivalent to classical prolate spheroidal coordinates, if we replace the radial coordinate with $r = h_1 \sinh\lambda$ and use (4.149). Finally the spherical case can be obtained by taking $h_2 = 0$ in the oblate case (4.150) or $h_1 = 0$ in the prolate one (4.151). Several remarks are here in order:

1. The main driving idea in Tabanov is that of preservation of spheroidal limits by simple substitution. While many of the subsequent developments could have been presented using classical ellipsoidal coordinates, we have found that using Tabanov's main idea simplifies and clarifies many arguments.
2. The classical ellipsoidal coordinates (4.144) are symmetric with respect to concomitant permutations of (x, y, z) and (a, b, c); the natural coordinates do break this symmetry. In reality, for problems formulated for the inside or the outside of some ellipsoid, we will see that the new natural coordinates preserve the only existing symmetry, the one between angular coordinates.
3. Contrary to the classical oblate and prolate spheroidal coordinates where one uses the focal distance to scale the radial coordinate (which makes the spherical case a degenerate one), we do not use here any scaling. Practically, one can use for all "length" type variables r, h_1, h_2 a fixed scaling that does not depend on the shape of the reference ellipsoid.
4. The definitions (4.147) for k, k' becomes degenerate when h_1, h_2 tend simultaneously to zero while their ratio tends to a finite limit. Then we obtain new natural variables for the well-known sphero-conical orthogonal coordinates (see

Morse and Feschbach 1953). In other words, the polar spherical limit can be recovered by simple substitution only when passing first through either the oblate or the prolate spheroidal cases. We will later see that this poses no significant problem.

4.4.2 Laplace's Equation in Natural Ellipsoidal Coordinates

For a curvilinear coordinate system with local coordinates ξ, the basis of tangent vectors is defined by $\mathrm{g}_\alpha = \frac{\partial \mathrm{r}}{\partial \xi^\alpha}$ with r the position vector. Components of a vector field in this basis $\mathrm{v} = v^\alpha \mathrm{g}_\alpha$ are called contravariant,[4] while those with respect to the dual basis $\mathrm{v} = v_\alpha \mathrm{g}^\alpha$ are called covariant components. For orthogonal coordinate system where the matrix of scalar products $\langle \boldsymbol{g}_\alpha, \boldsymbol{g}_\beta \rangle = h_\alpha^2 \delta_{\alpha\beta}$ is diagonal, the terms h_α are called Lamé coefficients and there is a preference to use as basis the normalized tangent vectors defined by $\mathrm{e}_\alpha = \frac{1}{h_\alpha}\mathrm{g}_\alpha = h_\alpha \mathrm{g}^\alpha$. Components of a vector field in this basis $v = v^\alpha \mathrm{e}_\alpha$ are called physical components and there is no distinction between upper and lower indices (as the physical basis e_α is orthonormal it is equivalent to its dual). Unless otherwise stated we will use physical components.

Now, it is straightforward to show (see Tabanov) that the curvilinear coordinate system defined by (4.146) with $\xi = (r, \theta, \phi)$ is orthogonal. The Lamé coefficients are readily calculated:

$$\begin{aligned} h_r^2 &= \frac{(r^2 + h_2^2 \cos^2\theta)(r^2 + h_2^2 + h_1^2 \sin^2\phi)}{(r^2 + h_2^2)(r^2 + h_1^2 + h_2^2)} \\ h_\theta^2 &= \frac{(r^2 + h_2^2 \cos^2\theta)(k^2 \sin^2\phi + k'^2 \sin^2\theta)}{1 - k'^2 \cos^2\beta} \\ h_\phi^2 &= \frac{(r^2 + h_2^2 + h_1^2 \sin^2\phi)(k^2 \sin^2\phi + k'^2 \sin^2\theta)}{1 - k^2 \cos^2\phi} \end{aligned} \tag{4.152}$$

Motivated by these expression, we introduce the following notations:

$$\begin{gathered} m_1 = (k^2 \sin^2\phi + k'^2 \sin^2\theta)^{1/2}, \quad m_2 = (r^2 + h_2^2 + h_1^2 \sin^2\phi)^{1/2} \\ m_3 = (r^2 + h_2^2 \cos^2\beta)^{1/2} \\ s_\theta = \sqrt{1 - k'^2 \cos^2\theta}, \quad s_\phi = \sqrt{1 - k^2 \cos^2\phi} \\ s_r = (r^2 + h_2^2)^{1/2}(r^2 + h_1^2 + h_2^2)^{1/2} \end{gathered} \tag{4.153}$$

The Laplace equation in the new coordinate system is given by:

[4] Hereafter we use the usual convention of summing over repeated indices.

$$\frac{\partial}{\partial r}\left(\frac{h_\theta h_\phi}{h_r}\frac{\partial \Phi}{\partial r}\right)+\frac{\partial}{\partial \theta}\left(\frac{h_r h_\phi}{h_\theta}\frac{\partial \Phi}{\partial \theta}\right)+\frac{\partial}{\partial \phi}\left(\frac{h_\theta h_r}{h_\phi}\frac{\partial \Phi}{\partial \phi}\right)=0 \tag{4.154}$$

It admits solutions found by separation of variables $\Phi = U(r)V(\theta)W(\phi)$:

$$\begin{gathered}\left[s_r\partial_r(s_r\partial_r)+c_1(h_1^2+h_2^2)-c_2(r^2+h_2^2)\right]U=0\\ \left[s_\theta\partial_\theta(s_\theta\partial_\theta)-c_1+c_2k'^2\sin^2\theta\right]V=0\\ \left[s_\phi\partial_\phi\left(s_\phi\partial_\phi\right)+c_1+c_2k^2\sin^2\phi\right]W=0\end{gathered} \tag{4.155}$$

where c_1, c_2 are separation constants. These three second-order ordinary differential equations are all equivalent to Lamé's equation (see Arscott 1964) which itself has several useful forms: the first an algebraic one, while the last two are equivalent to Ince's trigonometric form. Other widely used forms are the Jacobian and Weierstrassian ones.

The usual way of solving these differential equations is to bring them to a common form. For example, using the following changes of variable: $h_1^2t^2 = r^2+h_1^2+h_2^2$ for the first differential equation, $k^2t^2 = 1-k'^2\cos^2\theta$ for the second one and $t=\cos\phi$ for the third one, all three reduce to the following form:

$$\left[(t^2-1)(k^2t^2-1)\partial_t^2+t(1+k^2-k^2t^2)\partial_t+h-c_2k^2t^2\right]X(t)=0 \tag{4.156}$$

where $h = c_1+c_2k^2$ is another separation constant. This is precisely the algebraic form used by Dobner and Ritter (1998) and later by Garmier and Barriot (2001) (in a different but equivalent form) and represents the foundation for all recent numerical implementations of Lamé functions.

However, the problem with this approach is that the first and second changes of variables (those for r and θ) become degenerate in the spheroidal limits and only the third one (that for ϕ) behaves reasonably. On the contrary, the differential equations in the form (4.155) respect Tabanov's principle—they reduce to the spheroidal limits by simple substitution.

For example, in the oblate case where $h_1 = 0, k = 0, k' = 1$, the differential Eqs. (4.155) reduce to:

$$\begin{gathered}\left(\partial_r^2+\frac{r}{\sqrt{r^2+h_2^2}}\partial_r+\frac{c_1h_2^2}{r^2+h_2^2}-c_2\right)U=0\\ \left(\partial_\theta^2+\frac{\cos\theta}{\sin\theta}\partial_\theta-\frac{c_1}{\sin^2\theta}+c_2\right)V=0\\ \left(\partial_\phi^2+c_1\right)W=0\end{gathered} \tag{4.157}$$

Here we recognize in the second equation the trigonometric form of Legendre's associated differential equation while the last one has a simple trigonometric solution. Together they imply that the separation constants are given by $c_2 = n(n+1)$ and $c_1 = m^2$ where $n, 0\le m\le n$ are integers. With regard to the first equation, it represents an unusual form of the same Legendre's differential equation, one that

respects Tabanov's principle for the spherical limit. Indeed, plugging $h_2 = 0$ directly in $(4.157)_1$ and solving, we get correctly the solid spherical harmonics:

$$\Psi_{\text{sph}} = r^n P_n^m(\cos\theta)\begin{pmatrix}\cos m\phi\\ \sin m\phi\end{pmatrix} \tag{4.158}$$

In the general oblate spheroidal case defined by $(4.157)_1$, one usually makes a new change of variable $h_2 z = ir$ to obtain the following well-known expression for solid oblate spheroidal harmonics (of the first kind):

$$\Psi_{\text{obl}} = P_n^m(z)P_n^m(\cos\theta)\begin{pmatrix}\cos m\phi\\ \sin m\phi\end{pmatrix}, \quad z = \frac{ir}{h_2} \tag{4.159}$$

Unfortunately, this change of variable does not respect Tabanov's principle and does not give the spherical limit for a direct substitution $h_2 = 0$. We note that a similar analysis can be made for the prolate case.

In conclusion, even for the oblate and prolate cases, we prefer a treatment based on the unusual form (4.157) that respects Tabanov's principle.

4.4.3 *Some Properties of Surface Ellipsoidal Harmonics*

We list now some important properties of Lamé functions. First, the three differential Eqs. (4.155) admit polynomial solutions[5] in r, $\cos\theta$ and $\cos\phi$ respectively, iff the second separation constant is taken as:

$$c_2 = n(n+1) \tag{4.160}$$

where n is an integer. For each such n there are $m = 1, \cdots, 2n+1$ solutions for the other separation variable c_1 and therefore $2n+1$ linearly independent solutions for each of the differential equations in (4.155). These give rise to $2n+1$ normal solutions to Laplace's equation:

$$\Psi_{\text{ell}} = E_n^m(r)E_n^m(\cos\theta)E_n^m(\cos\phi) \tag{4.161}$$

These are called solid ellipsoidal harmonics of the first kind. We note the similarity of these harmonics with the spherical ones given by (4.158) and oblate ones given by (4.159). There is a deeper reason for this similarity—in all these cases, the solid harmonics of degree n are nothing else but harmonic polynomials[6] of total degree n in the Cartesian coordinates (x, y, z).

[5]Multiplied by some leading terms involving square roots.

[6]These polynomials are also homogeneous only in the spherical case.

We will need two results concerning the surface ellipsoidal harmonics. These are defined by:

$$Y_n^m(\theta,\phi) = E_n^m(\cos\theta)E_n^m(\cos\phi) \tag{4.162}$$

and are similar to the surface spherical harmonics. First, they are orthogonal on the surface $S(r = \text{cst.})$ of every ellipsoid confocal with the reference ellipsoid, with respect to a certain weight measure:

$$\iint_{S(r)} \frac{Y_{n_1}^{m_1} Y_{n_2}^{m_2}}{\sqrt{r^2 + h_2^2\cos^2\theta}\sqrt{r^2 + h_2^2 + h_1^2\sin^2\phi}} dS = \gamma_{n_1}^{m_1}\delta_{m_1 m_2}\delta_{n_1 n_2} \tag{4.163}$$

where γ_n^m are some normalization constants. This can be proven by applying Green's theorem to the harmonic functions $E_{n_1}^{m_1}(r)Y_{n_1}^{m_1}$ and $E_{n_2}^{m_2}(r)Y_{n_2}^{m_2}$ in the interior of the ellipsoid $S(r)$, noting that the derivative with respect to the surface normal n is $\partial_n = \partial_r/h_r$ and finally using the linear independence of $E_{n_1}^{m_1}(r), E_{n_2}^{m_2}(r)$.

Using now the definition of the surface measure $dS = h_\theta h_\phi d\theta d\phi$ we obtain from (4.163) the following orthogonality property that does not involve the radial coordinate r any more:

$$\int_{\theta=0}^{\pi}\int_{\phi=0}^{2\pi} \frac{Y_{n_1}^{m_1} Y_{n_2}^{m_2}(k^2\sin^2\phi + k'^2\sin^2\theta)}{\sqrt{1-k'^2\cos^2\theta}\sqrt{1-k^2 cos^2\phi}} d\theta d\phi = \gamma_{n_1}^{m_1}\delta_{m_1 m_2}\delta_{n_1 n_2} \tag{4.164}$$

The second property we need is that the surface ellipsoidal harmonics $Y_n^m(\theta,\phi)$ are the eigenvectors of a certain second order differential operator acting on the surface of the ellipsoid. This is similar to the spherical case, where it is well known that surface harmonics are eigenvectors of the angular or surface Laplacian:

$$L_{\text{sph}}^2 Y_n^m = n(n+1)Y_n^m \tag{4.165}$$

where

$$L_{sph}^2 = -\frac{1}{\sin\theta}\frac{\partial}{\partial\theta}\left(\sin\theta\frac{\partial}{\partial\theta}\right) - \frac{1}{\sin^2\theta}\frac{\partial^2}{\partial\phi^2} \tag{4.166}$$

Passing now to the ellipsoidal case, we consider a surface ellipsoidal harmonics $Y(\theta,\phi) = V(\theta)W(\phi)$ where V, W are solutions of

$$\begin{aligned}\left[s_\theta\partial_\theta(s_\theta\partial_\theta) - c_1 + c_2 k'^2\sin^2\theta\right]V = 0\\ \left[s_\phi\partial_\phi(s_\phi\partial_\phi) + c_1 + c_2 k^2\sin^2\phi\right]W = 0\end{aligned} \tag{4.167}$$

for the same separation constant c_1 and where $c_2 = n(n+1)$. Multiplying the first equation by W and second one by V and adding them, we obtain the following result:

$$L^2_{\text{ell}} Y = n(n+1)Y \tag{4.168}$$

where the second order differential operator on the left side is defined by:

$$L^2_{\text{ell}} = -\frac{s_\theta \partial_\theta (s_\theta \partial_\theta) + s_\phi \partial_\phi (s_\phi \partial_\phi)}{k'^2 \sin^2\theta + k^2 \sin^2\phi} \tag{4.169}$$

Again, we note that this operator reduces to the spherical one for $k = 0, k' = 1$. However, and contrary to spherical case, L^2_{ell} is not equal to the surface Laplacian on the surface of some confocal ellipsoid. Without going into details, one can still show that it represents some surface Laplacian but for a different metric.

4.4.4 Incompressible Vector Fields by Piola Transforms

The Mie decomposition (or toroidal-poloidal decomposition) applies to incompressible vector fields in a spherical setting (see Backus 1986). Any such vector field with div v = 0 inside a ball can be written as:

$$\mathbf{v} = \operatorname{curl} t\mathbf{r} + \operatorname{curl}\operatorname{curl} p\mathbf{r} \tag{4.170}$$

where t, p are arbitrary function and $\mathbf{r} = r\mathbf{e}_r$ is the position vector. The usual proof relies on a special form of the Helmholtz decomposition that takes advantage of the simple expression of the position vector in spherical coordinates (Backus et al. 1996). As such, this proof does not extend to ellipsoidal coordinates (nor to the simpler spheroidal ones). The biggest advantage of the Mie decomposition is that the functions t, p restricted on the surface of a sphere are real scalars, and therefore can be each expanded in a sum of surface spherical harmonics. This significantly simplifies the application of boundary conditions for $\mathbf{v}$. On the contrary, such an expansion in surface spherical harmonics does not apply to individual components (in spherical coordinates) of the original vector field.

For coordinate systems that possess a rotational symmetry, there is another simple decomposition for axisymmetric incompressible vector fields:

$$\mathbf{v} = \operatorname{curl} q\mathbf{e}_\phi \tag{4.171}$$

where q is another arbitrary function. The Lee and Mear family for the prolate and oblate spheroidal case can be written in this form, although the resulting expression for q is not very illuminating.

When passing from a ball to a spherical shell, the Mie decomposition applies again but does not capture all available incompressible fields. Indeed, all fields of the form (4.170) have zero total flux through the outer surface (and by incompressibility also on the inner surface). The Hodge decomposition theorem (Cantarella et al. 2002) applied to a spherical shell (or any 3D region with one hole having therefore a non-trivial second homology group) shows that we need to seek a harmonic gradient or a vector field which is the gradient of a harmonic function:

$$\mathbf{v} = \nabla\eta, \quad \Delta\eta = 0 \tag{4.172}$$

and where η is constant on each component of the boundary. For a spherical shell, such a function is readily available:

$$\eta = \frac{-A}{r} + B, \quad \mathbf{v} = \nabla\eta = \frac{A}{r^2}\mathbf{e}_r \tag{4.173}$$

We note that the missing velocity field is nothing else than the cavity expansion field for a spherical void.

The first extension of the Mie decomposition to a non-spherical geometry has been proposed by Schmitt and Jault (2004) in the oblate spheroidal setting. Their method has a geometrical flavor that is not explicit in their presentation but will be clarified in the sequel. Let us contemplate an ellipsoidal shell N such that the inner and outer boundaries are confocal. If we are able to write down a diffeomorphism from this solid to a spherical shell M, then we can relate incompressible vector fields on each solid by a Piola transform and the Mie decomposition on the spherical shell will be pulled-back to some useful decomposition of the original vector field.

The notations we use are as follows:

$$\begin{array}{ccc} \xi = (r', \theta', \phi') & U \overset{x'=T'(\xi)}{\underset{\text{spherical}}{\longrightarrow}} & M = \text{spherical shell} \\ \Phi \uparrow & & \uparrow \Psi = T'\Phi T^{-1} \\ \eta = (r, \theta, \phi) & V \overset{x=T(\eta)}{\underset{\text{ellipsoidal}}{\longrightarrow}} & N = \text{ellipsoidal shell} \end{array} \tag{4.174}$$

Each manifold (with boundary) has its own local coordinates—natural coordinates (r, θ, ϕ) for the ellipsoidal shell and polar coordinates (r', θ', ϕ') for the spherical shell. The diffeomorphism will be given explicitly by a map Φ from local to local coordinates as shown in (4.174). Let us note the Jacobians of various maps:

$$J_\Phi = \det\left(\frac{\partial\xi}{\partial\eta}\right), J_\eta = \det\left(\frac{\partial x}{\partial\eta}\right), J_\xi = \det\left(\frac{\partial x'}{\partial\xi}\right), \tag{4.175}$$

such that the Jacobian of the composition map Ψ is given by:

$$J_\Psi = J_\xi J_\Phi J_\eta^{-1} \tag{4.176}$$

We switch now to the use of natural (contravariant or covariant) components of vector fields with respect to the basis $\mathbf{g}_\alpha = \frac{\partial}{\partial \xi^\alpha}$ or its dual $\mathbf{g}^\alpha = d\xi^\alpha$ on M and $\mathbf{g}_\beta = \frac{\partial}{\partial \eta^\beta}$ or its dual $\mathbf{g}^\beta = d\eta^\beta$ on N.[7]

Let $\mathbf{v} = v^\alpha \mathbf{g}_\alpha$ be a contravariant vector field on M. Define its Piola transform to be the contravariant vector field $\mathbf{V} = V^\beta \mathbf{g}_\beta$ on N with components given by:

$$\mathbf{V} = J_\Psi (\nabla \Phi)^{-1} \mathbf{v}, \quad V^\beta = J_\Psi \frac{\partial \eta^\beta}{\partial \xi^\alpha} v^\alpha \tag{4.177}$$

Then one can show that the divergence of these fields are related by:

$$\mathrm{DIV}\, \mathbf{V} = J_\Psi \,\mathrm{div}\, \mathbf{v} \tag{4.178}$$

or, in components:

$$\frac{1}{J_\eta} \frac{\partial \left(J_\eta V^\beta \right)}{\partial \eta^\beta} = J_\Psi \left[\frac{1}{J_\xi} \frac{\partial (J_\xi V^\alpha)}{\partial \xi^\alpha} \right] \tag{4.179}$$

We now need a similar Piola type transform that commutes not with the divergence but with the curl operator. Let $\mathbf{u} = u_\alpha \mathbf{g}^\alpha$ be a covariant vector field on M. Define its Piola "curl" transform to be the covariant vector field $\mathbf{U} = U_\beta \mathbf{g}^\beta$ on N with components given by:

$$\mathbf{U} = (\nabla \Phi)\mathbf{u}, \quad U_\beta = \frac{\partial \xi^\alpha}{\partial \eta^\beta} u_\alpha \tag{4.180}$$

Then one can show that the curl of these vectors are related by:

$$\mathrm{CURL}\, \mathbf{U} = J_\Psi (\nabla \Phi)^{-1} \mathrm{curl}\, \mathbf{u} \tag{4.181}$$

or, in components:

$$\frac{\epsilon^{\delta \beta \gamma}}{J_\eta} \frac{\partial U_\gamma}{\partial \eta^\beta} = J_\Psi \frac{\partial \eta^\delta}{\partial \xi^\alpha} \left(\frac{\epsilon^{\alpha \beta \gamma}}{J_\xi} \frac{\partial u_\gamma}{\partial \xi^\beta} \right) \tag{4.182}$$

where ϵ is the Levi-Civita alternating symbol.

Note that both Piola transforms are pulling vector fields from M back to N. If the transformation Φ is actually a diffeomorphism, then we can reverse this pull-back and transfer freely vector fields from one manifold to the other. A second

[7] We use the same notation for the basis on M and N as there is no confusion possible.

observation is that the Jacobian J_Ψ used in the Piola transforms should always include the local coordinate Jacobians as in (4.176) in order that the pull-back vectors are true vectors (behave as 1-tensors under a change of coordinates).

We are now ready to describe the method discovered by Schmitt and Jault (2004). Start with some incompressible vector field $\mathbf{V}$ on N. Use the Piola transform associated to the inverse transformation Φ^{-1} to pull it back to a vector field $\mathbf{v}$ on the spherical shell M. The two vector fields are then related by Eq. (4.177). Due to Eq. (4.178), the new field is again incompressible. It admits therefore a Mie decomposition given by:

$$\mathbf{v} = \frac{A}{r'^2}\mathbf{g}_{r'} + \operatorname{curl} tr'\mathbf{g}_{r'} + \operatorname{curl}\operatorname{curl} pr'\mathbf{g}_{r'} \tag{4.183}$$

where $p = p(r', \theta', \phi')$ and $t = t(r', \theta\prime, \phi\prime)$ are arbitrary functions. Let now $\mathbf{u}$ be defined as:

$$\mathbf{u} = tr'\mathbf{g}_{r'} + \operatorname{curl} pr'\mathbf{g}_{r'} \tag{4.184}$$

but written as a covariant vector. We can then pull it back to obtain:

$$\mathbf{V} = J_\Psi(\nabla\Phi)^{-1}\frac{A}{r'^2}\mathbf{g}_{r'} + \mathrm{CURL}[(\nabla\Phi)\mathbf{u}] \tag{4.185}$$

Let us analyze in more detail this decomposition. The vector pulled back from $\mathbf{u}$ is a sum of two terms—the first one is a simple curl applied to some vector field. The second part represents a second order operator applied to some vector field but is *not* of the form curl curl like in the original Mie decomposition. Practically, we need to apply one curl on M and the second curl on N after pull-back. Maybe there is a Piola type transform for the curl curl operator? Unfortunately, the answer is no and this for a deep reason. Piola transforms are actually pull-backs of differential forms and as such they do not use the metric properties of the underlying manifolds. On the contrary, the Mie decomposition with its double curl part requires the metric (essentially to raise or lower indices of tensorial fields). Because our transformation is a diffeomorphism but not an isometry, there is no reason that we can pull-back the curl curl part. Put otherwise, the final decomposition (4.185) can be rewritten so as to contain a double curl term but in a different metric, the one pulled-back by the transformation.[8]

[8]The entire argument applies equally well to another second order operator—the Laplacian written as div grad. There is no reason an arbitrary diffeomorphism will preserve harmonic functions. But transformed harmonic functions are still harmonic is we redefine the Laplacian using the transformed metric. This simple idea is the key to all recent work on cloaking transformations.

4.4.5 The Ellipsoidal Mie Decomposition for Incompressible Vector Fields

Let us now apply this method to an ellipsoidal shell. The key point now is to choose a reasonable transformation Φ. In the oblate spheroidal case, Schmitt and Jault (2004) have chosen the simplest such diffeomorphism—in our notation, a simple function $r' = F(r)$ for the radial coordinate and the identity for the angular coordinates. This transforms an oblate spheroid to a sphere by contraction in the x, y plane and an expansion along the z axis.

We have tried the same option for the ellipsoidal case to no avail—while we were able to obtain a family of incompressible fields, these were not at all adapted to an expansion in ellipsoidal surface harmonics. The winning solution is to use an affine transformation of the surface of an ellipsoid to that of a sphere (see Arscott 1964) given by:

$$\left\{\begin{array}{ccc} \sqrt{1-k'^2\cos^2\theta}\cos\phi & = & \sin\theta'\cos\phi' \\ \sin\theta\,\sin\phi & = & \sin\theta'\sin\phi' \\ \cos\theta\sqrt{1-k^2\cos^2\phi} & = & \cos\theta' \end{array}\right. \tag{4.186}$$

One can easily calculate θ', ϕ' from these equations to obtain the full transformation $(r', \theta', \phi') = \Phi(r, \theta, \phi)$:

$$\begin{aligned} r' &= F(r) = \left(r + \sqrt{r^2 + h_2^2}\right)/2 \\ \theta' &= G(\theta, \phi) = \cos^{-1}\left(\cos\theta\sqrt{1-k^2\cos^2\phi}\right) \\ \phi' &= H(\theta, \phi) = \tan^{-1}\left(\tan\phi\,\frac{\sin\theta}{\sqrt{1-k'^2\cos^2\theta}}\right) \end{aligned} \tag{4.187}$$

The specific choice for the function $F(r)$ shown here is essentially that of Schmitt and Jault (2004). We have been guided by the following criteria—it should have a finite limit for $r = 0$ corresponding to the focal ellipse of the confocal family (with the exception of the prolate case with $h_2 = 0$ where the focal ellipse degenerates to a segment), it should have everywhere a nonzero derivative and it should tend to the identity at large values of r when the confocal ellipsoid tends to a spherical form. Actually, we will see that the final result does not depend explicitly on the choice of $F(r)$ and any single valued function will do as long it provides a diffeomorphism for all values of h_1, h_2.

We are now able to calculate the gradient of the transformation (4.187)

$$\nabla\Phi = \begin{pmatrix} \partial_r F & 0 & 0 \\ 0 & \partial_\theta G & \partial_\phi G \\ 0 & \partial_\theta H & \partial_\phi H \end{pmatrix} \tag{4.188}$$

and the Jacobians (4.175) and (4.176):

$$J_\xi = h_{r'} h_{\theta'} h_{\phi'} = r'^2 \sin\theta', \quad J_\eta = h_r h_\theta h_\phi$$
$$J_\Phi = \frac{\partial_r F(k^2 \sin^2\phi + k'^2 \sin^2\theta)}{s_\theta s_\phi (\sin^2\theta + k^2 \cos^2\theta \cos^2\phi)^{1/2}} \tag{4.189}$$

where s_θ, s_ϕ are functions defined in (4.153). Note for future use that:

$$\sin\theta' = (\sin^2\theta + k^2 \cos^2\theta \cos^2\phi)^{1/2} \tag{4.190}$$

so that the full Jacobian is:

$$J_\Psi = \frac{\partial_r F r'^2 (r^2 + h_2^2)^{1/2} (r^2 + h_1^2 + h_2^2)^{1/2}}{(r^2 + h_2^2 \cos^2\beta)(r^2 + h_2^2 + h_1^2 \sin^2\phi)} \tag{4.191}$$

It is apparent in this final expression that Ψ is really a diffeomorphism for any value of h_1, h_2. We are ready now to apply the program outlined above and we start with the expansion field with contravariant components $(G/r'^2, 0, 0)$, which by pull-back gives us, by using (4.185) and (4.191):

$$V^r = \frac{G(r^2 + h_2^2)^{1/2} (r^2 + h_1^2 + h_2^2)^{1/2}}{(r^2 + h_2^2 \cos^2\beta)(r^2 + h_2^2 + h_1^2 \sin^2\phi)}, \quad V^\theta = V^\phi = 0 \tag{4.192}$$

To compare this to previous known results, let us calculate the physical components of this expansion field:

$$\tilde{V}_r = \frac{1}{h_r} V^r = \frac{G}{(r^2 + h_2^2 \cos^2\beta)^{1/2} (r^2 + h_2^2 + h_1^2 \sin^2\phi)^{1/2}} \tag{4.193}$$

while the other two components are zero and where the tilde is a reminder that these are the physical components. This is already a remarkable result and is a good example of the power of the Piola transform method. In the spherical case with $h_1 = h_2 = 0$ it reduces to the well-known Gurson spherical expansion field. In the oblate spheroidal case with $h_1 = 0$ and making the change of variable $r = h_2 \sinh\lambda$ we obtain:

$$\tilde{V}_\lambda = \frac{G}{h_2^2 (\sinh^2\lambda + \cos^2\beta)^{1/2} \cosh\lambda} \tag{4.194}$$

which is precisely (modulo some scaling factor) the expansion field appearing in the Lee and Mear (1992) oblate family. The same is true for the prolate case. Also it is easy to show that the expansion field (4.193) corresponds exactly to the harmonic gradient as required by Hodge theory. This is rather unexpected as in general the

Piola transform method does not preserve harmonic functions or vectors. A final observation is that the expansion field (4.193) does not respect conditions of homogeneous strain rate on any confocal ellipsoid; nevertheless it must be present in all velocity fields that change the volume of the void.

Let us now consider the curl part of the Mie decomposition for the ellipsoidal case. We start with the vector **u** given in (4.184) and calculate its covariant components:

$$(u_{r'}, u_{\theta'}, u_{\phi'}) = (r't, \frac{r'}{\sin\theta'}\partial_{\phi'}p, -r'\sin\theta'\,\partial_{\theta'}p) \tag{4.195}$$

We use now the Piola "curl" transform (4.180) to pull back this vector. This gives:

$$(U_r, U_\theta, U_\phi) = \begin{pmatrix} \partial_r F & 0 & 0 \\ 0 & \partial_\theta G & \partial_\theta H \\ 0 & \partial_\phi G & \partial_\phi H \end{pmatrix} \begin{pmatrix} u_{r'} \\ u_{\theta\prime} \\ u_{\phi\prime} \end{pmatrix} \tag{4.196}$$

Let us first consider the radial component:

$$U_r = r'\partial_r F t = F(r)t(r', \theta', \phi')\partial_r F \equiv T(r, \theta, \phi) \tag{4.197}$$

where, as announced, we have included the radial part of the transformation in a new arbitrary function. For the angular components, we need to transform all derivatives in the expression (4.195) for u from the (r', θ', ϕ') variables to the (r, θ, ϕ) variables. In order to make this more transparent, let us introduce the following matrices:

$$J = \begin{pmatrix} \partial_\theta G & \partial_\phi G \\ \partial_\theta H & \partial_\phi H \end{pmatrix}, M = \begin{pmatrix} \frac{1}{\sin\theta'} & 0 \\ 0 & \sin\theta' \end{pmatrix}, R = \begin{pmatrix} 0 & 1 \\ -1 & 0 \end{pmatrix} \tag{4.198}$$

Then one can show that the angular part of the vector field U is given by:

$$(U_\theta, U_\phi) = J^T M R J^{-T} \begin{pmatrix} r'\partial_\theta p \\ r'\partial_\phi p \end{pmatrix} \tag{4.199}$$

Similar to the radial component, let us first define a new arbitrary function by: $P(r, \theta, \phi) = r'p(r', \theta', \phi')$. After a lengthy but elementary calculation, we obtain for the matrix product above the following simple expression:

$$J^T M R J^{-T} = \begin{pmatrix} 0 & \frac{s_\phi}{s_\theta} \\ -\frac{s_\theta}{s_\phi} & 0 \end{pmatrix} \tag{4.200}$$

Combining these results we obtain for the vector field **U** the following covariant components:

$$(U_r, U_\theta, U_\phi) = \left(T,\ \frac{s_\phi}{s_\theta}\partial_\phi P,\ -\frac{s_\theta}{s_\phi}\partial_\theta P\right) \tag{4.201}$$

where T, P are arbitrary functions. It is easy now to calculate the curl of this vector field. Passing from natural components to physical ones and adding the expansion field (4.193), we obtain the sought after Mie decomposition for the ellipsoidal case:

$$\begin{cases} \tilde{V}_r = \frac{G + L_{ell}^2 P}{(r^2 + h_2^2\cos^2\beta)^{1/2}(r^2 + h_2^2 + h_1^2\sin^2\phi)^{1/2}} \\ \tilde{V}_\theta = \frac{1}{h_r h_\phi}\left(\partial_\phi T + \frac{s_\theta}{s_\phi}\partial^2_{r\theta} P\right) \\ \tilde{V}_\phi = \frac{1}{h_r h_\theta}\left(-\partial_\theta T + \frac{s_\phi}{s_\theta}\partial^2_{r\phi} P\right) \end{cases} \tag{4.202}$$

Here, the functions s_θ, s_ϕ are defined by (4.153), while the second order surface operator L^2_{ell} is defined by (4.169). We recall these definitions for ease of use:

$$L^2_{\text{ell}} = -\frac{s_\theta\partial_\theta(s_\theta\partial_\theta) + s_\phi\partial_\phi(s_\phi\partial_\phi)}{k'^2\sin^2\theta + k^2\sin^2\phi}$$
$$s_\theta = \sqrt{1 - k'^2\cos^2\theta},\ s_\phi = \sqrt{1 - k^2\cos^2\phi}$$

Let us now consider boundary conditions for the velocity field $\mathbf{V}$ imposed on some ellipsoid surface confocal with the reference ellipsoid and how these determine the functions P, T on the same surface.

First, it is easy to derive from (4.202) the following equations:

$$\begin{aligned} G + L^2_{\text{ell}} P &= m_2 m_3 \tilde{V}_r \\ L^2_{\text{ell}} T &= -\frac{s_\phi}{s_r}\frac{m_3}{m_1^2}\partial_\phi(m_1 m_2^2 \tilde{V}_\theta) + \frac{s_\theta}{s_r}\frac{m_2}{m_1^2}\partial_\theta(m_1 m_3^2 \tilde{V}_\phi) \end{aligned} \tag{4.203}$$

where m_1, m_2, m_3, s_r are defined in (4.153). We know that the surface operator L^2_{ell} admits ellipsoidal surface harmonics as eigenvectors. This invites us to decompose both functions P, T as sums of ellipsoidal surface harmonics multiplied by some arbitrary functions of the pseudo-radial variable:

$$\begin{aligned} P(r,\theta,\phi) &= \sum_{n=1}^{\infty}\sum_{m=1}^{2n+1} P_{nm}(r) Y_n^m(\theta,\phi) \\ T(r,\theta,\phi) &= \sum_{n=1}^{\infty}\sum_{m=1}^{2n+1} T_{nm}(r) Y_n^m(\theta,\phi) \end{aligned} \tag{4.204}$$

Plugging these expressions in the Mie decomposition (4.202) we obtain:

$$\begin{cases} \tilde{V}_r = \frac{1}{m_2 m_3}\left[G + n(n+1)P_{nm}Y_n^m\right] \\ \tilde{V}_\theta = \frac{1}{h_r h_\phi}\left[T_{nm}\partial_\phi Y_n^m + \frac{s_\theta}{s_\phi}\partial_r(P_{nm})\partial_\theta Y_n^m\right] \\ \tilde{V}_\phi = \frac{1}{h_r h_\theta}\left[-T_{nm}\partial_\theta Y_n^m + \frac{s_\phi}{s_\theta}\partial_r(P_{nm})\partial_\phi Y_n^m\right] \end{cases} \tag{4.205}$$

where there is an implicit sum over repeated indices $n, m = 1, \ldots 2n+1$ and we recall that each ellipsoidal surface harmonic is a product of Lamé polynomials:

$$Y_n^m(\theta, \phi) = E_n^m(\cos\theta) E_n^m(\cos\phi) \tag{4.206}$$

The functions $P_{nm}(r), T_{nm}(r)$ can be further decomposed as series of functions of the pseudo-variable r. We can use either some orthonormal basis like Chebyshev polynomials or Lamé functions of first and second kind, in a way similar to the prolate and oblate cases treated in Lee and Mear (1992), Gologanu (1997). In the next section we will propose a simpler decomposition.

The ellipsoidal Mie decomposition (4.205) reduces, in the spherical case, to the usual Mie decomposition. In the oblate and prolate spheroidal cases, it is a genuine generalization of the Lee and Mear (1992) family of axisymmetric incompressible vector fields to the general, non-axisymmetric case. We recall that the general case for an oblate spheroidal geometry was already obtained by Schmitt and Jault (2004). The ellipsoidal case is completely new to our knowledge.

4.5 Calibration of Gurson Type Models via the Mie Decomposition

We use now the ellipsoidal Mie decomposition of incompressible vector fields to determine, via a spectral method, the macroscopic yield criterion for an ellipsoidal unit cell, containing a confocal void and made of a rigid-plastic material with general anisotropic plasticity. In particular, we obtain a calibration method for Gurson-type models by using in the spectral method a small number of vector fields approximating the velocity field describing the expansion of the cavity.

4.5.1 The Homogenization Limit Analysis Problem

Consider an ellipsoidal void V in a confocal unit cell Ω. We use an ellipsoidal coordinate system with Tabanov's natural ellipsoidal coordinates defined by Eqs. (4.146), consisting in a pseudo-radial variable r and two pseudo-angular variables θ, ϕ. The void surface and the outer surface of the cell are defined by $r = r_1$ and $r = r_2$, respectively, while the focal ellipse is given by $r = 0$. The demi-axis along x, y, z of a generic confocal ellipsoid defined by $r = \text{cst.}$ are $(r^2 + h_1^2 + h_2^2)^{1/2}$, $(r^2 + h_2^2)^{1/2}$ and respectively r. The matrix is made of a rigid-plastic material with an arbitrary, pressure-independent and anisotropic yield criterion defined by some convex region κ in stress space with dissipation function w. Then the homogenization problem in the kinematic formulation is to find the macroscopic yield region K via the macroscopic dissipation function given by:

$$W(\mathbf{D}) = \inf_{\mathrm{v}} \left\{ \frac{1}{|\Omega|} \int\limits_{\Omega \setminus \mathrm{V}} w(\mathbf{d}(\mathbf{v})) \middle| \mathbf{v} = \mathbf{D}\mathbf{x}|_{\partial\Omega}, \mathrm{div}\mathbf{v} = 0 \right\} \tag{4.207}$$

The ellipsoidal Mie decomposition (4.205) of the velocity field automatically assures the incompressibility condition. Taking a partial sum of the infinite series in the Mie decomposition $\mathbf{v} = a_k \mathbf{v}^{(k)}$ and replacing the triple integral in (4.207) with a Gaussian quadrature with points x_i and weights ω_i, we obtain:

$$W^a(\mathbf{D}) = \inf_{a_k} \left\{ \sum_i \omega_i w \left(\sum_k a_k \mathbf{d}(\mathbf{v}^{(k)}(x_i)) \right) \middle| La = s \right\} \tag{4.208}$$

where the linear constraints $La = s$ arise from the boundary conditions $\mathbf{v} = \mathbf{D}\mathbf{x}|_{\partial\Omega}$ and will be explicitly given in the next subsection. Note that this is a convex minimization problem with linear constraints that depend linearly on $\mathbf{D}$, and therefore the approximate macroscopic dissipation function W^a will be automatically convex. There are several possible choices for the 3D Gaussian quadrature in (4.208): either a tensorial product of one-dimensional Gaussian quadratures in each variable r, θ, ϕ or the product of a Gaussian quadrature in r with a Lebedev type quadrature for θ, ϕ (see Lebedev and Laikov 1999). The physical components of the strain rate $\mathbf{d}(\mathbf{v})$ in a general orthogonal coordinates (q_1, q_2, q_3) with Lame coefficients (h_1, h_2, h_3) are:

$$\begin{cases} d_{ii} = \frac{1}{h_i} \frac{\partial v_i}{\partial q_i} + \sum\limits_{j \neq i} \frac{v_j}{h_i h_j} \frac{\partial h_i}{\partial q_j}, & i = 1, 2, 3 \\ 2d_{ij} = \frac{h_i}{h_j} \frac{\partial}{\partial q_j} \left(\frac{v_i}{h_i} \right) + \frac{h_j}{h_i} \frac{\partial}{\partial q_i} \left(\frac{v_j}{h_j} \right), & i \neq j \end{cases} \tag{4.209}$$

We now show that we can calculate numerically the dissipation function in (4.208), without the need of an analytic expression. For an arbitrary point x in the matrix, let $\mathbf{d} = \sum_k a_k \mathbf{d}(\mathbf{v}^{(k)}(x)) = \sum_k a_k \mathbf{d}^{(k)}$ and let $\boldsymbol{\sigma}$ denote the projection of the direction $\mathbf{d}$ on the microscopic yield convex κ. Then, by (4.18) and (4.19), the dissipation function and its derivative with respect to a_k are given by:

$$\mathbf{d} = \sum_k a_k \mathbf{d}^k, \quad w(\mathbf{d}) = \boldsymbol{\sigma} : \mathbf{d} = \mathrm{pr}_\kappa(\mathbf{d}) : \mathbf{d}, \quad \frac{\partial w}{\partial a_k} = \mathrm{pr}_\kappa(\mathbf{d}) : \mathbf{d}^{(k)} \tag{4.210}$$

We note that the above derivative with respect to a_k is required by most numerical solvers for the convex minimization problem (4.208).

Let us now find the intersections $t^{\pm}$ of some arbitrary direction $t\,\boldsymbol{\Sigma}$ in stress space with the yield surface or boundary of the macroscopic yield convex. For all $t\,\boldsymbol{\Sigma}$ located inside the yield convex, the definition of the dissipation function gives:

$$(t\boldsymbol{\Sigma}) : \mathbf{D} \leq W^a(\mathbf{D}). \tag{4.211}$$

Using the homogeneity of degree 1 of W^a, it is easy to show that:

$$t^{\pm} = \inf_{\Sigma:\mathrm{D}=\pm 1} W^a(\mathbf{D}) = \inf_{\substack{a_k \\ L'a=s'}} \left\{ \sum_i \omega_i w \left(\sum_k a_k \mathbf{d}(\mathbf{v}^{(k)}(x_i)) \right) \right\} \tag{4.212}$$

where the linear constraints $L'a = s'$ are given explicitly in the next subsection.

4.5.2 Boundary Conditions

We now give an explicit treatment of the boundary conditions $\mathbf{v} = \mathbf{D}\mathbf{x}$ on the outer boundary of the cell. Let us start with some general expressions, valid for an arbitrary Dirichlet boundary condition $\mathbf{v} = \mathbf{u}$ on the external surface.

We have observed that we obtain the simplest expressions if we use natural covariant components for the vector fields. Considering therefore the ellipsoidal Mie decomposition of $\mathbf{v}$ in covariant components, we obtain, for $r = r_2$:

$$\begin{cases} u_r = v_r = \frac{h_r}{m_2 m_3} \left[G + n(n+1) P_{nm} Y_n^m \right] \\ u_\theta = v_\theta = \frac{h_\theta}{h_r h_\phi} \left[T_{nm} \partial_\phi Y_n^m + \frac{s_\theta}{s_\phi} \partial_r (P_{nm}) \partial_\theta Y_n^m \right] \\ u_\phi = v_\phi = \frac{h_\phi}{h_r h_\theta} \left[-T_{nm} \partial_\theta Y_n^m + \frac{s_\phi}{s_\theta} \partial_r (P_{nm}) \partial_\phi Y_n^m \right] \end{cases} \tag{4.213}$$

where $P_{nm}(r), T_{nm}(r)$ are arbitrary functions and $Y_n^m(\theta, \phi)$ are the ellipsoidal surface harmonics. Using the orthogonality property (4.164) of the ellipsoidal surface harmonics, the first equation gives directly:

$$\begin{aligned} G &= \frac{s_{r_2}}{\gamma_0^0} \int_0^{\pi} \int_0^{2\pi} \frac{u_r m_1^2}{s_\theta s_\phi} d\phi d\theta, \\ P_{nm}(r_2) &= \frac{s_{r_2}}{\bar{\gamma}_n^m} \int_0^{\pi} \int_0^{2\pi} \frac{u_r Y_n^m m_1^2}{s_\theta s_\phi} d\phi d\theta \end{aligned} \tag{4.214}$$

where $\bar{\gamma}_n^m = n(n+1)\gamma_n^m$ are related to the normalization constants from (4.164). The last two equations in (4.213) provide the following conditions:

$$\begin{aligned} T_{nm}(r_2) &= \frac{1}{\bar{\gamma}_n^m}\int_0^{\pi}\int_0^{2\pi}\left(\frac{\partial(m_3^2 u_\phi)}{\partial\theta} - \frac{\partial(m_2^2 u_\theta)}{\partial\phi}\right)d\phi d\theta, \\ \frac{\partial P_{nm}}{\partial r}(r_2) &= \frac{1}{\bar{\gamma}_n^m}\int_0^{\pi}\int_0^{2\pi}\left(\frac{m_2^2}{s_\phi}\frac{\partial(s_\theta u_\theta)}{\partial\theta} - \frac{m_3^2}{s_\theta}\frac{\partial(s_\phi u_\phi)}{\partial\phi}\right)d\phi d\theta \end{aligned} \tag{4.215}$$

We observe that Dirichlet boundary conditions on the external surface impose not only well-defined values for all functions P_{nm}, T_{nm} on this surface, but also the derivatives of P_{nm} with respect to the pseudo-radial variable.

Consider now the particular case where $\mathbf{u} = \mathbf{D}\mathbf{x}$ with a diagonal macroscopic strain rate (in the reference frame of the void). The covariant components are:

$$\begin{cases} u_r = r_2\left(D_{xx}s_\theta^2\cos^2\phi + D_{yy}\sin^2\theta\,\sin^2\phi + D_{zz}s_\phi^2\cos^2\theta\right) \\ u_\theta = \mathrm{sc}\,\theta\left(D_{xx}\rho_{12}^2 k'^2\cos^2\phi + D_{yy}\rho_2^2\sin^2\phi - D_{zz}r^2 s_\phi^2\right) \\ u_\phi = \mathrm{sc}\,\phi\left(-D_{xx}\rho_{12}^2 k'^2 s_\theta^2 + D_{yy}\rho_2^2\sin^2\theta + D_{zz}r^2k^2\cos^2\theta\right) \end{cases} \tag{4.216}$$

where $\mathrm{sc}\beta = \sin\beta\,\cos\beta$ and we have used the following notations:

$$a_2 = (r_2^2 + h_1^2 + h_2^2)^{1/2}, \quad b_2 = (r_2^2 + h_2^2)^{1/2}, \quad c_2 = r_2. \tag{4.217}$$

Note that a_2, b_2, c_2 are precisely the demi-axis of the ellipsoidal unit cell, that $s_{r_2} = a_2 b_2$ and that $\Lambda_2 = a_2 b_2 c_2$ is proportional (up to a factor of $4\pi/3$) to the volume of the cell. Plugging (4.216) into (4.214) and (4.215), we obtain right hand sides that are zero for all n, m with the following exceptions:

$$\begin{aligned} G &= \Lambda_2 D_m \\ P_{20}(r_2) &= \frac{\Lambda_2\left[(D_{zz}-D_{yy})K + (D_{yy}-D_{xx})k'^2\right]}{9k'^2(K-1)(K+k^2)} \\ P_{22}(r_2) &= \frac{\Lambda_2\left[(D_{zz}-D_{yy})(K-2) + (D_{xx}-D_{yy})k'^2\right]K}{24k'^2(K-1)(K+k'^2)} \\ T_{32}(r_2) &= \frac{h_1^2c_2^2(D_{zz}-D_{yy}) + h_2^2a_2^2(D_{xx}-D_{yy})}{90a_2b_2} \\ \frac{\partial P_{20}}{\partial r} &= \frac{P_{20}(r_2)}{\Lambda_2}\frac{\partial(\Lambda_2)}{\partial r_2} - \frac{1}{a_2b_2}\frac{D_m h_2^2(Ka_2^2 + k^2c_2^2)}{3k'^2(K-1)(K+k^2)} \\ \frac{\partial P_{22}}{\partial r} &= \frac{P_{22}(r_2)}{\Lambda_2}\frac{\partial(\Lambda_2)}{\partial r_2} - \frac{1}{a_2b_2}\frac{D_m h_2^2\left[(K-2)a_2^2 - k^2c_2^2\right]}{8k'^2(K-1)(K+k'^2)} \end{aligned} \tag{4.218}$$

Here we have used the following notation:

$$K = \sqrt{k^4 - k^2 + 1} + 1 \tag{4.219}$$

Note that these conditions are valid only for $0 \le k^2 \le 1/2$ due to the following fact. In calculating Eqs. (4.218), we have used some specially crafted scaling for the Lame polynomials that respects Tabanov's principle and gives the correct limit in the oblate case by the direct substitution $k = 0, k' = 1, h_1 = 0$. Unfortunately, these expressions do not respect Tabanov's principle for the prolate case $(k = 1)$, where a

different scaling must be used. One advantage of this division is that we can label the ellipsoidal surface harmonics in a similar way to the spherical ones:

$$\begin{cases} Y_2^0 = \frac{K+3k'^2\cos^2\theta+k^2-3}{2}\frac{K-3k^2\cos^2\phi+k^2}{2} \\ Y_2^2 = 2(K-3k'^2\cos^2\theta+k'^2)\left(\cos^2\phi-\frac{K-k^2+1}{3K}\right) \\ Y_3^{\bar{2}} = 30\sin\theta\,\cos\theta\sqrt{1-k'^2\cos^2\theta}\sin\phi\,\cos\phi\sqrt{1-k^2\cos^2\phi} \end{cases} \tag{4.220}$$

Note that these expressions give the correct limit in the oblate spheroidal case by direct substitution $k=0, k'=1, h_1=0$:

$$\begin{cases} Y_2^0 = (3\cos^2\theta-1)/2 = P_2^0(\cos\theta) \\ Y_2^2 = 3\sin^2\theta\,\cos 2\phi = P_2^2(\cos\theta)\cos 2\phi \\ Y_3^{\bar{2}} = 15\sin^2\theta\,\cos\theta\,\sin 2\phi = P_3^2(\cos\theta)\sin 2\phi \end{cases} \tag{4.221}$$

with $P_n^m(\cos\theta)$ representing the Legendre associated polynomials. The alternate expressions for the boundary conditions (4.218) and the ellipsoidal surface harmonics (4.220) valid for $\frac{1}{2}\le k^2\le 1$ and giving the prolate limit by simple substitution $k=1, k'=0, h_2=0$, are given by:

$$\begin{gathered} G = \Lambda_2 D_m \\ P_{20}(r_2) = \frac{\Lambda_2\left[(D_{xx}-D_{yy})K+(D_{yy}-D_{zz})k^2\right]}{9k^2(K-1)(K+k'^2)} \\ P_{22}(r_2) = \frac{\Lambda_2\left[(D_{xx}-D_{yy})(K-2)+(D_{zz}-D_{yy})k^2\right]K}{24k^2(K-1)(K+k^2)} \\ T_{32}(r_2) = \frac{h_1^2c_2^2(D_{zz}-D_{yy})+h_2^2a_2^2(D_{xx}-D_{yy})}{90a_2b_2} \\ \frac{\partial P_{20}}{\partial r} = \frac{P_{20}(r_2)}{\Lambda_2}\frac{\partial(\Lambda_2)}{\partial r_2} - \frac{1}{a_2b_2}\frac{D_m h_1^2(Kc_2^2+k'^2a_2^2)}{3k^2(K-1)(K+k'^2)} \\ \frac{\partial P_{22}}{\partial r} = \frac{P_{22}(r_2)}{\Lambda_2}\frac{\partial(\Lambda_2)}{\partial r_2} - \frac{1}{a_2b_2}\frac{D_m h_1^2\left[(K-2)c_2^2-k^2a_2^2\right]}{8k^2(K-1)(K+k^2)} \end{gathered} \tag{4.222}$$

and:

$$\begin{cases} Y_2^0 = \frac{K-3k'^2\cos^2\theta+k'^2}{2}\frac{K+3k^2\cos^2\phi+k'^2-3}{2} \\ Y_2^2 = 2\left(\cos^2\theta-\frac{K+k^2}{3K}\right)(K-3k^2\cos^2\phi+k^2) \end{cases} \tag{4.223}$$

where the expression for $Y_3^{\bar{2}}$ is unchanged and has not been repeated. We note that the two representations (4.220) and (4.223) for the ellipsoidal surface harmonics give identical results for $k=1/2$.

As already noted, the boundary conditions (4.218) or (4.222) are supplemented by:

$$\begin{cases} P_{nm}(r_2) = 0, & \forall(n,m)\neq(2,0)\text{ or }(2,2) \\ \frac{\partial P_{nm}}{\partial r}(r_2) = 0, & \forall(n,m)\neq(2,0)\text{ or }(2,2) \\ T_{nm}(r_2) = 0, & \forall(n,m)\neq(3,2) \end{cases} \tag{4.224}$$

The above boundary conditions provide directly the linear constraints in the expression (4.208) of the macroscopic dissipation function as a function of the macroscopic strain rate. However, when searching for the intersection of the macroscopic yield surface with some direction $\mathbf{\Sigma}$ in stress space via the minimization problem (4.212), we need a different approach. The first three equations in (4.218) can be inverted to obtain the following expressions, all taken at $r = r_2$:

$$\begin{aligned} D_{xx} &= \frac{G}{\Lambda_2} - \frac{3P_{20}}{2\Lambda_2}(K+k^2)(2K-k^2-3) + \frac{4P_{22}}{K\Lambda_2}(K+k'^2)(2K-k'^2) \\ D_{yy} &= \frac{G}{\Lambda_2} + \frac{3P_{20}}{2\Lambda_2}(K+k^2)(K+k^2-3) - \frac{4P_{22}}{K\Lambda_2}(K+k'^2)^2 \\ D_{zz} &= \frac{G}{\Lambda_2} + \frac{3P_{20}}{2\Lambda_2}(K+k^2)(K-2k^2) - \frac{4P_{22}}{K\Lambda_2}(K+k'^2)(K-2k'^2) \end{aligned} \tag{4.225}$$

The same approach applied to (4.222) gives:

$$\begin{aligned} D_{xx} &= \frac{G}{\Lambda_2} + \frac{3P_{20}}{2\Lambda_2}(K+k'^2)(K-2k'^2) - \frac{4P_{22}}{K\Lambda_2}(K+k^2)(K-2k^2) \\ D_{yy} &= \frac{G}{\Lambda_2} + \frac{3P_{20}}{2\Lambda_2}(K+k'^2)(K-k^2-2) - \frac{4P_{22}}{K\Lambda_2}(K+k^2)^2 \\ D_{zz} &= \frac{G}{\Lambda_2} - \frac{3P_{20}}{2\Lambda_2}(K+k'^2)(2K+k^2-4) + \frac{4P_{22}}{K\Lambda_2}(K+k^2)(2K-k^2) \end{aligned} \tag{4.226}$$

These expressions, when plugged in the last three equations in (4.218) or (4.222), provide three linear constraints. Among these, two contain the derivatives of P_{20}, P_{22}. For them, it suffices to replace D_m with A/Λ_2 to obtain the sought after expressions. For the remaining equation, we obtain:

$$\begin{aligned} T_{32} &= \frac{2h_2^2(Ka_2^2+k^2c_2^2)P_{22}}{5(K+k^2)a_2b_2\Lambda_2} - \frac{h_2^2\left[(K-2)a_2^2-k^2c_2^2\right](K+k^2)P_{20}}{20a_2b_2\Lambda_2} \\ T_{32} &= \frac{2h_1^2(Kc_2^2+k^2a_2^2)P_{22}}{5(K+k'^2)a_2b_2\Lambda_2} - \frac{h_1^2\left[(K-2)c_2^2-k'^2a_2^2\right](K+k'^2)P_{20}}{20a_2b_2\Lambda_2} \end{aligned} \tag{4.227}$$

where the first expression applies to $0 \le k^2 \le 1/2$. and the second to $1/2 \le k^2 \le 1$. A supplementary constraint arises from plugging the same expressions for the macroscopic strain rate into $\mathbf{\Sigma} : \mathbf{D} = \pm 1$. For the particular case of a hydrostatic stress with $\mathbf{\Sigma} = \mathrm{diag}(1,1,1)$, this gives the linear constraint:

$$3G = \pm\Lambda_2 \tag{4.228}$$

Some comments are due now. If one searches for a velocity field that respects conditions of homogeneous strain rate an *all* ellipsoids confocal with the cavity, then the boundary conditions (4.218) or (4.222) applied to all r_2 provide two

differential equations for the functions P_{20}, P_{22} plus the constraints $(4.218)_1$ or $(4.222)_1$ involving G. Solving these equations, one recovers precisely the velocity field discovered in Leblond and Gologanu (2008), expressed in covariant components in ellipsoidal natural coordinates. Unfortunately, this velocity field has a relatively complex expression involving elliptic integrals. In the next subsection we will present a simpler approach for building a large family of velocity fields describing the expansion of the cavity. A second comment is related to the off-diagonal components of **D**. Each such component, if not zero, provides three supplementary equations for some $P_{2m}(r_2)$, its derivative and some $T_{3m}(r_2)$. Due to limited space, we do not give here the full expressions for these equations.

4.5.3 Calibration of Gurson Type Models

We have now all ingredients to search numerically for a "good" velocity field $\mathbf{v}^{\mathrm{A}}$ describing the expansion of the cavity. We recall that this velocity field is associated to a pure hydrostatic stress via the minimization problem:

$$p = \inf_{\substack{\mathrm{div}\mathbf{v}^A=0,\quad \mathbf{v}^A=\mathbf{D}\mathbf{x}|_{\partial\Omega} \\ D_{xx}+D_{yy}+D_{zz}=1,\ D_{xy}=D_{xz}=D_{yz}=0}} \frac{1}{|\Omega|}\int_{\Omega\setminus V} w(\mathbf{d}(\mathbf{v}^A)) \tag{4.229}$$

In order to solve this problem we choose $\mathbf{v}^{\mathrm{A}}$ among the velocity fields described by the Mie decomposition (4.205) with the only non-zero terms given by $G, P_{20}(r), P_{22}(r), T_{32}(r)$ and with the corresponding ellipsoidal surface harmonics defined by (4.220) or (4.223). This decomposition assures the incompressibility of the velocity field. Next, we know that the condition $D_{xx}+D_{yy}+D_{zz}=1$ implies that G has a fixed value given by (4.228). The values of P_{20}, P_{22} at $r=r_2$ are arbitrary, but their derivatives and the value of T_{32}, all at $r=r_2$, are given by $(4.218)_{5,6}$ or $(4.222)_{5,6}$ and $(4.227)_1$ or $(4.227)_2$ respectively. All choices above correspond to two cases, the first defined by $0 \le k^2 \le 1/2$ and the second by $1/2 \le k^2 \le 1$. This family of velocity fields is used to solve the minimization problem (4.229), or after discretization, the minimization problem (4.212) with the three linear constraints described above. The only missing ingredient is some explicit expression for the functions $P_{20}(r), P_{22}(r), T_{32}(r)$ of the pseudo-radial variable. Let $P(r)$ be one of these three functions. As mentioned before, a simple choice for $P(r)$ is a finite Chebyshev series in the interval (r_1, r_2). A second choice is given by truncating the following infinite series:

$$P(r) = \sum_{i=0}^{\infty} P_i r^i + \sum_{i=1}^{\infty} \frac{\bar{P}_i}{\left(r^2+h_2^2\right)^{i/2}} \tag{4.230}$$

The first series in the right hand side of (4.230) gives, when truncated, a simple polynomial and therefore is equivalent to a finite Chebyshev series; however, the latter is numerically stable for high degrees, contrary to (4.230). The choice of the second series in the right hand side of (4.230) has been guided by two criteria. First, the i-th term in this series should behave like $1/r^i$ for large values of the pseudo-radial variable (corresponding to an ellipsoid that approaches a sphere). Second, all terms should have finite limits at $r = 0$, corresponding to the focal ellipse, with the exception of the prolate case with $h_2 = 0$ where this ellipse degenerates to an interval. This is similar to the behaviour of the Lee and Mear family in the oblate and prolate cases, but has the supplementary advantage that it does not involve complex functions like the associated Legendre functions of the second kind.

Once we know an approximate but accurate velocity field $\mathbf{v}_0^A$ describing the expansion of the void we use it to determine several points on the macroscopic Gurson criterion. First, the minimum found when solving (4.229) gives us an approximation of the hydrostatic stress located on the yield surface. Plugging the solution $\mathbf{v}_0^A$ in the expressions (4.225) or (4.226) giving the macroscopic strain rates D_{xx}, D_{yy}, D_{zz}, we obtain directly the normal to the yield criterion at the hydrostatic point and therefore the parameters $\alpha_1 = D_{xx}, \alpha_2 = D_{yy}, \alpha_3 = D_{zz}$. Note that the condition $\alpha_1 + \alpha_2 + \alpha_3 = 1$ is automatically assured due to $D_{xx} + D_{yy} + D_{zz} = 1$ imposed from the start. Next, the same macroscopic strain rates can be used to determine the two points on the yield criterion with known normal, given by (4.110) and (4.111). The full determination of these points requires also the mean strain rates $\mathbf{D}^{A,V}$ on the void, due to the velocity field $\mathbf{v}_0^A$. These can be calculated from the definitions (4.109) for an arbitrary velocity field in the ellipsoidal Mie decomposition but we do not give them here as the resulting expressions involve complete elliptic integrals involving k^2, k'^2 and therefore do not respect Tabanov's principle of having spheroidal limits given by simple substitution. A possible solution is to search for solutions using Carlson's symmetric functions. We have thus found solutions that respect Tabanov's principle but unfortunately are not symmetric in the ellipsoid axis as we expected and therefore yield very long expressions that are not given here. An alternative solution is to use numerical integration for the mean strain rates on the void. We note also that the same mean strain rates provide, via Eqs. (4.112), the evolution laws for the shape of the void.

These three points located on the macroscopic criterion and having known normal give a total of nine equations for the following nine parameters of the Gurson-type models: $k, \alpha_1, \alpha_2, C_{11}, C_{12}, C_{21}, C_{22}, \eta_1, \eta_2$. One can treat this as a parameter identification problem and solve it by the advanced methods described in Chapter 1. Using this method we can determine the parameters of a Gurson-type model as functions of void and unit cell geometries via the porosity f and the focal parameters h_1, h_2. One can tabulate these results covering a wide range of geometries and use interpolation in these tables in order to use the Gurson type model in a finite element simulation.

Finally, we need to provide a value for the parameter g, playing a similar role to the porosity in Gurson-type models. In fact, this parameter is directly related to the behaviour of the strain rate for the expansion velocity field $\mathbf{v}_0^A$ and more precisely to its limits for $r = 0$ and $r = +\infty$. In our case, the velocity field $\mathbf{v}_0^A$ is not fixed a priori, but varies with the geometries of the void and unit cell. The only fixed component of $\mathbf{v}_0^A$ is the one related to the harmonic gradient velocity field corresponding to G in the ellipsoidal Mie decomposition. The analysis of the strain rate of this field is simpler than the one done in Madou et al. (2012a) and based on the velocity field respecting conditions of homogeneous boundary strain rate on each confocal ellipsoid (Leblond and Gologanu 2008). However, the results are the same and we adopt therefore the definition given in Madou and Leblond (2012b):

$$g = \frac{a_1 b_1^2}{a_2 b_2 c_2} = \frac{a_1 b_1^2}{\Lambda_2} \tag{4.231}$$

This definition gives a non-zero value also in the case where the void reduces to a crack defined by the focal ellipse. However, in the prolate spheroidal case where the focal ellipse degenerates to a segment, we have $b_1 = 0$ and therefore $g = f = 0$, and the Gurson-type criterion reduces to the yield criterion of the matrix or a material without voids.

4.6 Conclusions

We have presented a short introduction to Gurson-type models for predicting the fracture of ductile metals. We continued with an application of some anisotropic extension of the Gurson-Tvergaard-Needleman model to the prediction of fracture in a sheet deep drawing simulation, including the identification of material parameters from tensile tests on sheets. Having concluded that the optimal Gurson-type model for sheets would consider ellipsoidal voids and non-quadratic anisotropic yield criteria, we focused on three such advanced yield criteria—Yld91, Yld2004-18p and BBC2005. We presented new methods based on convex analysis to derive analytical expressions for the dissipation functions of these yield criteria. The expressions thus obtained are not fully explicit and require some supplementary minimizations; however we have shown that such forms are compatible with the development of Gurson-type models. In the second step we extended Gurson's model to non-quadratic yield criteria where the "cosh" term is replaced by some other function. Unfortunately, we were able to obtain only parametric forms for these new Gurson type models. In order to calibrate these new models, we have extended the Lee and Mear family of spheroidal axisymmetric and incompressible velocity fields to the general ellipsoidal case. The method we used is based on a Piola transform of the spherical Mie decomposition to a new ellipsoidal Mie decomposition. This forms the basis of a spectral method to solve the limit-analysis

problem for an ellipsoidal void in a confocal unit cell. Using this spectral method to find an approximate solution in the case of a hydrostatic macroscopic stress provides the optimal velocity field describing the expansion of the cavity. The knowledge of this velocity field for a given geometry permits the calibration of the remaining parameters in Gurson-type models. At variance with previous works, we did not try to fit analytical approximations to the calibrated parameters. For a given yield criterion, we propose to use our fast calibration to tabulate all parameters as functions of void geometry and porosity and to use interpolation in these tables in a finite element simulation. We hope that the new tools and techniques presented in this Chapter open the way to build Gurson-type models for new anisotropic yield criteria and general ellipsoidal voids.

References

Abbasi M, Ketabchi M, Izadkhah H, Fatmehsaria DH, Aghbash AN (2011) Identification of GTN model parameters by application of response surface methodology. Procedia Eng 10:415–420

Abbassi F, Belhadj T, Mistou S, Zghal A (2013) Parameter identification of a mechanical ductile damage using Artificial Neural Networks in sheet metal forming. Mat Design 45:605–615

Agoras M, Ponte Castañeda P (2014) Anisotropic finite-strain models for porous viscoplastic materials with microstructure evolution. Int J Sol Struct 51(5):981–1002

Arscott FM (1964) Periodic differential equations: an introduction to Mathieu, Lame and Allied functions. Pergamon Press, Oxford

Backus G (1986) Poloidal and toroidal fields in geomagnetic field modelling. Rev Geophys 24 (1):75–109

Backus G, Parker R, Constable C (1996) Foundations of geomagnetism. Cambridge University Press, Cambridge

Banabic D, Balan T, Comsa DS (2000) A new yield criterion for orthotropic sheet metals under plane–stress conditions. In: The 7th conference on'TPR 2000', Cluj Napoca, pp 217–224

Banabic D, Aretz H, Comsa DS, Paraianu L (2005) An improved analytical description of orthotropy in metallic sheets. Int J Plasticity 21:493–512

Barlat F, Lian K (1989) Plastic behaviour and stretchability of sheet metals. Part I: a yield function for orthotropic sheets under plane stress conditions. Int J Plasticity 5:51–66

Barlat F, Lege DJ, Brem JC (1991) A six-component yield function for anisotropic materials. Int J Plast 7:693–712

Barlat F et al (2005) Linear transformation-based anisotropic yield functions. Int J Plast 21:1009–1039

Benzerga AA, Besson J (2001) Plastic potentials for anisotropic porous solids. Eur J Mech A-Solids 20:397–434

Benzerga AA, Leblond J-B (2010) Ductile fracture by void growth to coalescence. Adv App Mech 44:169–305

Besson J (2010) Continuum models of ductile fracture: a review. Int J Damage Mech 19:3–52

Burnett DS, Holford RL (1998) Multipole-based 3-D infinite elements: an ellipsoidal acoustic element and a spherical electromagnetic element. In: Geers TL (ed) IUTAM symposium on computational methods for unbounded domains. Fluid mechanics and its applications. Springer, pp 53–62

Cantarella J, DeTurck D, Gluck H (2002) Vector calculus and the topology of domains in 3-space. Am Math Mon 109:409–442

Cazacu O, Plunkett B, Barlat F (2006) Orthotropic yield criterion for hexagonal closed packed metals. Int J Plast 22:1171–1194

Chen Z, Dong X (2009) The GTN damage model based on Hill'48 anisotropic yield criterion and its application in sheet metal forming. Comput Mater Sci 44:1013–1021

Danas K, Castañeda PP (2009) A finite-strain model for viscoplastic anisotropic porous media: I—theory. Eur J Mech A-Solids 28:387–401

Dobner H, Ritter S (1998) Verified computation of Lamé functions with high accuracy. Computing 60:81–89

Fratini L, Lombardo A, Micari F (1996) Material characterization for the prediction of ductile fracture occurrence: an inverse approach. J Mater Proc Techn 60:311–316

Garajeu M, Michel J-C, Suquet P (2000) A micromechanical approach of damage in viscoplastic materials by evolution in size shape and distribution of voids. Comput Methods Appl Mech Eng 183:223–246

Garmier R, Barriot JP (2001) Ellipsoidal harmonic expansions of the gravitational potential: theory and application. Celestial Mech Dyn Astron 79:235–275

Gologanu M, Leblond J-B, Devaux J (1993) Approximate models for ductile metals containing non-spherical voids—case of axisymmetric prolate ellipsoidal cavities. J Mech Phys Solids 41:1723–1754

Gologanu M, Leblond J-B, Devaux J (1994) Approximate models for ductile metals containing nonspherical voids—case of axisymmetric oblate ellipsoidal cavities. J Eng Mater Techn 116:290–297

Gologanu M, Leblond JB, Perrin G, Devaux J (1997) Recent extensions of Gurson's model for porous ductile metals. In: Suquet P (ed) Continuum micromechanics. Springer, Vienna, pp 61–130

Gologanu M (1997) Etude de quelques problemes de rupture ductile des metaux. These de Doctorat, Universite Paris 6

Gurson AL (1977) Continuum theory of ductile rupture by void nucleation and growth Part I-yield criteria and flow rules for porous ductile media. J Eng Mater Techn 99:2–15

Hill R (1948) A theory of the yielding and plastic flow of anisotropic metals. Roy Soc Lond Proc A 193:281–297

Kami A, Mollaei Dariani B, Sadough Vanini A, Comsa DS, Banabic D (2014a) Application of a GTN damage model to predict the fracture of metallic sheets subjected to deep-drawing. Proc Rom Acad A 15:300–309

Kami A, Mollaei Dariani B, Sadough Vanini A, Comsa DS, Banabic D (2014b) Numerical determination of the forming limit curves of anisotropic sheet metals using GTN damage model. J Mater Proc Techn 216:472–483

Keralavarma SM, Benzerga AA (2008) An approximate yield criterion for anisotropic porous media. CR Mech 336:685–692

Keralavarma SM, Benzerga AA (2010) A constitutive model for plastically anisotropic solids with non-spherical voids. J Mech Phys Solids 58:874–901

Koplik J, Needleman A (1988) Void growth and coalescence in porous plastic solids. Int J Solids Struct 24:835–853

Lebedev VI, Laikov DN (1999) A quadrature formula for the sphere of the 131st algebraic order of accuracy. Dokl Math 59:477–481

Leblond JB, Gologanu M (2008) External estimate of the yield surface of an arbitrary ellipsoid containing a confocal void. CR Mech 336:813–819

Lee B, Mear M (1992) Axisymmetric deformation of power–law solids containing a dilute concentration of aligned spheroidal voids. J Mech Phys Solids 40:1805–1836

Lewis AS (1996) Convex analysis on the hermitian matrices. SIAM J Opt 6:164–177

Liao KC, Pan J, Tang SC (1997) Approximate yield criteria for anisotropic porous ductile sheet metals. Mech Mater 26:213–226

Madou K, Leblond J-B (2012a) A Gurson-type criterion for porous ductile solids containing arbitrary ellipsoidal voids—I: limit-analysis of some representative cell. J Mech Phys Solids 60:1020–1036

Madou K, Leblond J-B (2012b) A Gurson-type criterion for porous ductile solids containing arbitrary ellipsoidal voids—II: determination of yield criterion parameters. J Mech Phys Solids 60:1037–1058
McClintock FA (1968) A criterion for ductile fracture by the growth of holes. J Appl Mech 35:363–371
Michel J-C, Suquet P (1992) The constitutive law of nonlinear viscous and porousmaterials. J Mech Phys Solids 40:783–812
Monchiet V, Gruescu C, Charkaluk E, Kondo D (2006) Approximate yield criteria for anisotropic metals with prolate or oblate voids. CR Mech 334:431–439
Monchiet V, Cazacu O, Charkaluk E, Kondo D (2008) Macroscopic yield criteria for plastic anisotropic materials containing spheroidal voids. Int J Plast 24:1158–1189
Morin L, Leblond JB, Kondo D (2015) A Gurson-type criterion for plastically anisotropic solids containing arbitrary ellipsoidal voids. Int J Solids Struct 77:86–101
Morse PM, Feshbach H (1953) Methods of theoretical physics. McGraw-Hill, New York
Nicodim I, Ciobanu I, Banabic D (2013) Effect of the constitutive law on the prediction of the wall thickness distribution of square cup. In: Proceedings of the 11th international MeTM conference, Cluj-Napoca, Romania, pp 173–176
Rice JR, Tracey DM (1969) On the ductile enlargement of voids in triaxial stress fields. J Mech Phys Solids 17:201–217
Rockafellar RT (1997) Convex analysis. Princeton University Press, Princeton
Schmitt D, Jault AD (2004) Numerical study of a rotating fluid in a spheroidal container. J Comput Phys 197:671–685
Simo JC, Hughes TJR (1998) Computational inelasticity. Springer, New York
Suquet P (1988) Discontinuities and plasticity. In Moreau J (ed) Non-smooth mechanics and applications. Springer, Vienna
Stewart JB, Cazacu O (2011) Analytical yield criterion for an anisotropic material containing spherical voids and exhibiting tension–compression asymmetry. Int J Solids Struct 48:357–373
Tabanov MB (1998) Normal forms of equations of wave functions in new natural ellipsoidal coordinates. AMS Trans 193:225–238
Talbot DRS, Willis JR (1985) Variational principles for inhomogeneous nonlinear media. IMA J Appl Math 35:39–54
Tagata T, Matsuo M, Iwasaki H, Higashi K (2004) Forming Limit Diagram for a superplastic 5083 aluminium alloy. Mat Trans 45:2516–2520
Tekoğlu C (2014) Representative volume element calculations under constant stress triaxiality, lode parameter, and shear ratio. Int J Solids Struct 51:4544–4553
Tvergaard V (1981) Influence of voids on shear band instabilities under plane strain conditions. Int J Fract 17:389–407
Tvergaard V (1982) On localization in ductile materials containing spherical voids. Int J Fract 18:237–252
Tvergaard V (1990) Material failure by void growth to coalescence. Adv Appl Mech 27:83–151
Tvergaard V, Needleman A (1984) Analysis of the cup-cone fracture in a round tensile bar. Acta Metall 32:157–169
Wang DA, Pan J, Liu SD (2004) An anisotropic Gurson yield criterion for porous ductile sheet metals with planar anisotropy. Int J Damage Mech 13:7–33

Chapter 5
Advanced Models for the Prediction of Forming Limit Curves

Dorel Banabic, Dan-Sorin Comsa, Philip Eyckens, Abdolvahed Kami and Mihai Gologanu

5.1 Failure in Sheet Metal Forming Operations

During the forming of flat sheet metal into a more complex shape, a number of plastic instabilities may occur subsequently. A 'plastic instability' occurs when the zone of plastic deformation is suddenly confined to a smaller zone. The first plastic instability which usually occurs in forming processes is the onset of diffuse necking, in which plastic deformation is confined to a smaller zone, but with typical dimensions that are still in the order of magnitude of the part's dimensions. In common industrial practice, the presence of a diffuse neck in a formed part is considered to be acceptable (Dieter

The original version of the chapter was revised: The erratum to this chapter is available at 10.1007/978-3-319-44070-5_8

D. Banabic (✉) · D.-S. Comsa · M. Gologanu
Technical University of Cluj Napoca, 28 Memorandumului,
400114 Cluj Napoca, Romania
e-mail: banabic@tcm.utcluj.ro
URL: http://www.certeta.utcluj.ro

D.-S. Comsa
e-mail: dscomsa@tcm.utcluj.ro

M. Gologanu
e-mail: gologanu@protonmail.com

P. Eyckens
Department of Materials Engineering, KU Leuven,
44 Kasteelpark Arenberg, 3001 Leuven, Belgium
e-mail: philip.eyckens@kuleuven.be

A. Kami
Amirkabir University of Technology, 424 Hafez Avenue, Tehran, Iran
e-mail: vahed.kami@gmail.com
URL: http://aut.ac.ir/aut/

D. Banabic (ed.), *Multiscale Modelling in Sheet Metal Forming*,
ESAFORM Bookseries on Material Forming,
DOI 10.1007/978-3-319-44070-5_5

1988). The 'formability' or 'forming limit' is thus determined by the onset of another type of plastic instability. For most materials and forming processes, this plastic instability is localized necking and so the terms 'formability' and 'forming limit' have been associated with localized necking in the literature.

In the next paragraphs, the different sequences of plastic instabilities which were found in the literature are described in more detail, giving an overview of the possible stages in the failure process. In each case, the final step for metal sheets, which are all ductile materials, is the onset of ductile failure, i.e. the coalescence of voids (resulting from the processes of void initiation and growth).

5.1.1 *Diffuse Necking—Localized Necking—Ductile Fracture*

As often observed in uniaxial tensile tests of sheet metal, diffuse necking is followed by localized necking. While the size of a diffuse neck is of the order of magnitude of the sample width, the width of the localized neck is only of the order of the sheet thickness (its length being of the order of magnitude of the sample width). After the onset of localized necking, strain is concentrated within the neck while the surrounding material returns to the elastic state. Consequently, the thickness within the neck drops drastically compared to the elastic surrounding. Localized necking is therefore also known as thinning instability. In the developed localized neck, a plane strain state exists with zero extension along the neck length (Marciniak and Kuczynski 1967).

After the onset of localized necking, the failure process can continue with ductile fracture through void coalescence within the neck, resulting in a cup-and-cone type of fracture in the terminology of fractography.

5.1.2 *Diffuse Necking—Localized Necking—Shear Instability—Ductile Fracture*

As shown in Bird et al. (1987) and Timothy (1989), the appearance of a macroscopic shear localization (over multiple grains) within the developed neck is possible, which is illustrated in Fig. 5.1. In Bird et al. (1987) and Carlson and Bird (1987), it is observed that shear localization initiates at the free surface within the neck, and that multiple shear bands can be found within a single localized neck.

5.1.3 *Diffuse Necking—Shear Instability—Ductile Fracture*

Various authors have reported sheet metal failure without localized necking. Examples that were found in the literature all deal with aluminium alloy sheets.

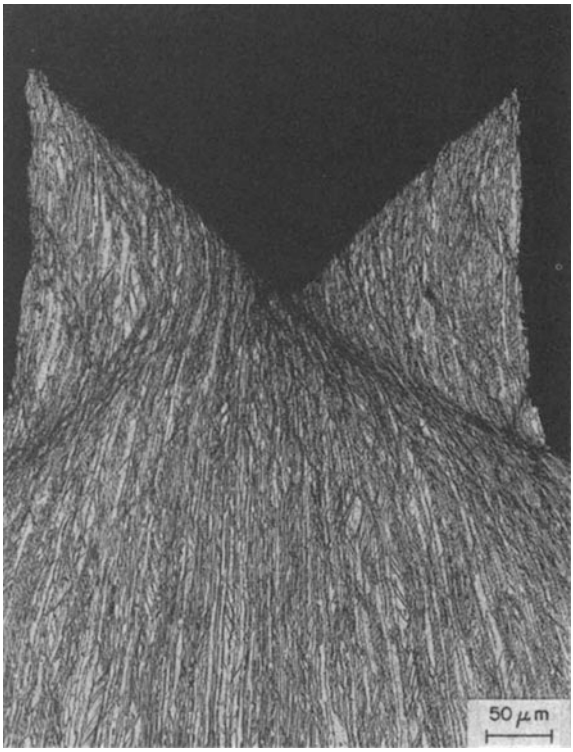

Fig. 5.1 Through-thickness section of ferrite-austenite steel deformed by plane strain punch stretching. Failure develops along two intersecting through-thickness, sample-scale shear bands (Carlson and Bird 1987)

In Duncan and Bird (1978), the metallographic cross-section of one aluminium alloy shows a well-developed neck after tensile testing, while another alloy shows no necking but instead failure has occurred along a plane at oriented at about 45° to the sheet normal. A very similar observation is presented in Chien et al. (2004), but on two other aluminium alloys. Failure along the plane at 45° to the sheet normal is assumed to be the result of shear localization along this direction.

Also in Hu et al. (2008) these two types of failure are also seen, but in this case for the same alloy either after direct chill casting (DC) or strip casting (CC). The distribution of second phase particles is different under these casting conditions: for DC, particle distribution is more homogeneous and necking is pronounced in a tensile test, while for CC, more stringers of particles are present and a shear-type of failure is seen. Lademo et al. (2008) present two different failure types for an extruded and subsequently cold rolled AlZnMg alloy. In the fully annealed condition, uniaxial tensile test specimens showed shear bands within a developed neck, while after partial annealing parallel and intersecting shear bands over the sheet thickness and oblique to the sheet normal direction were observed. The authors attribute this difference to the strong anisotropy of the sheet in the partially annealed condition, resulting from the retained β-fibre deformation texture, while fully annealed, the sheet has a texture close to random.

Sang and Nishikawa (1983) present the fracture profile of a number of aluminium alloys under plane strain stretching at various temperatures. The observed

fracture evolves from a shear-type fracture with no or small necking at low temperatures to a highly pronounced neck with cup-and-cone fracture at higher temperatures. The fracture morphology at room temperature depends on the alloy.

In pure bending of sheet metal, a similar failure mechanism is found, although shear bands do not extent throughout the whole sheet thickness. No references in the literature were found that report the appearance of localized necking in sheet under bending. Steninger and Melander (1982) subjected various steel grades to pure bending tests until failure. It is reported that after a certain homogeneous deformation of the outer fibres, shear bands appear near the outer surface, in which cracks are subsequently formed by void coalescence.

5.2 Forming Limit Diagram: Introduction

The formability is the capability of sheet metal to undergo plastic deformation to a given shape without defects. The defects have to be considered separately for the fundamental sheet metal forming procedures of deep-drawing and stretching. The difference between these types of stamping procedures is based on the mechanics of the forming process (see more details in Banabic et al. (2010a)).

The maximum values of the principal strains ε_1 and ε_2 can be determined by measuring the strains at failure (necking, fracture, wrinkling etc.) on sheet components covered with grids of circles. Gensamer (1946) was the first researcher who performed a thorough analysis of the strain localization phenomena in the case of sheet metals evolving along different load paths. He published a formability diagram that could be considered as the precursor of the FLCs. The research in this field was pioneered by Keeler (1961), Keeler and Backofen (1963) based on the observations of Gensamer (1946) that instead of using global indices the local deformations have to be considered (in the Fig. 5.2 is presented the Gensamer diagram reflected in mirror).

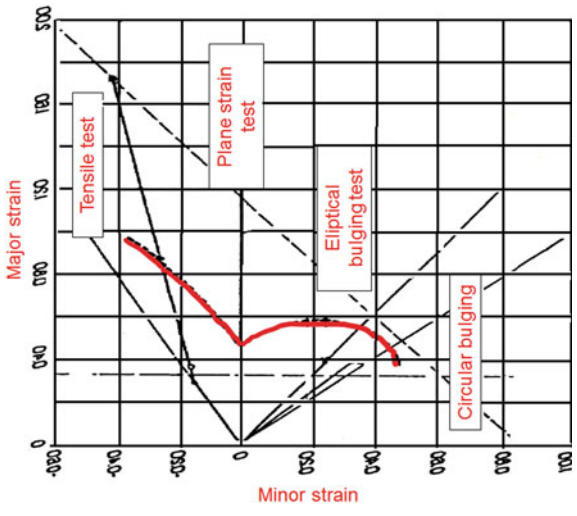

Fig. 5.2 The Forming Limit Diagram defined by Gensamer presented in mirror

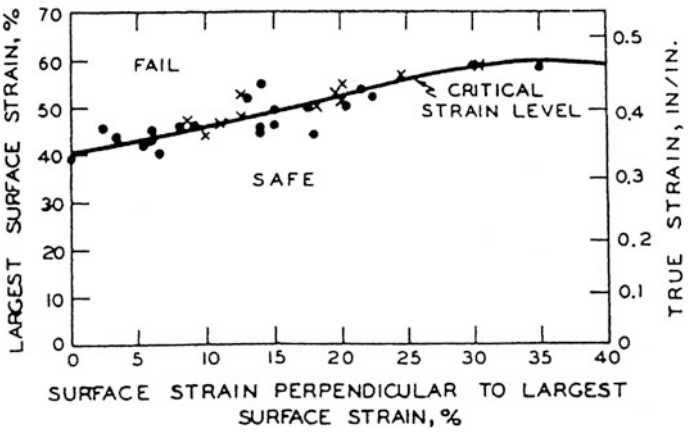

Fig. 5.3 Forming Limit Diagram defined by Keeler (1978)

During forming the initial circles of the grid become ellipses. Keeler plotted the major strains against the minor strains obtained from such ellipses at fracture of parts after biaxial stretching ($\varepsilon_1 > 0; \varepsilon_2 > 0$) (see Fig. 5.3 and Keeler (1978)).

For numerous materials the critical area between the domains has been detected both by means of laboratory tests and by forming of industrial components. These measurements were conducted for various materials. The excellent correlation of the results was a proof that the forming limits in sheet metal forming can be evaluated very well by determining the Forming Limit Curve (FLC).

Later, Goodwin (1968) plotted the curve for the tension/compression domain ($\varepsilon_1 > 0; \varepsilon_2 < 0$) by using different mechanical tests. In this case, transverse compression allows for obtaining high values of tensile strains like in rolling or drawing.

The diagrams of Keeler (*right* side) and Goodwin (*left* side) are currently called the Forming Limit Diagram (FLD), see Fig. 5.4 and Keeler (1978). Connecting all of the points corresponding to limit strains leads to a Forming Limit Curve (FLC). The FLC splits the 'fail' (i.e. above the FLC) and 'save' (i.e. below the FLC) regions.

The Forming Limit Curve FLC is plotted on a Forming Limit Diagram (FLD). The intersection of the limit curve with the vertical axis (which represents the plane strain deformation ($\varepsilon_2 = 0$)) is an important point of the FLD and is noted FLD_0. The position of this point depends mainly on the strain hardening coefficient and also on thickness.

Today, depending on the kind of limit strains that is measured different types of FLD's are determined: for necking and for fracture, see Fig. 5.5.

From subsequent experimental and theoretical research, even two more types of FLDs have emerged: the wrinkling limit diagram by Havranek (1977) (see Fig. 5.6) and the Stress Forming Limit Diagram (SFLD) by Arrieux and Boivin (1987) (see Fig. 5.7). The latter is not sensitive to the strain path.

In order to extend the application of stress limit curves to a 3D stress state (presence of through-thickness components of compressive stress), Simha et al.

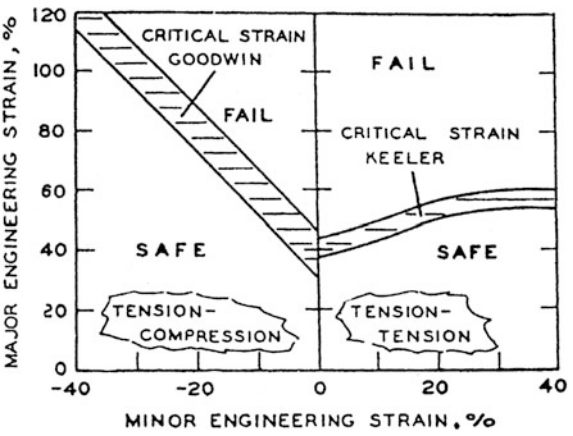

Fig. 5.4 Forming Limit Diagram defined by Keeler (1978)

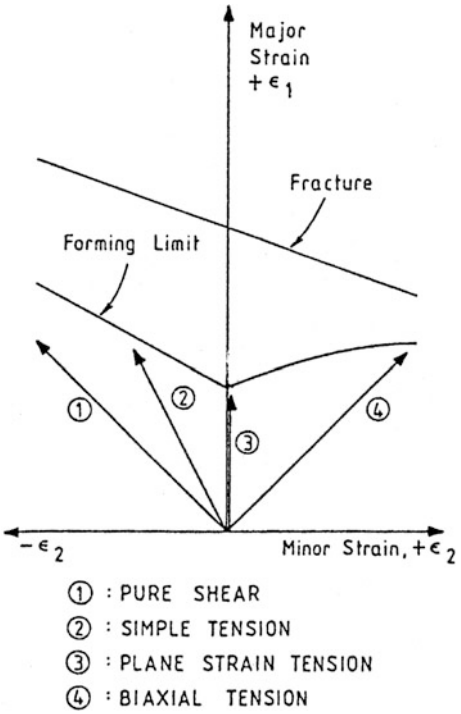

Fig. 5.5 Forming Limit Diagrams for necking and for fracture

(2007a) has introduced a new concept, namely Extended Stress-Based Limit Curve (XSFLC). The XSFLC represents the equivalent stress and mean stress at the onset of necking during in-plane loading. Figure 5.8 shows the three formulations of the Forming Limit Curve concept, namely: strain-based FLC (εFLC), stress-based FLC (σFLC) and Extended Stress-Based FLC (XSFLC), respectively. The equivalent stress and the mean stress are obtained through the expressions

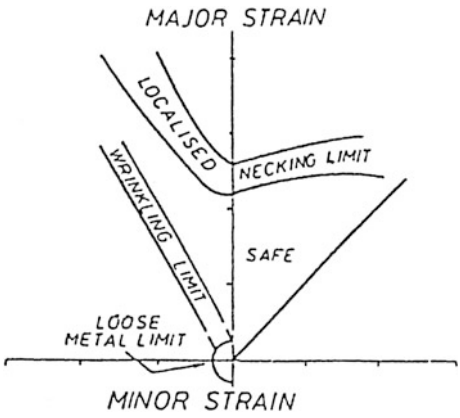

Fig. 5.6 Forming Limit Diagram for wrinkling

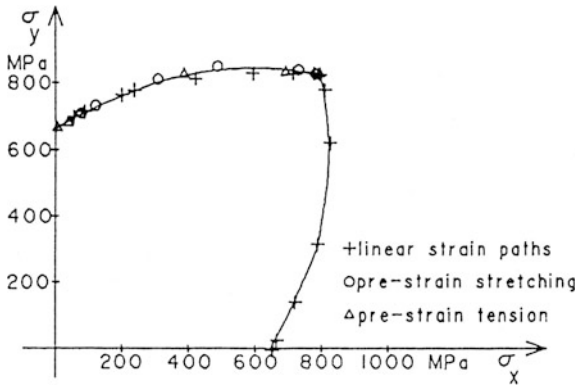

Fig. 5.7 Stress Forming Limit Diagram defined by Arrieux and Boivin (1987)

$$\sigma_{eq} = \sqrt{\sigma_1^2 + \sigma_2^2 - \sigma_1\sigma_2}; \tag{5.1}$$

$$\sigma_{mean} = \frac{\sigma_1 + \sigma_2}{3}, \tag{5.2}$$

where σ_{eq} is the equivalent stress, and σ_{mean} the mean stress, which is assumed to be positive in tension.

Figure 5.8 also presents the loading paths for the three cases: uniaxial stress, plane strain and biaxial stress. A thorough analysis of the conditions for the use of the XSFLC as a Formability Limit Curve under three-dimensional loading is presented in Simha et al. (2007b).

Forming Limit Curves are valid for one particular material alloy, temper and gauge combination. However material properties vary from batch to batch due to variation in the production process. Therefor a single Forming Limit Curve cannot be an exact description of the forming limit. Janssens et al. (2001) have proposed a

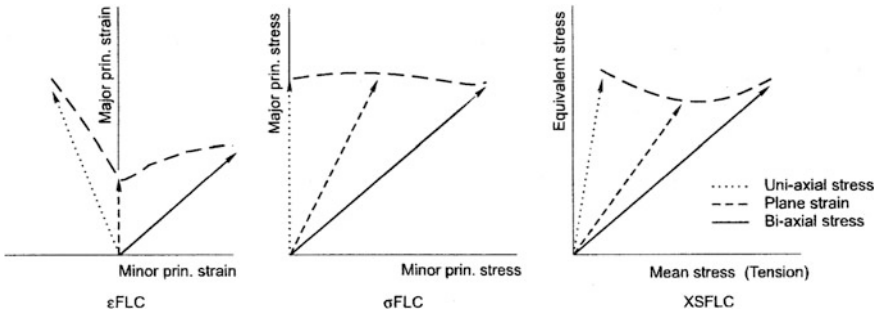

Fig. 5.8 Schematic of the Strain-Based Forming Limit Curve (εFLC), the Strain-Based Forming Limit Curve (σFLC) and the extended Strain-Based Forming Limit Curve (XSFLC) (Simha et al. 2007b)

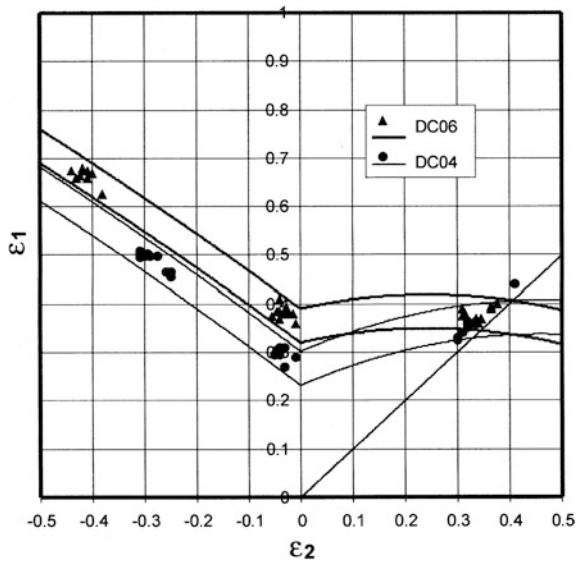

Fig. 5.9 Forming Limit Band (FLB) for two steel grades (Janssens et al. 2001)

more general concept, namely the Forming Limit Band (FLB) as a region covering the entire dispersion of the Forming Limit Curves (Fig. 5.9).

5.3 Experimental Formability Tests

The FLC should cover the entire deformation domain specific to the sheet metal forming processes. In general, the strain combinations span between those induced by uniaxial and equibiaxial surface loads. The subsequent discussion will insist on the experimental methods commonly used for investigating the deformation domain

of the FLCs. First an overview is given of some experimental techniques designed for the determination of the whole or a partial forming limit diagram (FLD), i.e. Nakazima tests, Marciniak, tests stretch-bending tests, hydraulic bulging tests and tests performed in a tensile test machine (see more details in Banabic et al. (2010a). After the experimental formability techniques, experimental results on the influence of different factors (sheet curvature, thickness, temperature and strain rate on formability are discussed.

5.3.1 An Overview of Experimental Formability Tests

The most used procedures for the experimental determination of the FLCs are those based on the punch stretching principle. Keeler (1961) was the first researcher who adopted such a method. He used circular specimens and spherical punches with different radii in order to modify the load path. In general, the punch stretching test developed by Keeler is able to investigate only the right end of the tension-tension FLC branch. Hecker (1972) extended Keeler's methodology to the whole tension-tension domain by improving the lubrication of the contact surface between punch and specimen. A notable development of this experimental procedure is due to Nakazima and Kikuma (1967). He used a hemispherical punch having a constant radius in combination with rectangular specimens with different widths (Fig. 5.10).

In this way, Nakazima was able to explore both the tension-compression and the tension-tension domains of the FLC. The Nakazima forming limit test is the most widely-spread method for experimental determination of the FLD. It uses a hemispherical punch with large diameter (in the order of 100 mm) to deform a clamped specimen until failure. Due to the punch curvature, a strain gradient exists in the sheet thickness direction, and also in the plane of the sheet. By using circular specimens with lateral notches, Hasek (1978) removed the main disadvantage of Nakazima test, namely the wrinkling of the wide specimens. Under biaxial

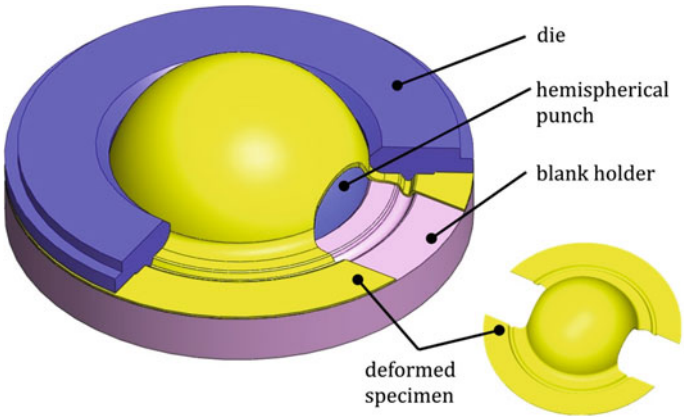

Fig. 5.10 Schematic view of the Nakazima test

stretching, the largest straining is not necessarily found at the punch apex (Keeler and Brazier 1975). The strain mode is determined by choosing the specimen width and/or lubrication conditions (Charpentier 1975). It was early recognised that the experimental determination of a FLC through the Nakazima test was prone to various test conditions such as punch geometry, lubrication conditions and limit strain measurement method. Consequently, several laboratory procedures were proposed for comparison purposes of different materials, such as the CRM-method (Bragard 1989). In this method, the limit strains are determined by a parabolic fit of the non-homogeneous strain field after the onset of necking. The use of Digital Image Correlation (DIC) for use of in-process strain measurement on a surface of the sheet, results in a more automated and thus less user-dependent measurement of the necking strains, as discussed in Geiger and Merklein (2003). Through DIC measurements, a relative small non-linearity of the strain path in the Nakazima test is found in Leppin et al. (2008): due to the hemispherical punch, a small initial equibiaxial strain is found on the convex sheet surface, independent of the sheet geometry. As a result, FLC_0 determined from the Nakazima test is slightly shifted to the right in the FLD.

In the Marciniak forming limit test, first described in Marciniak et al. (1973), a punch with flat bottom deforms the sheet until failure in the flat part of the sheet occurs. Failure at the punch edge is avoided through use of an auxiliary sheet with a hole with appropriate dimensions in between the punch and test sheet. The flat region of the test sheet deforms homogeneously, except in the site where strain localization takes place. In the original paper, the test and auxiliary sheets are fully clamped around the punch, and the strain mode is determined by the punch geometry (having a circular, elliptical or rectangular bottom face). Grosnostajski and Dolny (1980) improved Marciniak's test by changing the geometry of the specimen and carrier blank.

A standardized procedure for determination of the FLC based on Nakazima and Marciniak tests, using a 100 mm diameter cylindrical or hemispherical punch respectively, is found in ISO norm 12004 (2008). Various deformation modes are achieved by different sheet sample geometries. Additional information on the this standard can be found in Hotz and Timm (2008). In Vegter et al. (2008), the use of a rubber disc in the tribological system in the Nakazima test is analyzed through FE simulations. Although not described in the ISO norm 12004, it is quite common to use such a disc in order to achieve the highest strains and thus the neck at the apex of the Nakazima punch, a condition which is required in this norm.

In stretch-bending tests, a rectangular blank is clamped at two opposite edges and deformed under a cylindrical punch which has its axis along the direction of the clamped sheet edges. The punch diameter can vary from the order of the sheet thickness much larger values. The distribution and evolution of the strain field in stretch-bending can be quite complex. Uko et al. (1977) presents experimental results for HSLA steel under stretch-bending in which the inside surface thickness strain changes from compressive to tensile during testing. The observed deformation mode is near-plane strain (small negative minor strains).

The variability of sheet formability and sheet formability testing for a standardized stretch-bending test, named OSUFT, is explored in Karthik et al. (2002). Sensitivity of numerous parameters (the hold-down force, sheet thickness, sample width, deformation speed, lubrication conditions and seasoning of the tooling) to the punch stroke at failure was investigated. The variability of this test between different test laboratories was shown to be much less compared to Nakazima tests using plane-strain samples, making it more useful for material comparison purposes.

In Kitting et al. (2008), micrographic cross-sections are shown of failed sheet deformed through stretch-bending with varying punch radii. It can be seen that the double-sided neck observed at large radii changes into a single-sided neck at the convex sheet side for smaller radii. Also, punch penetration in the sheet can be seen in case the punch radius is of the order of the sheet thickness.

The positive-positive region (right branch) of the FLC can be reproduced in a hydraulic bulging device equipped with dies having circular or elliptic apertures. Different load paths belonging to the tension-tension domain result by varying the eccentricity of the elliptic aperture (Ranta-Eskola 1979). In hydraulic bulging, a fully clamped sheet is deformed through a die with circular or elliptical aperture through fluid pressure, usually oil. The deformation mechanism in hydraulic bulge testing with circular die aperture has been experimentally studied by Ranta-Eskola (1979). It is shown that at the bulge apex, sheet thinning is maximal, so it is the preferential site for plastic instability and failure. It is also pointed out that the sheet assumes a spherical shape at the apex, although the strain state can differ from equibiaxial loading due to in-plane anisotropy.

Forming limit tests in tensile test machines have been proposed for deformation modes of the left-hand side of the FLD. The uniaxial tension of flat specimens having circular notches (proposed by Brozzo and de Lucca (1971)) allows the exploration of the tension-compression range (left branch of the FLC). By using relatively wide specimens, it is also possible to reach the plane strain point. In Sang and Nishikawa (1983) and later in Timothy (1989), a plane strain state in a tensile test machine is obtained through the use of a clamping device with knife edges to prevent deformation in the width direction. Later, a methodology to obtain the full left-hand side of the FLD from tensile test specimens with different geometries has been proposed by Holmberg et al. (2004). As a conclusion, the uniaxial tension is suitable only for investigating the positive-negative domain of the FLC.

Figure 5.11 compares the results provided by different experimental methods developed in the seventh and eighth decades of the previous century. One may notice that none of those procedures are able to reproduce the whole deformation domain of the FLC. Aiming to overcome this drawback, as well as the discrepancies of the limit strains provided by different methodologies, a specialized IDDRG workgroup elaborated a standard proposal for the FLC determination recommending the use of the Nakazima or Marciniak tests. The proposal issued by IDDRG was subsequently adopted at international level in the form of the ISO 12004 standard ISO (2008). A description of the experimental procedures analyzed by the IDDRG workgroup and their comparison by means of a “robin test” performed in different laboratories participating in the standardization activity is given

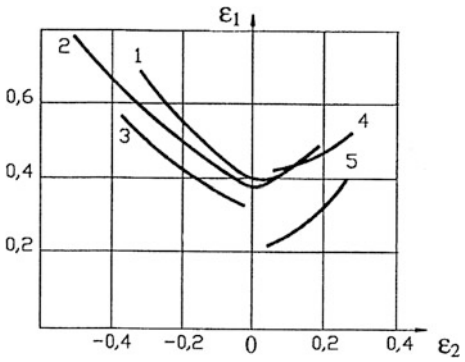

Fig. 5.11 FLCs determined using different experimental methods: 1—Hasek; 2—Nakazima; 3—uniaxial tension; 4—Keeler; 5—hydraulic bulge test

in Hotz and Timm (2008). A presentation of the determination of the FLCs is described in Geiger and Merklein (2003).

Banabic et al. (2013) proposed a new procedure for the experimental determination of the FLCs. The methodology is based on the hydraulic bulging of a double specimen (Fig. 5.12).

The upper blank has a pair of holes pierced in symmetric positions with respect to the centre, while the lower one acts both as a carrier and a deformable punch. By modifying the dimensions and position of the holes, it is possible to investigate the entire deformation range of the FLC. Figure 5.13 provides a synthetic presentation of the numerical results obtained in the case of the AA6016-T4 aluminium alloy. The results provided by the hydraulic bulging experiments performed with the same geometries of the specimens are also plotted on the diagram. One may notice a very good agreement between the numerical simulation and the experimental data, as well as the fact that the characteristic strain paths are closed to linearity in all cases.

The most important advantages of the method are the capability of investigating the whole strain range specific to the sheet metal forming processes, simplicity of the equipment, and reduction of the parasitic effects induced by the friction, as well as the occurrence of the necking in the polar region. The comparison between the FLCs determined using the new procedure and the Nakazima test shows minor differences. Figure 5.14 compares the FLCs obtained using the methodology proposed by the authors and the Nakazima test (according to the specifications of the international standard ISO 12004-2). In both cases, the limit strains have been measured using the ARAMIS system (Banabic et al. 2013).

5.3.2 *Experimental Formability Observations Concerning the Influence of Sheet Curvature*

A comparative study between the Nakazima and Marciniak tests for aluminium killed steel, Brass and cold rolled aluminium (Ghosh and Hecker 1975) showed a clear trend of higher formability determined from the Nakazima test. It is however

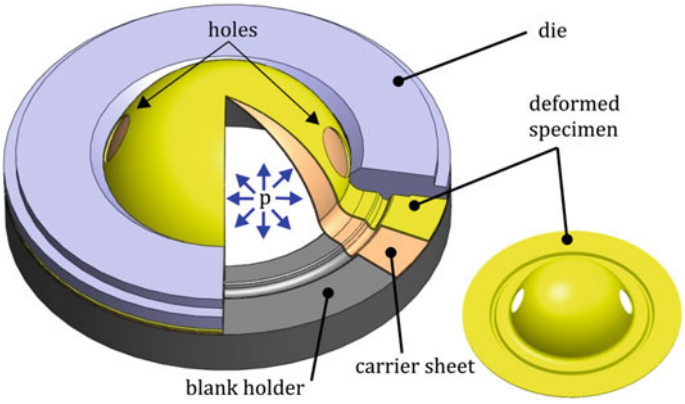

Fig. 5.12 Schematic view of the new formability test

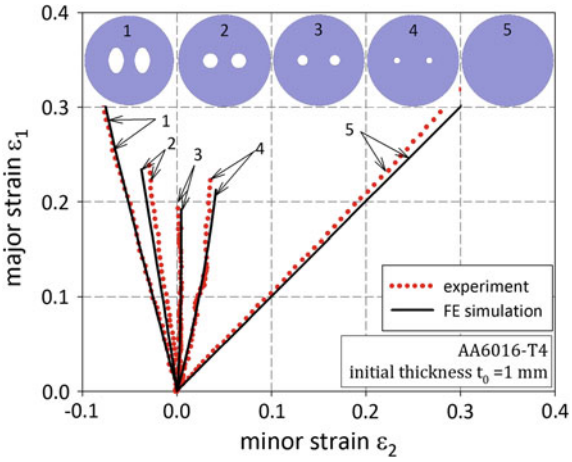

Fig. 5.13 Strain paths obtained in the hydraulic bulge tests: comparison between the numerical simulation and experimental data

preliminary to conclude from this study that sheet curvature during forming is the only reason for this since it was chosen to reduce the sheet thickness in the Nakazima test instead of using an auxiliary sheet.

In Levy (2002), an empirical law is presented for a number of steel grades to assess the increase in formability in sheet material after it has been subjected to a form of bending, being multiple bending during drawbead flow or bending occurring at corner radii of press tooling. As a rule of thumb, it is concluded that for material which has been subjected to this kind of stretch-bending, the FLD can be shifted upwards by an amount equal to 60 % of the thinning strain that was achieved in the drawbead or under small tool corners.

The beneficial effect of simultaneous bending and unbending during plane strain stretching was shown in Emmens and van den Boogaard (2008), in which a tensile

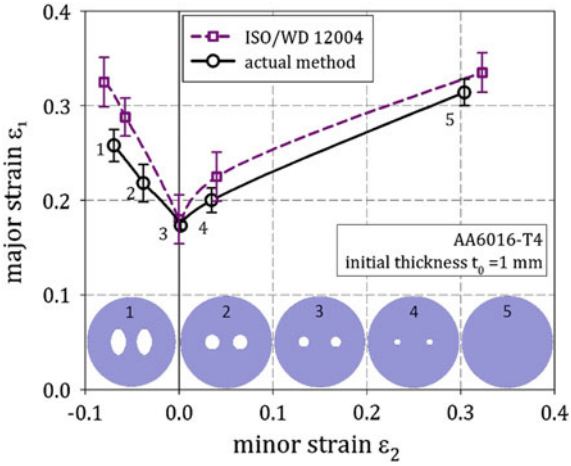

Fig. 5.14 Forming Limit Diagram of the AA6016-T4 alloy

test specimen was additionally subjected to small bending strains under three moving rollers.

5.3.3 *Experimental Formability Observations Concerning the Influence of Sheet Thickness*

The influence of the sheet thickness on the limit strains has been studied by Haberfield and Boyles (1973), Romano et al. (1976), Hiam and Lee (1978), Kleemola and Kumpulainen (1980) etc.

The plane strain intercept of the FLC (denoted FLC_0), was already in the 1970s found to be dependent on the sheet thickness for a number of hot and cold rolled steels by Keeler and Brazier (1975), resulting in higher limit strains for thicker sheets.

Possible influencing factors which result in a general higher forming limit of thicker sheets are discussed in Marciniak (1977). The factors that depend on sheet thickness include through-thickness gradients of strain, stress and triaxiality, friction forces, tool contact pressure, and sheet metal homogeneity.

In Karthik et al. (2002), a standardized stretch-bend test (OSUFT) was used to show that thicker sheets failed at higher punch strokes, even though less draw-in under the drawbeads occurred for thicker sheets.

The influence of sheet thickness on the FLD is characterized by the following relationships Tisza and Kovács (2012):

- the FLD for necking depends on sheet thickness (t_0) (see Fig. 5.15);
- as the thickness rises, the curve rises on the plot ($\varepsilon_1; \varepsilon_2$);
- The influence is high for pure expansion and vanishes for pure compression;
- The influence of the thickness on the FLD_0 increases linearly;

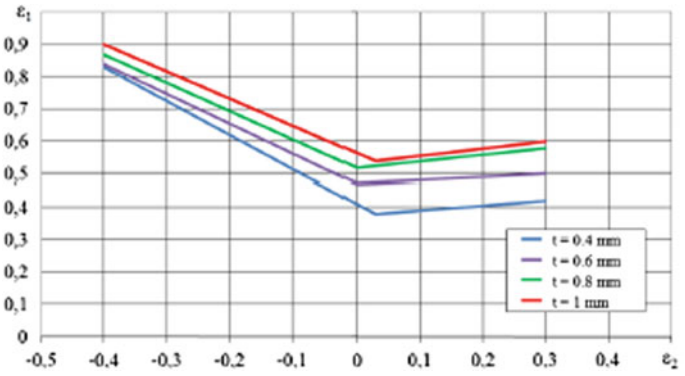

Fig. 5.15 Influence of the thickness on the FLC

- Along a linear strain path the rise of the FLD is proportional to the increase of thickness but this influence vanishes above a critical value.

The engineer can decide if an unsuccessful forming process may be improved by increasing the sheet thickness. This is especially important if the stress acting during the forming process is tensile in both principal directions.

5.3.4 Experimental Formability Observations Concerning the Combined Influence of Sheet Curvature and Thickness

Ghosh and Hecker (1975) showed that the choice of the experimental method used for the FLC determination (in-plane versus out-of-plane) influences the position of the limit curves. The influence of the punch curvature on the stretching limits has been studied first by Charpentier (1975). In Charpentier (1975) and Demeri (1986), it is shown that the limit strain is increased by increasing the sheet thickness, or by decreasing the punch radius in the Nakazima test. It is also observed that the strain distribution is less homogeneous for smaller punch radii. For the same non-dimensional bending curvature t/R (the ratio of sheet thickness to punch radius), it appears that the limit strain increase of a thicker sheet and a smaller punch radius is higher compared to a thinner sheet stretched under a smaller punch radius (Charpentier 1975) (see Fig. 5.16) (the experimental data was taken from Charpentier (1975)). Shi and Gerdeen (1991) performed a theoretical analysis of this influence using the Marciniak-Kuckzinsky model.

Based on an experimental campaign of punch-stretching of steel alloys with various punch radii and sheet thicknesses, Tharrett and Stoughton (2003a) proposed that the strain on the concave side be used for comparison with FLC_0 (concave-side rule), rather than the mid-plane strain which is a more conservative criterion.

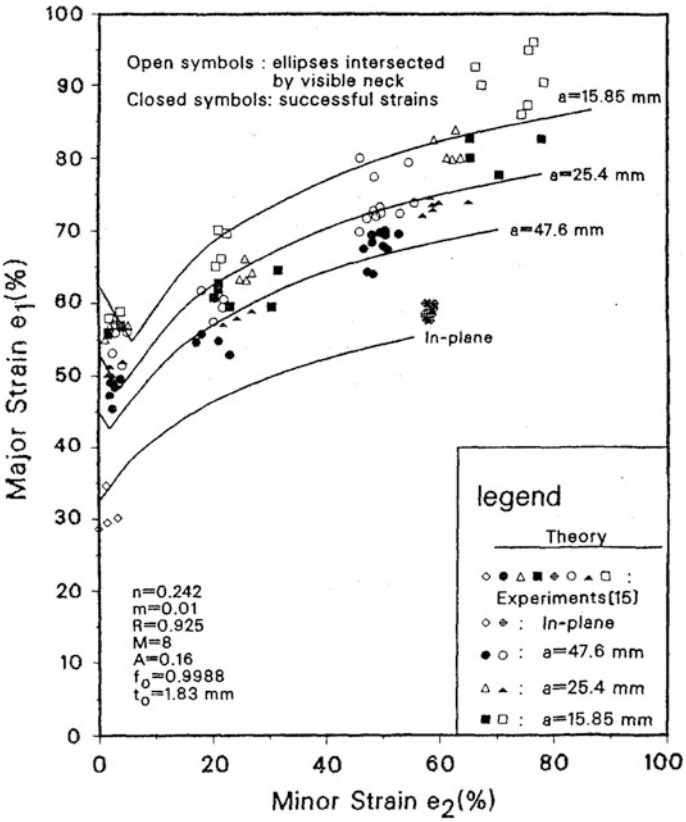

Fig. 5.16 Influence of punch curvature on the FLC (Charpentier 1975)

However, for two FCC materials (70/30 Brass and AA6010), this method resulted in an overestimate of the forming limit (Tharrett and Stoughton 2003b).

5.3.5 *Experimental Formability Observations Concerning the Influence of Temperature*

The influence of the temperature on the limit strains was studied first by Lange (1975) and later by Ayres and Wenner (1978), Kumpulainen et al. (1983), van den Boogaard (2002), Li and Ghosh (2004), Abedrabbo et al. (2006), etc. According to these researchers, the temperature has a different influence on the formability of different metallic alloys. For example, the formability of the AA 5754 alloy has a significant increase when the temperature rises even with small amounts (from 250 to 350 °C) (Fig. 5.17 and Li and Ghosh (2004)), while temperature variations in the

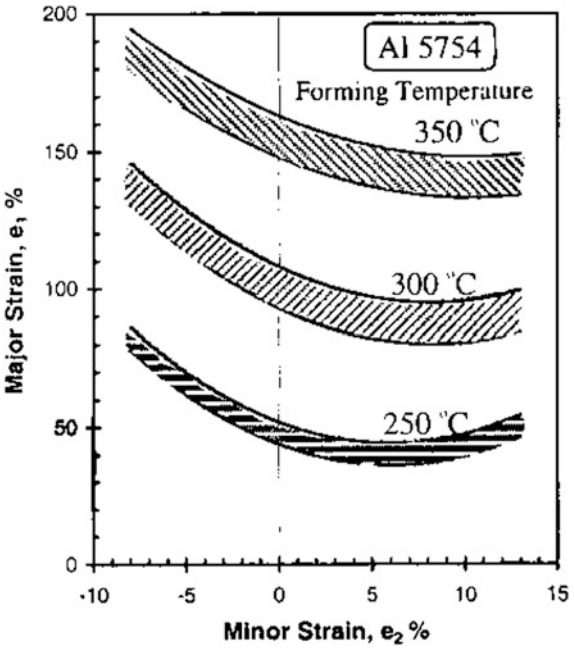

Fig. 5.17 Influence of the temperature on the FLC for the 5754 aluminium alloy (Li and Ghosh 2004)

same range have a very little influence on the formability of the AA 6111-T4 alloy (Fig. 5.18 and Li and Ghosh (2004)). The increase of the formability by raising the temperature of the material is frequently used in the case of the sheet metals having a poor formability at room temperature (some aluminium or magnesium alloys, high-strength steels, etc.).

5.3.6 *Experimental Formability Observations Concerning the Influence of Strain Rate*

Drewes and Martini (1976) followed later by Ayres and Wenner (1978) and Percy (1980) have analyzed the influence of the strain rate on the limit strain. In general, the increase of the strain rate causes a downward displacement of the FLC, that is a diminishment of the formability. Such an example is shown in Fig. 5.19 and Percy (1980) and corresponds to the SPCEN-SD steel. Similar results were also obtained by Ayres and Wenner (1978). On the other hand, more recently, Balanethiram and Daehn (1994) have reported a significant increase of the formability when the strain rate is also increased for an OFHC copper. Gerdooei and Dariani (2009) have explained this effect based on the Johnson-Cook law. The different behaviour of the metallic materials from this point of view is a consequence of the different values of the strain-rate sensitivity index, as well as of the different mechanical response when the strain rate is modified.

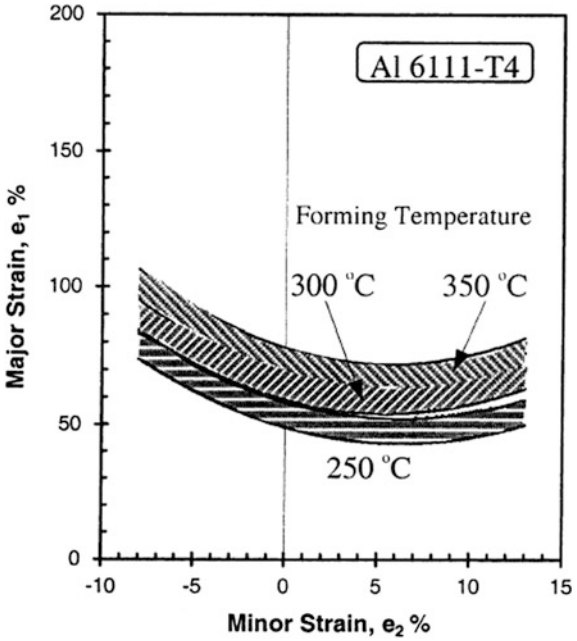

Fig. 5.18 Influence of the temperature on the FLC for the 6111-T4 aluminium alloy (Li and Ghosh 2004)

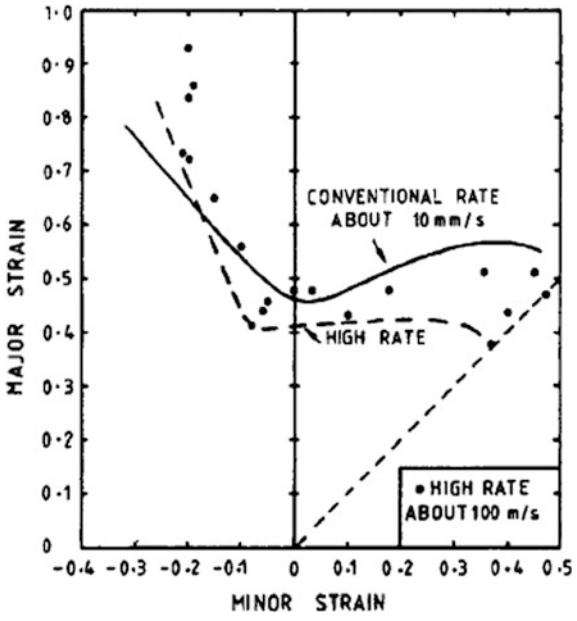

Fig. 5.19 Influence of the strain-rate on the FLC for SPCEN-SD steel (Percy 1980)

5.4 Forming Limit Models

Various theoretical models have been developing for the calculation of forming limit curves (Fig. 5.20). The first ones were proposed by Swift (1952) and Hill (1952) assuming homogeneous sheet metals (the so-called models of diffuse necking and localized necking), respectively). The Swift model has been developed later by Hora, so-called Modified Maximum Force Criterion-MMFC, (Hora and Tang 1994). Marciniak (1965) proposed a model taking into account that sheet metals are non-homogeneous from both the geometrical and the structural point of view. Storen and Rice (1975) developed a model based on the bifurcation theory. Dudzinski and Molinari (1991) used the method of linear perturbations for analyzing the strain localization and computing the limit strains.

Since the theoretical models are rather complex and need a profound knowledge of continuum mechanics and mathematics while their results are not always in agreement with experiments, some semi-empirical models have been developed in recent years.

In the next sections the most commonly used models are presented briefly with the focus on those based on the necking phenomenon (Swift and Hill), the Marciniak-Kuczynski and MMFC models.

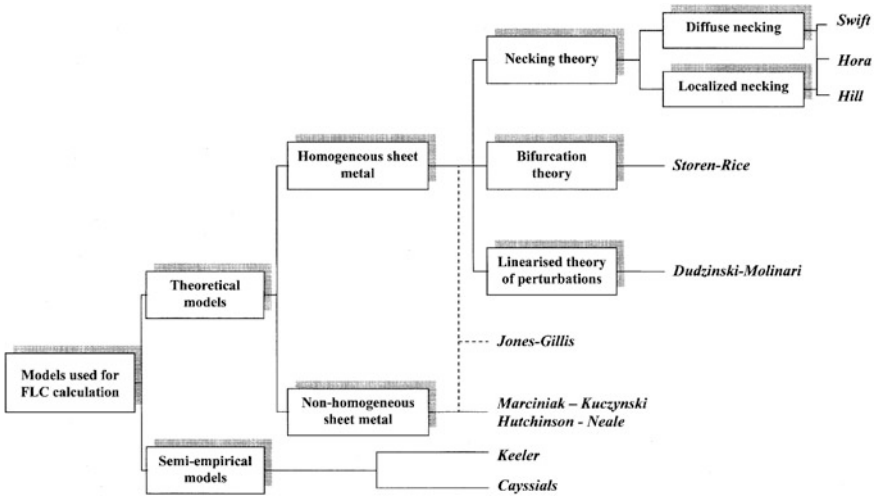

Fig. 5.20 Theoretical models used in FLC calculation

5.4.1 Diffuse Necking Models

5.4.1.1 Swift's Model

Considère (1885) approached for the first time the problem of plastic instability in uniaxial tension. In the case of ductile materials, two domains may be distinguished in the region of plastic straining. In the first domain the hardening influence on the traction force is stronger than the influence of the cross-section reduction. This is the so-called 'domain of stable plastic straining', being characterized by the fact that an increase of the traction force is needed in order to obtain an additional deformation of the specimen. In the second domain material hardening cannot compensate the decrease of the traction force due to the reduction of the specimen's cross-section. This is the so-called 'domain of unstable plastic straining', being characterized by a decrease of the traction force, although the stress continues to increase.
The beginning of necking corresponds to the maximum of the traction force. From the mathematical point of view, this condition can be written in the form

$$dF = 0 \tag{5.3}$$

By simple mathematical manipulations the following condition of plastic instability is obtain:

$$\frac{d\sigma}{d\varepsilon} = 1 + \sigma \tag{5.4}$$

Assuming a Ludwik-Hollomon strain-hardening law,

$$\sigma = k\bar{\varepsilon}^n \tag{5.5}$$

condition (5.4) becomes

$$\bar{\varepsilon} = n \tag{5.6}$$

Hence, according to Considère's criterion, a material obeying the Ludwick-Hollomon hardening law starts to neck when the strain is equal to the hardening coefficient.

Swift (1952) used the Considère criterion to determine the limit strains in biaxial tension. He analysed a sheet element loaded along two perpendicular directions and applied the Considère criterion for each direction. Assuming a strain hardening described by Eq. (5.5), he obtained the following expressions of the limit strains:

$$\varepsilon_1^* = \frac{\sigma_1\left(\frac{\partial f}{\partial \sigma_1}\right)^2 + \sigma_2\left(\frac{\partial f}{\partial \sigma_2}\right)\left(\frac{\partial f}{\partial \sigma_1}\right)}{\sigma_1\left(\frac{\partial f}{\partial \sigma_1}\right)^2 + \sigma_2\left(\frac{\partial f}{\partial \sigma_2}\right)^2} n \tag{5.7}$$

$$\varepsilon_2^* = \frac{\sigma_2\left(\frac{\partial f}{\partial \sigma_1}\right)^2 + \sigma_1\left(\frac{\partial f}{\partial \sigma_1}\right)\left(\frac{\partial f}{\partial \sigma_2}\right)}{\sigma_1\left(\frac{\partial f}{\partial \sigma_1}\right)^2 + \sigma_2\left(\frac{\partial f}{\partial \sigma_2}\right)^2} n \tag{5.8}$$

where f is the yield function.

By using different yield functions, it is possible to evaluate the limit strains as functions of the loading ratio α and the mathematical parameters of the material (hardening coefficient n, anisotropy coefficient r, strain-rate sensitivity m, etc.). As an example, if the Hill 1948 yield criterion is used, the limit strains are as follows:

$$\varepsilon_1^* = \frac{[1 + r(1-\alpha)]\left(1 - \frac{2r}{1+r}\alpha + \alpha^2\right)}{(1+r)(1+\alpha)\left[1 - \frac{1+4r+2r^2}{(1+r)^2}\alpha + \alpha^2\right]} n \tag{5.9}$$

$$\varepsilon_2^* = \frac{[(1+r)\alpha - r]\left(1 - \frac{2r}{1+r}\alpha + \alpha^2\right)}{(1+r)(1+\alpha)\left[1 - \frac{1+4r+2r^2}{(1+r)^2}\alpha + \alpha^2\right]} n \tag{5.10}$$

The expressions of the limit strains associated to some other yield criteria (such as Hill 1979 and Hill 1993) are presented in Banabic and Dannenmann (2001). By computing the values of ε_1^* and ε_2^* for different loading ratios α and recording them in a rectangular coordinate system ε_1, ε_2 the necking limit curve is obtain.

5.4.1.2 Modified Maximum Force Criterion (MMFC)

The 'Modified Maximum Force Criterion' (MMFC) for diffuse necking proposed by Hora and Tang (1994) is based on Considère's maximum force criterion. The idea behind the MMFC-Model is to factor in an additional increase in hardening, which is triggered by the deviation from the initial, homogeneous stress condition —e.g. uniaxial tension—to the stress condition of local necking and with this to the point of plane strain (Fig. 5.21).

The mathematical expression of the criterion is:

$$\frac{\partial \sigma_{11}}{\partial \varepsilon_{11}} + \frac{\partial \sigma_{11}}{\partial \beta}\frac{\partial \beta}{\partial \varepsilon_{11}} = \sigma_{11} \tag{5.11}$$

Herein, β represents the strain rate ratio given by

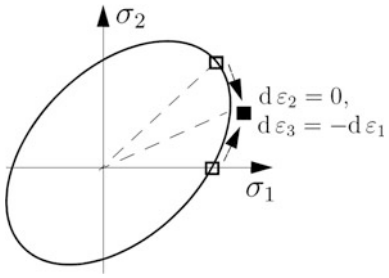

Fig. 5.21 Basic principle of the MMFC criterion

$$\beta = \frac{\dot{\varepsilon}_{22}}{\dot{\varepsilon}_{11}} \tag{5.12}$$

The MMFC model can be written in a form independent of the yield criterion, i.e. it can accommodate any yield criterion. According to Hora and Tang (1994) the following relations are defined:

$$\alpha = \frac{\sigma_{22}}{\sigma_{11}}, \quad \bar{\sigma} = \frac{\sigma_{11}}{f(\alpha)}, \quad \bar{\varepsilon} = g(\alpha)\varepsilon_{11}. \tag{5.13}$$

The stress ratio α takes the values $0 \leq \alpha \leq 1$, i.e. it ranges from uniaxial tension ($\alpha = 0$) to equibiaxial tension ($\alpha = 1$). $\bar{\sigma}$ is the equivalent stress defined by the yield criterion which is utilized in the necking analysis, see below. $\bar{\varepsilon}$ is the equivalent plastic strain.

$$g(\alpha) = f(\alpha)[1 + \alpha \cdot \beta(\alpha)] \tag{5.14}$$

The function $f(\alpha)$ is obtained from:

$$f(\alpha) = \frac{1}{\bar{\sigma}(\sigma_{11} = 1, \sigma_{22} = \alpha)} \tag{5.15}$$

Assuming the instantaneous yield stress is represented by the Swift hardening law, Hora's necking criterion then reads (Hora and Tang 1994)

$$Y'(\bar{\varepsilon}) \cdot f(\alpha) \cdot g(\alpha) - Y(\bar{\varepsilon}) \cdot \frac{f'(\alpha) \cdot g(\alpha) \cdot \beta(\alpha)}{\beta'(\alpha)\bar{\varepsilon}} = f(\alpha)Y(\bar{\varepsilon}) \tag{5.16}$$

with $\beta' = d\beta/\mathrm{d}\alpha, \quad \mathrm{f}' = \mathrm{df}/\mathrm{d}\alpha, \quad Y' = dY/d\bar{\varepsilon}$.

The primary unknown $\bar{\varepsilon}$ can be easily calculated as the solution of the necking criterion given by Eq. (5.16) (which is, in general, a non-linear equation) using Newton's method. Once the equivalent plastic strain at the onset of necking for a

chosen linear strain path is calculated from Eq. (5.16), the major and minor in-plane strains corresponding to the onset of necking are found from

$$\varepsilon_{11}^{*} = \frac{\bar{\varepsilon}^{*}}{g}, \quad \varepsilon_{22}^{*} = \beta \cdot \varepsilon_{11}^{*} \tag{5.17}$$

$\bar{\varepsilon}^{*}$ is the root of the necking criterion Eq. (5.16).

In order to take into account the influence of the thickness on the limit strains, an enhanced MMFC (eMMFC) has been recently proposed by Hora and his co-workers (Hora et al. 2003). A term is added to the original formulation (5.11). The eMMFC is expressed as

$$\frac{\partial \sigma_{11}}{\partial \varepsilon_{11}}\left[1 + \frac{t}{2r} + e(E,t)\right] + \frac{\partial \sigma_{11}}{\partial \beta}\frac{\partial \beta}{\partial \varepsilon_{11}} \geq \sigma_{11} \tag{5.18}$$

where, t is the thickness, r is the sheet curvature radius and $e(t, E = const) = E_0\left(\frac{t}{t_0}\right)^{p}$ represents the influence of the thickness. The parameters E_0, p and t_0 are determined using experimental data (Hora and Tong 2006).

Recently, Hora et al. (2013) investigated the influence of the yield loci and strain-hardening laws on the Forming Limit Curves using the MMFC model. Different explicit expressions of the MMFC model have been proposed based on some simplifications. A new formulation of the MMFC model Manopulo et al. (2015) has been proposed to accommodate this model with the Homogeneous Anisotropic Hardening (HAH) model proposed by Barlat et al. (2011). Using the new approach, the role of the distortional hardening on strain localization has been analyzed.

Banabic and Soare (2009) make more precise statements about the nature of the numerical instability of the MMFC model, asses the predictive capabilities of the criterion, and introduce a fitting parameter for its plane strain calibration. In order to improve the prediction of limit strains using the MMFC model, Paraianu et al. (2009), (2010) chose to introduce two fitting coefficients in the original model.

The advantage of the MMFC criteria can be found in their independence of the inhomogeneity assumption. These criteria could be used to calculate FLC for non-linear strain paths. A drawback of the MMFC models is the fact that they can be affected by a singularity that emerges if the yield locus contains straight line segments, as in the case of Barlat et al. (2003) or BBC 2005 (Banabic et al. 2005a) yield criteria. Banabic et al. (2015) removed this limitation of the MMFC criterion by modifying the initial formulation. As an example, the singularity noticed by Aretz (2004) in the case of the AA2090-T3 aluminium alloy is no more present when using the new formulation proposed in Banabic et al (2015) (see Fig. 5.22).

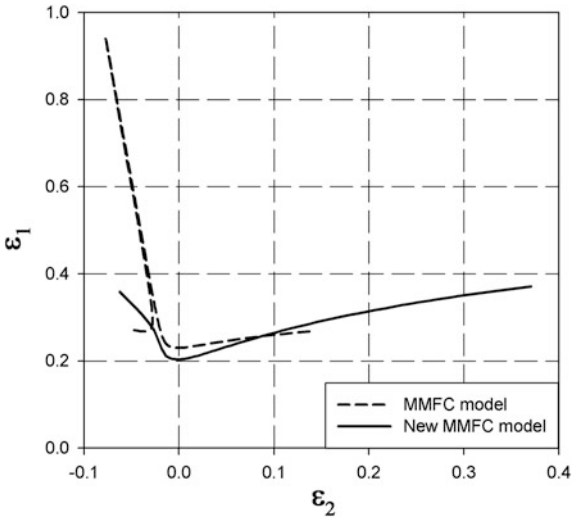

Fig. 5.22 FLC of the AA2090-T3 aluminium alloy predicted by classic and new MMFC models

5.4.2 *Localized Necking Model (Hill's Model)*

In the case of uniaxial tension, the localized necking develops along a direction which is inclined with respect to the loading direction. Hill (1952) assumed that the necking direction is coincident with the direction of zero-elongation and thus the straining in the necking region is due only to the sheet thinning.

The method used for obtaining the limit strains in this case is presented in Banabic and Dörr (1995). The expressions of these strains are as follows:

$$\varepsilon_1^* = \frac{\frac{\partial f}{\partial \sigma_1}}{\frac{\partial f}{\partial \sigma_1} + \frac{\partial f}{\partial \sigma_2}} n \tag{5.19}$$

$$\varepsilon_2^* = \frac{\frac{\partial f}{\partial \sigma_2}}{\frac{\partial f}{\partial \sigma_1} + \frac{\partial f}{\partial \sigma_2}} n \tag{5.20}$$

It can be seen that

$$\varepsilon_1^* + \varepsilon_2^* = n \tag{5.21}$$

This is the equation of a line parallel with the second bisectrix of the rectangular coordinate system ε_1, ε_2 and intersecting the vertical axis at the point (0, n).

According to Eq. (5.21), the FLC computed on the basis of the Hill's model does not depend on the yield criterion, but only on the value of the hardening coefficient.

5.4.3 Assessing the Formability of Metallic Sheets by Means of Localized and Diffuse Necking Models

5.4.3.1 Constitutive Equations

In what follows, sheet metals are assimilated to orthotropic membranes exhibiting a rigid-plastic behaviour. Their formability is analyzed in the context of active loading processes subjected to the constraints

$$\begin{aligned} &\sigma_{33}=0, \quad \sigma_{12}=0, \quad \sigma_{23}=0, \quad \sigma_{31}=0, \\ &\dot{\varepsilon}_{12}=0, \quad \dot{\varepsilon}_{23}=0, \quad \dot{\varepsilon}_{31}=0, \end{aligned} \tag{5.22}$$

where $\sigma_{ij}=\sigma_{ji}$ and $\dot{\varepsilon}_{ij}=\dot{\varepsilon}_{ji}$ respectively denote stress and strain-rate components expressed in the orthotropy frame defined by the rolling direction RD (axis 1), transverse direction TD (axis 2), and normal direction ND (axis 3). It is not difficult to observe that Eqs. (5.22) enforce a particular plane-stress state characterized by the absence of shearing effects. Under such circumstances, σ_{ii} and $\dot{\varepsilon}_{ii}(i=1,2,3)$ automatically become principal values of the corresponding stress and strain-rate tensors. In order to emphasize this significance, the following notations are adopted:

$$\sigma_{ii}=\sigma_i, \quad \dot{\varepsilon}_{ii}=\dot{\varepsilon}_i, \quad i=1,2,3. \tag{5.23}$$

The rigid-plastic behaviour of sheet metals is described by the yield criterion

$$\bar{\sigma}(\sigma_1,\sigma_2)=y(\bar{\varepsilon})>0, \quad \bar{\varepsilon}\geq 0, \tag{5.24}$$

the flow rule

$$\dot{\varepsilon}_i=\dot{\bar{\varepsilon}}\frac{\partial\bar{\sigma}}{\partial\sigma_i}, \quad \dot{\bar{\varepsilon}}>0, \quad i=1,2, \tag{5.25}$$

and the incompressibility condition

$$\dot{\varepsilon}_1+\dot{\varepsilon}_2+\dot{\varepsilon}_3=0. \tag{5.26}$$

Equations (5.24) and (5.25) operate with the equivalent stress $\bar{\sigma}$ (defined as a strictly convex and first-degree homogeneous function $\bar{\sigma}=\bar{\sigma}(\sigma_1,\sigma_2)$), the equivalent strain $\bar{\varepsilon}$, and the yield parameter (controlled by a strictly increasing hardening law $y=y(\bar{\varepsilon})$). For any load state having the property $\sigma_1>0$, the quantities $\bar{\sigma}$ and $\partial\bar{\sigma}/\partial\sigma_i(i=1,2)$ can be written in the form

$$\begin{aligned} &\bar{\sigma}(\sigma_1,\sigma_2)=\sigma_1 f(\alpha), \quad \frac{\partial\bar{\sigma}}{\partial\sigma_i}=g_i(\alpha), \\ &\alpha=\sigma_2/\sigma_1, \quad \sigma_1>0, \quad i=1,2, \end{aligned} \tag{5.27}$$

where

$$\begin{aligned} f(\alpha) &= \bar{\sigma}(1,\alpha) > 0, \\ g_1(\alpha) &= f(\alpha) - \alpha f'(\alpha), \quad g_2(\alpha) = f'(\alpha). \end{aligned} \tag{5.28}$$

Equations (5.27) and (5.28) are easily deducible from the following mathematical properties of the first-degree homogeneous function $\bar{\sigma}$:

$$\bar{\sigma}(q\sigma_1, q\sigma_2) = q\bar{\sigma}(\sigma_1, \sigma_2), \quad \forall q > 0, \tag{5.29}$$

$$\bar{\sigma}(\sigma_1, \sigma_2) = \sigma_1 \frac{\partial \bar{\sigma}}{\partial \sigma_1} + \sigma_2 \frac{\partial \bar{\sigma}}{\partial \sigma_2}. \tag{5.30}$$

With the aim of simplifying the future manipulations of the constitutive relationships, one denotes by g_3 the opposite of the sum $g_1 + g_2$:

$$g_3(\alpha) = -[g_1(\alpha) + g_2(\alpha)]. \tag{5.31}$$

As soon as Eqs. (5.27) and (5.31) are taken into account, Eq. (5.24) becomes

$$\sigma_1 = y(\bar{\varepsilon})/f(\alpha) > 0, \quad \alpha = \sigma_2/\sigma_1, \quad \bar{\varepsilon} \geq 0, \tag{5.32}$$

while Eqs. (5.25) and (5.26) get the unified formulation

$$\dot{\varepsilon}_i = \dot{\bar{\varepsilon}} g_i(\alpha), \quad \alpha = \sigma_2/\sigma_1, \quad \sigma_1 > 0, \quad \dot{\bar{\varepsilon}} > 0, \quad i = 1, 2, 3. \tag{5.33}$$

The models described in the next section make use of the strain-path concept. This term designates a sequence of load states defined by a relationship between $\dot{\varepsilon}_1$ and $\dot{\varepsilon}_2$. Only strain paths that induce a continuous thinning of the metallic sheet are relevant to the following analysis. Such a characteristic is enforced by the restriction $\dot{\varepsilon}_3 < 0$ or, equivalently, $\dot{\varepsilon}_1 + \dot{\varepsilon}_2 > 0$ (see Eq. (5.26)). The analysis is further limited to the case when $\dot{\varepsilon}_1$ is the major principal value of the strain-rate tensor, i.e. $\dot{\varepsilon}_1 > 0$ and $-\dot{\varepsilon}_1 < \dot{\varepsilon}_2 \leq \dot{\varepsilon}_1$. Any strain path having these properties can be represented in the form

$$\dot{\varepsilon}_1 > 0, \quad \dot{\varepsilon}_2 = \beta \dot{\varepsilon}_1, \quad \beta_{\text{inf}} < \beta \leq \beta_{\text{sup}}, \tag{5.34}$$

where the bounds of the β—range correspond to the pure shear deformation

$$\dot{\varepsilon}_1 > 0, \quad \dot{\varepsilon}_2 = -\dot{\varepsilon}_1 \quad \rightarrow \quad \beta_{\text{inf}} = -1, \tag{5.35}$$

and balanced biaxial elongation

$$\dot{\varepsilon}_1 > 0, \quad \dot{\varepsilon}_2 = \dot{\varepsilon}_1 \quad \rightarrow \quad \beta_{\text{sup}} = 1. \tag{5.36}$$

Under conditions (5.34)–(5.36), σ_1 is a strictly positive quantity. Equations (5.33)–(5.36) can be thus combined to express β as a function of α i.e.

$$\beta = g_2(\alpha)/g_1(\alpha), \quad g_1(\alpha) > 0, \quad \alpha_{\text{inf}} < \alpha \leq \alpha_{\text{sup}}, \tag{5.37}$$

where the bounds of the α—range result by solving the equations

$$\beta_{\text{inf}} = g_2(\alpha_{\text{inf}})/g_1(\alpha_{\text{inf}}), \quad g_1(\alpha_{\text{inf}}) > 0 \quad \rightarrow \quad \alpha_{\text{inf}}, \tag{5.38}$$

and

$$\beta_{\text{sup}} = g_2\left(\alpha_{\text{sup}}\right)/g_1\left(\alpha_{\text{sup}}\right), \quad g_1\left(\alpha_{\text{sup}}\right) > 0 \quad \rightarrow \quad \alpha_{\text{sup}}. \tag{5.39}$$

If $\bar{\sigma} = \bar{\sigma}(\sigma_1, \sigma_2)$ is strictly convex, Eqs. (5.38) and (5.39) have unique solutions. Assuming the same strict convexity constraint, one may prove that Eq. (5.37) also defines a one-to-one mapping $\alpha \leftrightarrow \beta$, with $\alpha_{\text{inf}} < \alpha \leq \alpha_{\text{sup}}$ and $\beta_{\text{inf}} < \beta \leq \beta_{\text{sup}}$.

The plane-strain state ($\dot{\varepsilon}_1 > 0$ and $\dot{\varepsilon}_2 = 0$) is of special interest for the models discussed below. In this case, conditions (5.34) enforce

$$\dot{\varepsilon}_1 > 0, \quad \dot{\varepsilon}_2 = 0 \quad \rightarrow \quad \beta_{\text{FLC}_0} = 0, \tag{5.40}$$

the associated value of the principal stress ratio being uniquely determined by Eq. (5.37) rewritten as follows:

$$g_2(\alpha_{\text{FLC}_0}) = 0, \quad g_1(\alpha_{\text{FLC}_0}) > 0 \quad \rightarrow \quad \alpha_{\text{FLC}_0}. \tag{5.41}$$

5.4.3.2 Localized and Diffuse Necking Models

From a theoretical perspective, localized necking is associated with the loss of carrying capability in a zero-extension plane. According to Hill (1952), the angle made by this plane with TD is (see Fig. 5.23a, as well as Eqs. (5.34)–(5.36) and (5.40))

$$\phi = \arctan\sqrt{-\dot{\varepsilon}_2/\dot{\varepsilon}_1}, \quad \dot{\varepsilon}_1 > 0, \quad -\dot{\varepsilon}_1 < \dot{\varepsilon}_2 \leq 0. \tag{5.42}$$

One may notice that the square root in Eq. (5.42) has no significance for strictly positive values of the argument $\dot{\varepsilon}_2/\dot{\varepsilon}_1$. In such cases corresponding to biaxial elongation regimes ($\dot{\varepsilon}_1 > 0$ and $0 < \dot{\varepsilon}_2 \leq \dot{\varepsilon}_1$—see Eqs. (5.34)–(5.36) and (5.40)), the localized necking mechanism is inhibited because zero-extension planes do not exist.

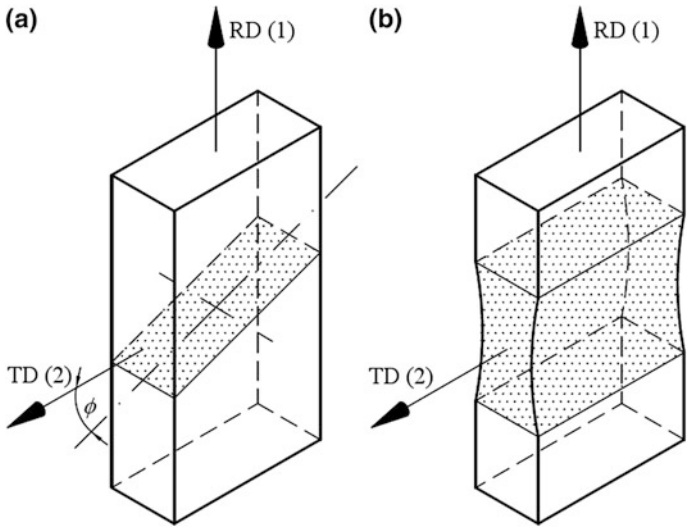

Fig. 5.23 Localized (**a**) and diffuse (**b**) necking domains (see the *shaded* regions)

For linear strain paths individualized by constant ratios $\dot{\varepsilon}_2/\dot{\varepsilon}_1$ in the range $-1 < \dot{\varepsilon}_2/\dot{\varepsilon}_1 \leq 0$, Hill's model predicts that metallic sheets lose their carrying capability when

$$\frac{\dot{\sigma}_1}{\sigma_1} + \dot{\varepsilon}_3 = 0. \tag{5.43}$$

With the help of Eqs. (5.32)–(5.41) and (5.43) becomes

$$\frac{h(\bar{\varepsilon})}{y(\bar{\varepsilon})} + g_3(\alpha) = 0, \quad \alpha_{\text{inf}} < \alpha \leq \alpha_{\text{FLC}_0}, \quad \alpha = \text{const.}, \tag{5.44}$$

where

$$h(\bar{\varepsilon}) = y'(\bar{\varepsilon}) > 0 \tag{5.45}$$

is the hardening modulus. Equation (5.44) can be used to determine the equivalent strain in the stage of localized necking, for a given value of the parameter α. Let $\bar{\varepsilon}_{\text{Hill}}(\alpha)$ denote the solution of Eq. (5.44). Due to the fact that rupture immediately follows the loss of carrying capability in the zero-extension plane (Hill 1952), $\bar{\varepsilon}_{\text{Hill}}(\alpha)$ defines a limit value of the equivalent strain.

One assumes that diffuse necking begins as soon as the major cross-sectional force is maximized, i.e. when (Dorn and Thomsen 1947; Mattiasson et al. 2006)

$$\frac{\dot{\sigma}_1}{\sigma_1} - \dot{\varepsilon}_1 = 0. \tag{5.46}$$

In the particular case of a linear strain path, Eqs. (5.32)–(5.39) and (5.45) bring (5.46) to the form

$$\frac{h(\bar{\varepsilon})}{y(\bar{\varepsilon})} - g_1(\alpha) = 0, \quad \alpha_{\text{inf}} < \alpha \leq \alpha_{\text{sup}}, \quad \alpha = \text{const.} \tag{5.47}$$

For a given value of the parameter α, Eq. (5.47) can be used to determine the equivalent strain accumulated by the metallic sheet up to the onset of diffuse necking. Let ${}^{0}\bar{\varepsilon}_{\text{EMFC}}(\alpha)$ denote[1] the solution of Eq. (5.47).

In its evolutionary phase, diffuse necking is described as a transition towards the plane-strain state at the level of a straight band perpendicular to RD (see Figs. 5.23b and 5.2). Three hypotheses are formulated with reference to this process (Mattiasson et al. 2006):

- The linear character of the strain path is preserved in the non-necking regions.
- The minor principal strain-rate remains uniformly distributed in the metallic sheet, i.e.

$$\underset{\sim}{\dot{\varepsilon}}_2 = \dot{\varepsilon}_2. \tag{5.48}$$

- The major cross-sectional force is kept at a maximum value inside the necking band, i.e. (see Eq. (5.46) for comparison).

$$\frac{\underset{\sim}{\dot{\sigma}}_1}{\underset{\sim}{\sigma}_1} - \underset{\sim}{\dot{\varepsilon}}_1 = 0. \tag{5.49}$$

Equations (5.48) and (5.49) use underlined symbols for the parameters of the necking band vs. plain symbols for the parameters of the non-necking domains. The subsequent relationships also adhere to this typographic convention.

With the help of Eqs. (5.28), (5.32)–(5.39), (5.45), Eqs. (5.48) and (5.49) can be rewritten in the explicit forms

$$\begin{aligned} &\dot{\underset{\sim}{\bar{\varepsilon}}} g_2\left(\underset{\sim}{\alpha}\right) = \dot{\bar{\varepsilon}} g_2(\alpha), \quad \dot{\underset{\sim}{\bar{\varepsilon}}} > 0, \quad \dot{\bar{\varepsilon}} > 0, \\ &\alpha_{\text{inf}} < \underset{\sim}{\alpha} \leq \alpha_{\text{sup}}, \quad \alpha_{\text{inf}} < \alpha \leq \alpha_{\text{sup}}, \quad \alpha = \text{const.}, \end{aligned} \tag{5.50}$$

[1] EMFC is an acronym for "Extended Maximum Force Criterion" Mattiasson et al. (2006).

and

$$\begin{aligned}
&\left[\frac{h\left(\underset{\sim}{\bar{\varepsilon}}\right)}{y\left(\underset{\sim}{\bar{\varepsilon}}\right)} - g_1\left(\underset{\sim}{\alpha}\right)\right]\dot{\underset{\sim}{\bar{\varepsilon}}} - \frac{g_2\left(\underset{\sim}{\alpha}\right)}{f\left(\underset{\sim}{\alpha}\right)}\dot{\underset{\sim}{\alpha}} = 0,\\
&\underset{\sim}{\bar{\varepsilon}} \geq {}^0\bar{\varepsilon}(\alpha), \quad \dot{\underset{\sim}{\bar{\varepsilon}}} > 0, \quad \alpha_{\text{inf}} < \underset{\sim}{\alpha} \leq \alpha_{\text{sup}}, \quad \alpha_{\text{inf}} < \alpha \leq \alpha_{\text{sup}},\\
&\alpha = \text{const.},
\end{aligned} \tag{5.51}$$

respectively. The necking progress is controlled by Eqs. (5.50) and (5.51), together with the initial conditions

$${}^0\underset{\sim}{\bar{\varepsilon}} = {}^0\bar{\varepsilon} = {}^0\bar{\varepsilon}_{\text{EMFC}}(\alpha), \quad {}^0\underset{\sim}{\alpha} = \alpha, \quad \alpha_{\text{inf}} < \alpha \leq \alpha_{\text{sup}}, \quad \alpha = \text{const.} \tag{5.52}$$

The discussion below focuses on describing the manner in which Eqs. (5.50)–(5.52) are used to determine the limit level of the equivalent strain $\bar{\varepsilon}_{\text{EMFC}}(\alpha)$ that corresponds to a given value of the parameter α.

If $\alpha = \alpha_{\text{FLC}_0}$, Eq. (5.50) and condition (5.41) enforce $\underset{\sim}{\alpha} = \alpha_{\text{FLC}_0}$. Under such circumstances, Eq. (5.51) degenerates to Eq. (5.47), both of them being also coincident with Eq. (5.44) particularized for $\alpha = \alpha_{\text{FLC}_0}$. The onset of diffuse necking is thus immediately followed by rupture when the metallic sheet evolves along a plane-strain path, i.e.

$$\bar{\varepsilon}_{\text{EMFC}}(\alpha_{\text{FLC}_0}) = {}^0\bar{\varepsilon}_{\text{EMFC}}(\alpha_{\text{FLC}_0}) = \bar{\varepsilon}_{\text{Hill}}(\alpha_{\text{FLC}_0}). \tag{5.53}$$

On the other hand, if $\alpha \neq \alpha_{\text{FLC}_0}$, Eq. (5.50) and condition (5.41) also enforce $\underset{\sim}{\alpha} \neq \alpha_{\text{FLC}_0}$. In this case, the evolution of the necking band towards the plane-strain state is possible (see Fig. 5.24). Due to the fact that $\dot{\bar{\varepsilon}}/\dot{\underset{\sim}{\bar{\varepsilon}}} \to 0$ for $\underset{\sim}{\alpha} \to \alpha_{\text{FLC}_0}$ (see Eq (5.50) and condition (5.41)), a bottom threshold of the ratio $\dot{\bar{\varepsilon}}/\dot{\underset{\sim}{\bar{\varepsilon}}}$ must be fixed in order to avoid numerical difficulties when solving Eqs. (5.50) and (5.51):

$$\dot{\bar{\varepsilon}}/\dot{\underset{\sim}{\bar{\varepsilon}}} \geq \eta, \quad \eta = 10^{-3} \div 10^{-2} = \text{const.} \tag{5.54}$$

If Eq. (5.50) is taken into account, condition (5.54) becomes

$$\begin{aligned}
&g_2\left(\underset{\sim}{\alpha}\right)/g_2(\alpha) \geq \eta,\\
&\alpha_{\text{inf}} < \underset{\sim}{\alpha} \leq \alpha_{\text{sup}}, \quad \underset{\sim}{\alpha} \neq \alpha_{\text{FLC}_0}, \quad \alpha_{\text{inf}} < \alpha \leq \alpha_{\text{sup}},\\
&\alpha \neq \alpha_{\text{FLC}_0}, \quad \alpha = \text{const.},
\end{aligned} \tag{5.55}$$

or, equivalently (see also Eqs. (5.52) and Fig. 5.24),

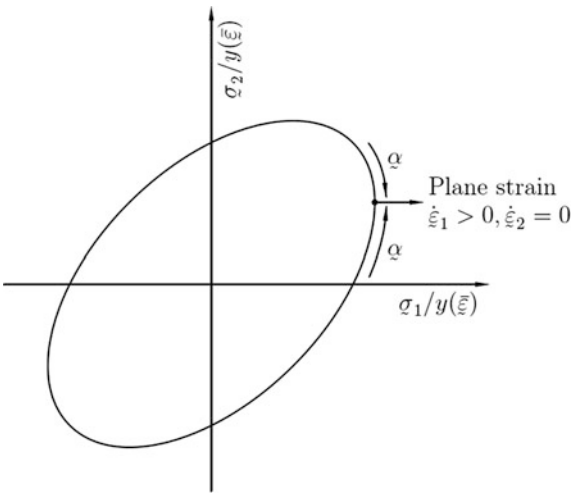

Fig. 5.24 Transition towards the plane-strain point of a normalized yield locus (the underlined symbols shown in the sketch denote parameters of the diffuse necking band)

$$\underset{\sim}{\alpha}_{\text{inf}} \le \underset{\sim}{\alpha} \le \underset{\sim}{\alpha}_{\text{sup}},$$

$$\begin{cases} \underset{\sim}{\alpha}_{\text{inf}} = \alpha, \quad \underset{\sim}{\alpha}_{\text{sup}} = \alpha_{\text{FLC}_{-\eta}}, & \text{if } \alpha_{\text{inf}} < \alpha < \alpha_{\text{FLC}_0}, \quad \alpha = \text{const.}, \\ \underset{\sim}{\alpha}_{\text{inf}} = \alpha_{\text{FLC}_{+\eta}}, \quad \underset{\sim}{\alpha}_{\text{sup}} = \alpha, & \text{if } \alpha_{\text{FLC}_0} < \alpha \le \alpha_{\text{sup}}, \quad \alpha = \text{const.}, \end{cases} \tag{5.56}$$

with $\alpha_{\text{FLC}_{\mp\eta}}$ determined as follows:

$$\begin{aligned} g_2\left(\alpha_{\text{FLC}_{-\eta}}\right)/g_2(\alpha) &= \eta, \quad \alpha < \alpha_{\text{FLC}_{-\eta}} < \alpha_{\text{FLC}_0}, \quad \text{if } \alpha_{\text{inf}} < \alpha < \alpha_{\text{FLC}_0}, \\ g_2\left(\alpha_{\text{FLC}_{+\eta}}\right)/g_2(\alpha) &= \eta, \quad \alpha_{\text{FLC}_0} < \alpha_{\text{FLC}_{+\eta}} < \alpha, \quad \text{if } \alpha_{\text{FLC}_0} < \alpha \le \alpha_{\text{sup.}} \end{aligned} \tag{5.57}$$

In the case $\alpha \neq \alpha_{\text{FLC}_0}$, the limit value $\bar{\varepsilon}_{\text{EMFC}}(\alpha)$ results by integrating Eqs. (5.50) and (5.51) over a time interval that corresponds to the evolution of the parameter $\underset{\sim}{\alpha}$ between the bounds $\underset{\sim}{\alpha}_{\text{inf}}$ and $\underset{\sim}{\alpha}_{\text{sup}}$. This task is accomplished in a sequence of $i_{\max}$ steps,

$$i_{\max} = 1 + \left\lfloor \frac{\underset{\sim}{\alpha}_{\text{sup}} - \underset{\sim}{\alpha}_{\text{inf}}}{\Delta\underset{\sim}{\alpha}\Big|_{\max}} \right\rfloor, \quad \Delta\underset{\sim}{\alpha}\Big|_{\max} = 10^{-5} \div 10^{-4} = \text{const.} \tag{5.58}$$

Equation (5.58) uses $\lfloor \blacksquare \rfloor$ as a symbol of the floor function. Each step of the computational procedure starts by incrementing $\underset{\sim}{\alpha}$ (see also conditions (5.52) and (5.56)):

$$
\begin{aligned}
&{}^{i}\underset{\sim}{\alpha} = {}^{i-1}\underset{\sim}{\alpha} + \Delta\underset{\sim}{\alpha}, \quad {}^{0}\underset{\sim}{\alpha} = \alpha, \quad i = 1, \ldots, i_{\max},\\
&\alpha_{\inf} < \alpha \leq \alpha_{\sup}, \quad \alpha \neq \alpha_{\mathrm{FLC}_0}, \quad \alpha = \text{const.},\\
&\Delta\underset{\sim}{\alpha} = \frac{\underset{\sim}{\alpha}_{\sup} - \underset{\sim}{\alpha}_{\inf}}{i_{\max}} \operatorname{sgn}(\alpha_{\mathrm{FLC}_0} - \alpha) = \text{const.}
\end{aligned}
\tag{5.59}
$$

Equation (5.59) and many of the subsequent relationships involve quantities with upper-left index qualifiers. Their significance is explained below:

${}^{i-1}\blacksquare \rightarrow$	State parameters associated to the reference configuration of the metallic sheet (known quantities either evaluated in the previous computational step or initialized by means of Eqs. (5.52))
${}^{i}\blacksquare \rightarrow$	State parameters associated to the current configuration of the metallic sheet (except for ${}^{i}\underset{\sim}{\alpha}$, all these quantities are unknowns that must be determined)

For solution purposes, Eqs. (5.50) and (5.51) are also rewritten in the incremental forms (see also Eqs. (5.52))

$$
\begin{aligned}
&\left({}^{i}\underset{\sim}{\bar{\varepsilon}} - {}^{i-1}\underset{\sim}{\bar{\varepsilon}}\right) g_2\left({}^{i}\underset{\sim}{\alpha}\right) = \left({}^{i}\bar{\varepsilon} - {}^{i-1}\bar{\varepsilon}\right) g_2(\alpha),\\
&{}^{0}\underset{\sim}{\bar{\varepsilon}} = {}^{0}\bar{\varepsilon} = {}^{0}\bar{\varepsilon}_{\mathrm{EMFC}}(\alpha), \quad i = 1, \ldots, i_{\max},\\
&{}^{i}\underset{\sim}{\bar{\varepsilon}} > {}^{i-1}\underset{\sim}{\bar{\varepsilon}}, \quad {}^{i}\bar{\varepsilon} > {}^{i-1}\bar{\varepsilon}, \quad \alpha_{\inf} < \alpha \leq \alpha_{\sup},\\
&\alpha \neq \alpha_{\mathrm{FLC}_0}, \quad \alpha = \text{const.},
\end{aligned}
\tag{5.60}
$$

and

$$
\begin{aligned}
&\left[\frac{h\left({}^{i}\underset{\sim}{\bar{\varepsilon}}\right)}{y\left({}^{i}\underset{\sim}{\bar{\varepsilon}}\right)} - g_1\left({}^{i}\underset{\sim}{\alpha}\right)\right]\left({}^{i}\underset{\sim}{\bar{\varepsilon}} - {}^{i-1}\underset{\sim}{\bar{\varepsilon}}\right) - \frac{g_2\left({}^{i}\underset{\sim}{\alpha}\right)}{f\left({}^{i}\underset{\sim}{\alpha}\right)}\Delta\underset{\sim}{\alpha} = 0,\\
&{}^{0}\underset{\sim}{\bar{\varepsilon}} = {}^{0}\bar{\varepsilon}_{\mathrm{EMFC}}(\alpha), \quad i = 1, \ldots, i_{\max},\\
&{}^{i}\underset{\sim}{\bar{\varepsilon}} > {}^{i-1}\underset{\sim}{\bar{\varepsilon}}, \quad \alpha_{\inf} < \alpha \leq \alpha_{\sup}, \quad \alpha \neq \alpha_{\mathrm{FLC}_0}, \quad \alpha = \text{const.},
\end{aligned}
\tag{5.61}
$$

respectively. One may notice that Eq. (5.61) is able to determine ${}^{i}\underset{\sim}{\bar{\varepsilon}}$. As soon as Eq. (5.61) is solved for the unknown ${}^{i}\underset{\sim}{\bar{\varepsilon}}$, Eq. (5.60) allows evaluating ${}^{i}\bar{\varepsilon}$:

$$
\begin{aligned}
&{}^{i}\bar{\varepsilon} = {}^{i-1}\bar{\varepsilon} + \left({}^{i}\underset{\sim}{\bar{\varepsilon}} - {}^{i-1}\underset{\sim}{\bar{\varepsilon}}\right)\frac{g_2\left({}^{i}\underset{\sim}{\alpha}\right)}{g_2(\alpha)},\\
&{}^{0}\underset{\sim}{\bar{\varepsilon}} = {}^{0}\bar{\varepsilon} = {}^{0}\bar{\varepsilon}_{\mathrm{EMFC}}(\alpha), \quad i = 1, \ldots, i_{\max},\\
&\alpha_{\inf} < \alpha \leq \alpha_{\sup}, \quad \alpha \neq \alpha_{\mathrm{FLC}_0}, \quad \alpha = \text{const.}
\end{aligned}
\tag{5.62}
$$

The incremental procedure presented above must be performed $i_{\max}$ times. The solution ${}^{i_{\max}}\bar{\varepsilon}$ obtained in the last step characterizes the formability of the metallic sheet from the point of view of the diffuse necking model:

$$
\bar{\varepsilon}_{\mathrm{EMFC}}(\alpha) = {}^{i_{\max}}\bar{\varepsilon}, \quad \alpha_{\inf} < \alpha \leq \alpha_{\sup}, \quad \alpha \neq \alpha_{\mathrm{FLC}_0}, \quad \alpha = \text{const.} \tag{5.63}
$$

Both $\bar{\varepsilon}_{\mathrm{Hill}}(\alpha)$ and $\bar{\varepsilon}_{\mathrm{EMFC}}(\alpha)$ should be used to define a limit value of the equivalent strain for a given value of the stress ratio α:

$$
\bar{\varepsilon}(\alpha) = \begin{cases} \min[\bar{\varepsilon}_{\mathrm{Hill}}(\alpha), \bar{\varepsilon}_{\mathrm{EMFC}}(\alpha)], & \text{if } \alpha_{\inf} < \alpha \leq \alpha_{\mathrm{FLC}_0}, \\ \bar{\varepsilon}_{\mathrm{EMFC}}(\alpha), & \text{if } \alpha_{\mathrm{FLC}_0} < \alpha \leq \alpha_{\sup}. \end{cases} \tag{5.64}
$$

Under the assumption $\alpha = \text{const.}$, the formability is equally characterized by two of the principal logarithmic strains (see Eqs. (5.33))

$$
\varepsilon_i(\alpha) = \bar{\varepsilon}(\alpha) g_i(\alpha), \quad \alpha_{\inf} < \alpha \leq \alpha_{\sup}, \quad \alpha = \text{const.}, \quad i = 1, 2, 3. \tag{5.65}
$$

A common practice is to use $\varepsilon_1 = \varepsilon_1(\alpha)$ and $\varepsilon_2 = \varepsilon_2(\alpha)$ for this purpose. If $\varepsilon_2 = \varepsilon_2(\alpha)$ is a one-to-one mapping,[2] $\varepsilon_1 = \varepsilon_1(\alpha)$ and $\varepsilon_2 = \varepsilon_2(\alpha)$ can be replaced by a single function $\varepsilon_1 = \varepsilon_1(\varepsilon_2)$ that defines the Forming Limit Curve.

5.4.4 *Marciniak-Kuckzynski (M-K) Model*

5.4.4.1 Overview

Shortly after the introduction of the Forming Limit Diagram concept, on the basis of the experimental investigations concerning the strain localization of some specimens subjected to hydraulic bulging or punch stretching, Marciniak (1965) and Marciniak and Kuczynski (1967) developed a limit curve prediction model. This model is based on the hypothesis of the existence of imperfections in sheet metals. According to Marciniak's hypothesis, sheet metals have, from manufacturing, geometrical imperfections (thickness variations) and/or structural imperfections (inclusions, gaps). In the forming process these imperfections progressively evolve and the

[2]This requirement is always met when $\bar{\sigma} = \bar{\sigma}(\sigma_1, \sigma_2)$ is a strictly convex function.

plastic forming of the sheet metal is almost completely localized in them, leading to the necking of the sheet metal. The realism of this hypothesis has been experimentally analyzed by Azrin and Backofen (1970). This model has been intensely used and developed by researchers due to the advantages it offers: it has an intuitive physical background; it correctly predicts the influence of different process or material parameters on the limit strains; the predictions are precise enough; the model can be easily coupled with Finite Element simulation software for sheet metal forming processes. The main drawbacks of this model are: the prediction results are very sensitive to the constitutive equations used, as well as to the values of the non-homogeneity parameter; in the case of advanced material models, the equation system of the model is quite difficult to solve and lacks robustness.

A few years later, Marciniak (1968) made a thorough analysis of the strain localization phenomenon from the right side of the FLD and extended his initial model to cover this area. The models have periodically been brought in discussion by specialists in dedicated symposia (see Koistinen and Wang (1978), Hecker et al. (1978), Wagoner et al. (1989), Hora (2006), Hora and Volk (2014)) or in special sections in conferences (NUMISHEET, NUMIFORM, IDDRG, ESAFORM, etc.). Further developments of the Marciniak models are synthetically described in the review papers (Banabic et al. 2010b; Banabic 2010).

The analysis of the necking process has been performed assuming a geometrical non-homogeneity in the form of a thickness variation. This variation is usually due to some defects in the technological procedure used to obtain the sheet metal. The thickness variation is generally gentle. However, the theoretical model assumes a sudden variation in order to simplify the calculations (Fig. 5.25).

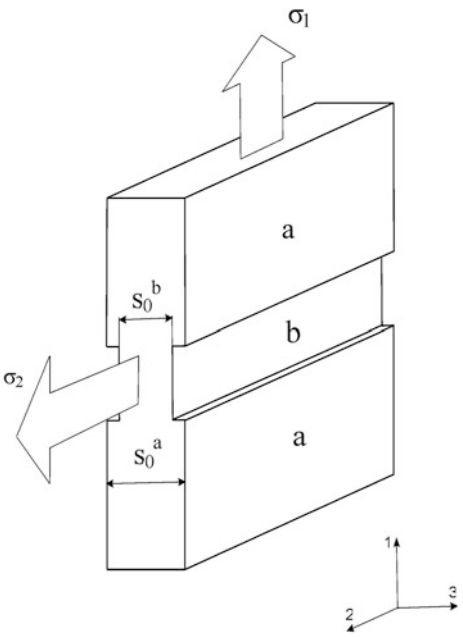

Fig. 5.25 Geometrical model of the M-K theory

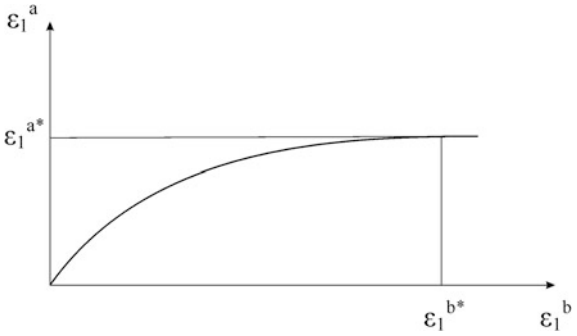

Fig. 5.26 The dependence $\varepsilon_1^a(\varepsilon_1^b)$

The theoretical model proposed by Marciniak and Kuczynski (1967) assumes that the specimen has two regions: region *'a'* having a uniform thickness s_0^a, and region *'b'* having the thickness s_0^b (Fig. 5.25). The initial geometrical non-homogeneity of the specimen is described by the so-called 'coefficient of geometrical non-homogeneity', η, expressed as the ratio of the thickness in the two regions:

$$\eta = \frac{s_0^b}{s_0^a} \tag{5.66}$$

The strain and stress states in the two regions are analysed with respect to the principal strain ε_1^b in region *'b'* and the principal strain ε_1^a in region *'a'*. When the ratio $\varepsilon_1^b/\varepsilon_1^a$ becomes too high (infinite in theory, above 10 in practice), one may consider that the deformation of the specimen is localized in region *'b'* (Fig. 5.26).

The shape and position of the curve $\varepsilon_1^a(\varepsilon_1^b)$ depend on the value of the coefficient η. If $\eta = 1$ (geometrically homogeneous sheet), the curve becomes coincident with the first bisectrix. Thus this theory cannot model the strain localization for geometrically homogeneous sheets.

The value of the principal strain ε_{1a} in region 'a' corresponding to non-significant straining of this region as compared to region 'b' (the straining being localized in region 'b') represents the limit strain ε_{1a}* (Fig. 5.26). This strain together with the second principal strain ε_{2a}* in region 'a' define a point of the Forming Limit Curve. By varying the strain ratios $\rho = d\varepsilon_2/d\varepsilon_1$, different points on the FLC are obtained. By scrolling the range $0 < \rho < 1$, the FLC for biaxial tension ($\varepsilon_1 > 0$, $\varepsilon_2 > 0$) is obtained. In this range the orientation of the geometrical non-homogeneity with respect to the principal directions is assumed to be the same during the entire forming process.

The Marciniak model (1965) was further developed by Marciniak and Kuczynski (1967) and Marciniak et al. (1973), usually being briefly denominated the M-K model.

The M-K model was extended to the negative range of the FLD's ($\varepsilon_2 < 0$) by Hutchinson and Neale (H-N model) (Hutchinson and Neale 1978a, 1978b, 1978c).

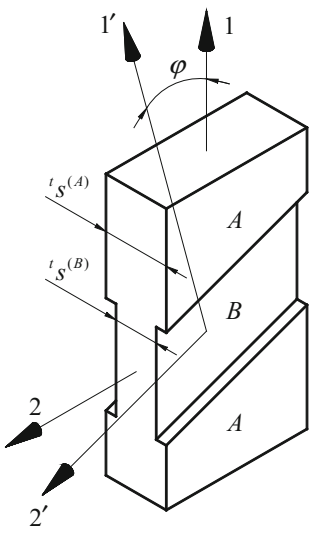

Fig. 5.27 Schematic view of the thickness imperfection assumed by the H-N model

The geometric H-N model is presented in Fig. 5.27. According with the original paper of Hutchinson and Neale (1978b), the inclination of the non- homogeneity varies with the main strains by a law having the form:

$$\tan(\varphi + d\varphi) = \frac{1 + d\varepsilon_1^a}{1 + d\varepsilon_2^a} \tan\ \varphi \tag{5.67}$$

and the non-uniformity coefficient varies by a law having the form:

$$\eta_1 = \eta_0 (d\,\varepsilon_3^b - d\,\varepsilon_3^a), \tag{5.68}$$

where, η_1 and η_0 are the current and initial non-uniformity coefficients, respectively.

5.4.4.2 Implicit Formulation of the M-K and H-N Models

Both M-K and H-N models assume that the strain localization is caused by a thickness imperfection represented as a groove in Fig. 5.27. According to this hypothesis, two regions of the sheet metal should be distinguished: *A*—non-defective zone; *B*—groove. At different stages of the straining process (identified by the time parameter *t*), the ratio

$$^{t}f = {}^{t}s^{(B)} / {}^{t}s^{(A)}, \quad 0 < {}^{t}f < 1 \tag{5.69}$$

is used to describe the amplitude of the imperfection ($^{t}s^{(A)}$ and $^{t}s^{(B)}$ denote the current thickness of regions *A* and *B*, respectively—see Fig. 5.27).

Throughout this section, the sheet metal is considered to behave as an orthotropic membrane under the plane-stress conditions

$$\begin{aligned} {}^t\sigma_{i3} &= {}^t\sigma_{3i} = 0, \quad i = 1,2,3, \\ {}^t\dot{\varepsilon}_{\alpha 3} &= {}^t\dot{\varepsilon}_{3\alpha} = 0, \quad \alpha = 1,2,3. \end{aligned} \tag{5.70}$$

The constraints written above are valid both for region A and region B. Equation (5.70) involves the components of the stress and strain-rate tensors expressed in the plastic orthotropy frame (1 and 2 are the indices associated to the rolling and transverse directions, respectively—see Fig. 5.27, while 3 is the index corresponding to the normal direction—not shown in Fig. 5.27).

One also assumes that the sheet metal is subjected to loads which do not produce tangential stresses and strains in the plastic orthotropy frame:

$${}^t\sigma_{12} = {}^t\sigma_{21} = 0, \quad {}^t\dot{\varepsilon}_{12} = {}^t\dot{\varepsilon}_{21} = 0. \tag{5.71}$$

This constraint will be applied not only to the non-defective zone (as in the classical formulation of the H-N model), but also to the groove. Under such circumstances, the diagonal components of the stress and strain-rate tensors automatically become eigenvalues. In order to emphasize their significance, the following notations will be used:

$${}^t\sigma_i (i = 1,2,3)$$—principal stresses $({}^t\sigma_1 = {}^t\sigma_{11}, {}^t\sigma_2 = {}^t\sigma_{22}, {}^t\sigma_3 = {}^t\sigma_{33} = 0)$

$${}^t\dot{\varepsilon}_i (i = 1,2,3)$$—principal strain rates $({}^t\dot{\varepsilon}_1 = {}^t\dot{\varepsilon}_{11}, {}^t\dot{\varepsilon}_2 = {}^t\dot{\varepsilon}_{22}, {}^t\dot{\varepsilon}_3 = {}^t\dot{\varepsilon}_{33})$.

The mechanical response of the sheet metal will be described by a rigid-plastic model. The main ingredient of the constitutive model is the yield criterion:

$${}^t\bar{\sigma}({}^t\sigma_1, {}^t\sigma_2) = {}^tY({}^t\bar{\varepsilon}). \tag{5.72}$$

Equation (5.72) involves the following quantities:

${}^t\bar{\sigma} = {}^t\bar{\sigma}({}^t\sigma_1, {}^t\sigma_2) \geq 0$—equivalent stress (homogeneous function of the first degree)

${}^t\bar{\varepsilon} \geq 0$—equivalent (plastic) strain

${}^tY = {}^tY({}^t\bar{\varepsilon}) > 0$—yield parameter controlled by a strictly increasing hardening law.

The non-zero components of the strain-rate tensor (considered fully plastic) are defined by the flow rule

$${}^t\dot{\varepsilon}_\alpha = {}^t\dot{\bar{\varepsilon}} \frac{\partial {}^t\bar{\sigma}}{\partial {}^t\sigma_\alpha}, \quad \alpha = 1,2, \tag{5.73}$$

and the incompressibility constraint

$$ {}^{t}\dot{\varepsilon}_3 = -{}^{t}\dot{\varepsilon}_1 - {}^{t}\dot{\varepsilon}_2. \tag{5.74} $$

In order to preserve the simplicity of the formulation, one assumes that region A evolves along linear strain paths defined as follows:

$$ {}^{t}\dot{\varepsilon}_1^{(A)} > 0, \quad {}^{t}\dot{\varepsilon}_2^{(A)} = \rho^{(A)} \cdot {}^{t}\dot{\varepsilon}_1^{(A)}, \quad -1 < \rho^{(A)} \leq 1. \tag{5.75} $$

Each strain path investigated when calculating a Forming Limit Curve will be identified by a constant value of the parameter $\rho^{(A)}$. Equation (5.75) automatically implies that ${}^{t}\dot{\varepsilon}_2^{(A)}$ has the status of a minor principal strain-rate.

As shown in Fig. 5.27, the orientation of the groove is described by the angular parameter φ. One adopts the hypothesis $0° \leq \varphi < 45°$, thus considering that the necking band is closer to the direction of the minor principal strain-rate ${}^{t}\dot{\varepsilon}_2^{(A)}$. In order to find a formula for the calculation of the angular parameter φ, a local frame associated to the groove is defined. Its planar axes are individualized by the indices 1' and 2', being oriented as shown in Fig. 5.27. Let

$$ \begin{aligned} {}^{t}\dot{\varepsilon}_{2'2'}^{(A)} &= {}^{t}\dot{\varepsilon}_1^{(A)} \sin^2\varphi + {}^{t}\dot{\varepsilon}_2^{(A)} \cos^2\varphi \\ &= {}^{t}\dot{\varepsilon}_1^{(A)} \left[\sin^2\varphi + \rho^{(A)} \cos^2\varphi\right] \end{aligned} \tag{5.76} $$

be the strain-rate along the necking band. If $-1 < \rho^{(A)} \leq 0$, Eq. (5.76) could be used to find a zero-extension direction. Indeed, by enforcing

$$ {}^{t}\dot{\varepsilon}_{2'2'}^{(A)} = {}^{t}\dot{\varepsilon}_1^{(A)} \left[\sin^2\varphi + \rho^{(A)} \cos^2\varphi\right] = 0, \quad -1 < \rho^{(A)} \leq 0, \tag{5.77} $$

one obtains

$$ \tan^2\varphi + \rho^{(A)} = 0, \quad -1 < \rho^{(A)} \leq 0, \tag{5.78} $$

i.e.

$$ \varphi = \arctan\sqrt{-\rho^{(A)}}, \quad -1 < \rho^{(A)} \leq 0. \tag{5.79} $$

Equation (5.79) defines the orientation of the necking band for the left branch of the Forming Limit Curve. In fact, this formula is similar to that found by Hill for the same type of strain paths (Hill 1952).

If $0 < \rho^{(A)} \leq 1$, Eq. (5.76) does not allow the existence of zero-extension directions in the plane of the sheet metal. In such cases, as in the classical M-K model, one assumes that the necking band is oriented along the direction of the minor principal strain-rate ${}^{t}\dot{\varepsilon}_2^{(A)}$:

$$\varphi = 0^\circ, \quad 0 < \rho^{(A)} \leq 1. \tag{5.80}$$

Equations (5.79) and (5.80) can be unified in the general formula

$$\varphi = \arctan \sqrt{\max[-\rho^{(A)}, 0]}, \quad -1 < \rho^{(A)} \leq 1. \tag{5.81}$$

It is easily noticeable that, for linear strain paths $\left(\rho^{(A)} = \text{const.}\right)$, Eq. (5.81) implies the constancy of the angular parameter φ.

For any load state having the property ${}^t\sigma_1 > 0$, the equivalent stress could be expressed as follows:

$${}^t\bar{\sigma} = {}^t\sigma_1 \cdot F({}^t\zeta), \quad {}^t\zeta = {}^t\sigma_2/{}^t\sigma_1, \quad {}^t\sigma_1 > 0. \tag{5.82}$$

Equation (5.82) results from the fact that ${}^t\bar{\sigma}$ is a first-degree homogeneous function. The partial derivatives $\partial {}^t\bar{\sigma}/\partial {}^t\sigma_\alpha (\alpha = 1, 2)$ are also homogeneous functions but of zero-degree. As a consequence, they are expressible under the form

$$\frac{\partial {}^t\bar{\sigma}}{\partial {}^t\sigma_\alpha} = G_\alpha({}^t\zeta), \quad {}^t\zeta = {}^t\sigma_2/{}^t\sigma_1, \quad {}^t\sigma_1 > 0, \quad \alpha = 1, 2. \tag{5.83}$$

The functions F and $G_\alpha (\alpha = 1, 2)$ are related only to the particular formulation of the equivalent stress adopted in the model. Equations (5.82) and (5.83) lead to the following expressions of the yield criterion and flow rule (see also Eqs. (5.72) and (5.73)):

$${}^t\sigma_1 \cdot F({}^t\zeta) = {}^tY({}^t\bar{\varepsilon}), \quad {}^t\zeta = {}^t\sigma_2/{}^t\sigma_1, \quad {}^t\sigma_1 > 0, \tag{5.84}$$

$${}^t\dot{\varepsilon}_\alpha = {}^t\dot{\bar{\varepsilon}} \cdot G_\alpha({}^t\zeta), \quad {}^t\zeta = {}^t\sigma_2/{}^t\sigma_1, \quad {}^t\sigma_1 > 0, \quad \alpha = 1, 2. \tag{5.85}$$

The linear strain paths defined as in Eq. (5.75) fulfil the condition ${}^t\sigma_1^{(A)} > 0$. Under these circumstances, Eq. (5.85) can be applied to region A:

$$\begin{aligned} &{}^t\dot{\varepsilon}_\alpha^{(A)} = {}^t\dot{\bar{\varepsilon}}^{(A)} \cdot G_\alpha\left[{}^t\zeta^{(A)}\right], \quad {}^t\zeta^{(A)} = {}^t\sigma_2^{(A)}/{}^t\sigma_1^{(A)}, \\ &{}^t\sigma_1^{(A)} > 0, \quad \alpha = 1, 2. \end{aligned} \tag{5.86}$$

Equations (5.86) and (5.75) allow to obtain a relationship between $\rho^{(A)}$ and ${}^t\zeta^{(A)}$:

$$G_2\left[{}^t\zeta^{(A)}\right] = \rho^{(A)} \cdot G_1\left[{}^t\zeta^{(A)}\right]. \tag{5.87}$$

It is again noticeable that, for linear strain paths $\left(\rho^{(A)} = \text{const.}\right)$, Eq. (5.87) implies the constancy of the principal stress ratio, i.e.

$$ {}^{t}\zeta^{(A)} = {}^{t}\sigma_2^{(A)} \Big/ {}^{t}\sigma_1^{(A)} = \zeta^{(A)} = \text{const.} \tag{5.88} $$

At the level of region A, Eqs. (5.84) and (5.85) can thus be written in the particular forms

$$ {}^{t}\sigma_1^{(A)} \cdot F\left[\zeta^{(A)}\right] = {}^{t}Y\left[{}^{t}\bar{\varepsilon}^{(A)}\right], \tag{5.89} $$

$$ {}^{t}\dot{\varepsilon}_{\alpha}^{(A)} = {}^{t}\dot{\bar{\varepsilon}}^{(A)} \cdot G_{\alpha}\left[\zeta^{(A)}\right], \quad \alpha = 1, 2. \tag{5.90} $$

Because the stress state in region B also fulfils the condition ${}^{t}\sigma_1^{(B)} > 0$, the corresponding ratio

$$ {}^{t}\zeta^{(B)} = {}^{t}\sigma_2^{(B)} / {}^{t}\sigma_1^{(B)}, \quad {}^{t}\sigma_1^{(B)} > 0, \tag{5.91} $$

can be defined. ${}^{t}\zeta^{(B)}$ generally varies even if the strains in the non-defective zone evolve along a linear path. Due to this fact, Eqs. (5.84) and (5.85) should be written as follows when making reference to region B:

$$ {}^{t}\sigma_1^{(B)} \cdot F\left[{}^{t}\zeta^{(B)}\right] = {}^{t}Y\left[{}^{t}\bar{\varepsilon}^{(B)}\right], \tag{5.92} $$

$$ {}^{t}\dot{\varepsilon}_{\alpha}^{(B)} = {}^{t}\dot{\bar{\varepsilon}}^{(B)} \cdot G_{\alpha}\left[{}^{t}\zeta^{(B)}\right], \quad \alpha = 1, 2. \tag{5.93} $$

As in the classical formulation of the H-N model, two sets of constraints will be enforced at the interface between the regions A and B (see Fig. 5.29):

- Continuity of the strain-rate along the necking band

$$ {}^{t}\dot{\varepsilon}_{2'2'}^{(A)} = {}^{t}\dot{\varepsilon}_{2'2'}^{(B)} \tag{5.94} $$

- Equilibrium of the normal and tangential loads acting on the interface from both sides

$$ {}^{t}\sigma_{1'1'}^{(A)} \cdot {}^{t}s^{(A)} = {}^{t}\sigma_{1'1'}^{(B)} \cdot {}^{t}s^{(B)}, \tag{5.95} $$

$$ {}^{t}\sigma_{1'2'}^{(A)} \cdot {}^{t}s^{(A)} = {}^{t}\sigma_{1'2'}^{(B)} \cdot {}^{t}s^{(B)}. \tag{5.96} $$

By making use of the thickness-defect parameter ${}^{t}f$ (see Eq. (5.69)), one rewrites Eqs. (5.95) and (5.96) in the equivalent forms

$$ {}^{t}\sigma_{1'1'}^{(A)} = {}^{t}f \cdot {}^{t}\sigma_{1'1'}^{(B)}, \tag{5.97} $$

$$ {}^{t}\sigma_{1'2'}^{(A)} = {}^{t}f \cdot {}^{t}\sigma_{1'2'}^{(B)}. \tag{5.98} $$

The rotated tensor components involved in Eqs. (5.97) and (5.98) can be also expressed in terms of the principal stresses, thus obtaining

$$ \begin{aligned} &{}^{t}\sigma_{1}^{(A)} \cos^2 \varphi + {}^{t}\sigma_{2}^{(A)} \sin^2 \varphi \\ &\quad = {}^{t}f \cdot \left[{}^{t}\sigma_{1}^{(B)} \cos^2 \varphi + {}^{t}\sigma_{2}^{(B)} \sin^2 \varphi \right], \end{aligned} \tag{5.99} $$

$$ \begin{aligned} &\left[{}^{t}\sigma_{1}^{(A)} - {}^{t}\sigma_{1}^{(B)} \right] \sin \varphi \cdot \cos \varphi \\ &\quad = {}^{t}f \cdot \left[{}^{t}\sigma_{1}^{(B)} - {}^{t}\sigma_{2}^{(B)} \right] \sin \varphi \cdot \cos \varphi. \end{aligned} \tag{5.100} $$

Because $0^\circ \leq \varphi < 45^\circ$, the above relationships may be rewritten as follows:

$$ {}^{t}\sigma_{1}^{(A)} + {}^{t}\sigma_{2}^{(A)} \tan^2 \varphi = {}^{t}f \cdot \left[{}^{t}\sigma_{1}^{(B)} + {}^{t}\sigma_{2}^{(B)} \tan^2 \varphi \right], \tag{5.101} $$

$$ \left[{}^{t}\sigma_{1}^{(A)} - {}^{t}\sigma_{1}^{(B)} \right] \tan \varphi = {}^{t}f \cdot \left[{}^{t}\sigma_{1}^{(B)} - {}^{t}\sigma_{2}^{(B)} \right] \tan \varphi. \tag{5.102} $$

Finally, with the help of the principal stress ratios associated to regions A and B (see Eqs. (5.88), (5.91)), (5.101) and (5.102) become

$$ {}^{t}\sigma_{1}^{(A)} \cdot \left[1 + \zeta^{(A)} \tan^2 \varphi \right] = {}^{t}f \cdot {}^{t}\sigma_{1}^{(B)} \cdot \left[1 + {}^{t}\zeta^{(B)} \tan^2 \varphi \right], \tag{5.103} $$

$$ {}^{t}\sigma_{1}^{(A)} \cdot \left[1 - \zeta^{(A)} \right] \tan \varphi = {}^{t}f \cdot {}^{t}\sigma_{1}^{(B)} \cdot \left[1 - {}^{t}\zeta^{(B)} \right] \tan \varphi. \tag{5.104} $$

In general, Eq. (5.103) cannot reduce to the trivial case 0 = 0. Under such circumstances, it is possible to divide Eqs. (5.104) by (5.103). After some simple manipulations, one obtains the following relationship between the principal stress ratios associated to regions A and B:

$$ \left[\zeta^{(A)} - {}^{t}\zeta^{(B)} \right] \sin \varphi = 0. \tag{5.105} $$

For the strain paths characterized by the condition $-1 < \rho^{(A)} < 0$, Eq. (5.81) defines an angular parameter $0^\circ < \varphi < 45^\circ$. In this case, Eq. (5.105) enforces ${}^{t}\zeta^{(B)} = \zeta^{(A)} =$ const. The principal stress ratios associated to regions A and B are thus rigorously coincident and constant when $-1 < \rho^{(A)} < 0$.

The plane-strain path $\rho^{(A)} = 0$ needs a separate discussion, as in this case Eq. (5.81) defines an angular parameter $\varphi = 0^\circ$ and Eq. (5.105) degenerates to the

trivial form 0 = 0. When $\varphi = 0°$, the local frame associated to the groove is superimposed to the plastic orthotropy frame (1 = 1' and 2 = 2'). The constraints given by Eqs. (5.77) and (5.94) now reduce to ${}^t\dot{\varepsilon}_2^{(A)} = {}^t\dot{\varepsilon}_2^{(B)} = 0$, meaning that region B evolves along the same plane-strain path and enforcing again the constancy of the principal stress ratio: ${}^t\zeta^{(B)} = \zeta^{(A)} = \text{const}$. One may thus conclude

$$ {}^t\zeta^{(B)} = \zeta^{(A)} = \text{const.}, \quad \text{if } -1 < \rho^{(A)} \leq 0. \tag{5.106} $$

For all the strain paths characterized by the condition $0 < \rho^{(A)} \leq 1$, Eq. (5.81) defines an angular parameter $\varphi = 0°$. In this case, Eq. (5.105) also degenerates to the trivial form 0 = 0, but Eq. (5.94) will not enforce the constancy of the stress ratio in region B as it takes the more general form ${}^t\dot{\varepsilon}_2^{(A)} = {}^t\dot{\varepsilon}_2^{(B)}$.

One may notice that, whatever is the value of the parameter $\rho^{(A)}$ in the range $-1 < \rho^{(A)} \leq 1$, the equilibrium constraint given by Eq. (5.103) reduces to

$$ {}^t\sigma_1^{(A)} = {}^tf \cdot {}^t\sigma_1^{(B)}, \tag{5.107} $$

due to Eqs. (5.106) and (5.81). For all the strain paths characterized by the condition $-1 < \rho^{(A)} \leq 0$, the above relationship becomes even simpler when combined with Eqs. (5.89), (5.92) and (5.106):

$$ {}^tY\left[{}^t\bar{\varepsilon}^{(A)}\right] = {}^tf \cdot {}^tY\left[{}^t\bar{\varepsilon}^{(B)}\right], \quad \text{if } -1 < \rho^{(A)} \leq 0. \tag{5.108} $$

Equation (5.108) makes redundant the second equilibrium constraint expressed by Eq. (5.104). In fact, Eq. (5.108) has been deduced using Eq. (5.106) which is a corollary of Eq. (5.104).

In the case $0 < \rho^{(A)} \leq 1$, Eqs. (5.89) and (5.92) can be exploited to reformulate Eq. (5.107) as follows:

$$ \begin{aligned} &{}^tY\left[{}^t\bar{\varepsilon}^{(A)}\right] \Big/ F\left[\zeta^{(A)}\right] = {}^tf \cdot {}^tY\left[{}^t\bar{\varepsilon}^{(B)}\right] \Big/ F\left[{}^t\zeta^{(B)}\right], \\ &\text{if } 0 < \rho^{(A)} \leq 1. \end{aligned} \tag{5.109} $$

Again, Eq. (5.109) should not be accompanied by Eq. (5.104) because the second equilibrium constraint now degenerates to the trivial form 0 = 0.

The strain-compatibility enforced by Eq. (5.94) also deserves a discussion. In the case $-1 < \rho^{(A)} \leq 0$, this constraint becomes trivial (0 = 0) and redundant due to Eqs. (5.81) and (5.106) already included in the model. For the remaining strain paths $0 < \rho^{(A)} \leq 1$, Eq. (5.94) reduces to the simpler formulation (see also Eqs. (5.80), (5.90) and (5.93))

$$ {}^{t}\dot{\bar{\varepsilon}}^{(A)} \cdot G_2\left[\zeta^{(A)}\right] = {}^{t}\dot{\bar{\varepsilon}}^{(B)} \cdot G_2\left[{}^{t}\zeta^{(B)}\right], \quad \text{if } 0 < \rho^{(A)} \leq 1. \tag{5.110} $$

Equation (5.110) is non-trivial and accompanies Eq. (5.109) in the model used to calculate the right branch of the Forming Limit Curve.

The discussion below will focus on the presentation of the computational strategy used to solve the strain localization model. The evolution of the sheet metal up to the necking is analyzed for individual strain paths. Each of these paths is defined by a constant value of the parameter $\rho^{(A)}$ in the range $-1 < \rho^{(A)} \leq 1$. The straining process is analyzed in an incremental manner. Let $[T, T + \Delta T]$ be the discrete time interval corresponding to one of the steps performed in the analysis. All the parameters associated to the T moment are known quantities both for the non-defective area and the groove. The corresponding configuration of the sheet metal is thus taken as a reference state. In particular, the parameters associated to the moment $T = 0$ are defined by the conditions ${}^{0}\bar{\varepsilon}^{(A)} = {}^{0}\bar{\varepsilon}^{(B)} = 0$, and ${}^{0}\varepsilon_{\alpha}^{(A)} = {}^{0}\varepsilon_{\alpha}^{(B)} = 0$ $(\alpha = 1, 2)$. The initial value of the thickness ratio $0 < {}^{0}f < 1$ is also prescribed. As concerns the parameters corresponding to the $T + \Delta T$ moment, they are unknown quantities and should be evaluated.

The computation is conducted by applying small increments of the equivalent strain to region A. In order to obtain sufficiently accurate results, these increments should remain small. During the numerical tests performed by the authors, $\Delta\bar{\varepsilon}^{(A)} = 10^{-3} \div 10^{-4}$ has proved to be a good selection range.

Due to the fact that $\rho^{(A)}$ uniquely defines the ratio of the principal stresses in region A, the parameter $\zeta^{(A)}$ should be evaluated only once, namely at the beginning of each strain path. This task is accomplished by solving the equation (see Eqs. (5.87) and (5.88))

$$ \rho^{(A)} \cdot G_1\left[\zeta^{(A)}\right] - G_2\left[\zeta^{(A)}\right] = 0 \tag{5.111} $$

with respect to the unknown $\zeta^{(A)}$. In general, numerical procedures must be used to evaluate $\zeta^{(A)}$. During the tests performed by the authors, the bisection method has worked very well, especially when combined with a bracketing strategy.

As soon as $\zeta^{(A)}$ is known, the increments of the principal strains in region A can be evaluated from Eq. (5.90) rewritten as

$$ \Delta\varepsilon_{\alpha}^{(A)} = \left[\Delta\bar{\varepsilon}^{(A)}\right] \cdot G_{\alpha}\left[\zeta^{(A)}\right], \quad \alpha = 1, 2. \tag{5.112} $$

One may also notice that, for a given strain path, $\Delta\varepsilon_{\alpha}^{(A)}$ $(\alpha = 1, 2)$ are constant quantities and should be computed only once.

At this stage, the parameters associated to the non-defective area of the sheet metal can be updated using the formulae

$$
\begin{aligned}
{}^{T+\Delta T}\bar{\varepsilon}^{(A)} &= {}^{T}\bar{\varepsilon}^{(A)} + \Delta\bar{\varepsilon}^{(A)},\\
{}^{T+\Delta T}\varepsilon_{\alpha}^{(A)} &= {}^{T}\varepsilon_{\alpha}^{(A)} + \Delta\varepsilon_{\alpha}^{(A)}, \quad \alpha = 1,2.
\end{aligned}
\tag{5.113}
$$

The solution procedure is now prepared to evaluate the groove parameters corresponding to the $T+\Delta T$ moment. If $-1<\rho^{(A)}\leq 0$ (left branch of the forming limit curve), the principal stress ratios are the same in regions A and B (see Eq. (5.106)). In this case, only the increment of the equivalent strain $\Delta\bar{\varepsilon}^{(B)}$ should be found as a solution of Eq. (5.108) written for the $T+\Delta T$ moment:

$$
\begin{aligned}
&{}^{T+\Delta T}Y\left[{}^{T+\Delta T}\bar{\varepsilon}^{(A)}\right] = {}^{T+\Delta T}f\cdot{}^{T+\Delta T}Y\left[{}^{t}\bar{\varepsilon}^{(B)} + \Delta\bar{\varepsilon}^{(B)}\right],\\
&\text{if } -1<\rho^{(A)}\leq 0,
\end{aligned}
\tag{5.114}
$$

where the current thickness ratio ${}^{T+\Delta T}f$ is expressible from Eqs. (5.69) and (5.74)

$$
\begin{aligned}
{}^{T+\Delta T}f &= \frac{{}^{T+\Delta T}s^{(B)}}{{}^{T+\Delta T}s^{(A)}} = {}^{0}f\exp\left[{}^{T+\Delta T}\varepsilon_3^{(B)} - {}^{T+\Delta T}\varepsilon_3^{(A)}\right]\\
&= {}^{0}f\exp\left[{}^{T+\Delta T}\varepsilon_1^{(A)} + {}^{T+\Delta T}\varepsilon_2^{(A)} - {}^{T}\varepsilon_1^{(B)} - {}^{T}\varepsilon_2^{(B)} - \Delta\varepsilon_1^{(B)} - \Delta\varepsilon_2^{(B)}\right],
\end{aligned}
\tag{5.115}
$$

with $\Delta\varepsilon_{\alpha}^{(B)}$ $(\alpha = 1,2)$ resulting from Eqs. (5.93) and (5.106):

$$
\begin{aligned}
&\Delta\varepsilon_{\alpha}^{(B)} = \left[\Delta\bar{\varepsilon}^{(B)}\right]\cdot G_{\alpha}\left[\zeta^{(A)}\right],\\
&\text{if } -1<\rho^{(A)}\leq 0, \quad \alpha = 1,2.
\end{aligned}
\tag{5.116}
$$

Equation (5.114) can be solved only in a numerical manner. Again, during the tests performed by the authors, the bisection method has proved excellent performances in combination with a bracketing strategy. After $\Delta\bar{\varepsilon}^{(B)}$ is determined, the increments of the principal strains in region B can be easily evaluated from Eq. (5.116).

In the case $0<\rho^{(A)}\leq 1$ (right branch of the Forming Limit Curve), the principal stress ratio associated to region B is no longer constant. As a consequence, two unknown quantities should be determined. They are the current principal stress ratio ${}^{T+\Delta T}\zeta^{(B)}$ and the increment of the equivalent strain $\Delta\bar{\varepsilon}^{(B)}$. Fortunately, the strain-rate along the necking band does not vanish if $0<\rho^{(A)}\leq 1$. Under such circumstances, Eq. (5.110) can be put in an incremental form and used to express $\Delta\bar{\varepsilon}^{(B)}$ as a dependency on ${}^{T+\Delta T}\zeta^{(B)}$ (see also Eq. (5.112)):

$$
\Delta\bar{\varepsilon}^{(B)} = \frac{\Delta\varepsilon_2^{(A)}}{G_2\left[{}^{T+\Delta T}\zeta^{(B)}\right]}, \quad \text{if } 0<\rho^{(A)}\leq 1.
\tag{5.117}
$$

$\Delta\bar{\varepsilon}^{(B)}$ given by Eq. (5.117) should be replaced in Eq. (5.109) written for the $T+\Delta T$ moment, thus obtaining

$$
\begin{aligned}
&{}^{T+\Delta T}Y\left[{}^{T+\Delta T}\bar{\varepsilon}^{(A)}\right] \Big/ F\left[\zeta^{(A)}\right] \\
&= {}^{T+\Delta T}f \cdot {}^{T+\Delta T}Y\left[{}^{T}\bar{\varepsilon}^{(B)} + \frac{\Delta\varepsilon_2^{(A)}}{G_2\left[{}^{T+\Delta T}\zeta^{(B)}\right]}\right] \Big/ F\left[{}^{T+\Delta T}\zeta^{(B)}\right], \qquad (5.118)\\
&\text{if } 0<\rho^{(A)}\leq 1.
\end{aligned}
$$

The current thickness ratio ${}^{T+\Delta T}f$ is still defined by Eq. (5.115), but the principal strain increments $\Delta\varepsilon_\alpha^{(B)}$ $(\alpha=1,2)$ result now from a more complicated flow rule (see Eqs. (5.93) and (5.117)):

$$
\begin{aligned}
&\Delta\varepsilon_1^{(B)} = \left[\Delta\varepsilon_2^{(A)}\right]\frac{G_1\left[{}^{T+\Delta T}\zeta^{(B)}\right]}{G_2\left[{}^{T+\Delta T}\zeta^{(B)}\right]}, \quad \Delta\varepsilon_2^{(B)} = \Delta\varepsilon_2^{(A)}, \qquad (5.119)\\
&\text{if } 0<\rho^{(A)}\leq 1.
\end{aligned}
$$

In conclusion, Eqs. (5.115) and (5.119) will bring Eq. (5.118) to a formulation involving only ${}^{T+\Delta T}\zeta^{(B)}$ as unknown. Again, the numerical solution can be found using the bisection method combined with a bracketing strategy. After ${}^{T+\Delta T}\zeta^{(B)}$ is determined, Eqs. (5.117) and (5.119) allow the evaluation of the increments $\Delta\bar{\varepsilon}^{(B)}$ and $\Delta\varepsilon_\alpha^{(B)}$ $(\alpha=1,2)$, respectively.

At this stage, the parameters associated to the defective area of the sheet metal can be updated using the formulae

$$
\begin{aligned}
{}^{T+\Delta T}\bar{\varepsilon}^{(B)} &= {}^{T}\bar{\varepsilon}^{(B)} + \Delta\bar{\varepsilon}^{(B)},\\
{}^{T+\Delta T}\varepsilon_\alpha^{(B)} &= {}^{T}\varepsilon_\alpha^{(B)} + \Delta\varepsilon_\alpha^{(B)}, \quad \alpha=1,2.
\end{aligned} \qquad (5.120)
$$

The procedure described above is simple and efficient. Both for the left and right branches of the Forming Limit Curve, the problem consists in solving a unique non-linear equation. At the level of region A, it is always possible to find a solution by numerical techniques. Region B needs a more careful treatment from this point of view. Generally, strains accumulate faster in the groove. As previously shown, the model tries to enforce the equilibrium of the tractions along the interface with the non-defective area of the sheet metal. At higher strain levels, the bearing capability of the groove can be limited by the hardening law. In such cases, it is not possible to find the solution at the level of region B. The bearing limitation can be trapped by testing the value of the equivalent strain increment $\Delta\bar{\varepsilon}^{(B)}$ during the bracketing procedure. If the search for an initial guess fails even for very large increments $\Delta\bar{\varepsilon}^{(B)}$ one may deduce that region B has already attained its bearing

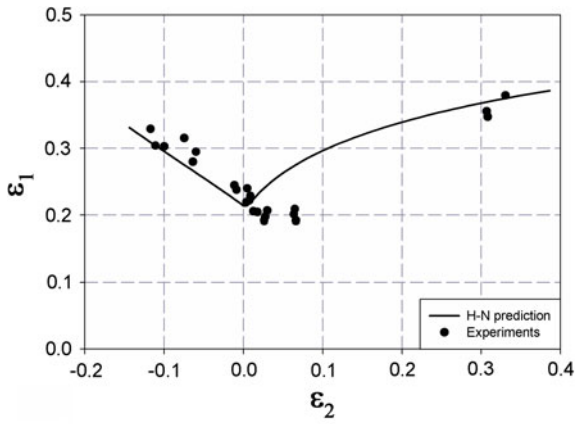

Fig. 5.28 H-N prediction versus experiments (Volk et al. 2008) for AA5182-O aluminium alloy

limit. From a mechanical point of view, this situation corresponds to the occurrence of the necking phenomenon in the groove. As a consequence, the current values of the principal strains in region *A* should be considered as defining the limit state of the sheet metal.

The occurrence of the necking must be also checked after finding a numerical solution for the groove. Normally, the ratio $\Delta\bar{\varepsilon}^{(B)}/\Delta\bar{\varepsilon}^{(A)}$ should be tested. If this quantity becomes very large ($\Delta\bar{\varepsilon}^{(B)}/\Delta\bar{\varepsilon}^{(A)} > 100$, for example), one may conclude that the necking has been initiated. The inspection of the strain path should be stopped as the current values of the principal strains in region *A* define the limit state. If the ratio $\Delta\bar{\varepsilon}^{(B)}/\Delta\bar{\varepsilon}^{(A)}$ is not great enough, the computation will continue after applying a new increment of the equivalent plastic strain $\Delta\bar{\varepsilon}^{(A)}$ to region *A*.

Different formulations of the equivalent stress (von Mises, Hill 1948; Barlat 1989, and Banabic et al. 2005a) and hardening laws (Hollomon, Swift, Voce, Ghosh, Hockett-Sherby, and AUTOFORM) have been implemented in the strain localization model presented above. In all cases, the numerical tests have shown a very good stability and robustness of the solution procedure. In order to validate the performances of the computational algorithm, its predictions have been compared with experimental data corresponding both to steel and aluminium alloys. As an example, Fig. 5.28 shows the comparison between the numerical results and the experimental data included in Benchmark 1 of the NUMISHEET 2008 conference (Volk et al. 2008) for the case of the AA5182-O aluminium alloy.

5.4.4.3 Comparison of the FLC's Predicted by Different Theoretical Models

During the last five decades, the theoretical model developed by Marciniak and Kuczynski Marciniak (1965) has been intensively used for calculating forming limit curves. More recently, several other approaches have been proposed. Among them,

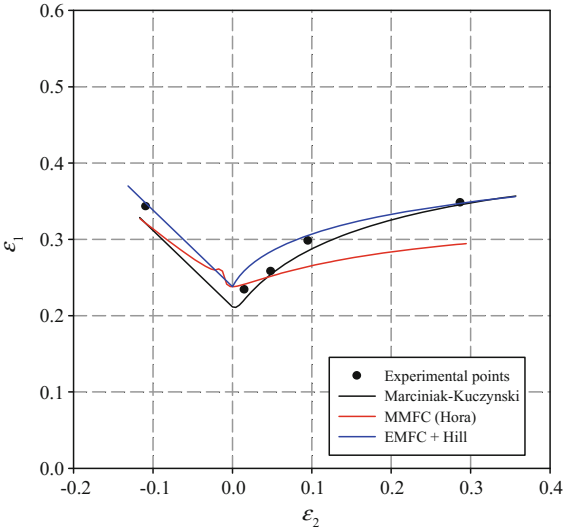

Fig. 5.29 Comparison of the FLCs predicted by Marciniak-Kuckzynski model, Modified Maximum Force Criterion (Hora) and Edhanced Maximum Force + Hill Criteria with experimental data for AA6016-T4 aluminium alloy

Hora's MMFC model (Hora and Tang 1994) and its extension to the so-called EMFC model developed by Mattiasson and his co-workers Mattiasson et al. (2006) are also attractive due to their simplicity and good performances.

Figure 5.29 shows a comparison of the FLC's predicted by the theoretical models mentioned above with experimental data obtained by the authors in the case of an AA6016-T4 sheet metal (1 mm thickness). All the calculations have been performed using the same plasticity model namely, the BBC2005 yield criterion and Swift's hardening law. As one may notice in Fig. 5.29, the FLC's predicted by the M-K and EMFC models are in very good agreement with the experimental data. The quality of the predictions given by the MMFC model is poorer. It seems that Hora's assumption of a sudden evolution towards the plane-strain state in the necking region causes an understimation of the formability along the right branch of the FLC. From this point of view, the hypotheses on which the EMFC model is based are more realistic. It is also noticeable the characteristic peak on the left branch of the FLC predicted by the MMFC model. This strange behaviour is the consequence of a mathematical singularity that cannot be removed from Hora's MMFC model (see Sect. 5.4.1.2 and Aretz (2004) for details).

5.4.4.4 Non-zero Thickness Stress

In sheet forming processes that imply a non-zero sheet curvature, e.g. in punch stretching and hydraulic bulging, the thickness stress varies from a minimum (i.e. compressive stress) at the concave side of the sheet to zero at the (stress-free) convex side. This stress component is much smaller than in-plane stresses (at least for not too high sheet curvatures) and are therefore usually neglected in sheet

forming limit models. Under certain conditions however, the average thickness compressive stress can be very high and non-negligible, e.g. in double-sided hydroforming, during which pressure is applied to both sides of the sheet with a certain pressure difference, and in pinching regions in pressing operations (where there is double-side tool contact).

The effect of the normal pressure on the formability of sheet metals is well known and already used from long time ago in industry by Keeler (1970). During some forming operations (hydrostatic forming, incremental forming) the sheet is subjected to a significant normal pressure. Bridgman (1952) studied first time the influence of the hydrostatic pressure on the formability. Later this influence has been the subject of numerous experimental investigations, especially by Spitzig and Richmond (1984). The general conclusion was that the yield stress decrease and the formability increase with superimposed hydrostatic pressure. The increase in formability is usually explained by the closing of the micro-voids in the sheet and the slowing down of the nucleation of new ones due to the normal pressure exerted by the surrounding fluid Padwal et al. (1992). A systematic analysis of sheet failure under normal pressure without assuming ductile damage has been done in the last decades. The first theoretical analysis was performed by Ciumadin et al. (1990). Using a simple analytical model (similar with the Marciniak-Kuczynski model) they succeed to calculate the FLC for different values of the hydrostatic pressure. Gotoh et al. (1995) used the classical Swift's and Hill's criterion of instability and Stören and Rice's condition together with the constitutive model developed by himself for localized necking. In Smith et al. (2003) and later in Matin and Smith (2005), forming limit equations are derived for a sheet deformation under a constant and non-zero ratio of sheet thickness stress over major in-plane stress. These models are based on the assumption of a strain-path independent FLSD, which is extended in the sense that the forming limit stress is also assumed to be independent of the sheet thickness stress. In Smith et al. (2003), the ratio of minor to major in-plane stresses are assumed to be constant during deformation, while in Matin and Smith (2005), it is the ratio of minor to major in-plane strains which is fixed.

Banabic and Soare (2008), Wu et al. (2009), Allwood and Shouler (2009) have analyzed the influence of the normal pressure on the Forming Limit Curve using an enhanced Marciniak model. The results presented in the last papers are closed one to another one. In the Fig. 5.32 is presented this influence based on the modified Marciniak model (Banabic and Soare 2008).

Figure 5.30 shows a significant increasing of the limit strains for any strain path (more significant in the equi-biaxial region) with the increasing of the superimposed hydrostatic pressure. Allwood and Shouler (2009) included in the MK model a six component stress tensor and proposed a new generalized forming limit diagram (GFLD) showing the influence on the limit strains both of the normal and through thickness stresses (see Fig. 5.31 and Allwood and Shouler (2009)).

The effect of the through-thickness normal stress on the forming limit diagram has been studied extensively in the last five years using different anisotropic yield criteria by Assempour et al. (2010), Liu and Meng (2012), Zhang et al. (2012), (2014a, b), Nurcheshmeh and Green (2014), Lang et al. (2015), Wang et al. (2015).

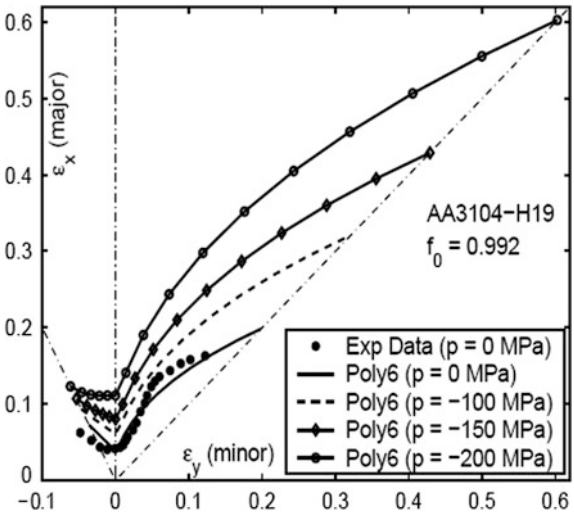

Fig. 5.30 Forming Limit Curves for several values of the normal pressure for AA3104-H19 aluminium alloy

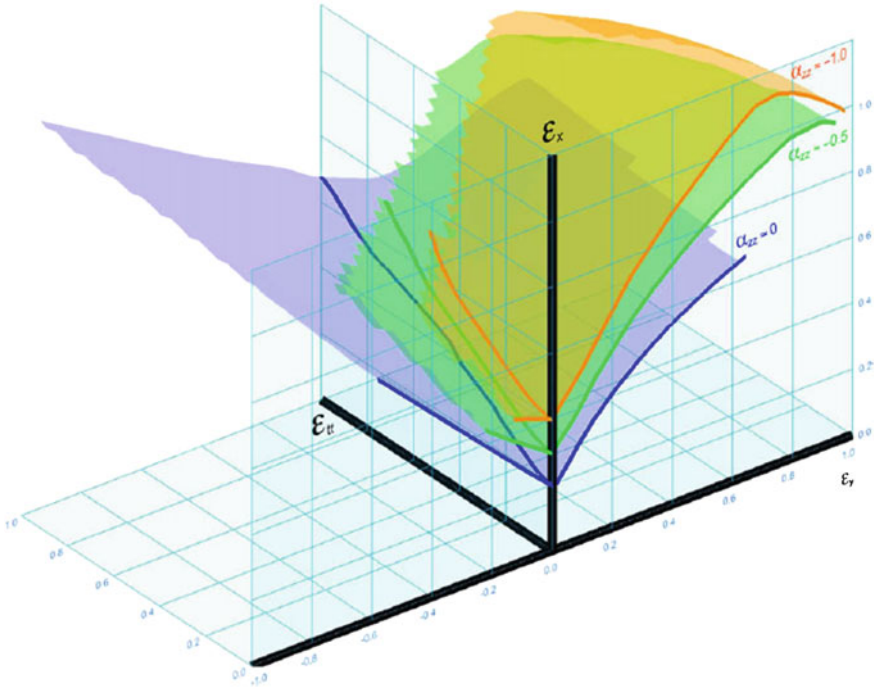

Fig. 5.31 The generalized Forming Limit Diagram for AA1050 aluminium alloy (Allwood and Shouler 2009)

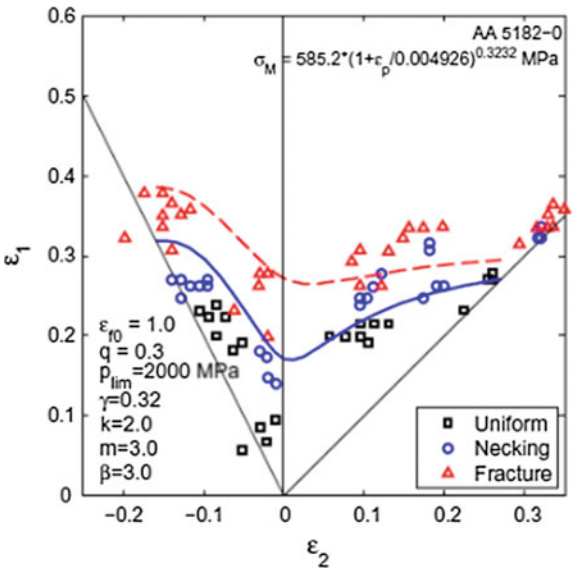

Fig. 5.32 The experimental localization and fracture curves for AA 5182-0 (Xue 2010). Experimental data from Banabic et al. (2005b)

A clarification of the influence of the hydrostatic pressure on the yield and flow of the metallic materials has been presented by Soare and Barlat (2014). A new approach to analyze the effect of hydrostatic pressure on the deformability of sheet metals was introduced by Xue (2010). He extended the one dimensional Considère condition for arbitrary three dimensional loadings (taking into account the hydrostatic pressure) and applied it to sheet metal forming. The bifurcation point for the localized deformation is considered from the sense of energy dissipation. Xue (2010) applied his models to calculate both the necking and the fractured limit strains, respectively (see Fig. 5.32 and Xue (2010) for the AA5182-0 aluminium alloy). With the proposed method the influence of the pressure on the limit strains has been also analysed.

The trend in formability that all these models show is that a more negative thickness stress (i.e. more compression) delays the onset of the localized necking instability, which is the same trend found in some experimental investigations mentioned above.

5.4.4.5 Non-zero Through-Thickness Shear Stress

Through-thickness shearing (TTS) in sheet metal is induced through sliding friction, especially against highly curved tooling for which normal contact pressure is high. Typical examples of these conditions may be found in incremental sheet forming and in the deep drawing over relatively sharp die corners and across draw beads. Research on the effect of TTS on formability has been originally initiated by the unusually high formability observed in incremental sheet forming (Allwood and Shouler 2009; Eyckens et al. 2009, 2011).

Before extending the MK framework to include TTS and giving some numeric examples on the effect of TTS on FLCs, we first look into a mathematical description of TTS. If the sheet undergoes in-plane deformation combined with through-thickness shearing, the strain mode can no longer be captured by a single variable. The plastic strain rate tensor **D** can in this case be expressed as:

$$[\mathbf{D}] = \begin{bmatrix} 1 & 0 & \rho_{13} \\ 0 & \rho_{22} & \rho_{23} \\ \rho_{13} & \rho_{23} & -(1+\rho_{22}) \end{bmatrix} D_{11} \tag{5.121}$$

Here D_{11} is the major in-plane strain rate. In (5.121) it is used as a scaling factor to define the in-plane strain mode ρ_{22}, and also two independent 'through-thickness shear modes': ρ_{13} (in the direction 1, i.e. the major in-plane strain direction) and ρ_{23} (in the direction 2, i.e. the minor in-plane strain direction). From tensor analysis the relative through-thickness shearing along all other direction in the sheet plane may be derived, cf. (Eyckens et al. 2011). A typical result is visualized in the polar plot given by Fig. 5.33. The lengths of the lines that start from the origin of the coordinate system and that are bound by the grey-shaded area, reflect the magnitude of relative TTS along the respective directions. Along the 1- and 2-directions, these lengths correspond to ρ_{13} and ρ_{23} , respectively. Two enclosing, circle-shaped lobes can be seen: one has a positive sign of TTS associated with it, while the other has negative sign. Along the in-plane direction that separates these lobes, no TTS is acting. It may be shown that such a direction always exists, for any possible combination of ρ_{13} and ρ_{23} . At 90° with respect to this direction of 'zero TTS', the TTS has the maximal magnitude among all in-plane directions. The maximal magnitude of TTS is called *the imposed TTS*, and written as ρ_{TTS}. It is imposed along the direction given by the angle α_{TTS} with respect to the major in-plane straining direction. There is a one-to-one conversion between the sets of $(\rho_{TTS}, \alpha_{TTS})$ on one hand and (ρ_{13}, ρ_{23}) on the other hand.

The generalization of the MK formability framework towards TTS, concerns both the force equilibrium equations and the geometric compatibility equations (Eyckens et al. 2009).

Extension of force equilibrium is straightforward: equilibrium equations of the in-plane normal and the in-plane shear components of force, are supplemented with one equilibrium equation of the out-of-plane shear component of force. The resulting set of 3 equilibrium equations is the scalar equivalent of the imposed equilibrium of the force vectors on either side of the boundary plane between matrix and groove: $\vec{f}^{a} = \vec{f}^{b}$

Geometric compatibility between matrix and groove is generally expressed in terms of the velocity gradients, which intrinsically considers not only the strain rate but also the rate of rigid body rotation. The compatibility conditions refer to components of the velocity gradient tensors within the matrix ($\mathbf{L}^{a}$) and the groove ($\mathbf{L}^{b}$), as expressed in a reference frame that is aligned with the (instantaneous) directions along the groove (t-direction) and normal to the groove within the sheet

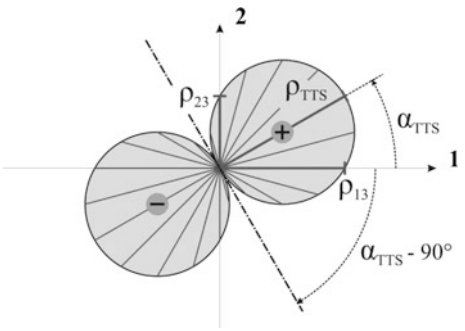

Fig. 5.33 Polar plot giving an example of the direction (α_{TTS}) and magnitude (ρ_{TTS}) of the *imposed* through-thickness shear (TTS) onto a sheet, as well as the resulting TTS along any other in-plane direction (straight lines bounded by the *grey* area). Figure reproduced from Eyckens et al. (2011)

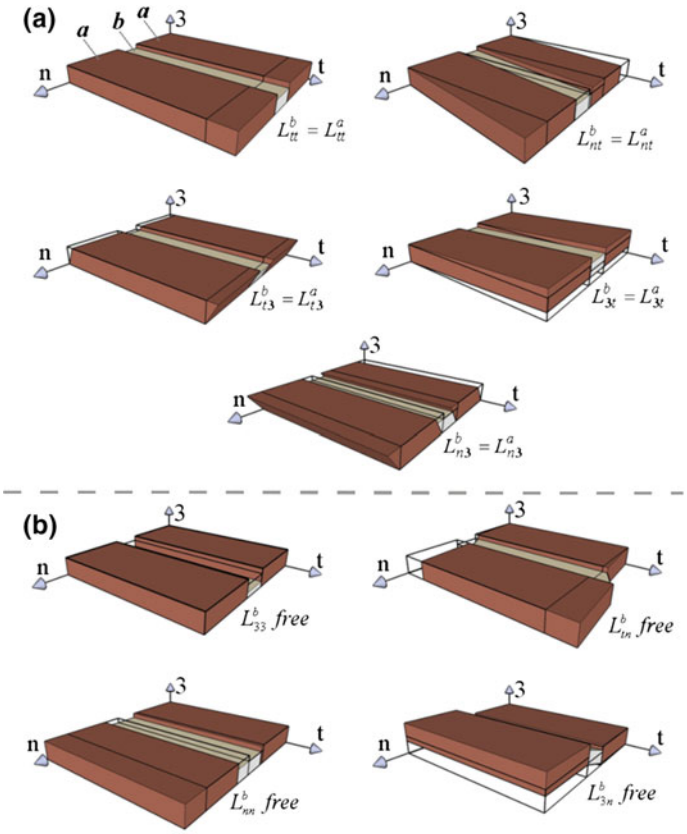

Fig. 5.34 **a** Geometric compatibility conditions and **b** unconstrained (i.e. 'free') components of the velocity gradient of the groove material. The initial configuration is depicted with wireframe. Figure reproduced from Eyckens et al. (2009)

plane (n-direction). As demonstrated in Fig. 5.34a, 5 out of the 9 independent components of the velocity gradient need to be equal in both regions in order to ensure compatibility. Consequently, the remaining 4 components of the velocity gradient within the groove, are not constrained by their counterparts in the matrix material, as illustrated Fig. 5.34b.

Results from this extended MK model demonstrate that TTS *may* have a beneficial effect on formability, and that this depends not only on the magnitude but also on the direction of imposed TTS. Let us consider first the case of plane strain deformation with additional TTS along the direction of zero extension (minor in-plane strain direction), which is sketched in Fig. 5.35a. The (fixed) direction of the MK groove that determines the limit of formability, coincides in this case to the minor in-plane strain direction. The imposed through-thickness shearing induces non-zero out-of-plane shear stress σ_{t3} in both matrix and groove, while in the sheet plane, the plane strain deformation induces non-zero σ_{nn} (= σ_{11}) and σ_{tt} (= σ_{22}). It can be shown that for a von Mises material loaded under these deformation conditions, the stress mode **u** (in both matrix and groove) is contained in the hyperplane $\sigma_{nn} = 2\sigma_{tt,}$ as shown in the 3-dimensional yield locus section. The matrix' stress mode $\mathbf{u}^a$ is fixed (monotonic loading). The groove stress mode $\mathbf{u}^b$ however evolves during deformation, from close to $\mathbf{u}^a$ towards the plane strain stress mode (indicated by a cross marked 'PS'). This stress mode change is accompanied with a relative increase of σ_{nn}-component of stress, thereby delaying the onset of strain localization within the groove that is governed by equilibrium of the normal force component.

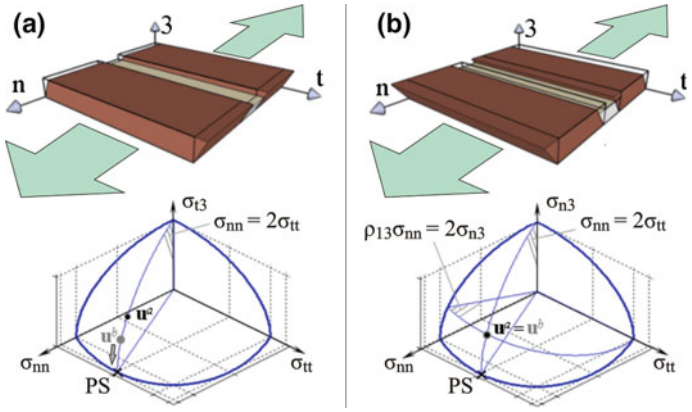

Fig. 5.35 Plane strain loading superimposing TTS along **a** the direction of zero extension (coinciding with groove direction *t*) and **b** the major in-plane strain direction (coinciding with groove normal direction *n*). For both **a** and **b**, the relevant 3-dimensional section in stress space for a von Mises material is shown: major in-plane stress (σ_{nn}), minor in-plane stress (σ_{tt}) and the non-zero out-of-plane shear stress (σ_{t3} for **a** and σ_{n3} for **b**, respectively). For case **a**, the groove stress mode $\mathbf{u}^b$ evolves towards the plane strain point 'PS' during deformation, while in case **b** it remains constant and equal to the matrix' stress mode $\mathbf{u}^a$. Figure composed from Eyckens et al. (2009)

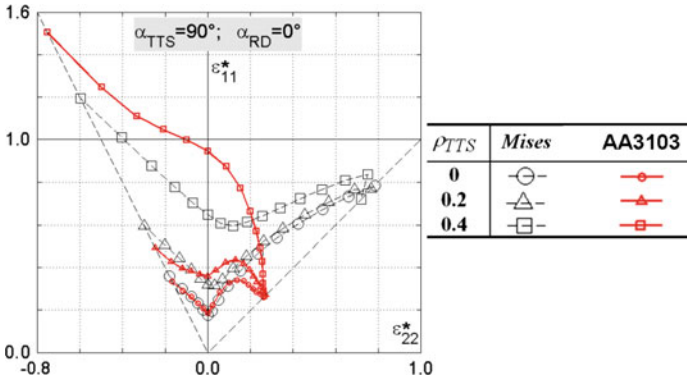

Fig. 5.36 Calculated FLCs for materials with von Mises yield locus and with an anisotropic yield locus of AA3103 aluminium alloy, having various degrees of magnitude of imposed through-thickness shear ρ_{TTS} (different symbols). Direction of imposed TTS is given by: $\alpha_{TTS} = 90°$. Figure reproduced from Eyckens et al. (2011)

The results are however very different for plane strain with superimposed TTS along the *major* in-plane strain, cf. Fig. 5.35b. The critical direction of the MK groove with respect to formability, is also in this case along the direction of zero extension. TTS induces a non-zero σ_{n3}-component of stress. It can be derived from force equilibrium that the ratio σ_{n3}/σ_{nn} is equal for both matrix and groove, which leads to the second hyperplane containing $\mathbf{u}^a$ and $\mathbf{u}^b$ that is drawn in Fig. 5.35b. As a result, the groove stress mode is required to be equal to the matrix stress mode, meaning that the stabilizing mechanism of groove stress mode evolution towards the plane strain point does not occur.

Figure 5.36 shows FLC predictions with increasing TTS along the minor in-plane strain direction (i.e. $\alpha_{TTS} = 90°$). Except for equibiaxial loading, imposing TTS along this direction generally improves formability. Figure 5.37 further illustrates the high sensitivity of the forming limit with respect to the direction of imposed TTS. TTS along the major in-plane strain direction ($\alpha_{TTS} = 0°$) does not significantly affect FLC (compare to FLC curve of $\rho_{TTS} = 0$ in the Fig. 5.38). The beneficial effect of TTS on the FLC is maximal if it is imposed along the minor in-plane strain direction ($\alpha_{TTS} = 90°$).

5.4.5 Crystal Plasticity Based FLC Prediction

Crystal plasticity modelling considers the main microstructural aspects of metallic alloys, namely the distribution of the individual metallic crystals or grains (with associated crystal orientation), possibly augmented with information of the morphologic appearance of microstructure, second phase particles (if present), or other microstructural aspects. Crystal plasticity modelling is in essence a multi-scale

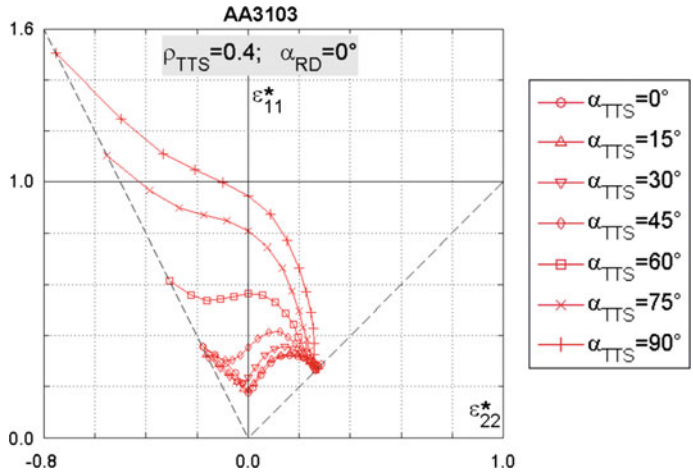

Fig. 5.37 Calculated FLCs for materials with an anisotropic yield locus of AA3103 aluminium alloy, with varying imposed directions of TTS (α_{TTS}). The magnitude of imposed TTS is $\rho_{TTS} = 0.4$. Figure reproduced from Eyckens et al. (2011)

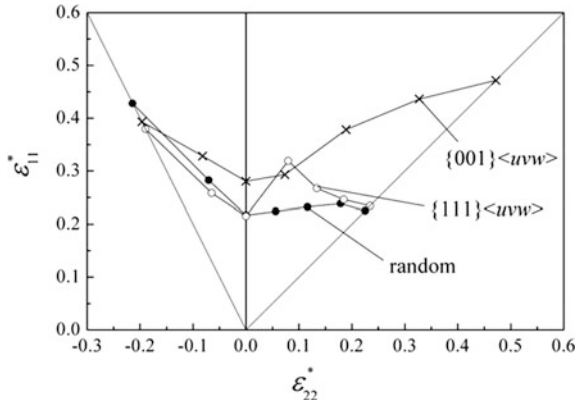

Fig. 5.38 Three theoretical FCC textures leading to significant differences in FLCs, from Yoshida and Kuroda (2012)

approach, linking the physical processes that accommodate plastic deformation on the scale of the crystal (e.g. plastic slip, deformation twinning) to the homogenized or macroscopic behaviour of the polycrystalline metallic aggregate. The microstructure determines the yield locus shape, which is intrinsically incorporated in crystal plasticity modelling. For single-phase materials with near-equiaxed grain morphology, the dominant microstructural feature linked to yield locus shape is the crystallographic texture. Deformation-induced evolution of texture will result in yield locus shape changes. Such effects can be readily studied by crystal plasticity.

In recent year, two different approaches have been mainly followed to couple crystal plasticity calculations to sheet formability prediction, namely the MK framework and FE modelling. They will be discussed next.

The development of ductile damage or voids in the microstructure, and their correlation to macroscopic forming limits, is another topic that has received significant attention in recent literature. An overview of such studies is also included.

5.4.5.1 Crystal Plasticity in MK Analysis

The pioneering studies in this field adopted a crystal-plasticity-derived yield locus in MK model framework (Barlat 1989; Bassani et al. 1979), thereby neglecting effects of deformation texture or other microstructural evolutions. In later years, the influence of deformation-induced texture evolution was explicitly investigated by direct coupling of the crystal plasticity as a material model. Due to limited computation power, the earlier investigations often made additional assumptions, e.g. that necking band is perpendicular to major strain direction (Zhou and Neale 1995), or that texture evolution should be identical in groove and surrounding matrix (Ratchev et al. 1994). In Tóth et al. (1996), the study of the formability of three measured aluminium textures shows the effect of texture evolution to equalize the forming limits of the different textures and lower them (in most strain paths of the right-hand side of the FLD). These earlier studies often adopt the Taylor-Bisschop-Hill polycrystal plasticity model.

Over the last decade, significant attention has been given to the study of 'idealized textures', in particular for aluminium (FCC structure). Such theoretical textures consist of randomly-generated orientations with certain spread around a single orientation (Wu et al. 2004a) or orientation fibre (Yoshida and Kuroda 2012). Formability is not only very sensitive to the chosen ideal orientation, but also to the texture spread around the central orientation (Wu et al. 2004a). This dependency can be linked to the sharpness of yield locus in the biaxial range (Wu et al. 2004a). The effect of the cube texture component (main recrystallization texture component in aluminium) is studied with a rate-dependent plasticity model in Wu et al. (2004a), where it was found that the spread around the ideal texture component determines the yield locus surface near equibiaxial stretching deformation to affect the formability under this deformation mode. However, the initial shape of yield locus does not completely determine formability in right-hand side of FLD. So-called distortional or textural hardening, i.e. yield locus shape change due to texture evolution, is as important a factor (Signorelli et al. 2009). In aluminium alloys for example, the cube fibre textures gives high forming limits due to the beneficial distortional hardening effect, in spite of an unfavourable initial yield locus shape with low r-value (Yoshida and Kuroda 2012).

In summary, in aluminium materials (FCC), rolling texture components generally have a negative effect on biaxial formability (Yoshida et al. 2007), whereas the cube texture (recrystallization texture component) can be beneficial (Wu et al. 2004a; Yoshida et al. 2007). Fewer studies have been done on BCC cubic materials such as ferritic steels; the study of Inal et al. (2005) suggests that sensitivity of texture evolution on formability is much less for BCC compared to FCC materials. For Mg sheet alloy (HCP crystal structure), besides dislocation-based plasticity also

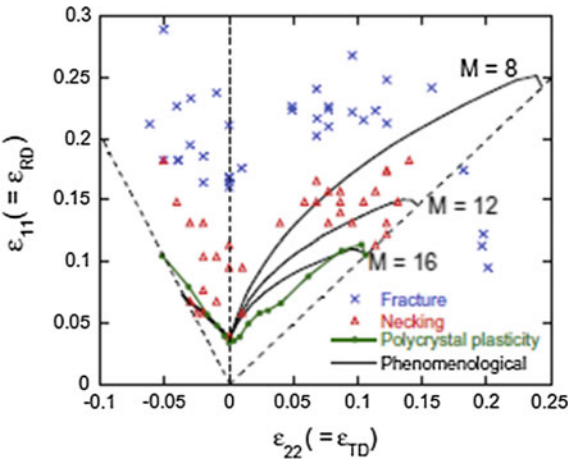

Fig. 5.39 Comparison of advanced phenomenological and crystal plasticity material models in FLC prediction, from Chiba et al. (2013)

the mechanical twinning needs to be considered (Neil and Agnew 2009). Additional hardening due to twinning can promote the resistance to localized necking. Also in Wang et al. (2011), formability of Mg alloy is investigated, both with Taylor and VPSC models. Results show that texture evolution decreases forming limit under uniaxial and biaxial deformation paths, while it has little effect under near-plane strain deformation. Numerical investigation also reveals that formability can be significantly improved by altering the texture, in particular a rotation of the basal texture component.

Coupling of crystal plasticity with formability analysis that is highly no-linear requires sufficient attention to algorithmic implementation. For time integration scheme of MK model with crystal plasticity-based material modelling, it is referred to Knockaert et al. (2002); where focus is put on the consequences of texture evolution on the overall algorithm. Kim et al. (2013) compare Newton-Raphson and Nelder-Mead time integration schemes for crystal plasticity-based MK simulations.

In the current state-of-the art, crystal plasticity-based formability modelling does indeed give insightful guidelines with respect to optimized microstructure (Yoshida et al. 2009; Yoshida and Kuroda 2012; Wang et al. 2011). Figure 5.38 gives an example of increased theoretical formability through texture optimization. Even though this makes crystal plasticity an appealing approach to predict formability, often no clear improvement in FLC prediction is obtained from crystal plasticity with respect to recent phenomenological material modelling approaches (Chiba et al. (2013), cf. Fig. 5.39).

Advanced crystal plasticity models, which incorporate grain interaction and non-equiaxed grain morphology, can improve accuracy of FLC predictions compared to more basic Taylor crystal plasticity model, in which the local deformation inside each crystal is unaffected by its environment in the microstructure (Signorelli et al. 2009). For complex microstructures such as multi-phase materials, a

microstructural representative volume element (RVE) may be defined through FE modelling to produce the constitutive behaviour in formability modelling framework. In Tadano et al. 2013, such RVE material modelling approach for single-phased material is used in MK analysis.

5.4.5.2 Formability Modelling Through Crystal Plasticity in FEM (CPFEM)

In Wu et al. (2004b), the FE mesh under consideration corresponds to a unit cell of the polycrystalline material. Each integration point corresponds to a grain and obeys single crystal plasticity theory. A discretized aluminium texture is used to assign grain orientations to specific integration points of the mesh, which is done arbitrarily. It is shown that a forming limit band rather than a single curve is obtained when several arbitrary assignments of grains to the FE mesh are considered. Texture evolution results in higher formability predictions on the right-hand side of the FLD for the material under study. It is emphasized that this approach does not require the 'fitting' parameter of the initial imperfection of the MK model, but on the other hand it is indicated that forming limits depend on the number of elements (i.e. grains) considered in the analysis. In Yoshida (2014), deformation-induced surface roughening and strain localization is investigated by crystal plasticity FE analysis, in particular regarding their dependency on grain size and number of grains over the sheet thickness. If the sheet has relatively few grains over the sheet thickness (less than 30), plane strain formability is found to be reduced due to significant surface roughening.

In Inal et al. (2002a, b) the Taylor theory of rate-dependent crystal plasticity is used in a plane-strain Crystal Plasticity Finite Element Model (CPFEM) to simulate the localization of deformation under plane strain tension. Strain localization occurs in two phases, firstly a through thickness neck is initiated, after which shear bands are formed within the neck. Texture evolution and strain rate sensitivity were identified as crucial parameters for shear band localization, since shear localization was shown to be completely suppressed when texture evolution during deformation was not considered or when strain rate sensitivity was taken to be high enough.

Hu et al. (2008) apply CPFEM (using a plane stress model) to simulate the onset of necking in uniaxial tension of an aluminium alloy containing second phase particles about an order of magnitude smaller than the average grain size. They found that necking band formation is determined mainly by the arrangement of the soft and hard grains in the model, with only a small influence of particle volume fraction and type of particle distribution (i.e. homogeneous or aligned in stringers). Also post-necking behaviour was studied with a plane strain model, showing the large influence of the type of particle distribution: a homogeneous distribution leads to a well-developed neck (i.e. a large fracture strain) with cup-and-cone ductile fracture, while low fracture strains are found in combination with a shear-type fracture in the presence of particle stringers. Experimentally it is also found that the

presence of stringers (which is related to the method of sheet casting) produce a shear-type dominant failure with small necking.

5.4.6 *Void Growth Based FLC Prediction*

In Saanouni (2008), the isotropic damage model of Gurson is implemented into implicit and explicit FE analysis to predict the onset of necking in a hydraulic bulging process. The same material model is also used for prediction of the onset of ductile fracture in numerous bulk forming processes. Haddag et al. (2008) presents a FLC obtained from the implementation of the isotropic damage model of Lemaitre into implicit FE code. The damage parameters were obtained by inverse modelling from uniaxial, plane strain and equibiaxial tension tests and a simple shear test. The same authors apply a similar constitutive modelling approach to Rice's bifurcation theory for FLC prediction in Haddag et al. (2009). Achani et al. (2007) use the isotropic damage model of Cockcroft and Latham to predict the onset of necking in a plane strain tension test after model parameter identification using a pure shear test. In Uthaisangsuk et al. (2008), the Nakazima test is simulated with FEM including the Gurson-Tvergaard-Needleman damage model. The damage parameters are estimated based on metallographic observations and other experimental techniques. The shape of the FLC obtained from the different FE simulations appears to be different than the experimental FLC, although the position of the numeric FLD corresponds reasonably well to the experiment.

5.4.6.1 Modelling of FLC using the GTN Model

One of the recently proposed approaches for FLC construction is the application of damage model. The determination of forming limits of metallic sheets using the GTN damage model has been performed according to different approaches. The most common ones include the approaches that use the numerical simulation of the traditional formability tests prdoposed by Nakazima an Kikuma (1967) and Marciniak and Kuczynski (1967) and the approaches that combine the GTN model with the Marciniak-Kuczynski model (Marciniak and Kuczynski 1967). This section introduces these approaches and their application in the construction of FLCs.

5.4.6.2 FLC Prediction by Numerical Simulation of Traditional Formability Tests

The Nakazima and Marciniak tests are standard traditional tests for the determination of FLCs. In these tests, metallic sheets with different shapes are stretched against a punch up to the onset of necking/fracture. By measuring the planar limit

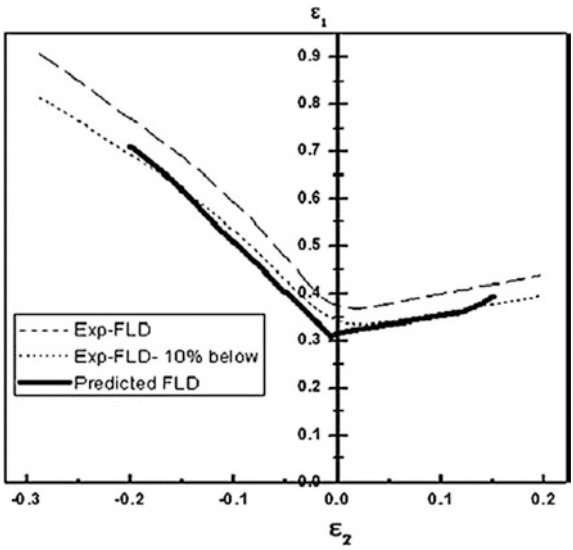

Fig. 5.40 Comparison of FLDs obtained by experiments and GTN model Abbasi et al. (2012b)

strains at the onset of necking, the Forming Limit Diagram (FLD) is plotted. Like the experimental tests, the forming limit strains of metallic sheets can be predicted by numerical simulation of Nakazima and Marciniak tests. On the other hand, the accuracy of the predicted limit strains will be affected by the necking criterion used in the simulations. One of the useful tools for the prediction of necking and determination of limit strains is the application of the GTN damage model. The GTN model defines the plastic behaviour of the sheet metal and its failure due to void evolution.

The effect of void growth on the forming limits was investigated by employing Gurson damage model (Gurson 1977) in the FE analysis, within the framework of membrane theory, of a punch stretching test (Chu 1980). The effect of other mechanisms of void evolution i.e. void nucleation and coalescence can be included in the investigations by using the GTN damage model (Abbasi et al. 2011, 2012a; Yoon et al. 2013). Abbasi et al. (2011), (2012a) predicted the FLC of an IF steel using an isotropic GTN damage model. A set of rectangular specimens with a length of 200 mm and different widths of 25, 50, 75, 100, 125, 150, 175 and 200 mm were simulated according to the Hecker test (Banabic et al. 2000). All specimens were formed until the final void volume fraction f_F for an element was fulfilled. The value of major and minor strains at the element with void volume fraction of f_F was selected as the failure strains. The constructed FLC based on the measured failure strains was in good agreement with experiments (see Fig. 5.40).

As the metallic sheets are commonly produced by rolling, they exhibit high levels of anisotropy. Investigations using anisotropic GTN damage models show that the plastic anisotropy of the matrix in ductile sheet metal influences both the deformation behaviour and damage evolution of the material Chen and Dong

Table 5.1 Values of GTN model parameters

GTN parameter	q_1	q_2	q_3	f_0	f_N	S_N	$\bar{\varepsilon}_N$	f_C	f_F
Value	1.5	1	2.25	0.00035	0.05	0.1	0.3	0.05	0.15

(2009). Regarding this fact, Brunet et al. (1996) employed an anisotropic Gurson-Tvergaard model Gurson (1977), Tvergaard (1981) with Hill'48 quadratic yield criterion Hill (1948) in the analysis of necking in the simulation of a deep drawing process. The FLC of a mild steel sheet was determined by the numerical simulation of Marciniak tests. Kami et al. (2015) also used the anisotropic GTN model with Hill'48 quadratic yield criterion to determine the FLC of anisotropic sheet metals. The commercial ABAQUS/Explicit finite element code and the VUMAT implementation of the anisotropic GTN damage model were used to calculate the limit strains of an AA6016-T4 sheet. The hardening behaviour of the metallic sheet is described by Swift's law:

$$Y(\bar{\varepsilon}^p) = 525.8(0.113 + \bar{\varepsilon}^p)^{0.27} \tag{5.122}$$

The Hill'48 coefficients i.e. F, G, H, L, M, and N were calculated as 0.648, 0.644, 0.356, 1.5, 1.5 and 1.174, respectively. The GTN model parameters were calibrated using the force-displacement curve obtained from uniaxial tensile tests. Table 5.1 shows the values of the calibrated GTN model parameters:

The Forming Limit Curve has been constructed according to the specifications of the international standard ISO 12004-2 (2008) and by performing the Nakazima tests. Different strain paths have been tested by using different geometries of the specimens according to Fig. 5.41. The values of the width parameter w are 30, 55, 70, 90, 120, 145, and 185 mm, the last of them corresponding to a fully circular specimen. The Forming Limit Curve obtained by numerical simulations has been validated by comparison with experimental results.

To calculate the limit strains, the numerical simulations have been continued up to fracture. Three groups of nodes distributed along paths normal to the fracture section have been selected and the values of the major and the minor strains at these nodes have been measured on the frame corresponding to the stage just before the onset of fracture. One of the node paths used to measure the principal strains is shown in Fig. 5.42. Having the fracture section as shown in Fig. 5.42a, b facilitates the selection of node paths for strain measurement. The first node path passes through the middle of the fracture section (see Fig. 5.42), while the other two paths are located on each side of the first path with an approximate distance of 2 mm, being also parallel to each other. The values of the strains associated to these node paths were analyzed with the ARAMIS software and according to Bragard's method (Bragard et al. 1972; D'Haeyer and Bragard 1975) to determine the corresponding point on the Forming Limit Curve.

The Forming Limit Curve obtained using the ARAMIS software is presented in Fig. 5.43. This figure indicates that the results obtained by numerical simulation using the GTN damage model are in good agreement with the experimental data.

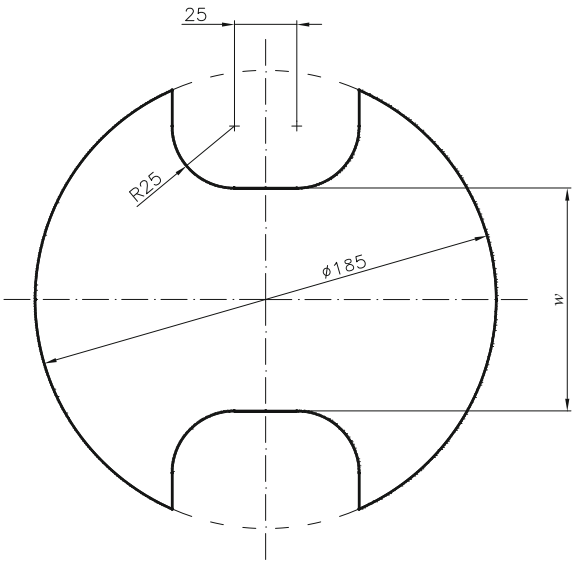

Fig. 5.41 Dimensional characteristics of the circular and notched specimens used in the Nakazima tests with hemispherical punch, Ø100 mm

The comparison becomes even more favourable when confronted with the predictions of the MK and MMFC models see Fig. 5.43. One may notice from the diagram that the quality of the GTN predictions is far better, especially along the right branch of the Forming Limit Curve, where both MK and MMFC models overestimate the formability of the metallic sheet.

The finite element simulation with the GTN damage model as the material constitutive model was also used for the construction of Forming Limit Stress Diagram (FLSDs) (Uthaisangsuk et al. 2008; He et al. 2011). For this purpose, the Nakazima tests were simulated with sheet metal samples having the same length of 190 mm and varying widths from 55 up to 195 mm (Uthaisangsuk et al. (2008)). The FLSD obtained in this way was used for the prediction of crack initiation due to a two-step forming and hole expansion tests. The same investigation was performed by the application of FLD obtained by the experimental tests. It was observed that the FLSD obtained by the GTN model was able to predict the failure with reasonable accuracy. On the other hand, the experimental FLD failed to predict the crack initiation (Uthaisangsuk et al. (2008)). A similar work was reported by He et al. (2011) in which the FLSD of an AA5052-O1 sheet was determined using the GTN damage model. The cited authors performed numerical simulations of the Nakazima test on different samples with 10 mm to 180 mm widths (see Fig. 5.44).

The numerical simulation was allowed to continue until the onset of necking where the damaged elements with zero stress appear in the necking region. Three elements with close stress values (the stress difference between every two elements is within 10 %) were selected in the necking region and the mean value of the principal maximum and middle stresses at these elements were defined as the limit

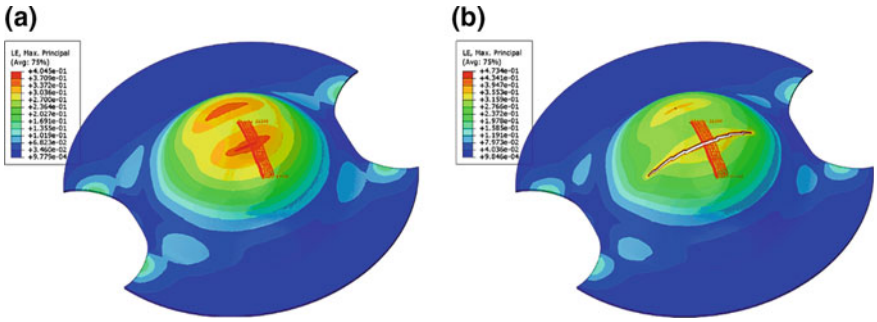

Fig. 5.42 Distribution of the major logarithmic strain of the notched specimen with w = 130 mm **a** at the onset of necking and **b** after fracture

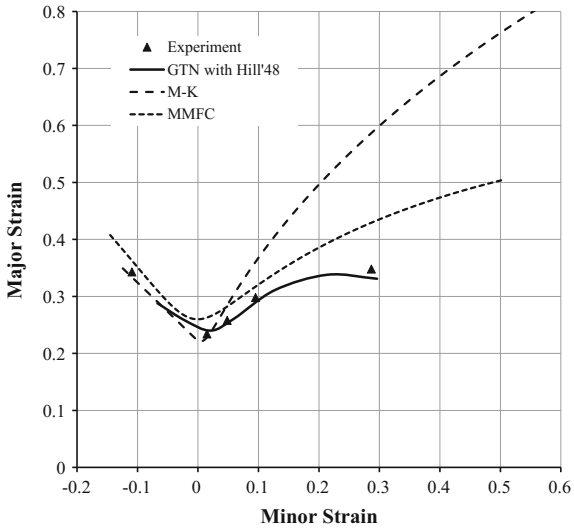

Fig. 5.43 Comparison between the FLC's obtained by different methods

stresses. The stress values were measured at the last loading increment without the appearance of cracked elements. The same procedure has been used for the determination of limit strains. The numerical FLD obtained by using this approach showed good agreement with experimental results (He et al. 2011).

The GTN damage model was also used to predict FLDs for different types of sheets, dual phase and multi-phase steels (Uthaisangsuk et al. 2009, 2011; Ramazani et al. 2012), Tailor-welded blanks (TWBs) (Abbasi et al. 2012b, 2012c) and sandwich sheets (Parsa et al. 2013; Liu et al. 2013). Ramazani et al. (2012) determined the FLC of the DP600 steel by the numerical simulation of the Nakazima test. Furthermore, the ability of the GTN model to predict the damage in forming was assessed by FE simulation of a cross-die test. The results showed that the GTN damage model predicts the fracture with reasonable accuracy (Ramazani et al. 2012).

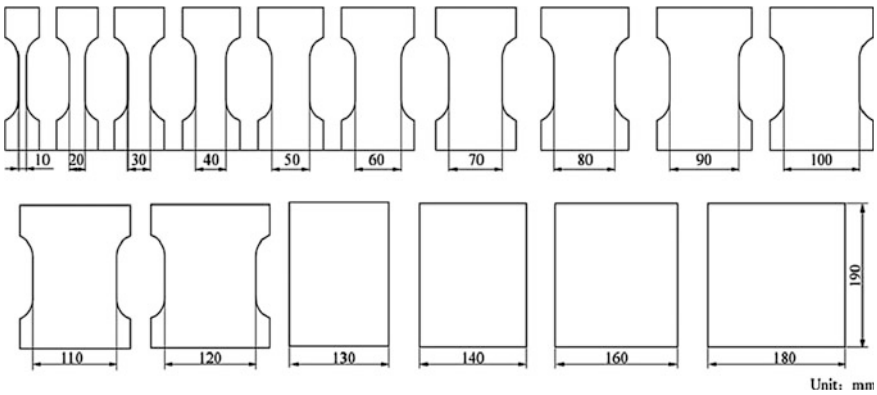

Fig. 5.44 Nakazima test samples used for the numerical construction of the FLSD for an AA5052-O1 metallic sheet

Almost the same procedure in Abbasi et al. (2012a) was used for the FLC prediction of IF-steel TWBs (Abbasi et al. 2012b, 2012c). The results showed that the predicted FLD by the GTN model does not properly agree with the FLD relevant to fracture initiation, but it is in fairly good conformance with the FLD that separates the safe region from other regions.

The GTN damage model was employed to construct the FLC of Al3105/polypropylene/Al3105 (Parsa et al. (2013)) and AA5052/polyethylene/AA5052 sandwich sheets (Liu et al. 2013). The FLC of these sandwich sheets was determined by numerical simulations of the Nakajima test where the GTN model was used as the constitutive model of the metallic face sheets. The effect of layer's thickness on the formability of these sandwich sheets was investigated.

To find the limit strains, Liu et al. (2013) analyzed the evolution of the equivalent plastic strain in the neck region. As Fig. 5.45 illustrates, the evolution of the equivalent plastic strain in the localized neck point "a" and its vicinity point "b" were plotted as a function of the dome height. By comparing the equivalent plastic strain curves of these two points, one may notice that the strain values at these two points show similar tendencies during most of the deformation process, and this portion of the deformation process is called stability period. With the proceeding of deformation process, the equivalent plastic strain value at point "a" begins to show a rapid increase, which indicates that the instability period starts. When the equivalent plastic strain increment at point "a" exceeds by 7 times that at point "b", the localized necking is assumed to occur and the final major and minor strains of element "a" calculated by linear interpolation are considered as the limit strains for the construction of forming limit diagrams.

Besides the above mentioned studies, the GTN damage model was used for the investigation of formability under double-sided pressure forming Liu and Meng (2012) and also in the study of geometry and grain size effects on the formability of sheet metals in micro/meso scale plastic deformation (Xu et al. 2015). Liu et al. (2012)

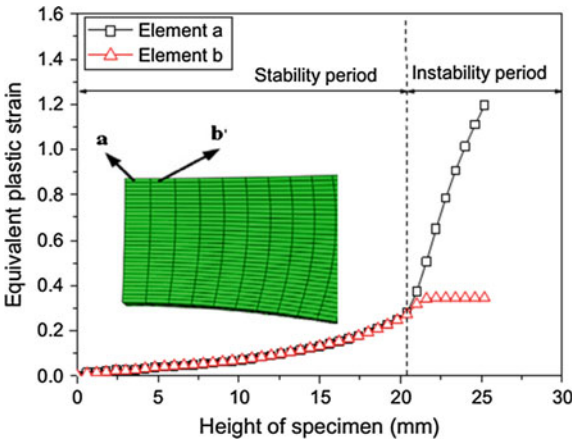

Fig. 5.45 Equivalent plastic strain distribution of localized neck element "a" and its neighbour element "b" Liu et al. (2013)

studied the effects of double-sided pressure on the formability of an AA5052-O aluminium alloy sheet metal under tension-compression deformation state. The left branch of the FLD was determined by numerical simulation of Nakazima tests under different double-sided pressure conditions. The GTN model was able to predict the limit strains in the left branch of the FLD with acceptable accuracy.

Xu et al. (2015) investigated the geometry and grain size effects on the formability of sheet metals in micro/meso scale plastic deformation using experiments and numerical simulation. For this purpose, the forming limit experiments were conducted based on the miniaturized (Holmberg et al. 2004) (for the left branch of FLC) and Marciniak (for the right branch of FLC) tests to estimate the formability of sheet metals under different loading conditions. The dimensions of the specimens used in these tests are shown in Fig. 5.46. The traditional Marciniak test was performed with the punch diameter of 10 mm, die diameter of 14 mm and the hole in the driving sheet centre of 3 mm diameter.

For the numerical construction of FLC at micro/meso scale, an extended coupled damage model was first developed based on GTN and the Thomason (1985) models via considering the geometry and grain size effects on void evolution. The extended model was then employed in the numerical simulations of both Holmberg and Marciniak tests. In these simulations, when the void volume fraction just reaches to final void volume fraction f_F the major and minor strains are considered as the limit strains. The forming limits determined in this way are shown in Fig. 5.47 for a copper sheet with the thickness of 0.4 mm and different grain sizes of 23.7, 58.9 and 132.2 μm and (Xu et al. 2015). As one may notice, the extended GTN is qualitatively able to predict the changes in limit strains with the change of grain size (the numerically predicted limit strains decrease with the increase of grain size as in the case of experiments). Nevertheless, the extended GTN model underestimates the limit strains under biaxial stretch condition. The reason for this inaccuracy may be related to the identification procedure of the extended GTN model parameters. It

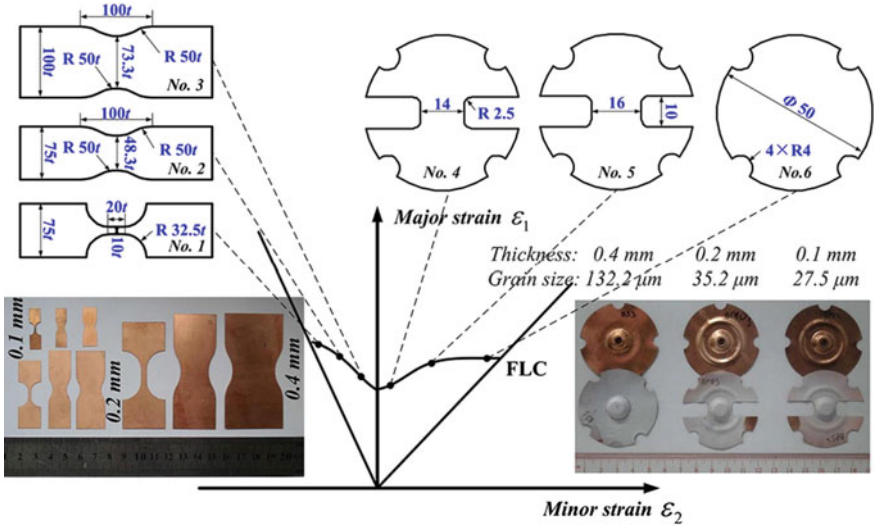

Fig. 5.46 The dimensions of the Holmberg and Marciniak specimens used for the construction of FLC Xu et al. (2015)

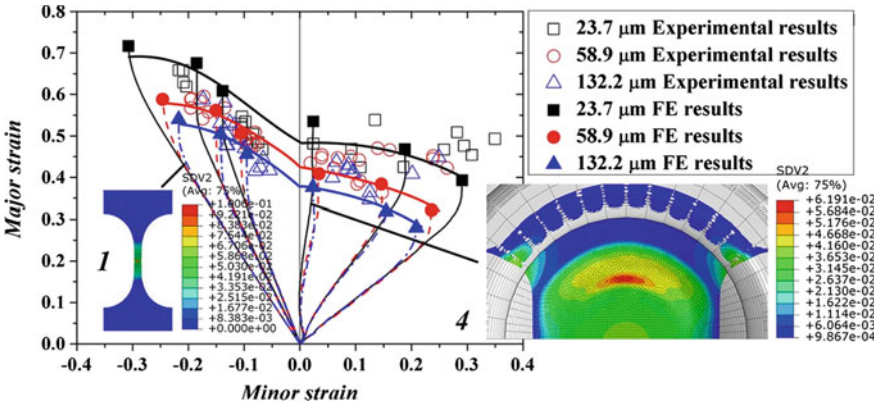

Fig. 5.47 Comparison of limit strains in a copper sheet with the thickness of 0.4 mm and grain sizes of 23.7, 58.9 and 132.2 µm (Xu et al. 2015)

is revealed that Thomason model tends to overestimate the ductility at low triaxiality (Benzerga 2002), hence the parameters identified based on the uniaxial tensile tests could be less accurate when applied to the biaxial stretch condition with higher triaxiality. In addition, the coalescence behaviour affected by shear loading is not considered either. This might also contribute to the difference between the experimental and predicted FLCs (Xu et al. 2015).

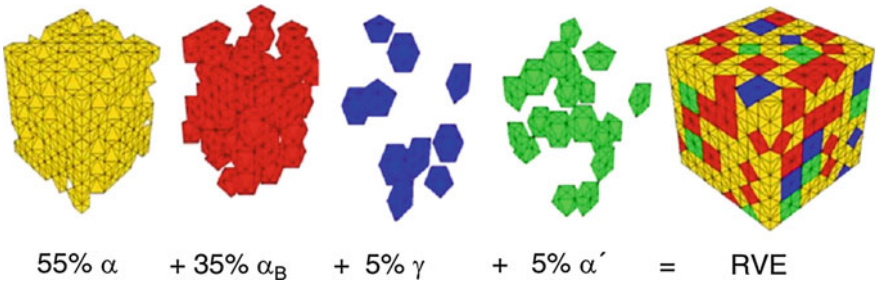

Fig. 5.48 Representative volume elements (RVE) for a TRIP microstructure consisting of ferrite, bainite, austenite and martensite (Uthaisangsuk et al. 2009)

Uthaisangsuk et al. (2009), (2011) used a 3D representative volume element (RVE) to characterize multiphase microstructures of DP600 and TRIP600 steels and their distribution on the micro-level. Figure 5.48 illustrates an example of the RVE for a TRIP steel its microstructure consisting of ferrite, bainite, austenite and martensite (Uthaisangsuk et al. 2009). The GTN damage model was used in the finite element simulations of RVE for calculating the failure moment. The FLC's of DP600 and TRIP600 steels were constructed based on the results of these simulations.

The RVE was defined as a cube and the experimentally measured constituent phase fractions were taken into account. To describe the random distribution of phases, a statistical algorithm was implemented. The RVE's were used to investigate the critical areas of sheet samples in the Nakazima stretching-test. Therefore, boundary conditions for the RVEs were obtained from the local deformation fields in the macroscopic simulations (simulation of Nakazima tests with real dimensions of sheet samples). The influences of the local stress state on the crack initiation in the microstructure were considered by varying the sample dimensions. The GTN model was only employed for the softer ferritic matrix in the RVE model, where void initiation and void growth were observed in the experiments.

The comparison between the results of the RVE model and the experimental FLCs of DP600 and TRIP600 steels is presented in Fig. 5.49. As this figure shows, the limit strains predicted by the RVE model with GTN damage model underestimated the FLD curves in the biaxial stress condition whereas in the uniaxial tension and plane strain range the failure predictions exhibited similar strain levels as the experimental results. The reader is recommended to refer to Uthaisangsuk et al. (2009) for more discussions.

Figure 5.50 shows the macroscopically simulated Nakazima samples and their corresponding RVE's for the microstructure of TRIP600 at the moment of failure for the specimen having the dimensions 20 and 190 mm. The white regions are austenite and bainite, for which the GTN damage criterion was not applied. The failed elements reaching the critical damage values were observed close to the upper side of the RVE model for all sample geometries. This area belongs to the surface of the sheet samples, where cracking emerged in the experiments (Uthaisangsuk et al. 2009).

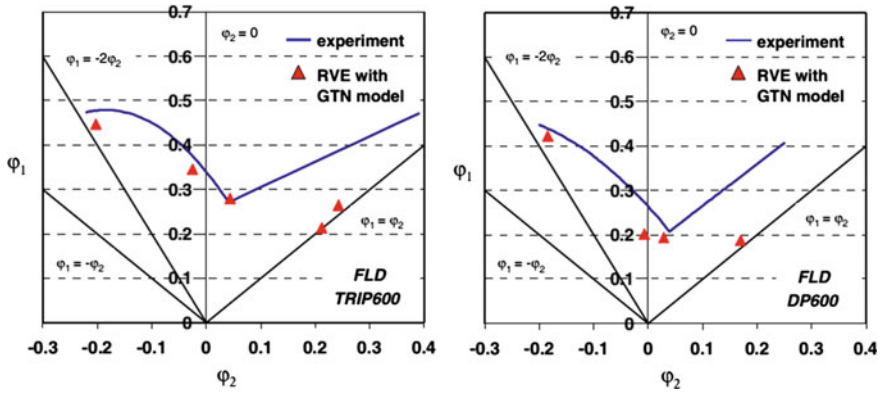

Fig. 5.49 Comparison of numerical calculated strains at failure with experimental FLC's for DP600 and TRIP600 steels (Uthaisangsuk et al. 2009)

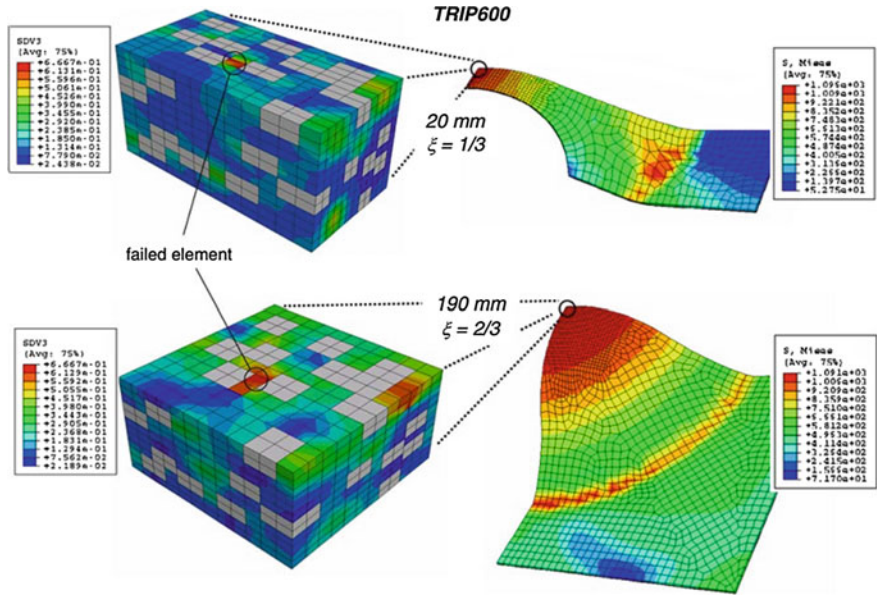

Fig. 5.50 FE results from macroscopic and RVE simulations for the 20 and 190 mm sheet samples made from steel TRIP600 (Uthaisangsuk et al. 2009)

5.4.6.3 FLC Prediction by Combined M-K and GTN Models

The M-K model (Marciniak and Kuczynski 1967) assumes that the strain localization results from a thickness imperfection schematically represented as a groove in Fig. 5.27 and (Marciniak and Kuczynski 1967; Hutchinson and Neale 1978a).

According to this hypothesis, two regions of the sheet metal should be distinguished: *A*—non-defective zone; *B*—groove. At different stages of the straining process, the parameter $f = s^{(B)}/s^{(A)}, 0 < f < 1$, is used to describe the amplitude of the imperfection ($s^{(A)}$ and $s^{(B)}$ denote the current thickness of regions *A* and *B*, respectively—see Fig. 5.27. The mechanical interconnection *A*–*B* is defined by a set of relationships enforcing the continuity of the strain-rate along the groove and the equilibrium of the normal and tangential loads acting on the interface from both sides (Banabic et al. 2010a). In the case of the MK model, necking is a consequence of the fact that the thickness strain tends to accumulate faster in region *B*.

To overcome some drawbacks of the MK model like the unrealistic assumption of a thickness defect, some researchers proposed to include void concentration in the defective zone. One approach developed according to this idea is the combination of MK and Gurson damage models. In this way, both ductile fracture caused by the evolution of voids and sheet metal instability contributes in the prediction of necking and limit strains.

Needleman and Triantafyllidis (1978) used the MK model in combination with Gurson damage model (Gurson 1977) to study the effect of void growth on the formability of biaxially stretched sheets. The imperfection was described by an increased initial volume concentration of voids in the incipient neck. The effect of the strain-hardening exponent and difference in initial void concentration between the material inside and outside the neck on the forming limit strains was studied Needleman and Triantafyllidis (1978). Because voids also evolve by nucleation, better predictions of plastic instability will be achieved when the nucleation of voids is taken into account in the Gurson model. The study on the effect of void nucleation on the forming limit of biaxially stretched sheets confirmed that the void nucleation has a significant effect on the limit strains Chu and Needleman (1980). The combined Gurson and MK models were also employed to study the effect of material properties on the forming limits of voided sheet metals (Melander 1983; Ragab et al. 2002).

Zadpoor et al. (2009) compared four different approaches of phenomenological ductile fracture modelling, the MK model, a modified Gurson damage model and a combined Gurson and MK approach to understand which of them can successfully predict the forming limits of high strength aluminium alloys like AA2024-T3. In the combined Gurson and MK approach, an initial imperfection in the sheet metal was assumed and a population of initial voids that are subject to further nucleation, growth and coalescence as deformation takes place was considered in both uniform and imperfection zones. The schematic drawing of this model is presented in Fig. 5.51. Once the void volume fraction of the imperfection zone reached the failure void volume fraction, the sheet was assumed to have failed and the strain values in the uniform zone were recorded as forming limits.

The results showed that the combination of the porous metal plasticity with the MK model improves the quality of the predictions of the porous metal plasticity model in the high end of the stress triaxiality values. Furthermore, it was found that the combined GTN and MK models and the modified Gurson model are more

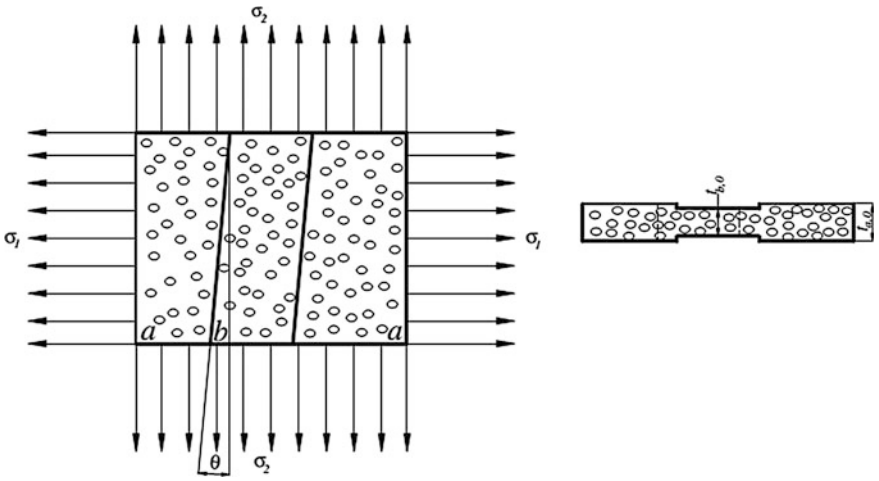

Fig. 5.51 Schematic drawing of the combined Gurson and MK models (Zadpoor et al. 2009)

computationally expensive in comparison with the MK and the phenomenological ductile fracture models. Based on these results it was concluded that the phenomenological ductile fracture models can predict the forming limits with better accuracy and lower computational costs in comparison with the combined GTN and MK models (Zadpoor et al. 2009).

To include material anisotropy, an approximate macroscopic yield criterion based on the Gurson damage model (Gurson 1977) was developed by Liao et al. (1997) under plane stress conditions:

$$\Phi = \left(\frac{\sigma_{eq}}{\sigma_0}\right)^2 + f^* \left[2 \cosh\left(\sqrt{\frac{1+2R}{6(1+R)}}\frac{6\sigma_m}{2\sigma_0}\right) - f^*\right] - 1, \tag{5.123}$$

where, R is the anisotropy parameter, defined as the ratio of the transverse plastic strain rate to the through-thickness plastic strain rate under in-plane uniaxial loading conditions. Later, this model was used to investigate the failure of sheet metals under forming operations (Huang et al. 2000). The MK method was employed to predict plastic localization by assuming a slightly higher void volume fraction inside randomly oriented imperfection bands in a material element of interest. The effects of the anisotropy parameter R, the material/geometric inhomogeneities, and the potential surface curvature on the plastic localization were investigated Huang et al. (2000).

The finite element model of combined Gurson and MK model is presented in Fig. 5.52 and Simha et al. (2007a, b) used this model to construct a limit curve in terms of the invariants of mean stress and equivalent stress which is called extended stress-based formability curve (XSFLC) using the GTN damage model. The authors used a material model consisting of a homogeneous zone and a zone that contains

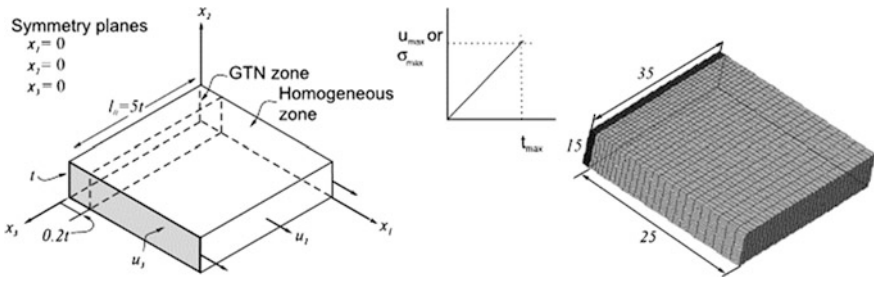

Fig. 5.52 Schematic material model. Symmetry and displacement boundary conditions are shown. When $u_3 = 0$, the model is loaded along the plane strain path (Simha et al. 2007b)

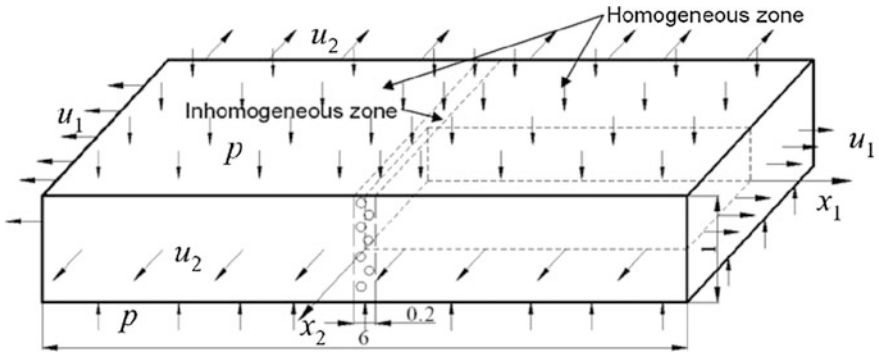

Fig. 5.53 Schematic of the MK model combined with Gurson model (Liu et al. 2012)

voids (material inhomogeneity) to simulate the necking under plane strain and uniaxial stress load paths.

The GTN material model was used to simulate the necking through finite element computations. Then, a strain-based FLC is constructed for this model and this FLC is transformed into a XSFLC. By changing the ratio of displacement in x_3 direction to displacement in x_1 direction, different in-plane loading paths are applied to the model. The XSFLC was constructed for different values of the work hardening exponent and initial void volume fraction. The applicability of this model was satisfactory for the case of straight tube hydroforming with no end feed.

The applicability of the combined Gurson and MK models in the prediction of FLC's of metal sheets under superimposed double-sided pressure was also investigated Liu et al. (2012). It was assumed that the imperfection zone has a certain initial volume fraction of voids. The schematic model is shown in Fig. 5.53. To find the limit strains, it was assumed that the failure takes place when the plastic strain increment in the inhomogeneous zone is 10 times larger than that in the homogeneous zone. The major and minor strains in the homogeneous zone were considered as the limit strains for the FLC construction (Liu et al. 2012). Figure 5.54 shows the predicted FLC's at different values of the initial void volume fraction of the

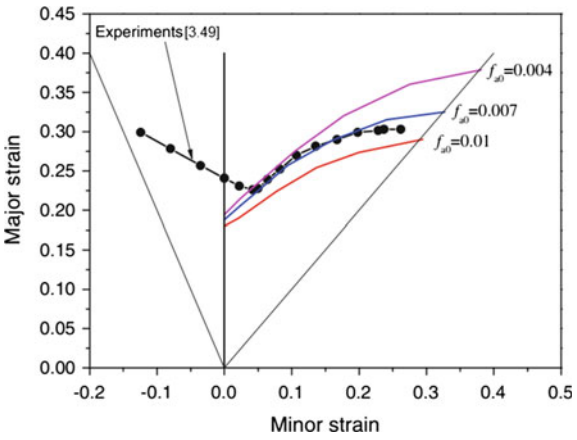

Fig. 5.54 Comparison of FLC's for different values of the initial void volume fraction in the inhomogeneous zone (Liu et al. 2012)

inhomogeneous zone f_{a0}. As one may notice, the limit strains decrease with the increase of f_{a0}.

The interested reader is suggested to refer to Chien et al. (2004) and Son and Kim (2003) for more examples of the construction of FLC using the combined GTN and MK models.

In addition to the above mentioned works, the GTN model was employed according to other approaches for FLC prediction. A brief description of these approaches will be presented here. A numerical necking criterion based on the stress state in the neck was proposed by Brunet et al. (1998) and Brunet and Morestin (2001) for the determination of limit strains. The necking criterion was based on the load-instability and plane strain localization assumptions (Hora's model (Hora and Tong 1994)) in which the failure of the material is defined by Gurson–Tvergaard damage model with Hill'48 and Barlat and Lian (1989) yield criteria. Similar studies using a non-local version of Gologanu–Leblond–Devaux model (Gologanu et al. 1993, 1994, 1997) were made to define the limit strains of anisotropic sheet metals (Brunet et al. 2004, 2005). Wang et al. (2013) used the anisotropic GTN damage model with Hill's quadratic yield criterion for the prediction of fracture in warm stamping of an AZ31 magnesium alloy sheets and also for the construction of FLC's at different temperatures. By the numerical simulation of the warm stamping process and recording the major and minor strains at the predicted place of fracture the FLC's at different temperatures were constructed. The effect of temperature on the void growth, coalescence and fracture behaviour of the Mg alloy sheets were analyzed using the anisotropic GTN model (Wang et al. 2013). Jeong and Pan (1995) employed a modified yield criterion based on the Gurson model and the Coulomb's yield criterion in the finite element modelling of a voided cube. Using these constitutive relations, Forming Limit Diagrams of rubber-modified plastics were constructed by measuring the critical localization strains under plane-stress biaxial loading. Grange et al. (2000) extended the GTN model to take into account the plastic anisotropy and viscoplasticity. They used this

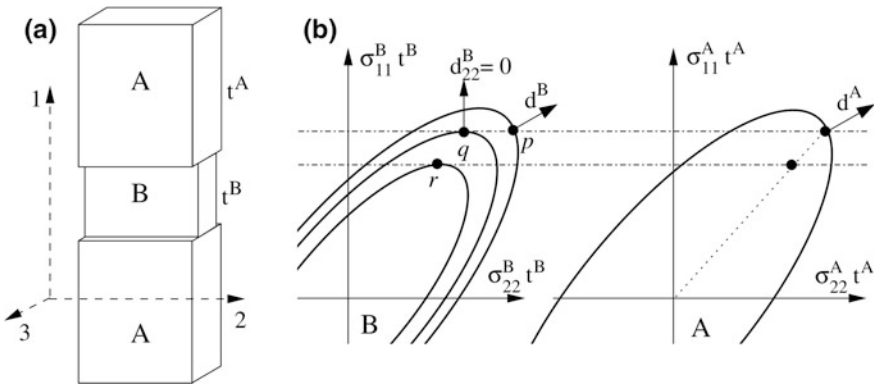

Fig. 5.55 MK model: thickness defect along a narrow band (**a**) and limit load interpretation of the onset of necking (**b**)

extended model for the FLC construction for a zirconium alloy containing various amounts of hydrogen.

5.4.6.4 Theoretical Model for Forming Limit Diagram Predictions Without Initial Inhomogeneity

Limit Analysis Interpretation of the MK Model

We will now show that the M-K model for the onset of necking admits a simple interpretation in terms of limit analysis or limit loads. Figure 5.55a shows the typical configuration of the homogeneous regions A along with the thickness defective region B. As it typical for the first quadrant of the FLD, we consider only the case where the region B is perpendicular to the direction of the major strain Ox_1. To simplify the discussion we also suppose that the coordinate system of Fig. 5.55a is aligned with the rolling and transverse directions of the sheet, and therefore also with the orthotropy axes of the yield locus. In the region A we impose a constant strain rate ratio:

$$\frac{d_{22}^A}{d_{11}^A} = \rho, \quad 0 \le \rho \le 1, \quad d_{12}^A = 0, \tag{5.124}$$

where d is the strain rate and all variables carry a superscript showing the region they belong to. The last equation is implied by the condition that the strain rates d_{11}, d_{22} are principal strain rates. Equations (5.124) and conditions of plastic normality and plane stress uniquely define the stress tensor σ^A in region A. The equilibrium and compatibility conditions for the two regions are given by:

$$\sigma_{11}^A t^A = \sigma_{11}^B t^B, \quad \sigma_{12}^A t^A = \sigma_{12}^B t^B, \quad d_{22}^A = d_{22}^B, \tag{5.125}$$

where t is the actual thickness. These conditions also uniquely define the stress and strain rate for the region B.

In the usual approach to the numerical solution of the MK model, these differential equations are integrated using an implicit Euler solver. During deformation, the strain rate in the region B rotates toward the plane strain condition where $d_{22}^B = 0$. Because of Eqs. (5.125), and the normality condition for region B, this implies that $d_{11}^B \to \infty$ when $d_{22}^B \to \infty$. In turn, this implies an infinitely fast decrease of the thickness in region B which is the MK definition for incipient necking. In practice, the solver is stopped as soon as d_{11}^B / d_{22}^B becomes larger than a predefined value, usually 10.

We now propose an alternative explanation for the incipient necking predicted by the MK model. In Fig. 5.55b we have plotted the intersection of the yield loci for both regions A and B with the hyper-plane $\sigma_{12} = \sigma_{13} = \sigma_{23} = \sigma_{33} = 0$. In order to impose the equilibrium condition given by the first of Eqs. (5.125), we have scaled the yield loci with the respective actual thicknesses. Starting with the known scaled stress $\sigma_{11}^A t^A$ in the region A, we seek the intersection of the line $\sigma_{11}^B t^B = \sigma_{11}^A t^A$ with the scaled yield locus of the region B. There are three possibilities, labelled with (p, q, r) in Fig. 5.55b: two points of intersection, one tangent point, and no intersection.

For case (p), the two points have normals with different signs of d_{22}^B and therefore the correct choice is governed by the third of Eq. (5.125) and the sign of d_{22}^A. The second case (r) is precisely the onset of necking in the MK model. As it easily inferred from Fig. 5.55b, this case has two equivalent interpretations:

$$d_{22}^B = 0 \Leftrightarrow \sigma_{11}^B = \sup\left\{\sigma_{11} | \exists \sigma_{22}, \Phi^B(\sigma_{11}, \sigma_{22}) \leq 0\right\}, \tag{5.126}$$

where Φ^B is the convex yield function for the region B. The second equation above shows that at the onset of necking the region B has reached its limit load for the x_1 direction. The third case (r) reinforces this limit-load interpretation: when there is no intersection, the equilibrium condition requires that the stresses in region A are inside the convex yield locus. This means that region A is rigid, with no plastic deformation, and this implies:

$$d_{11}^A = d_{22}^A = 0, \quad d_{22}^B = d_{22}^A = 0 \tag{5.127}$$

so that region B is necessarily in the plane strain condition. We observe that this last case is incompatible with an imposed strain rate ratio in region A as required by Eq. (5.125); in this case the simplest solution is to switch to a constant stress ratio (shown with a dotted line in Fig. 5.55b).

In conclusion, we have shown that the onset of necking in the MK model is characterized by the attainment of a limit load for the defective region and a

transition from a state of plastic deformation in both regions to one of plastic deformation inside the defective region and a rigid one inside the defect-free region.

Coalescence Models for Ductile Porous Materials

Initially the voids in a ductile porous material grow due the incompressibility of the surrounding material. In their pioneering work, Koplik and Needleman (1988) have numerically analyzed an elementary cell in a material with periodic voids, submitted to conditions of constant *s*tress ratio (with axisymmetric loading and predominant axial stress); after some deformation the plastic flow becomes localized in the ligaments between the voids thus leading to an accelerated growth and subsequent coalescence of voids. An analytical model for the same elementary cell has been proposed by Gologanu et al. (2001), based on a sandwich model with three layers—a highly porous one surrounded by two sound layers. There are two possible regimes—one with rigid outer layers and the other with plastic sound layers. The evolution of intervoid distances may trigger the rigid/plastic regime and therefore the onset of coalescence. Recently, Leblond and Mottet (2008) have extended this analysis to the case of a combined axisymmetric and shear loading, treating within the same model the coalescence of voids and the formation of shear bands along voided sheets.

Independently, Thomason (1985) has provided an analytical solution for the critical normal stress acting on a periodic planar array of rectangular voids where only the ligaments between voids are under plastic flow, the upper and lower blocks being rigid. He then used this particular solution to determine the onset of coalescence by the following limit analysis recipe: use a non-localized plastic flow solution (given by some homogenized model for porous solids) as long as the normal stress given by this theory is below the critical stress; otherwise switch to the rigid blocks/plastic ligaments model.

Another successful model has been proposed by Perrin (1992). Similarly to the above models he follows the evolution of the distribution of voids and once a highly porous layer is formed, he applies to it the localized band bifurcation analysis of Rudnicki and Rice (1975).

Figure 5.56 shows a typical coalescence model. The essential ingredients are the anisotropic distribution of voids due to the plastic deformation (**a**), the consideration of the horizontal sound layers A and highly porous layer B (**b**) and finally the limit load interpretation for the onset of coalescence, completely analogous to the one in Fig. 5.55b pertaining to the onset of necking in the M-K model: when stresses in the sound region attain the maximal stress supported by the porous layer at q, there is a change in plastic regime toward a rigid behaviour of the sound regions (stresses in the sound region are inside the yield locus Φ^A at r) while the porous layer remains in a strain-state compatible with this rigid behaviour $d_{22}^B = d_{33}^B = 0$.

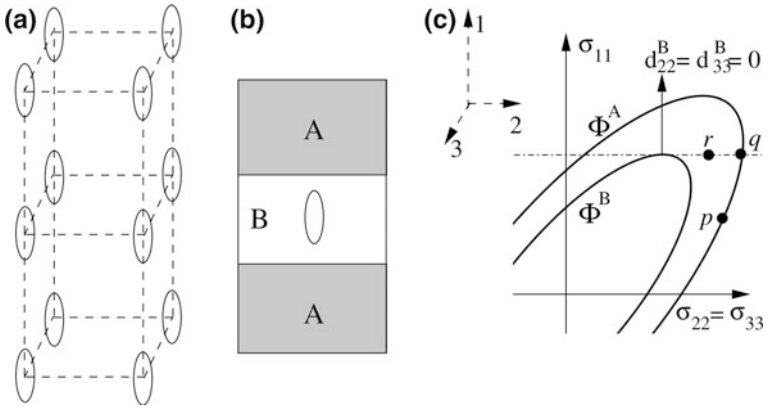

Fig. 5.56 Typical coalescence model based on limit analysis: distribution of voids after some deformation (**a**), elementary cell showing sound and highly porous layers (**b**) and limit load interpretation of the onset of coalescence with stress states in the sound regions before coalescence p, at the onset of coalescence q and during coalescence r (**c**)

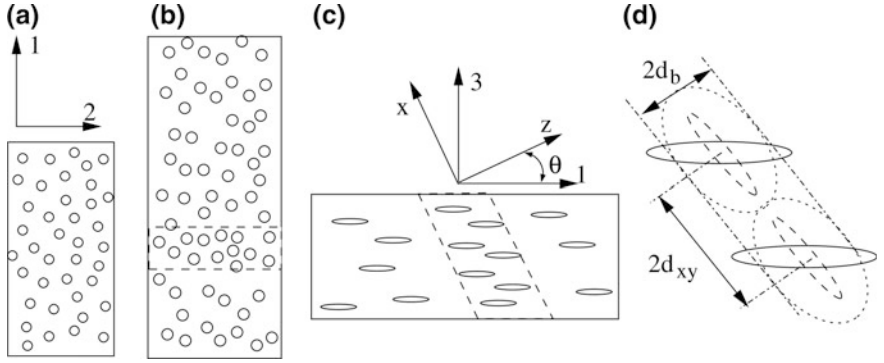

Fig. 5.57 LA necking model: Spherical voids with an initial homogeneous distribution (**a**), in plane virtual localization band after a plastic deformation with vertical major strain (**b**), through-thickness virtual localization band after a biaxial deformation that rendered the voids oblate (**c**), method for determining the increased porosity in a virtual localization band (**d**)

5.4.6.5 Necking Model Based on Limit Analysis for Porous Sheets

Based on the observed analogy between the onset of sheet necking as predicted by the MK model (Marciniak and Kuczynski 1967) and the onset of coalescence of voids in a porous bulk solid, we develop now a new necking model without an initial imperfection based on limit analysis (LA).

Let us consider a porous sheet with a matrix obeying a rigid-plastic law with von Mises yield criterion. An initial isotropic distribution of voids (Fig. 5.57a) will evolve into an anisotropic one after a deformation of the sheet (Fig. 5.57b).

We model the voided sheet using the ellipsoidal Gurson model from Gologanu et al. (1997) without taking into account the distribution of voids. At each moment we test for localization inside virtual bands with various normals n (Fig. 5.57c). For this test we do take into account the anisotropic distribution of voids that leads to an increased porosity inside the band. We first need to determine the mean void interspacings $2d_{xy}$ and $2d_z$ in the plane of the band and in the perpendicular direction z, parallel to n; then we need to estimate the thickness of the band $2d_b$ or equivalently the ratio $c = d_b/d_z$ and finally we need a model for the limit load the band can still sustain.

Let us denote F the deformation gradient at the actual time. By assuming that the void interspacings are governed by the evolution of some elementary area and length, Leblond and Mottet (2008) were able to determine an expression for the ratio $r = d_{xy}/d_z$. It is easy to generalize their result to the case of a distribution of voids that has already been submitted to some deformation gradient F_0 prior to the analyzed deformation process, again starting from an isotropic distribution:

$$r \equiv d_{xy}/d_z = \sqrt{\det(FF_0)}\left(nFF_0F_0^TF^Tn\right)^{-3/4} \tag{5.128}$$

where n is the normal to the band (parallel to direction z).

The choice of the band thickness for coalescence models has been widely discussed in the literature. For example Thomason's model is based on the choice $2d_b$ equal to the void height in the direction n, in order to best model plastic flow localization in the ligaments between voids. Based on experimental observations on sheet rupture showing that necking in general precedes void coalescence, we follow here the proposal of Perrin (1992) and Gologanu et al. (2001) and choose the thickness d_b such that the resulting elementary cell surrounding the void is the best possible approximation for an ellipsoid confocal with the void. This choice is compatible with using an ellipsoidal Gurson model for determining the limit load of the band; this model needs the porosity f^p and the shape factor S^p inside the band.

A supplementary difficulty appears if the band is not parallel to the void axes or if the void is not axisymmetric in the plane of the band. In this case, we determine an equivalent axisymmetric void by the following recipe: we project the initial void onto the plane xy to obtain an ellipse, we replace this ellipse with a circle of radius a_{xy} of same area and we determine the height a_z of the new void by imposing equal volumes for the original and new voids. In the sequel we will need only the following special case: the initial void is aligned with the sheet axes and has semiaxes a_1, a_2, a_3 and the normal to the band is given by $n = (n_1, 0, n_3)$.

$$\begin{aligned} a_{xy} &= a_2^{1/2}\left(a_3^2n_1^2 + a_1^2n_3^2\right)^{1/4}, \quad a_z = \frac{a_1a_3}{\left(a_3^2n_1^2 + a_1^2n_3^2\right)^{1/2}}, \\ \exp(S^p) &= w^p = \frac{a_z}{a_{xy}}. \end{aligned} \tag{5.129}$$

We note that for a initial void that is also axisymmetric (either prolate or oblate), the last equation defines uniquely the shape factor S^p of the projected void as a function of the initial shape factor S.

The confocality condition and the porosity are given now explicitly by:

$$d_b^2 - d_{xy}^2 = a_z^2 - a_{xy}^2, \quad f = \frac{4\pi a_{xy}^2 a_z}{24 d_{xy}^2 d_z} \tag{5.130}$$

Using Eqs. (5.128), (5.129) and (5.130) we obtain the final result for the porosity f^p inside the band:

$$c = \frac{f}{f^p} = \left[r^2 + \left(\frac{6fr^2w^2}{\pi} \right)^{2/3} \left(1 - \frac{1}{w^2} \right) \right]^{1/2} \tag{5.131}$$

For a spherical void, this expression reduces to $c = r$ as proposed by Leblond and Mottet (2008).

We still need to provide an expression for the limit load of the virtual localization band. Let σ^p be the stress on the inclined band in Fig. 5.57d due to stress equilibrium and strain compatibility with the uniform sheet:

$$\sigma_{zz}^p = \sigma_{11} \cos^2 \theta, \quad \sigma_{xz}^p = \sigma_{11} \sin^2 \theta, \quad \sigma_{yz}^p = 0, \quad d_{yy}^p = 0. \tag{5.132}$$

We note that at variance with coalescence models we do not impose $d_{xx}^p = d_{xy}^p = 0$ but rather $\sigma_{xx}^p = \sigma_{xy}^p = 0$ resulting from plane stress conditions. Let $\Phi^p(\sigma, f^p, S^p) = 0$ be the yield surface of the porous band, where we have omitted the dependence on other state parameters. Then the limit load problem for the band can be written as:

$$\alpha_{\max} = \sup \left\{ \alpha \mid \Phi^p(\alpha\sigma, f^p, S^p) \leq 0, \frac{\partial \Phi^p}{\partial \sigma_{22}} = 0 \right\} = 1. \tag{5.133}$$

There is no analytical solution of this equation; we solve it numerically using a formulation described elsewhere.

There is a supplementary condition for incipient necking that has generally been neglected in coalescence studies. The attainment of the limit load in the band is not sufficient, as the subsequent deformation of this band and increased hardening inside the band may instantaneously deactivate the limit load condition. For a vertical through thickness band this new condition is simply:

$$d\left(\sigma_{11}^p t\right)/d\tau \leq 0, \quad \dot{\sigma}_{11}^p + \sigma_{11}^p d_{33} \leq 0 \tag{5.134}$$

where the derivatives with respect to time τ must be taken for a porous band that remains compatible with rigid blocks outside the band. The last equation is similar to the one used by Hill for the second quadrant and identical to Eq. (7) in Stören

and Rice (1975) for the bifurcation along a band perpendicular to the major strain axis, without any consideration of a vertex on the yield surface. This shows that the new model contains as a special case the bifurcation theory of Stören and Rice, applied not to the uniform sheet but to a virtual band with increased porosity.

We do not present here the supplementary condition for an inclined band as we have found that it is always preceded by the limit load condition for strain paths close to the biaxial one, exactly where we expect that inclined bands may be first to localize.

The final model we use is that for a non-inclined band incipient necking is attained when both conditions are true:

$$\alpha_{\max} \leq 1, \quad \dot{\sigma}^p_{11} + \sigma^p_{11} d_{33} \leq 0 \tag{5.135}$$

while for an inclined band only the first condition is used.

Numerical Results

We first consider the simplest possible model for a porous sheet with a matrix having a rigid-plastic behaviour with von Mises yield surface, Swift hardening with $K = 417$ MPa, $\varepsilon_0 = 0.01$ and a hardening exponent 0.245 and an initial porosity 0.01. We also suppose that voids are initially spherical and remain so during sheet deformation. Figure 5.58 compares the prediction of the new LA necking model with the MK model. The LA necking model shows two different regions: the first region, close to the plane-strain conditions, is one where the bifurcation condition Eq. (5.134) is attained before the limit load condition Eq. (5.133), while for the second region the reverse is true. For this spherical Gurson model the limit load in an inclined band was attained always after it was attained in the non-inclined band. The MK model results shown on the same Figure correspond to the case of an initial damage imperfection without thickness imperfection—the region B is porous

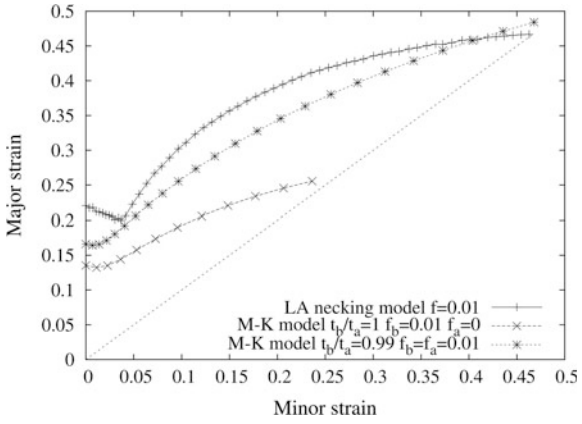

Fig. 5.58 Numerical FLD predictions for a spherical Gurson model: LA necking model versus MK model

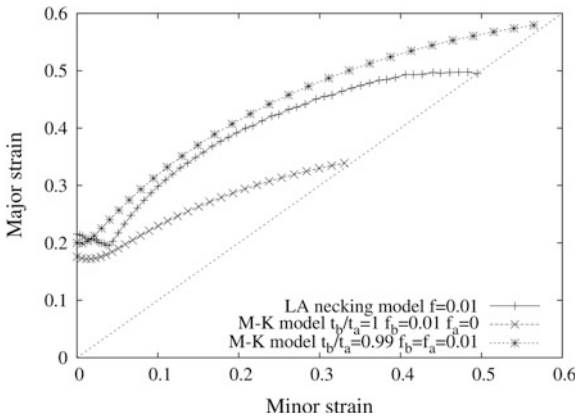

Fig. 5.59 Numerical FLD predictions for an ellipsoidal Gurson model: LA necking model versus MK model

but region *A* is sound, while the other curve corresponds to the dual case where the porosity is the same in both regions but there is an initial thickness imperfection with thickness ratio 0.99. We now consider the same porous material as before but we let the shape of the voids evolve toward oblate ellipsoids. Figure 5.59 compares again the results of the new LA necking model and MK models. In this case one observes that there appears a third region around the biaxial strain condition, where some inclined band attains the limit load before the non-inclined band.

5.4.7 Other Models

5.4.7.1 Bifurcation Models

Bifurcation models seek the conditions under which localized plastic plane-strain deformation is possible in a narrow band without loss of stress equilibrium. The first bifurcation model, that of Hill (1952), was limited to the left-hand side of the Forming Limit Curve since for deformation modes in the right-hand side, there exists no plain-strain direction for materials with smooth yield loci and normal plastic flow. By adopting the deformation theory of plasticity and allowing for vertex-formation on the yield locus, the extension to the right-hand side of the FLD was made by Stören and Rice (1975).

More recently, this bifurcation model has nevertheless been successfully used with the flow theory of plasticity, more commonly accepted in sheet metal forming. Flow theories in which non-normal plastic flow is allowed, are used in Hashiguchi and Protasov (2004), Ito et al. (2000), while Haddag et al. (2007) added the damage model of Chaboche into flow theory.

5.4.7.2 Perturbation Models

Dudzinski and Molinari (1991) proposed the use of the linearized theory of stability in order to determine the limit strains. This approach which considers the sheet to have homogeneous properties, is the linear perturbation technique for sheet necking analysis (Boudeau 1995; Boudeau and Gelin 1996). In this approach, a perturbation to the strain state at equilibrium is introduced, from which the limit strain is found as the conditions under which the perturbation increases in time. Recently, Jouve (2015) revisited the Dudzinski and Molinari theory and developed a 3D linear stability analysis to study the onset of the development of necking plastic instabilities.

5.4.8 Semi-empirical Models

Despite all the recent enhancements of the computational models (see Sect. 5.4.4), they are not able to give very accurate predictions of the limit strains in all the cases encountered in practical applications (different materials, thickness, forming rates, temperatures, strain paths, etc.). Due to this fact, the commercial finite-element codes still make use of experimental FLD's or FLD's calculated with semi-empirical models. Some of the widely-used semi-empirical models will be presented next.

Keeler and Brazier (1975) proposed an empirical relationship for calculating the limit strains corresponding to plane strain, ε_{10}:

$$\varepsilon_{10}(\%) = (23.3 + 14.13 \cdot t)\frac{n}{0.21} \tag{5.136}$$

where t is the sheet thickness (t $\leq$ 3 mm).

Assuming that the shape of the FLD remains the same and having determined the value of ε_{10}, it is possible to obtain the FLD by translating the Keeler-Goodwin curve along the vertical coordinate axis.

Cayssials (1998), (1999) developed the Keeler-Brazier model by including both the coefficient of strain-rate sensitivity m and the 'internal damage' parameters. The limit strain is the solution of the equation

$$a(\varepsilon_{10} - n)^3 + b(\varepsilon_{10} - n)^2 + c(\varepsilon_{10} - n) - 10 \cdot mt = 0 \tag{5.137}$$

where a, b and c are material constants. As a first approximation, ε_{10} can be expressed as follows:

$$\varepsilon_{10} = n + 5mt \tag{5.138}$$

Cayssials and Lemoine (2005) have extended the formulation (5.137) by including the anisotropy coefficient thus obtaining:

$$a(\varepsilon_{10}-n)^3+b(\varepsilon_{10}-n)^2+c(\varepsilon_{10}-n)- \\ -14\frac{\sqrt{(2+4r)}}{\sqrt{(r+1)(r+2)}}mt=0 \tag{5.139}$$

where r is the anisotropy coefficient.

More, by coupling the former model with the Stören and Rice model (Stören and Rice 1975) has been possible the extension of the new model also for drawing and stretching areas. So, the new model is able to predict the FLC for the complete domain, both for linear and non-linear strain paths, using only the mechanical parameters (yield stress, strain hardening coefficient, strain rate sensitivity index and anisotropy coefficient) and thickness of the material. The results obtained are in very good agreement with the experimental data for new grades of steel alloys (UHSS, DP, TRIP etc.) (Cayssials and Lemoine 2005).

Held et al. (2009) proposed a new semi-empirical approach for FLC prediction, which is valid for all sheet metal materials used in car body production. This approach uses a correlation of mechanical properties of uniaxial tensile test an experimentally determined limit strains.

Abspoel et al. (2013) proposed a new method to predict accurately the FLCs for a wide range of steel grades and thicknesses. The method is based on the correlations founded between the characteristic points of the FLC and the mechanical parameters. Four characteristic points were considered: uniaxial tension necking point, plane strain point, intermediate biaxial stretch point and equi-biaxial stretch point.

5.5 Commercial Programs for FLC Prediction

Based on the above mentioned models have been developed more commercial programs for the limit strains prediction.

5.5.1 FORM-CERT Program

Based on a Marciniak-Kuckzynski model, Jurco and Banabic (2005a, b); Banabic (2006) have developed so-called FORM-CERT commercial code. The BBC 2005 yield criterion is implemented in this model. This yield criterion can be reduced to simpler formulations (Hill 1948, Hill 1979, Barlat 1989, etc.). In this way, the yield

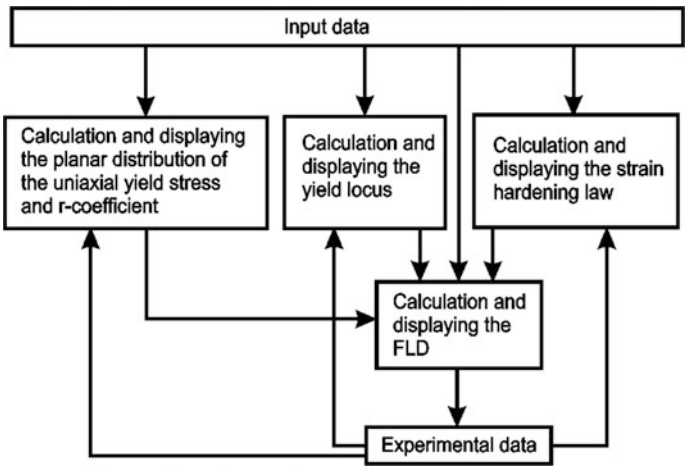

Fig. 5.60 Structure of the FORM-CERT program

criterion can be also used in the situations when only 2, 4, 5, 6, or 7 mechanical constants are available. The program consists in four modules: a graphical interface for input, a module for the identification and visualization of the yield surfaces, of the strain hardening laws and a module for calculating and visualizing the forming limit curves. The numerical results can be compared with experimental data, using the import/export facilities included in the program. FORM-CERT can be used as a standalone application for calculating FLC's and comparing them with experimental data, or as an auxiliary tool for the finite-element simulation of sheet metal forming processes. In its current structure, the program offers useful functionalities both for research and industrial laboratories. A short description of this program will be presented in the next sections.

The program FORM-CERT developed in the CERTETA research centre consists in the following modules:

- Identification module associated to the yield criterion (responsible for evaluating the coefficients of the yield criterion, as well as for the graphical output of the yield locus and planar distribution of the yield stress and *r*-coefficient).
- Module for calculating and displaying the strain hardening law.
- Module for calculating and displaying the forming limit diagram.

Figure 5.60 shows a structural diagram of the program. This diagram presents the modules mentioned above, as well as their interaction. We shall describe next the functionality of each module.

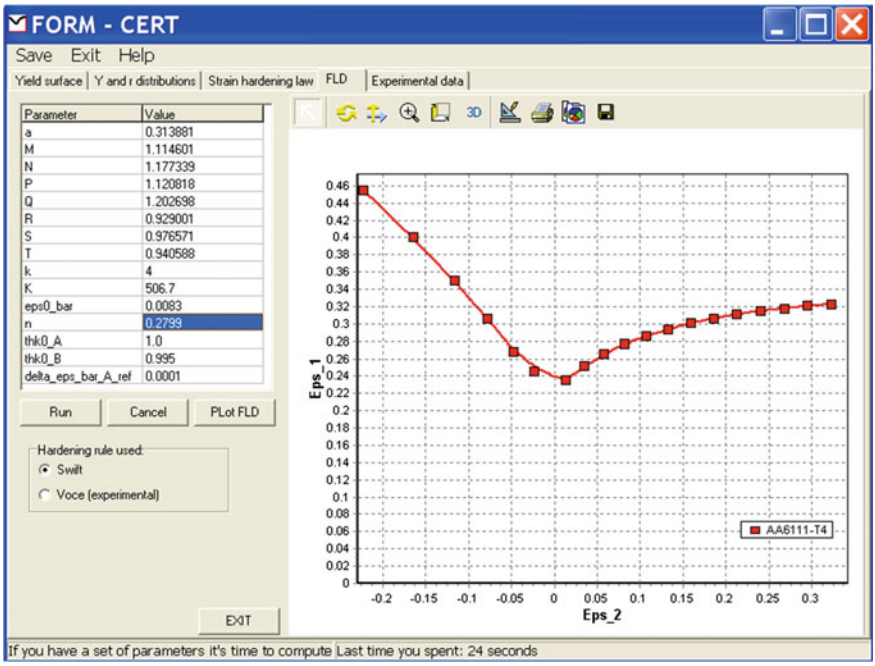

Fig. 5.61 Graphical user interface of the FLD module

5.5.1.1 Calculation and Displaying the FLC

This is the main module of the program. The MK model (see Sect. 5.4.4) of the strain localization process has been implemented in the FORM-CERT program.

The graphical user interface provided by this module is divided in two regions (Fig. 5.61). The first one receives the input data: coefficients of the yield criterion and strain hardening law calculated by the modules mentioned bellow, a parameter specifying the thickness non-homogeneity factor and also the value of the strain increment used for computing the FLC.

At present, the FLD module works only for linear strain paths. The second region of the graphical user interface is used for plotting the FLC predicted. Several curves can be superimposed on the same diagram and also compared with experimental data (imported from ASCII files via the 'Experimental data' panel).

5.5.1.2 "Experimental Data" Module

This module is structured as a panel for acquiring input data (Fig. 5.62). The user has the possibility to type this data or to import it from ASCII files. The data can be plotted on diagrams or exported to other modules of the FORM-CERT program. All

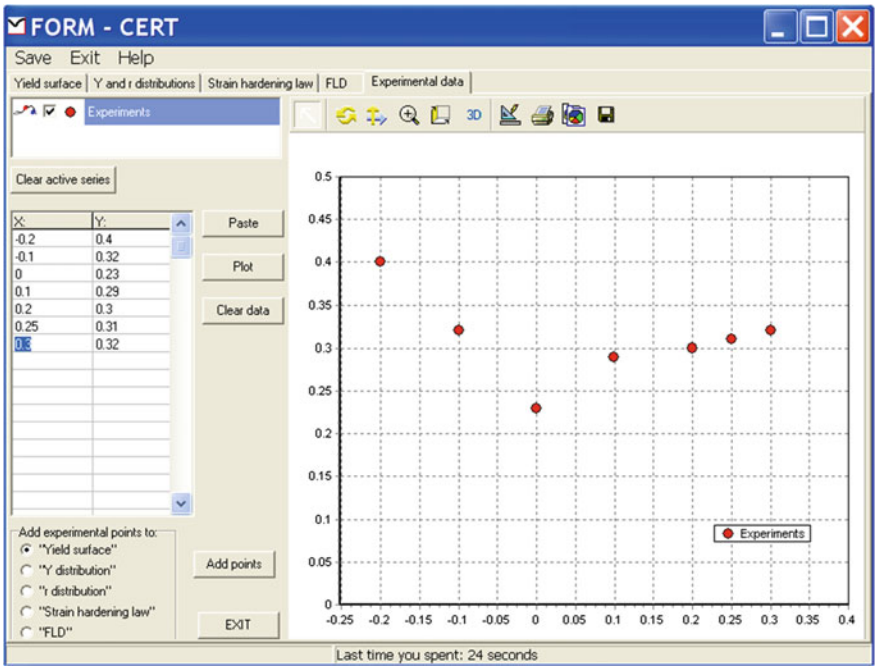

Fig. 5.62 Graphical user interface of the 'Experimental data' module

the diagrams generated by the modules mentioned above can be processed and also exported in different graphical formats (Bitmap, Windows Metafile, GIF, JPEG, Postscript, PDF, etc.). In addition, the results of the computations can be exported in a numerical format (via ASCII, XML, Excel, and HTML files).

5.5.2 *Other Programs*

Hora and his co-workers have developed MATFORM code (http://www.fominnotech.ethz.com) based on the MMFC model (Hora and Tang 1994; Hora et al. 2003; Hora 2006). This code is able to calculate and plot the limit strains and also the visualization of the strain hardening curve and yield loci using Hill (1948), Hill 1979, Hill 1990 and Barlat (1989) criteria. The program is useful for evaluation of most common experiments like tensile, bulge, Miauchi, torsion dilatometer and tube hydroforming tests. The program is very well documented and is able to export the constitutive models in FEM specific form for the application in the mostly spread FEM-codes like Autoform or PamStamp.

Using the CRACH algorithm (based on the MK model), Gese and Dell (2006); Dell et al. (2007), (2008) have developed two software: CrachLAB, a product for

prediction of the initial FLC and CrachFEM a product for coupling with the FEM codes. Criteria for ductile and shear fracture have been included in CrachFEM to cover the whole variety of fracture modes for sheet materials. The material model used to calculate instability describes: the initial anisotropy (using Hill 1948 criterion), the combined isotropic-kinematic hardening and the strain rate sensitivity. CrachFEM is now included in the FEM codes PamStamp and PamCrash of ESI Group.

5.6 Conclusions

In the past, the FLC models provided an approximate description of the experimental results. Such models were used especially for obtaining qualitative information concerning the necking/tearing phenomena.

At present, the FLC models allow a sufficiently accurate prediction of the limit strains, but each model suffers from its own limitations. There is no model that can be applied to any sort of sheet metal, any type of crystallographic structure, any strain-path or any variation range of the process parameters (strain rate, temperature, pressure, etc.).

The future research will be focused on a more profound analysis of the phenomena accompanying the necking and fracture of the sheet metals. On the basis of the analysis, more realistic models will be developed in order to obtain better predictions of the limit strains. New models will be developed for prediction of the limit strains for special sheet metal forming processes: superplastic forming, forming at very high pressure, incremental forming etc. Commercial codes allowing the quick and accurate calculation of the FLC's both for linear and complex strain-paths will be developed. The texture models will be also implemented in such commercial programs. The FLC computation will be included in the finite element codes used for the simulation of the sheet metal forming processes. The aim is to develop automatic decision tools (based on artificial intelligence methods) useful in the technological design departments. The stochastic modelling of the FLC's will be developed in order to increase the robustness of the sheet metal forming simulation programs. More refined, accurate and objective experimental methods for the experimental determination of the limit strains (e.g. methods based on thermal or acoustic effects) will be also developed.

References

Abbasi M, Ketabchi M, Izadkhah H, Fatmehsaria DH, Aghbash AN (2011) Identification of GTN model parameters by application of response surface methodology. Procedia Eng 10:415–420

Abbasi M, Shafaat MA, Ketabchi M, Haghshenas DF, Abbasi M (2012a) Application of the GTN model to predict the forming limit diagram of IF-Steel. J Mech Sci Technol 26:345–352

Abbasi M, Bagheri B, Ketabchi M, Haghshenas DF (2012b) Application of response surface methodology to drive GTN model parameters and determine the FLD of tailor welded blank. Comp Mater Sci 53:368–376

Abbasi M, Ketabchi M, Ramazani A, Abbasi M, Prahl U (2012c) Investigation into the effects of weld zone and geometric discontinuity on the formability reduction of tailor welded blanks. Comp Mater Sci 59:158–164

Abedrabbo N, Pourboghrat F, Carsley J (2006) Forming of aluminium alloys at elevated temperatures—Part 2: numerical modelling and experimental verification. Int J Plast 22:342–373

Abspoel M, Scholting ME, Droog JMM (2013) A new method for predicting forming limit curves from mechanical properties. J Mat Proc Technol 213:759–769

Achani D, Eriksson M, Hopperstad OS, Lademo OG (2007) Modelling of local necking and fracture in aluminium alloys. In: César de Sá JMA, Santos DA (eds) Proceedings of NUMIFORM 2007, Porto, Portugal

Allwood JM, Shouler DR (2009) Generalised forming limit diagrams showing increased forming limits with non-planar stress states. Int J Plast 25:1207–1230

Aretz H (2004) Numerical restrictions of the modified maximum force criterion for prediction of forming limits in sheet metal forming. Model Simul Mater Sci Eng 12:677–692

Arrieux R, Boivin M (1987) Determination of the forming limit stress curve for anisotropic sheets. CIRP Ann 36:195–198

Assempour A, Nejadkhaki HK, Hashemi R (2010) Forming limit diagrams with the existence of through-thickness normal stress. Comp Mat Sci 48:504–508

Ayres RA, Wenner ML (1978) Strain and strain–rate hardening effect on punch stretching of 5182-O aluminium at elevated temperature. Sheet Metal Indus 55:1208–1216

Azrin M, Backofen WA (1970) The deformation and failure of a biaxially stretched sheet. Metall Trans 1:2857–2861

Balanethiram VS, Daehn GS (1994) Hyperplasticity-increased forming limits at high workpiece velocities. Scripta Metall 31:515–520

Banabic D (2006) Numerical prediction of FLC using the M-K-model combined with advanced material models. In: Hora P (ed) Numerical and experimental methods in prediction of forming limits in sheet forming and tube hydroforming processes, pp 37–42. ETH Zürich

Banabic D (2010) A review on recent developments of Marciniak-Kuczynski model. Comp Meth Mat Sci 10:225–237

Banabic D, Dannenmann E (2001) The influence of the yield locus shape on the limits strains. J Mat Proc Technol 109:9–12

Banabic D, Dörr RI (1995) Modelling of the sheet metal forming. Transilvania Press, Cluj Napoca (in Romanian)

Banabic D, Soare S (2008) On the effect of the normal pressure upon the forming limit strains. In: Hora P (ed) Proceedings of the 7th international conference and workshop on numerical simulation of 3D sheet metal forming processes. interlaken, pp 199–204

Banabic D, Soare S (2009) Assessment of the modified maximum force criterion for aluminium metallic sheets. Key Eng Mat 410–411:511–520

Banabic D, Bunge HJ, Pöhlandt K, Tekkaya AE (2000) Forming limits of sheet metal. In: Banabic D (ed) Formability of metallic materials. Springer, Berlin, pp 173–214

Banabic D, Aretz H, Comsa DS, Paraianu L (2005a) An improved analytical description of orthotropy in metallic sheets. Int J Plast 21:493–512

Banabic D, Aretz H, Paraianu L, Jurco P (2005b) Application of various FLD modelling approaches. Modell Simul Mater Sci Eng 13:759–769

Banabic D et al (2010a) Sheet metal forming processes. Springer, Heidelberg

Banabic D, Barlat F, Cazacu O, Kuwabara T (2010b) Advances in anisotropy and formability. Int J Mater Form 3:165–189

Banabic D, Lazarescu L, Paraianu L, Ciobanu I, Nicodim I, Comsa DS (2013) Development of a new procedure for the experimental determination of the forming limit curves. Ann CIRP 62:255–258

Banabic D, Lăzărescu L, Comşa DS (2015) Predictive performances of the Marciniak-Kuczynski model and Modified Maximum Force Criterion, Key Eng Mat 651–653:96–101

Barlat F (1989) Forming limit diagrams—predictions based on some microstructural aspects of materials. In: Wagoner RH, Chan KS, Keeler SP (eds) Forming limit diagrams: concepts, methods, and applications. The Minerals, Metals and Materials Society, Warrendale, pp 275–302

Barlat F, Lian J (1989) Plastic behaviour and stretchability of sheet metals. Part I: yield function for orthotropic sheets under plane stress conditions. Int J Plast 5:51–66

Barlat F, Brem JC, Yoon JW, Chung K, Dick RE, Choi SH, Pourboghrat F, Chu E, Lege DJ (2003) Plane stress yield function for aluminium alloy sheets. Part 1. Theory Int J Plast 19:1297–1319

Barlat F, Gracio JJ, Lee MG, Rauch EF, Vincze G (2011) An alternative to kinematic hardening in classical plasticity. Int J Plast 27:1309–1327

Bassani JL, Hutchinson JW, Neale KW (1979) On the prediction of necking in anisotropic sheets. In: Lippmann H (ed) Metal forming plasticity (IUTAM symposium). Springer, Germany, pp 1–13

Benzerga AA (2002) Micromechanics of coalescence in ductile fracture. J Mech Phys Solids 50:1331–1362

Bird JE, Newman KE, Narasimhan K, Carlson JM (1987) Heterogeneous initiation and growth of sample-scale shear bands during necking of Al-Mg sheet. Acta Metall 35:2971–2982

Boudeau N (1995) Prediction of instability in local elasto-plastic instabilities (in French). Ph.D. thesis, University of Franche-Compte, Besancon

Boudeau N, Gelin JC (1996) Post-processing of finite element results and prediction of the localized necking in sheet metal forming. J Mat Proc Technol 60:325–330

Bragard A (1989) The contribution of CRM to the FLD concept. In: Wagoner RH, Chan KS, Keeler SP (eds) Forming limit diagrams: concepts, methods, and applications. The minerals, metals and materials society, Warrendale, pp 9–19

Bragard A, Baret JC, Bonnarens H (1972) A simplified method to determine the FLD onset of localized necking. Rap Cent Rech Metall 33:53–63

Bridgman PW (1952) Studies in large plastic flow and fracture—with special emphasis on the effects of hydrostatic pressure. McGraw-Hill, New York

Brozzo P, de Lucca B (1971) On the interpretation of the formability limits of metals sheets and their evaluation by means of elementary tests. In: Proceedings of ICSTIS, Tokyo, pp 966–988

Brunet M, Morestin F (2001) Experimental and analytical necking studies of anisotropic sheet metals. J Mat Proc Technol 112:214–226

Brunet M, Morestin F, Mguil S (1996) The prediction of necking and failure in 3D. Sheet forming analysis using damage variable. J Phys IV 06:C6–473–C6-482

Brunet M, Mguil S, Morestin F (1998) Analytical and experimental studies of necking in sheet metal forming processes. J Mat Proc Technol 80–81:40–46

Brunet M, Morestin F, Walter H (2004) Damage identification for anisotropic sheet metals using a non-local damage model. Int J Damage Mech 13:35–57

Brunet M, Morestin F, Walter-Leberre H (2005) Failure analysis of anisotropic sheet-metals using a non-local plastic damage model. J Mat Proc Technol 170:457–470

Carlson JM, Bird JE (1987) Development of sample-scale shear bands during necking of ferrite-austenite sheet. Acta Metall 35:1675–1701

Cayssials F (1998) A new method for predicting FLC. In: IDDRG congress meeting working group III, Brussel, pp 1–6

Cayssials F (1999) The version of the 'Cayssials' FLC model. IDDRG Meeting Working Group III, Birmingham, pp 1–7

Cayssials F, Lemoine X (2005) Predictive model for FLC (arcelor model) upgraded to UHSS steels. In: Boudeau N (ed) Proceedings of the IDDRG conference, Besancon, pp 17.1–17.8

Charpentier PL (1975) Influence of punch curvature on the stretching limits of sheet steel. Metall Trans A 6A:1665–1669

Chen Z, Dong X (2009) The GTN damage model based on Hill'48 anisotropic yield criterion and its application in sheet metal forming. Comp Mat Sci 44:1013–1021

Chiba R, Takeuchi H, Kuroda M, Hakoyama T, Kuwabara T (2013) Theoretical and experimental study of forming limit strain of half-hard AA1100 aluminium alloy sheet. Comp Mat Sci 77:61–71

Chien WY, Pan J, Tang SC (2004) A combined necking and shear localization analysis for aluminium sheets under bi-axial stretching conditions. Int J Plast 20:1953–1981

Chu CC (1980) An analysis of localized necking in punch stretching. Int J Solids Struct 16:913–931

Chu CC, Needleman A (1980) Void nucleation effects in biaxially stretched sheets. J Eng Mat Technol 102:249–256

Ciumadin AS, Ersov BI, Ziaja D (1990) Effect of hydrostatic pressure on the forming limit deformation of sheet metals. Kuznecino-stampovocinoe proizvodsvo 9:241-24

Considère M (1885) L'emploi du fer et l'acier dans les constructions. Ann des Ponts et Chausses 9:574–775

D'Haeyer R, Bragard A (1975) Determination of the limiting strains at the onset of necking. Rap Cent Rech Metall 42:33–35

Dell H, Gese H, Oberhofer G (2007) CrachFEM—A comprehensive approach for the prediction of sheet metal failure. In: César de Sá JMA, Santos AD (eds) Materials processing and design: modeling, simulation and applications NUMIFORM 2007, Porto, pp 165–170

Dell H, Gese H, Oberhofer G (2008) Advanced yield loci and anisotropic hardening in the material model MF GENYLD+CRACHFEM. In: Hora P (ed) Proceedings of the 7th international conference and workshop on numerical simulation of 3D sheet metal forming processes, part 2. Interlaken, pp 49–54

Demeri MY (1986) Strain analysis of the hemispherical stretch-bend test. J App Metalworking 4:183–187

Dieter GE (1988) Mechanical metallurgy. McGraw-Hill, New York

Dorn JE, Thomsen EG (1947) The ductility of metals under general conditions of stress and strain. Trans Am Soc Met 39:741–772

Drewes EJ, Martini A (1976) Einfluss der Umformgeschwindigkeit auf die Grenzformaenderungen und die Formaenderungsverteilung von Feinblech. Archiv fuer Eissenhuettenwessen 47:167–172

Dudzinski D, Molinari A (1991) Perturbation analysis of thermoviscoplastic insta-bilities in biaxial loading. Int J Solids Struct 5:601–628

Duncan JL, Bird JE (1978) Die forming approximations for aluminium sheet. Sheet Metal Indus 51:1015–1025

Emmens WC, van den Boogaard AH (2008) Tensile tests with bending: a mechanism for incremental forming. In: Proceedings of the 11th ESAFORM conference on material forming (ESAFORM 2008), Lyon, France

Eyckens P, Van Bael A, Van Houtte P (2009) Marciniak-Kuczynski type modelling of the effect of through-thickness shear on the forming limits of sheet metal. Int J Plast 25:2249–2268

Eyckens P, Van Bael A, Van Houtte P (2011) An extended Marciniak-Kuczynski model for anisotropic sheet subjected to monotonic strain paths with through-thickness shear. Int J Plast 27:1577–1597

Fukui Y, Nakanishi K (1988) Effects of sheet thickness on the in-plane stretch forming limit in an aluminium sheet. JSME Int J 31:679–685

Geiger M, Merklein M (2003) Determination of forming limit diagrams—a new analysis method for characterization of materials formability. CIRP Ann Manuf Technol 52:213–216

Gensamer M (1946) Strength and ductility. Trans ASM 36:30–60

Gerdooei M, Mollaei Dariani B (2009) Strain rate-dependent Forming Limit Diagrams for sheet metals. J Eng Manuf 222:1651–1659

Gese H, Dell H (2006) Numerical prediction of FLC with the program CRACH. In: Hora P (ed) Numerical and experimental methods in prediction of forming limits in sheet forming and tube hydroforming processes, ETH Zürich, pp 43–49

Ghosh AK, Hecker SS (1975) Stretching limits in sheet metals: in-plane versus out-of-plane deformations. Metall Trans 5A:2161–2164

Gologanu M, Leblond JB, Devaux J (1993) Approximate models for ductile metals containing non-spherical voids—Case of axisymmetric prolate ellipsoidal cavities. J Mech Phys Solids 41:1723–1754

Gologanu M, Leblond JB, Devaux J (1994) Approximate models for ductile metals containing nonspherical voids—case of axisymmetric oblate ellipsoidal cavities. J Eng Mat Technol 116:290–297

Gologanu M, Leblond JB, Perrin G, Devaux J (1997) Recent extensions of Gurson's model for porous ductile metals. In: Suquet P (ed) Continuum Micromechanics. Springer, Vienna, pp 61–130

Gologanu M, Leblond JB, Perrin G, Devaux J (2001) Theoretical models for void coalescence in porous ductile solids—I: Coalescence "in layers". Int J Sol Struct 38:5581–5594

Goodwin GM (1968) Application of strain analysis to sheet metal forming problems in the press shop. Soc Auto Eng 680093:380–387

Gotoh M, Chung T, Iwata N (1995) Effect of out-of-plane stress on the forming limit strains of sheet metals. JSME Int J 38:123–132

Grange M, Besson J, Andrieu E (2000) An anisotropic Gurson type model to represent the ductile rupture of hydrided Zircaloy-4 sheets. Int J Fract 105:273–293

Grosnostajski J, Dolny A (1980) Determination of FLC by means of Marciniak punch. Mem Sci Rev Met 4:570–576

Gurson AL (1977) Continuum theory of ductile rupture by void nucleation and growth Part I-yield criteria and flow rules for porous ductile media. J Eng Mater Technol 99:2–15

Haberfield AB, Boyles MW (1973) Laboratory determined the FLC of sheet steel. Sheet Metal Indus 50:400–411

Haddag B, Balan T, Abed-Meraim F (2007) Investigation of advanced strain-path dependent material models for sheet metal forming simulations. Int J Plast 23:951–979

Haddag B, Abed-Meraim F, Balan T (2008) Strain localization and damage prediction during sheet metal forming. In: ESAFORM 2008, Lyon, France

Haddag B, Abed-Meraim F, Balan T (2009) Strain localization analysis using a large deformation anisotropic elastic–plastic model coupled with damage. Int J Plast 25:1970–1996

Hasek V (1978) Untersuchung und theoretische Beschreibung wichtiger Einflussgrossen auf das Grenzformaenderungschaubild. Blech, 25:213–220, 285–292, 493–499, 619–627

Hashiguchi K, Protasov A (2004) Localized necking analysis by the subloading surface model with tangential-strain rate and anisotropy. Int J Plast 20:1909–1930

Havranek B (1977) The effect of mechanical properties on wrinkling in conical shells. J Mech Working Technol 1:115–129

He M, Li F, Wang Z (2011) Forming Limit Stress Diagram prediction of aluminium alloy 5052 based on GTN model parameters determined by in situ tensile test. Chin J Aeronaut 24:378–386

Hecker SS (1972) A simple FLC technique and results on some aluminium alloy. In: Proceedings of 7th IDDRG congress, Amsterdam, pp 51–71

Hecker SS, Ghosh AK, Gegel HL (eds) (1978) Formability: analysis modeling and experimentation. Met Soc AIME, New York

Held C, Dadrich J, Denninger R, Schleich R, Weidenmann KA, Liewald M (2009) Semi-empirische Berechnungsmethode zur Bestimmung des Grenzforma¨nder-ungsdiagramms auf Basis mechanischer Kennwerte. Mat-wiss. u. Werkstofftech. 40:831–835

Hiam J, Lee A (1978) Factors influencing the FLC of sheet steel. Sheet Metal Indus 50:400–411

Hill R (1948) A theory of the yielding and plastic flow of anisotropic metals. Roy Soc Lond Proc A 193:281–297

Hill R (1952) On discontinuous plastic states with special reference to localized necking in thin sheets. J Mech Phys Solid 1:19–30

Hill R (1979) Theoretical plasticity of textured aggregates. Math. Proc. Cambridge Philosophical Soc. 85:179–191

Hill R (1993) A user-friendly theory of orthotropic plasticity in sheet metals. Int. J. Mech. Sci. 15:19–25

Holmberg S, Enquist B, Thilderkvist P (2004) Evaluation of sheet metal formability by tensile tests. J Mater Process Technol 145:72–83

Hora P (2006) Proceedings of FLC 2006 workshop. Numerical and experimental methods in prediction of forming limits in sheet forming and tube hydroforming processes. ETH Zürich, Zürich

Hora P (2014) Proceedings of FTF 2014 workshop. Time-dependent methods for the evaluation of FLC, ETH Zürich, Zürich

Hora P, Tong L (1994) Prediction methods for ductile sheet metal failure using FE-simulation. In: da Rocha B (ed) Proceedings of IDDRG congress, Porto, pp 363-375

Hora P, Tong L (2006) Numerical prediction of FLC using the enhanced modified maximum force criterion (eMMFC). In: Hora P (ed) Numerical and experimental methods in prediction of forming limits in sheet forming and tube hydroforming processes. ETH Zürich, Zürich, pp 31–36

Hora P, Tong L, Reissner J (2003) Mathematical prediction of FLC using macroscopic instability criteria combined with micro structural crack propagation models. In: Khan A (ed) Proceedings of plasticity 2003 conference, pp 364–366

Hora P, Tong L, Berisha B (2013) Modified maximum force criterion, a model for the theoretical prediction of forming limit curves. Int J Mat Form 6:267–279

Hotz W, Timm J (2008) Experimental determination of forming limit curves (FLC). In: Hora P (ed) Numisheet 2008 (Proceedings of 7th international conference workshop on numerical simulation of 3D sheet metal forming processes), Interlaken, Switzerland, 1–5 September 2008, pp 271–278

Hu XH, Jain M, Wilkinson DS, Mishra RK (2008) Micro-structure-based finite element analysis of strain localization behaviour in AA5754 aluminium sheet. Acta Mat 56:3187–3201

Huang HM, Pan J, Tang SC (2000) Failure prediction in anisotropic sheet metals under forming operation with consideration of rotating principal stretch directions. Int J Plast 16:611–633

Hutchinson RW, Neale KW (1978a) Sheet necking I. In: Koistinen DP, Wang NM (eds) Mechanics of sheet metal forming. Plenum Press, New York, pp 111–126

Hutchinson RW, Neale KW (1978b) Sheet necking II. In: Koistinen DP, Wang NM (eds) Mechanics of sheet metal forming. Plenum Press, New York, pp 127–153

Hutchinson RW, Neale KW (1978c) Sheet necking III. In: Koistinen DP, Wang NM (eds) Mechanics of sheet metal forming. Plenum Press, New York, pp 269–285

Inal K, Wu PD, Neale KW (2002a) Finite element analysis of localization in FCC polycrystalline sheets under plane stress tension. Int J Solids Struct 39:3469–3486

Inal K, Wu PD, Neale KW (2002b) Instability and localized deformation in polycrystalline solids under plane-strain tension. Int J Solids Struct 39:983–1002

Inal K, Neale KW, Aboutajeddine A (2005) Forming limit comparisons for FCC and BCC sheets. Int J Plast 21:1255–1266

International Standard ISO 12004-2 (2008) Metallic materials-sheet and strip determination of forming limit curves. Part 2: determination of forming limit curves in the laboratory. International organization for standardization, Geneva

Ito K, Satoh K, Goya M, Yoshida T (2000) Prediction of limit strain in sheet metal forming processes by 3D analysis of localized necking. Int J Mech Sci 42:2233–2248

Janssens K, Lambert F, Vanrostenberghe S, Vermeulen M (2001) Statistical evaluation of the uncertainty of experimentally characterised forming limits of sheet steel. J Mater Process Technol 112:174–184

Jeong HY, Pan J (1995) A macroscopic constitutive law for porous solids with pressure-sensitive matrices and its implications to plastic flow localization. Int J Solids Struct 32:3669–3691

Jouve D (2015) Analytic study of the onset of plastic necking instabilities during biaxial tension tests on metallic plates. Eur J Mech A Solids 50:59–69

Jurco P, Banabic D (2005) A user-frienldy program for calculating forming limit diagrams. In: Banabic D (ed) Proceedings of 8th ESAFORM conference material forming, Cluj Napoca, pp 423–427

Jurco P, Banabic D (2005) A user-friendly program for analyzing the anisotropy and formability of sheet metals. In: Boudeau N (ed) Proceedings of IDDRG 2005 conference, Besancon, pp 26.1–26.8

Kami A, Mollaei Dariani B, Sadough Vanini A, Comsa DS, Banabic D (2015) Numerical determination of the forming limit curves of anisotropic sheet metals using GTN damage model. J Mater Process Technol 216:472–483

Karthik V, Comstock RJ, Hershberger DL, Wagoner RH (2002) Variability of sheet formability and formability testing. J Mater Process Technol 121:350–362

Keeler SP (1961) Plastic instability and fracture in sheet stretched over rigid punches. Ph.D. thesis, Massachusetts Institute of Technology, Boston

Keeler SP (1970) La formabilité est améliorée par pression hydrostatique. Machine Moderne, 65:43–45

Keeler SP (1978) Forming limit criteria—sheets. In: Burke JJ, Weiss V (eds) Advances in deformation processing. Plenum Press, New York, pp 127–158

Keeler SP, Backofen WA (1963) Plastic instability and fracture in sheets stretched over rigid punches. Trans ASM 56:25–48

Keeler SP, Brazier WG (1975) Relationship between laboratory material characterization and press-shop formability. In: Microalloying 75 (Proceedings of international symposium high-strength, low-alloy steels), Washington, DC, pp 517–530

Kim JH, Lee MG, Kim D, Barlat F (2013) Numerical procedures for predicting localization in sheet metals using crystal plasticity. Comp Mat Sci 72:107–115

Kitting D, Ofenheimer A, Jain M, Pauli H, Rabler G (2008) Experimental characterisation of failure of stretch-bend steel sheets. In: Hora P (ed) Numisheet 2008 (Proceedings of 7th international confernece workshop on numerical simulation of 3D sheet metal forming processes), 1–5 September 2008, Interlaken, pp 315–320

Kleemola HJ, Kumpulainen JO (1980) Factors influencing the FLD. Influence of sheet thickness. J Mater Process Technol 3:303–311

Knockaert R, Chastel Y, Massoni E (2002) Forming limits prediction using rate-independent polycrystalline plasticity. Int J Plast 18:231–247

Koistinen DP, Wang NM (eds) (1978) Mechanics of sheet metal forming. Plenum Press, New York

Koplik J, Needleman A (1988) Void growth and coalescence in porous plastic solids. Int J Solids Struct 24:835–853

Kumpulainen JO, Ranta-Eskola AJ, Rintamaa RHO (1983) Effects of temperature on deep-drawing of sheet metals. Trans ASME J Eng Mat Technol 105:119–127

Lademo OG, Pedersen KO, Berstad T, Furu T, Hopperstad OS (2008) An experimental and numerical study on the formability of textured AlZnMg alloys. Eur J Mech A Solids 27:116–140

Lang L et al (2015) Investigation on the effect of through thickness normal stress on forming limit at elevated temperature by using modified M-K model. Int J Mat Form 8:2011–2228

Lange E (1975) Die Bedeutung von Kennwerten und Verfahren zur Beurteilung des Umformverhaltens beim Tiefziehen von Feinblechen (I). Baender Blech Rohre 5:511–514

Leblond JB, Mottet G (2008) A theoretical approach of strain localization within thin planar bands in porous ductile materials. Comptes-Rendus Mécanique 336:176–189

Leppin C, Li J, Daniel D (2008) application of a method to correct the effect of non-proportional strain paths on nakazima test based forming limit curves. In: Hora P (ed) Numisheet 2008 (Proceedings of 7th international confernece workshop on numerical simulation of 3D sheet metal forming processes), 1–5 September 2008, Interlaken, pp 217–221

Levy BS (2002) The enhanced FLC effect—project team research report. The Auto/Steel Partnership, Southfield, MI. (http://www.a-sp.org)

Li D, Ghosh AK (2004) Biaxial warm forming behaviour of aluminium sheet alloys. J Mater Process Technol 145:281–293
Liao KC, Pan J, Tang SC (1997) Approximate yield criteria for anisotropic porous ductile sheet metals. Mech Mater 26:213–226
Liu JG, Meng QY (2012) Left-side of the Forming Limit Diagram (FLD) under superimposed double-sided pressure. Adv Mat Res 472:653–656
Liu J, Wang Z, Meng Q (2012) Numerical investigations on the influence of superimposed double-sided pressure on the formability of biaxially stretched AA6111-T4 sheet metal. J Mater Eng Perform 21:429–443
Liu J, Liu W, Xue W (2013) Forming Limit Diagram prediction of AA5052/polyethylene/AA5052 sandwich sheets. Mater Des 46:112–120
Manopulo N, Hora P, Peters P, Gorji M, Barlat F (2015) An extended Modified Maximum Force Criterion for the prediction of localized necking under non-proportional loading. Int J Plast 75:189–203
Marciniak Z (1965) Stability of plastic shells under tension with kinematic boundary condition. Arch Mech Stosorwanej 17:577–592
Marciniak Z (1968) Analysis of necking preceding fracture of sheet metal under tension. La Metallurgia Ital 8:701–709
Marciniak Z (1977) Sheet metal forming limits. In: Koistinen DP, Wang NM (eds) Mechanics of sheet metal forming: material behaviour and deformation analysis. Plenum Press, New York, pp 215–235
Marciniak Z, Kuczynski K (1967) Limit strains in the processes of stretch-forming sheet metal. Int J Mech Sci 9:609–620
Marciniak Z, Kuczynski K, Pokora T (1973) Influence of the plastic properties of a material on the forming limit diagram for sheet metal in tension. Int J Mech Sci 15:789–800
Matin PH, Smith LM (2005) Practical limitations to the influence of through-thickness normal stress on sheet metal formability. Int J Plast 21:671–690
Mattiasson K, Sigvant M, Larsson M (2006) Methods for forming limit prediction in ductile metal sheets. In: Santos AD, Barata da Rocha ADC (eds) Proceedings of IDDRG 2006 conference, Porto, pp 1–9
Melander A (1983) A new model of the forming limit diagram applied to experiments on four copper-base alloys. Mater Sci Eng 58:63–88
Nakazima K, Kikuma T (1967) Forming limits under biaxial stretching of sheet metals (in Japanese). Testu-to Hagane 53:455–458
Needleman A, Triantafyllidis N (1978) Void growth and local necking in biaxially stretched sheets. J Eng Mater Technol 100:164–169
Neil JC, Agnew SR (2009) Crystal plasticity-based forming limit prediction for non-cubic metals: application to Mg alloy AZ31B. Int J Plast 25:379–398
Nurcheshmeh M, Green DE (2014) The effect of normal stress on the formability of sheet metals under non-proportional loading. Int J Mech Sci 82:131–139
Padwal SB, Chaturvedi RC, Rao US (1992) Influence of superimposed hydrostatic tension on void growth in the neck of a metal sheet in biaxial stress fields (I, II). J Mater Proc Technol 32:91–107
Paraianu L, Dragos G, Bichis I, Comsa DS, Banabic D (2009) An improved version of the modified maximum force criterion (MMFC) used for predicting the localized necking in sheet metals. Proc Rom Acad 10:237–243
Paraianu L, Dragos G, Bichis I, Comsa DS, Banabic D (2010) A new formulation of the modified maximum force criterion (MMFC). Int J Mat Form 3:243–246
Parsa MH, Ettehad M, Matin PH (2013) Forming limit diagram determination of Al 3105 sheets and Al 3105/Polypropylene/Al 3105 sandwich sheets using numerical calculations and experimental investigations. J Eng Mater Technol 135:031003
Percy JH (1980) The effect of strain rate on the FLD for sheet metal. Ann CIRP 29:151–152
Perrin G (1992) Contribution a l'étude théorique et numérique de la rupture ductile des métaux, Ph.D. thesis, Ecole Polytechnique, Palaiseau, France

Ragab AR, Saleh C, Zaafarani NN (2002) Forming limit diagrams for kinematically hardened voided sheet metals. J Mater Process Technol 128:302–312

Ramazani A, Abbasi M, Prahl U, Bleck W (2012) Failure analysis of DP600 steel during the cross-die test. Comp Mater Sci 64:101–105

Ranta-Eskola AJ (1979) Use of the hydraulic bulge test in biaxial tensile testing. Int J Mech Sci 21:457–465

Ratchev P, Van Houtte P, Verlinden B, De Smet P, Neutjens P, Baartman R, Drent P (1994) Prediction of Forming Limit Diagrams of Al-Mg rolled sheets taking texture into account. Text Microstruct 22:219–231

Romano G, Rault D, Entringer M (1976) Utilization des courbes limites de formage et du mode de repartition des deformations comme critere de jugement de l'amptitude d'un acier extradoux a l'emboutissage. Mem Sci Rev Metal 73:372–383

Rudnicki JW, Rice JR (1975) Conditions for the localization of deformation in pressure-sensitive dilatant materials. J Mech Phys Solids 23:371–394

Saanouni K (2008) On the numerical prediction of the ductile fracture in metal forming. Eng Fract Mech 75:3545–3559

Sang H, Nishikawa Y (1983) A plane strain tensile apparatus. J Met 35:30–33

Shi MF, Gerdeen JC (1991) Effect of strain gradient and curvature on Forming Limit Diagrams for anisotropic sheets. J Mat Shaping Technol 9:253–268

Signorelli JW, Bertinetti MA, Turner PA (2009) Predictions of forming limit diagrams using a rate-dependent polycrystal self-consistent plasticity model. Int J Plast 25:1–25

Simha CHM, Gholipour J, Bardelcik A, Worswick MJ (2007a) Prediction of necking in tubular hydroforming using an extended stress-based FLC. ASME J Eng. Mater Technol 129:136–147

Simha CHM, Grantab R, Worswick MJ (2007b) Computational analysis of stress-based forming limit curves. Int J Solids Struct 44:8663–8684

Smith LM et al (2003) Influence of transverse normal stress on sheet metal formability. Int J Plast 19:1567–1583

Soare S, Barlat F (2014) About the influence of hydrostatic pressure on the yielding and flow of metallic polycrystals. J Mech Phys Solids 67:87–99

Son HS, Kim YS (2003) Prediction of forming limits for anisotropic sheets containing prolate ellipsoidal voids. Int J Mech Sci 45:1625–1643

Spitzig WA, Richmond O (1984) The effect of pressure on the flow stress of metals. Acta Metall 32:457–463

Steninger J, Melander A (1982) The relation between bendability, tensile properties and particle structure of low carbon steel. Scand J Metall 11:55–71

Storen S, Rice JR (1975) Localized necking in thin sheets. J Mech Phys Solids 23:421–441

Swift HW (1952) Plastic instability under plane stress. J Mech Phys Solids 1:1–18

Tadano Y, Yoshida K, Kuroda M (2013) Plastic flow localization analysis of heterogeneous materials using homogenization-based finite element method. Int J Mech Sci 72:63–74

Tharrett MR, Stoughton TB (2003) Stretch-bend forming limits of 1008 Ak steel. SAE SP (2003-01-1157), pp 123–129

Tharrett MR, Stoughton TB (2003b) Stretch-bend forming limits of 1008 Ak steel, 70/30 Brass, and 6010 Aluminium. In: Khan AS, Kazmi R, Zhou J (eds) Dislocations, plasticity and metal forming (The tenth international symposium plasticity current applications), Quebec, Canada, 7–11 July 2003. Neat Press, USA, pp 199–201

Thomason PF (1985) A three-dimensional model for ductile fracture by the growth and coalescence of microvoids. Acta Metall 33:1087–1095

Timothy SP (1989) A modified technique to measure formability in plane-strain tension. In: Wagoner RH, Chan KS, Keeler SP (eds) Forming limit diagrams: concepts, methods, and applications. The Minerals, Metals and Materials Society, Warrendale, pp 21–36

Tisza M, Kovács ZP (2012) New methods for predicting the formability of sheet metals. Prod Process Syst 5:45–54

Tóth LS, Hirsch J, Van Houtte P (1996) On the role of texture development in the forming limits of sheet metals. Int J Mech Sci 38:1117–1126
Tvergaard V (1981) Influence of voids on shear band instabilities under plane strain conditions. Int J Fract 17:389–407
Tvergaard V (1982) On localization in ductile materials containing spherical voids. Int J Fract 18:237–252
Tvergaard V, Needleman A (1984) Analysis of the cup-cone fracture in a round tensile bar. Acta Metall 32:157–169
Uko DK, Sowerby R, Duncan JL (1977) Strain distribution in the bending-under-tension test. CIM Bull 70:127–134
Uthaisangsuk V, Prahl U, Münstermann S, Bleck W (2008) Experimental and numerical failure criterion for formability prediction in sheet metal forming. Comp Mat Sci 43:43–50
Uthaisangsuk V, Prahl U, Bleck W (2009) Characterisation of formability behaviour of multiphase steels by micromechanical modelling. Int J Fract 157:55–69
Uthaisangsuk V, Prahl U, Bleck W (2011) Modelling of damage and failure in multiphase high strength DP and TRIP steels. Eng Fract Mech 78:469–486
van den Boogaard AH (2002) Thermally enhanced forming of aluminium sheet. Modeling and experiments. Ph.D. thesis, University of Twente
Vegter H, ten Horn CHLJ, Abspoel M (2008) Modeling of the forming limit curve by MK analysis and FE simulations. In: Hora P (ed) Numisheet 2008 (Proceedings of 7th international conference workshop on numerical simulation of 3D sheet metal forming processes), 1–5 September 2008, Interlaken, pp 187–192
Volk W, Illig R, Kupfer H, Wahlen A, Hora P, Kessler L, Hotz W (2008) Benchmark 1—virtual forming limit curves. In: Hora P (ed) Numisheet 2008 (Proceedings of 7th international conference workshop on numerical simulation of 3D sheet metal forming processes), 1–5 September 2008, Interlaken, pp 3–9
Wagoner RH, Chan KS, Keeler SP (eds) (1989) Forming limit diagrams: concepts, methods and applications. TMS, Warrendale
Wang H, Wu PD, Boyle KP, Neale KW (2011) On crystal plasticity formability analysis for magnesium alloy sheets. Int J Solids Struct 48:1000–1010
Wang R, Chen Z, Li Y, Dong C (2013) Failure analysis of AZ31 magnesium alloy sheets based on the extended GTN damage model. Int J Min Met Mater 20:1198–1207
Wang H, Wu PD, Lee SY, Wang J, Neale KW (2015) Numerical study of the effects of shear deformation and super-imposed hydrostatic pressure on the formability of AZ31B sheet at room temperature. Int J Mech Sci 92:70–79
Wu PD, MacEwen SR, Lloyd DJ, Neale KW (2004a) Effect of cube texture on sheet metal formability. Mat Sci Eng A 364:182–187
Wu PD, MacEwen SR, Lloyd DJ, Neale KW (2004b) A mesoscopic approach for predicting sheet metal formability. Modell Simul Mater Sci Eng 12:511
Wu PD, Embury JD, Lloyd DJ, Huang Y, Neale KW (2009) Effects of superimposed hydrostatic pressure on sheet metal formability. Int J Plast 25:1711–1725
Xu ZT, Peng LF, Fu MW, Lai XM (2015) Size effect affected formability of sheet metals in micro/meso scale plastic deformation: experiment and modeling. Int J Plast 68:34–54
Xue L (2010) Localization conditions and diffused necking for damage plastic solids. Eng Fract Mech 77:1275–1297
Yoon JS, Noh HG, Song WJ, Kang BS, Kim J (2013) Comparison of experimental and numerical failure criterion for formability prediction of automotive part. Adv Mater Res 658:354–360
Yoshida K (2014) Effects of grain-scale heterogeneity on surface roughness and sheet metal necking. Int J Mech Sci 83:48–56
Yoshida K, Kuroda M (2012) Numerical investigation on a key factor in superior stretchability of face-centered cubic polycrystalline sheets. Int J Mech Sci 58:47–56

Yoshida K, Ishizaka T, Kuroda M, Ikawa S (2007) The effects of texture on formability of aluminium alloy sheets. Acta Mater 55:4499–4506

Yoshida K, Tadano Y, Kuroda M (2009) Improvement in formability of aluminium alloy sheet by enhancing geometrical hardening. Comp Mat Scis 46:459–468

Zadpoor AA, Sinke J, Benedictus R (2009) Formability prediction of high strength aluminium sheets. Int J Plast 25:2269–2297

Zhang F, Chen J, Chen J, Lu J, Liu G, Yuan S (2012) Overview on constitutive modeling for hydroforming with the existence of through-thickness normal stress. J Mater Process Technol 212:2228–2237

Zhang F, Chen J, Chen J, Zhu X (2014a) Forming limit model evaluation for anisotropic sheet metals under through-thickness normal stress. Int J Mech Sci 89:40–46

Zhang F, Chen J, Chen J (2014b) Effect of through-thickness normal stress on forming limits under Yld 2003 yield criterion and M-K model. Int J Mech Sci 89:92–100

Zhou Y, Neale KW (1995) Predictions of forming limit diagrams using a rate-sensitive crystal plasticity. Int J Mech Sci 37:1–20

Chapter 6
Anisotropic Damage in Elasto-plastic Materials with Structural Defects

Sanda Cleja-Ţigoiu

6.1 Introduction

We propose here a mathematical formalism, developed within the continuum damage mechanics that allows us to describe the macroscopic behaviour of elasto-plastic material with damaged microstructure. The damage of the material at the microscopic level means the existence of the microcracks or microvoids, that will be modeled by the presence of certain internal state variables, called the damage tensor or scalar damage parameters, which evolve during the irreversible processes.

The continuum damage mechanics investigates from continuum mechanics point of view the internal microstructural changes, concerning the mechanical modeling of the distributed cavities and cracks, which induce the initiation of the macro cracks. The failure is characterized by dominant macro cracks, which are generated as an ultimate stage during the damage (microstructural) process of the material.

The continuum damage mechanics formulates mathematically the mechanical behaviour of the materials deteriorate by the existence of the microcavities and microcracks. Within the continuum damage mechanics two types of problems arise when describing the state of damaged material. The first type is related to the physical nature and the mathematical description of the damage variables, while the second type concerns the elaboration of the constitutive framework, which allows a coherent description of the behaviour of materials with damaged microstructure.

S. Cleja-Ţigoiu (✉)
University of Bucharest, 14 Academiei, Sector 1, 010014 Bucharest, Romania
e-mail: stigoiu@yahoo.com; tigoiu@fmi.unibuc.ro
URL: http://fmi.unibuc.ro/en/

D. Banabic (ed.), *Multiscale Modelling in Sheet Metal Forming*,
ESAFORM Bookseries on Material Forming,
DOI 10.1007/978-3-319-44070-5_6

The damage state can be described mathematically by using scalar and tensorial variables, referring to *isotropic damage* and *anisotropic damage*, which are described by the appropriate evolution equations. The **scalar damage variables** are adequate for the isotropic damage, when a random distribution of microvoids and microcracks characterizes the damaged structure. The scalar damage variables have been extensively used in continuum damage mechanics.

Murakami (1983) discusses mechanical modeling and the damage variables used to describe the damage state and appreciated the primary notions introduced by Kachanov (1986), Rabotnov (1969) as basic for the development of continuum damage mechanics. Murakami (1983, 1988) refers to the existence of the distributed microvoids, which imply microcavities and microcracks, as *damage*, and call the nucleation and the growth of the voids as their *evolution*.

In the anisotropic damage the void growth and micro-shear crack mechanism are active simultaneously. Brünig (2003), Brünig and Ricci (2005) provide a finite strain framework for ductile anisotropic continuum damage based on thermodynamic law for isothermic processes and coupled with plasticity and damage, and the extension to nonlocal plasticity and nonlocal damage can be found in Brünig and Ricci (2005) and Brünig et al. (2013).

In Sect. 6.2, we exemplify some scalar variables, like the *void volume fraction* and *effective area reduction*. We make reference to the effect of *triaxiality* on the ductile damage, and we recall the initial concept of the undamaged configuration in correlation with the anisotropic damage.

In Sect. 6.3, we present the models proposed by Brünig (2003), Brünig and Ricci (2005), which are using the *multiple undamaged (fictitious) configurations* and the specific metric coefficients to describe measures of damage. The macroscopic background is the same for the two above-mentioned papers. We also present the damage model by Ekh et al. (2004) proposed within the crystal plasticity formalism, when the evolution rule for the damage is formulated with respect to the crystalline slip system. The model is based on the fictitious configuration and the equivalence principle of the free energy in the fictitious undamaged configuration and the intermediate configuration, used in the multiplicative decomposition of the deformation gradient.

In Sect. 6.3, we also briefly presented the Chaboche and Lemaitre models, (Chaboche and Lemaitre 1990; Lemaitre 1992), in the compact formulation of damage laws as it was reviewed, presented and numerically implemented by de Souza Neto et al. (2008). Although there is a model developed within the small elasto-plastic formalism and it is based on one scalar damage variable only, and our aims is to discuss the finite elasto-plastic models coupled with the anisotropic damage, we included this model in our presentation due to the large number of extensions. We mention here the paper by Lämmer and Tsakmakis (2000), Malcher et al. (2012).

Two types of constitutive models have been proposed in this chapter, in Sects. 6.4 and 6.5. The first model, discussed in Sect. 6.4, is based on the existence of an undamaged (fictitious) configuration; the anisotropic damage is described in

terms of the (second order) damage tensor, $\mathbf{F}^d$, which is a deformation like tensorial variable. The damage tensor $\mathbf{F}^d$, characterizes the passage from a certain plastically deformed configuration (in our case considered to be also stress free configuration) to an undamaged (fictitious) configuration and depicted a measure of anisotropic damage. $\mathbf{F}^d$ is involved in the multiplicative decomposition of the deformation gradient $\mathbf{F}$ into its elastic (reversible), $\mathbf{F}^e$, damaged $\mathbf{F}^d$ and plastic, $\mathbf{F}^p$, components, namely $\mathbf{F} = \mathbf{F}^e\mathbf{F}^d\mathbf{F}^p$. In the proposed framework we describe the material behaviour with respect to the stress free (fictitious) undamaged configuration; the model is compatible with the second law of thermomechanics, expressed as the Clausius-Duhem dissipation inequality. The case of isotropic damage when a scalar field replaces the tensorial damage variable, and the multiplicative decomposition of the deformation gradient is reduced to the initial one, $\mathbf{F} = \mathbf{F}^e\mathbf{F}^p$, is also considered as a special case.

The second model is presented in Sect. 6.5, and it is developed within the constitutive framework of second order finite elasto-plasticity, formulated by Cleja-Ţigoiu (2007, 2010). The presence of the second order damage tensor is related to the measure of non-metricity of the so-called plastic connection. The model is described within the second order plasticity, based on the multiplicative decomposition of the deformation gradient $\mathbf{F} = \nabla\chi$ (where the function χ describes the motion of the body) into its elastic and plastic components $\mathbf{F}^e, \mathbf{F}^p$, called *distortions*

$$\mathbf{F} = \mathbf{F}^e\mathbf{F}^p, \tag{6.1}$$

as well as on the rule of the motion connection decomposition $\boldsymbol{\Gamma} = (\mathbf{F})^{-1}\nabla\mathbf{F}$ into its elastic and plastic counterparts.

The behaviour of elasto-plastic materials with damaged microstructure is described in terms of specific differential geometry elements which characterize the internal mechanical state, following Kröner (1992), de Wit (1981). In the proposed elasto-plastic models the defects of lattice structure, like dislocations and disclinations, can be involved through the Cartan torsion of the so-called plastic connection, see Cleja-Ţigoiu (2010, 2002), while the point defects, microvoids and microcracks, in the damaged zone are modeled in terms of the non-metric tensor which belongs to the plastic connection, apart from Cleja-Ţigoiu and Ţigoiu (2011), where the gradient of the elastic strain measures the damage. The non-metric property of the plastic connection is described in terms of a symmetric second order tensor, **h,** which is potential for the non-metric (extra-matter) tensor **Q.**

The continuum damage mechanics also deals with the constitutive and evolution equations which describe the damage and plastic behaviour.

Energetic arguments, like dissipation inequality, along the isothermal deformation processes and power conjugated variables, will be used in order to complete the models. The dissipative nature for the irreversible behavior is modeled by the requirement to satisfy the principle of the free energy imbalance for the isothermal processes. The free energy imbalance principle reformulates the classical second law of thermodynamics within the second order finite elasto-plasticity, following

Gurtin's idea presented in Gurtin (2002), Gurtin et al. (2010), see Cleja-Ţigoiu (2007, 2010). The constitutive and evolution equations are derived to be compatible with free energy imbalance. The resulting models are strongly dependent on the postulated expressions for the free energy and the internal power.

Our exposure in Sect. 6.2 constitutes a concise and critical presentation of the contributions and results which led to basic ideas for the development of elasto-plastic anisotropic damaged materials. We shortly recall the meaning of extensively used scalar damage variables, with reference to the volume void fraction, and to the first micromechanical model for ductile fracture, the Gurson (1977) model, which introduces a strong coupling between the plastic deformation and damage. Modifications of the Gurson model for shear have been proposed and experimentally validated by Nahshon and Hutchinson (2008), Xue (2008), the key point being the extension of the evolution equation for the void volume fraction. Lassance et al. (2007) consider the Gurson model to be representative of the void growth only. The authors introduce and validate an extended version of the Gurson (1977) model, which involves also many other recent improvements of the aforementioned model. The paper applies the micromechanics-based methodology to investigate the damage resistance of certain Al-alloys.

We expose certain ideas, as fictitious damaged and undamaged configurations, effective stress, and so on, which have been fruitfully utilized in modeling the anisotropic damage.

Section 6.3 is devoted to the constitutive models for elasto-plastic materials with microstructural defects (like microcracks and microcavities), which describe the inelastic deformations, including the anisotropic damage and based on the fictitious configurations. We refer to the models described by Murakami (1988), Brünig (2003), Ekh et al. (2004), Menzel et al. (2002), and so on.

Different models connecting damage and elasto-plasticity are based on deformation type damage variables, see the models proposed by Brünig (2003), Brünig and Ricci (2005), Brünig et al. (2008), Menzel et al. (2002), Ekh et al. (2004, 2005) and we also mention de Borst et al. (1999).

Two types of damage (second order) tensors like deformation fields have been introduced in the literature, both of them assuming the hypothesis of the existence of the undamaged (fictitious) configuration. In general the damage deformation tensor, denoted here by $\mathbf{F}^d$, characterizes the passage from an undamaged (fictitious) configuration to a certain plastically deformed configuration, as a measure of anisotropic damage. $\mathbf{F}^d$ is viewed sometimes like a purely internal state variable, see Menzel et al. (2002), Ekh et al. (2004, 2005) which does not influence the multiplicative decomposition of the deformation gradient into its component, apart from the models proposed by Brünig (2003), Brünig and Ricci (2005).

To avoid the confusions which appear, when this mention is missing we pay attention to the configurations on which the tensor fields are defined. We tried to use our notations only, as much as possible, with the aim to unify the notations from different papers, in order to make evident the differences between the models and field definitions, thus facilitating the comparison of the various presented models.

When we refer to the finite elasto-plasticity based on the deformation gradient multiplicative decomposition into elastic and plastic components, we have in mind the concept of the so-called local relaxed (or stress free) configuration, physically motivated by the mechanism of plastic deformations within the crystalline materials, see Cleja-Ţigoiu and Soós (1990). The global stress free configuration does not exist for elasto-plastic materials with crystalline structure. We assume that the local stress free configurations can be uniquely associated to any material point, apart from the orthogonal transformation that can be an element of the material symmetry group. That is why we reconsidered the figures from the papers by Brünig (2003), Murakami (1988), Ekh et al. (2004). The indeterminacy in choosing the stress free configuration has been solved by considering the same crystallographic orientation for the appropriate material neighborhoods, in the initial and relaxed configurations, i.e. the so-called *isoclinic configuration.*

We tacitly used the same idea representing graphs of the undamaged configurations.

Another important fact is related to the *objectivity assumptions*, see Cleja-Ţigoiu (1990), Cleja-Ţigoiu and Soós (1990), which states that if the two motions of the body differ locally by a superposed rigid motion the set of the associated local relaxed configurations can be the same, and moreover the associated internal state variables have equal values. Let us remark that the elastic type constitutive equation in terms of the Cauchy stress tensor has to be *objective*, namely relative to the change of frame in the actual configuration, characterized by an orthogonal mapping $\mathbf{Q}$. The tensor $\mathbf{F}^e$ sustains the transformation, i.e. $\mathbf{F}^{*e} = \mathbf{Q}\mathbf{F}^e$, and $\mathbf{F}^{*d} = \mathbf{F}^d$ and $\mathbf{F}^{*p} = \mathbf{F}^p$. On the other hand in order to a certain elastic type constitutive equation satisfies *the stress free condition* it is necessary for the Cauchy stress to be zero, $\mathbf{T} = 0$, if the elastic strain, say $\mathbf{C}^e = (\mathbf{F}^e)^T\mathbf{F}^e$, is the identity tensor.

In our presentation we do not considered the vector damage variables, which were introduced to characterize the effect of the cracks distributed on certain planes. The damage vector is considered to be perpendicular on the plane of the cracks.

6.1.1 List of Notation

Further the following notations will be used:

- $\mathscr{E}$—the three dimensional Euclidean space, with the vector space of translations $\mathscr{V}$;
- *Lin*—the set of the linear mappings from $\mathscr{V}$ to $\mathscr{V}$, *Sym*–i.e. the set of symmetric tensors, $Orth \subset Lin$ the set of all orthogonal second order tensors;
- $\mathbf{u} \cdot \mathbf{v}, \mathbf{u} \otimes \mathbf{v}$ denote scalar and tensorial products of vectors;
- $\mathbf{a} \otimes \mathbf{b}$ and $\mathbf{a} \otimes \mathbf{b} \otimes \mathbf{c}$ are defined to be a second order tensor and a third order tensor and are defined by $(\mathbf{a} \otimes \mathbf{b})\mathbf{u} = \mathbf{a}(\mathbf{b} \cdot \mathbf{u})$, $(\mathbf{a} \otimes \mathbf{b} \otimes \mathbf{c})\mathbf{u} = (\mathbf{a} \otimes \mathbf{b})\ (\mathbf{c} \cdot \mathbf{u})$, for all vectors $\mathbf{u}$;

- for $\mathbf{A} \in Lin$—a second order tensor, we introduce the notations: $\{\mathbf{A}\}^S, \{\mathbf{A}\}^a$ for the symmetric and skew-symmetric parts of the tensor and tr$\mathbf{A}$ for the trace of $\mathbf{A} \in Lin$;
- the tensorial product $\mathbf{A} \otimes \mathbf{a}$ for $\mathbf{a} \in \mathscr{V}$, is a third order tensor, with the property $(\mathbf{A} \otimes \mathbf{a})\mathbf{v} = \mathbf{A}(\mathbf{a} \cdot \mathbf{v})$, $\forall \mathbf{v} \in \mathscr{V}$;
- $\mathbf{I}$ is the identity tensor in Lin and $\mathbf{A}^T$ denotes the transpose of $\mathbf{A} \in Lin$;
- for $\mathcal{A}$ in Lin, the third order field $(\mathcal{A} \times \mathbf{I})$ is defined by $((\mathcal{A} \times \mathbf{I})\mathbf{u})\mathbf{v} = (\mathcal{A}\mathbf{u}) \times \mathbf{v}$, for all vectors $\mathbf{u}$ and $\mathbf{v}$;
- $\partial_{\mathbf{A}}\phi(x)$ denotes the partial differential of the function ϕ with respect to the field $\mathbf{A}$;
- $\nabla\mathbf{A}$ is the derivative (or the gradient) of the field $\mathbf{A}$ in a coordinate system $\{\mathbf{x}^a\}$ (with respect to the reference configuration), $\nabla\mathbf{A} = \frac{\partial A_{ij}}{\partial x^k}\mathbf{e}^i \otimes \mathbf{e}^j \otimes \mathbf{e}^k$, for $\mathbf{A} = A_{ij}\mathbf{e}^i \otimes \mathbf{e}^j$, namely the calculation follows as the basis is fixed;
- the gradient with respect to the configuration $\mathscr{K}$ is defined by $\nabla_{\mathscr{K}}\mathbf{H} = (\nabla\mathbf{H})(\mathbf{F}^p)^{-1}$ in terms of the gradient with respect to the reference configuration, due to the fact that $\mathbf{F}^p$ denotes the map which put into correspondence the reference and damaged configuration, $\mathscr{K}$;
- the operator $\odot$ associates to the third order tensors $\mathscr{A}, \mathscr{B}$ the second order tensor, denoted $\mathscr{A} \odot \mathscr{B}$ and defined by

$$(\mathscr{A} \odot \mathscr{B}) \cdot \mathbf{L} = \mathscr{A}[\mathbf{I}, \mathbf{L}] \cdot \mathscr{B} = \mathscr{A}_{isk} L_{sn} \mathscr{B}_{ink}, \tag{6.2}$$

  for all second order tensor $\mathbf{L}$;
- the transpose of the third order tensor field $\mathscr{N}$ is given by $\mathscr{N}^T\mathbf{u} = (\mathscr{N}\mathbf{u})^T$, for any $\mathbf{u}$.
- *curl* of a second order tensor field $\mathbf{A}$ is defined by the second order tensor field

$$\begin{aligned} &(\mathrm{curl}\mathbf{A})(\mathbf{u} \times \mathbf{v}) := (\nabla\mathbf{A}(\mathbf{u}))\mathbf{v} - (\nabla\mathbf{A}(\mathbf{v}))\mathbf{u} \quad \forall \mathbf{u}, \mathbf{v} \in \mathscr{V} \text{ and} \\ &(curl\mathbf{A})_{pi} = \varepsilon_{ijk}\frac{\partial A_{pk}}{\partial x^j} \end{aligned} \tag{6.3}$$

  are the component of $curl\mathbf{A}$ given in a Cartesian basis. ε_{ijk} denotes the components of Ricci permutation tensor.
- $\mathcal{H}$ denotes the Heaviside function, defined by $\mathcal{H}(x) = 0 \; \forall \, x < 0$, and $\mathcal{H}(x) = 1 \; \forall \, x \geq 0$

6.2 Damage State

The damage state is described by scalar and tensorial variables. We exemplify the scalar variables, like the *void volume fraction* and *effective area reduction*. We make reference to the effect of *triaxiality* on the ductile damage, and we recall the initial formulation of the undamaged configuration concept in correlation with the anisotropic damage.

6.2.1 Isotropic Damage

Kachanov (1986) introduced the scalar damage variable ω, $(0<\omega<1)$. The damage variable can be interpreted as being the *effective area (net area) reduction* caused by the microcracks and microcavities.

Consider a damaged solid and a volume element of a sufficiently large size with respect to the inhomogeneity and sufficiently small size to be viewed as a material neighborhood of a given material point.

Let us denote by $A(n)$ the area of the section of the volume element identified by the normal **n**, and the effective area of resistance by $\bar{A}(n)$, i.e. the remaining area after eliminating the microcavities and microcracks, assuming $\bar{A}(n)<A(n)$. Thus the *effective area (net area) reduction* ω is the ratio between the net current area, $\bar{A}(n)$, and the area of the given section, $A(n)$, i.e.

$$\omega = \frac{\bar{A}(n)}{A(n)}. \tag{6.4}$$

From a physical point of view the so-called damage variable, $d = 1 - \omega$, is the relative (or corrected) area of the cracks and cavities cut by a plane normal to the direction **n**.

In the uniaxial tension the applied force on a section of the representative element is $\sigma A(n)$, and the *effective stress*, denoted by $\bar{\sigma}$, is defined in terms of Cauchy stress σ by $\bar{\sigma} = \frac{\sigma}{1-d}$, as a consequence of the assumed equality

$$\sigma A(n) = \bar{\sigma}\bar{A}(n). \tag{6.5}$$

In the one dimensional case $\bar{A}(n)$ appears to be the effective load-carried area of the current damaged state. The *fictitious undamaged bar* with the cross-section area $\bar{A}(n)$ and subjected to the same applied force has been considered *mechanically equivalent* and it is called *fictitious undamaged state* (Murakami 1988).

Lemaitre and Chaboche (1978), Lemaitre (1985) characterized the damage state by the change of the elastic constants of the materials. The authors assumed the *hypothesis of elastic strain equivalence*, namely the elastic type constitutive equation of the *damaged material* is derived by the constitutive equation for the *elastic undamaged material*, by replacing the Cauchy stress tensor, σ, by the *effective stress* $\bar{\sigma}$.

$$\begin{aligned} \varepsilon^e &= \frac{\sigma}{\bar{E}} = \frac{\bar{\sigma}}{E} = \frac{\sigma}{E(1-d)} \\ d &= 1 - \frac{\bar{E}}{E}, \quad \bar{\sigma} = \frac{\sigma}{1-d} = E\frac{\sigma}{\bar{E}}, \end{aligned} \tag{6.6}$$

where $\bar{E}$ and E are elastic constants of the damaged and undamaged materials.

6.2.2 Void Volume Fraction

Another scalar damage variable, namely the void volume fraction, f, has been extensively considered in various micromechanical models for ductile fraction. This parameter is the ratio between the volume of microvoids, f_{voids}, and the representative volume element, f_{rve}, i.e. $f = \frac{f_{voids}}{f_{rve}}$. The Gurson model, (Gurson 1977), is the first micromechanical model for ductile fracture, which introduces a strong coupling between the plastic deformation and damage. The main result of the Gurson model estimates the yield function for the porous metal, which is given by

$$\Phi = \frac{\sigma_{eq}^2}{\sigma_y^2} + 2f\cosh\left(\frac{1}{2}\frac{\mathrm{tr}\boldsymbol{\sigma}}{\sigma_y}\right) - 1 - f, \tag{6.7}$$

where the hardening behaviour is described by $\sigma_y = h(\bar{\varepsilon}^p)$ related through the energy balance

$$\sigma_y \dot{\bar{\varepsilon}}^p (1-f) = \boldsymbol{\sigma} \cdot \dot{\boldsymbol{\varepsilon}}^p. \tag{6.8}$$

The evolution equations for the plastic strain, void volume fraction and Cauchy stress, respectively, $(\boldsymbol{\varepsilon}^p, f, \boldsymbol{\sigma})$, are given by:

The associate flow rule is characterized by

$$\dot{\varepsilon}^p = \lambda \frac{\partial \Phi}{\partial \sigma}, \tag{6.9}$$

with λ defined by the Kuhn-Tucker condition $\lambda \geq 0, \quad \Phi \leq 0, \quad \lambda\, \Phi = 0$, and consistency condition $\lambda\, \dot{\Phi} = 0$.

The law of the variation of the void volume fraction, caused by the accumulation of plastic deformation, is given by

$$\dot{f} = (1-f)\mathrm{tr}\, \dot{\varepsilon}^p, \tag{6.10}$$

as the voids started to nucleate, and the rate type elastic constitutive equation is described by

$$\dot{\boldsymbol{\sigma}} = \mathscr{E}(\dot{\boldsymbol{\varepsilon}}^p - \dot{\boldsymbol{\varepsilon}}), \tag{6.11}$$

in terms of the Cauchy stress tensor.

The Gurson model has been extended to include void shape dependences and so on, see Siruguet and Leblond (2004) and the reference that can be found, for instance in Lassance et al. (2007), Nahshon and Hutchinson (2008). These extensions are based on "the solutions for the voids subjected to axisymmetric stress and exclude the possibility of *shear localization* and fracture under the low triaxiality, if void nucleation is not invoked", as remarked Nahshon and Hutchinson (2008). We

make a special reference to the paper by Lassance et al. (2007), as the attention is focused on the non-symmetric microstructural defects. The authors considered that "the presence of coarse, elongated particles is the key microstructural feature behaviour" of Al-alloy. The authors evidenced that the *elongated* β-type particles are transformed into *rounded* α-type particles, by heat treatment. "At the ambient temperature the α particles and the β particles oriented with the long axis perpendicular to the loading direction undergo interface decohesion, while the β particles oriented perpendicular to the loading direction break into several fragments." They concluded that "the ductility increases with decreasing amount of β particles, increasing temperature and strain rates, and decreasing stress triaxiality." The review performed in the aforementioned paper contains well structured references.

6.2.3 *Effect of Stress Triaxiality*

The effect of stress triaxiality on ductile fracture and the evolution of the fracture ductility is put experimentally into evidence and discussed by Bao and Wierzbicki (2004, 2005), Brünig et al. (2013, 2008), Nahnshon and Hutchinson (2008), see also the references in the aforementioned papers. "Fracture ductility is understood as the ability of a material to accept large amount of deformation without fracture. Equivalent strain to fracture is good measurement of fracture ductility," see Bao and Wierzbicki (2004).

The *stress triaxiality* is defined by the ratio η

$$\begin{aligned} &\eta = \frac{\sigma_H}{\sigma_e}, \qquad \text{where} \\ &\sigma_H = \tfrac{1}{3}\,\mathrm{tr}\mathbf{T}, \quad \sigma_{eq} = \sqrt{\tfrac{3}{2}\,\mathrm{Dev}\mathbf{T}\cdot\mathrm{Dev}\mathbf{T}}, \quad \mathrm{Dev}\mathbf{T} = \mathbf{T} - \tfrac{1}{3}\,\mathrm{tr}\mathbf{T}\mathbf{I}. \end{aligned} \tag{6.12}$$

σ_H is the mean stress and σ_{eq} is the second invariant of the stress deviator $\mathrm{Dev}\mathbf{T}$.

Based on the experimental and numerical results Bao and Wierzbicki (2004, 2005) concluded that the equivalent strain to fracture, denoted by $\bar{\varepsilon}_f$, can be represented as a function of stress triaxiality. The relations between the effective plastic strain at fracture and triaxiality is not monotonous. Three branches have been put into evidence, being governed by shear mode for negative triaxiality, by void growth dominant failure for large triaxiality and by a combination of shear and voids growth mode for the stress triaxiality between the two regimes mentioned above. $\bar{\varepsilon}_f$ is supposed to be analytically represented in terms of the stress triaxiality, i.e. $\bar{\varepsilon}_f = f(\eta)$ which is specific for a given material. Finally the best fit of the experimental data have been presented as average stress triaxiality versus equivalent strain to fracture, i.e. the fracture locus has been defined. The authors mentioned that the displacement to the fracture has been determined during the experiments and by the force displacement response. The significant drop in

loading has been taken to be the point of the initiation of the fracture. It is observed that after its initiation the crack grows very rapidly during the test.

To capture the effect of stress state on the ductile damage and failure, Brünig et al. (2013, 2008) introduced the damage potential functions and damage criteria which are expressed in terms of stress intensity, stress triaxiality and Lode parameter. The damage rule takes into account the isotropic and anisotropic parts corresponding to isotropic growth of voids and anisotropic evolution of micro-shear-cracks, respectively. The parameters can be identify by experiments or by numerical simulations on microscale.

Malcher et al. (2012) considered three isotropic hardening models, which include stress triaxiality and Lode angles, (as a measure of the third invariant of the stress): the extension of the Gurson model, proposed by Tveergard and Needleman (1984), the Lemaitre model (1985), and Bai and Wierzbicki model (2008). Due to the fact that Bai and Wierzbicki (2008) did not include in the model a damage variable, but included the stress triaxiality and Lode angle, Malcher et al. (2012) considered a modified model, by introducing the fracture indicator (a post-processed variable). In the numerical simulations, the specimens with different geometries have been employed in order to generate various stress and strain states, which covered a wide range of triaxiality and Lode angles. The authors concluded that for higher level of stress triaxiality the model proposed by Bai and Wierzbicki (2008) combined with the fracture indicator is more in agreement with the experimental results. Contrary, for a low level of the triaxiality the modified Gurtin model (Tveergard and Needleman 1984) is in agreement with experiments with reference to the equivalent plastic strain. The final conclusion in Malcher et al. (2012): the analyzed models need to be improved, as the models have limitations on the values of the displacement to fracture, the equivalent plastic strain to fracture or in term of fracture localization, under combined loading conditions.

6.2.4 *Undamaged Configuration*

The second and higher order tensors are introduced to characterize the complex three-dimensional distribution and evolution of the microvoids and microcracks, i.e. the material anisotropic damage. Murakami (1983), Murakami and Ohno (1980, 1981), described the anisotropic damage by a second order symmetric tensor, $\mathbf{D}$,

$$\mathbf{D} = \sum_{i=1}^{i=3} D_i \mathbf{n}_i \otimes \mathbf{n}_i, \tag{6.13}$$

where D_i and $\mathbf{n}_i$ are the principal values and directions. D_i can be interpreted as the void area density in the plane perpendicular to direction of the damage $\mathbf{n}_i$.

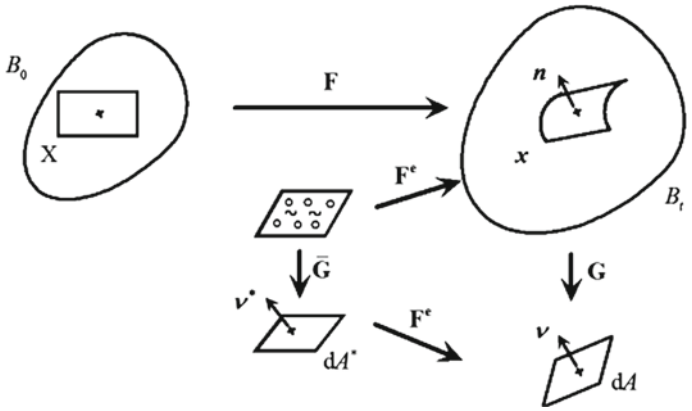

Fig. 6.1 $\mathbf{F}^e$ the elastic part of the deformation gradient; $\mathbf{G}$ and $\bar{\mathbf{G}}$ linear transformations from the current deformed body $\mathscr{B}_t$, and from the stress free and damaged configuration, respectively, to the fictitious associated configurations

By assuming that the principal effect of the material damage consists of the net area decrease due to the three-dimensional distribution of micro defects, Murakami (1988) considered an area vector element in the current (actual) damaged configuration, say $\boldsymbol{\nu}\, dA$ and postulated that there exists a *fictitious undamaged configuration*, and the equivalent load-carrying area vector is denoted by $\boldsymbol{\nu}^*\, dA^*$. Here $\boldsymbol{\nu}$ and $\boldsymbol{\nu}^*$ are unit normals to the appropriate areas, see Fig. 6.1.

If $\mathbf{G}$ denotes the tensor which characterizes the passage from the current deformed damaged configuration to fictitious undamaged configuration associated with the previous one, then by applying the Nanson formula we obtain

$$\begin{aligned} &\boldsymbol{\nu}\, dA = (\det\mathbf{G})\mathbf{G}^{-T}\mathbf{n}\, da \quad \text{or} \\ &\boldsymbol{\nu}\, dA = (\mathbf{I}-\mathbf{D})\mathbf{n}\, da, \quad \text{where}\, \mathbf{I}-\mathbf{D} = (\det\mathbf{G})\mathbf{G}^{-T}. \end{aligned} \tag{6.14}$$

Here $\boldsymbol{\nu}\, dA$ denotes the associated area vector in the undamaged configuration associated to $\mathbf{n}\, da$, the vector area in deformed damaged configuration, $\mathscr{B}_t$. The definition (6.14) introduces a *fictitious deformation* from the current damaged configuration to the so called *fictitious undamaged* configuration, $\mathbf{G}$. The tensor $\mathbf{D}$ (and $\mathbf{G}$) depends on the current state of deformation, as Murakami (1988) observed. Due to the fact that only the *irreversible change of the structure* is responsible for the damage, Murakami (1988) associated the undamaged (fictitious) configuration with the deformed stress free configuration. Consequently, a similar formula to (6.14) is derived

$$\boldsymbol{\nu}^*\, dA^* = (\mathbf{I}-\overline{\mathbf{D}})\bar{\mathbf{n}}\, d\bar{a}, \tag{6.15}$$

where $\mathbf{I}-\overline{\mathbf{D}}$ is associated with $\overline{\mathbf{G}}$ and $\boldsymbol{v}^*\, dA^*$ is the area vector in the undamaged (fictitious) stress-free configuration, while $\bar{\mathbf{n}}\, d\bar{a}$ denotes the associated area vector in the damaged stress free configuration. The following formula is derived in Murakami (1988)

$$\begin{aligned}(\det\overline{\mathbf{G}})\overline{\mathbf{G}}^{-T} &= (\mathbf{F}^e)^T(\det\mathbf{G})\mathbf{G}^{-T}(\mathbf{F}^e)^{-T},\\ \overline{\mathbf{D}} &= (\mathbf{F}^e)^T\mathbf{D}(\mathbf{F}^e)^{-T},\end{aligned} \tag{6.16}$$

in terms of $\mathbf{F}^e$, which realizes the passage from the stress free configuration to the current damaged configuration.

Remark Let us remark that the formulae (6.16) hold only under the assumption that just $\mathbf{F}^e$ realizes the passage from the undamaged and stress free configuration and fictitious undamaged configuration (associated with the current deformed configuration). Moreover, the second order field $\overline{\mathbf{D}}$ and consequently the damage transformation $\overline{\mathbf{G}}$ are symmetric.

The effect of the Cauchy stress, say $\boldsymbol{\sigma}$, acting on the body is given by the *effective stress tensor*

$$\bar{\boldsymbol{\sigma}} = \frac{1}{2}((\mathbf{I}-\mathbf{D})^{-1}\boldsymbol{\sigma} + \boldsymbol{\sigma}(\mathbf{I}-\mathbf{D})^{-1}), \tag{6.17}$$

introduced by Murakami and Ohno (1981). The tensor $(\mathbf{I}-\mathbf{D})^{-1}$ represents the stress effect increase due to damage.

Due to the hypothesis concerning the symmetry of the damage $\mathbf{D}$, Murakami expressed the idea that this damage state should correspond to the orthotropic symmetry only, see Murakami (1988).

Remark The formula (6.17) can be rewritten as

$$\bar{\boldsymbol{\sigma}} = \frac{1}{2}\sum_{i=1}^{i=3}\frac{1}{1-D_i}(\mathbf{n}_i\otimes(\boldsymbol{\sigma}\mathbf{n}_i) + \boldsymbol{\sigma}\mathbf{n}_i\otimes\mathbf{n}_i),\ \text{where}\ \frac{1}{1-D_i} = \frac{\bar{A}_i}{A_i} \tag{6.18}$$

Consequently, if $\mathbf{n}_i$ is a proper vector for $\boldsymbol{\sigma}$, the formula (6.18) could be considered as an extension to the anisotropic damage of the uniaxial formula $\bar{\sigma}_i = \frac{\sigma_i}{1-D_i}$, (see the formulae (6.4) and (6.5)).

The evolution equation of the damage is expressed, following Murakami and Ohno (1980, 1981) by

$$\dot{\mathbf{D}} = \mathbf{H}(\bar{\boldsymbol{\sigma}}, (\mathbf{I}-\mathbf{D})^{-1}, \kappa), \tag{6.19}$$

where κ denotes a hardening parameter.

In Chap. 5 of the book by Voyiadjis and Kattan (2005), the *fourth-order anisotropic damage effect tensor* $\mathbf{M}$ is the key point in describing the anisotropic

damage. **M** expresses the linear transformation giving rise to the effective stress tensor $\bar{\boldsymbol{\sigma}}$ in terms of the Cauchy stress tensor $\boldsymbol{\sigma}$, as in Murakami and Ohno (1981), namely

$$\bar{\boldsymbol{\sigma}} = \mathbf{M}\boldsymbol{\sigma}, \quad \text{where} \quad \mathbf{M}\boldsymbol{\sigma} = \frac{1}{2}(\boldsymbol{\sigma}(\mathbf{I}-\mathbf{D})^{-1} + (\mathbf{I}-\mathbf{D})^{-1}\boldsymbol{\sigma}). \tag{6.20}$$

The explicit representation of the fourth-order damage tensor **M** using the second order damage tensor **D**[1] is important in implementation of the constitutive models of damage. The representation of **M**, as a matrix (6,6) is given in terms of the six components of **D**, or using the proper values **D**, but this time in the tensorial representation with respect to the proper vector of **D**. In Chap. 7 of the book by Voyiadjis and Kattan (2005), the *fourth-order anisotropic damage effect tensor* **M** remains a general one, without any correlation with certain second order damage tensor, and a general elasto-plastic model connected with damage is proposed in an Eulerian formalism. A modified elasto-plastic stiffness tensor includes the effect of damage through the use of the undamaged stress configuration and the hypothesis of elastic energy equivalence.

The fourth order damage tensors have been also introduced, see for instance Murakami and Imaizumi (1982), Lubarda and Krajcinovic (1995), Voyiadjis and Park (1996), to take into account the damage induced material anisotropy.

6.3 Models with Damage State Variables

Two constitutive models for ductile anisotropic continuum damage, based on thermodynamic law for isothermic processes and connected with plasticity and damage, to capture the dissipative nature of the inelastic deformation are presented in Sect. 6.3.1 following Brünig (2003), Brünig and Ricci (2005), and in Sect. 6.3.2 following Ekh et al. (2004). Section 6.3.3 makes references to Lemaitre and Chaboche model (1990).

6.3.1 Model with Multiple Undamaged Configurations

Brünig (2003), Brünig and Ricci (2005) provide a finite strain framework, using the *multiple undamaged (fictitious) configurations* and specific metric coefficients to describe measures of damage. The extension to nonlocal plasticity and nonlocal damage can be found in Brünig and Ricci (2005), the macroscopic background being the same in all the aforementioned papers. Three types of undamaged

[1] **D** is denoted by Φ in Voyiadjis and Kattan (2005).

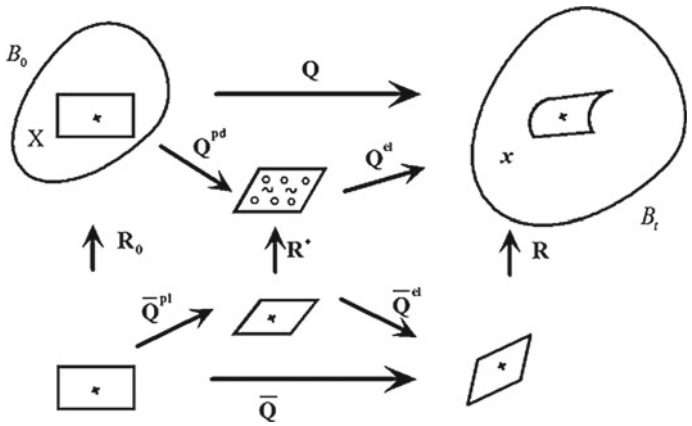

Fig. 6.2 The framework considered by Brünig (2003): $\mathbf{R}_0, \mathbf{R}^*$ and $\mathbf{R}$ are defined on the appropriate undamaged configurations obtained by fictitious removing the defects of the initial, stress-free intermediar and actual configurations: $\mathbf{Q}^{pd}, \mathbf{Q}^{el}$, the inelastic (plastic and damage) and elastic parts of the metric transformation tensor $\bar{\mathbf{Q}}^{pl}$, $\bar{\mathbf{Q}}^{el}$, the effective plastic and elastic parts of the effective metric transformation $\bar{\mathbf{Q}}$

configurations have been introduced, namely initial, $\mathscr{E}_0$, intermediate, $\mathscr{E}^*$, and current, $\mathscr{E}$, undamaged configurations, respectively, see Fig. 6.2. The current undamaged configuration $\mathscr{E}$ and the initial undamaged configuration of the body, $\mathscr{E}_0$, are obtained from the current configuration (denoted by $\mathscr{B}_t$ in Fig 6.2) and initial configuration, $\mathscr{B}_0$, by "fictitious removing all the damage" of the deformed body and initial body, respectively. The elastic unloaded configuration, $\mathscr{B}^*$, is associated to the deformed body $\mathscr{B}$ and the corresponding fictitious elastically unloaded and undamaged configuration is denoted by $\mathscr{E}^*$. We remark that all these configurations are local and only the initial and the deformed configurations are global. The set of undamaged configurations is similar to those provided by Murakami (1988), except the unloading initial configuration.

In Fig. 6.2, we represented here the locally appropriate neighborhoods associated to a given material point in the body, **X**, only.

We pointed out certain specific key points in formulating the background of the model.

i. The multiplicative decomposition of the so-called *metric transformation tensor*, $\mathbf{Q}$, into its inelastic (plastic and damage) part, $\mathbf{Q}^{pd}$, and elastic part, $\mathbf{Q}^{el}$, is considered, namely $\mathbf{Q} = \mathbf{Q}^{pd}\mathbf{Q}^{el}$.[2] A similar multiplicative decomposition is introduced, this time with reference to the undamaged configurations. The

[2]The correct written form of the above decomposition and which corresponds to the mentioned figures in the papers (Brünig 2003; Brünig and Ricci 2005) is $\mathbf{Q} = \mathbf{Q}^{el}\mathbf{Q}^{pd}$.

definitions of the elastic strain and damage strain tensors, are differently introduced

$$\begin{aligned}&\mathbf{A}^{el}=\frac{1}{2}\ln\mathbf{Q}^{el},\quad \mathbf{A}^{da}=\frac{1}{2}\ln\mathbf{R}^{*},\quad \text{defined in Brünig (2003)}\\&\mathbf{A}^{el}=\frac{1}{2}(\mathbf{I}-(\mathbf{Q}^{el})^{-1}),\quad \mathbf{A}^{da}=\frac{1}{2}(\mathbf{I}-(\mathbf{R}^{*})^{-1}),\quad \text{in Brünig and Ricci (2005).}\end{aligned}\tag{6.21}$$

These tensors are defined on the appropriate vector spaces associated with $\mathscr{B}^{*}$ and $\mathscr{E}^{*}$, respectively in the first definitions and with $\mathscr{B}$ and $\mathscr{B}^{*}$, respectively in the second definition. Consequently, these tensor fields are not referring to the same configurations and their composition is generally unjustified.

ii. The appropriate strain rate tensors have been introduced in Brünig (2003), Brünig and Ricci (2005), Brünig et al. (2013), and an additive decomposition of the strain rate tensor defined by $\dot{\mathbf{H}}=\frac{1}{2}(\mathbf{Q})^{-1}\dot{\mathbf{Q}}$, into the elastic and inelastic strain rates have been derived. We also remark that the strain rates $\dot{\mathbf{H}}^{el}=\frac{1}{2}(\mathbf{Q}^{el})^{-1}\,\dot{\mathbf{Q}}^{el}$ and $\dot{\mathbf{H}}^{da}=\frac{1}{2}(\mathbf{R}^{*})^{-1})\dot{\mathbf{R}}^{*}$ are associated with the configurations $\mathscr{B}^{*}$ and $\mathscr{E}^{*}$, respectively, if we look at their written expressions.[3]

Comments. Generally strong restrictions have to be imposed on the considered tensor fields in order to provide the imposed algebraic symmetry. For instance, although $(\mathbf{Q})^{-1}$ and $\dot{\mathbf{Q}}$ are symmetric tensors if $\mathbf{Q}$ is symmetric, the tensors $(\mathbf{Q})^{-1}\dot{\mathbf{Q}}$ and $\dot{\mathbf{Q}}(\mathbf{Q})^{-1}$ could not be symmetric. In order to avoid these unjustified issues, the linear and invertible transformations should be introduced in order to define the passage between various configurations, say for instance $\mathbf{F}^{e}$ instead of $\mathbf{Q}^{el}$. Consequently the symmetric and positive definite tensors which characterize the corresponding metric tensors can be naturally provided, but they do not enter the multiplicative decomposition.

iii. The elastic type constitutive equation, presented by Brünig (2003) formula (6.82), and by Brünig and Ricci (2005) formula (6.78), characterizes the Kirchhoff tensor $\mathbf{T}$ in terms of elastic strain, $\mathbf{A}^{el}$ (see the definitions given by (6.21)),

$$\begin{aligned}\mathbf{T}=2(G+\eta_2\,\mathrm{tr}\mathbf{A}^{da})\mathbf{A}^{el}+[(K-\frac{2}{3}G+2\eta_1\,\mathrm{tr}\mathbf{A}^{da})\mathrm{tr}\mathbf{A}^{el}+\\+\eta_3(\mathbf{A}^{da}\cdot\mathbf{A}^{el})]\mathbf{I}+\eta_3(\mathrm{tr}\mathbf{A}^{el})\mathbf{A}^{da}+\eta_4(\mathbf{A}^{da}\mathbf{A}^{el}+\mathbf{A}^{el}\mathbf{A}^{da}).\end{aligned}\tag{6.22}$$

and containing the damage strain measure, $\mathbf{A}^{da}$.

[3]The correct definition for $\dot{\mathbf{H}}^{el}$ ought to be $\dot{\mathbf{H}}^{el}=\frac{1}{2}((\mathbf{Q}^{el})^{-1}\,\dot{\mathbf{Q}}^{el}+\dot{\mathbf{Q}}^{el}\,(\mathbf{Q}^{el})^{-1})$.

Remark The constitutive Eq. (6.22), say together with $(6.21)_2$ which characterizes an elastic behaviour contains two measure of deformations with respect to different configurations, the elastic strain $\mathbf{A}^{el}$, with respect to the deformed configuration, while $\mathbf{A}^{da}$ is defined on the stress free and damaged configuration. Moreover, the Kirchhoff tensor $\mathbf{T}$ and $\mathbf{A}^{el}$ are objective fields, while $\mathbf{A}^{da}$ is not.

Remark Due to the wrong writing in the composed tensor fields, which do not correspond to their images plotted in Fig. 6.1 from Brünig (2003), Brünig and Ricci (2005), further we do not make reference to the appropriate formulae presented in the aforementioned papers. We underline now some principal ideas that follow from the papers (Brünig 2003; Brünig and Ricci 2005), and that are fruitful in describing anisotropic damage.

In the damage-coupled elasto-plastic models, these dissipative processes, namely plastic flow and damage, are treated by the constitutive models proposed in Brünig (2003), Brünig and Ricci (2005), Brünig et al. (2013), as different in their nature and effects on mechanical properties of the materials and structures. Brünig (2003) motivated the differences by the fact that "The pure plastic flow develops by dislocation motion and sliding phenomena along the some preferential crystallographic planes, whereas damage-related irreversible deformations are due to residual opening of micro defects after unloading." The free energy functions are introduced separately with respect to the fictitious undamaged configuration, $\mathscr{E}^*$, and to the current damaged configuration $\mathscr{B}^*$. The plastic strain rate tensor is determined via a non-associative plastic flow rule. The damaged surface is characterized in terms of the stress tensor with respect to stress free damaged configuration, $\mathscr{B}^*$.

The energies involved in plastic flow and damage processes are postulated to be independent. The free energy function of the damaged elasto-plastic material, see formula (6.61) by Brünig (2003), is considered to be represented in terms of three functions

$$\Phi = \Phi^{el}(\mathbf{A}^{el}, \mathbf{A}^{da}) + \Phi^{pl}(\gamma) + \Phi^{da}(\mu), \tag{6.23}$$

where Φ^{el} is dependent on the elastic strain $\mathbf{A}^{el}$ and damage strain tensor $\mathbf{A}^{da}$, the plastic and damage parts, Φ^{pl} and Φ^{da}, are dependent on the plastic and damage scalars, internal variables, γ and μ, respectively. The effective specific free energy $\bar{\Phi}$ of the fictitious undamaged configuration, see formula (6.50) by Brünig (2003), is decomposed into two parts, an effective elastic one and an effective plastic part, respectively,

$$\bar{\Phi} = \bar{\Phi}^{el}(\overline{\mathbf{A}}^{el}) + \bar{\Phi}^{pl}(\gamma). \tag{6.24}$$

Brünig (2003) states that the model "does not need strain equivalence, stress equivalence or strain energy approaches often used in continuum damage theory," but the equality of the appropriate elastic type metric transformations, $\mathbf{Q}^{el}$ and $\overline{\mathbf{Q}}^{el}$,

is introduced. Thus the equivalence of the elastic strain tensors, $\mathbf{A}^{el} = \overline{\mathbf{A}}^{el}$, is accepted. Moreover, two types of the dissipation principles, one related to the plastically deformed body coupled with anisotropic damage and the other one concerning the undamaged fictitious configurations are considered. The correlation between these dissipative principles is realized by the equality $\mathbf{A}^{el} = \overline{\mathbf{A}}^{el}$.

In the **effective undamaged configuration**, $\mathscr{C}^*$, the plastic yield condition is described in terms of the effective stress tensor $\overline{\mathbf{T}}$ by

$$f^{pl}(\overline{\mathbf{T}}, c) = 0, \tag{6.25}$$

where c denotes the so-called *strength coefficient of the matrix material.* As a specific form, the linear influence of the hydrostatic stress is considered in the expression for the yield condition given by

$$f^{pl}(\bar{I}_1, \bar{J}_2, c) = \sqrt{\bar{J}_2} - c\left(1 - \frac{a}{c}\,\bar{I}_1\right) = 0, \tag{6.26}$$

where $\bar{I}_1 = \mathrm{tr}\overline{\mathbf{T}}, \quad \bar{J}_2 = \frac{1}{2}\mathrm{dev}\overline{\mathbf{T}} \cdot \mathrm{dev}\overline{\mathbf{T}}$. A non-associative flow rule is defined using the plastic potential function, say $g^{pl} = \sqrt{\bar{J}_2}$.

Brünig and Ricci (2005) proposed a non-local continuum theory of anisotropic damage, which incorporates a non-local yield condition

$$f^{pl}(\overline{\mathbf{T}}, c) \equiv f^{pl}(\bar{I}_1, \bar{J}_2, c) = (1 - \frac{a}{c}\bar{I}_1)^{-1}\sqrt{\bar{J}_2} - c(\gamma, \nabla^2\gamma) = 0, \tag{6.27}$$

where γ is the scalar internal variable and c denotes the strength coefficient of the material.

The **anisotropically damaged configurations** are used by Brünig (2003), Brünig et al. (2008) to describe the behaviour of the damaged materials, with reference to the damage. The damage dissipation potential is introduced as a function dependent on the stress tensor with respect to the configuration $\mathscr{B}^*$, $\widetilde{\mathbf{T}}$, and the appropriate damage criterion is given by

$$f^{da}(\widetilde{\mathbf{T}}, \tilde{\sigma}) = 0, \tag{6.28}$$

where $\tilde{\sigma}$ denotes the damage threshold. The damage strain rate is prescribed by the damage potential, denoted g^{da}, which is defined in terms of the same stress measure $\widetilde{\mathbf{T}}$, as

$$\dot{\mathbf{H}}^{da} = \mu \partial_{\widetilde{\mathbf{T}}} g^{da}. \tag{6.29}$$

Analyzing experimental results, the following damage criterion has been considered to be adequate for describing the damage behaviour in ductile materials, see Brünig (2003),

$$f^{da}(\tilde{I}_1, \tilde{J}_2, \tilde{\sigma}) = \tilde{I}_1 + \tilde{\beta}\sqrt{\tilde{J}_2} - \tilde{\sigma} = 0 \tag{6.30}$$

where $\tilde{\sigma}$ is dependent on the scalar internal variable μ, and its gradient $\nabla\mu$, which is involved in a non-local theory. The scalar function $\tilde{\beta}$ describes the influence of the deviatoric part of the stress on damage. In order to define the damage evolution equation, the damage potential has been introduced by

$$g^{da}(\widetilde{\mathbf{T}}) = \alpha\tilde{I}_1 + \beta\sqrt{\tilde{J}_2}, \tag{6.31}$$

where α and β are damage parameters. The non-associated damage rule is derived in Brünig and Ricci (2005) under the form

$$\dot{\mathbf{H}}^{ad} = \tilde{\mu}(\alpha\mathbf{I} + \beta\frac{1}{\sqrt{2\tilde{J}_2}}\,\mathrm{dev}\,\widetilde{\mathbf{T}}), \tag{6.32}$$

with the remark that the first term is related to the growth of microvoids, while the second term considers the "dependence of the evolution of the size, shape and orientation of the micro defects."

Remark The rate independent models have been adopted in the papers (Brünig 2003; Brünig and Ricci 2005), and the necessity to introduce the consistency conditions is considered, but without any references to the correlations between the damage and yield functions.

Remark The applicability of the models proposed in Brünig (2003), Brünig and Ricci (2005) have been proved by the numerical simulations performed and analyzed in the above mentioned papers.

6.3.2 *Crystal Plasticity Model Coupled with Anisotropic Damage*

Menzel et al. (2002) developed a framework of continuum damage based on the fictitious configuration and the equivalence principle of the free energy in the fictitious configuration and the intermediate configuration, see Fig. 6.3. The intermediate configuration (which is called the local relaxed configuration in our description (Cleja-Ţigoiu and Soós 1990)) is associated with the multiplicative decomposition of the deformation gradient into its elastic and plastic parts. The second order tensor $\mathbf{F}^d$, called the *integrity tensor*, characterizes the passage from an *undamaged* (*fictitious*) *configuration* to the intermediate configuration and it is not involved in the multiplicative decomposition of the deformation gradient. The damage model proposed by Ekh et al. (2004) appeals to the crystal plasticity model and the evolution rule for the damage is formulated with respect to the crystalline

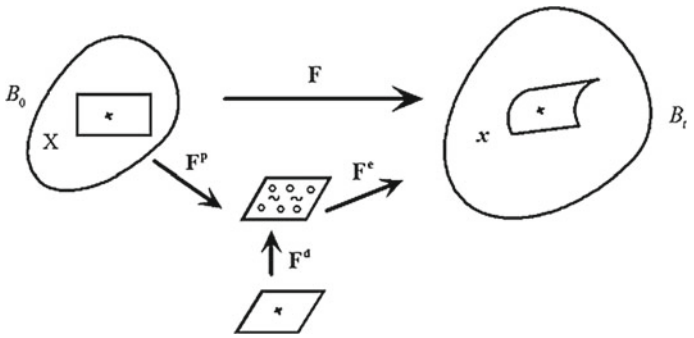

Fig. 6.3 The elastic and plastic parts, $\mathbf{F}^e$ and $\mathbf{F}^p$, of the deformation gradient. $\mathbf{F}^d$ the damage tensor defined on the undamaged and stress-free local configuration

slip systems. Not only the damage tensor $\mathbf{F}^d$ but also scalar integrity measure b_α, which are a set of scalar damage variables are involved in the expression of the *effective Schmid stress*, $\bar{\tau}_\alpha$, which is associated with the α-slip system. The α-slip system is denoted by $(\bar{\mathbf{s}}_\alpha, \bar{\mathbf{m}}^\alpha)$, when we refer to the intermediate configuration and by $(\mathbf{s}_\alpha \equiv \mathbf{F}^e\bar{\mathbf{s}}_\alpha, \mathbf{m}^\alpha \equiv (\mathbf{F}^e)^{-T}\bar{\mathbf{m}}_\alpha)$ with respect to the actual configuration.

The reference, local intermediate and actual configurations, as well as the (local) undamaged stress free configuration are represented in Fig. 6.3. We introduce the tensor field, denoted by $\widehat{\mathbf{F}}$, which realizes the passage from the undamaged to the actual (deformed) configuration in Fig. 6.4.

- The free energy with respect to the stress free and damaged configuration is dependent on the elastic strain (elastic right Cauchy- Green tensor), the damage tensor, internal scalar variables denoted by $\{k_\alpha\}$, representing the hardening variables on each slip systems,

$$\varphi = \varphi(\mathbf{C}^\mathbf{e}, \mathbf{F}^d, \{k_\alpha\}). \tag{6.33}$$

The free energy is additively represented by the elastic φ^e and hardening part $\varphi^{(h)}$

$$\varphi = \varphi^e(\mathbf{C}^e, \mathbf{b}^d) + \varphi^{(h)}(\{k_\alpha\}), \quad \text{where} \quad \mathbf{b}^d = \mathbf{F}^d(\mathbf{F}^d)^T \tag{6.34}$$

with the damage influence on the elastic part of free energy. The following **assumption** motivated by the principle of the *elastic* strain energy equivalence has been introduced by Menzel and Steinmann (2003), the *elastic* free energy with respect to the stress free and damaged configuration and to the effective configuration, respectively, have equal values, i.e.

$$\varphi^e(\mathbf{C}^e, \mathbf{b}^d) = \hat{\varphi}^e(\widehat{\mathbf{C}}), \quad \text{where} \quad \widehat{\mathbf{C}} = (\mathbf{F}^d)^T \mathbf{C}^e \mathbf{F}^d. \tag{6.35}$$

Under the **supplementary condition** stipulating that the $\hat{\varphi}^e$ is *isotropic* with respect to its argument, $\widehat{\mathbf{C}}$, the following representation follows

$$\varphi^e(\mathbf{C}^e, \mathbf{b}^d) = \hat{\varphi}(j_k(\widehat{\mathbf{C}})), \tag{6.36}$$

where $j_k(\widehat{\mathbf{C}}) = \mathrm{tr}((\mathbf{C}\mathbf{b}^d)^k)$, $k = 1, 2, 3$, i.e. the invariants of the mentioned tensor.

As a consequence of the thermodynamic restrictions imposed by the Clausius-Duhem inequality

$$\mathbf{T} \cdot \dot{\mathbf{F}}(\mathbf{F})^{-1} - \dot{\varphi} \geq 0, \tag{6.37}$$

written with respect to the actual configuration, the free energy density is potential for the stress tensor. The symmetric Piola-Kirchhoff stress tensor with respect to the intermediate configuration can be expressed as

$$\frac{\overline{\mathbf{T}}}{\tilde{\rho}} = 2\partial_{\mathbf{C}^e} \varphi^e(\mathbf{C}^e, \mathbf{b}^d). \tag{6.38}$$

Thus a thermodynamic stress which is power conjugated to the rate of damage in a slip system is associated with the damage tensor $\mathbf{b}^d$ via the relationship

$$\boldsymbol{\beta}^d = -2\partial_{\mathbf{b}^d} \varphi^e(\mathbf{C}^e, \mathbf{b}^d) \tag{6.39}$$

being defined by a similar procedure as that used to define the symmetric Piola-Kirchhoff stress tensor, see (6.38).

The thermodynamic stresses κ_α are associated with the hardening variables k_α and are defined as in the standard materials by

$$\boldsymbol{\kappa}_\alpha = -\partial_{k_\alpha} \varphi^h(\{k_\alpha\}). \tag{6.40}$$

The dissipation inequality (6.37) together with (6.38)–(6.40) is reduced to the inequality

$$\mathbf{C}^e \frac{\widetilde{\mathbf{T}}}{\tilde{\rho}} \cdot \dot{\mathbf{F}}^p (\mathbf{F}^p)^{-1} + \boldsymbol{\beta}^d \mathbf{b}^d \cdot \dot{\mathbf{F}}^d (\mathbf{F}^d)^{-1} + \sum_\alpha \mu_\alpha \kappa_\alpha \dot{k}^\alpha \geq 0. \tag{6.41}$$

- The yield function is assumed to be dependent on damage and thermodynamic stresses, and is defined in terms of *effective resolved shear stress*, denoted by $\tilde{\tau}_\alpha$,

$$\Phi_\alpha = \tilde{\tau}_\alpha - [Y_\alpha + \kappa_\alpha], \quad \tilde{\tau}_\alpha = \frac{1}{b_\alpha}\tau_\alpha, \quad \tau_\alpha = \bar{\mathbf{s}}_\alpha \cdot \mathbf{C}^e \frac{\widetilde{\mathbf{T}}}{\tilde{\rho}} \bar{\mathbf{m}}^\alpha. \tag{6.42}$$

τ_α is called the *resolved shear stress* and b_α are scalar parameters which characterize the evolution of damage.

The flow rule is of the associative type and is formulated for $\mathbf{F}^p$ and for $\mathbf{F}^d$.

The rate of plastic part of deformation gradient is associated to the yield function (6.42) as

$$\dot{\mathbf{F}}^p(\mathbf{F}^p)^{-1} = \sum_\alpha \mu_\alpha \frac{\partial \Phi_\alpha}{\partial \overline{\mathbf{M}}}, \quad \overline{\mathbf{M}} = \mathbf{C}^e \frac{\widetilde{\mathbf{T}}}{\tilde{\rho}}. \tag{6.43}$$

In order to define the *damage rule*, the authors introduced in Ekh et al. (2004) the *integrity resolved shear*, similarly to the resolved shear stress (6.42), namely

$$\bar{\beta}_\alpha = \bar{\mathbf{s}}_\alpha \cdot \mathbf{M}^d \bar{\mathbf{m}}_\alpha, \quad \mathbf{M}^d = \boldsymbol{\beta}^d \mathbf{b}^d. \tag{6.44}$$

- There exists a damage potential $\Gamma_\alpha(\bar{\beta}_\alpha, \mathbf{b}_\alpha)$ associated with each slip system α, such that

$$\dot{\mathbf{F}}^d(\mathbf{F}^d)^{-1} = \sum_\alpha \mu_\alpha \frac{\partial \Gamma_\alpha}{\partial \mathbf{M}^d} = \sum_\alpha \mu_\alpha \frac{\partial \Gamma_\alpha}{\partial \bar{\beta}_\alpha}(\bar{\mathbf{s}}_\alpha \otimes \bar{\mathbf{m}}_\alpha) = \sum_\alpha \dot{b}_\alpha(\bar{\mathbf{s}}_\alpha \otimes \bar{\mathbf{m}}_\alpha). \tag{6.45}$$

- The stress-type hardening parameters, the so-called drag-stress corresponding to the isotropic hardening variables $\{k_\alpha\}$ are defined by the appropriate evolution equations in α-slip system

$$\dot{k}_\alpha = \mu_\alpha \frac{\partial \Phi_\alpha}{\partial \kappa_\alpha} \equiv -\mu_\alpha. \tag{6.46}$$

- The scalar parameters which characterize the evolution of damage are described by the appropriate evolution equations given by

$$\dot{b}_\alpha = \sum_\alpha \mu_\alpha \frac{\partial \Gamma_\alpha}{\partial \bar{\beta}_\alpha}. \tag{6.47}$$

Finally the dissipation inequality is expressed as follows:

$$\sum_\alpha \mu_\alpha \left[\Phi_\alpha + Y_\alpha + \bar{\beta}_\alpha \frac{\partial \Gamma_\alpha}{\partial \bar{\beta}_\alpha} \right] \geq 0. \tag{6.48}$$

In the case of the rate-dependent plasticity μ_α is defined in terms of non-negative and monotonically increasing overstress functions $\eta_\alpha(\Phi_\alpha)$

$$\mu_\alpha = \frac{1}{t_{*\alpha}} \langle \eta_\alpha(\Phi_\alpha) \rangle. \tag{6.49}$$

The functions $\eta_\alpha(\Phi_\alpha)$ have the properties $\eta_\alpha(\Phi_\alpha) = 0$ if $\Phi_\alpha \leq 0$, and $\eta_\alpha(\Phi_\alpha) > 0$ if $\Phi_\alpha > 0$, and $t_{*\alpha}$ is the relaxation time.

Here the function $\langle x \rangle = \frac{1}{2}(x + |x|)$ is defined for all x real numbers.

Remark In the numerical application, given by Ekh et al. (2004) the small deformation strain model is considered, and the scalar damage parameters have been chosen $b_\alpha = 1 - d_\alpha$, and μ_α have been introduced corresponding to rate dependent (viscoplastic) models.

Comments. We refer now to a certain physical meaning that can be assigned to the damage variable within the crystal plasticity framework. In the viscoplastic model considered by Cleja-Ţigoiu and Paşcan (2014) the evolution in time of the plastic distortion is described by multislip in an appropriate crystallographic system, with hardening laws dependent on the scalar dislocation densities, denoted by ρ_α in α-slip system. The evolution in time of the scalar dislocation densities is described by non-local (i.e. diffusion-like) evolution equations, which can be reduced to differential ones when the diffusion parameter, k, is vanishing. The problems concerning the deformation of the sheet made up from such viscoplastic crystalline material, which is generated by different slip systems that could be simultaneously activated, were numerically solved. In compression problem, for the boundary impenetrable to dislocations all eight activated slip systems were considered together with the activation condition. The large band-zones of relative minimum and maximum values of the total dislocation densities, denoted by ρ_{tot}, can be seen for k = 0.

The non-homogeneous band zones with the alternating maximum and minimum values of plastic distortion components, as well as for stress components, follow the localized zones of ρ_{tot}. Analyzing the numerical solutions for the boundary value problem we conclude that the total dislocation density accumulated during the elasto-plastic process can be interpreted as a scalar damage variable. The damage is essentially anisotropic, due to the presence of different slip systems activated, the damage variable as the total dislocation density is well defined from the physical point of view.

6.3.3 Lemaitre and Chaboche Models

We present now the models of coupled elasto-plasticity and damage constitutive equations for small deformations, with only scalar damage variables, namely the unified formulation of damage laws, following the exposure that can be found in Sect. 6.3.1 (Malcher et al. 2012; Lemaitre and Chaboche 1990; Lemaitre 1992, and so on). The models proposed by Lemaitre and Chaboche are based on the concept of *effective stress* and the hypothesis of *strain equivalence* and are largely applied and extended in the literature of the continuum damage field.

In Chap. 12 of the book (de Souza Neto et al. 2008), the authors reviewed and discussed some elasto-plastic damage models and their numerical implementation.

We listed the principal hypotheses adopted in the models.

i. The *existence of the free energy* density, φ, as function of the state variables $(\boldsymbol{\varepsilon}^e, R, \mathbf{X}, D)$, where $\boldsymbol{\varepsilon}^e$ is the elastic strain, R and D are scalar hardening and scalar damage variables, and $\mathbf{X}$ denotes the second order tensor, describing the kinematic hardening. The free energy function is described in terms of both elastic part φ^e, dependent on damage and irreversible part, φ^p, i.e.

$$\begin{aligned} \varphi &= \varphi(\boldsymbol{\varepsilon}^e, R, \mathbf{X}, D), \\ \varphi &= \varphi^e(\boldsymbol{\varepsilon}^e, D) + \varphi^p(R, \mathbf{X}). \end{aligned} \tag{6.50}$$

ii. Under the assumption that the elastic part of the free energy is given by

$$\varphi^e = \frac{1}{2}(1-D)\mathscr{E}\boldsymbol{\varepsilon}^e \cdot \boldsymbol{\varepsilon}^e, \tag{6.51}$$

the Cauchy stress is derived from the free energy, viewed as thermodynamic potential,

$$\boldsymbol{\sigma} = \rho\frac{\partial\varphi}{\partial\boldsymbol{\varepsilon}^e} = \rho(1-D)\mathscr{E}\boldsymbol{\varepsilon}^e, \tag{6.52}$$

where ρ is the mass density.

Equivalently the damage elastic law can be written in terms of *effective stress*, as

$$\begin{aligned} \boldsymbol{\sigma}_{eff} &= \frac{1}{\rho(1-D)}\boldsymbol{\sigma}, \\ \boldsymbol{\sigma}_{eff} &= \mathscr{E}\boldsymbol{\varepsilon}^e. \end{aligned} \tag{6.53}$$

The thermodynamic force conjugated to the scalar damage variable, D, is defined by

$$Y = -\rho\frac{\partial\varphi}{\partial D}. \tag{6.54}$$

Using the invertibility of the elastic stiffness tensor $\mathcal{E}$, in the case of isotropic elastic behaviour, the expression of Y leads to another important feature of the damage, the influence of the triaxiality. Y is dependent on the *triaxiality by the factor* R_v,

$$\begin{aligned} Y &= \frac{1}{2\rho(1-D)^2}\boldsymbol{\sigma}\cdot\mathscr{E}^{-1}\boldsymbol{\sigma} \equiv -\frac{\sigma_{eq}R_v}{2E\rho(1-D)^2}, \\ R_v &= \frac{2}{3}(1+v)+3(1-2v)\left(\frac{\sigma_H}{\sigma_{eq}}\right). \end{aligned} \tag{6.55}$$

Y corresponds to the variation of internal energy density due to damage growth at constant stress.

iii. The plastic part of the free energy function is defined by

$$\varphi^p(R,\mathbf{X}) = \varphi^I(R) + \frac{a}{2}\mathbf{X}\cdot\mathbf{X}, \tag{6.56}$$

where a is material constant. The thermodynamic forces associated with isotropic hardening and kinematic hardening

$$\kappa = \rho\frac{\partial\varphi^p}{\partial R} = \kappa(R), \quad \boldsymbol{\alpha} = \rho\frac{\partial\varphi^p}{\partial\mathbf{X}}, \tag{6.57}$$

$\boldsymbol{\alpha}$ is called the *back stress*.

The *yield function* ϕ is defined by

$$\phi(\boldsymbol{\sigma},\kappa,\boldsymbol{\alpha},D) = \tfrac{1}{1-D}\left(Dev\boldsymbol{\sigma}-\boldsymbol{\alpha}\right)_{eq} - \sigma_Y - \kappa, \tag{6.58}$$

where σ_Y is the uniaxial yield stress.

The *potential of dissipation* is given by

$$\begin{aligned} \varphi &= \phi + \tfrac{b}{2a}\tfrac{1}{1-D}\boldsymbol{\alpha}\cdot\boldsymbol{\alpha} + F_D(Y), \\ F_D(Y) &= \tfrac{r}{(1-D)(s+1)}\left(\tfrac{Y}{r}\right)^{s+1}H(\overline{\varepsilon}^p - p_D). \end{aligned} \tag{6.59}$$

a, b are constants which characterize the so-called Armstrong-Frederick hardening law. In order to have similarity between the terms containing $\boldsymbol{\alpha}$ in the expression of the potential of dissipation we introduced here $\frac{1}{1-D}$.

The function F_D is the key point in representing the damage evolution, r and s are material constants and p_D is a material constant, which represents the *damage threshold*.

The plastic behaviour of the material is described using the potential of dissipation by

$$\begin{aligned}
\dot{\boldsymbol{\varepsilon}}^p &= \lambda \frac{\partial \varphi}{\partial \boldsymbol{\sigma}} \equiv \lambda \frac{1}{1-D}\mathbf{N}, \\
\dot{\boldsymbol{\alpha}} &= \lambda \frac{\partial \varphi}{\partial \boldsymbol{\alpha}} \equiv \lambda \frac{1}{1-D}(a\mathbf{N} - b\boldsymbol{\alpha}), \\
\dot{D} &= \lambda \frac{\partial F_D}{\partial Y} \mathscr{H}(\bar{\boldsymbol{\varepsilon}}^p - p_D) \equiv \lambda \frac{1}{1-D}\left(\frac{Y}{r}\right)^s H(\bar{\varepsilon} - p_D), \\
\dot{R} &= \lambda,
\end{aligned} \tag{6.60}$$

where $\bar{\varepsilon}^p$ is the equivalent plastic strain, and p_D is a material constant, which represents the *damage threshold*. Here the function $\mathbf{N}$ characterizes the direction of the plastic strain rate given by

$$\mathbf{N} = \frac{3}{2}\frac{Dev\boldsymbol{\sigma} - \boldsymbol{\alpha}}{(Dev\sigma - \boldsymbol{\alpha})_{eq}}. \tag{6.61}$$

Damage Thresholds. In the pure tension case there exists a certain value of the plastic strain, ε_D^p below for which no damage caused by microcracks occurs, namely if $\varepsilon_p < \varepsilon_{pD}$ then $D = 0$. On the other hand there exists a value of damage, $D = D_c$ which marks the macro crack initiation.

Damage is always related to some irreversible strain either at the microlevel or the mesolevel, this property is considered by the presence of λ in the evolution equation for D, which is written in (6.60). The damage remains equal to zero if $\bar{\boldsymbol{\varepsilon}}^p < p_D$, and the evolution occurs if $\bar{\boldsymbol{\varepsilon}}^p \geq p_D$. p_D is a function of the applied stress and $\bar{\boldsymbol{\varepsilon}}^p$ is the equivalent plastic strain. In the evolution equation of damage, (6.60), the Heaviside function has been introduced to emphasize the role of the *damage threshold.*

As **an extension** of the Lemaitre and Chaboche models, we mention that in Lämmer and Tsakmakis (2000) proposed the elasto-plastic models coupled with damage (described in terms of scalar damage variable) for small and finite deformations. In the finite strain models the strain measure on the intermediate configuration has been defined as

$$\hat{\boldsymbol{\Gamma}} = \frac{1}{2}(\mathbf{C}^e - \mathbf{c}^p), \text{ with } \mathbf{C}^e = (\mathbf{F}^e)^T\mathbf{F}^e \text{ and } \mathbf{c}^p = (\mathbf{F}^p)^{-T}(\mathbf{F}^p)^{-1} \text{ (in our notation).}$$

The additive decomposition of the appropriate strain measure into its elastic and plastic part is introduced by

$$\begin{aligned}
&\hat{\boldsymbol{\Gamma}} = \hat{\boldsymbol{\Gamma}}^e + \hat{\boldsymbol{\Gamma}}^p, \quad \text{where} \\
&\hat{\boldsymbol{\Gamma}}^e = \tfrac{1}{2}(\mathbf{C}^e - \mathbf{I}), \quad \hat{\boldsymbol{\Gamma}}^p = \tfrac{1}{2}(\mathbf{I} - \mathbf{c}^p)
\end{aligned} \tag{6.62}$$

The Oldroyd derivative is given in terms of $\hat{\mathbf{L}}^p = \dot{\mathbf{F}}^p(\mathbf{F}^p)^{-1}$, in order to have the equality written below

$$\begin{aligned} &\overset{(\Delta)}{\hat{\boldsymbol{I}}}{}^p = \hat{\mathbf{D}}^p, \quad \hat{\mathbf{D}}^p = \tfrac{1}{2}(\hat{\mathbf{L}}^p + (\hat{\mathbf{L}}^p)^T), \quad \text{where} \\ &\overset{(\Delta)}{\hat{\boldsymbol{I}}}{}^p = \frac{d}{dt}\hat{\boldsymbol{I}}^p + (\hat{\mathbf{L}}^p)^T\hat{\boldsymbol{I}}^p + \hat{\boldsymbol{I}}^p\hat{\mathbf{L}}^p \end{aligned} \tag{6.63}$$

The three models have been developed by Lämmer and Tsakmakis (2000). These models differ in the definitions of the yield function and the law describing the hardening effects. In models A only the stress tensor is replaced by the effective stress, in B the stress tensor and the back stress are replaced by the appropriate effective fields, while in C the scalar hardening variables is also replaced by its effective associate field. The models are developed within the thermomechanical framework and the influence of triaxiality is involved in the models, using a similar arguments as in the Lemaitre and Chaboche model, see the formula (6.55), in Sect. 6.3.3.

6.4 Model with Stress-Free Undamaged Configuration and Deformation-like Damage Tensor F^d

We present here some results partially published by Cleja-Ţigoiu (2011), concerning the elasto-plastic models with second order defect density tensor, under the hypothesis of large deformation. In the model proposed here we assume the existence of the stress-free, undamaged configuration. We introduced simplifications in the succession of the damaged and the undamaged configurations, that has been presented in the above mentioned papers by Brünig (2003), Brünig and Ricci (2005).

Remark We consider only one undamaged configuration, associated with the stress free (intermediate) local configuration, namely $\mathbf{R}^* = \mathbf{F}^d$, we refer to Fig. 6.2. The deformation like damage tensor $\mathbf{F}^d$ is an invertible one, and it is not apriori a symmetric tensor. The initial configuration of the body does not contain microvoids and microcracks (more precisely these initial micro defects can be neglected), which means that $\mathbf{R}^0 = \mathbf{I}$. In Figs. 6.2 and 6.4 all these elements can be seen. We remark the differences between the considered configurations plotted in Figs. 6.4 and 6.3, where the plastic part of deformation is viewed like in the deformation gradient multiplicative decomposition. Contrary, in this section the damage tensor is involved into the multiplicative decomposition, establishing a similarity with the models briefly presented in Sect. 6.3.1. We mention that $\bar{\mathbf{Q}}^{pl}$, which is considered to be symmetric and positive definite in Brünig (2003), Brünig and Ricci (2005), is replaced by an invertible tensor $\mathbf{F}^p$, which is called plastic distortion in our model.

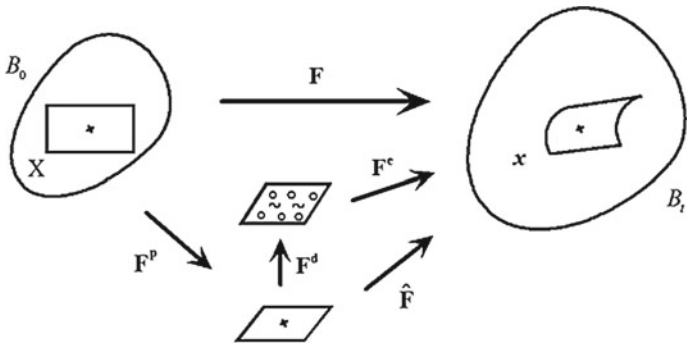

Fig. 6.4 Elastic, plastic and damage tensors as parts of the deformation gradient $\mathbf{F}$, $\mathbf{F} = \mathbf{F}^e\mathbf{F}^d, \mathbf{F}^p$, with $\mathbf{F}^d$ the transformation from the undamaged and stress free configuration to the damaged and stress free configuration

Let us consider k the reference configuration and the actual (deformed) configuration $\chi(\cdot, t)$ of the body $\mathscr{B}$, where χ represents a motion of the body.

Ax. 1. We **assume** that at any time t, for any $\mathbf{X} \in \mathscr{B}$ there exist:

- $\tilde{\mathscr{K}}$ a *stress free, damaged configuration* and
- $\mathscr{K}$ a stress free, undamaged configuration.

Starting from these assumptions, we define the local deformations: $\mathbf{F}^e$ the elastic component, which characterizes the passage from $\tilde{\mathscr{K}}$ to $\chi(\cdot, t)$, $\mathbf{F}^p$ the plastic component, which characterizes the passage from the reference configuration to $\mathscr{K}$ and $\mathbf{F}^d$ the damage deformation tensor, which characterizes the passage from the stress free, undamaged (fictitious) configuration $\mathscr{K}$ to the damaged one, $\tilde{\mathscr{K}}$.

Mass densities ρ^d, ρ^p, ρ are written in *stress free damaged and undamaged configurations, respectively, and in actual configuration* and are related by the following relationships

$$\rho \det\mathbf{F}^e = \rho^d, \quad \rho^d \det\mathbf{F}^d = \rho^p. \tag{6.64}$$

Ax. 2. For any motion χ, $\forall \mathbf{X}, \forall t$, the deformation gradient $\mathbf{F} := \nabla\chi(\mathbf{X}, t)$ is multiplicatively decomposed into its $\mathbf{F}^p$ plastic, $\mathbf{F}^d$ damage and $\mathbf{F}^e$-elastic parts

$$\mathbf{F} = \mathbf{F}^e\mathbf{F}^d\mathbf{F}^p, \quad \hat{\mathbf{F}} = \mathbf{F}^e\mathbf{F}^d. \tag{6.65}$$

All the tensor fields are invertible.

6.4.1 Elastic Type Response Dependent on Damage

In describing the behaviour of elasto-plastic body with damaged structure the following stress tensors are introduced with respect to the appropriate configurations

$\mathbf{T}(\mathbf{x},t)$—the Cauchy stress in the actual configuration $\chi(\cdot,t)$, where $\mathbf{x}=\chi(\mathbf{X},t)$;
$\tilde{\mathbf{T}}(\mathbf{x},t)$—the Piola-Kirchhoff stress in the stress free and damaged configuration, denoted by $\tilde{\mathscr{K}}$;
$\bar{\mathbf{T}}(\mathbf{x},t)$—the Piola-Kirchhoff stress in the stress free and undamaged configuration, denoted by $\mathscr{K}$, the so-called *effective stress*.

These stress measures are related by the following relationships

$$\begin{aligned}\tilde{\mathbf{T}} &= \det(\mathbf{F}^e)(\mathbf{F}^e)^{-1}\mathbf{T}(\mathbf{F}^e)^{-T},\\ \bar{\mathbf{T}} &= (\det\mathbf{F}^d)(\mathbf{F}^d)^{-1}\tilde{\mathbf{T}}(\mathbf{F}^d)^{-T},\\ \bar{\mathbf{T}} &= (\det\hat{\mathbf{F}})(\hat{\mathbf{F}})^{-1}\mathbf{T}(\hat{\mathbf{F}})^{-T}.\end{aligned} \tag{6.66}$$

The Mandel type stress tensors are defined with respect to the configurations $\bar{\mathcal{K}}$ and $\mathcal{K}$ by

$$\frac{1}{\rho^d}\tilde{\boldsymbol{\Sigma}}=\frac{1}{\rho\det\mathbf{F}^e}(\mathbf{F}^e)^T\mathbf{F}^e\tilde{\mathbf{T}},\quad \frac{1}{\rho^p}\bar{\boldsymbol{\Sigma}}=\frac{1}{\rho\det\hat{\mathbf{F}}}(\hat{\mathbf{F}})^T\hat{\mathbf{F}}\bar{\mathbf{T}}. \tag{6.67}$$

We omitted the presence of t in the notations concerning the damaged configurations.

Ax. 3. The behaviour of the material is elastic with respect to stress free and damaged configuration, in terms of the Piola-Kirchhoff stress tensor, $\tilde{\mathbf{T}}$,

$$\begin{aligned}&\tilde{\mathbf{T}}(\mathbf{x},t)=\rho_d\mathbf{h}_{\tilde{\mathscr{K}}}(\boldsymbol{\Delta}^e,\alpha),\\ &\quad\text{where}\quad \boldsymbol{\Delta}^e(\mathbf{X},t)=\frac{1}{2}(\mathbf{C}^e-\mathbf{I}),\quad \mathbf{C}^e=(\mathbf{F}^e)^T\mathbf{F}^e\end{aligned} \tag{6.68}$$

or equivalently in terms of the Cauchy stress tensor

$$\mathbf{T}=\rho\mathbf{F}^e\mathbf{h}_{\tilde{\mathscr{K}}}(\boldsymbol{\Delta}^e,\alpha)(\mathbf{F}^e)^T. \tag{6.69}$$

The strain tensors which appear in the relationships defined herein are defined by

$$\hat{\mathbf{F}}=\mathbf{F}^e\mathbf{F}^d,\quad \hat{\mathbf{C}}:=\hat{\mathbf{F}}^T\hat{\mathbf{F}},\quad \mathbf{C}^d=(\mathbf{F}^d)^T\mathbf{F}^d. \tag{6.70}$$

Let us remark that as a consequence of (6.70)

$$\mathbf{F} = \hat{\mathbf{F}}\mathbf{F}^p, \quad \hat{\mathbf{C}} := (\mathbf{F}^p)^{-T}\mathbf{C}(\mathbf{F}^p)^{-1}, \quad \text{where} \quad \mathbf{C} = \mathbf{F}^T\mathbf{F}. \tag{6.71}$$

Let us calculate the elastic strain measure which has been introduced in (6.68), via the relationship (6.70)

$$\begin{aligned} \boldsymbol{\Delta}^e &= \frac{1}{2}(\mathbf{F}^d)^{-T}(\hat{\mathbf{C}} - (\mathbf{F}^d)^T\mathbf{F}^d)(\mathbf{F}^d)^{-1} \\ \text{or} \quad \hat{\mathbf{C}} - \mathbf{C}^d &= 2(\mathbf{F}^d)^T(\boldsymbol{\Delta}^e)\mathbf{F}^d. \end{aligned} \tag{6.72}$$

Ax. 4. *The elastic constitutive equation* in stress free and undamaged configuration in terms of the effective stress is expressed in relation to the strain through

$$\bar{\mathbf{T}}(\mathbf{x}, t) = \rho^p \hat{\mathbf{h}}_{\mathscr{K}}(\hat{\mathbf{C}} - \mathbf{C}^d, \boldsymbol{\alpha}). \tag{6.73}$$

Remark The new elastic type constitutive function introduced in (6.73), $\hat{\mathbf{h}}_{\mathscr{K}}$, is related to the old one given by (6.68), $\mathbf{h}_{\tilde{\mathscr{K}}}$, through the relationship

$$\mathbf{h}_{\tilde{\mathscr{K}}}(\boldsymbol{\Delta}^e, \boldsymbol{\alpha}) := \mathbf{F}^d \hat{\mathbf{h}}_{\mathscr{K}}(\hat{\mathbf{C}} - \mathbf{C}^d, \boldsymbol{\alpha})(\mathbf{F}^d)^T, \tag{6.74}$$

together with (6.72).

In other words, the dependence of the constitutive function on the configuration $\tilde{\mathscr{K}}$ has been postulated in terms of dependence on the damage tensor $\mathbf{F}^d$, which makes the passage from the stress free and damaged configuration $\tilde{\mathscr{K}}$ to the stress free and undamaged configuration, $\mathscr{K}$.

As a consequence of the stipulated definitions and properties, *the elastic type constitutive equation characterizes Cauchy stress, with respect to the stress free and undamaged configuration*, via $(6.66)_3$, as it follows

$$\mathbf{T} = \rho \hat{\mathbf{F}} \mathbf{h}_{\mathscr{K}}(\hat{\mathbf{C}} - \mathbf{C}^d, \boldsymbol{\alpha})(\hat{\mathbf{F}})^T, \tag{6.75}$$

$\mathbf{F}^d$, being involved like an internal variable.

The stress free (*or relaxation*) *restriction is formulated*, following our development given in Cleja-Ţigoiu and Soós (1990), under the form

$$\hat{\mathbf{h}}_{\mathscr{K}}(\mathbf{S}, \boldsymbol{\alpha}) = 0, \text{for} \quad \mathbf{S} \in Sym \quad \text{if and only if} \quad \mathbf{S} = 0. \tag{6.76}$$

Here in the considered case, the relaxation restriction takes place if and only if $\hat{\mathbf{C}} := (\mathbf{F}^d)^T\mathbf{F}^d \equiv \mathbf{C}^d$, or if and only if $\mathbf{C}^e := (\mathbf{F}^e)^T\mathbf{F}^e = \mathbf{I}$.

6.4.2 Equations for Damage and Plasticity

We adopt the point of view formulated by Brünig (2003), Brünig and Ricci (2005), saying that *by combining plasticity and damage it seems to be natural that plasticity can only affect the undamaged material skeleton*.

Following the constitutive framework of finite elasto-plasticity, as it has been postulated by Cleja-Tigoiu and Sóos (1990, 1990), the evolution equation for $\mathbf{F}^p$, as well as for $\mathbf{F}^d$, which appears to be like an internal variable, will be written with respect to the stress free configuration. Here we choose the *stress free and undamaged* configuration.

(**Ev.1**). The rate of *plastic part of deformation* is described in terms of the Piola-Kirchhoff type stress measure, $\bar{\mathbf{T}}$,

$$\dot{\mathbf{F}}^p(\mathbf{F}^p)^{-1} = \mu_1 \mathscr{B}_{\mathscr{K}}(\bar{\mathbf{T}}, \boldsymbol{\alpha}), \tag{6.77}$$

associated with the yield conditions

$$\bar{f}(\bar{\mathbf{T}}, \boldsymbol{\alpha}) \leq 0 \quad \mu_1 \geq 0, \quad \mu_1 \bar{f}(\bar{\mathbf{T}}, \boldsymbol{\alpha}) = 0, \quad \mu_1 \dot{\bar{f}}(\bar{\mathbf{T}}, \boldsymbol{\alpha}) = 0. \tag{6.78}$$

Let us remark that the rate of damage tensor $\mathbf{F}^d$ can be expressed by $\mathbf{L}^d := \dot{\mathbf{F}}^d(\mathbf{F}^d)^{-1}$ with respect to $\widetilde{\mathscr{K}}$ and by $\mathbf{l}^d$ with respect to the stress free and undamaged configuration $\mathscr{K}$. Here the two rates of damage tensor $\mathbf{F}^d$ are related through

$$\mathbf{l}^d = (\mathbf{F}^d)^{-1}\mathbf{L}^d\mathbf{F}^d, \quad \text{where} \quad \mathbf{l}^d := (\mathbf{F}^d)^{-1}\dot{\mathbf{F}}^d. \tag{6.79}$$

(**Ev.2**). The evolution equation for damage tensorial variable $\mathbf{F}^d$, will be written in terms of the stress measure $\bar{\mathbf{T}}$ and $\mathbf{F}^d$,

$$(\mathbf{F}^d)^{-1}\dot{\mathbf{F}}^d = \mu_2 \mathscr{D}_{\mathscr{K}}(\bar{\mathbf{T}}, \mathbf{F}^d). \tag{6.80}$$

We add two hypothesis concerning the evolution of the damage:

(**Ev.3**). The evolution equation is associated with the *damage criterion*

$$g_{\mathscr{K}}(\bar{\mathbf{T}}, \mathbf{F}^d) \geq 0. \tag{6.81}$$

For $\mathbf{F}^d = \mathbf{I}$, $g_{\mathscr{K}}(\bar{\mathbf{T}}, \mathbf{I}) \geq 0$ together with the elastic type constitutive Eq. (6.73) characterizes the activation condition for the damage.

Remark In the model the initial value of $\hat{\mathbf{C}}$ at which the damage may initiate satisfies the condition

$$g_{\mathscr{K}}(\hat{\mathbf{h}}_0(\hat{\mathbf{C}} - \mathbf{I}, 0), \mathbf{I}) = 0, \tag{6.82}$$

Remark. In our model we suppose that the damage can occur only if a certain threshold in the stress space (which also means a certain criterion in (elastic) strain space due to the possible composition with the constitutive Eq. (6.73)) is reached or is exceeded.

(Ev. 4). No evolution of the damage is produced if there is no variation of the plastic part of deformation, which will be formalized by the condition to have the same plastic multiplier, $\mu_1 = \mu_2 \equiv \mu$

6.4.3 *Dissipative Nature of the Irreversible Behaviour*

We introduce the **assumption**: The elasto-plastic behaviour of the material with damaged structure is restricted to satisfy the **free energy imbalance** in $\mathscr{K}$, i.e. in the *stress free and undamaged configuration*,

$$-\dot{\varphi}_{\mathscr{K}} + \mathscr{P}_{int} \geq 0, \tag{6.83}$$

where $\varphi_{\mathscr{K}}$ is the given free energy density and $\mathscr{P}_{int}$ denotes the internal power expanded during the elasto-plastic process.

The Clausius-Duhem type inequality is reformulated as *free energy imbalance* principle in $\mathscr{K}$, and is considered to be written for any virtual (isothermal) processes. The thermomechanical restrictions on the constitutive framework are derived based on the formulated principle of dissipation.

The free energy with respect to the stress free and damaged configuration is dependent on the elastic strain (elastic right Cauchy- Green tensor), $\mathbf{C}^e$, the damage tensor, $\mathbf{F}^d$, internal variables denoted by $\boldsymbol{\alpha}$,

$$\varphi_{\mathscr{K}} = \varphi(\mathbf{C}^e, \mathbf{F}^d, \boldsymbol{\alpha}, (\mathbf{F}^p)^{-1}), \tag{6.84}$$

as well as being dependent on the configuration relative to which the constitutive representation has done, namely on $(\mathbf{F}^p)^{-1}$.

In finite elasto-plasticity it is supposed that the free energy density can be additively represented by the elastic and irreversible part

$$\varphi_{\mathscr{K}} = \varphi^e(\mathbf{C}^e, \mathbf{F}^d) + \varphi^{(iv)}(\mathbf{F}^d, (\mathbf{F}^p)^{-1}, \boldsymbol{\alpha}), \tag{6.85}$$

with the damage influence on the elastic part of free energy. Motivated by the principle of the elastic free energy equivalence, see Menzel et al. (2002), the free energy with respect to the effective configuration is postulated here under the form

$$\varphi_{\mathscr{K}} = \hat{\varphi}^e(\hat{\mathbf{C}} - \mathbf{C}^d) + \varphi^{(iv)}(\mathbf{F}^d, (\mathbf{F}^p)^{-1}, \boldsymbol{\alpha}), \tag{6.86}$$

In the expression of the elastic part of the free energy function, written in (6.85), the relative strain measure $\hat{\mathbf{C}} - \mathbf{C}^d$ is introduced by (6.72).

The internal power is calculated in terms of the fields expressed with respect to the deformed configuration, namely the Cauchy stress tensor $\mathbf{T}$ and gradient of the velocity vector $\mathbf{v}$, by

$$\mathscr{P}_{int} = \frac{1}{\rho}\mathbf{T}\cdot\{\mathbf{L}\}^S, \text{ with } \quad \mathbf{L} = \nabla\mathbf{v} \equiv \dot{\mathbf{F}}(\mathbf{F})^{-1}, \text{ and } \{\mathbf{L}\}^S = \frac{1}{2}(\mathbf{L}+\mathbf{L}^T). \tag{6.87}$$

The kinematical relationships are derived from (6.65),

$$\begin{aligned} &\mathbf{L} = \nabla\mathbf{v} \equiv \mathbf{L}^e + \mathbf{F}^e\mathbf{L}^d(\mathbf{F}^e)^{-1} + \hat{\mathbf{F}}\mathbf{L}^p(\hat{\mathbf{F}})^{-1}, \quad \hat{\mathbf{F}} = \mathbf{F}^e\mathbf{F}^d \quad \text{with} \\ &\mathbf{L}^e = \dot{\mathbf{F}}^e(\mathbf{F}^e)^{-1}, \quad \mathbf{L}^d = \dot{\mathbf{F}}^d(\mathbf{F}^d)^{-1}, \quad \mathbf{L}^p = \dot{\mathbf{F}}^p(\mathbf{F}^p)^{-1}. \end{aligned} \tag{6.88}$$

Proposition *The internal power is expressed in terms of the elastic, plastic and damage power, represented here by the scalar product of the appropriate rates with the power conjugate stress measures, respectively,*

$$\frac{1}{\rho}\mathbf{T}\cdot\mathbf{L} = \frac{1}{\rho^d}\tilde{\boldsymbol{\Sigma}}\cdot\dot{\mathbf{F}}^d(\mathbf{F}^d)^{-1} + \frac{1}{\rho^p}\bar{\boldsymbol{\Sigma}}\cdot\dot{\mathbf{F}}^p(\mathbf{F}^p)^{-1} + \frac{\mathbf{T}}{\rho}\cdot\dot{\mathbf{F}}^e(\mathbf{F}^e)^{-1}. \tag{6.89}$$

where $\tilde{\boldsymbol{\Sigma}}$ and $\bar{\boldsymbol{\Sigma}}$ are the Mandel type stresses, which are introduced by (6.67).

We prove the above relationships. We pay attention to the first and second terms written in (6.89).

When we take the scalar product written below we get

$$\frac{1}{\rho}\mathbf{T}\cdot\mathbf{F}^e\mathbf{L}^d(\mathbf{F}^e)^{-1} = \frac{1}{\rho}(\mathbf{F}^e)^T\mathbf{T}(\mathbf{F}^e)^{-T}\cdot\mathbf{L}^d = \frac{1}{\rho^d}(\mathbf{F}^e)^T\mathbf{F}^e\tilde{\mathbf{T}}\cdot\mathbf{L}^d = \frac{1}{\rho^d}\tilde{\boldsymbol{\Sigma}}\cdot\mathbf{L}^d \tag{6.90}$$

and

$$\frac{1}{\rho}\mathbf{T}\cdot\hat{\mathbf{F}}\mathbf{L}^p(\hat{\mathbf{F}})^{-1} = (\hat{\mathbf{F}})^T\frac{1}{\rho}\mathbf{T}(\hat{\mathbf{F}})^{-T}\cdot\mathbf{L}^p = (\hat{\mathbf{F}})^T\hat{\mathbf{F}}\frac{1}{\rho\det\hat{\mathbf{F}}}\bar{\mathbf{T}}\cdot\mathbf{L}^p = \frac{1}{\rho^p}\bar{\boldsymbol{\Sigma}}\cdot\mathbf{L}^p. \tag{6.91}$$

as a consequence of the defined stress measures by (6.66) and (6.67).

The rate of free energy density written with respect to the stress free and undamaged configuration can be calculated starting from (6.86)

$$\begin{aligned} \dot{\varphi}_{\mathscr{K}} = {} & \partial_{\overline{\mathbf{C}}}\varphi^{(e)}\cdot(\dot{\hat{\mathbf{C}}} - \dot{\mathbf{C}}^{\mathbf{d}}) + \partial_{\mathbf{F}^{\mathbf{d}}}\varphi^{(\mathbf{iv})}\cdot\dot{\mathbf{F}}^{\mathbf{d}} + \\ & + \partial_{(\mathbf{F}^p)^{-1}}\varphi^{(iv)}\cdot(-(\mathbf{F}^p)^{-1}\dot{\mathbf{F}}^p(\mathbf{F}^p)^{-1}) + \partial_{\boldsymbol{\alpha}}\varphi^{(iv)}\cdot\dot{\boldsymbol{\alpha}} \end{aligned} \tag{6.92}$$

The time derivatives of the following fields can be derived

$$\begin{aligned} &\dot{\hat{\mathbf{F}}}(\hat{\mathbf{F}})^{-1} = \mathbf{L} - \hat{\mathbf{F}}\mathbf{L}^p(\hat{\mathbf{F}})^{-1}, \\ &\dot{\hat{\mathbf{C}}} = (\dot{\hat{\mathbf{F}}})^{\mathbf{T}}\hat{\mathbf{F}} + (\hat{\mathbf{F}})^{\mathbf{T}}\dot{\hat{\mathbf{F}}} = 2\hat{\mathbf{F}}^{\mathbf{T}}\mathbf{D}\hat{\mathbf{F}} - ((\mathbf{L}^p)^{\mathbf{T}}\hat{\mathbf{C}} + \hat{\mathbf{C}}\mathbf{L}^p) \end{aligned} \tag{6.93}$$

as a consequence of the formulae (6.71) together with (6.88). From $(6.70)_3$ we get

$$\dot{\mathbf{C}}^d = 2(\mathbf{F}^d)^T\{\mathbf{L}^d\}^S\mathbf{F}^d. \tag{6.94}$$

Proposition *Within the constitutive framework formulated above the following formulation for the free energy imbalance has been derived*

$$\begin{aligned}&\left\{\frac{\mathbf{T}}{\rho} - 2\,\hat{\mathbf{F}}\partial_{\bar{\mathbf{C}}}\varphi^{(e)}(\hat{\mathbf{F}})^T\right\}\cdot\{\tilde{\mathbf{L}}\}^S + \{2\,\mathbf{F}^d\partial_{\overline{\mathbf{C}}}\varphi^{(e)}(\mathbf{F}^d)^T - \partial_{\mathbf{F}^d}\varphi^{(iv)}(\mathbf{F}^d)^T\}\cdot\tilde{\mathbf{L}}^d + \\ &+\{2\hat{\mathbf{C}}\partial_{\bar{\mathbf{C}}}\varphi^{(e)} + \mathbf{F}^{p-T}\partial_{(\mathbf{F}^p)^{-1}}\varphi^{(iv)}\}\cdot\tilde{\mathbf{L}}^p - \partial_{\boldsymbol{\alpha}}\varphi^{(iv)}\cdot\underline{\boldsymbol{\alpha}} \geq 0,\end{aligned} \tag{6.95}$$

$\forall\quad \tilde{\mathbf{L}}, \tilde{\mathbf{L}}^p, \quad \tilde{\mathbf{L}}^d$, *and* $\underline{\boldsymbol{\alpha}}$

In order **to prove** the above formula we replace the internal power defined by (6.87) and the derivative with respect to time of the free energy density calculated in (6.92) together with (6.93) and (6.94) in the expression of the free energy imbalance (6.83). Thus

$$\begin{aligned}&\frac{\mathbf{T}}{\rho}\cdot\{\mathbf{L}\}^S - 2\partial_{\bar{\mathbf{C}}}\varphi^{(e)}\cdot(\hat{\mathbf{F}})^T\{\mathbf{L}\}^S\mathbf{F}^e + \\ &\quad + 2\partial_{\bar{\mathbf{C}}}\varphi^{(e)}\cdot\{\hat{\mathbf{C}}\mathbf{L}^p\}^S + 2\partial_{\bar{\mathbf{C}}}\varphi^{(e)}\cdot(\mathbf{F}^d)^T\{\mathbf{L}^d\}^S\mathbf{F}^d - \\ &- \partial_{\mathbf{F}^d}\varphi^{(iv)}\cdot\mathbf{L}^d(\mathbf{F}^d) + \mathbf{F}^{p-T}\partial_{(\mathbf{F}^p)^{-1}}\varphi^{(iv)}\cdot\mathbf{L}^p - \partial_{\boldsymbol{\alpha}}\varphi^{(iv)}\cdot\dot{\boldsymbol{\alpha}} \geq 0.\end{aligned} \tag{6.96}$$

Here we replaced $\dot{\mathbf{F}}^p$ and $\dot{\mathbf{F}}^d$ by $\mathbf{L}^p\mathbf{F}^p$ and $\mathbf{L}^d\mathbf{F}^d$, respectively.

If the virtual rate of appropriate fields has been also introduced, the formula (6.95) follows from (6.96).

Theorem *The following thermodynamic restrictions are provided from the free energy imbalance:*

I. *The free energy density is potential for the Cauchy stress tensor*

$$\frac{\mathbf{T}}{\rho} = 2\hat{\mathbf{F}}\partial_{\bar{\mathbf{C}}}\varphi^{(e)}(\hat{\mathbf{F}})^T \quad \text{or} \quad \frac{\bar{\mathbf{T}}}{\rho^p} = 2\,\partial_{\bar{\mathbf{C}}}\hat{\varphi}^e, \tag{6.97}$$

with the notation $\bar{\mathbf{C}} \equiv \hat{\mathbf{C}} - \mathbf{C}^d$, *if the free energy density is written under the form* (6.86).

II. *The residual dissipation inequality becomes*

$$\left\{\mathbf{C}^d\frac{\bar{\mathbf{T}}}{\rho^p}-(\mathbf{F}^d)^T\partial_{\mathbf{F}^d}\varphi^{(iv)}\right\}\cdot\tilde{\mathbf{I}}^d+ \\ +\left\{\hat{\mathbf{C}}\frac{\bar{\mathbf{T}}}{\rho^p}+\mathbf{F}^{p-T}\partial_{(\mathbf{F}^p)^{-1}}\varphi^{(iv)}\right\}\cdot\tilde{\mathbf{L}}^p-\partial_{\boldsymbol{\alpha}}\varphi^{(iv)}\cdot\underline{\boldsymbol{\alpha}}\geq 0. \tag{6.98}$$

Here $\mathbf{l}^d=(\mathbf{F}^d)^{-1}\dot{\mathbf{F}}^d$ *is the rate of damage tensor relative to the stress free and undamaged configuration.*

Proof Let us consider that during the deformation process with arbitrarily given $\tilde{\mathbf{L}}$, no evolution of irreversible behaviour occurs, i.e. $\tilde{\mathbf{L}}^p=0,\quad \tilde{\mathbf{L}}^d=0$ and $\dot{\tilde{\boldsymbol{\alpha}}}=0$. Then the elastic type restriction (6.97) on the constitutive function follows from (6.96). When we replace (6.97) and the rate of damage $\mathbf{l}^d$ in (6.95) the dissipation inequality (6.98) follows.

We introduce the assumption that the viscoplastic type constitutive equations characterize the irreversible behaviour of the elasto-plastic material coupled with damage. The expressions of viscoplastic constitutive equations are suggested by the reduced dissipation inequality (6.98).

Ax. 5. *The evolution equations for plastic part of deformation and damage* are postulated to be given by

$$\lambda_d\tilde{\mathbf{l}}^d=\mathbf{C}^d\frac{\bar{\mathbf{T}}}{\rho^p}-(\mathbf{F}^d)^T\partial_{\mathbf{F}^d}\varphi^{(iv)}, \\ \lambda_p\tilde{\mathbf{L}}^p=\hat{\mathbf{C}}\frac{\bar{\mathbf{T}}}{\rho^p}+\mathbf{F}^{p-T}\partial_{(\mathbf{F}^p)^{-1}}\varphi^{(iv)}, \\ \lambda_a\dot{\boldsymbol{\alpha}}=-\partial_{\boldsymbol{\alpha}}\varphi^{(iv)}. \tag{6.99}$$

Ax. 6. The evolution Eqs. (6.99) are compatible with the reduced dissipative inequality, namely the constitutive functions λ_d, λ_p and λ_a are given to satisfy the inequality

$$\lambda_d\mathbf{L}^d\cdot\mathbf{L}^d+\lambda_p\mathbf{L}^p\cdot\mathbf{L}^p+\lambda_a\dot{\boldsymbol{\alpha}}\cdot\dot{\boldsymbol{\alpha}}\geq 0. \tag{6.100}$$

6.4.4 Constitutive Models

In this model $\mathbf{F}^d$ is a second order invertible tensor, which characterizes the passage from the stress free and undamaged configuration, i.e. a fictitious configuration, which is denoted by $\mathscr{K}$ to the stress free and damaged configuration, say $\tilde{\mathscr{K}}$.

- The elastic type constitutive equation gives rise either to the Cauchy stress tensor or to the Piola-Kirchhoff stress tensor (effective stress) by

$$\mathbf{T} = \rho\hat{\mathbf{F}}\mathbf{h}_{\mathscr{K}}(\hat{\mathbf{C}} - \mathbf{C}^d, \boldsymbol{\alpha})(\hat{\mathbf{F}})^T, \Leftrightarrow \quad \bar{\mathbf{T}} = \rho^p \mathbf{h}_{\mathscr{K}}(\hat{\mathbf{C}} - \mathbf{C}^d, \boldsymbol{\alpha}) \tag{6.101}$$

The elastic type constitutive function can be expressed in terms of the free energy density, following (6.97), by

$$\mathbf{h}_{\mathscr{K}}(\hat{\mathbf{C}} - \mathbf{C}^d, \boldsymbol{\alpha}) \equiv \partial_{\hat{\mathbf{C}}}\varphi^{(e)}(\hat{\mathbf{C}} - \mathbf{C}^d, \boldsymbol{\alpha}). \tag{6.102}$$

- The evolution equation for the plastic part of deformation, written in (6.77) together with the $(6.99)_2$ is characterized by

$$\dot{\mathbf{F}}^p(\mathbf{F}^p)^{-1} = \mu_1\left(\hat{\mathbf{C}}\frac{\bar{\mathbf{T}}}{\rho^p} + \mathbf{F}^{p-T}\partial_{(\mathbf{F}^p)^{-1}}\varphi^{(iv)}\right), \quad \mu_1 = \frac{1}{\lambda_p} \tag{6.103}$$

- The evolution equation for the damage tensor, written in (6.80) together with $(6.99)_1$ is characterized by

$$(\mathbf{F}^d)^{-1}\dot{\mathbf{F}}^d = \mu_2\left(\mathbf{C}^d\frac{\bar{\mathbf{T}}}{\rho^p} - (\mathbf{F}^d)^T\partial_{\mathbf{F}^d}\varphi^{(iv)}\right), \quad \mu_2 = \frac{1}{\lambda_d}. \tag{6.104}$$

- The evolution equation for hardening variables $\boldsymbol{\alpha}$ is given by (6.99)

$$\dot{\boldsymbol{\alpha}} = -\mu_3\partial_{\boldsymbol{\alpha}}\varphi^{(iv)}, \quad \mu_3 = \frac{1}{\lambda_a} \tag{6.105}$$

Finally, we consider the **model with isotropic damage**, as a particular case of the previously presented model. The damage tensor is reduced to

$$\mathbf{F}^d = \kappa\mathbf{R}^d, \quad \mathbf{R}^d \in Orth, \quad \kappa = 1 - d. \tag{6.106}$$

The multiplicative decomposition of the deformation gradient is reduced to $\mathbf{F} = \mathbf{F}^e\mathbf{F}^p$. The scalar damage variable is viewed as a scalar internal variable, that variation in time being described by the specific evolution equation. The tensors $\mathbf{C}^d$ and $\hat{\mathbf{F}}$, defined by $(6.70)_3$ and $(6.65)_2$, result

$$\mathbf{C}^d = \kappa^2\,\mathbf{I} \quad , \quad \hat{\mathbf{F}} = \kappa\mathbf{F}^e(\mathbf{R}^d). \tag{6.107}$$

We use the polar decomposition of the elastic part of the deformation gradient, $\mathbf{F}^e = \mathbf{V}^e\,\mathbf{R}^e$, where $\mathbf{R}^e \in Orth$.

Proposition *There exists a stress free and undamaged configuration associated to* $\tilde{\mathscr{K}}$, *which can be characterized in term of* $\hat{\mathbf{F}} = \kappa \mathbf{V}^e$, *where* $\mathbf{V}^e \in Sym$, *representing the left hand side, elastic stretch Cauchy-Green tensor.*

- The elastic type constitutive equation in terms either of the Cauchy stress tensor or of the Piola-Kirchoff stress tensor (effective stress) is expressed by the free energy density, following (6.97)

$$\begin{aligned} &\mathbf{T} = \rho \hat{\mathbf{F}} \partial_{\mathbf{C}^e} \varphi^{(e)}(\kappa^2(\mathbf{C}^e - \mathbf{I}), \boldsymbol{\alpha})(\hat{\mathbf{F}})^T, \quad \text{equivalently} \\ &\bar{\mathbf{T}} = \rho^p \partial_{\mathbf{C}^e} \varphi^{(e)}(\kappa^2(\mathbf{C}^e - \mathbf{I}), \boldsymbol{\alpha}) \end{aligned} \tag{6.108}$$

- The evolution equation for the plastic part of deformation, written in (6.77) is characterized by

$$\dot{\mathbf{F}}^p(\mathbf{F}^p)^{-1} = \mu_1 \partial_{\mathbf{C}^e} \varphi^{(e)} \left(\mathbf{C}^e \frac{\bar{\mathbf{T}}}{\rho^p} + \mathbf{F}^{p-T} \partial_{(\mathbf{F}^p)^{-1}} \varphi^{(iv)} \right). \tag{6.109}$$

- The evolution equation for the damage tensor, written in (6.80) is characterized by

$$\dot{\kappa} = \mu_2 \kappa^2 \left(\kappa tr \left(\frac{\bar{\mathbf{T}}}{\rho^p} \right) - tr(\partial_{\mathbf{F}^d} \varphi^{(iv)}) \right). \tag{6.110}$$

- The evolution equation for hardening variables is given by

$$\dot{\boldsymbol{\alpha}} = -\mu_3 \partial_{\boldsymbol{\alpha}} \varphi^{(iv)}. \tag{6.111}$$

6.5 Models with Non-metric Property

We present here some ideas that can be found in the paper by Cleja-Ţigoiu and Ţigoiu (2013), that require further development. The behaviour of elasto-plastic materials with damaged microstructure is described in terms of specific differential geometry elements which characterize the internal mechanical state, following Kröner (1992), de Wit (1981). In the proposed elasto-plastic models the defects of lattice structure, like dislocations and disclinations, can be involved through the Cartan torsion of the so-called plastic connection, see Cleja-Ţigoiu (2007, 2010, 2014).

The point defects, microvoids and microcracks in the damaged zone are modeled in terms of the *non-metric tensor which belongs to the plastic connection*, apart from Cleja-Ţigoiu and Ţigoiu (2011) where the gradient of the elastic strain measures the damage. The non-metric property of the plastic connection is

described in terms of a symmetric second order tensor, $\mathbf{h}^d$, which is potential for the non-metric (extra-matter) tensor **Q.** The symmetric second order tensor $\mathbf{h}^d$, is called here the *damage tensor.*

6.5.1 Constitutive Hypotheses

We present here the basic ideas developed within the finite elasto-plasticity with second order deformations provided by Cleja-Ţigoiu (2007, 2010), Cleja-Ţigoiu and Ţigoiu (2013).

Let us consider the function χ which defines the motion of the body, $\mathscr{B}$. The deformation gradient associated with the motion is defined by $\mathbf{F} = \nabla\chi$ and the expression of the second order gradient of the motion χ, pulled back to the reference configuration is given by $(\mathbf{F})^{-1}\nabla\mathbf{F}$, and is denoted by $\boldsymbol{\Gamma}$, namely $\boldsymbol{\Gamma} = (\mathbf{F})^{-1}\nabla\mathbf{F}$. Here $\nabla\mathbf{F}$ and $\boldsymbol{\Gamma}$ are represented as third order fields in a certain coordinate system.

Hypotheses The plastic behaviour is characterized in terms of the pair $(\mathbf{F}^p, \overset{(\mathrm{p})}{\boldsymbol{\Gamma}})$, whose components *are incompatible.*

The second order tensor field $\mathbf{F}^p$, which is called plastic distortion, or the plastic part of the deformation gradient, and $\overset{(\mathrm{p})}{\boldsymbol{\Gamma}}$ is characterized by a third order field in a curvilinear coordinate system and represents the Christoffel-Riemann coefficient of a connection, called here plastic connection.

Assumptions The plastic distortion does not satisfy the first integrability condition, i.e. *the plastic distorstion is incompatible.* The plastic connection $\overset{(\mathrm{p})}{\boldsymbol{\Gamma}}$ does not satisfy the second integrability condition, i.e. i.e. the plastic connection is incompatible.

We recall the classical results concerning the theorems (in the smooth case).

(First Integrability Theorem) Let $\mathscr{U}$ be a simply connected domain in R^3 and $\mathbf{F} : \mathscr{U} \to Lin$. The following three assertions are equivalent

$$\begin{aligned} &a. \quad \mathbf{F} \text{ is a gradient, which means the existence of a vector field } \mathbf{Z} \text{ such that } \mathbf{F} = \nabla\mathbf{Z};\\ &b. \quad (\nabla\mathbf{F}(\mathbf{x})(\mathbf{u}))\mathbf{v} - (\nabla\mathbf{F}(\mathbf{x})\mathbf{v})\mathbf{u} = 0, \quad \forall\,\mathbf{x} \in \mathscr{U}, \forall\mathbf{u}, \mathbf{v} \in \mathscr{V}\\ &c. \quad (\operatorname{curl}\mathbf{F}(\mathbf{x}))(\mathbf{u} \times \mathbf{v}) = \mathbf{0}, \quad \forall \quad \mathbf{x} \in \mathscr{U}, \forall\mathbf{u}, \mathbf{v}. \end{aligned} \tag{6.112}$$

Definition A connection $\boldsymbol{\Gamma}$ is integrable if there exists a tensor field $\mathbf{F}$ such that the partial differential equation (written in a local representation) is satisfied

$$\boldsymbol{\Gamma} = \mathbf{F}^{-1}\nabla\mathbf{F}, \quad \forall \quad \mathbf{x} \in \mathscr{U}, \tag{6.113}$$

Definition The fourth order Riemann-curvature tensor $\mathscr{R}$, attached to $\boldsymbol{\Gamma}$, is defined by

$$\mathscr{R}(\mathbf{u},\mathbf{v}) = ((\nabla \boldsymbol{\Gamma})\mathbf{u})\mathbf{v} - ((\nabla \boldsymbol{\Gamma})\mathbf{v})\mathbf{u} + (\boldsymbol{\Gamma}\mathbf{u})(\boldsymbol{\Gamma}\mathbf{v}) - (\boldsymbol{\Gamma}\mathbf{v})(\boldsymbol{\Gamma}\mathbf{u}). \tag{6.114}$$

The equation written in definition (6.113) is known as the **second integrability condition**. The following theorem states a relationship between the two definitions.

Theorem *The second integrability condition takes place if the Riemann-curvature tensor $\mathscr{R}$ belonging to $\boldsymbol{\Gamma}$ is vanishing, which means the Frobenius condition holds.*

Three type of configurations are used in the models, namely the reference and the deformed configurations at time t, $\chi(\cdot,t)$, as well as the **so-called damaged (anholonomic) configuration**, generically denoted by $\mathscr{K}$, and which is viewed as the pair $(\mathbf{F}^p, \overset{(\mathrm{p})}{\boldsymbol{\Gamma}})$.

The model is described within the *second order plasticity*, based on the multiplicative decomposition of the deformation gradient $\mathbf{F} = \nabla\chi$ (where the function χ describes the motion of the body) into its elastic and plastic components $\mathbf{F}^e, \mathbf{F}^p$, called *distortions*

$$\mathbf{F} = \mathbf{F}^e\mathbf{F}^p, \tag{6.115}$$

as well as on the rule of the $\boldsymbol{\Gamma} = (\mathbf{F})^{-1}\nabla\mathbf{F}$ motion connection decomposition into its elastic and plastic counterparts, which are defined as it follows

$$\boldsymbol{\Gamma} = (\mathbf{F}^p)^{-1}\overset{(\mathrm{e})}{\boldsymbol{\Gamma}}_{\mathscr{K}}[\mathbf{F}^p,\mathbf{F}^p] + \overset{(\mathrm{p})}{\boldsymbol{\Gamma}}. \tag{6.116}$$

For any third order tensor $\boldsymbol{\Gamma}$, and for any second order tensors, $\mathbf{F}_1, \mathbf{F}_2$, the third order tensor $\boldsymbol{\Gamma}[\mathbf{F}_1,\mathbf{F}_2]$ is defined by

$$(\boldsymbol{\Gamma}[\mathbf{F}_1,\mathbf{F}_2]\mathbf{u})\mathbf{v} = (\boldsymbol{\Gamma}(\mathbf{F}_1\mathbf{u}))\,\mathbf{F}_2\mathbf{v}, \tag{6.117}$$

for all vectors $\mathbf{u}$ and $\mathbf{v}$.

In the formula (6.116) giving rise to the *decomposition of the second order deformation*, the elastic connection with respect to the damaged configuration has been introduced, as a direct consequences of the appropriate relationships between the three order fields, when we pass from the reference configuration to the damaged configuration $\mathscr{K}$ by the plastic distortion $\mathbf{F}^p$,

$$\begin{aligned} &\overset{(\mathrm{e})}{\boldsymbol{\Gamma}}_{\mathscr{K}} = \mathbf{F}^p\,\overset{(\mathrm{e})}{\boldsymbol{\Gamma}}[(\mathbf{F}^p)^{-1},(\mathbf{F}^p)^{-1}], \text{ where} \\ &\overset{(\mathrm{e})}{\boldsymbol{\Gamma}} = \boldsymbol{\Gamma} - \overset{(\mathrm{p})}{\boldsymbol{\Gamma}}. \end{aligned} \tag{6.118}$$

Remark We shortly justify the rationale put down at the composition rule involved in the above formula, following Cross (1973), Wang (1973). The formula (6.116) is a relationships between the second order derivatives for a composition rule written for two applications.

We **assume** that the plastic connection $\overset{(\mathrm{p})}{\boldsymbol{\Gamma}}$ has *non-metric property with respect to the metric tensor* $\mathbf{C}^p = (\mathbf{F}^p)^T\mathbf{F}^p$, apart from the hypothesis adopted by Cleja-Ţigoiu (2007, 2010).

Consequently *there exists* a third order tensor $\mathbf{Q}$, such that $\mathbf{Qu} \in Sym$ and

$$-(\nabla\mathbf{C}^p)\mathbf{u} + (\mathbf{C}^p\overset{(\mathrm{p})}{\boldsymbol{\Gamma}}\mathbf{u})^T + \mathbf{C}^p(\overset{(\mathrm{p})}{\boldsymbol{\Gamma}}\mathbf{u}) = \mathbf{Qu}, \tag{6.119}$$

hold for all vectors $\mathbf{u}$.

The following representation for the plastic connection can be derived, see Cleja-Ţigoiu and Ţigoiu (2013),

$$\overset{(\mathrm{p})}{\boldsymbol{\Gamma}} = \overset{(\mathrm{p})}{\mathscr{A}} + (\mathbf{C}^p)^{-1}(\boldsymbol{\Lambda}\times\mathbf{I} + \tfrac{1}{2}\mathbf{Q}), \quad \overset{(\mathrm{p})}{\mathscr{A}} = (\mathbf{F}^p)^{-1}\nabla\mathbf{F}^p, \tag{6.120}$$

Here the third order tensor field $\boldsymbol{\Lambda}$ is a measure of *disclination*, being defined in such a way to have the equality $((\boldsymbol{\Lambda}\times\mathbf{I})\mathbf{u})\mathbf{v} = (\boldsymbol{\Lambda}\mathbf{u})\times\mathbf{v}$.

$\overset{(\mathrm{p})}{\mathscr{A}}$ defines the so-called *Bilby type plastic connection*.

Following Kröner (1992) we assume the existence of a second order tensor, $\mathbf{h}^d$, which is a potential for the non-metric (extra-matter) tensor $\mathbf{Q}$, namely $\mathbf{Q} = \nabla\mathbf{h}^d$. As a direct property of the above introduced definitions, the plastic metric tensor $\mathbf{C}^p$ is corrected by $\mathbf{h}^d$, to restore the metric property of the plastic connection, i.e.

$$-\nabla(\mathbf{C}^p + \mathbf{h}^d)\mathbf{u} + (\mathbf{C}^p\overset{(\mathrm{p})}{\boldsymbol{\Gamma}}\mathbf{u})^T + \mathbf{C}^p(\overset{(\mathrm{p})}{\boldsymbol{\Gamma}}\mathbf{u}) = 0, \quad \forall \quad \mathbf{u} \in \mathscr{V}. \tag{6.121}$$

Remark The plastic distortion $\mathbf{F}^p$ and the tensorial damage variable $\mathbf{h}^d$ are *incompatible*, which means that they are not the derivative of certain vector fields, see de Wit (1981). The second order torsion tensor, $\mathscr{N}^p$, related to the third order Cartan torsion $\mathbf{S}^p$,

$$\begin{aligned}&(\mathbf{S}^p\tilde{\mathbf{u}})\tilde{\mathbf{v}} = \mathscr{N}^p(\tilde{\mathbf{u}}\times\tilde{\mathbf{v}}), \quad \forall \quad \tilde{\mathbf{u}},\tilde{\mathbf{v}};\\ &\mathscr{N}^p = (\mathbf{F}^p)^{-1}\mathrm{curl}\mathbf{F}^p + (\mathbf{C}^p)^{-1}(\mathrm{curl}\mathbf{h}^d + (\mathrm{tr}\,\boldsymbol{\Lambda})\mathbf{I} - (\boldsymbol{\Lambda})^T)\end{aligned} \tag{6.122}$$

The following *defect fields* have been introduced

$$\begin{array}{lll} \boldsymbol{\alpha} & := (\mathbf{F}^p)^{-1}\mathrm{curl}(\mathbf{F}^p) & \text{dislocation density} \\ \boldsymbol{\alpha}^d & = (\mathbf{C}^p)^{-1}\mathrm{curl}\mathbf{h}^d & \text{damage defect density} \\ \boldsymbol{\alpha}^{\Lambda} & := \mathrm{tr}\,\boldsymbol{\Lambda}\mathbf{I} - (\boldsymbol{\Lambda})^T & \text{disclination density}, \end{array} \tag{6.123}$$

which characterize the incompatibilities existing in the materials, following for instance Kröner (1992) and de Wit (1981).

Remark The *damage defect density* $\boldsymbol{\alpha}^d = (\mathbf{C}^p)^{-1}\mathrm{curl}\mathbf{h}^d$ is not symmetric and contains the plastic metric tensor and the damage tensor $\mathbf{h}^d$. Thus there is a measure of damage explicitly dependent on the plastic distortion.

For the shake of simplicity we do not consider here the disclination among the lattice defect, apart from Cleja-Ţigoiu (2010), Cleja-Ţigoiu (2014), where the influence of the lattice defect modeled by $\boldsymbol{\Lambda}$ has been emphasized.

In the model the damage variable $\mathbf{h}^d$ was defined on the reference configuration, and we introduce the tensorial damage variable $\mathbf{H}$ which is pushed forward to the damaged configuration of $\mathbf{h}^d$. We also define the appropriate gradients of the aforementioned fields, as follows

$$\begin{aligned} \mathbf{H} &= (\mathbf{F}^p)^{-T}\mathbf{h}^d(\mathbf{F}^p)^{-1}, \\ \nabla_{\mathscr{K}}\mathbf{H} &= (\nabla\mathbf{H})(\mathbf{F}^p)^{-1}. \end{aligned} \tag{6.124}$$

6.5.2 Dissipation Postulate

The models are *dissipative* and the constitutive equations for the macro forces as well as the appropriate evolution laws which involves the micro forces are derived to be compatible with the free energy imbalance principle, formulated in Gurtin et al. (2010) and adapted here to involve the internal expanded power during the irreversible (plastic) process coupled with damage, as in Cleja-Ţigoiu (2007), Cleja-Ţigoiu (2010).

Let us denote by $\varphi_{\mathscr{K}}$ the expression of the free energy function with respect to the damaged configuration and by $(\mathscr{P}_{int})_{\mathscr{K}}$ the density of the internal expended power.

Ax. 1. The elasto-plastic behavior of the material is restricted to satisfy in *damaged configuration* the imbalanced free energy condition

$$-\dot{\varphi}_{\mathscr{K}} + (\mathscr{P}_{int})_{\mathscr{K}} \geq 0 \quad \text{for any virtual (isothermic) processes}. \tag{6.125}$$

The model is strongly dependent on the postulated expression for the free energy density, as well as of the postulated form for the virtual internal power in the damaged configuration.

Ax. 2. The *free energy density* function in the damaged configuration is postulated to be dependent on the second order elastic deformation, in terms of $\mathbf{C}^e = (\mathbf{F}^e)^T\mathbf{F}^e$, and to be dependent on the damaged configuration, through the part of second order plastic deformation $((\mathbf{F}^p)^{-1}, \overset{(\mathrm{p})}{\mathscr{A}}_{\mathscr{K}})$

$$\varphi = \varphi_{\mathscr{K}}(\mathbf{C}^e, (\mathbf{F}^p)^{-1}, \overset{(\mathrm{p})}{\mathscr{A}}_{\mathscr{K}}, \mathbf{H}, \nabla_{\mathscr{K}}\mathbf{H}), \tag{6.126}$$

As the tensorial damage variable and its gradient have been introduced among the independent variables in the expression of the free energy density, the power conjugated variables with their rates should be introduced in the expression postulated for the virtual internal power.

Within the constitutive framework developed by Cleja-Ţigoiu (2010) and adapted to the problem which we discuss here and which refers to damage, the free energy imbalance principle can be reformulated taking into account the expression of the *virtual internal power* in $\mathscr{K}$.

$$\begin{aligned}(\mathrm{virt}\mathscr{P}_{int})_{\mathscr{K}} = &\frac{1}{2}\frac{\boldsymbol{\pi}}{\tilde{\rho}}\cdot\delta\mathbf{C}^e + \frac{1}{\tilde{\rho}}\boldsymbol{\mu}_{\mathscr{K}}\cdot((\mathbf{F}^e)^{-1}(\nabla_\chi\mathbf{L}[\mathbf{F}^e,\mathbf{F}^e]) - \nabla_{\mathscr{K}}\mathbf{L}^p)\\ &+\frac{1}{\tilde{\rho}}\boldsymbol{\Upsilon}^p\cdot\tilde{\mathbf{L}}^p + \frac{1}{\tilde{\rho}}\boldsymbol{\mu}^p\cdot\nabla_{\mathscr{K}}\tilde{\mathbf{L}}^p + \frac{1}{\tilde{\rho}}\boldsymbol{\Upsilon}^d\cdot\delta\mathbf{H} + \frac{1}{\tilde{\rho}}\boldsymbol{\mu}^d\cdot\nabla_{\mathscr{K}}\delta\mathbf{H}.\end{aligned} \tag{6.127}$$

$(\boldsymbol{\pi}, \boldsymbol{\mu}_{\mathscr{K}})$ are the macroforces in $\mathscr{K}$, namely Piola-Kirchhoff stress tensor and stress momentum pulled back to the configuration with torsion, $\mathscr{K}$, see Cleja-Ţigoiu (2007). The macroforces in $\mathscr{K}$ are power conjugated to $\dot{\mathbf{C}}^e$ and to the gradient of the velocity gradient in the actual configuration, $\nabla_\chi\mathbf{L}$, pulled back to the configuration $\mathscr{K}$.

$\boldsymbol{\mu}^p, \boldsymbol{\mu}^d$ are *micro stress momenta* (third order tensors) which are conjugated to the gradients of the rate of plastic distortion $\mathbf{L}^p$ and of the rate of $\mathbf{H}$, respectively. The internal virtual power (6.127) is written for any virtual rate of plastic distortion $\tilde{\mathbf{L}}^p$, and any virtual variation of damage tensor, $\delta\mathbf{H}$, and for their gradients $\nabla_{\mathscr{K}}\tilde{\mathbf{L}}^p$ and $\nabla_{\mathscr{K}}\delta\mathbf{H}$, respectively. Based on the following kinematic relationships

$$\dot{\mathbf{C}}^e = 2\,(\mathbf{F}^e)^T\{\mathbf{L}\}^s\mathbf{F}^e - 2\,\{\mathbf{C}^e\mathbf{L}^p\}^s, \quad \text{as} \quad \mathbf{C}^e = (\mathbf{F}^p)^{-T}\mathbf{C}(\mathbf{F}^p)^{-1}, \tag{6.128}$$

which are written in terms of $\mathbf{L}$ and $\mathbf{L}^p$, the virtual variation $\delta\,\mathbf{C}^e$ is derived. To do that, $\mathbf{L}$ and $\mathbf{L}^p$ are replaced by their virtual expression, $\tilde{\mathbf{L}}$ and $\tilde{\mathbf{L}}^p$.

Assuming that during the elasto-plastic process no evolution of plastic distortion and damage is produced when an elastic process is considered, the following statement can be proved.

Proposition *A fist consequence follows from the principle of the free energy imbalance, namely the free energy is potential for the macro force, namely the Cauchy stress is expressed by*

$$\mathbf{T}(\mathbf{x},t) = 2\rho\mathbf{F}^e\partial_{\mathbf{F}^e}\varphi(\mathbf{F}^e)^T. \tag{6.129}$$

Balance Equations for Micro Forces. We mention that the micro forces are power conjugated to the rate of kinematic variables and of their gradients, in the plastic and damage mechanism. They satisfy their own *micro balance equations* in the damaged configuration, $\mathscr{K}$, which are postulated (see Cleja-Ţigoiu (2007), Cleja-Ţigoiu (2010)) to be given by

$$\boldsymbol{\Upsilon}^p = div_{\mathscr{K}}\,(\boldsymbol{\mu}^p - \boldsymbol{\mu}_{\mathscr{K}}) + \tilde{\rho}\,\mathbf{B}^p_m, \quad \boldsymbol{\Upsilon}^d = div_{\mathscr{K}}\,\boldsymbol{\mu}^d + \tilde{\rho}\,\mathbf{B}^d_m \tag{6.130}$$

with the appropriate boundary conditions on $\partial\mathscr{K}(\mathscr{P},t)$. When we pass to the reference configuration the micro balance (6.130) can be written in the following form

$$\begin{aligned} J^p\,\boldsymbol{\Upsilon}^p_{\mathscr{K}} &= div\,(J^p\,(\boldsymbol{\mu}^p - \boldsymbol{\mu}_{\mathscr{K}})(\mathbf{F}^p)^{-T}) + \rho_0\,\mathbf{B}^p_m,\\ J^p\boldsymbol{\Upsilon}^d &= div\,(J^p\,\boldsymbol{\mu}^d(\mathbf{F}^p)^{-T})) + \rho_0\,\mathbf{B}^d_m, \quad J^p = |\det\mathbf{F}^p|. \end{aligned} \tag{6.131}$$

Here $\mathbf{B}^p_m$ and $\mathbf{B}^d_m$ are the mass density forces associated with the plastic and damage mechanism.

The balance equation *for macro force, i.e. the Cauchy stress tensor*, is reduced to the classical balance equation $\operatorname{div}\mathbf{T} + \rho\mathbf{b} = 0$.

6.5.3 Constitutive and Evolution Equations with Respect to the Reference Configuration

In order to describe the behaviour of the elasto-plastic material with damaged structure, modeled by the tensorial variable $\mathbf{h}^d$ and its gradient $\nabla\mathbf{h}^d$, the form of the free energy density could be postulated directly with respect to the reference configuration,

The free energy in $\mathscr{K}$ can be expressed in a *pulled back* to the reference configuration form

$$\varphi = \bar{\varphi}(\mathbf{C}, \mathbf{F}^p, \overset{(\mathrm{p})}{\mathscr{A}}, \mathbf{h}^d, \nabla \mathbf{h}^d) \tag{6.132}$$

taking into account the appropriate relationships between the fields when we pass from the damaged configuration $\mathscr{K}$ to the reference configuration by $(\mathbf{F}^p)^{-1}$.

The free energy density is assumed to be dependent on $\mathbf{h}^d$, and its gradient, namely the non-metric (extra-matter) tensor $\mathbf{Q}$.

We develop the kinematic of the process which leads to the evolution equations which prescribe $\dot{\mathbf{h}}^d$, and

$$\mathbf{l}^p = \left(\frac{d}{dt}(\mathbf{F}^p)^{-1}\right)\mathbf{F}^p = -(\mathbf{F}^p)^{-1}\mathbf{L}^p\mathbf{F}^p \tag{6.133}$$

when the dissipation inequality is also revised.

First we proceed to directly reformulate the imbalanced form of the free energy principle with respect to the reference configuration, taking into account the following expression of the internal power, namely

$$\begin{aligned}(\mathscr{P}_{int})_{\mathscr{K}} = &\frac{1}{2}\frac{\boldsymbol{\pi}}{\tilde{\rho}} \cdot \dot{\mathbf{C}}^e + \frac{1}{\tilde{\rho}}\boldsymbol{\mu}_{\mathscr{K}} \cdot ((\mathbf{F}^e)^{-1}(\nabla_\chi \mathbf{L}[\mathbf{F}^e, \mathbf{F}^e]) - \nabla_{\mathscr{K}}\mathbf{L}^p) + \\ &+ \frac{1}{\tilde{\rho}}\boldsymbol{\Upsilon}^p \cdot \mathbf{L}^p + \frac{1}{\tilde{\rho}}\boldsymbol{\mu}^p \cdot \nabla_{\mathscr{K}}\mathbf{L}^p + \frac{1}{\tilde{\rho}}\boldsymbol{\Upsilon}^d \cdot \frac{D}{Dt}\mathbf{H} + \frac{1}{\tilde{\rho}}\boldsymbol{\mu}^d \cdot \nabla_{\mathscr{K}}\frac{D}{Dt}\mathbf{H}.\end{aligned} \tag{6.134}$$

Second, we compute the time derivative of the free energy density function taking into account the derivative formulae for the appropriate fields.

- $\delta\mathbf{H}$ which is involved in the expression of the virtual internal power, (6.127), is defined to be the rate of $\mathbf{h}^d$ pushed away to the configuration $\mathscr{K}$, namely

$$\tfrac{D}{Dt}(\mathbf{H}) = (\mathbf{F}^p)^{-T}\dot{\mathbf{h}}^d(\mathbf{F}^p)^{-1}, \tag{6.135}$$

- The gradient with respect to $\mathscr{K}$ applied to the previous rate, i.e. $\nabla_{\mathscr{K}}\delta\mathbf{H}$, leads to

$$\nabla_{\mathscr{K}}\left(\tfrac{D}{Dt}(\mathbf{H})\right) = (\mathbf{F}^p)^{-T}\{\nabla(\dot{\mathbf{h}}^d) - (\dot{\mathbf{h}}^{d\,(\mathrm{p})}\mathscr{A}) - (\dot{\mathbf{h}}^{d\,(\mathrm{p})}\mathscr{A})^T\}[(\mathbf{F}^p)^{-1}, (\mathbf{F}^p)^{-1}], \tag{6.136}$$

  where the transpose of the third order tensor field $\mathscr{N}$ is given by $\mathscr{N}^T\mathbf{u} = (\mathscr{N}\mathbf{u})^T$, for any $\mathbf{u}$.
- The rate of the appropriate fields which enter the expression of the internal power associated to the processes is calculated in terms of $\mathbf{l}^p$ as given by the formulae

$$\begin{aligned}
&\dot{\mathbf{C}}^e = (\mathbf{F}^p)^{-T}\{\dot{\mathbf{C}} + \mathbf{C}\mathbf{l}^p + (\mathbf{l}^p)^T\mathbf{C}\}(\mathbf{F}^p)^{-1}\\
&\nabla_{\mathscr{K}}\mathbf{L}^p = -\mathbf{F}^p\{\nabla\mathbf{l}^p + \overset{(\mathrm{p})}{\mathscr{A}}[\mathbf{I},\mathbf{l}^p] - \mathbf{l}^p\overset{(\mathrm{p})}{\mathscr{A}}\}[(\mathbf{F}^p)^{-1},(\mathbf{F}^p)^{-1}],\\
&\left(\frac{d}{dt}(\overset{(\mathrm{p})}{\mathscr{A}})\right) = -\nabla\mathbf{l}^p + \mathbf{l}^p\overset{(\mathrm{p})}{\mathscr{A}} - \overset{(\mathrm{p})}{\mathscr{A}}[\mathbf{I},\mathbf{l}^p].
\end{aligned} \tag{6.137}$$

Second, we introduce the new appropriate measures for the forces which enter the reformulated expression for the principle of the imbalanced free energy when we passed from the damaged configuration to the reference one, namely

$$\begin{aligned}
&\frac{\mathbf{m}_0^d}{\rho_0} = \frac{1}{\tilde{\rho}}(\mathbf{F}^p)^{-1}\boldsymbol{\mu}^d[(\mathbf{F}^p)^{-T},(\mathbf{F}^p)^{-T}], \quad \frac{\mathbf{m}_0^p}{\rho_0} = \frac{1}{\tilde{\rho}}(\mathbf{F}^p)^T\boldsymbol{\mu}^p[(\mathbf{F}^p)^{-T},(\mathbf{F}^p)^{-T}]\\
&\frac{\boldsymbol{\Upsilon}_0^p}{\rho_0} = (\mathbf{F}^p)^{-1}\frac{1}{\tilde{\rho}}\boldsymbol{\Upsilon}^d(\mathbf{F}^p)^{-T}, \quad \frac{\boldsymbol{\Upsilon}_0^p}{\rho_0} = (\mathbf{F}^p)^T\frac{1}{\tilde{\rho}}\boldsymbol{\Upsilon}^p(\mathbf{F}^p)^{-T},\\
&\boldsymbol{\Sigma}_0 = \mathbf{C}\boldsymbol{\pi}_0, \quad \frac{\boldsymbol{\pi}_0}{\rho_0} = (\mathbf{F}^p)^{-1}\frac{1}{\tilde{\rho}}\boldsymbol{\pi}(\mathbf{F}^p)^{-T},
\end{aligned} \tag{6.138}$$

where $\boldsymbol{\Sigma}_0$ and $\boldsymbol{\pi}_0$ denote Mandel stress measure and Piola-Kirchhoff stress tensor, respectively, with respect to the reference configuration.

As a consequence of the formulated dissipated postulate the expression for the macro forces is derived.

- We introduce micro stress momenta associated with the damage and dislocations by the non-dissipative (energetic) constitutive relations, the so-called *energetic micro forces*

$$\tfrac{1}{\rho_0}\mathbf{m}_0^d = \partial_{\nabla\mathbf{h}^d}\varphi, \quad \tfrac{1}{\rho_0}\mathbf{m}_0^p = \partial_{\overset{(\mathrm{p})}{\mathscr{A}}}\varphi. \tag{6.139}$$

- The rates of the plastic distorsion and of the quasi-plastic strain, $\mathbf{F}^p$ and $\mathbf{h}^d$, and the constitutive functions have to be *compatible with the dissipation inequality*, and they are postulated as follows

$$\begin{aligned}
&\frac{1}{\rho_0}(\boldsymbol{\Sigma}_0 - \boldsymbol{\Upsilon}_0^p) + (\mathbf{F}^p)^T\partial_{\mathbf{F}^p}\varphi = \xi_1\,\mathbf{l}^p,\\
&\frac{1}{\rho_0}(\boldsymbol{\Upsilon}_0^d - \partial_{\mathbf{h}^d}\varphi) - 2\{\partial_{\nabla\mathbf{h}^d}\varphi\odot\overset{(\mathrm{p})}{\mathscr{A}}\}^S = \xi_2\,\dot{\mathbf{h}}^d,
\end{aligned} \tag{6.140}$$

where the operator $\odot$ associates to the third order tensors $\mathscr{A}$ and $\mathscr{B}$ the second order tensor, denoted $\mathscr{A}\odot\mathscr{B}$ and defined by

$$(\mathscr{A}\odot\mathscr{B})\cdot\mathbf{L}=\mathscr{A}[\mathbf{I},\mathbf{L}]\cdot\mathscr{B}=\mathscr{A}_{isk}L_{sn}\mathscr{B}_{ink}, \tag{6.141}$$

for all second order tensor $\mathbf{L}$.

The micro forces are eliminated from the evolution equations for plastic deformation and damage tensor, $\mathbf{h}^d$ via their own balance equations. The non-local evolution equations can be either associated for instance with an appropriate yield function in terms of effective stress and damage back stress tensor, or described as the viscoplastic ones.

The rate independent elasto-plastic model with anisotropic damage can be derived as it follows:

- The scalar constitutive functions ξ_1,ξ_2 are defined in such a way to be compatible with the dissipation inequality

$$\xi_1\,\mathbf{l}^p\cdot\mathbf{l}^p+\xi_2\,\dot{\mathbf{h}}^d\cdot\dot{\mathbf{h}}^d\geq 0. \tag{6.142}$$

Let us introduce *internal variables like stress*

1. the *back stress*, denoted by $\boldsymbol{\Sigma}_{back}$, which is introduced in order to describe the hardening of the material,

$$\boldsymbol{\Sigma}_{back}:=\boldsymbol{\Upsilon}_0^p-\rho_0(\mathbf{F}^p)^T\partial_{\mathbf{F}^p}\varphi \tag{6.143}$$

2. the *damage stress* variable

$$\mathbf{b}:=\boldsymbol{\Upsilon}_0^d-\rho_0\partial_{\mathbf{h}^d}\varphi-2\rho_0\{\partial_{\nabla\mathbf{h}^d}\varphi\odot\overset{(\mathrm{p})}{\mathscr{A}}\}^S. \tag{6.144}$$

When the micro forces are eliminated via the micro balance Eq. (6.131) together with the energetic representation for micro stress momenta (6.139) the following expressions are provided for the back stress and damage stress

$$\begin{aligned}\boldsymbol{\Sigma}_{back}&=\frac{1}{J^p}\mathrm{div}(\rho_0\mathbf{F}^p\partial_{\overset{(\mathrm{p})}{\mathscr{A}}}\varphi[\mathbf{I},(\mathbf{F}^p)^T]))-\rho_0(\mathbf{F}^p)^T\partial_{\mathbf{F}^p}\varphi,\\ \mathbf{b}&:=-\rho_0\partial_{\mathbf{h}}\varphi+\frac{1}{J^p}\mathrm{div}(\rho_0\mathbf{F}^p\partial_{\nabla\mathbf{h}}\varphi)[\mathbf{I},(\mathbf{F}^p)^T].\end{aligned} \tag{6.145}$$

As a consequence of the micro balance equations together with the energetic definitions for the micro stress momenta the reduced dissipation inequality referring to the *irreversible behavior coupled with damage* can be derived under the form

$$(\boldsymbol{\Sigma}_0-\boldsymbol{\Sigma}_{back})\cdot\mathbf{l}^p+\mathbf{b}\cdot\dot{\mathbf{h}}^d\geq 0. \tag{6.146}$$

We introduce the rate-independent model, following the idea proposed by Grudmundson (2004), which is in the sprit of classical plasticity.

In terms of *effective fields* we introduce a *convex function* with respect to its arguments, say for instance like in classical plasticity, namely

$$\hat{\Psi} := \sqrt{|\boldsymbol{\Sigma}_0 - \boldsymbol{\Sigma}_{back}|^2 + |\mathrm{b}|^2}, \tag{6.147}$$

and a yield function

$$\hat{\mathscr{F}} := \hat{\Psi} - R(\zeta), \quad \text{with} \quad R(\zeta) > 0, \quad R'(\zeta) > 0, \quad R(0) = k > 0, \tag{6.148}$$

with R a scalar constitutive function dependent on the scalar hardening variable of the deformation type, say ζ, which has to be introduced by a differential type equation.

The relationships (6.140) will be viewed as evolution equations to describe the rates of plastic distortion, through $\mathbf{l}^p$, and for the scalar dislocation density $\frac{d}{dt}\rho^d$, namely

$$\begin{aligned} \mathbf{l}^p &:= \lambda \frac{\Sigma_0 - \Sigma_{back}}{R(\zeta)} \mathscr{H}(\hat{\mathscr{F}}), \\ \frac{d}{dt}\mathbf{h} &:= \lambda \frac{\mathrm{b}}{R(\zeta)} \mathscr{H}(\hat{\mathscr{F}}), \\ \dot{\zeta} &:= \lambda \mathscr{H}(\hat{\mathscr{F}}), \end{aligned} \tag{6.149}$$

λ has the role of plastic multiplier and satisfies Kuhn-Tucker and consistency condition.

6.5.4 Model Proposed by Aslan et al. (2011)

We make references to the class of anisotropic elasto-viscoplastic micromorphic media which was provided by Aslan et al. (2011), within the constitutive framework of finite deformation, based on the multiplicative decomposition. The degrees of freedom of the proposed model are the displacement vector $\mathbf{u}$ and the *micro deformation variable* $\hat{\chi}^p$, which is generally a *non-symmetric second order tensor*.

The *relative deformation tensor*, denoted by $\mathbf{e}^p$, is defined by

$$\mathbf{e}^p = (\mathbf{F}^p)^{-1}\hat{\chi}^p - \mathbf{I}, \tag{6.150}$$

and measures the departure of the micro deformation from the plastic distortion as

$$\mathbf{e}^p = 0, \quad \text{if and only if} \quad \hat{\chi}^p = \mathbf{F}^p. \tag{6.151}$$

We remark that $\mathbf{e}^p$ is a second order tensor defined on the reference configuration and $\hat{\chi}^p$ is defined on the reference configuration with the value in the intermediate configuration.

The *gradient of the set of degrees of freedom*

$$(\mathbf{F}, \mathbf{K}), \quad \mathbf{F} = \mathbf{I} + \nabla \mathbf{u}, \quad \mathbf{K} = \text{Curl}\hat{\chi}^p. \tag{6.152}$$

The state variables are introduced by the set the following fields

$$\left(\mathbf{E}^e \equiv \frac{1}{2}((\mathbf{F}^e)^T\mathbf{F}^e - \mathbf{I}), \mathbf{e}^p, \mathbf{K}, \boldsymbol{\alpha}\right). \tag{6.153}$$

The free energy density function φ is assumed to be dependent on the state variables

$$\varphi = \varphi(\mathbf{E}^e, \mathbf{e}^p, \mathbf{K}, \boldsymbol{\alpha}). \tag{6.154}$$

The internal power density is introduced by the following expression

$$p^{(i)} = \boldsymbol{\sigma} \cdot \mathbf{L} + \mathrm{s} \cdot \dot{\hat{\chi}}^p + \mathbf{M} \cdot \text{Curl}\, \dot{\hat{\chi}}^p, \tag{6.155}$$

where $(\boldsymbol{\sigma}, \mathbf{s}, \mathbf{M})$ denote stress-like fields which are power conjugated to the velocity gradient, rate of microdeformation, $\dot{\hat{\chi}}^p$ and its curl. The consequences that can be derived from the dissipation principle defined by $p^{(i)} - \rho\dot{\varphi} \geq 0$ were investigated by Aslan et al. (2011).

The balance equation for the Cauchy stress, $\boldsymbol{\sigma}$, div $\sigma = 0$, as well as the appropriate balance equation for micro stresses, $Curl\,\mathbf{M} + \mathbf{s} = 0$, have been introduced to be satisfied by the pair of forces $(\mathbf{s}, \mathbf{M})$, which are power conjugated to $\dot{\hat{\chi}}$ and $Curl\,\dot{\hat{\chi}}$, respectively.

Conclusions. Certain *similarities* can be established between the model (Aslan et al. 2011) and the models with non-metric property.

a. $(\mathbf{F}, \mathbf{K})$ and $(\mathbf{F}^p, \overset{(\mathrm{p})}{\boldsymbol{\Gamma}})$ describe the second order effect;
b. $\mathbf{e}^p$ and $\mathbf{h}^d$ are anisotropic second order damage tensors;
c. The appropriate balance equations have been formulated for *micro forces*;
d. The specific dissipation inequalities characterize the dissipative nature of plastic deformation and damage.

The physical motivation and mathematical description of the damage are completely different. $\mathbf{e}^p$ *measures the discrepancy* between the micro deformation and the plastic distortions, while $\mathbf{h}^d$ *characterizes the lost of the metricity* of the geometrical structure, as a consequence of the existence of microvoids and microcracks. No evolution equation has been introduced in Aslan et al. (2011) for the micro deformation or for the relative deformation tensor. In the model with non-metric property the evolution equation for the tensorial damage variable is coupled with the evolution equation for plastic distortion.

6.6 Conclusion

In the models proposed in this chapter, the key point is the presence of the tensorial variables which describe the anisotropic damage connected to the large plastic deformation. The physical nature and the mathematical description of the damage variables are related to the presence of the microcracks and microvoids, developed at the microstructural level. We pay attention to the configurations on which the tensor fields are defined to avoid the confusions which appear when this mention is missing.

The model presented in Sect. 6.4 is based on the fictitious undamaged and stress free configuration and on the existence of the second order tensor, $\mathbf{F}^d$ which realizes the passage from this configuration to the damaged and stress free configuration. Only one type of undamaged configuration has been necessary to develop the proposed model, like in Ekh et al. (2004). Contrary to Menzel et al. (Ekh et al. 2004) the damage anisotropic tensor $\mathbf{F}^d$ is involved in the gradient deformation multiplicative decomposition, and the plastic distortion $\mathbf{F}^p$ describes the passage from the reference configuration to the undamaged and stress free configuration. The damage tensor field $\mathbf{F}^d$ is not symmetric, as it is considered by Brünig (2003), Murakami (1988). The composed tensor $\mathbf{F}^d\mathbf{F}^p$ characterizes damage and plastic coupled effect, when the passage from the reference configuration to the damaged stress free configuration occurs.

In the model proposed in Sect. 6.5 we defined the damage tensor to be the second order symmetric tensor field $\mathbf{h}^d$, which characterizes a measure of *non-metric property* for the geometry of elasto-plastic material with damaged structure. The rationale of our choice is motivated by the fact that the local metric property of the material with crystalline structure is lost in the material with damaged microstructure. The symmetric tensor field $\mathbf{h}^d$, which is not a metric tensor, restores the metricity of the so-called plastic connection, with respect to the reference configuration. In the two models the evolution equations for the plastic distortion and tensorial damage variable are derived to be compatible with the appropriate dissipation principle, the classical one for the first model and the free energy imbalance principle for the second one.

References

Aslan O, Coedero NM, Gaubert A, Forest S (2011) Micromorphic approach to single crystal plasticity damage. Int J Eng Sci 49:1311–1325

Bai Y, Wierzbicki T (2008) A new model of metal plasticity and fracture with pressure and Lode dependence. Int J Plast 24:1071–1096

Bao Y, Wierzbicki T (2004) On the fracture locus in the equivalent strain and stress triaxiality space. Int J Mech Sci 46:81–98

Bao Y, Wierzbicki T (2005) On the cut-off value of negative triaxiality for fracture. Eng Fract Mech 72:1049–1069

Brünig M (2003) An anisotropic ductile damage model based on irreversible thermodynamics. Int J Plast 19:1679–1713

Brünig M, Ricci S (2005) Nonlocal continuum theory of anisotropically damaged metals. Int J Plast 21:1346–1382

Brünig M, Chyra O, Albrecht D, Driemeier L, Alves M (2008) A ductile damage criterion at various stress triaxialities. Int J Plast 24:1731–1755

Brünig M, Gerke S, Hagenbrock V (2013) Micro-mechanical studies on the effect of the triaxiality and the Lode parameter on ductile damage. Int J Plast 50:49–65

Cleja-Tigoiu S (2011) Elasto-plastic model with second order defect density tensor. In: AIP conference proceedings, vol 1353, pp 1505–1510. doi:10.1063/1.3589730

Cleja-Ţigoiu S (1990) Large elasto-plastic deformations of materials with relaxed configurations-I: constitutive assumptions, II: role of the complementary plastic factor. Int J Eng Sci 28(171–180):273–284

Cleja-Ţigoiu S (2002) Couple stresses and non-Riemannian plastic connection in finite elasto-plasticity. Z Angew Math Phys 53:996–1013

Cleja-Ţigoiu S (2007) Material forces in finite elasto-plasticity with continuously distributed dislocations. Int J Fract 147:67–81

Cleja-Ţigoiu S (2010) Elasto-plastic materials with lattice defects modeled by second order deformations with non-zero curvature. Int J Fract 166:61–75

Cleja-Ţigoiu S (2014) Dislocations and disclinations: continuously distributed defects in elasto-plastic crystalline materials. Arch Appl Mech 84:1293–1306

Cleja-Ţigoiu S, Paşcan R (2014) Slip systems and flow patterns in viscoplastic metallic sheets with dislocations. Int J Plast 61:64–93

Cleja-Ţigoiu S, Soós E (1990) Elastoplastic models with relaxed configurations and internal state variables. Appl Mech Rev 43:131–151

Cleja-Ţigoiu S, Ţigoiu V (2011) Strain gradient effect in finite elasto-plastic damaged materials. Int J Damage Mech 20:484–514

Cleja-Ţigoiu S, Ţigoiu V (2013) Modeling anisotropic damage in elasto-plastic materials with structural defects. In: Oñate E, Owen DRJ, Peric D, Suarez B (eds) Computational plasticity XII: fundamentals and aplications. CIMNE, Barcelona, pp 453–463

Cross JJ (1973) Mixtures of fluids and isotropic solids. Arch Mech 25:1025–1039

de Borst R, Pamin J, Geers M (1999) On coupled gradient-dependent plasticity and damage theories with a view to localization analysis. Eur J Mech A-Solids 18:939–962

de Souza Neto EA, Perić D, Owen DRJ (2008) Computational methods for plasticity: theory and applications. Wiley

de Wit R (1981) A view of the relation between the continuum theory of lattice defects and non-Euclidean geometry in the linear approximation. Int J Eng Sci 19:1475–1506

Ekh M, Lillbacka R, Runesson K (2004) A model framework for anisotropic damage coupled to crystal (visco)plasticity. Int J Plast 20:2143–2159

Ekh M, Lillbacka R, Runesson K, Steinmann P (2005) A framework for multiplicative elastoplasticity with kinematic hardening coupled to anisotropic damage. Int J Plast 21:397–434

Grudmundson P (2004) A unified treatment of strain gradient plasticity. J Mech Phys Solids 52:1379–1406

Gurson AL (1977) Continuum theory of ductile rupture by voids nucleation and growth-Part I. Yield criteria and flow rules for porous ductile media. J Eng Mater-T ASME 99:2–15
Gurtin ME (2002) A gradient theory of single-crystal viscoplasticity that accounts for geometrically necessary dislocations. J Mech Phys Solids 50:5–32
Gurtin ME, Fried E, Anand L (2010) The mechanics and thermodynamics of continua. Cambridge University Press
Kachanov LM (1986) Introduction to continuum damage mechanics. Martinus Nijhoff, Dordrecht
Kröner E (1992) The internal state mechanical state of solids with defects. Int J Solids Struct 29:1849–1857
Lämmer H, Tsakmakis Ch (2000) Discussion of coupled elastoplasticity and damage constitutive equations for small and finite deformations. Int J Plast 16:495–523
Lassance D, Fabrégue D, Delannay F, Pardoen T (2007) Micromechanics of room and high temperature fracture in 6xxx Al alloys. Prog Mater Sci 52:62–129
Lemaitre J (1985) A continuous damage mechanics model for ductile fracture. J Eng Mater-T ASME 107:83–89
Lemaitre J (1992) A course on damage mechanics. Springer-Verlag, Berlin
Lemaitre J, Chaboche JL (1978) Aspect Phénoméde la Rupture par Endommangement. J Mech Appl 2:317–365
Lemaitre J, Chaboche JL (1990) Mechanics of solid materials. Cambridge University Press
Lubarda VA, Krajcinovic D (1995) Some fundamental issues in rate theory of damage-elastoplasticity. Int J Plast 11:763–797
Malcher L, Andrade Pires FM, César de Sá JMA (2012) An assessment of isotropic constitutive models for ductile fracture under high and low stress triaxiality. Int J Plast 30–31:81–115
Menzel A, Steinmann P (2003) Geometrically nonlinear anisotropic inelasticity based on the fictitious configurations: application to the coupling of continuum damage and multiplicative elasto-plasticity. Int J Numer Meth Eng 56:2233–2266
Menzel A, Ekh M, Steinmann P, Runesson K (2002) Anisotropic damage coupled to plasticity: modelling based on the effective configuration concept. Int J Numer Meth Eng 54:1409–1430
Murakami S (1983) Notion of continuum damage mechanics and its application to anisotropic creep damage theory. J Eng Mater-T ASME 105:99–105
Murakami S (1988) Mechanical modeling of material damage. J Appl Mech 55:280–286
Murakami S, Imaizumi T (1982) Mechanical description of creep damage state and its experimental verification. J Mec Theor Appl 1:743–761
Murakami S, Ohno N (1980) A continuum theory of creep and creep damage. In: Ponter ARS, Hayhurst DR (eds) Creep in structures. IUTAM 8th Symposium, Leicester, UK, pp 422–443
Murakami S, Ohno N (1981) A continuum theory of creep and creep damage. In: Ponter ARS, Hayhurst DR (eds) Creep in structures. Spinger, Berlin, pp 422–444
Nahshon K, Hutchinson JW (2008) Modication of the Gurson model for shear failure. Eur J Mech A-Solids 27:1–17
Rabotnov YN (1969) Creep problems of structural members. North Holland, Amsterdam
Siruguet K, Leblond J-B (2004) Effect of void locking by inclusions upon the plastic behavior of porous ductile solids-I: theoretical modeling and numerical study of void growth. Int J Plast 20:225–254
Tveergard V, Needleman A (1984) Analysis of the cup-cone fracture in a round tensile bar. Acta Metall Mater 32:157–169
Voyiadjis GZ, Kattan, PI (2005) Damage mechanics. Taylor & Francis
Voyiadjis GZ, Park T (1996) Kinematics of damage for the characterization of the onset of macro-crack initiation in metals. Int J Damage Mech 5:68–92
Wang CC (1973) Inhomogeneities in second-grade fluid bodies and isotropic solid bodies. Arch Mech 25:765–780
Xue L (2008) Constitutive modeling of void shearing effect in ductile fracture of porous materials. Eng Fract Mech 75:3343–3366

Chapter 7
Modelling the Portevin-Le Chatelier Effect—A Study on Plastic Instabilities and Pattern Formation

Cristian Făciu

Dedicated to Academician Nicolae Cristescu on the occasion of his 87th birthday and to the 150th anniversary of the Romanian Academy.

7.1 Introduction

From macroscopic point of view the Portevin-Le Chatelier effect is an oscillatory plastic flow, resulting in inhomogeneous and discontinuous deformation that may be observed in metallic alloys subjected to load-or displacement-controlled experiments in a certain range of strain, strain-rate and temperature. From microscopic point of view the PLC effect is usually explained by a model called dynamic strain ageing (DSA) which characterizes the interaction between moving dislocations and between dislocations and diffusing solute atoms. The concept of DSA, first introduced by Cottrell and Bilby (1949) in the frame of the dislocation theory (see Cottrell 1953), generalized by Louat (1981) and later developed by others (see for instance Rizzi and Hähner 2004 and the references therein) is based on the pinning and unpinning of dislocations by impurity clouds.

In the present work, after reminding the main experimental and physical aspects of this phenomenon we introduce the principal ideas for incorporating the microstructural processes specific to the DSA into the phenomenological constitutive modelling. Our goal is to focus on macroscopic constitutive equations appropriate from the point of view of continuum mechanics. One way to realize this bridge from the microstructural aspects to the macroscopic mechanical behavior

C. Făciu (✉)
Simion Stoilow Institute of Mathematics of the Romanian Academy,
21 Calea Grivitei Street, 010702 Bucharest, Romania
e-mail: Cristian.Faciu@imar.ro
URL: http://www.imar.ro/∼cfaciu

D. Banabic (ed.), *Multiscale Modelling in Sheet Metal Forming*,
ESAFORM Bookseries on Material Forming,
DOI 10.1007/978-3-319-44070-5_7

associated with the PLC instabilities can be achieved by using the theory of flow localization due to the DSA proposed by McCormick (1988). In this framework, we survey the literature related with such macroscopic phenomenological approaches able to describe both the global responses, as observed typically in the stress-strain curves, but also the spontaneous appearance of strain localization.

In Sect. 7.2, following a line developed by Mesarovics (1995), Zhang et al. (2001), Böhlke et al. (2009) we give a detailed description of an elastic-viscoplastic model of McCormick type incorporating DSA and negative strain-rate sensitivity.

Starting from the idea that the PLC effect as well as all phenomena related with strain localization and band propagation are characterized by deformation which is inhomogeneous both in space and time, we consider that the appropriate framework for a phenomenological approach is the *field theory* approach. That means, in order to establish the predictions of a constitutive set of relations we have to add the general law of mechanics, for instance, the balance of momentum, the balance of mass and to investigate the resulting set of partial differential equations (PDEs) for initial-boundary value problems which simulate laboratory experiments.

In order to outline the basic ideas we consider for simplicity in Sect. 7.3 the case of a bar subjected to a one-dimensional stress state. We show that the field theory approach leads in this case to a hyperbolic semilinear PDEs system with source terms. The hyperbolic character of the system is due to the fact that we do not neglect the inertial term in the balance of momentum, although the PLC effect manifests only for strain-rate ranging between $10^{-6}\,s^{-1}$ and $10^{-2}\,s^{-1}$, which usually are considered as static tests.

We accurately formulate initial-boundary value problems corresponding to strain- and stress-controlled tests. Moreover, we do not add as usual a machine equation in order to describe the machine effect, but we formulate in a new way mixed stress- and strain-controlled boundary conditions which include a parameter describing the influence of the testing machine.

A numerical investigation of uniaxial tensile tests is done using an explicit finite difference scheme based on the method of characteristics described in Appendix. It is shown that, without introduction of a geometric defect or other heterogeneity, the PDEs system is able to describe quantitatively the remarkable features of the PLC effect, that is, the staircase response for a soft testing device, the jerky flow for the hard device depending on the imposed strain-rate, but also strain localization phenomena and pattern formation.

In the mathematical framework developed, we consider in Sect. 7.4.1 a spatial homogeneous process in stress, strain and ageing time, as the solution of an ideal initial-boundary value problem. That corresponds to a constant cross-head velocity controlled experiment having a linear distribution of the velocity in the bar at the initial moment. A linear stability analysis of this homogeneous solution allows to determine a critical condition on some material parameters for the PLC effect. Moreover, one determines the range of strain-rates and mechanical parameters for which there exists a jerky flow. One shows that the boundaries of the unstable PLC

domain correspond to a Hopf bifurcation with limit cycle behavior. Section 7.4.2 concerns the calibration and verification of the constitutive model.

7.1.1 Experimental and Physical Aspects

The phenomenon of discontinuous deformation in tensile tests had already been observed in the first part of the 19th century in dead weight tests. By adding successively weights to the end of copper strips, the French physicist Savart (1837) observed that the deformation does not increase continuously, but by sudden jumps, feature known now as "staircase" like stress-strain behavior. He was the first to consider this phenomenon as an intrinsic material property of plastic deformation. More careful and systematic tests have been considered by his student Masson (1841) who performed tests on different alloys at different temperatures. That is way sometimes this phenomenon is referred as Savart–Masson effect (see the historical comments in Bell (1973), Scott et al. (2000), Rizzi and Hähner (2004)). The use of "hard" testing machines, i.e. of strain-controlled experiments, at the beginning of 20th century, had allowed Portevin and Le Chatelier (1923) to investigate in a systematically manner the serrated yielding in aluminium alloys at different elongation rates and to definitively remove a common belief that such irregularities and discontinuous deformation are only a machine-produced effect of little importance. In recognition of their results, starting with the work of Cottrell (1953), this phenomenon of discontinuous deformation of metals, in quasi-static tests, bears their name.

Thus, the PLC effect is an unstable, irregular plastic flow resulting in an inhomogeneous deformation that may be observed in some dilute metallic alloys. These are, for example, steels and aluminium alloys which are important industrial materials used for car bodies, aircraft fuselage and different type of casing. The localized deformation associated with the PLC effect leads to the formation of narrow bands of intense plastic deformation that leaves undesirable traces on the surface of the final product. Moreover, it affects most materials properties *by increasing*: the flow stress, the ultimate tensile strength and the work hardening rate and *by decreasing*: the ductility of metals, the strain-rate sensitivity coefficient and the fracture toughness (see Yilmaz 2011).

From *macroscopic point of view* the PLC effect is characterized by the following aspects. In *constant strain-rate* tensile experiments, i.e. when the end of the test specimen is subjected to a constant velocity motion, the PLC effect appears in certain ranges of temperature and strain-rate and manifests by a discontinuous deformation, which corresponds to serrated stress - strain curves ("jerky flow"). The most distinct feature is the localization of strain in the form of visible bands, apparently moving along the surface of the specimen gauge. The apparition of each strain band corresponds to a burst of plastic activity.

While for most metallic alloys the stress-strain curves obtained in tensile tests moves up when the strain-rate increases, for the alloys which show the PLC effect the reverse phenomenon happens, that is, they move down. This behavior is known

as *negative strain-rate sensitivity* (NSRS) of the flow stress. It is illustrated in Fig. 7.1 where one can see that the highest strength and the highest stress-strain curve is obtained for the lowest strain-rate, i.e. for 6×10^{-4} s^{-1}. As the strain-rate increases to 6×10^{-3} s^{-1} and ultimately to 6×10^{-2} s^{-1} the two stress-strain curves are lower, thereby indicating a negative strain-rate effect. At constant strain-rate, the amplitude of the serrations increases gradually with strain and then finally saturates at large strains. Moreover, the amplitude of serrations decreases with increasing strain-rate.

Experimental observations have shown that different types of serrations correspond to different ways the PLC bands nucleate and move along the specimen leading finally to specific band patterns. These are designated as type A, type B and type C, serrations and correspondingly as type A, type B and type C, PLC bands (see for instance Chihab et al. 1987). They are illustrated in Fig. 7.2. The transition between *band types* or, equivalently, *serration types* may occur upon changes in strain-rate and temperature. Usually, higher strain-rates are associated with type A bands, lower strain-rates with type C bands and intermediate levels with type B bands.

Type C bands nucleate randomly and appear as hopping bands throughout the specimen gauge and the corresponding serrations have a relative constant amplitude and frequency. Type B bands propagate in a gauge in an intermittent manner with approximately equal intervals having amplitudes and frequencies somewhat irregular and smaller than those of a type C curve. Type A bands propagate apparently continuously in a gauge resembling a longitudinal wave (see Ait-Amokhtar and Fressengeas 2010), with arbitrarily located small stress drops embedded in the regular flow in the tensile test curve.

Different optical methods, laser scanning extensometry, infrared thermographic techniques, or digital image correlation methods, (see for instance Chihab et al. 1987; Neuhäuser et al. 2004; Ait-Amokhtar et al. 2008; Benallal et al. 2008a, b;

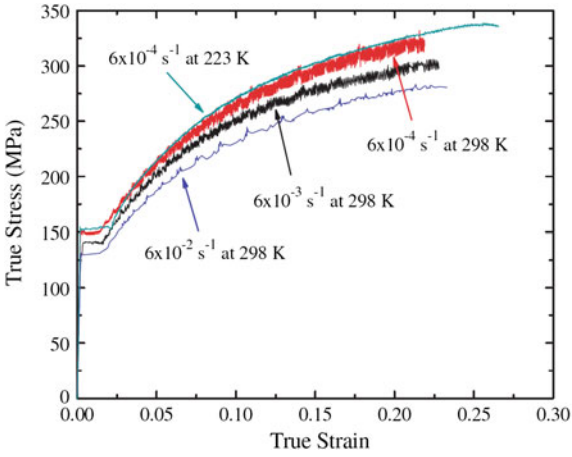

Fig. 7.1 True stress-strain curves of AA5754 alloy at various strain-rates and temperatures (reproduced with permission from Halim et al. 2007 Elsevier Ltd.)

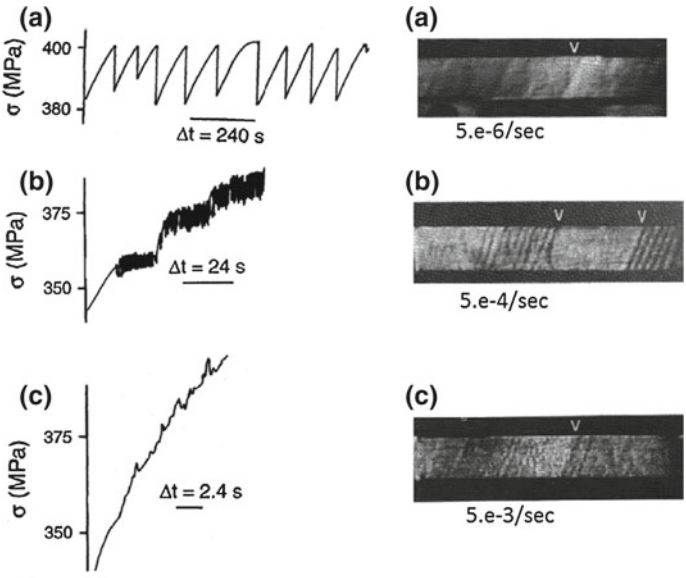

Fig. 7.2 Stress-time curves for an Al–Mg alloy at $T = 300\,^{\circ}\mathrm{K}$ showing the change from type C to type B, and then to type A serrations with increasing strain-rate. **a** Type C; $5 \times 10^{-6}\ \mathrm{s}^{-1}$, **b** type B; $5 \times 10^{-4}\ \mathrm{s}^{-1}$ and **c** type A; $5 \times 10^{-3}\ \mathrm{s}^{-1}$ (reproduced with permission from Chihab et al. (1987) and Yilmaz (2011) Elsevier Ltd.)

Zdunek et al. 2008; Ait-Amokhtar and Fressengeas 2010 and the references therein) have allowed to correlate the spatio-temporal characteristics of the PLC effect with the associated serrations observed in conventional tensile tests.

Thus, if one looks at a zoom of the "saw teeth" stress–strain curve of a constant strain-rate test (see Fig. 7.3) obtained using Digital Image Correlation technique by Zdunek et al. (2008) one observes that it is composed by a rapid stress drop followed by a slow reloading part and this process runs almost cyclically. One notes also that each stress drop accompanies a local dynamic event evidenced by the nucleation of a strain band and the subsequent strain band buildup (see the strain distribution in images 3–4 and 7–8). On the other side, when the stress increases quasistatically there is no strain nucleation and the bands remain unchanged (see the strain distribution in images 1–2 and 5–6). In this way, cyclic strain accumulation occurs leading to a strain pattern formation along the specimen. In other words, the plastic flow appears as "strain bursts-and-arrests" and the strain band propagation can be of type "go-and-stop".

The experimental effort on the PLC effect has been mainly devoted to constant strain-rate tests and the atypical load-extension curves obtained have led to the acceptance of the term "serrated flow" as a synonym for the expression "Portevin-Le Chatelier effect".

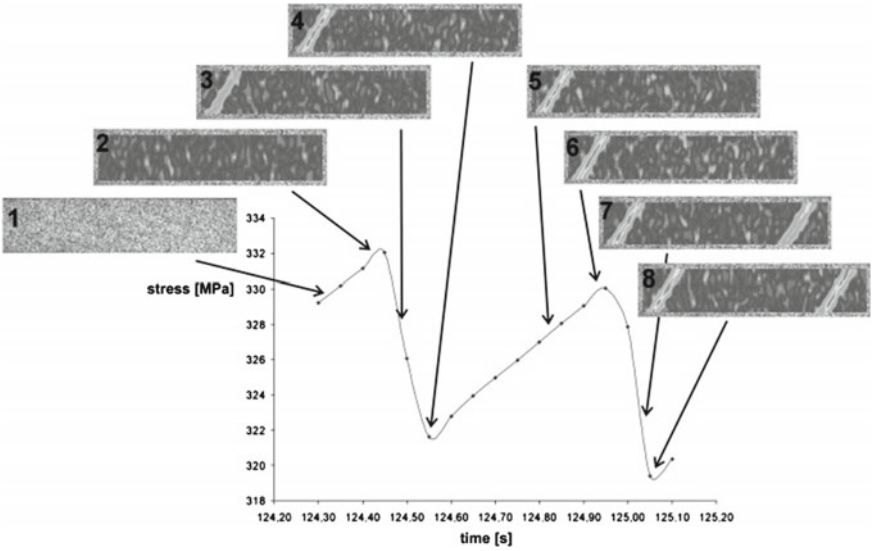

Fig. 7.3 Correlation between stress drops and pattern formation: strain band localization during a stress drop and no change in strain distribution during the stress increase (reproduced from Zdunek et al. (2008) Elsevier Ltd.)

Considerably less attention has been paid to *constant stress-rate* tests. In these experiments the PLC effect manifests by stress-strain curves which are no longer "serrated", but exhibit "staircase steps". As it is described by Fellner et al. (1991) there are two ways to conduct a constant-$\dot{\sigma}$ test. The first modality is to perform dead-load experiments using a creep machine by programmed addition of water, for example, which allow a careful control of the loading rate. This is a so-called dead-load tensile machine and the experiment is called a *true constant-$\dot{\sigma}$* test. In this case "almost perfect" steps can be obtained as it is illustrated in Fig. 7.4. The second way, but the most common in laboratory experiments, is to use a conventional tensile testing machine with electronic control systems. Such a machine is used as a hard testing machine for constant extension-rate tests, but when one inserts a spring of weak stiffness between the specimen and the grips of the machine it is used as a soft testing machine for constant loading-rate tests. In this case, the steps of the staircase present always a decrease of the stress and even successive "oscillations" (see Figs. 3–4 in Fellner et al. 1991). The machine effect on the "staircase shape" is not negligible as it can be seen from the physical experiments in Fig. 7.5 obtained using a Zwick testing machine equipped with digital recording. This experiment can be considered a *"pseudoconstant-$\dot{\sigma}$"* test.

It is important to note that, unlike the constant strain-rate tensile experiments in which the serrations on the stress-strain curves are accompanied by the appearance of visible localized deformations bands along the gauge length, in true constant stress-rate experiments no well defined stretcher-strain markings can be revealed on the surface of the specimen (Fellner et al. 1991).

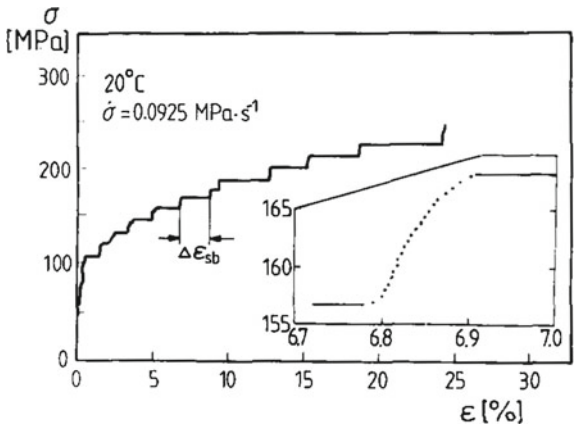

Fig. 7.4 Strain bursts in a dead-load tensile machine with constant stress-rate for annealed AlMg3 (reproduced from Fellner et al. (1991) Elsevier Ltd.)

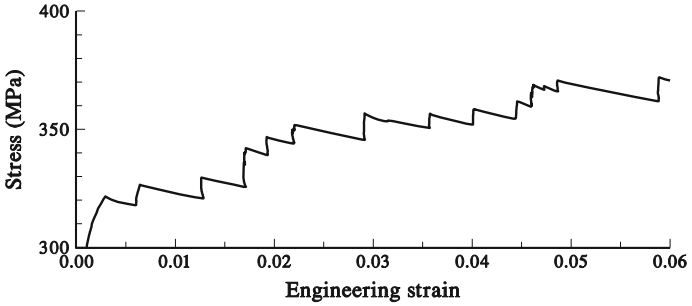

Fig. 7.5 Strain bursts in a Zwick testing machine in a nearly constant stress-rate test ≈ 0.076 MPa/s for a 5182H28 alloy (reproduced with permission from Făciu et al.1998 EDP Sciences)

However, Cuddy and Leslie (1972), testing several alloys of iron, by means of a creep tensile test machine, with an incrementally increased stress, have put into evidence that deformation bands can be detected by the oscilloscope traces of the outputs of a double extensometer. These bands spread immediately over the entire gauge length of the specimen while the stress remains constant and large strain increments are recorded.

More sophisticated experiments at constant stress-rate have been performed by Neuhäuser et al. (2004), Chmelík et al. (2007) using acoustic emission and laser extensometry techniques in order to detect the movement of a deformation band. It has been shown that the deformation band movement is characterized most appropriately by a repeated nucleation of bands. This appears as a piecewise continuous propagation at higher and strongly scattered values of propagation velocity as compared to the A-type in strain-rate controlled tests. They claim that "in fact there is a new generic type of PLC bands at the stress-rate controlled deformation".

From *microscopic point of view* the plastic flow in metals can be explained by using the theory of dislocations (see for instance Cottrell 1953; Nabarro 1967). In general, when dislocations move without interacting each other, or without interacting with point defects, the plastic flow is steady and stable. When the motion of dislocations is disturbed by different kind of interactions the plastic flow becomes unstable as it happens in the case of PLC effect. This phenomenon is usually explained by a model called *dynamic strain ageing* (DSA) which characterizes the interaction between moving dislocations and between dislocations and diffusing solute atoms (see Cottrell and Bilby 1949). It is considered that when the dislocations meet obstacles like solute atoms, or interstitial particles, they are temporary arrested for a certain time. If sufficient stress is applied these dislocations will overcome these obstacles and will quickly move to the next obstacle where they are stopped again and the process is repeated. This microscopic mechanism, referred to as dislocation pinning by solutes (Cottrell 1953), is believed to be the main factor controlling instabilities in plastic flow and in particularly the PLC effect. The dynamic strain ageing as micro mechanism of plastic instability phenomenon described by dislocation–solute and dislocation–dislocation interactions is in agreement with the experimental macroscopic correlation of the spatio-temporal characteristics of the PLC effect, obtained by different imaging techniques, as it is illustrated, for example, in Fig. 7.3. The idea of DSA has been further developed by van den Beukel (1975), Mulford and Kocks (1979), Louat (1981), McCormick (1988), Springer et al. (1998), Rizzi and Hähner (2004).

7.1.2 Main Ideas for the Constitutive Modelling of the PLC Effect

Phenomenological viscoplastic models used to describe the PLC effect are mainly based on two directions. One is motivated by the empirical material law adopted by Penning (1972) in his analysis of the tension tests for materials with negative strain-rate sensitivity. This relay on the assumption that in uniaxial tension, the stress σ is defined as a function of plastic strain ε^p and plastic strain-rate $\dot{\varepsilon}^p$ in the form

$$\sigma = \sigma_Y + \sigma_H(\varepsilon^p) + \sigma_V(\dot{\varepsilon}^p), \tag{7.1}$$

where σ_Y is the yield stress, σ_H is the strain hardening variable, and σ_V is the viscous stress governing the strain-rate sensitivity of the flow stress. It is assumed that the viscous stress is non-negative, but in order to include negative strain-rate sensitivity, σ_V is taken as a decreasing function of $\dot{\varepsilon}^p$ in a bounded region of the plastic strain-rate, i.e. there is a N-shaped relationship between the plastic strain-rate and flow stress. This model has been extended by Kubin and Estrin (1985) by adding the so-called "machine equation"

$$\frac{\sigma(t)}{M} = \frac{V^*}{L}t - \frac{1}{L}\int_0^L \varepsilon(x,t)\mathrm{d}x, \tag{7.2}$$

where M is the combined elastic modulus of the specimen and the testing machine, L is the length of the specimen and V^* is the imposed end velocity. This approach has led to a nonlinear integro differential system involving a spatial variable x and a temporal variable t which allowed to model constant stress-rate experiments. Penning's constitutive equation has been modified by Hähner (1993) by incorporating second order strain-gradients $\partial^2\varepsilon^p/\partial x^2$ to capture a spatial coupling of the PLC effect. A generalization of the material law (7.1) for a three dimensional viscoplastic model has been considered by Benallal et al. (2003, 2006).

The second direction is based on the constitutive relations introduced by McCormick (1988) to describe the dynamic strain ageing. The model assumes that the plastic flow occurs as a result of thermally activated escape of dislocations that have been pinned by solute atoms and can be described by an Arrhenius-type law. This implies that the plastic strain-rate $\dot{\varepsilon}^p$ is related to the stress σ and the average local solute concentration near dislocations C by relation

$$\dot{\varepsilon}^p = \dot{\varepsilon}_0 \exp\left(\frac{\sigma - \sigma_H(\varepsilon^p)}{S} - HC(t_a)\right) \Leftrightarrow \sigma = \sigma_H(\varepsilon^p) + SHC(t_a) + S\ln\left(\frac{\dot{\varepsilon}^p}{\dot{\varepsilon}_0}\right), \tag{7.3}$$

where $\dot{\varepsilon}_0$ is a characteristic strain-rate, S and H are material constants controlling the instantaneous and steady-state strain-rate sensitivity of the solid. Here $\sigma_H(\varepsilon^p)$ describes the stress hardening part of the flow stress. The solute concentration C, according to the original model proposed by Cottrell and Bilby (1949) and modified by Louat (1981), depends on average age of dislocations according to relation

$$C(t_a) = 1 - exp\left(-\left(\frac{t_a}{t_D}\right)^n\right), \tag{7.4}$$

where t_D is the characteristic time for solute diffusion across dislocations, n is a phenomenological material constant and t_a is the time that a representative mobile dislocation is pinned by obstacles. The age of dislocations t_a evolves according to a phenomenological kinetic law which will be described bellow.

An obvious inconvenience of the Arrhenius-type relation (7.3) is that when it is coupled with an elastic unloading condition, and σ is lower than the flow stress, it yields a finite plastic strain-rate (see Estrin 1996). Therefore, a different flow rule has been proposed by Böhlke et al. (2009), whereby the plastic strain-rate $\dot{\varepsilon}^p$ is related to the stress σ not by an exponential function as in (7.3), but by a power law, coupled with an unloading condition, i.e.

$$\dot{\varepsilon}^p = \dot{\varepsilon}_0\left(\frac{\sigma - \sigma_H(\varepsilon^p)}{S} - HC(t_a)\right)^m, \tag{7.5}$$

where $m > 0$ is a material constant which describes the strain-rate sensitivity of the material. By using this flow rule a geometrically non-linear elastic–viscoplastic constitutive model has been used for simulation of material response under various applied strain-rates.

For steady-state conditions the ageing time t_a may be taken to be equal to the *waiting time of dislocations*, t_w, as given by the Orowan equation, which relates the plastic strain-rate to dislocation densities and the average velocity of mobile dislocations, $v_D = \frac{l}{t_w}$, by relations

$$t_w = \frac{\rho_m b l}{\dot{\varepsilon}^p} = \frac{\rho_m b \rho_i^{-1/2}}{\dot{\varepsilon}^p} = \frac{\Omega}{\dot{\varepsilon}^p} \tag{7.6}$$

where ρ_m is the mobile dislocation density, ρ_i is the immobile dislocation density, l is the effective obstacle spacing, that is, the effective mean free path between obstacles, and b is the length of the Burgers vector. Ω is in fact the strain produced by all mobile dislocations moving to the next obstacle on their path. Since according to (7.6), Ω varies with the dislocation densities it follows that from phenomenological point of view it varies with the plastic strain, that is, $\Omega = \Omega(\varepsilon^p)$. The strain dependence of Ω can be calculated using a dislocation model (see Zhang et al. 2001) and taken as

$$\Omega = \omega_1 + \omega_2 (\varepsilon^p)^{\beta} \tag{7.7}$$

where ω_1, ω_2 and β are constants.

Relation (7.6) reflects the generally accepted fact that a decrease in plastic strain-rate causes an increase in the waiting time spent by dislocations at obstacles, which in turn will increase the magnitude of the stress drop in a jerky flow.

According to McCormick and Ling (1995), measurements of transient behavior following abrupt changes in $\dot{\varepsilon}^p$ or σ indicate that t_a is not an instantaneous function of $\dot{\varepsilon}^p$, but rather may be approximated by a first order relaxation kinetics law (see Ling and McCormick 1993). That means, the effective *ageing time* t_a is not identical to the average *waiting time* t_w a dislocation is arrested at localized obstacles. The fundamental assumption proposed by McCormick (1988) is that the effective ageing time t_a "relaxes" towards t_w with time t according to the evolution law

$$\frac{\mathrm{d}t_a}{\mathrm{d}t} = \frac{t_w - t_a}{\tau}, \tag{7.8}$$

where the characteristic relaxation time τ is taken to be equal to t_w.

Therefore, from (7.8) and (7.6) the age of dislocations t_a evolves with time, plastic strain and plastic strain-rate according to the phenomenological kinetic law

$$\frac{\mathrm{d}t_a}{\mathrm{d}t} = 1 - \frac{t_a}{t_w}, \quad \text{where} \quad t_w = \frac{\Omega(\varepsilon^p)}{\dot{\varepsilon}^p}. \tag{7.9}$$

Let us note that if $t_w \gg t_a$, then from (7.9) it follows that $\frac{\mathrm{d}t_a}{\mathrm{d}t} \cong 1$, in agreement with the fact that the solute concentration at arrested dislocations cannot increase faster than that allowed by the passage of time (McCormick 1988).

McCormick's model has been used in a large number of theoretical and numerical studies. It has been extended to the three-dimensional case by interpreting relation (7.3) as a relation between the von Mises equivalent deviatoric stress and the equivalent plastic strain. Analytical and numerical stability and bifurcation analysis have been done by Mesarovics (1995). There are several studies in the literature in which such kind of three-dimensional constitutive approaches have been investigated numerically by using the finite element method. The first numerical study in a 3D context has been done in McCormick and Ling (1995) by discretizing the tensile specimen into a number of axisymmetric sections and simultaneously solving the constitutive equations for dynamic strain ageing in each section. A reference approach is that in Zhang et al. (2001) where finite element simulations of dynamic strain ageing in flat and notably round specimens have been implemented by using the ABAQUS code. The model has been also used by Graff et al. (2004) and investigated in a finite element code for strain localization phenomena associated with static and dynamic strain ageing in notched specimens. In Jiang et al. (2007) a phenomenological model that includes spatial coupling is developed on the basis of McCormick's constitutive assumptions. In this case the specimen is numerically divided into N sections with equal width, perpendicular to the axial direction and coupled through the acting load. An experimental and numerical investigation of the PLC effect in the aluminium alloy AA5083-H116 was carried out by Benallal et al. (2008a) using the explicit non-linear finite element code LS-DYNA for different specimen geometries. In Zhang et al. (2012) a simple modification of McCormick's model has been made by introducing a power law dependence in the right part of Eq. $(7.9)_1$ to modify the transient kinetics of the strain-rate response of the material. Numerical simulations of PLC band formation and necking in a tensile specimen have been performed using the explicit dynamic finite element code ABAQUS. By using the flow rule (7.5), Böhlke et al. (2009) have considered a geometrically non-linear elastic-viscoplastic constitutive model for simulation of material response under various applied strain-rates. A related elastic-viscoplastic approach with that proposed by Böhlke et al. (2009) has been used by Mazière and Dierke (2012) to investigate the PLC critical strain in an aluminum alloy.

More complex constitutive laws derived from a depth analysis of physical mechanisms have been developed and are suitable, but more difficult to implement. For instance, Rizzi and Hähner (2004) have introduced two intrinsic time scales in the evolution equations and a characteristic length scale through a diffusion-like term with spatial second-order gradient. Soare and Curtin (2008a, b) have

developed a different kinetic model of dynamic strain ageing. Picu (2004) has introduced a new mechanism leading to negative strain-rate sensitivity in dilute solid solutions.

7.2 An Elastic-Viscoplastic Model with "Negative Strain-Rate Sensitivity" of McCormick Type

We consider in the following a phenomenological three dimensional elastic-viscoplastic constitutive model, of "overstress" type, that accounts for negative strain-rate sensitivity. The model formulation is motivated by McCormick's ideas presented in the previous section.

For simplicity reasons the formulation of the problem and its analysis is limited here to small strains and isotropic materials. We denote by $\boldsymbol{\varepsilon}$ the small strain tensor and by $\boldsymbol{\sigma}$ the stress tensor, and by

$$\boldsymbol{e} = \boldsymbol{\varepsilon} - \frac{1}{3}\mathrm{tr}(\boldsymbol{\varepsilon})\boldsymbol{I} \quad \text{and} \quad \boldsymbol{s} = \boldsymbol{\sigma} - \frac{1}{3}\mathrm{tr}(\boldsymbol{\sigma})\boldsymbol{I}, \tag{7.10}$$

their deviatoric parts, respectively. $\boldsymbol{I}$ is the second-order identity tensor.

We consider the additive decomposition of the strain tensor $\boldsymbol{\varepsilon}$ into an elastic and inelastic part, i.e.

$$\boldsymbol{\varepsilon} = \boldsymbol{\varepsilon}^{el} + \boldsymbol{\varepsilon}^{in}. \tag{7.11}$$

with the classical assumption of purely isochoric inelasticity of metals, i.e. $\mathrm{tr}(\boldsymbol{\varepsilon}^{in}) = 0$, it follows that the inelastic strain tensor is a deviatoric one and $\boldsymbol{\varepsilon}^{in} = \boldsymbol{e}^{in}$.

One assumes that the volume deforms only elastically, i.e. the mean strain and the mean stress satisfies the linear relation

$$\mathrm{tr}(\boldsymbol{\sigma}) = 3K\,\mathrm{tr}(\boldsymbol{\varepsilon}), \tag{7.12}$$

where K is the bulk modulus. By assuming that in the elastic domain we have an isotropic Hookean elastic material response, the relation between the stress deviator and the deviatoric part of the elastic strain read as

$$\boldsymbol{s} = 2\mu\boldsymbol{e}^{el}, \tag{7.13}$$

where μ is the shear modulus.

Therefore, the stress tensor can be written as

$$\boldsymbol{\sigma} = \boldsymbol{s} + \frac{1}{3}\mathrm{tr}(\boldsymbol{\sigma})\boldsymbol{I} = 2\mu\boldsymbol{e}^{el} + K\,\mathrm{tr}(\boldsymbol{\varepsilon})\boldsymbol{I} = 2\mu\boldsymbol{\varepsilon}^{el} + \lambda\,\mathrm{tr}(\boldsymbol{\varepsilon}^{el})\boldsymbol{I}, \tag{7.14}$$

where μ and λ are the Lamé coefficients and $K = (2\mu + 3\lambda)/3$.

The inelastic strain tensor is expressed in the fairly general form of the Lévy-von Mises type equation by which its rate is proportional with the deviatoric part of the stress tensor as

$$\dot{\boldsymbol{\varepsilon}}^{in} = \frac{3}{2}\frac{\dot{\varepsilon}^p}{\sigma_{eq}}\boldsymbol{s}, \tag{7.15}$$

where

$$\sigma_{eq} \equiv \sqrt{\frac{3}{2}\boldsymbol{s}\cdot\boldsymbol{s}}, \tag{7.16}$$

and

$$\dot{\varepsilon}^p \equiv \sqrt{\frac{2}{3}\dot{\boldsymbol{\varepsilon}}^{in}\cdot\dot{\boldsymbol{\varepsilon}}^{in}}. \tag{7.17}$$

denote *the equivalent von Mises stress* and *the equivalent inelastic strain-rate*. Here and in the following the over-dot denotes the derivative with respect to time t.

The use of the von Mises equivalent quantities implies plastic isotropy of the material. The specificity of the constitutive model is introduced through a particular form of a kinetic equation relating the equivalent stress σ_{eq} and the equivalent inelastic strain-rate $\dot{\varepsilon}^p$. To describe the PLC effect we choose here as a flow rule a power law of type (7.5), i.e.

$$\dot{\varepsilon}^p = \dot{\varepsilon}_0 \left\langle \frac{\sigma_{eq} - Y(\varepsilon^p, t_a)}{\sigma_D} \right\rangle^m, \tag{7.18}$$

The angle brackets $< \cdot >$ means as usual $< x > = \max(0, x)$ and allow to characterize both the elastic and viscoplastic domains and the loading/unloading conditions. The quantities $\dot{\varepsilon}_0$, m and σ_D are material parameters influencing the kinetics of the viscoplastic processes. The factor $\dot{\varepsilon}_0$, which is proportional to the density of mobile dislocations, is considered constant, $m > 0$ is a constant rate sensitivity parameter and σ_D is a characteristic stress for a dimensionless quantity inside the bracket.

The function $Y = Y(\varepsilon^p, t_a)$ represents the *flow stress*, which depends on the *accumulated plastic strain* ε^p defined as,

$$\varepsilon^p = \int_0^t \sqrt{\frac{2}{3}\dot{\boldsymbol{\varepsilon}}^{in}\cdot\dot{\boldsymbol{\varepsilon}}^{in}}\,\mathrm{d}\tilde{t}, \tag{7.19}$$

and on an internal variable t_a, called *dynamic ageing time*. It is obvious that the rate of the accumulated plastic strain coincides with the equivalent inelastic strain-rate.

The accumulated plastic strain satisfies $\varepsilon^p(0) = 0$, i.e. the body is initially in a virgin state and $\varepsilon^p(t) \geq 0$ increases with time in any elastic-viscoplastic process. One can view ε^p as a macroscopic measure of dislocations stored in the microscopic structure.

Since the expression $\sigma_{eq} - Y(\varepsilon^p, t_a)$ is called *overstress* function, as it characterizes the deviation of the equivalent stress with respect to the flow stress, one says that this elastic-viscoplastic constitutive approach is of *overstress type*. It is obvious, according to (7.18), that the temporal changes in the accumulated plastic strain ε^p are due to the variation of the overstress function and are associated with dissipative effects.

By combining relations (7.11), (7.13), (7.15) and (7.18) one can write the constitutive rate-type equation in terms of the rate of the deviatoric parts of total strain tensor and stress tensor as

$$\dot{\boldsymbol{e}} = \frac{\dot{\boldsymbol{s}}}{2\mu} + \frac{3}{2}\frac{\dot{\varepsilon}_0}{\sigma_{eq}}\left\langle \frac{\sigma_{eq} - Y(\varepsilon^p, t_a)}{\sigma_D} \right\rangle^m \boldsymbol{s}. \tag{7.20}$$

From this expression one can see that we have obtained an elastic-viscoplastic rate-type model with *linear instantaneous response* between the total strain deviator $\boldsymbol{e}$ and the stress deviator $\boldsymbol{s}$. For this class of constitutive relations see also Cristescu and Suliciu (1982, Chap. VIII).

We assume that the flow stress can be decomposed in two additive parts

$$Y(\varepsilon^p, t_a) = \sigma_H(\varepsilon^p) + \sigma_B(\varepsilon^p, t_a), \tag{7.21}$$

where the first term $\sigma_H(\varepsilon^p)$ describes the hardening of the material and the second one $\sigma_B(\varepsilon^p, t_a)$ takes the dynamic strain ageing into account.

One can assume for $\sigma_H(\varepsilon^p)$ a strain dependence obeying a Voce-type equation (see Ling et al. 1993; Böhlke et al. 2009) as

$$\sigma_H(\varepsilon^p) = \sigma_0 + (\sigma_\infty - \sigma_0)\left(1 - \exp\left(-\left(\frac{\Theta_0 \varepsilon^p}{\sigma_\infty - \sigma_0}\right)\right)\right), \tag{7.22}$$

where σ_0 and σ_∞ denote the initial and the saturation values of the stress and Θ_0 is a hardening parameter.

Motivated by relations (7.3) and (7.4), based on the generalization made by Louat (1981) of the relation proposed by Cottrell and Bilby (1949) for the time variation of the solute concentration around dislocations, one can take, according to Böhlke et al. (2009), the part of the stress accounting for the PLC effect as

$$\sigma_B(\varepsilon^p, t_a) = (\sigma_1 + \sigma_2 \varepsilon^p)\left(1 - \exp\left(-\left(\frac{t_a}{t_D}\right)^n\right)\right), \tag{7.23}$$

where t_D is the characteristic time for solute diffusion across dislocations and $n > 0$ is a material parameter.

Let us note that, if one takes the ageing time t_a equal to the waiting time of dislocations t_w, then according to (7.6), one can write relation (7.23) as

$$\sigma_B(\varepsilon^p, t_w) = (\sigma_1 + \sigma_2 \varepsilon^p)\left(1 - \exp\left(-\left(\frac{\Omega(\varepsilon^p)}{t_D \dot{\varepsilon}^p}\right)^n\right)\right). \tag{7.24}$$

It is obvious that when the rate of the accumulated plastic strain $\dot{\varepsilon}^p$ increases, then the waiting time t_w decreases and the stress σ_B also decreases, pointing out in this way a negative strain-rate sensitivity of the flow stress.

Taking into account the relaxation law (7.9), introduced by McCormick (1988), and by using a linear relation of type (7.7) one obtains the following form of the evolution equation for the dynamic ageing time t_a

$$\dot{t}_a = -\frac{\dot{\varepsilon}^p}{\omega_1 + \omega_2 \varepsilon^p} t_a + 1, \tag{7.25}$$

where $\dot{\varepsilon}^p$ is the equivalent inelastic strain-rate (7.18), ε^p is the accumulated plastic strain (7.19) and ω_1 and ω_2 are constant material parameters.

By using expression (7.18), relation (7.25) can be written as

$$\dot{t}_a = -\frac{\dot{\varepsilon}_0}{\omega_1 + \omega_2 \varepsilon^p}\left\langle \frac{\sigma_{eq} - Y(\varepsilon^p, t_a)}{\sigma_D} \right\rangle^m t_a + 1. \tag{7.26}$$

Therefore, the constitutive relations relating the unknowns quantities: the stress $\boldsymbol{\sigma}$, the strain $\boldsymbol{\varepsilon}$, and the internal variable t_a are given by the evolution Eqs. (7.20) and (7.26) completed with relations (7.11–7.17) and (7.19).

These constitutive relations have to be supplemented with the balance of momentum law

$$\rho \frac{\partial \boldsymbol{v}}{\partial t} = \mathrm{div}\boldsymbol{\sigma}, \quad \rho \frac{\partial v_i}{\partial t} = \frac{\partial \sigma_{ij}}{\partial x_j} \tag{7.27}$$

where ρ is the mass density of the material and $\boldsymbol{v} = \boldsymbol{v}(x, t)$ denotes the velocity field and div is the divergence operator with respect to the actual coordinates, written in a Cartesian system in relation $(7.27)_2$.

Let us note that, although the PLC effect manifests only in almost static tests ranging, in general, between 10^{-6} s^{-1} and 10^{-2} s^{-1}, the inertial term in the balance of momentum (7.27) must not be neglected in order to capture the phenomena of strain nucleation and strain localization which accompany the PLC effect as local dynamic events.

7.3 One-Dimensional Stress State

Let us consider a thin bar with uniform cross-section and length L in an undeformed and free-stress state. In studying uniaxial load, or straining, of the bar it is common to make a one-dimensional approximation in which the only non-vanishing stress component is the longitudinal one which is assumed to be uniform in a cross-section. That means, the stress tensor and its deviator in a Cartesian system of coordinate having one of its axes directed along the bar read as

$$\boldsymbol{\sigma} = \begin{pmatrix} \sigma_{11} & 0 & 0 \\ 0 & 0 & 0 \\ 0 & 0 & 0 \end{pmatrix}, \quad \boldsymbol{s} = \begin{pmatrix} \frac{2}{3}\sigma_{11} & 0 & 0 \\ 0 & -\frac{1}{3}\sigma_{11} & 0 \\ 0 & 0 & -\frac{1}{3}\sigma_{11} \end{pmatrix}, \tag{7.28}$$

and the strain tensor and its deviator as

$$\boldsymbol{\varepsilon} = \begin{pmatrix} \varepsilon_{11} & 0 & 0 \\ 0 & \varepsilon_{22} & 0 \\ 0 & 0 & \varepsilon_{22} \end{pmatrix}, \quad \boldsymbol{e} = \begin{pmatrix} \frac{2}{3}(\varepsilon_{11} - \varepsilon_{22}) & 0 & 0 \\ 0 & -\frac{1}{3}(\varepsilon_{11} - \varepsilon_{22}) & 0 \\ 0 & 0 & -\frac{1}{3}(\varepsilon_{11} - \varepsilon_{22}) \end{pmatrix}. \tag{7.29}$$

One assumes also that all the mechanical quantities intervening in the constitutive description depends only on time t and on the spatial variable X corresponding to the axis of the bar.

7.3.1 Constitutive Relations

In this case we denote for simplicity $\sigma = \sigma_{11}$ and $\varepsilon = \varepsilon_{11}$. The elastic deformation of volume (7.11) allows to determine the transversal strain as

$$\varepsilon_{22} = -\frac{\varepsilon}{2} + \frac{\sigma}{6K}. \tag{7.30}$$

Relations (7.11)–(7.13) describing the linear elastic response of the material lead to

$$\varepsilon_{11}^{el} = \frac{(\lambda+\mu)\sigma}{\mu(2\mu+3\lambda)} = \frac{\sigma}{E}, \quad \varepsilon_{22}^{el} = -\frac{\lambda}{2\mu(2\mu+3\lambda)}\sigma, \tag{7.31}$$

where $E = \frac{\mu(3\lambda+2\mu)}{\lambda+\mu}$ is the Young modulus.

By using the additive decomposition of the strain tensor in its elastic and inelastic part, and the fact that the inelastic part is a deviatoric tensor one gets

$$\varepsilon_{11}^{in} = \varepsilon - \frac{\sigma}{E}, \quad \text{and} \quad \varepsilon_{22}^{in} = -\frac{1}{2}\varepsilon_{11}^{in}. \tag{7.32}$$

The equivalent von Mises stress (7.16), the equivalent inelastic strain-rate (7.17) and relation (7.15) read as

$$\sigma_{eq} = |\sigma|, \quad \dot{\varepsilon}^p = \left|\dot{\varepsilon}_{11}^{in}\right| = \left|\dot{\varepsilon} - \frac{\dot{\sigma}}{E}\right|, \quad \dot{\varepsilon} - \frac{\dot{\sigma}}{E} = \frac{\sigma}{|\sigma|}\left|\dot{\varepsilon} - \frac{\dot{\sigma}}{E}\right|. \tag{7.33}$$

The accumulated plastic strain (7.19) becomes

$$\varepsilon^p(t) = \int_0^t \left|\dot{\varepsilon}_{11}^{in}(s)\right| \mathrm{d}s = \int_0^t \left|\dot{\varepsilon}(s) - \frac{\dot{\sigma}(s)}{E}\right| \mathrm{d}s \geq 0. \tag{7.34}$$

Then, the tensorial viscoplastic constitutive relation (7.20) reduces to a single equation

$$\dot{\varepsilon} = \frac{\dot{\sigma}}{E} + \dot{\varepsilon}_0 \left\langle \frac{|\sigma| - Y(\varepsilon^p, t_a)}{\sigma_D} \right\rangle^m \frac{\sigma}{|\sigma|}. \tag{7.35}$$

Let us consider the case of a *tensile* test, that is $\sigma > 0$. Then, according to $(7.33)_3$, $|\dot{\varepsilon} - \dot{\sigma}/E| = \dot{\varepsilon} - \dot{\sigma}/E > 0$, and the accumulated plastic strain (7.34) becomes $\varepsilon^p(t) = \varepsilon(t) - \sigma(t)/E$, if the bar at the initial moment is undeformed, i.e. $\varepsilon(0) - \sigma(0)/E = 0$. Then, the constitutive Eq. (7.35) can be written as

$$\dot{\sigma} = E\dot{\varepsilon} - E\dot{\varepsilon}_0 \left\langle \frac{\sigma - Y\left(\varepsilon - \frac{\sigma}{E}, t_a\right)}{\sigma_D} \right\rangle^m. \tag{7.36}$$

For the *compressive* case, that is when $\sigma < 0$, according to $(7.33)_3$, we have $|\dot{\varepsilon} - \dot{\sigma}/E| = -\dot{\varepsilon} + \dot{\sigma}/E > 0$, and the accumulated plastic strain (7.34) is $\varepsilon^p(t) = -\varepsilon(t) + \sigma(t)/E$, if the bar at the initial moment is undeformed, i.e. $\varepsilon(0) - \sigma(0)/E = 0$. Then, the constitutive Eq. (7.35) can be written as

$$\dot{\sigma} = E\dot{\varepsilon} - E\dot{\varepsilon}_0 \left\langle \frac{-\sigma - Y\left(-\varepsilon + \frac{\sigma}{E}, t_a\right)}{\sigma_D} \right\rangle^m. \tag{7.37}$$

By combining relations (7.36) and (7.37) we can write the constitutive Eq. (7.35) in the form

$$\frac{\partial \sigma}{\partial t} - E\frac{\partial \varepsilon}{\partial t} = G(\varepsilon, \sigma, t_a), \tag{7.38}$$

where

$$G(\varepsilon,\sigma,t_a)=-\frac{E\dot{\varepsilon}_0}{\sigma_D^m}\begin{cases}\left(\sigma-Y\left(\varepsilon-\frac{\sigma}{E},t_a\right)\right)^m, & \text{if } \sigma>Y\left(\varepsilon-\frac{\sigma}{E},t_a\right)\\ 0, & \text{if } -Y\left(-\varepsilon+\frac{\sigma}{E},t_a\right)\le\sigma\le Y\left(\varepsilon-\frac{\sigma}{E},t_a\right)\\ \left(-\sigma-Y\left(-\varepsilon+\frac{\sigma}{E},t_a\right)\right)^m, & \text{if } \sigma<-Y\left(-\varepsilon+\frac{\sigma}{E},t_a\right).\end{cases}$$

The evolution equation for the dynamic ageing time (7.25) can then be written as

$$\frac{\partial t_a}{\partial t}=H(\varepsilon,\sigma,t_a), \tag{7.39}$$

where

$$H(\varepsilon,\sigma,t_a)=\begin{cases}\frac{G(\varepsilon,\sigma,t_a)}{E\left(\omega_1+\omega_2\left(\varepsilon-\frac{\sigma}{E}\right)\right)}t_a+1, & \text{if } \sigma>Y\left(\varepsilon-\frac{\sigma}{E},t_a\right)\\ 1, & \text{if } -Y\left(-\varepsilon+\frac{\sigma}{E},t_a\right)\le\sigma\le Y\left(\varepsilon-\frac{\sigma}{E},t_a\right)\\ \frac{G(\varepsilon,\sigma,t_a)}{E\left(\omega_1+\omega_2\left(-\varepsilon+\frac{\sigma}{E}\right)\right)}t_a+1, & \text{if } \sigma<-Y\left(-\varepsilon+\frac{\sigma}{E},t_a\right).\end{cases}$$

Here function $Y=Y(\varepsilon^p,t_a)$ is given by relations (7.21)–(7.23).

7.3.2 *Field Equations and Initial-Boundary Value Problems*

To investigate the predictions of the model we have to consider besides the constitutive relations (7.38) and (7.39) the partial differential equations governing the longitudinal motion of a thin bar with constant mass density ρ in the reference configuration. These are the balance of momentum and the compatibility equation between strain and velocity

$$\rho\frac{\partial v}{\partial t}-\frac{\partial\sigma}{\partial X}=0,\quad \frac{\partial\varepsilon}{\partial t}-\frac{\partial v}{\partial X}=0, \tag{7.40}$$

where t is time, $X\in[0,L]$ is the (Lagrangian) spatial coordinate along the bar and v is the particle velocity. Once more, the inertial term is not neglected in order to be able to capture the local dynamic events.

Hence, the complete PDEs system in the unknown $\sigma=\sigma(X,t)$, $\varepsilon=\varepsilon(X,t)$, $t_a=t_a(X,t)$ and $v=v(X,t)$ composed by the Eqs. (7.38), (7.39) and (7.40) can be written as

$$\frac{\partial}{\partial t}\begin{pmatrix}v\\ \varepsilon\\ \sigma\\ t_a\end{pmatrix}+\begin{pmatrix}0 & 0 & -1/\rho & 0\\ 1 & 0 & 0 & 0\\ -E & 0 & 0 & 0\\ 0 & 0 & 0 & 0\end{pmatrix}\frac{\partial}{\partial X}\begin{pmatrix}v\\ \varepsilon\\ \sigma\\ t_a\end{pmatrix}=\begin{pmatrix}0\\ 0\\ G(\varepsilon,\sigma,t_a)\\ H(\varepsilon,\sigma,t_a)\end{pmatrix}. \tag{7.41}$$

The type of the system is given by its characteristic directions $\mathrm{d}X/\mathrm{d}t = r$ which are defined as the eigenvalues of the 4×4 matrix in (7.41). These are $(\mathrm{d}X/\mathrm{d}t)^2 = E/\rho > 0$ and $(\mathrm{d}X/\mathrm{d}t)^2 = 0$. They are real and positive and consequently the system is *hyperbolic*. Moreover, it is *semilinear with source terms* since all the nonlinear terms, i.e. G and H, are among the free terms of the system.

As we have seen in Sect. 7.1.1 the PLC phenomenon is usually investigated by two kind of experiments: either a tensile testing at constant applied strain-rate ("hard testing machine experiment"), or a tensile testing at constant applied stress-rate ("soft testing machine experiment").

To simulate such kind of uniaxial quasi-static experiments we have to consider a bar initially at rest, in its natural state of strain and stress, with one of its end fixed. The other end is subjected to one of the following conditions.

(*A*) *Strain–controlled experiment – cross-head velocity controlled experiment.*
The left-end of the bar in this tensile test is moved with a constant negative velocity V^*. Thus, we have to find the solution of the system (7.41) which satisfies the initial and boundary conditions.

$$\begin{aligned} &\varepsilon(X,0) = 0, \quad \sigma(X,0) = 0, \quad t_a(X,0) = 0, \quad v(X,0) = 0, \quad \text{for } X \in [0,L], \\ &v(0,t) = V^*, \quad v(L,t) = 0 \quad \text{for any } t > 0. \end{aligned} \tag{7.42}$$

This experiment corresponds to an engineering constant strain-rate $\dot{\varepsilon}_e = |V^*|/L$.

(*B*) *Stress–controlled experiment – true constant stress-rate experiment.*
The end of the bar is submitted to a constant increase of the load. Thus, we have to find the solution of the system (7.41) which satisfies the initial and boundary conditions.

$$\begin{aligned} &\varepsilon(X,0) = 0, \quad \sigma(X,0) = 0, \quad t_a(X,0) = 0, \quad v(X,0) = 0, \quad \text{for } X \in [0,L], \\ &\sigma(0,t) = \dot{\sigma}_e t, \quad v(L,t) = 0 \quad \text{for any } t > 0, \end{aligned} \tag{7.43}$$

where the applied stress-rate $\dot{\sigma}_e = \text{const.} > 0$.

(*C*) *Mixed stress- and strain-controlled experiment – pseudoconstant stress-rate experiment.*
As we have seen in the comments from Sect. 7.1.1 related with Figs. 7.4 and 7.5 a true constant stress-rate test is very difficult to be conducted in laboratory experiments by conventional testing machines due to the elastic interaction between specimen and the testing machine which is caused by the spring introduced between the specimen and the grips of the machine. In order to take into account the influence of the testing machine we consider that in fact the left-end condition is a mixture between a perfect hard testing-machine and a pure soft-testing machine by considering the following mixed initial-boundary value problem.

$$\varepsilon(X,0)=0,\quad \sigma(X,0)=0,\quad t_a(X,0)=0,\quad v(X,0)=0,\quad \text{for } X\in[0,L],$$
$$\beta\sigma(0,t)-(1-\beta)\sqrt{\rho E}v(0,t)=\beta\dot{\sigma}_e t-(1-\beta)\sqrt{\rho E}V^*, v(L,t)=0 \text{ for any } t>0, \tag{7.44}$$

where $\dot{\sigma}_e = \text{const.} > 0$, $V^* = \text{const.} < 0$ and β is a parameter with the property that $\beta \in [0,1]$.

It is obvious that when $\beta = 1$ we simulate a constant stress-rate test, while when $\beta = 0$ we simulate a constant strain-rate test ($\dot{\varepsilon}_e = V^*/L$). For $\beta \in (0,1)$ we have a mixed boundary condition. If β is near 1, this boundary condition should correspond to a "pseudoconstant" stress-rate experiment.

To solve these initial–boundary value problems for the system of PDEs (7.41), and see what the model predicts, we built an explicit second order finite difference numerical scheme based on the method of characteristics. This is described in Appendix.

7.3.3 A Numerical Investigation

The mechanical parameters of the model are listed in the fifth column of Tables 7.1 and 7.2 and are chosen in agreement with similar parameters in the literature, but so as to ensure the fulfillment of critical conditions for the emergence of typical instability phenomena for the PLC effect. These conditions are investigated in Sect. 7.4.

We consider here a bar of length $L = 20$ mm discretized by using 161 nodes, that means a space integration step $h = 0.125$ mm and a time integration step $\tau = 3.44 \times 10^{-8}$ s satisfying condition (7.71) for the Courant number $\nu = 0.9$. Since the numerical experiments simulate laboratory tests at extremely low strain-rates an important computation time was necessary.

Table 7.1 Mechanical parameters for classical part of elastic-viscoplastic relations (7.20)–(7.22)

Parameters	Zhang et al. (2001)	Benallal et al. (2008a, b), Zhang et al. (2012)	Böhlke et al. (2009)	This paper	Units
E	70	70	70	70	GPa
ρ	–	–	–	6550	kg/m^3
$\dot{\varepsilon}_0$	2.3×10^{-7}	10^{-8}	3.5×10^{-5}	3.5×10^{-6}	s^{-1}
σ_D	(0.41, 1.7)	2.23	15.	30	MPa
m	Exponential (7.3)	Exponential (7.3)	28	15	
σ_0	38.3	78.7	123	123	MPa
σ_∞	67.9	Power law	343	343	MPa
Θ_0	534.6		2800	2800	MPa

Table 7.2 Mechanical parameters for the DSA model described by (7.26) and (7.23)

Parameters	Zhang et al. (2001)	Benallal et al. (2008a, b), Zhang et al. (2012)	Böhlke et al. (2009)	This paper	Units
σ_1	$(7.92, 30.6)$	62.22	18.9	62.22	MPa
σ_2	–	0	189.26	622.2	MPa
t_D	$(0.126, 0.03)$	0.02	0.125	0.125	s
n	$1/3$	$1/3$	1/3	1/3	
ω_1	$(3.6 \times 10^{-5}, 7.9 \times 10^{-4})$	10^{-4}	6.81×10^{-4}	3.6×10^{-5}	
ω_2	–	0	3.6×10^{-4}	0	
$A = \frac{n\sigma_1}{\omega_1 E}$	$(0.23, 1.05)$	$2.96 > e$	$0.132 < e$	$8.23 > e$	
Temporal instability	No	Yes	No	Yes	

The numerical results show that the constitutive model is able to reproduce with reasonable accuracy most of the experimentally observed phenomena which accompany the PLC effect.

7.3.3.1 Strain-Controlled Experiments

We first consider the constant strain-rate experiment (7.42) where the free-end of the bar is moved with the constant velocity $V^* = 0.2$ mm/s, which corresponds to the engineering strain-rate $\dot{\varepsilon}_e = 10^{-3}\text{s}^{-1}$.

The computed stress–engineering strain curve, i.e. the end-stress $\sigma(0,t)$ versus $\varepsilon_e(t) = \frac{1}{L}\int_0^L \varepsilon(X,t)\text{d}X = (l(t) - L)/L$, where $l(t)$ is the actual length of the bar, is illustrated in Fig. 7.6. One obtains a serrated curve, with sudden stress drops ("jerky flow") and with a changes of the serrated plateaus. The emergence of different serrated yielding plateaus in a constant strain-rate experiment is often reported in laboratory tests on alloys which present the PLC effect as it is shown in Fig. 7.7. No geometric defect, or other heterogeneity was introduced in the PDEs system to initiate the unstable behavior of the solution.

The same as in the laboratory experiments, the serrations accompany the formation of bands of localized deformation in the bar. Indeed, the numerical experiment clearly illustrates how the strain bands nucleate, localize and propagate along the specimen. For instance, if one focuses on the zoom in Fig. 7.6 one can follow in Fig. 7.8 the evolution of the strain and strain-rate distribution in bar during the stress oscillations. Thus, between the points A and B the stress rises elastically and when it reaches a critical value it suddenly drops. During this slowly and almost elastic process the strain band distribution in the bar remains unchanged and there is

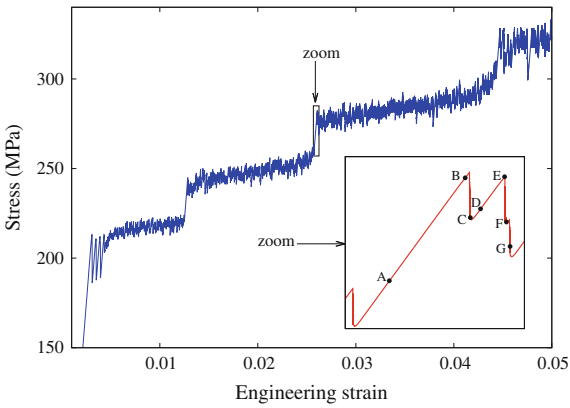

Fig. 7.6 Serrated stress-strain curve for numerical simulation of a hard-testing machine experiment with engineering strain-rate $\dot{\varepsilon}_e = 10^{-3}\ s^{-1}$. Insert: zoom of a portion and the position of points A, B, C, D, E, F, G where are recorded the distribution of strain ε and strain-rate $\dot{\varepsilon}$ in bar, illustrated in Fig. 7.8

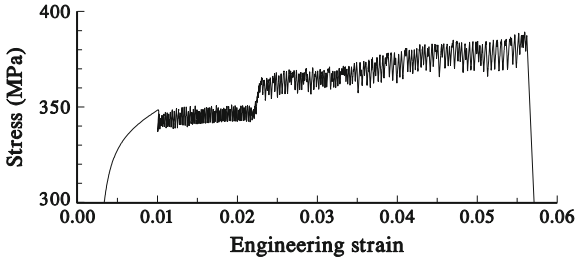

Fig. 7.7 Nominal stress versus engineering strain in constant strain-rate test at $\dot{\varepsilon}_e = 10^{-5}\ s^{-1}$ in 5182H28 alloy. Serrated flow with change of plateaus (reproduced with permission from Făciu et al. (1998) EDP Sciences)

no significant plastic activity. Only at point B, just before the stress drop, the plastic activity begins to activate and the strain-rate in the bar locally overcomes the value of the imposed strain-rate announcing the apparition of a new localization of strain. During the stress drop, at the level of point C, a new strain band appears and inside this band it is observed that the strain-rate is six hundred times larger than the applied strain-rate. At the end of the stress drop, the new band is already buildup and the plastic activity goes out at the point D.

Once the stress starts to rise again elastically, between the points D and E, the strain band distribution remains unchanged and the process is quasistatic (compare the strain and the strain-rate distribution at the points C, D and E in Fig. 7.8). Only at point E, just before a new stress drop, the strain-rate starts to increase locally marking the new nucleation zones. Two new dynamic events follow. A stress drop to the point F, which leads to the localization of the strain near the fixed end of the bar, followed immediately by a sudden stress decay at the point G which leads to the apparition of a new localization of strain. These two strain bursts are accompanied by an important increase of the strain-rate inside the new bands, which becomes at the point G more than four thousand times higher than the imposed strain-rate. This behavior is in agreement with the laboratory experiment illustrated in Fig. 7.3. The process continues in this way in a manner almost cyclic.

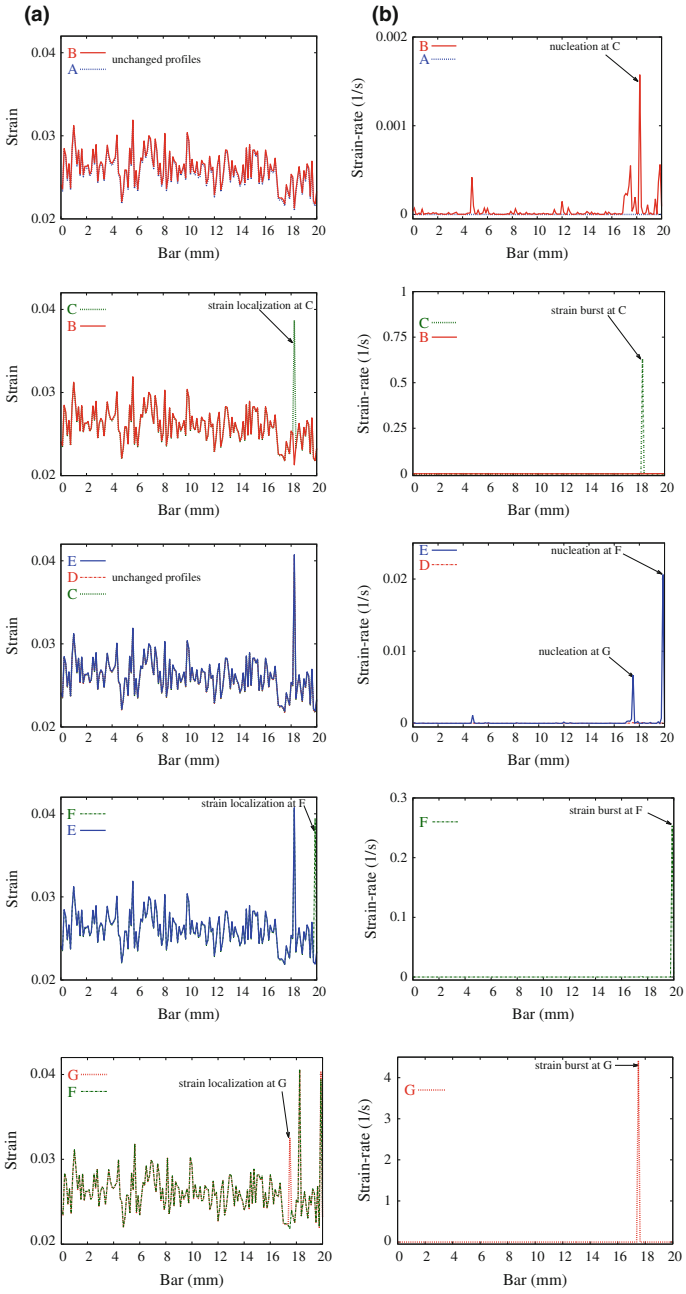

Fig. 7.8 **a** The distribution of strain ε and **b** The distribution of strain-rate $\dot{\varepsilon}$ in bar at the moments A, B, C, D, E, F, G in Fig. 7.6. Note the different scales used for the strain-rate distribution

It is obvious that the stress drop occurs in a time interval much smaller than that required for the new increase of the stress. Therefore, the sawtooth appearance of the stress-strain curve reflects an alternation between dynamic and quasi-static processes. Thus, Fig. 7.8 also illustrates how the stress drop is accompanied by local dynamic events followed by quasi-static ones. This behavior explains the mechanism of "go-and-stop" propagation of strain bands which is recorded in laboratory experiments.

An overview of the PLC band propagation in the numerical simulation in Fig. 7.6 is illustrated in Fig. 7.9. One can see that the strain bands nucleate in a way specifically to the type B bands, which appear as hopping bands propagating discontinuously, in an intermittent manner.

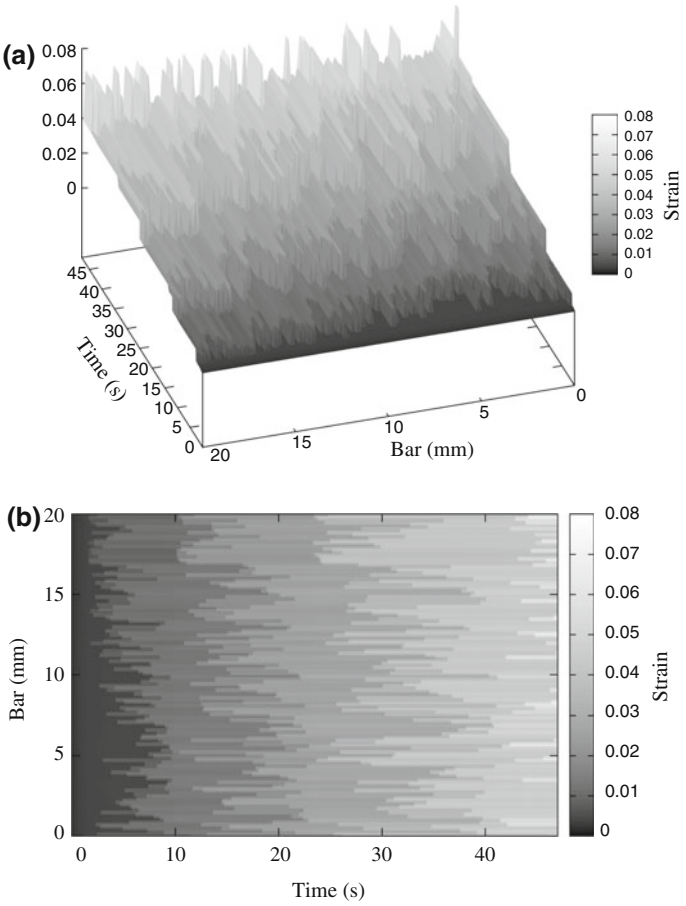

Fig. 7.9 Overall picture of the strain evolution in the bar during the cross-head velocity controlled experiment in Fig. 7.6. **a** Spatial representation of $\varepsilon = \varepsilon(X, t)$. **b** Its plane projection

Let us also note that each plateau of the serrated curve corresponds to a new stage of the strain growth in bar during the plastic deformation. Thus, for the numerical simulation illustrated in Fig. 7.6 there are four plateaus which lead to four stages of strain increase as can be seen in Fig. 7.9.

One observes that the increase of the local strain along a plateau, in general, is not larger than the maximal value of the engineering strain of the corresponding plateau. Indeed, see for instance the size of the strain bursts in Fig. 7.8 and compare with the value of the engineering strain at the end of the corresponding plateau.

Therefore, such numerical simulations could clarify the relation between the strain magnitude of a serrated yielding plateau and the way the strain increases inside a band during a stress drop. Thus, one could explain, depending on the "jerky" flow structure of the serrated curve, the possible occurrence of visible strain markings on the surface of a specimen during its unstable viscoplastic flow.

The 3D Fig. 7.10 illustrates how the plastic strain-rate is locally activated in a spectacular way in the process of band formation during each stress drop. Since these simulations are demanding not only with respect to the computation time, but also to the data storage it is possible to not capture here the largest strain-rates of the numerical simulation.

The evolution of the ageing time variable t_a describes the dynamic ageing process in which dislocations are alternately pinned by solute and released, or newly generated, when the stress attains some critical value.

This behavior is illustrated in Fig. 7.11. According to the evolution Eq. (7.26) when a particle of the bar suffers an elastic quasi-static process one has $\frac{dt_a}{dt} = 1$, that is, one has a linear increase of t_a with constant slope 1. This behavior can be clearly seen appearing regularly in Fig. 7.11. The increase of the ageing time during the slow elastic stress growth describes in fact the process of ageing of dislocations

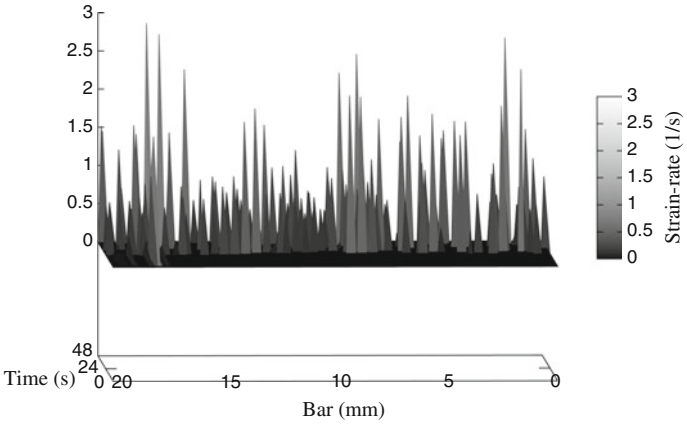

Fig. 7.10 Overall picture of the strain-rate $\dot{\varepsilon} = \dot{\varepsilon}(X, t)$ in the bar during the cross-head velocity controlled experiment in Fig. 7.6

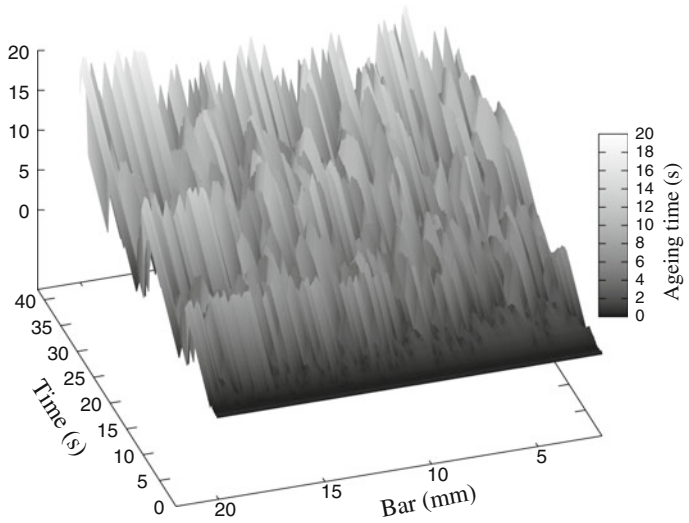

Fig. 7.11 Overall picture of the evolution of the ageing time $t_a = t_a(X, t)$ in the bar during the cross-head velocity controlled experiment in Fig. 7.6

when the band front is pinned. Afterwards, the ageing time of the particles which enter the viscoplastic domain starts to decay.

During the nucleation and localization process, when the stress sharply decreases and the strain-rate bursts leading to localized bands, the ageing time t_a decreases rapidly to the waiting time $t_w \approx \Omega/\dot{\varepsilon}_e = 3.5 \times 10^{-2}$s in the corresponding zones, as can be seen in Fig. 7.12 (compare the ageing time distribution in the bar at points B and C). This behavior is in agreement with Schwarz (1985) assertion that the propagation and localization occur at the position of less aged dislocations. This can

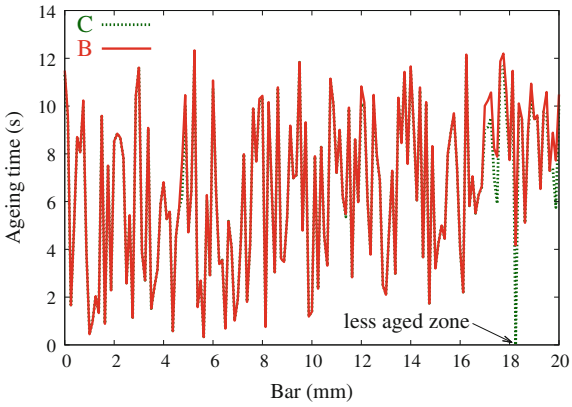

Fig. 7.12 The distribution of the ageing time t_a in bar during a stress drop—moments B and C in Fig. 7.6

be also observed globally in Fig. 7.11 where t_a decreases for short periods of time in the neighborhood of the new localized front bands.

Thus, the prediction of the model is in agreement with the observation made by Cuddy and Leslie (1972) that, as the bands appear along the gauge length, producing regular serrations on the load-extension curve, and surface markings on the specimen, there is an alternation between the ageing and breakaway of the dislocations.

We end the comments on strain-controlled experiments with Fig. 7.13 which illustrates how the strain-rate influences the yielding curve. One observes that, as the engineering strain-rate $\dot{\varepsilon}_e$ decreases, the stress-strain curves, in general, move up pointing out the way the constitutive equations describe the negative strain-rate sensitivity of the flow stress. For $\dot{\varepsilon}_e = 10^{-1}\text{s}^{-1}$ there is only a first drop, but no jerky flow appears. The reason is that at this "high" strain-rate we are outside the region of instability predicted by the analytical results in Sect. 7.4 for the material parameters in Tabels 7.1 and 7.2. As we have already seen, the numerical simulation performed at $\dot{\varepsilon}_e = 10^{-3}\text{s}^{-1}$ presents the characteristics of type B serrations and PLC bands propagation, with regular alternation of stress increases and decreases. For the increasing engineering strain-rate $\dot{\varepsilon}_e = 10^{-2}\text{s}^{-1}$, which according to the stability analysis in the next section, lies in the intermediate range of stable/unstable flow, the stress-strain curve presents the characteristics of a transition from type A to type B serrations with more irregular humps and valleys.

The stress drop amplitudes also show a slight strain dependence, in agreement with laboratory experiments, which points out a gradual increase of the serrations with strain (see Fig. 7.1). Thus, the overall agreement of the numerical simulations with experiments is found to be reasonable.

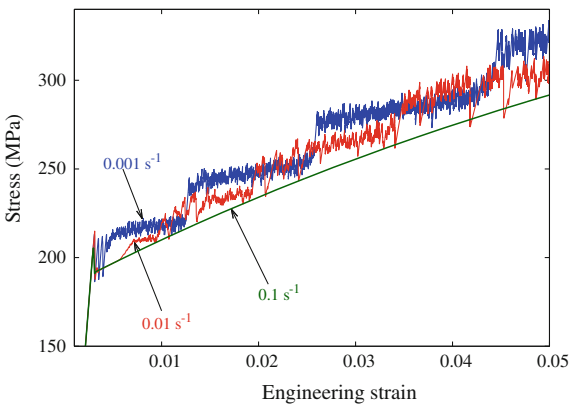

Fig. 7.13 Influence of the imposed engineering strain-rate $\dot{\varepsilon}_e$ on the serrated yielding

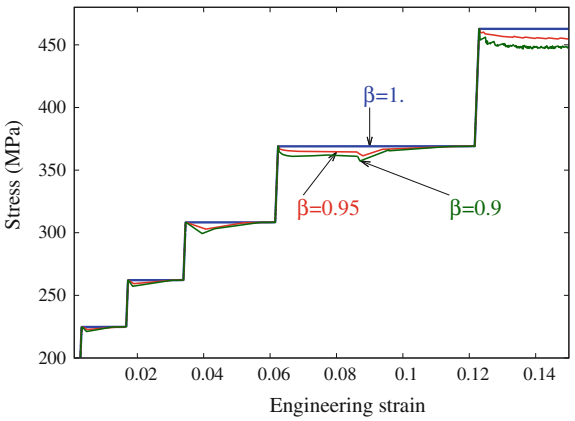

Fig. 7.14 Staircase type stress-strain curves in the numerical simulation of a soft-testing machine experiment. $\beta = 1$ corresponds to a true constant stress-rate test (7.43) at $\dot{\sigma}_e = 10$ MPa/s. $\beta = 0.95$ and $\beta = 0.9$ correspond to the mixed boundary condition (7.44) where $\dot{\sigma}_e = 10$ MPa/s and $V^* = 2.85 \times 10^{-3}$ mm/s ($\dot{\varepsilon}_e = 1.4 \times 10^{-3}$ s^{-1}, i.e. $\dot{\sigma}_e = E\dot{\varepsilon}_e$)

7.3.3.2 Stress-Controlled Experiments

We first consider a numerical simulation of the *true* constant stress-rate test (7.43) (or equivalently, (7.44) for $\beta = 1$) with $\dot{\sigma}_e = 10$ MPa/s. The computed end-stress $\sigma(0,t)$ vs. engineering strain $\varepsilon_e(t)$ illustrates in Fig. 7.14 how the model is able to predict a staircase structure with five steps, each one corresponding to a strain burst.

At the scale of the 3D picture in Fig. 7.15 the specimen appears to deform in a homogeneous manner along the almost horizontal treads, but also on the vertical risers where the sudden strain bursts occurs leading to the increase of deformation by steps. The transition from one strain burst plateau in Fig. 7.14 to the next one is a quasistatic process with practically no plastic activity. The alternation between these quasistatic and dynamic events is illustrated in Fig. 7.16 where it is depicted

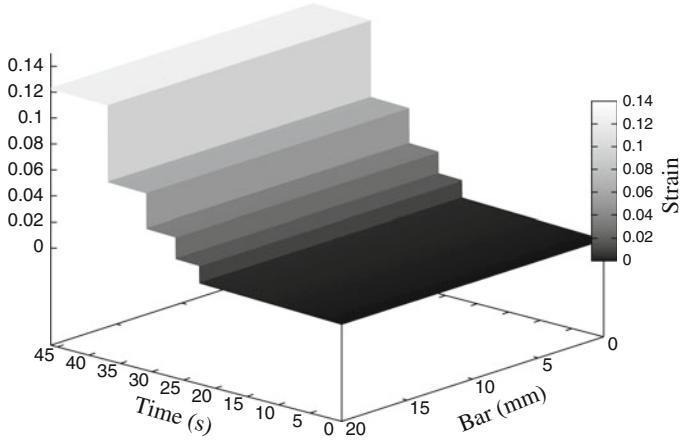

Fig. 7.15 Overall picture of the strain $\varepsilon = \varepsilon(X,t)$ in the bar during the true constant stress-rate experiment ($\beta = 1$) in Fig. 7.14

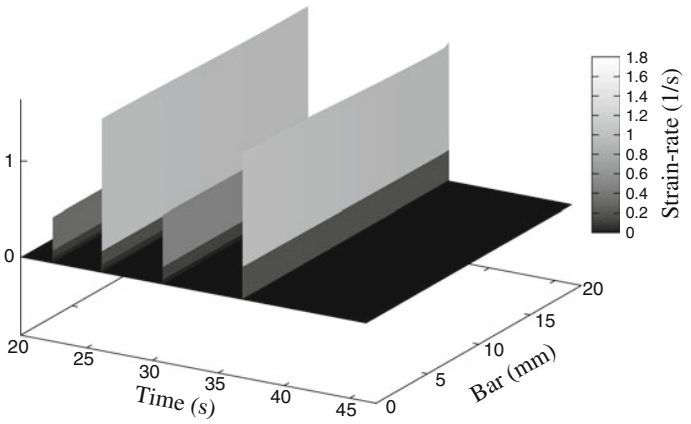

Fig. 7.16 Overall picture of the strain-rate $\dot{\varepsilon} = \dot{\varepsilon}(X,t)$ in the bar during the true constant stress-rate experiment ($\beta = 1$) in Fig. 7.14

the evolution of the strain-rate for the first four plateaus in Fig. 7.14. The prediction of the model for this ideal testing case is in agreement with the remark by Cuddy and Leslie (1972) according to which "in a soft machine where the applied load remains constant, the band spreads immediately over the entire gauge length."

The evolution of the ageing time variable t_a is illustrated in Fig. 7.17. One has a homogeneous and linear increase of the ageing time with constant slope 1 during the quasi-static elastic deformation of the bar. This corresponds to the ageing of dislocations when they are arrested at local obstacles.

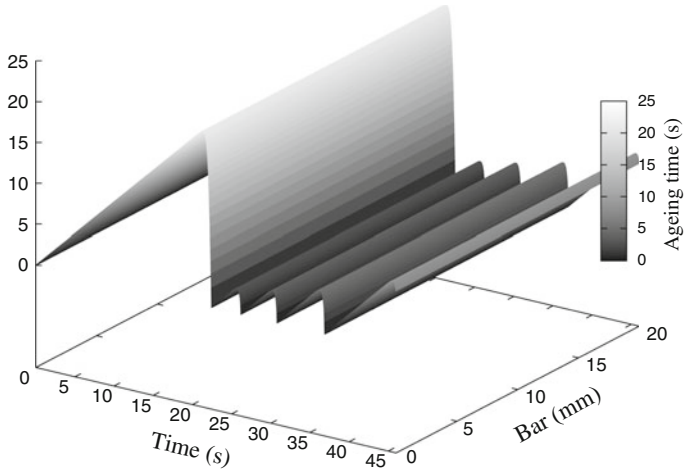

Fig. 7.17 Overall picture of the ageing time $t_a = t_a(X,t)$ in the bar during the true constant stress-rate experiment ($\beta = 1$) in Fig. 7.14

Afterwards, when the stress attains some critical value, a decay of t_a in the viscoplastic domain starts and is followed, during the strain burst, by a sudden drop near zero. This behavior corresponds to the moment when the dislocations become unlocked, start to move, accelerate rapidly and advance to the next obstacles. At the end, when the strain reaches a certain level, the advancing of the deformation front stops and the process is restarted.

As we have seen in the Sect. 7.1.1, the experimental literature points out that macroscopic features of the PLC effect, like the stress-engineering strain curves, depend strongly on the testing machine. In order to examine the sensitivity of the model to a perturbation of the mode of testing we considered the mixed initial-boundary value problem (7.44) to simulate the so called pseudoconstant-$\dot{\sigma}_e$ experiments. The way the model is able to simulate the influence of the machine effects is illustrated in Fig. 7.14 where the computed stress-strain curves obtained for $\beta = 0.95$ and $\beta = 0.9$ are represented. These numerical simulations with mixed boundary conditions are closer to the laboratory experiments of pseudoconstant stress-rate experiments illustrated in Fig. 7.5, or reported in Fellner et al. (1991, Figs. 3–4). Indeed, one gets numerically, the same as in the experiments mentioned earlier that, instead of a horizontal plateau during the strain burst, we firstly have a stress decay followed by an increase to the level of the horizontal plateau. The decrease is more important as the parameter β has a smaller value than 1. Much more than that, one observes, for $\beta = 0.9$ and for large strain, that the decrease of the stress is accompanied by oscillations. This behavior is in agreement with the remark made in Fellner et al. (1991) that *when 'constant-$\dot{\sigma}_e$' tests are carried out on electronically controlled tensile machines, it is not completely possible to avoid an initial stress drop and successive 'oscillations'*. Moreover, for such pseudoconstant-$\dot{\sigma}_e$ simulations like in Fig. 7.14 it is expected that the strain will no longer propagate in a homogeneous manner and some localization phenomena will appear during the strain burst.

7.4 A Methodology for Investigating Mechanical Parameters for Critical Conditions on PLC Effect

The question which arises is how one can identify the range of boundary conditions and the range of mechanical parameters of the model described in Sect. 7.2 for which the main characteristics of the PLC effect occur and how one can fit the numerical simulations with experimental tests.

In this section we give a partial answer to this problem. For instance, in order to determine for which input data, that is, for which mechanical parameters and imposed engineering strain-rate, there exists a jerky flow, we consider a stability analysis of a particular solution of the PDEs system (7.41). This allows the calibration and verification of the constitutive model. A stability and bifurcation analysis for investigating the PLC effect has been also used by Mesarovics (1995), Rizzi and Hähner (2004).

7.4.1 Temporal Stability Analysis of Serrated Curves

We analyze in the following the nature of temporal instabilities and, as a consequence, the existence or non-existence of serrations on the stress–engineering strain curve. For doing this, we consider instead of the strain-controlled problem (7.42) the following related initial-boundary value problem

$$\begin{aligned} &\varepsilon(X,0)=\varepsilon^*,\ \sigma(X,0)=\sigma^*,\ t_a(X,0)=t_a^*,\ v(X,0)=\frac{V^*}{L}(L-X),\ \text{for } X\in[0,L],\\ &v(0,t)=V^*=-L\dot{\varepsilon}_e<0,\quad v(L,t)=0,\quad \text{for any } t>0. \end{aligned} \tag{7.45}$$

That means, at the initial moment the bar is not at rest, but the velocity field is linear with respect to the spatial variable and satisfies the boundary conditions corresponding to a strain-controlled experiment.

In this special case the PDEs system (7.41) admits the following *spatial homogeneous solution* in the variables ε, σ and t_a, i.e.

$$\varepsilon=\varepsilon(t)=-\frac{V^*}{L}t=\dot{\varepsilon}_e t,\quad \sigma=\sigma(t),\quad t_a=t_a(t),\quad v=v(X)=\frac{V^*}{L}(L-X), \tag{7.46}$$

where $\sigma(t)$ and $t_a(t)$ are determined as solution of an ordinary differential equations (ODE) system. Taking into account that between ε and t there is a linear relation we can express the variable σ and t_a as function of ε. Functions $\sigma=\sigma(\varepsilon)$ and $t_a=t_a(\varepsilon)$ have to be solution of the Cauchy problem for the non-linear and *non-autonomous* system

$$\begin{cases} \frac{\mathrm{d}\sigma}{\mathrm{d}\varepsilon}=E+\frac{1}{\dot{\varepsilon}_e}G(\varepsilon,\sigma(\varepsilon),t_a(\varepsilon)), & \sigma(\varepsilon^*)=\sigma^*,\\ \frac{\mathrm{d}t_a}{\mathrm{d}\varepsilon}=\frac{1}{\dot{\varepsilon}_e}H(\varepsilon,\sigma(\varepsilon),t_a(\varepsilon)), & t_a(\varepsilon^*)=t_a^*. \end{cases} \tag{7.47}$$

To simplify the stability analysis of the system (7.47) we consider the case when the constitutive functions σ_H, σ_B in (7.21) and Ω in (7.7) do not depend on ε^p, i.e. when the ODE system is *autonomous*. That means $\sigma_\infty=0$, $\Theta_0=0$, $\sigma_2=0$ and $\omega_2=0$, i.e.

$$\sigma_H(\varepsilon^p)=\sigma_0,\quad \sigma_B(\varepsilon^p,t_a)=\sigma_1\left(1-\exp\left(-\frac{t_a}{t_D}\right)^n\right),\quad \Omega(\varepsilon^p)=\omega_1. \tag{7.48}$$

Thus, the solution of the system (7.47) satisfies the Cauchy problem

$$\begin{cases} \frac{\mathrm{d}\sigma}{\mathrm{d}\varepsilon}=E, & \sigma(\varepsilon^*)=0,\\ \frac{\mathrm{d}t_a}{\mathrm{d}\varepsilon}=\frac{1}{\dot{\varepsilon}_e}, & t_a(\varepsilon^*)=0, \end{cases} \tag{7.49}$$

if it lies in the *elastic domain*, that is, for

$$|\sigma| \leq \sigma_0 + \sigma_1(1 - \exp(-(t_a/t_D)^n),$$

and, it satisfies the Cauchy problem

$$\begin{cases} \frac{\mathrm{d}\sigma}{\mathrm{d}\varepsilon} = & f(\sigma, t_a) \equiv E - E\frac{\dot{\varepsilon}_0}{\dot{\varepsilon}_e}\left[\frac{\sigma-\sigma_0-\sigma_1(1-\exp(-(t_a/t_D)^n)}{\sigma_D}\right]^m, \\ & \sigma(\varepsilon^*) = \sigma^*, \\ \frac{\mathrm{d}t_a}{\mathrm{d}\varepsilon} = & g(\sigma, t_a) \equiv -\frac{\dot{\varepsilon}_0}{\omega_1\dot{\varepsilon}_e}\left[\frac{\sigma-\sigma_0-\sigma_1(1-\exp(-(t_a/t_D)^n)}{\sigma_D}\right]^m t_a + \frac{1}{\dot{\varepsilon}_e}, \\ & t_a(\varepsilon^*) = t_a^*. \end{cases} \tag{7.50}$$

if the solution belongs to the *viscoplastic domain in tension*, that is, for

$$\sigma > \sigma_0 + \sigma_1(1 - \exp(-(t_a/t_D)^n).$$

First, we investigate only the behavior of a homogeneous process in the viscoplastic domain, i.e. the solutions of the non-linear autonomous system (7.50). Thus, we do not consider at this moment the case when the homogeneous solution could enter in the elastic domain and has to satisfy the system (7.49). The combined elastic-viscoplastic homogeneous solution for the non-autonomous system is considered later and illustrated numerically for the mechanical parameters in Tables 7.1 and 7.2 in Fig. 7.24.

To sketch the phase portrait of a dynamical system it is useful to plot the nullclines, defined as the curve where $\frac{\mathrm{d}\sigma}{\mathrm{d}\varepsilon} = 0$ and $\frac{\mathrm{d}t_a}{\mathrm{d}\varepsilon} = 0$. The equilibrium points, or the fixed points of the system are defined as the intersection points of the curves $f(\sigma, t_a) = 0$ and $g(\sigma, t_a) = 0$. The system (7.50) has a unique fixed point

$$t_a^{fx} = \frac{\omega_1}{\dot{\varepsilon}_e}, \quad \sigma^{fx} = \sigma_0 + \sigma_1\left[1 - \exp\left(-\left(\frac{\omega_1}{t_D\dot{\varepsilon}_e}\right)^n\right)\right] + \sigma_D\left(\frac{\dot{\varepsilon}_e}{\dot{\varepsilon}_0}\right)^{1/m}. \tag{7.51}$$

Let us note that the ageing time component of the fixed point is just the waiting time of dislocations defined in (7.6).

To study the behavior of the prototypical autonomous system (7.50), we linearize the system around its equilibrium point. Let $(\delta\sigma, \delta t_a)$ be the components of a small disturbance of the fixed point. One shows that the disturbance evolves according to

$$\frac{\mathrm{d}}{\mathrm{d}\varepsilon}\begin{bmatrix}\delta\sigma \\ \delta t_a\end{bmatrix} = \begin{bmatrix}\frac{\partial f}{\partial\sigma} & \frac{\partial f}{\partial t_a} \\ \frac{\partial g}{\partial\sigma} & \frac{\partial g}{\partial t_a}\end{bmatrix}_{\left(\sigma^{fx}, t_a^{fx}\right)}\begin{bmatrix}\delta\sigma \\ \delta t_a\end{bmatrix} + \text{quadratic terms.} \tag{7.52}$$

The matrix of this linearized system is called the Jacobian matrix at the fixed point. The type and the stability of the equilibrium points depends on the eigenvalues λ_1 and λ_2 of the Jacobian matrix and can be characterized through the values

of its trace, determinant and discriminant of the characteristic equation, (see for instance Strogatz 1994) i.e.

$$\begin{aligned}
\mathrm{Tr} = \lambda_1 + \lambda_2 &= -\frac{1}{\omega_1} - \frac{m}{\sigma_D}\left(\frac{\dot{\varepsilon}_0}{\dot{\varepsilon}_e}\right)^{1/m}\left[E - \frac{n\sigma_1}{\omega_1}\left(\frac{\omega_1}{t_D\dot{\varepsilon}_e}\right)^n \exp\left(-\left(\frac{\omega_1}{t_D\dot{\varepsilon}_e}\right)^n\right)\right], \\
\mathrm{Det} = \lambda_1\lambda_2 &= \frac{mE}{\sigma_D\omega_1}\left(\frac{\dot{\varepsilon}_0}{\dot{\varepsilon}_e}\right)^{1/m}, \\
\Delta = (\lambda_1 + \lambda_2)^2 - 4\lambda_1\lambda_2 &= \Delta(\dot{\varepsilon}_e, \dot{\varepsilon}_0, \sigma_1, \sigma_0, \omega_1, t_D, \sigma_D, E, n, m).
\end{aligned} \tag{7.53}$$

The positive value of the determinant rules out the possibility of having a saddle point. Hence the stability of the fixed point can be established just by looking at the sign of trace. Therefore, the equilibrium point can be only

- a *stable node* if $\mathrm{Tr} < 0$ and $\Delta > 0$,
- a *stable focus* if $\mathrm{Tr} < 0$ and $\Delta < 0$,
- an *unstable focus* if $\mathrm{Tr} > 0$ and $\Delta < 0$,
- an *unstable node* if $\mathrm{Tr} > 0$ and $\Delta > 0$.

In this case the linearized system gives a qualitatively correct picture of the phase portrait near the equilibrium point (σ^{fx}, t_a^{fx}). Usually, if the phase portrait changes its topological structure as a parameter is varied, one says that a *bifurcation* occurs. From $(7.53)_3$ one sees that the phase portrait depends on the following 10 mechanical parameters which correspond to:

- boundary condition (7.45): $\dot{\varepsilon}_e$,
- kinetic parameters of viscoplastic constitutive Eq. (7.20): $\dot{\varepsilon}_0$, σ_D, m,
- McCormick's law (7.25) and flow stress due to ageing (7.23): ω_1, σ_1, t_D, n,
- flow stress due to plastic deformation (7.22): σ_0.
- elastic Young modulus E.

We consider, for instance, that only the *characteristic strain-rate factor* $\dot{\varepsilon}_0$, (or, equivalently the *characteristic time* of the viscoplastic constitutive equation $\tau = 1/\dot{\varepsilon}_0$) and the *engineering strain-rate* $\dot{\varepsilon}_e$ vary, while the other parameters are fixed. Then, the corresponding bifurcation plane, is characterized by the curves across which the trace Tr and the discriminant Δ change their signs (see Fig. 7.18).

We show that instability phenomena for the autonomous system (7.50) can occur if and only if the mechanical parameters satisfy the following condition

$$A \equiv \frac{n\sigma_1}{\omega_1 E} > e, \tag{7.54}$$

where e is Euler's number.

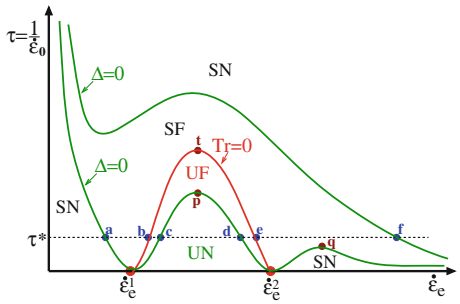

Fig. 7.18 Case $A > e$. Plane of bifurcation of the fixed point (7.51) corresponding to parameters $\tau = 1/\dot{\varepsilon}_0$ and $\dot{\varepsilon}_e$. SN stable node region ($\mathrm{Tr} < 0$, $\Delta > 0$); SF stable focus region ($\mathrm{Tr} < 0$, $\Delta < 0$); UF unstable focus region ($\mathrm{Tr} > 0$, $\Delta < 0$); UN unstable node region ($\mathrm{Tr} > 0$, $\Delta > 0$)

The fulfillment of this relation will also explain the existence of serrated curves for the non-homogeneous case considered in Sect. 7.3.3, i.e. for the strain-controlled initial-boundary value problems (7.42) for the PDEs system (7.41) (see Fig. 7.13).

To prove this statement let us introduce the notations

$$B \equiv \frac{m\omega_1 E}{\sigma_D}, \quad Z(\dot{\varepsilon}_e) \equiv \left(\frac{\omega_1}{t_D \dot{\varepsilon}_e}\right)^n. \tag{7.55}$$

First of all, observe that, if $A \leq e$, then $1 - Azexp(-z) \geq 0$, for any $z > 0$, and consequently, from $(7.53)_1$, it follows that $\mathrm{Tr}\,(\dot{\varepsilon}_0, \dot{\varepsilon}_e) \leq 0$, for any $\dot{\varepsilon}_0 > 0$ and $\dot{\varepsilon}_e > 0$. Therefore, in this case a fixed point can not be unstable.

If $A > e$, then $\mathrm{Tr}(\dot{\varepsilon}_0, \dot{\varepsilon}_e) > 0$ if and only if $0 < \tau = \frac{1}{\dot{\varepsilon}_0} < \tau_{tr}(\dot{\varepsilon}_e)$, where

$$\tau_{tr}(\dot{\varepsilon}_e) = \frac{1}{\dot{\varepsilon}_e} B^m [AZ(\dot{\varepsilon}_e) \exp(-Z(\dot{\varepsilon}_e)) - 1]^m, \quad \text{for } \dot{\varepsilon}_e \in \left(\dot{\varepsilon}_e^1, \dot{\varepsilon}_e^2\right), \tag{7.56}$$

and

$$\dot{\varepsilon}_e^1 = \dot{\varepsilon}_e^1(A, \omega_1, t_D) = \frac{\omega_1}{t_D (x_1)^{1/n}} < \frac{\omega_1}{t_D} < \dot{\varepsilon}_e^2 = \dot{\varepsilon}_e^2(A, \omega_1, t_D) = \frac{\omega_1}{t_D (x_2)^{1/n}}. \tag{7.57}$$

Here x_1, x_2 are the two solutions of the transcendental equation $exp(x) = Ax$ with the property that $x_2(A) < 1 < x_1(A)$.

An approximative solution of this equation, obtained using Newton's method, is

$$x_1 \cong \frac{(1 - A)\exp(1/A)}{A(\exp(1/A) - A)}, \quad x_2 \cong \frac{\sqrt{A}}{\sqrt{A} - 1}\left(3 \ln\left(\sqrt{A} - A\right)\right). \tag{7.58}$$

thus,

$$\dot{\varepsilon}_e^1 \cong \frac{\omega_1}{t_D}\left(\frac{\sqrt{A}-1}{\sqrt{A}(3\ln\sqrt{A}-1)}\right)^{1/n}, \quad \dot{\varepsilon}_e^2 \cong \frac{\omega_1}{t_D}\left(\frac{A(\exp(1/A)-A)}{\exp(1/A)(1-A)}\right)^{1/n}. \tag{7.59}$$

Thus, for $A > e$, $\tau = \tau_{tr}(\dot{\varepsilon}_e)$, is the unique positive curve in the bifurcation plane across which the trace changes its sign, i.e. across which the fixed point (7.51) switches from stable to unstable (see Fig. 7.18). $\dot{\varepsilon}_e^1$ and $\dot{\varepsilon}_e^2$ denote the intersection points of this curve with the axis $\tau = 0$. Therefore, the interval $(\dot{\varepsilon}_e^1, \dot{\varepsilon}_e^2)$ represents the maximal interval for the applied strain-rate $\dot{\varepsilon}_e$ in which a temporal instability can appear when $\dot{\varepsilon}_0 \to \infty$. Formulas (7.59) may give a direct hint about the way the mechanical parameters influence the range of the imposed engineering strain-rate $\dot{\varepsilon}_e$ for which a jerky flow can occur.

Furthermore, one can show that

$$\frac{\partial\dot{\varepsilon}_1^e}{\partial A}<0 \text{ and} \frac{\partial\dot{\varepsilon}_2^e}{\partial A}>0, \quad \frac{\partial\dot{\varepsilon}_1^e}{\partial\omega_1}>0 \text{ and} \frac{\partial\dot{\varepsilon}_2^e}{\partial\omega_1}<0, \quad \frac{\partial\dot{\varepsilon}_1^e}{\partial t_D}<0 \text{ and} \frac{\partial\dot{\varepsilon}_2^e}{\partial t_D}<0, \tag{7.60}$$

which lead to the following conclusions.

Remark 1 If the parameter A, $A > e$, increases, then the interval $(\dot{\varepsilon}_e^1, \dot{\varepsilon}_e^2)$ expands, while in the opposite case shrinks.

Remark 2 If the parameter ω_1 increases, then the interval $(\dot{\varepsilon}_e^1, \dot{\varepsilon}_e^2)$ shrinks, while in the opposite case expands.

Remark 3 If the parameter t_D decreases both the values of $\dot{\varepsilon}_e^1$ and $\dot{\varepsilon}_e^2$ increase.

The curve $\tau = \tau_{tr}(\dot{\varepsilon}_e)$ has a maximum at

$$\dot{\varepsilon}_e^3 = \dot{\varepsilon}_e^3(A,\omega_1,t_D,m,n) = \frac{\omega_1}{t_D(x_3)^{1/n}} \in \left(\frac{\omega_1}{t_D(1+1/m/n)^{1/n}}, \frac{\omega_1}{t_D}\right), \tag{7.61}$$

where x_3 is the solution of the equation $exp(x) = Ax(1+mn(1-x))$ in the interval (x_2, x_1) and $1<x_3<1+1/(mn)<x_1$. Indeed, this follows by analyzing its derivative,

$$\begin{aligned}\frac{\mathrm{d}\tau_{tr}(\dot{\varepsilon}_e)}{\mathrm{d}\dot{\varepsilon}_e} = \frac{B^m}{(\dot{\varepsilon}_e)^2}&[-1+AZ(\dot{\varepsilon}_e)\exp(-Z(\dot{\varepsilon}_e))]^{m-1}\\ &[1-AZ(\dot{\varepsilon}_e)(1+mn(1-Z(\dot{\varepsilon}_e)))\exp(-Z(\dot{\varepsilon}_e))].\end{aligned} \tag{7.62}$$

The maximum value at this point $\tau_{tr}^{max} = \tau_{tr}(\dot{\varepsilon}_e^3)$ determines the maximum value of the characteristic time τ, or equivalently, the minimum value of the characteristic strain-rate factor $\dot{\varepsilon}_0$ for which the fixed point (7.51) can become an *unstable focus*. This global maximum point is denoted by $\mathbf{t} = \mathbf{t}$ $(\dot{\varepsilon}_e^3, \tau_{tr}^{max})$ in Fig. 7.18.

Let us note that there are two positive curves across which the discriminant Δ change its sign, i.e. the eigenvalues change from real to complex (see Fig. 7.18). These are

$$\tau = \tau_{\Delta}^{\pm}(\dot{\varepsilon}_e) = \frac{1}{\dot{\varepsilon}_e} B^m \left(1 \pm \sqrt{AZ(\dot{\varepsilon}_e)\exp(-Z(\dot{\varepsilon}_e))}\right)^{2m}. \tag{7.63}$$

The graph of the function $\tau = \tau_{\Delta}^{-}(\dot{\varepsilon}_e)$ intersects the axis $\tau = 0$ at the points $\dot{\varepsilon}_e^1$ and $\dot{\varepsilon}_e^2$ defined by (7.57), where it reaches its minimum value. There are also two local maxima at the points

$$\dot{\varepsilon}_e^4 \equiv \frac{\omega_1}{t_D(x_4)^{1/n}} \in \left(\dot{\varepsilon}_e^3, \frac{\omega_1}{t_D}\right), \quad \text{and} \quad \dot{\varepsilon}_e^5 \equiv \frac{\omega_1}{t_D(x_5)^{1/n}} \in (\dot{\varepsilon}_e^2, \infty), \tag{7.64}$$

where x_5 and x_4 are the two solutions of the equation $exp(x) = Ax(1 + mn(1 - x))^2$, with the property that $x_5 \in (0, x_2)$ and $x_4 \in (1, x_3)$. Indeed, this follows by analyzing the expression of the derivative of this function, i.e.

$$\begin{aligned} \frac{\mathrm{d}\tau_{\Delta}^{-}(\dot{\varepsilon}_e)}{\mathrm{d}\dot{\varepsilon}_e} = \frac{B^m}{(\dot{\varepsilon}_e)^2}\left[-1 + \sqrt{AZ(\dot{\varepsilon}_e)\exp(-Z(\dot{\varepsilon}_e))}\right]^{2m-1} \\ \times \left[-1 + \sqrt{AZ(\dot{\varepsilon}_e)\exp(-Z(\dot{\varepsilon}_e))}(1 + mn(1 - Z(\dot{\varepsilon}_e)))\right]. \end{aligned} \tag{7.65}$$

The maximum value of the function τ_{Δ^-} at the point $\dot{\varepsilon}_e^4$ determines the maximum value of the characteristic time τ, or equivalently, the minimum value of the characteristic strain-rate factor $\dot{\varepsilon}_0$ for which the fixed point (7.51) can become an *unstable node*. These local maximum points are denoted by $\mathbf{p} = \mathbf{p}\left(\dot{\varepsilon}_e^4, \tau_{\Delta^-}(\dot{\varepsilon}_e^4)\right)$ and $\mathbf{q} = \mathbf{q}\left(\dot{\varepsilon}_e^5, \tau_{\Delta^-}(\dot{\varepsilon}_e^5)\right)$ in the bifurcation plane from Fig. 7.18.

7.4.2 Calibration of Mechanical Parameters

We analyze in the following the mechanical parameters of the model of dynamic strain ageing (DSA) presented in Sect. 7.2 and the way their values lead to the appearance of the PLC effect. Among these parameters we distinguish a first set, summarized in Table 7.1 which is related mainly to the classical elastic-viscoplastic approach used, and a second set, responsible for the evolution of the ageing time, i.e. of the DSA effect, which is shown in Table 7.2.

Material characterization and parameter identification from tension tests at a reference strain-rate for elastic-viscoplastic constitutive models of McCormick type has been considered, for instance, by Zhang et al. (2001) (for AlMgSi alloy), Benallal et al. (2008a) (for AA5083-H116 alloy plates), Böhlke et al. (2009) (for aluminium alloy 2024).

The term $\sigma_H(\varepsilon^p)$ which describes the effect of stress hardening associated with the dislocation density evolution in the stress flow (7.21) is given by a Voce-type equation in Zhang et al. (2001); Böhlke et al. (2009), by an extended Voce-rule in Benallal et al. (2008a, b) or by a power law in Zhang et al. (2012). This part of the constitutive approach does not influence the way the temporal instabilities related with the PLC effect manifests. We adopt here the same Voce-type equation as in Böhlke et al. (2009) (see Table 7.1), but we consider different values for the parameters m, σ_D and $\dot{\varepsilon}_0$. These latter quantities affect the stress component of the equilibrium point (7.51) and the kinetics of the viscoplastic processes in general. Only the elastic Young modulus E from Table 7.1, which is present in condition (7.54), influences the range of unstable PLC behavior.

The effect of DSA is accounted for by the additive term $\sigma_B(\varepsilon^p, t_a)$ in the flow stress, given by relation (7.23), and includes the material parameters t_D and n of the Cottrell-Bilby-Louat ageing kinetics. The maximum value of this contribution to the flow stress, i.e. $\sigma_1 + \varepsilon^p\sigma_2$, corresponds to the saturation of the local solute concentration on dislocations temporarily arrested at localized obstacles. This saturation value of the DSA related stress term is often considered constant (see Table 7.2). A linear plastic strain dependence has been introduced by Böhlke et al. (2009), instead of a plastic strain dependence introduced in the argument of the exponential function of the Cottrell-Bilby-Louat relation in Zhang et al. (2001).

Let us note that, parameter t_D, i.e. the characteristic time for solute diffusion across dislocations, intervenes only in formula of the stress component of the equilibrium point (7.51) and does not affect condition (7.54), that is, it does not influence the appearance of PLC effect. A discussion on how t_D is temperature dependent is done in Mesarovics (1995). We choose here for t_D the same value as in Böhlke et al. (2009).

According to the strain ageing kinetics proposed by Cottrell and Bilby (1949) the exponent n is 2/3. Starting with the paper by Springer and Schwink (1991) an exponent of $1/3$ has been used. Indeed, Ling and McCormick (1993) found that, for the Al-Mg-Si alloy, the exponent 1/3 is more appropriate to describe their results of strain-rate sensitivity measurements and this value is now accepted in the literature (see Table 7.2). Moreover, Ling et al. (1993) claim that the 1/3 value reflects pipe diffusion controlled strain ageing kinetics.

The evolution of the ageing time t_a in the DSA process is governed by the evolution Eq. (7.25) which includes essentially the material function $\Omega(\varepsilon^p) = \omega_1 + \varepsilon^p\omega_2$. Its value represents a strain increment produced when all arrested dislocations overcome localized obstacles and advance to the next pinned configuration. Mesarovics (1995) has evaluated by using the Orowan law (7.6) and some estimations of the densities of mobile and immobile dislocations that $\Omega \cong 10^{-4}$. The value of parameter Ω appears as essential in condition (7.54). Concerning the way Ω varies with the plastic strain Zhang et al. (2001) assumed the non-linear expression (7.7) while Böhlke et al. (2009) the linear one.

From Table 7.2 we see that for the mechanical parameters used by Zhang et al. (2001); Böhlke et al. (2009) condition (7.54) is not satisfied. Therefore, there is no

engineering strain-rate $\dot{\varepsilon}_e$ and no characteristic strain-rate factor $\dot{\varepsilon}_0$ for which the stress-strain curve of a homogeneous process, i.e. solution of the system (7.47), can be serrated. In other words, for these mechanical parameters the PLC effect can not occur. That is why, we used in this paper a larger value for σ_1, just as in Benallal et al. (2008a) and a lower value for ω_1, like in Zhang et al. (2001). With this choice condition (7.54) is fulfilled for $A = 8.23$ which is much larger than Euler's number e. We show in what follows how, under these circumstances, the unstable behavior specific for the PLC effect is captured.

We also notice that for the mechanical parameters used by Benallal et al. (2008a, b), Zhang et al. (2012) condition (7.54) is satisfied for a value of A slightly larger than e.

Further we illustrate how the stability/instability domains described by the curves (7.56) and (7.63) allow identification of the ranges of variation of the characteristic time $\tau = 1/\dot{\varepsilon}_0$ and of the engineering strain $\dot{\varepsilon}_e$ for which the PLC effect can appear. A similar bifurcation analysis can be done if one varies other material parameters of the model which are responsible for the PLC effect i.e., ω_1, t_D, σ_1, σ_D, m.

For the mechanical parameters in the fifth column in Tables 7.1 and 7.2 we have determined the main features of the bifurcation plane represented in Fig. 7.18 and we have summarized the corresponding results in Table 7.3.

Thus, if we choose the characteristic strain-rate factor $\dot{\varepsilon}_0^* = 3.5 \times 10^{-6}\ \mathrm{s}^{-1}$ then the intersection points of the horizontal line $\tau^* = 1/\dot{\varepsilon}_0^*$ with the curves which delimitate the domains of stability/unstability of the equilibrium point show that the range of the engineering strain-rate $\dot{\varepsilon}_e$ for which a jerky flow can appear is $(2.37 \times 10^{-5}\ \mathrm{s}^{-1}, 3.91 \times 10^{-3}\ \mathrm{s}^{-1})$. Indeed, this interval corresponds to the line segment (b, e) in Fig. 7.18 for which the fixed point is an unstable focus. This result is in agreement with the fact that the PLC effect can occur only for a range of engineering strain-rate and the numerical values obtained are appropriate to the ranges found experimentally.

According to the properties of the curves (7.56) and (7.63) in the bifurcation plane, if τ^* increases (i.e. $\dot{\varepsilon}_0^* = 1/\tau^*$ decreases), but without exceeding the value corresponding to the maximum point **t**, then the corresponding unstable focus interval for $\dot{\varepsilon}_e$ shrinks. For $\tau^* = 5.40 \times 10^9$ s (i.e. for $\dot{\varepsilon}_0^* = 1.85 \times 10^{-10}\ \mathrm{s}^{-1}$) the unstable interval reduces to the point $_e = 1.97 \times 10^{-4}\ \mathrm{s}^{-1}$.

If τ^* decreases (i.e., if $\dot{\varepsilon}_0^* = 1/\tau^*$ increases) then the corresponding interval of $\dot{\varepsilon}_e$ for which the fixed point is an unstable focus expands. The maximum interval is attained when $\tau^* \to 0$, that is $\dot{\varepsilon}_e \in \left(\dot{\varepsilon}_e^1 = 7.99 \times 10^{-6}\ \mathrm{s}^{-1}, \dot{\varepsilon}_e^2 = 1.05 \times 10^{-1}\ \mathrm{s}^{-1}\right)$ (see Table 7.3 and Fig. 7.18). Therefore, we can adjust the interval of the imposed strain-rate $\dot{\varepsilon}_e$ for which serrated curves appear with that found in laboratory tests for which the PLC effect manifests by an appropriate choice of the characteristic strain-rate factor $\dot{\varepsilon}_0$.

Moreover, the range of $\dot{\varepsilon}_e$ for which the equilibrium point (7.51) is an unstable point can be adapted, according to Remark 1–3 in Sect. 7.4.1, by increasing or decreasing the values of A, or ω_1, or t_D. We can also show that when m increases

Table 7.3 Type of equilibrium point (7.51) for parameters in Tables 7.1 and 7.2 and coordinates of the points in bifurcation plane from Fig. 7.18

Stability/Unstability intervals	Point on Fig. 7.18	$\dot{\varepsilon}_e\,(\mathrm{s}^{-1})$	$\tau\,(\mathrm{s})$	$\dot{\varepsilon}_0 = 1/\tau\,(\mathrm{s}^{-1})$
Stable node interval	$\uparrow$	$\uparrow$		
	a	5.99×10^{-7}	2.85×10^{5}	3.5×10^{-6}
Stable focus interval	$\downarrow$	$\downarrow$		
	$\dot{\varepsilon}_e^1$	7.99×10^{-6}	0	∞
Stable focus interval	$\uparrow$	$\uparrow$		
	b	2.37×10^{-5}	2.85×10^{5}	3.5×10^{-6}
Unstable focus interval	$\downarrow$	$\downarrow$		
	c	#	#	#
Unstable focus interval	$\updownarrow$	$\updownarrow$		
	t	1.97×10^{-4}	5.40×10^{9}	1.85×10^{-10}
Unstable focus interval	$\updownarrow$	$\updownarrow$		
	p	2.25×10^{-4}	14.93	6.69×10^{-2}
Unstable focus interval	$\updownarrow$	$\updownarrow$		
	d	#	#	#
Unstable focus interval	$\uparrow$	$\uparrow$		
	e	3.91×10^{-3}	2.85×10^{5}	3.5×10^{-6}
Stable focus interval	$\downarrow$	$\downarrow$		
	$\dot{\varepsilon}_e^2$	1.05×10^{-1}	0	∞
Stable focus interval	$\uparrow$	$\uparrow$		
	f	12.8	2.85×10^{5}	3.5×10^{-6}
Stable node interval	$\downarrow$	$\downarrow$		

There is no intersection between the graph of $\tau = \tau_{\Delta^-}(\dot{\varepsilon}_e)$ and $\tau^* = 1/\dot{\varepsilon}_0^* = 2.85 \times 10^5$ s

then the maximum values of the functions $\tau = \tau_{tr}(\dot{\varepsilon}_e)$ and $\tau = \tau_{\Delta^-}(\dot{\varepsilon}_e)$ attained at the points **t**, **p** and **q** increase.

In order to exemplify how the prediction of this bifurcation analysis is in agreement with the behavior of the solution of the autonomous nonlinear ODE system (7.50) we have considered for a fixed characteristic strain-rate factor $\dot{\varepsilon}_0^*$, or equivalently a fixed τ^* (see Table 7.3), different increasing values of the imposed strain-rate $\dot{\varepsilon}_e$, which covers in a successive manner the stable/unstable zones in Fig. 7.18.

If the pair $(\tau^*, \dot{\varepsilon}_e)$ lies in the *stable node region*, for instance below $\tau = \tau_{\Delta^-}(\dot{\varepsilon}_e)$, for $\dot{\varepsilon}_e < \dot{\varepsilon}_e^1$ (see Fig. 7.18) then the homogeneous solution in the viscoplastic domain is represented in Fig. 7.19. The process starts at the boundary between the elastic

and viscoplastic domain, i.e. the initial condition (σ, t_a) satisfies relations $\sigma = E\varepsilon = \sigma_0 + \sigma_1(1 - \exp(-(\varepsilon/\dot{\varepsilon}_e/t_D)^n)$ and $t_a = \varepsilon/\dot{\varepsilon}_e$.

One can see that there is no stress decay and the ageing time increases as long as the stress increases to its equilibrium value $\sigma_{eq}^{fx} = 211.5$ MPa, and afterwards the ageing time decays at the value of the waiting time $t_a^{fx} = \omega_1/\dot{\varepsilon}_e = 72$ s.

If the pair $(\tau^*, \dot{\varepsilon}_e)$ lies in the *stable focus area*, that is, between the points **a** and **b** in Fig. 7.18, then the homogeneous solution in the viscoplastic domain is illustrated in Fig. 7.20. One observes the appearance of a first stress decay followed by some small oscillations before to reach the equilibrium stress $\sigma_{eq}^{fx} = 214.4$ MPa. The ageing time behaves in the same manner, although the oscillations are not visible at the scale of the figure, and it stabilizes at the value of the waiting time $t_a^{fx} = \omega_1/\dot{\varepsilon}_e = 3.6$ s.

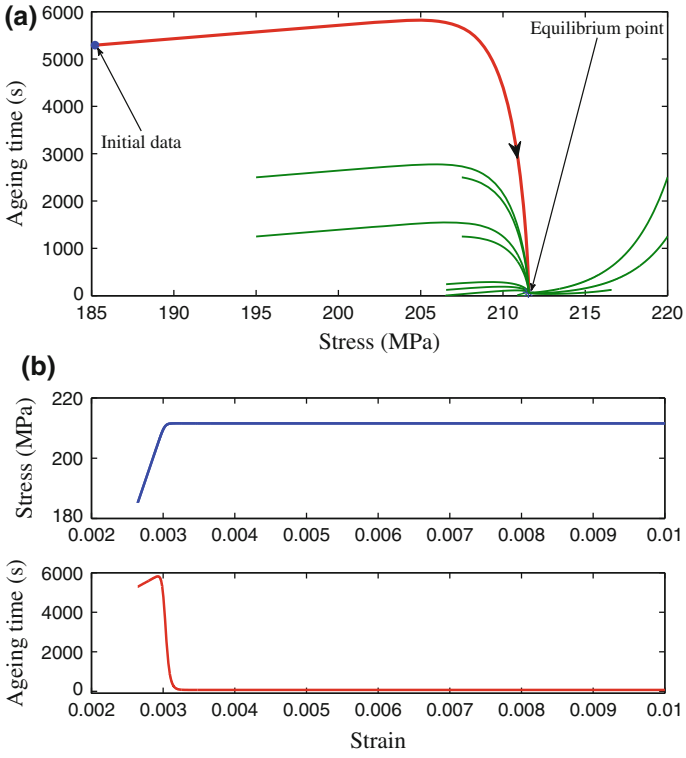

Fig. 7.19 *Stable Node Interval* $\dot{\varepsilon}_e = 5 \times 10^{-7}$ s^{-1} and $\dot{\varepsilon}_0^* = 3.5 \times 10^{-6}$ s^{-1} ($\tau^* = 2.85 \times 10^5$ s). Homogeneous process described by (7.50). **a** Phase portrait. **b** Stress and ageing time versus strain

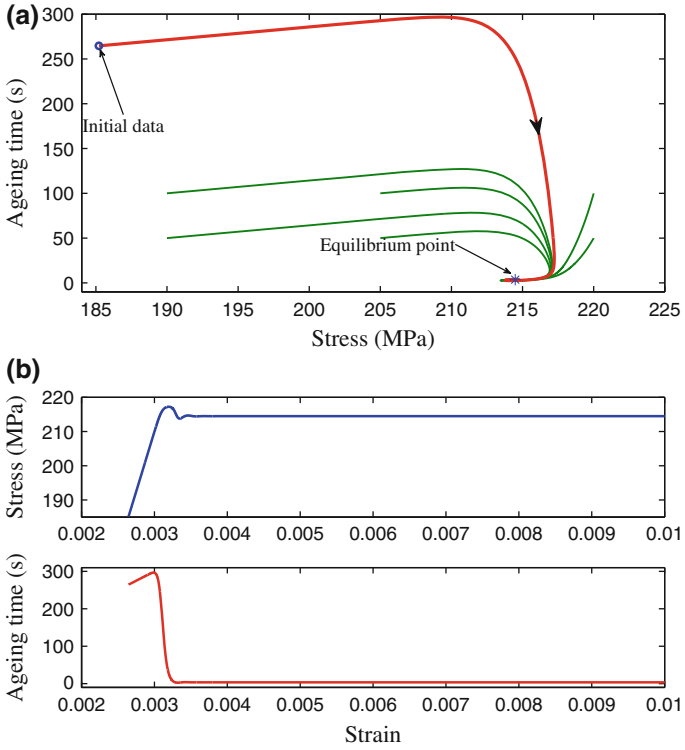

Fig. 7.20 *Stable Focus Interval* $\dot{\varepsilon}_e = 10^{-5}\ \mathrm{s}^{-1}$ and $\dot{\varepsilon}_0^* = 3.5 \times 10^{-6}\ \mathrm{s}^{-1}$ ($\tau^* = 2.85 \times 10^5$ s). Homogeneous process described by (7.50). **a** Phase portrait. **b** Stress and ageing time vs. strain

When the imposed strain-rate $\dot{\varepsilon}_e$ enters the estimated range of instability, that is, when the pair $(\tau^*, \dot{\varepsilon}_e)$ lies in the *unstable focus area* between the points **b** and **e** in Fig. 7.18, then the homogeneous solution in the viscoplastic domain is represented in Fig. 7.21. After a first drop of the stress and of the ageing time large oscillations, almost periodic, around the equilibrium point ($\sigma^{fx} = 196.8$ MPa, $t_a^{fx} = 0.036$ s) appear. The amplitude of the stress drop is around 23 MPa.

In this case the trajectories of the solutions in the phase plane spiral toward a *stable limit cycle*. This behavior illustrates that the nonlinear system is able to describe self-sustained oscillations. It is worth noting that the limit cycle shows a slow dynamics during one part of the cycle followed by a fast dynamics during the remaining part of the cycle. Indeed, one sees that the periodic oscillations consist of a slow increase of the stress which is followed by an abrupt fall in stress. This slow-fast dynamic process is in agreement with the characteristics of the PLC effect.

Oscillations of this type resemble with the so called "relaxation oscillations" of dynamical systems containing a small parameter which lead to singular perturbation. The prototype of this behavior is the van der Pol oscillator (see Strogatz 1994).

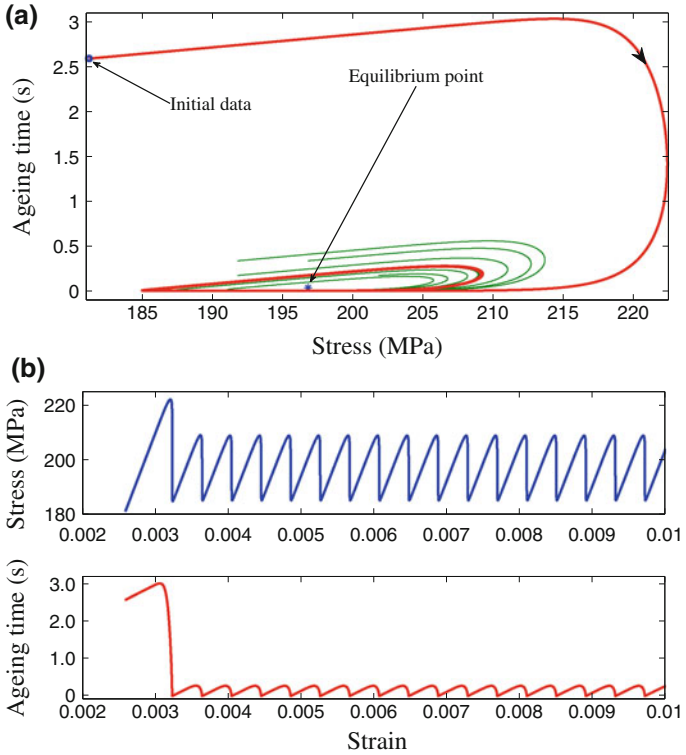

Fig. 7.21 *Unstable Focus Interval* $\dot{\varepsilon}_e = 10^{-3}\ \mathrm{s}^{-1}$ and $\dot{\varepsilon}_0^* = 3.5 \times 10^{-6}\ \mathrm{s}^{-1}$ ($\tau^* = 2.85 \times 10^5$ s). Homogeneous process described by (50). **a** Phase portrait. **b** Stress and ageing time vs. strain

Characteristic of the relaxation oscillations is the presence of phases in the cycle with different time scales: a phase of slow change followed by a short phase of rapid change in which the system practically jumps to the next stage of slow variation. In general, the specificity of these relaxation oscillations is that in a single period the solution describes two slow-fast alternation accompanied by two discontinuities, while for our nonlinear system (7.50) the solution experiences in a single period only one slow-fast alternation.

When, by increasing the imposed strain-rate, the pair $(\tau^*, \dot{\varepsilon}_e)$ enters again into a *stable focus region*, that is, it lies between the points **e** and **f** in Fig. 7.18, then the homogeneous process in the viscoplastic domain is represented in Fig. 7.22. The behavior of the solution is similar with that in Fig. 7.20, with the difference that the first stress drop is much more important and the oscillations are more visible before the solution reaches the equilibrium point ($\sigma^{fx} = 190.4$ MPa, $t_a^{fx} = 0.0036$ s).

We have also considered the case when the pair $(\tau, \dot{\varepsilon}_e)$ belongs to the *unstable node area*, that is, it lies below the curve $\tau = \tau_{\Delta^-}(\dot{\varepsilon}_e)$, for $\dot{\varepsilon}_e \in (\dot{\varepsilon}_e^1, \dot{\varepsilon}_e^2)$ in Fig. 7.18.

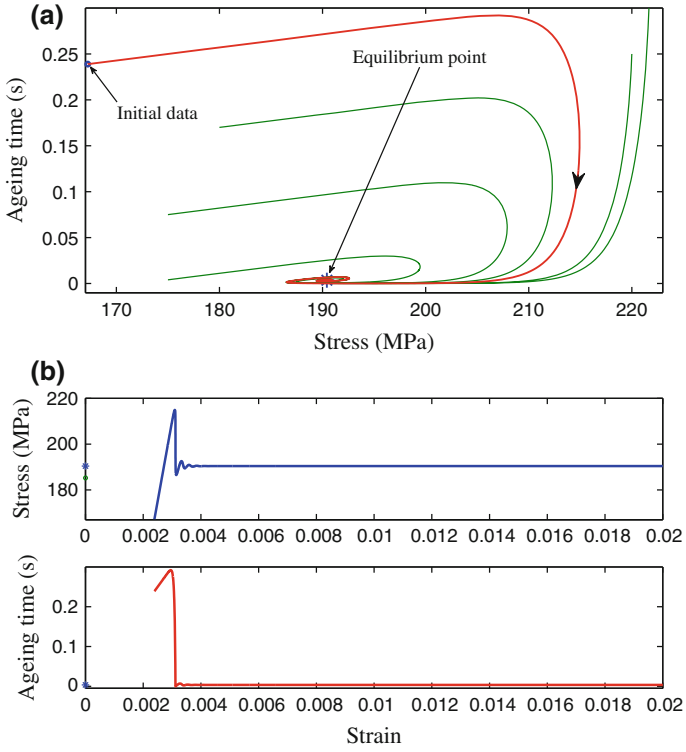

Fig. 7.22 *Stable Focus Interval* $\dot{\varepsilon}_e = 10^{-2}\ \mathrm{s}^{-1}$ and $\dot{\varepsilon}_0^* = 3.5 \times 10^{-6}\ \mathrm{s}^{-1}$ ($\tau^* = 2.85 \times 10^5$ s). Homogeneous process described by (7.50). **a** Phase portrait. **b** Stress and ageing time vs. strain

For instance, if we choose $\dot{\varepsilon}_e = 2.25 \times 10^{-4}\ \mathrm{s}^{-1}$, which corresponds to the local maximum point **p**, it follows that in order to be in the unstable area, according to Table 7.3, it is necessary that τ be less than 14.93 s, or equivalently $\dot{\varepsilon}_0$ be greater than $6.69 \times 10^{-2}\ \mathrm{s}^{-1}$. Such a situation is illustrated in Fig. 7.23. The same as in the case of the unstable focus fixed point the trajectories in the phase plane have the property that they approach a *stable limit cycle*. Numerical solutions illustrated in Fig. 7.23a show stable spirals giving rise to a limit cycle and to almost "periodic" oscillations. In this case both the stress and the ageing time show much larger oscillations around the equilibrium point ($\sigma^{fx} = 179.5$ MPa, $t_a^{fx} = 0.1636$ s). The amplitude of the stress drop increases to 50 MPa.

During a single period we record a slow and two fast variations of the solution. Indeed, the limit cycle consists of an extremely slow increase of the stress followed by a sudden discharge and a sudden rise of the stress. During the stress drop the ageing time reaches its minimum value, while it suffers a sudden increases during the sudden rise of the stress. This behavior is not typical to the PLC effect, but

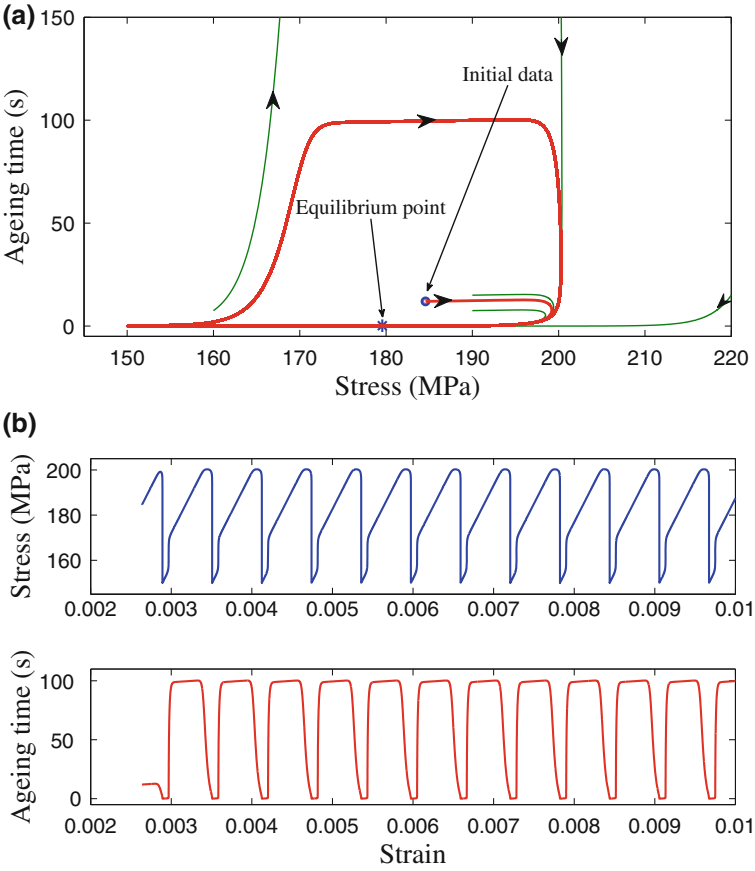

Fig. 7.23 *Unstable Node Area* $\dot{\varepsilon}_e = 2.2 \times 10^{-4}\ \mathrm{s}^{-1}$ and $\dot{\varepsilon}_0 = 6.\,\mathrm{s}^{-1}$ ($\tau = 0.16$ s). Homogeneous process described by (7.50). **a** Phase portrait. **b** Stress and ageing time vs. strain

illustrates how the nonlinear ODE system describes self-sustained oscillations for a large value of $\dot{\varepsilon}_0$.

The serrated stress-strain curves obtained in Figs. 7.21b and 7.23b show two important characteristic features: they are "horizontal" and have constant amplitude. The first is due to the fact that the strain hardening is neglected, while the second is a consequence of the assumption that the stress accounting for the PLC effect σ_B does not depend on ε^p, according to the constitutive relations (7.48) used in the bifurcation analysis.

Let us consider now the general case of the elastic-viscoplastic model with the strain hardening term $\sigma_H(\varepsilon^p)$ described by the Voce rule (7.22) and the term $\sigma_B(t_a, \varepsilon^p)$, responsible for the DSA effect, described by (7.23). The mechanical parameters are given in the fifth column in Tables 7.1 and 7.2.

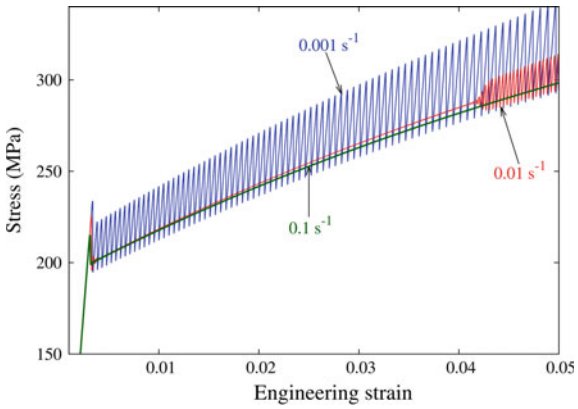

Fig. 7.24 Elastic-viscoplastic homogeneous process with strain hardening described by the non-autonomous system (7.47) for three imposed engineering strain-rates: $\dot{\varepsilon}_e = 10^{-3}\ \mathrm{s}^{-1}$, $\dot{\varepsilon}_e = 10^{-2}\ \mathrm{s}^{-1}$ and $\dot{\varepsilon}_e = 10^{-1}\ \mathrm{s}^{-1}$ when $\dot{\varepsilon}_0 = 3.5 \times 10^{-6}\ \mathrm{s}^{-1}$ ($\tau = 2.85 \times 10^5$ s)

In this case, the homogeneous process is described by the non-autonomous system (7.47) which includes both the elastic and the viscoplastic case. The numerical solutions obtained for three imposed engineering strain-rates $\dot{\varepsilon}_e$ are illustrated in Fig. 7.24.

The solution obtained for $\dot{\varepsilon}_e = 10^{-3}\ \mathrm{s}^{-1}$ has to be compared with the solution obtained in Fig. 7.21 when the fixed point is an unstable focus. One observes how the hardening rule leads to an increasing stress-strain serrated curve. Like in Fig. 7.21b there is an initial large stress drop, followed by large oscillations, but having now an increasing amplitude which ranges from 25.6 to 49.5 MPa. That is due to the fact that in the viscoplastic deformation process the term $\sigma_0 + \varepsilon^p \sigma_1$ which characterizes the saturation value of the DSA related stress term increases with plastic strain. This gradually increasing amplitude is in agreement with experimental facts (see for instance Fig. 7.1).

Moreover, it should be noted that a sawtooth is composed by a stress drop, which is a fast viscoplastic and dissipative process, while the reloading part, having the slope of the elastic Young modulus E, is a slow elastic process.

In the case of the higher strain-rate $\dot{\varepsilon}_e = 10^{-2}\ \mathrm{s}^{-1}$ the bifurcation analysis has predicted for the autonomous system, according to Fig. 7.22b, a stress-strain curve which is not serrated, since in this case we are outside the interval of instability described in Table 7.3. In the general case of the non-autonomous system (7.47) we see in Fig. 7.24 that the stress-strain curve preserves the same features as in the stable focus case for lower values of the engineering strain ε_e. Indeed, there is in the beginning a large stress drop followed by small oscillations which are damped and continued with a nice increasing smooth curve. If the strain becomes larger one can see that a serrated curve appears reflecting an unstable behavior of PLC type. This behavior is in agreement with the remarks in Sect. 7.4.1 that by increasing the value of the parameter $A = \frac{n\sigma_1}{\omega_1 E}$ the range of imposed strain-rate $\dot{\varepsilon}_e$ for which the

autonomous ODE system (7.50) has an unstable behavior expands. Indeed, in this case, if we consider the non-autonomous system (7.47) with frozen coefficients at ε^p then the parameter which characterizes the instability read as $A(\varepsilon^p) = \frac{n(\sigma_1 + \sigma_2 \varepsilon^p)}{\omega_1 E}$ and is increasing with the plastic strain. This explains the appearance of oscillations at this strain-rate for large value of the engineering strain ε_e.

If the strain-rate increases again by an order of magnitude, i.e. to 10^{-1}s^{-1}, one sees that the solution does not show unstable behavior for the range of strain in the figure, behavior which is in agreement with the stability/instability analysis.

Thus, the graphs obtained in Fig. 7.24 correspond to spatially homogeneous processes whose initial data are $(7.45)_1$ which is an ideal case since from the beginning we have supposed a linear distribution of the velocity in the bar. The real process corresponds to the initial-boundary value problem (7.42) which introduces from the start a small shock perturbation. This perturbation leads to spatial inhomogeneous solutions which have been analyzed in Sect. 7.3.3.1.

Therefore, the graphs in Fig. 7.24 have to be compared with those obtained in Fig. 7.13 for the non-homogeneous case. The similarities between the stress-strain curves confirm the bifurcation analysis performed and their differences highlight the influence of localization phenomena.

7.5 Conclusions and Outlook

The analyzed constitutive model for dynamic strain ageing provides a macroscopic description of the temporal and spatial features of the Portevin-Le Chatelier plastic instabilities in satisfactory agreement with experimental results. We have shown that, depending on the tensile testing conditions, the model describes both the serrated yielding and the staircase response. The sensitivity of the model to the boundary conditions can capture the influence of the testing machine on the stress - engineering strain curves as it is met in practice.

In order to improve the calibration of the mechanical parameters for critical conditions on PLC effect two directions require further analysis. The first one concerns the properties of the solutions of the autonomous dynamical system (7.50). We have seen that the appearance of a serrated stress-strain curve, i.e. of the unstable PLC behavior, is related to a Hopf bifurcation and that the emerging solution is a limit cycle in the phase plane. The shape and size of the limit cycle allows to estimate the amplitude of the periodic stress drops. But to find analytically the shape of the limit cycle for a dynamical system based on its equations is a tough problem. Therefore, in order to determine how the mechanical parameters of the model influence the serrations of a stress - strain curve one need to find a good estimate of a trapping region for the trajectories. That means to find a closed connected set in which all trajectories are confined (see Strogatz 1994).

A second direction is to investigate the influence of the parameters of the model on the localization phenomena which may develop in the dynamic strain ageing process. That means to perform a spatial stability analysis of the solutions of the

PDEs system (7.41). For doing this we have to analyze the stability of spatially homogeneous solutions to infinitesimal perturbations which is a necessary condition for the nucleation and propagation of strain bands.

Acknowledgments The author acknowledges support from the Romanian Ministry of Education and Research through Project PCCE ID-100/2010.

Appendix: Numerical Scheme

The numerical scheme used to solve the initial–boundary value problems (7.42)–(7.44) for the hyperbolic semilinear system of PDEs (7.41) is a variant of the standard method of characteristic (see for instance Mihăilescu-Suliciu and Suliciu 1985). A time integration step condition is used to ensure the numerical stability.

Let us note that by introducing the notations

$$p = \sigma + \sqrt{\rho E}v, \quad q = \sigma - \sqrt{\rho E}v, \quad r = \sigma - E\varepsilon, \tag{7.66}$$

we can write the system (7.41) in its characteristic form

$$\frac{\partial p}{\partial t} - C\frac{\partial p}{\partial X} = \tilde{G}(p,q,r,t_a), \quad \frac{\partial q}{\partial t} + C\frac{\partial q}{\partial X} = \tilde{G}(p,q,r,t_a), \tag{7.67}$$

$$\frac{\partial r}{\partial t} = \tilde{G}(p,q,r,t_a), \quad \frac{\partial t_a}{\partial t} = \tilde{H}(p,q,r,t_a), \tag{7.68}$$

where $C = \sqrt{E/\rho}$ is the longitudinal wave speed and

$$(\tilde{G},\tilde{H})(p,q,r,t_a) = (G,H)(\varepsilon,\sigma,t_a) = (G,H)\left(\frac{1}{E}\left(\frac{p+q}{2} - r\right), \frac{p+q}{2}, t_a\right).$$

Along the constant characteristic directions of the system the following relations are satisfied

$$\begin{aligned} \mathrm{d}p &= \tilde{G}(p,q,r,t_a)\mathrm{d}t \quad \text{on} \quad \mathrm{d}X = -C\mathrm{d}t, \\ \mathrm{d}q &= \tilde{G}(p,q,r,t_a)\mathrm{d}t \quad \text{on} \quad \mathrm{d}X = C\mathrm{d}t, \\ \mathrm{d}r &= \tilde{G}(p,q,r,t_a)\mathrm{d}t \quad \text{on} \quad \mathrm{d}X = 0, \\ \mathrm{d}t_a &= \tilde{H}(p,q,r,t_a)\mathrm{d}t \quad \text{on} \quad \mathrm{d}X = 0. \end{aligned} \tag{7.69}$$

The numerical solution is build in agreement to the stencil in Fig. 7.25. We partition the domain in space using a mesh $X_0,\ldots, X_i,\ldots, X_N$ and in time using a mesh $t_0,\ldots, t_j,\ldots$. We assume a uniform partition both in space and in time, so the difference between two consecutive space points will be h and between two

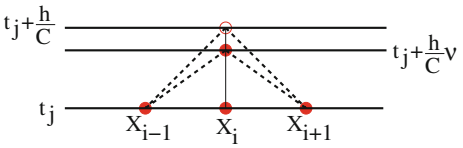

Fig. 7.25 Stencil for the method of characteristics

consecutive time points will be τ. We denote by $u(X_i, t_j) = u_i^j$ the values of a generic function u at the mesh points.

The *first order numerical approximation* is a set of four function (p, q, r, t_a) defined on the above mesh and satisfying the following iterative relations

$$\begin{aligned}
&\frac{p_i^{j+1} - p_i^j}{\tau} - \frac{C}{h}\left(p_{i+1}^j - p_i^j\right) = (1-\nu)\tilde{G}_i^j + \nu\tilde{G}_{i+1}^j,\\
&\frac{q_i^{j+1} - q_i^j}{\tau} + \frac{C}{h}\left(q_i^j - q_{i-1}^j\right) = (1-\nu)\tilde{G}_i^j + \nu\tilde{G}_{i-1}^j,\\
&r_i^{j+1} = r_i^j + \tau\tilde{G}_i^j, \quad t_{ai}^{j+1} = t_{ai}^j + \tau\tilde{H}_i^j,
\end{aligned} \tag{7.70}$$

where the Courant number ν has to satisfy condition

$$\nu \equiv C\frac{\tau}{h} \leq 1, \tag{7.71}$$

in order to ensure the numerical stability of the scheme (see Richtmyer and Morton 1967).

The iterative relations for this explicit scheme can be written as

$$\begin{aligned}
p_i^{j+1} &= (1-\nu)\left(p_i^j + \tau\tilde{G}_i^j\right) + \nu\left(p_{i+1}^j + \tau\tilde{G}_{i+1}^j\right),\\
q_i^{j+1} &= (1-\nu)\left(q_i^j + \tau\tilde{G}_i^j\right) + \nu\left(q_{i-1}^j + \tau\tilde{G}_{i-1}^j\right),\\
r_i^{j+1} &= r_i^j + \tau\tilde{G}_i^j, \quad t_{ai}^{j+1} = t_{ai}^j + \tau\tilde{H}_i^j,
\end{aligned} \tag{7.72}$$

or in terms of initial variables σ, ε, v, t_a the *first approximation* becomes

$$\begin{aligned}
\sigma_i^{j+1} &= (1-\nu)\sigma_i^j + \frac{\nu}{2}\left(\sigma_{i+1}^j + \sigma_{i-1}^j\right) + \frac{\nu}{2}\sqrt{\rho E}\left(v_{i+1}^j - v_{i-1}^j\right)\\
&\quad + \tau\left((1-\nu)G_i^j + \frac{\nu}{2}\left(G_{i+1}^j + G_i^j\right)\right),\\
v_i^{j+1} &= (1-\nu)v_i^j + \frac{\nu}{2}\left(v_{i+1}^j + v_{i-1}^j\right) + \frac{\nu}{2}\frac{1}{\sqrt{\rho E}}\left(\sigma_{i+1}^j - \sigma_{i-1}^j\right)\\
&\quad + \tau\frac{\nu}{2}\frac{1}{\sqrt{\rho E}}\left(G_{i+1}^j - G_{i-1}^j\right),\\
\varepsilon_i^{j+1} &= \varepsilon_i^j + \frac{1}{E}\left(\sigma_i^{j+1} - \sigma_i^j\right) - \tau\frac{1}{E}G_i^j, \quad t_{ai}^{j+1} = t_{ai}^j + \tau H_i^j.
\end{aligned} \tag{7.73}$$

The *second order numerical approximation* is a set of four function $\left(\overset{(2)}{p}, \overset{(2)}{q}, \overset{(2)}{r}, \overset{(2)}{t_a}\right)$ defined on the mesh and satisfying the following iterative relations

$$\begin{aligned}
&\frac{\overset{(2)}{p}{}_i^{j+1} - p_i^j}{\tau} - \frac{C}{h}\left(p_{i+1}^j - p_i^j\right) = \frac{(1-\nu)}{2}\left(\tilde{G}_i^j + \overset{(1)}{G}{}_i^{j+1}\right) + \frac{\nu}{2}\left(\tilde{G}_{i+1}^j + \overset{(1)}{G}{}_i^{j+1}\right),\\
&\frac{\overset{(2)}{q}{}_i^{j+1} - q_i^j}{\tau} + \frac{C}{h}\left(q_i^j - q_{i-1}^j\right) = \frac{(1-\nu)}{2}\left(\tilde{G}_i^j + \overset{(1)}{G}{}_i^{j+1}\right) + \frac{\nu}{2}\left(\tilde{G}_{i-1}^j + \overset{(1)}{G}{}_i^{j+1}\right),\\
&\overset{(2)}{r}{}_i^{j+1} = r_i^j + \frac{\tau}{2}\left(\tilde{G}_i^j + \overset{(1)}{G}{}_i^{j+1}\right), \quad \overset{(2)}{t_a}{}_i^{j+1} = t_{ai}^j + \frac{\tau}{2}\left(\tilde{H}_i^j + \overset{(1)}{H}{}_i^{j+1}\right),
\end{aligned} \tag{7.74}$$

where $\overset{(1)}{G}{}_i^{j+1} = \tilde{G}(p_i^{j+1}, q_i^{j+1}, r_i^{j+1}, t_{ai}^{j+1})$ and $\overset{(1)}{H}{}_i^{j+1} = \tilde{H}\left(p_i^{j+1}, q_i^{j+1}, r_i^{j+1}, t_{ai}^{j+1}\right)$ are computed using the first approximation (7.72).

The *second order numerical approximation* in terms of initial variables σ, ε, v, t_a becomes

$$\begin{aligned}
\overset{(2)}{\sigma}{}_i^{j+1} &= (1-\nu)\left(\sigma_i^j + \frac{\tau}{2}\left(G_i^j + \overset{(1)}{G}{}_i^{j+1}\right)\right) + \frac{\nu}{2}\left(\sigma_{i+1}^j + |\sigma_{i-1}^j\right) + \frac{\nu}{2}\sqrt{\rho E}\left(v_{i+1}^j - v_{i-1}^j\right)\\
&\quad + \nu\frac{\tau}{4}\left(2\overset{(1)}{G}{}_i^{j+1} + G_{i+1}^j + G_{i-1}^j\right),\\
\overset{(2)}{v}{}_i^{j+1} &= (1-\nu)v_i^j + \frac{\nu}{2}\left(v_{i+1}^j + v_{i-1}^j\right) + \frac{\nu}{2}\frac{1}{\sqrt{\rho E}}\left(\sigma_{i+1}^j - \sigma_{i-1}^j\right)\\
&\quad + \nu\frac{\tau}{4}\frac{1}{\sqrt{\rho E}}\left(G_{i+1}^j - G_{i-1}^j\right),\\
\overset{(2)}{\varepsilon}{}_i^{j+1} &= \varepsilon_i^j + \frac{1}{E}\left(\overset{(2)}{\sigma}{}_i^{j+1} - \sigma_i^j\right) - \frac{\tau}{2E}\left(G_i^j + \overset{(1)}{G}{}_i^{j+1}\right),\\
\overset{(2)}{t_a}{}_i^{j+1} &= t_{ai}^j + \frac{\tau}{2}\left(H_i^j + \overset{(1)}{H}{}_i^{j+1}\right),
\end{aligned} \tag{7.75}$$

where $\overset{(1)}{G}{}_i^{j+1} = G\left(\varepsilon_i^{j+1}, \sigma_i^{j+1}, t_{ai}^{j+1}\right)$ and $\overset{(1)}{H}{}_i^{j+1} = H\left(\varepsilon_i^{j+1}, \sigma_i^{j+1}, t_{ai}^{j+1}\right)$ are computed using the first approximation (7.73).

Boundary conditions

The *left boundary condition* $v(0,t) = V^*$, or equivalently, $p(0,t) - q(0,t) = 2\sqrt{\rho E}V^*$, for the *strain controlled experiment* (7.42), leads to the following iterative relations.

The *first order approximation* at the node X_0 read as

$$\begin{aligned}
\sigma_0^{j+1} &= (1-\nu)\left(\sigma_0^j + \sqrt{\rho E}V^* + \tau G_0^j\right) + \nu\left(\sigma_1^j + \sqrt{\rho E}v_1^j + \tau G_1^j\right) - \sqrt{\rho E}V^*,\\
v_0^{j+1} &= V^*,\\
\varepsilon_0^{j+1} &= \varepsilon_0^j + \frac{1}{E}\left(\sigma_0^{j+1} - \sigma_0^j\right) - \frac{\tau}{E}G_0^j, \quad t_{a0}^{j+1} = t_{a0}^j + \tau H_0^j.
\end{aligned} \tag{7.76}$$

and the *second order approximation* is

$$\begin{aligned}
\overset{(2)}{\sigma}{}_0^{j+1} &= (1-\nu)\left(\sigma_0^j + \sqrt{\rho E}V^* + \frac{\tau}{2}\left(\overset{(1)}{G}{}_0^{j+1} + G_0^j\right)\right)\\
&\quad + \nu\left(\sigma_1^j + \sqrt{\rho E}v_1^j + \frac{\tau}{2}\left(\overset{(1)}{G}{}_0^{j+1} + G_1^j\right)\right) - \sqrt{\rho E}V^*,\\
\overset{(2)}{v}{}_0^{j+1} &= V^*,\\
\overset{(2)}{\varepsilon}{}_0^{j+1} &= \varepsilon_0^j + \frac{1}{E}\left(\overset{(2)}{\sigma}{}_0^{j+1} - \sigma_0^j\right) - \frac{\tau}{2E}\left(G_0^j + \overset{(1)}{G}{}_0^{j+1}\right), \quad \overset{(2)}{t}{}_{a0}^{j+1} = t_{a0}^j + \frac{\tau}{2}\left(H_0^j + \overset{(1)}{H}{}_0^{j+1}\right).
\end{aligned} \tag{7.77}$$

where $\overset{(1)}{G}{}_0^{j+1} = G\left(\varepsilon_0^{j+1}, \sigma_0^{j+1}, t_{a0}^{j+1}\right)$ and $\overset{(1)}{H}{}_0^{j+1} = H\left(\varepsilon_0^{j+1}, \sigma_0^{j+1}, t_{a0}^{j+1}\right)$ are computed using the first approximation given by relations (7.76).

The *left boundary condition* $\sigma(0,t) = S^*(t)$, or equivalently, $p(0,t) + q(0,t) = 2S^*(t)$, for the *stress controlled experiment* (7.42), leads to the following iterative relations.

The *first order approximation* at the node X_0 read as

$$\begin{aligned}
\sigma_0^{j+1} &= S^*((j+1)\tau),\\
v_0^{j+1} &= (1-\nu)\left(v_0^j + \frac{S^*(j\tau)}{\sqrt{\rho E}} + \frac{\tau}{\sqrt{\rho E}}G_0^j\right)\\
&\quad + \nu\left(v_1^j + \frac{\sigma_1^j}{\sqrt{\rho E}} + \frac{\tau}{\sqrt{\rho E}}G_1^j\right) - \frac{S^*((j+1)\tau)}{\sqrt{\rho E}},\\
\varepsilon_0^{j+1} &= \varepsilon_0^j + \frac{1}{E}\left(\sigma_0^{j+1} - \sigma_0^j\right) - \frac{\tau}{E}G_0^j, \quad t_{a0}^{j+1} = t_{a0}^j + \tau H_0^j.
\end{aligned} \tag{7.78}$$

and the *second order approximation* is

$$
\begin{aligned}
&{}^{(2)}\sigma_0^{j+1} = S^*((j+1)\tau)\\
&{}^{(2)}v_0^{j+1} = (1-v)\left(v_0^j + \frac{S^*(j\tau)}{\sqrt{\rho E}} + \frac{\tau}{2\sqrt{\rho E}}\left(G_0^j + {}^{(1)}G_0^{j+1}\right)\right)\\
&\qquad + v\left(v_1^j + \frac{\sigma_1^j}{\sqrt{\rho E}} + \frac{\tau}{2\sqrt{\rho E}}\left(G_1^j + {}^{(1)}G_0^{j+1}\right)\right) - \frac{S^*((j+1)\tau)}{\sqrt{\rho E}},\\
&{}^{(2)}\varepsilon_0^{j+1} = \varepsilon_0^j + \frac{1}{E}\left({}^{(2)}\sigma_0 j+1 - \sigma_0^j\right) - \frac{\tau}{2E}\left(G_0^j + {}^{(1)}G_0^{j+1}\right), \quad {}^{(2)}t_{a\,0}^{j+1} = t_{a\,0}^j + \frac{\tau}{2}\left(H_0^j + {}^{(1)}H_0^{j+1}\right).
\end{aligned}
\tag{7.79}
$$

where ${}^{(1)}G_0^{j+1} = G\left(\varepsilon_0^{j+1}, \sigma_0^{j+1}, t_{a\,0}^{j+1}\right)$ and ${}^{(1)}H_0^{j+1} = H\left(\varepsilon_0^{j+1}, \sigma_0^{j+1}, t_{a\,0}^{j+1}\right)$ are computed using the first approximation given by relations (7.78).

References

Ait-Amokhtar H, Fressengeas C, Boudrahema S (2008) The dynamics of Portevin-Le Chatelier bands in an Al-Mg alloy from infrared thermography. Mat Sci Eng A-Struct 488:540–546

Ait-Amokhtar H, Fressengeas C (2010) Crossover from continuous to discontinuous propagation in the Portevin–Le Chatelier effect. Acta Mater 58:1342–1349

Bell JF (1973) Handbuch der Physik, Band VIa/I. Springer Verlag, Berlin, pp. 649–666

Benallal A, Børvik T, Clausen AH, Hopperstad OS (2003) Dynamic strain aging, negative strain-rate sensitivity and related instabilities. Tech Mech 23:160–166

Benallal A, Berstad T, Børvik T, Clausen AH, Hopperstad OS (2006) Dynamic strain aging and related instabilities: experimental, theoretical and numerical aspects. Eur J Mech A-Solid 25:397–424

Benallal A, Berstad T, Børvik T, Hopperstad OS, Koutiri I, de Nogueira Codes R (2008a) An experimental and numerical investigation of the behaviour of AA5083 aluminium alloy in presence of the Portevin–Le Chatelier effect. Int J Plast 24:1916–1945

Benallal A, Berstad T, de Nogueira Codes R, Børvik T, Hopperstad OS (2008b) Effects of strain rate on the characteristics of PLC deformation bands for AA5083-H116 aluminium alloy. Philos Mag 88:3311–3338

Böhlke T, Bondár G, Estrin Y, Lebyodkin MA (2009) Geometrically non-linear modeling of the Portevin-Le Chatelier effect. Comput Mat Sci 44:1076–1088

Chihab K, Estrin Y, Kubin LP, Vergnol J (1987) The kinetics of the Portevin-Le Chatelier bands in an Al-5at%Mg alloy. Scripta Metall Mater 21:203–208

Chmelík F, Klose FB, Dierke H, Šachl J, Neuhäuser H, Lukáč P (2007) Investigating the Portevin-Le Châtelier effect in strain rate and stress rate controlled tests by the acoustic emission and laser extensometry techniques. Mat Sci Eng A-Struct 462:53–60

Cottrell AH, Bilby B (1949) Dislocation theory of yielding and strain ageing of iron. Proc Phys Soc Lon Sect A 62:49–62

Cottrell AH (1953) Dislocations and plastic flow in crystals. Oxford University Press, Oxford

Cristescu N, Suliciu I (1982) Viscoplasticity. Martinus Nijhoff Publishers, Bucharest

Cuddy LJ, Leslie WC (1972) Some aspects of serrated yielding in substitutional solid solutions of iron. Acta Metall Mater 20:1157–1167

Estrin Y (1996) Dislocation-density-related constitutive modeling. In: Krausz AS, Krausz K (eds) Unified constitutive laws of plastic deformation. Academic Press, San Diego

Făciu C (1998) A new rate-type gradient-dependent viscoplastic approach for "stop-and-go" strain band propagation. Numerical vs. physical experiments. J Phys IV Fr 8:143–150

Fellner M, Hamerský M, Pink E (1991) A comparison of the Portevin-Le Chatelier effect in constant-strain-rate and constant-stress-rate tests. Mat Sci Eng A-Struct 136:157–161
Graff S, Forest S, Strudel J-L, Prioul C, Pilvin P, Béchade J-L (2004) Strain localization phenomena associated with static and dynamic strain ageing in notched specimens: experiments and finite element simulations. Mat Sci Eng A-Struct 387–389:181–185
Halim H, Wilkinson DS, Niewczas M (2007) The Portevin-Le Chatelier (PLC) effect and shear band formation in an AA5754 alloy. Acta Mater 55:4151–4160
Hähner P (1993) Modelling the spatio-temporal aspects of the Portevin-Le Chatelier effect. Mat Sci Eng A-Struct 164:23–34
Jiang HF, Zhang QC, Chen XD, Chen ZG, Jiang ZY, Wu XP, Fan JH (2007) Three types of Portevin-Le Chatelier effects: experiment and modelling. Acta Mater 55:2219–2228
Kubin L, Estrin Y (1985) Portevin - Le Chatelier effect in deformation with constant stress rate. Acta Metall Mater 33:397–407
Ling CP, McCormick PG (1993) The effect of temperature on strain rate sensitivity in an Al-Mg-Si alloy. Acta Metall Mater 41:3127–3131
Ling CP, McCormick PG, Estrin Y (1993) A load perturbation method of examining dynamic strain ageing. Acta Metall Mater 41:3323–3330
Louat N (1981) On the theory of the Portevin-Le Chatelier effect. Scripta Metall Mater 15:1167–1170
Masson AP (1841) Sur l'élasticité des corpes solides. Ann Chim Phys (third series) 3:461–462
Mazière M, Dierke H (2012) Investigations on the Portevin-Le Chatelier critical strain in an aluminum alloy. Comput Mat Sci 52:68–72
McCormick PG (1988) Theory of flow localisation due to dynamic strain ageing. Acta Metall Mater 36:3061–3067
McCormick PG, Ling CP (1995) Numerical modelling of the Portevin-Le Chatelier effect. Acta Metall Mater 43:1969–1977
Mesarovics SDJ (1995) Dynamic strain aging and plastic instabilities. J Mech Phys Solids 43:671–700
Mihăilescu-Suliciu M, Suliciu I (1985) On the method of characteristics in rate-type viscoelasticity. ZAMM-Z Angew Math Mech 65:479–486
Mulford RA, Kocks UF (1979) New observations on the mechanisms of dynamic strain aging and of jerky flow. Acta Metall Mater 27:1125–1134
Nabarro FRN (1967) Theory of crystal dislocations. Clarendon Press, Oxford
Neuhäuser H, Klose FB, Hagemann F, Weidenmüller J, Dierke H, Hähner P (2004) On the PLC effect in strain-rate and stress-rate controlled tests-studies by laser scanning extensometry. J Alloy Compd 378:13–18
Picu RC (2004) A mechanism for the negative strain-rate sensitivity of dilute solid solutions. Acta Mater 52:3447–3458
Penning P (1972) Mathematics of the Portevin-Le Chatelier effect. Acta Metall Mater 20:1169–1175
Portevin A, Le Chatelier F (1923) Sur un phénomène observé lors de l'essai de traction d'alliages en cours de transformation. CR Acad Sci 176:507–510
Richtmyer RD, Morton KW (1967) Difference methods for initial-value problems. Wiley, New York
Rizzi E, Hähner P (2004) On the Portevin - Le Chatelier effect: theoretical modeling and numerical results. Int J Plast 20:121–165
Savart F (1837) Recherches sur les vibrations longitudinales. Ann Chim Phys (second series) 65:337–340
Scott VF, Mertens F, Marder M (2000) Portevin - Le Chatelier effect. Phys Rev E 6:8195–8206
Schwarz RB (1985) The Portevin-LeChatelier effect: I. model for the type-B serrations. In: McQueen HJ et al (ed) Proceedings of ICSMA 7, vol. 1. Pergamon Press, Toronto, pp. 343–348
Soare MA, Curtin WA (2008a) Solute strengthening of both mobile and forest dislocations: The origin of dynamic strain aging in fcc metals. Acta Mater 56:4046–4061

Soare MA, Curtin WA (2008b) Single-mechanism rate theory for dynamic strain aging in fcc metals. Acta Mater 56:4091–4101

Strogatz SH (1994) Nonlinear dynamics and chaos. Perseus Books Publishing, Reading

Springer F, Schwink Ch (1991) Quantitative investigations on dynamic strain ageing in polycrystalline CuMn alloys. Scr Metall Mater 25:2739–2744

Springer F, Nortmann A, Schwink Ch (1998) A study of basic processes characterizing dynamic strain ageing. Phys Status Solidi A 170:63–81

van den Beukel A (1975) Theory of the effect of dynamic strain aging on mechanical properties. Phys Status Solidi A 30:197–206

Yilmaz A (2011) The Portevin-Le Chatelier effect: a review of experimental findings. Sci Technol Adv Mater 12(063001):1–16

Zdunek J, Brynk T, Mizera J, Pakieła Z, Kurzydłowski KJ (2008) Digital image correlation investigation of Portevin-Le Chatelier effect in an aluminium alloy. Mater Charact 59:1429–1433

Zhang S, McCormick PG, Estrin Y (2001) The morphology of Portevin-Le Chatelier bands: finite element simulation for Al-Mg-Si. Acta Mater 49:1087–1094

Zhang F, Bower AF, Curtin WA (2012) The influence of serrated flow on necking in tensile specimens. Acta Mater 60:43–50

Erratum to: Multiscale Modelling in Sheet Metal Forming

Dorel Banabic

Erratum to:
D. Banabic (ed.), *Multiscale Modelling in Sheet Metal Forming*, ESAFORM Bookseries on Material Forming, DOI 10.1007/978-3-319-44070-5

The original version of the book was inadvertently published with incorrect affiliation of Jerzy Gawad, Philip Eyckens, Albert van Bael and Paul van Houte in Chap. 1 and Chap. 3, Chap. 5 was published without inclusion of the contributor's name "Philip Eyckens", and in Chap. 7, Equation 7.75 content was published incorrectly. The erratum chapters and the book have been updated with the changes.

The updated original online version for this book can be found at 10.1007/978-3-319-44070-5

D. Banabic (✉)
CERTETA Research Center, Technical University of Cluj-Napoca, Cluj-Napoca, Romania
e-mail: banabic@tcm.utcluj.ro

D. Banabic (ed.), *Multiscale Modelling in Sheet Metal Forming*, ESAFORM Bookseries on Material Forming,
DOI 10.1007/978-3-319-44070-5_8

Author Index

D. Banabic (ed.), *Multiscale Modelling in Sheet Metal Forming*,
ESAFORM Bookseries on Material Forming,
DOI 10.1007/978-3-319-44070-5